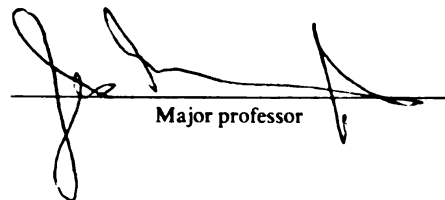This is to certify that the

dissertation entitled

**Electromagnetic Field Solutions
For The Natural Modes Of A Cylindrical Cavity
Loaded With Lossy Materials**

presented by

Edward Benjamin Manring

has been accepted towards fulfillment
of the requirements for

_____Ph.D._____ degree in _Electrical_
Engineering

Major professor

Date_9/29/92_

PLACE IN RETURN BOX to remove this checkout from your record.
TO AVOID FINES return on or before date due.

DATE DUE	DATE DUE	DATE DUE
MAY 1 2 1994 305556		
SEP 2 5 1995		
JUN 1 1 1996 071		
JUN		

ELECTROMAGNETIC FIELD SOLUTIONS
FOR THE NATURAL MODES OF A CYLINDRICAL CAVITY
LOADED WITH LOSSY MATERIALS

Volume I

By

Edward Benjamin Manring

A DISSERTATION

Submitted to
Michigan State University
in partial fulfillment of the requirements
for the degree of

DOCTOR OF PHILOSOPHY

Department of Electrical Engineering

1992

ABSTRACT

ELECTROMAGNETIC FIELD SOLUTIONS
FOR THE NATURAL MODES OF A CYLINDRICAL CAVITY
LOADED WITH LOSSY MATERIALS

By

Edward Benjamin Manring

A rigorous solution is presented for the natural mode fields of a circular cylindrical
cavity coaxially loaded with homogeneous, isotropic, lossy materials for loads of
arbitrary length and distance from the cavity end plates. Field expressions and
numerically stable characteristic equations are derived for the coaxially-loaded
waveguide, the coaxially-loaded cavity with cavity-length loads (cavity-short type),
and the coaxially-loaded cavity with loads of length less than cavity-length (cavity-
open type). Cavity-open type solutions are constructed using a mode-matching
technique which is shown to be more numerically stable than the mode-matching
method previously published for lossless loads. Theoretical and experimental resonant
frequency are shown to agree to within 0.2 % for a 1" diameter nylon load in a 6"
diameter cavity for the cavity-short type configuration and to within 0.06 % for all
lengths from zero to cavity-length of a 0.5" diameter nylon load in a 6" diameter
cavity for the cavity-open type configuration. A solution is included for the
azimuthally symmetric TM modes of the cavity-open type configuration for a
conducting load; this solution equally applies to the reentrant cavity. Numerical
solutions are presented for TE, TM, and hybrid modes of the coaxially-loaded
waveguide and the cavity-short type configuration, and the TM modes of the cavity-
open type configuration. Complex mode behavior is demonstrated in the waveguide
for lossless loads with high dielectric constant. For lossy loads, a backward wave
region is discovered in the low frequency range for TM modes. Mode charts
presented for the cavity-short type configuration show that mode behavior is highly

diverse and that modes cannot be consistently labeled by association with corresponding empty cavity modes which are approached as the load radius becomes small or the dielectric constant approaches unity. Very high loss factor loads are shown to behave like good conductors. It is shown that a small change in dielectric constant can cause a mode switch without affecting the resonant frequency or Q. Miscellaneous contributions include presentation of three previously untabulated indefinite Bessel function integrals, a complex zero-finding subroutine, and the discovery of natural mode field rotation in the presence of boundaries between lossy media.

To my wife,
Sandy,

whom I love with all my heart,
whose companionship has made my life
so much more joyful and fruitful,

and to my Savior,
Jesus Christ,

"through whom all things were made, and
without Him nothing was made that was
made."

"It is the God who commanded light to
shine out of darkness who has shone in our
hearts to give the light of the knowledge of
the glory of God in the face of Jesus
Christ."

ACKNOWLEDGMENTS

TABLE OF CONTENTS

LIST OF FIGURES

Chapter 1

INTRODUCTION

The purpose of the present work is to present analytical and numerical solutions for the electromagnetic fields of cylindrical waveguides and cavities coaxially-loaded with homogeneous, isotropic, lossy, cylindrically shaped materials.[†] The motivation for this study is the application of these solutions to microwave heating of lossy materials. Electromagnetic field solutions provide fundamental information on the interaction between microwaves and lossy materials in waveguides and resonant cavities. For materials processing purposes, knowledge of the electromagnetic fields reveals where energy is dissipated in the material, how efficiently energy is coupled into the material, and how material properties affect wave propagation or resonant conditions in the waveguide and cavity respectively. Since material properties change during processing, the electromagnetic fields are dynamically linked to the process cycle. Accurate field solutions make it possible to track material properties during the course of processing.

The coaxially-loaded waveguide is shown in Figure 1-1. The coaxially-loaded cavity investigated in this dissertation falls into three configurations called cavity-short type, cavity-image type, and cavity-open type. The most general of these, the cavity-open type, is shown in Figure 1-2. Special cases of the cavity-open type configuration exist when the length of the load is equal to the cavity length, cavity-short type, or when the load rests on one end of the cavity, cavity-image type. These are shown in Figures 1-3 and 1-4 respectively. The cavity-image type configuration also describes the cavity-open type configuration when the load material is located

---

[†]The term "cylindrical" often refers to waveguide and cavity systems of general cross section with no cross sectional variation in the axial variable. Here we use it in a more specialized sense to refer to cylindrical waveguides and cavities with circular cross section.

1
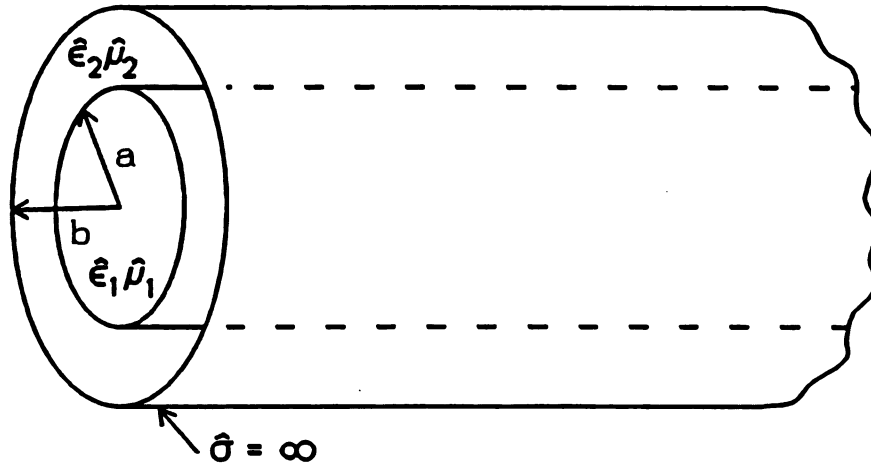
Figure 1-1 Coaxially-Loaded Waveguide.
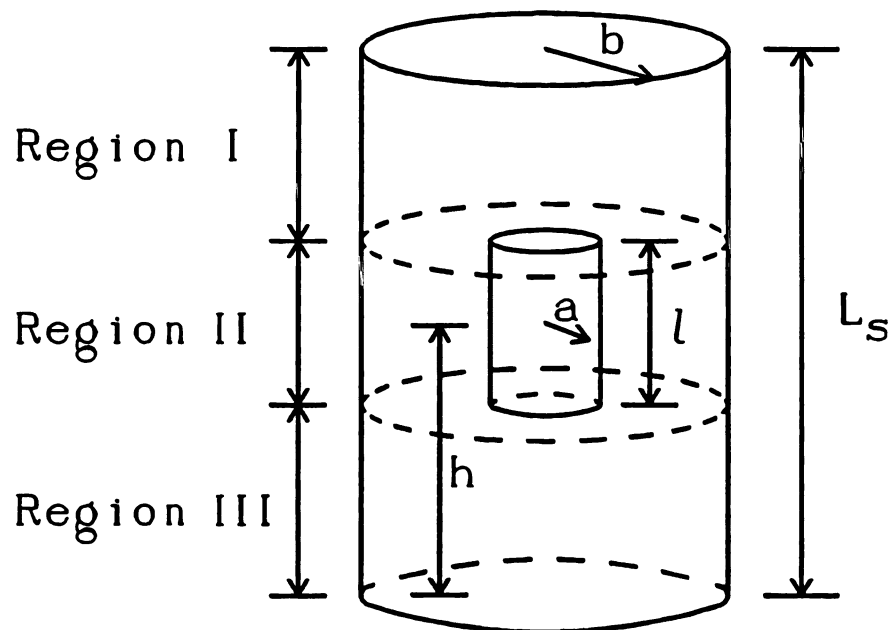
Figure 1-2 Cavity-Open Type Configuration.
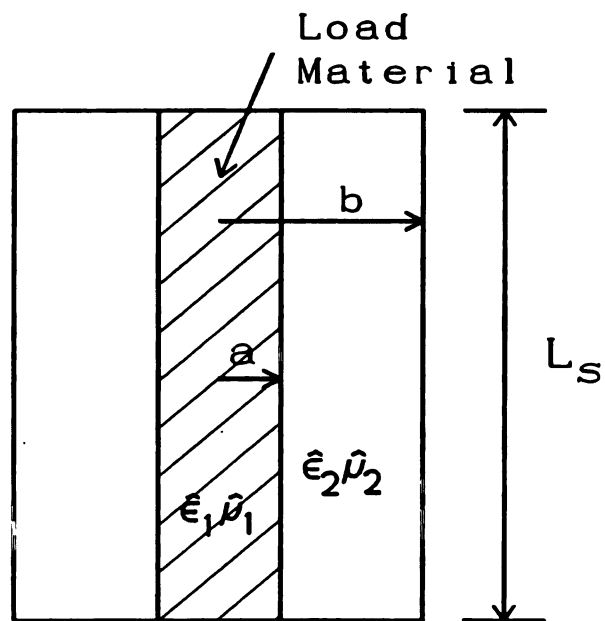
Figure 1-3 Cavity-Short Type Configuration.
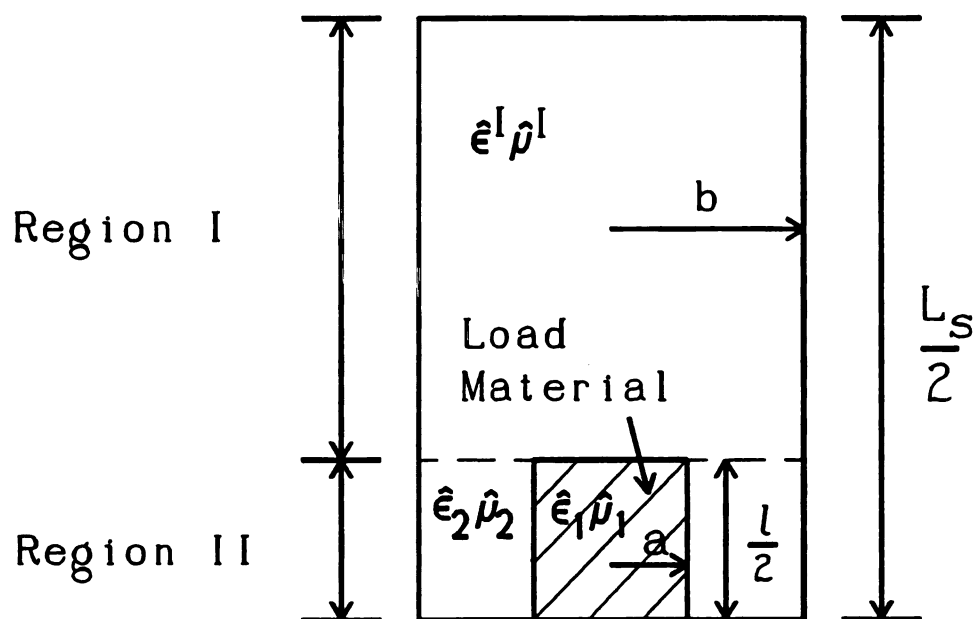
Figure 1-4 Cavity-Image Type Configuration.

exactly half way between the ends of the cavity. The features of these configurations are discussed in greater detail in Chapters 3 and 4.

Coaxially-loaded cylindrical waveguides and resonant cavities have found an immense range of applications in the 50 years since they were first studied. Particle acceleration, microwave circuit components, plasma generation and diagnosis, and materials processing are only the broad headings that classify most of the hundreds of different purposes they have served. Probably the chief reason that such attention has been given to the coaxial geometry is its circular symmetry which makes it simple to construct physically and renders its electromagnetic field parameters amenable to closed form analytic expression. Also, its symmetry is but one-dimensional and allows for junctions to be formed along planes perpendicular to the remaining free variable spacial component, in this case the axial variable.

That is not the case, for example, with the concentric spherical geometry, whose symmetry is two-dimensional. Aside from spheres being difficult to construct, any planar junction formed on a sphere distorts its symmetry. The axially invariant rectangular geometry presents a difficulty of a different kind: there are no closed form expressions for the wavenumbers of a rectangular waveguide with a smaller rectangular material located along the axis. Neither are there any cases in which purely TM or purely TE modes propagate in such a guide.[1] The corners of the rectangular load material make even perturbation analysis difficult for many modes and constitute potential hot spots in practical applications.

With all the attention that coaxially-loaded waveguides and cavities have received, there remain several unanswered questions about their behavior, especially for lossy loads. Although solutions have been presented, as will be discussed in Chapter 2, for lossy coaxially-loaded waveguides and cavity-short type cavities, and others have been presented for the cavity-open type cavity loaded with lossless

---

[1]If the material is altered so that it fills one dimension of the waveguide, closed form expressions for the wavenumbers are available and TE_{n0} modes exist with the electric field parallel to the material interface. Cf. R. E. Collin, *Field Theory of Guided Waves* (New York: McGraw-Hill, 1960), 224-25.

materials, no one has rigorously investigated the cavity-open or cavity-image type cavity loaded with lossy materials. As a second step, beyond perturbation methods, field solutions for these cavity configurations when the load is lossy are vital to our understanding of the exact interaction between lossy materials and the cavity fields. In materials processing and microwave cavity plasma applications, this information is important both in the design of cavity applicators and in understanding the behavior of existing cavity applicators for new load materials and modes.

Since solutions for the waveguide and cavity-short type configuration with lossy loads have been previously demonstrated, the principal contribution of this work is the presentation of analytical and numerical solutions to the cavity-open and cavity-image type configurations for lossy loads. This presentation proceeds as follows: Chapter 2 contains a review of past investigations of coaxially-loaded waveguides and cavities up to 1991. The papers reviewed are cataloged primarily by application and chronology. Chapters 3, and 4, with Appendices A, B, C, and F, present an analysis of the natural modes of lossy, coaxially-loaded cylindrical waveguides and cavities according to a rigorous solution of Maxwell's equations. For the cavity-open and cavity-image type configurations, mode-matching is used to find the eigenvalues.[t]

Chapter 5 is a reworking of a solution by D. M. Bolle published in 1962.[2] Bolle used mode-matching to solve for the resonant frequencies of a cylindrical cavity coaxially loaded with a conducting cylinder. The cylinder was located at the cavity center so that the configuration can be considered cavity-image type. The cavity-image type configuration with a conducting load and an electric wall is identical to the

---

[t]The equations in Chapters 3, 4, and 5 and Appendices C and F have been assiduously checked for errors. Most of them have not been simply copied from notebooks at publication time. Many of the programs written to solve them numerically have been founded directly on these equations as recorded in rough drafts of this work, so that the numerical solutions reflect the analysis as given by what is actually printed on these pages. That is not to claim that all equations presented here are inerrant, especially those which were not tested by numerical solution, but only to say that exceptional care was taken to prevent typographical errors.

[2]D. M. Bolle, "Eigenvalues for a Centrally Loaded Circular Cylindrical Cavity," *IRE Trans. Microwave Thry. Tech.* MTT-10 (3) (March 1962): 133-38.

reentrant cavity. Bolle's results are in error since the TEM mode contribution to the fields in the cavity region containing the conductor was neglected. Chapter 5 includes the development of the mode-matching equation and numerical results. The numerical results for the resonant frequency are compared with experiment showing excellent agreement. The solution is presented in order to demonstrate the principles and utility of mode-matching, and to examine the limiting case of high conductivity or loss factor for dielectric loads.[†]

Chapter 6 is a discussion of the relationship of the natural mode lossy cavity frequencies to the resonances of the sinusoidal steady-state and the material loaded cavity quality factor. It is shown that for quality factors greater than 50, the real part of the natural mode complex frequency closely approximates the sinusoidal steady-state resonant frequency. With the same restriction, the quality factor is one-half of the ratio of the real part of the complex frequency to the imaginary part of the complex frequency. For materials processing applications, the quality factor is often several thousand and rarely less than 50, so that this restriction is not prohibitive.

Numerical examples of the analysis of Chapters 3 and 4 are presented in Chapters 7, 8, and 9. Chapter 7 contains propagation diagrams, i.e., plots of system wavenumbers versus frequency, for the coaxially-loaded waveguide. Numerical results are compared with published values of the radial wavenumbers for given waveguide and load parameters. Complex mode propagation is demonstrated in the lossless case for high dielectric constant loads. Both propagation and attenuation patterns are examined for the lossy case. Numerical solutions for the cavity-short type configuration are found in Chapter 8. The axial wavenumber is constrained to be a real integer multiple of π normalized by the cavity length. Losses are no longer spacially distributed, as in the waveguide case, but are temporally distributed, represented by a complex natural frequency. Resonant frequencies are computed for several load materials and sizes and compared favorably to experiment. Field

---

[†]The effective equivalence of high conductivity and high loss factor is demonstrated in Chapter 3.

patterns are computed from a special time average magnitude defined in Appendix D. The natural frequencies of the modes are followed for a number of variables. The natural frequency versus load radius is plotted for several modes and materials over a load radius range of zero to the radius of the cavity. These plots demonstrate that the mode structure may change radically, changing from TE-like to TM-like and vice versa, as the load radius changes, especially for higher order modes and high loss factor materials.

Chapter 9 concludes the body of the dissertation with numerical examples of solutions for TM modes in the cavity-open and cavity-image type configurations. It is demonstrated that conventional formulations of the mode-matching equations produce a highly ill-conditioned characteristic matrix, and cannot be used to obtain reliable eigenvalues. Another formulation, worked out in Chapter 4, is shown to yield a well-conditioned characteristic matrix that provides accurate results for all load lengths. It is also shown how the resonant frequency and quality factor vary with the height of the load and its radius. All solutions are compared with experiments that show excellent agreement with computed resonant frequencies and qualitative agreement with computed quality factors. The quality factor discrepancy is due to the finite conductivity of the cavity walls and losses due to imperfections in the experimental cavity that were not accounted for by the theory. Quality factor agreement is better with larger loads when load losses dominate cavity wall losses and losses due to cavity imperfections.

Certain of the Appendices contain information that is of more general interest. For example, Appendix A contains a list of three previously unpublished indefinite integrals of products of Bessel functions. Also included are three previously unpublished Bessel function recurrence identities and two orthogonal definite integrals. Appendix B is an examination of the relationship between energy orthogonality and power orthogonality in inhomogeneously loaded waveguides of

arbitrary cross section. It is shown that energy orthogonality is actually a special case of power orthogonality when the modes are purely TM or purely TE.

It is shown in Appendix D that in the presence of boundaries between lossy materials, or between a lossy material and a lossless material, the natural fields of a loaded cavity rotate as they decay in time. The rotation is described by a time decaying ellipsoid whose parameters depend on the phases of the various field components. Since the time-average of a decaying field is zero, a relative time-average is defined for each field component. Due to the rotation, the relative value is not defined by simply neglecting the time-decay factor, but takes into account the differing phases of the various field components.

The numerical solutions presented in Chapters 7, 8, and 9 all involve finding the roots of complex functions of a complex variable. This can be a very difficult numerical problem and it proved so in this case. It was necessary to use two different approaches which are discussed in Appendix E. The FORTRAN source code is supplied for each. Similarly, it was necessary to evaluate Bessel functions with complex arguments. An address is given in the same Appendix where excellent subroutines may obtained for this purpose.

In the final Appendix, Appendix F, an analytical solution is derived for a slab-loaded cavity when the slab is located at an arbitrary height above the cavity bottom. This solution is the radial analog to the cavity-short type solution, but is much easier to solve because it involves only sine and cosine functions. It is used in Chapter 9 to check cavity-open type solutions as the load radius approaches the cavity radius. If cross sectional wavenumbers are known, the same solution may be used for slab-loaded cavities of arbitrary cross section.

Chapter 2
REVIEW OF PERTINENT LITERATURE

2.1 Introduction

The literature on coaxially-loaded cylindrical microwave cavities and waveguides is diverse, dealing with permittivity measurements, materials processing and heating, including direct ceramic sintering by microwaves, filters for microwave circuits, atomic clocks, particle accelerators, and plasma generation for applications in such a wide range of technology as heating of materials, ion generators, anisotropic etching of solid state circuit components, diamond thin film deposition, and deep space engines. The general field of this literature has been reviewed before.[1] Since the primary aim of the present study is to perform the theoretical analysis required to obtain the system eigenvalues, only literature pertinent to the chosen method of analysis is reviewed here.

As mentioned in Chapter 1, solutions are presented for the coaxially-loaded waveguide, the cavity-short type coaxially-loaded cavity, and the cavity-open type

---

[1]A review covering several of these areas is found in Haw-Hwa Lin, "Theoretical Formulation and Experimental Investigation of a Cylindrical Cavity Loaded with Lossy Dielectric Materials" (Ph.D. diss., Michigan State University, 1989). Literature on heating of materials, dielectric constant measurements, and techniques of measuring electric field strengths inside a cavity is reviewed in Edward B. Manring, "An Experimental Investigation of the Microwave Heating of Solid Non-Reactive Materials in a Circular Cylindrical Resonant Cavity" (M.S. thesis, Michigan State University, 1988). Literature on electric plasma propulsion and general use of the cavities developed at Michigan State University's Department of Electrical Engineering is reviewed by Lydell L. Frasch, "An Experimental and Theoretical Study of a Microwave Cavity Applicator Loaded with Lossy Materials" (Ph.D. diss., Michigan State University, 1987). Three new publications that deserve mention in the materials processing field are *Microwave Processing of Materials: Materials Research Society Symposia Proceedings 124, Symposium Held at Reno, Nevada 5-8 April 1988*, ed. W. H. Sutton, M. H. Brooks, and I. J. Chabinsky (Pittsburgh: Materials Research Society, 1988); *Microwave Processing of Materials II: Materials Research Society Symposia Proceedings 189, Symposium Held at San Francisco, California 17-20 April 1990*, ed. Wm. B. Snyder, et al. (Pittsburgh: Materials Research Society, 1991); *Microwaves: Theory and Application in Materials Processing: Ceramic Transactions 21, Symposium Held During the 93rd Meeting of the American Ceramic Society at Cincinnati, Ohio 29 April-3 May, 1991*, ed. D. E. Clark, F. D. Gac, W. H. Sutton (Westerville, Ohio: The American Ceramic Society, 1991).

coaxially-loaded cavity. The method used to solve for the latter configuration is called mode-matching. Since the coaxially-loaded waveguide and the cavity-short type loaded cavity are treated similarly, the literature will be divided into two categories: 1) waveguide and cavity-short type solutions, 2) mode-matching techniques and cavity-open type solutions. Coaxially-loaded waveguides and cavities have been studied for a wide variety of reasons over the past 50 years, therefore special attention is paid to the progressive applications motivating their development.

2.2 Waveguide and Cavity-Short Type Solutions

2.2.1 Dielectric Rod Waveguides

Waveguides involving dielectric rods come in various forms. Some consist of a simple rod-shaped material with a high enough dielectric constant that electromagnetic energy flowing through the rod is confined by total internal reflection. This is called a dielectric waveguide. Sometimes dielectric waveguides are enclosed in a second material called a cladding. A third form exists when the dielectric rod is encased in a metal. A dielectric rod surrounded by a cladding encased in metal is called a shielded dielectric waveguide or a coaxially-loaded waveguide. The foundational modern paper treating dielectric waveguides was written by E. Snitzer and published in 1961.[2] In it he refers to the first work done on dielectric waveguides at the turn of the century. Although others had already derived the characteristic equation and examined the first few modes, Snitzer demonstrated the behavior of the higher order modes, developed a reliable means of classifying them, and drew some very clear pictures of the electric and magnetic fields. His classification scheme has been widely accepted among those treating non-shielded dielectric waveguides. Mode classification schemes, including Snitzer's, are discussed in greater detail in Chapter 7.

The dielectric waveguide with cladding has been recently treated by Bruno and Bridges using a powder core to create a flexible millimeter-wave dielectric

---

[2]E. Snitzer, "Cylindrical Dielectric Waveguide Modes," *J. Opt. Soc. Am.* 51 (5) (May 1961): 491-98.

waveguide.[3] All flexible solids with low millimeter-wave losses have low dielectric constants. In order to confine the waves to the core region, the dielectric constant must be high. Bruno and Bridges's solution to this difficulty was to fill a hollow tube with the powder of a high dielectric constant, low loss material. In addition to presenting a clearly written paper, well-reasoned conclusions, and useful data, Bruno and Bridges make an original contribution in determining how to classify hybrid modes according to the relative axial field strengths of the electric and magnetic fields. They determine whether a hybrid mode is TE-like or TM-like by comparing the absolute value of the ratio of E_z to H_z (suppressing the ϕ-dependence) with the wave impedance of a plane wave traveling at the same phase velocity. This means of mode classification has physical intuitive appeal and provides an objective reference for determining the meaning of the ratio of E_z to H_z. The merits of Bruno and Bridges's mode classifications are discussed further in Chapter 7.

2.2.2 Coaxially-Loaded Waveguides for Particle Acceleration and Microwave Circuit Components

More directly related to the research presented in this dissertation are studies of the shielded dielectric or coaxially-loaded waveguide. The first study in America of the fields in a coaxially-loaded waveguide was reported in 1944 by L. Pincherle in which he demonstrates the method for obtaining the characteristic equations for ϕ-symmetric modes and how to solve them graphically.[4] Other investigations of ϕ-symmetric TM_{01} modes were reported in 1947 by S. Frankel and by G. G. Bruck

---

[3]William M. Bruno and William B. Bridges, "Flexible Dielectric Waveguides with Powder Cores," *IEEE Trans. Microwave Thry. Tech.* 36 (5) (May 1988): 882-90.

[4]L. Pincherle, "Electromagnetic Waves in Metal Tubes Filled Longitudinally with Two Dielectrics," *Phys. Rev.* 2:66 (5, 6) (September 1 and 15, 1944): 118-30. Beam and Wachowski refer to a similar publication in Germany the previous year by Von Herbert Bucholz, "Der Hohlleiter von kreisformigen Querschnitt mit Geschichtetem Dielektrischen Einsatz," *Annalen der Physik* (Leipzig) 43 (1943): 313-68, from which we may infer that the Nazis were the first to look into this question. Due to the war, however, it is certain that Pincherle's work was done independently.

and E. R. Wicher in the same issue of the *Journal of Applied Physics*.[5] Their
interests in the coaxially-loaded waveguide geometry stemmed from a desire to use
the TM_{01} waveguide mode for particle acceleration. For optimal particle acceleration
it is desirable that the phase velocity of the fields be near the velocity of the particles.
This had been accomplished in the past by carving spiral grooves or inserting fins in
the waveguide walls. The object of their investigations was to demonstrate that the
phase velocity might be reduced below the speed of light in a cylindrical waveguide
by lining the waveguide walls with a high permittivity dielectric.

In 1949 complete solutions for the coaxially-loaded waveguide, including the
non-ϕ-symmetric hybrid modes, were presented by Teasdale and Higgins.[6] More
results were published in 1951 by R. E. Beam and H. M. Wachowski in which the
labels HE and EH are applied for the first time to the coaxially-loaded waveguide
hybrid modes.[7] These labels were imported from the dielectric waveguide which
Beam also studied.[8] Others contributed throughout the 1950's to the expanding field
of knowledge of the propagation characteristics of the coaxially-loaded waveguide.
The motivation for this research had moved beyond particle acceleration to building
microwave circuit components like impedance transformers, matching devices, phase
shifters, and antenna feeds.

In 1959, P. J. B. Clarricoats published the first in a series of studies he
carried out over the next several years on coaxially-loaded waveguides. His
comprehensive survey of dielectric waveguides, both shielded and un-shielded,

[5]S. Frankel, "TM_{01} Mode in Circular Wave Guides with Two Coaxial Dielectrics," *J. App. Phys.* 18 (1947): 650-55; G. G. Bruck and E. R. Wicher, "Slow Transverse Waves in Cylindrical Guides," *J. App. Phys.* 18 (1947): 766-70.

[6]R. D. Teasdale and T. J. Higgins, "Electromagnetic Waves in Circular Waveguides Containing Two Coaxial Media," *Proc. Nat. Elec. Conf.* 5 (1949): 427-41.

[7]R. E. Beam and H. M. Wachowski, "Shielded Dielectric Rod Waveguides," *Trans. Amer. Inst. Elec. Eng.* 70 (1951): 874-80.

[8]R. E. Beam, M. M. Astrahan, W. C. Jakes, H. M. Wachowski, and W. L. Firestone, "Dielectric Tube Waveguides," Report ATI 94929, Ch. V, Northwestern University, Evanston, IL (1949), cited in Snitzer and in Bruno and Bridges.

covered 17 pages in the Proceedings of the Institution of Electrical Engineers in 1960.[9] In this Proceedings he demonstrates that propagation characteristics for the shielded and un-shielded dielectric waveguide are similar when the dielectric constant is sufficiently high and the radius of the dielectric is sufficiently less than the radius of the shield. He also discusses applications of the theory to ferrite materials. If Clarricoats is a fair representative, the British engineers do not seem to have taken up Beam's HE-EH hybrid mode naming scheme.

About the same time Clarricoats was investigating the coaxially-loaded waveguide, R. F. Harrington's *Time-Harmonic Electromagnetic Fields* was published in which he presents a generalized solution that can be adapted to the dielectric waveguide, the coaxially-loaded waveguide, the coated cylindrical conductor, or a corrugated cylindrical conductor.[10] Harrington's solution also applies to the coaxial waveguide, i.e., a cylindrical waveguide with a cylindrical conducting rod along the axis. The simplicity of Harrington's notation and procedure makes his analysis the easiest to follow. Being a text book, however, few numerical results from the equations are provided. The analysis of the coaxially-loaded waveguide found in Chapter 3 of this dissertation is an extension of Harrington's formulation.

2.2.3 Backward and Complex modes in Lossless Coaxially-Loaded Waveguides

Among the more interesting topics Clarricoats addressed in his series of studies was the existence of complex and backward modes in the lossless coaxially-loaded waveguide.[11] In particular, his paper with B. C. Taylor on "evanescent and propagating modes" discusses complex mode behavior in a coaxially-loaded

---

[9]P. J. B. Clarricoats, "Propagation Along Unbounded and Bounded Dielectric Rods—pts. 1 and 2," *Proc. Inst. Elec. Eng.*, 108 (3), pt. C (March 1961): 170-86.

[10]Roger F. Harrington, *Time-Harmonic Electromagnetic Fields* (New York: McGraw-Hill, 1961), 219-23.

[11]P. J. B. Clarricoats, "Circular-Waveguide Backward-Wave Structures," *Proc. Inst. Elec. Eng.* 110 (2) (Feb. 1963): 261-70; P. J. B. Clarricoats and K. R. Slinn, "Experimental Observation of Travelling Backward Waves in Dielectric-Loaded Circular Waveguide," *Proc. Inst. Elec. Eng.* 111 (6) (June 1964): 1090-92; P. J. B. Clarricoats and B. C. Taylor, "Evanescent and Propagating Modes of Dielectric-Loaded Circular Waveguide," *Proc. Inst. Elec. Eng.* 111 (12) (Dec. 1964): 1951-56.

waveguide for the first time. The authors demonstrate that the appearance of a backward propagating mode is associated with the appearance at a lower frequency of a complex mode, but complex modes do not necessarily give rise to higher frequency backward modes. The method used to prove the existence of the complex modes is instructive. Clarricoats and Taylor expand the characteristic equation at the edges of bands where purely real or purely imaginary propagation constants cease to exist. The expanded characteristic equation is used to show that an incremental change in ω cannot produce a purely real or purely imaginary γ solution, but a complex γ will solve the equation.

An abstract study of complex and backward modes was published by A. S. Omar and K. F. Schünemann in 1987 in which a rigorous proof was presented of the existence of complex and backward modes in inhomogeneously and anisotropically filled waveguides of general cross section.[12] Their paper also includes a discussion of power orthogonality between the modes, showing that the electric field of one complex mode couples to the magnetic field of another instead of to its own magnetic field. Thus, the complex modes must exist in coupled pairs. The effect of these modes on cavity resonances was later demonstrated by Chen and Zaki. They located a resonance in their cavity containing a lossless dielectric rod that could not be explained without considering complex modes.[13]

2.2.4 Microwave Plasma Diagnosis and Excitation

Even as particle acceleration was an early motivation for researching the coaxially-loaded waveguide, followed later by applications in microwave circuitry, in the 1960's microwave plasma applications became yet another reason to study the coaxially-loaded waveguide. Quasistatic solutions for coaxially-loaded waveguide modes were presented by Trivelpiece in 1958 and Trivelpiece and Gould in 1959 in

---

[12]Abbas S. Omar and Klaus F. Schünemann, "Complex and Backward Wave Modes in Inhomogeneously and Anisotropically Filled Waveguides," *IEEE Trans. Microwave Thry. Tech.* MTT-35 (3) (March 1987): 268-75.

[13]Chunming Chen and Kawthar A. Zaki, "Resonant Frequencies of Dielectric Resonators Containing Guided Complex Modes," *IEEE Trans. Microwave Thry. Tech.* 36 (10) (Oct. 1988): 1455-57.

which they present the discovery of space charge waves on stationary plasma columns.[14] The exact solution of the interaction of lossless plasmas with ϕ-symmetric coaxially-loaded cavity-short type modes was presented in 1960 by Buchsbaum, Mower, and Brown.[15] They found exact expressions for a lossless cold plasma column in TM_{0m0} and TE_{0mn} modes, and developed perturbation formulas for several other modes. An axial magnetic field was shown not to affect the calculations for the TM_{0m0} mode and could be accounted for by perturbation for TE_{0mn} modes. This work was followed up by Agdur and Enander the next year with an exact solution that included the non-ϕ-symmetric modes, although without considering the anisotropical behavior induced by an axial static B-field.[16] In addition to the ϕ-symmetric modes, Agdur and Enander identified the length-independent TM_{nm0} modes as non-hybrid. The dielectric properties of the plasma were determined using the cold plasma approximation, and losses were considered only as a perturbation to the lossless solution. They present several charts of resonant frequency versus plasma density and plasma frequency for a number of different modes. These are equivalent to mode charts for resonant frequency versus dielectric constant.

Two interesting features of the investigation of Agdur and Enander were the inclusion of radial variation in the plasma for some of the ϕ-symmetric modes and the discovery of TM-like modes that had no corresponding empty cavity relatives. These modes were labeled TM_{n0p}^{*} because the mode for the $n = 0$ case is related to the coaxial cavity TEM mode.[†] As the plasma density becomes small, the resonant

[14]A. W. Trivelpiece, "Slow Wave Propagation in Plasma Waveguides," (Ph.D. diss., California Institute of Technology, 1958); A. W. Trivelpiece and R. W. Gould, "Space Charge Waves in Cylindrical Plasma Columns," *J. App. Phy.* 30 (11) (Nov. 1959): 1784-93.

[15]S. J. Buchsbaum, L. Mower, and S. C. Brown, "Interaction Between Cold Plasmas and Guided Electromagnetic Waves," *Phys. Fluids* 3 (5) (Sept.-Oct. 1960): 806-819.

[16]B. Agdur and B. Enander, "Resonances of a Microwave Cavity Partially Filled with a Plasma" *J. App. Phy.* 33 (2) (Feb. 1962): 575-81.

[†]Trivelpiece and Gould had earlier shown the existence of these modes for the ϕ-symmetric case.

frequencies for the TM_{n0p}^{*} modes go to zero. Agdur and Enander, followed by others treating plasmas in coaxially-loaded cavities, use the asterisk (*) superscript to identify hybrid modes.

Losses were first rigorously included in the plasma model of Agdur and Enander three years later by Shohet and Moskowitz.[17] As pointed out earlier by Agdur and Enander, losses in the plasma occur due to collisions. In the models of both Agdur and Enander and Shohet and Moskowitz electron collisions are the chief source of losses. They enter the model by including a non-zero electron collision frequency in the equivalent dielectric constant expression. It is significant that Shohet and Moskowitz are the first, in treating either plasmas or dielectrics, to include losses rigorously in their numerical analysis of the coaxially-loaded cavity. Presumably, this is connected with the availability of numerical methods of evaluating Bessel functions with complex arguments. Shohet and Moskowitz show how the behavior of the resonant frequency versus plasma frequency can change radically near critical values of loss in the plasma.

The same sort of behavior is observed by Lin in the resonant frequency versus dielectric constant for a cavity-short type cavity loaded with a lossy dielectric rod.[18] Under lossless conditions, the resonant frequency of a dielectric-loaded cavity will drop with increasing dielectric constant or material size (for a plasma the opposite occurs since the effective dielectric constant is negative). When losses are present, as Shohet and Moskowitz show, an increase in the effective dielectric constant can cause a drop in resonant frequency for a plasma load, or as Lin shows, a rise in resonant frequency for a dielectric load.

Following the work of Agdur and Enander and Shohet and Moskowitz, several investigations of plasmas excited along the axis of cylindrical waveguides and cavities were carried out at Michigan State University. In 1971 Fredericks examined plasma columns using both the dielectric waveguide and coaxially-loaded waveguide models.

---

[17]J. L. Shohet and C. Moskowitz, "Eigenvalues of a Microwave-Cavity-Lossy-Plasma System," *J. App. Phy.* 36 (5) (May 1965): 1756-59.

[18]Lin, 192, 195.

The plasma was modeled as lossless, homogeneous, and isotropic with the equivalent dielectric constant being calculated for both the cold plasma and warm plasma approximations. The warm plasma supports Tonks-Dattner modes which disappear in the absence of the plasma. They are heavily damped for appreciable collision frequencies and exist only for low pressures. Hybrid modes were included in the analysis.[19] Asmussen, Mallavarpu, Hamann, and Park later used similar models, but with losses, as part of the design process in constructing microwave plasma applicators.[20] Since the plasma was contained in a quartz tube in the cavity, it was desirable to include the tube in the model to obtain more accurate results. Accordingly, a three region model of the cavity-short type configuration, including hybrid modes and losses in the plasma, was developed by Mallavarpu in 1976.[21] Mallavarpu noticed in his three region model the same kind of TM^*_{n0p} modes found by Agdur and Enander in their two region model. A fourth region was added later by Rogers because the plasma did not completely fill the tube in which it was contained. Rogers still included losses in his model, but due to the complicated nature of the four-region boundary value problem, and an experimental interest in the TM_{012} mode, only ϕ-symmetric solutions were sought.[22] Rogers's solution continues to be used for diagnosis of tube-contained plasma columns in cylindrical cavities.[23]

[19]Robert Michael Fredericks, "An Experimental and Theoretical Study of Resonantly Sustained Plasma in Microwave Cavities" (Ph.D. diss., Michigan State University, 1971).

[20]Jes Asmussen, Jr., Raghuveer Mallavarpu, John R. Hamann, and Hee Chung Park, "The Design of a Microwave Plasma Cavity," *Proc. IEEE* 62 (1) (Jan. 1974): 109-117.

[21]Raghuveer Mallavarpu, "An Investigation of the Electromagnetic Behavior of a Microwave Plasma Source Over a Wide Range of Pressures and Flow Rates" (Ph.D. diss., Michigan State University, 1976); R. Mallavarpu, J. Asmussen, and M. C. Hawley, "Behavior of a Microwave Cavity Discharge Over a Wide Range of Pressures and Flow Rates," *IEEE Trans. Plasma Sci.* PS-6 (4) (Dec. 1978): 341-54.

[22]James R. Rogers, "Properties of Steady State, High Pressure, Argon Microwave Discharges" (Ph.D. diss., Michigan State University, 1982).

[23]M. L. Passow, M. L. Brake, P. Lopez, W. B. McColl, and T. E. Repetti, "Microwave Resonant-Cavity-Produced Air Discharges," *IEEE Trans. Plasma Sci.* PS-19 (2) (April 1991): 219-28.

Models based on the coaxially-loaded cavity-short type cavity configuration continue to be used to characterize plasma discharges. Since most plasmas are not homogeneous, the inhomogeneity must be considered in order to gain an accurate understanding of the plasma/cavity interaction. This is particularly true for high-pressure plasma discharges. The problem is an especially difficult one, however, because the inhomogeneity of the plasma is coupled to the fields. To simplify the investigation of these phenomena, Offermanns examined a high-pressure mercury plasma column in the TM_{0m0} mode, which may be considered to have a one-dimensional field configuration.[24]

Offermans's plasma was considered to be longitudinally homogeneous with inhomogeneity only in the radial variable. The inhomogeneity was incorporated into the model by solving Maxwell's equations for the TM_{0m0} mode together with the plasma energy balance equation. These equations are linked because the Joulean heating term in the energy balance equation depends on the local electric field. The temperature from the energy balance equation, in turn, affects the local permittivity, ϵ, in the field equations. This is because the collision frequency and the plasma frequency/density, on which ϵ depends, are temperature dependent. The magnitude of the numerical problem may be comprehended by noting that it took between 8 and 24 hours of CPU time on an IBM 4341-11 to solve for each state.

2.2.5 Permittivity Measurement and Materials Processing

Apart from plasma applications, where it was necessary to include losses to understand more accurately the behavior of the plasma as it related to system eigenvalues, most analyses of the coaxially-loaded waveguide and cavity have been motivated by lossless or almost lossless applications. Two more applications of the technology, developed in the 1950's and 60's, demanded that losses be explicitly included in theoretical models: the first new application was materials processing, the

---

[24]Stephan Offermanns, "Electrodeless High-Pressure Microwave Discharges," *J. App. Phy.* 67 (1) (January 1990): 115-23; Stephan Offermanns, "Resonance Characteristics of a Cavity-Operated Electrodeless High-Pressure Microwave Discharge System," *IEEE Trans. Microwave Thry. Tech.* 38 (7) (July 1990): 904-11.

second was high frequency complex permittivity measurement. A combination of the two applications has been described by Asmussen, Lin, Manring, and Fritz for single-mode cavities using the same mode both to process the load material and to measure material properties during processing.[25] Both materials processing applications and permittivity measurement were treated in the beginning by perturbation theory.[26] This method, however, is inadequate for cavities containing large samples and materials with high dielectric constants or loss factors. This obstacle led Lin to investigate exact solutions for the coaxially-loaded waveguide and cavity with a lossy dielectric rod along the axis.[27]

Lin's contribution to the study of the coaxially-loaded waveguide lies chiefly in the large number of cases he solves for the lossy-load. When the load is lossy, and the frequency is the independent variable, there are six dependent variables in the solution for each mode: the waveguide radius, the load radius, and the real and imaginary parts of the complex dielectric constants of both the core region and the region between the core and the waveguide. ω-γ diagrams, where γ is the complex axial wavenumber, may be drawn for different values of each dependent variable for each of an infinite number of modes. That, incidentally, is one of the reasons that the subject of the coaxially-loaded waveguide has not been wrapped up in the 50 years that it has been studied.

In addition to reproducing some results for the cavity-short type cavity that others had reported earlier, and as mentioned above on page 16, Lin investigates the relatively unexplored relationship between α (α being defined by $\gamma = \beta - j\alpha$) and ω for the coaxially-loaded waveguide with a lossy core. He demonstrates that as the loss factor of the core rises, losses in the guide rise until a critical loss factor is reached, after which rising loss factor causes a decrease in propagation loss. This is

---

[25]J. Asmussen, H. H. Lin, B. Manring, and R. Fritz, "Single-Mode or Controlled Multimode Microwave Cavity Applicators for Precision Materials Processing," *Rev. Sci. Instrum.* 58 (8) (August 1987): 1477-86.

[26]A review of the literature on these applications is found in Lin and in Manring.

[27]Lin.

due, presumably, to the large core material loss factor being indistinguishable from a high electron conductivity. The equivalence of the two is discussed below in Chapter 3. As the loss factor rises, the skin depth of the material decreases, forcing the fields out of the material and inhibiting energy dissipation in the load. Among the more interesting features demonstrated by Lin's plots is that the light line crossing for the TM_{01} mode is independent of the ratio of the core diameter to the waveguide diameter.

2.2.6 Miscellaneous Recent Studies

Most studies of dielectric waveguides and coaxially-loaded cavities have been content to examine the propagation wavenumbers, and present no drawings of what the fields look like, Snitzer's early paper being an exception. K. A. Zaki and C. Chen remedy this deficiency by presenting diagrams of the transverse field patterns of several hybrid modes in a coaxially-loaded waveguide.[28] The fields are shown for an outer waveguide radius of 0.5" with a dielectric core radius of 0.394" at frequencies of 4 and 8 GHz. The relative dielectric constant of the core region was 37.6 with free-space between the core and the waveguide wall. Field component magnitude plots are also presented by Lin. These are similar to those found below in Chapter 8.

Many of the more recent studies of coaxially-loaded waveguides are concerned with metallic waveguides coated on the inside with one or more layers of dielectric material. Since the object of the coating is often to produce a high attenuation rate for selected modes, the dielectrics in these studies are usually lossy. Chou and Lee present an investigation of modal attenuation in waveguides coated with multiple layers of lossy dielectric and lossy magnetic materials.[29] They demonstrate the technique of dealing with multiple layers by manipulation of a series of 4×4 matrices

---

[28]Kawthar A. Zaki and Chunming Chen, "Intensity and Distribution of Hybrid-Mode Fields in Dielectric-Loaded Waveguides," *IEEE Trans. Microwave Thry. Tech.* MTT-33(12) (Dec. 1985): 1442-47.

[29]Ri-Chee Chou and Shung-Wu Lee, "Modal Attenuation in Multilayered Coated Waveguides," *IEEE Trans. Microwave Thry. Tech.* 36 (7) (July 1988): 1167-76.

rather than one large $4n \times 4n$ matrix, where n is the number of layers outside the core. This technique is not original with Chou and Lee, but their application presents a good example of its utility. They show that multiple layers can broaden the frequency range for modal attenuation compared to a single layer coating. They also show that a lossless layer on top of a lossy magnetic coating increases dominant mode attenuation by 20 dB per distance a where a is twice the waveguide wavelength.

The problem treated by Chou and Lee in their paper on multilayered coated waveguides is very similar to one examined earlier by Sphicopoulos, Bernier, and Gardiol in solving for the resonant frequency and cavity quality factor of a cylindrical cavity coaxially loaded with a multilayered material.[30] The concentric layers of dielectric materials extend the entire length of the cavity so that the axial wavenumber, γ, is real and equal to $\frac{q\pi}{L}$ where q is an integer and L is the cavity length. As Sphicopoulos, Bernier, and Gardiol point out, since q may be set to zero, making γ zero, non-ϕ-symmetric, length-independent TM_{mn0} modes exist. Normally non-ϕ-symmetric modes are neither TM nor TE, but are hybrid. When there are only two layers, the cavity of Sphicopoulos, Bernier, and Gardiol is the cavity-short type cavity of Figure 1-3 of Chapter 1.

Sphicopoulos, Bernier, and Gardiol use the 4×4 matrix manipulation technique, used later by Chou and Lee, instead of the $4n \times 4n$ matrix arising when boundary conditions are matched at the n boundaries between layers. They also include losses in the metal walls of the cavity. Since losses are allowed in the dielectrics, the wall losses could conceivably be taken care of by making the loss factor of the outermost layer very high, but the explicit inclusion of wall conductivity in the equations is elegantly incorporated and allows direct input of the wall conductivity in the characteristic equation. To allow losses in the cavity, the natural frequency must be complex. Sphicopoulos, Bernier, and Gardiol define the resonant

---

[30]T. Sphicopoulos, L. G. Bernier, and F. Gardiol, "Theoretical Basis for the Design of the Radially Stratified Dielectric-Loaded Cavities Used in Miniaturised Atomic Frequency Standards," *Proc. Inst. Elec. Eng.* 131 (2), pt. H (April 1984): 94-98.

frequency as the real part of the complex frequency and the cavity quality factor, Q, they define as

$$Q = \frac{\omega'}{2\omega''},$$ (2-1)

where ω' is the real part of the complex radian frequency, $\hat{\omega}$, and ω'' is the imaginary part, i.e., $\hat{\omega} = \omega' + j\omega''$. Their discussion does not attempt to justify the asserted significance of the real and imaginary parts of the frequency. In Chapter 6 of this dissertation those questions are addressed and resolved in agreement with Sphicopoulos, Bernier, and Gardiol. A last note on this paper is that it contains several plots of the magnitude of the field components versus radial coordinate. Although the cavity size and dielectric constant are different, the general shapes of the plots are similar to many of those presented in Chapter 8 of the present work.

The shorted dielectric rod resonator is similar in configuration to the cavity-short type coaxially-loaded cavity. The difference is that the shorted dielectric rod resonator has no radial conducting wall boundary. In spite of this difference, some modes behave similarly in either configuration, particularly those with fields confined to the dielectric rod. The absence of a radial wall for the dielectric rod resonator does introduce the possibility that energy may propagate away from the dielectric rod region. Modes exhibiting this sort of behavior are called "leaky modes" while those whose energy is confined to the dielectric are called "trapped modes." A study of the shorted dielectric rod resonator has been presented by Kobayashi and Tanaka in which they consider both trapped and leaky modes.[31]

Although no dielectric or conducting losses are present in the system, a complex frequency must be invoked to account for the energy loss due to propagation away from the resonator for the leaky modes. In addition to standard types of mode charts, of which they present several detailed ones, they demonstrate the effect of rod radius and dielectric constant on Q for the leaky modes. One plot shows how Q

---

[31]Yoshio Kobayashi and Shuzo Tanaka, "Resonant Mods of a Dielectric Rod Resonator Short-Circuited at Both Ends by Parallel Conducting Plates," *IEEE Trans. Microwave Thry. Tech.* MTT-28 (10) (Oct. 1980): 1077-85.

increases with dielectric constant for all length-independent TM modes, especially the higher order modes. Q also increases with rod diameter for most length-dependent modes, although it is shown that the Q of the HE_{121} mode (after Snitzer's notation) for $\epsilon_r = 10$ drops with increasing rod diameter until the diameter reaches 20% of the rod length. Q for length-independent modes is not affected by changes in rod diameter. Kobayashi and Tanaka did not compare their results with a cavity-short type loaded cavity, but it would be useful to investigate the relationship between the leaky and trapped modes of the shorted dielectric resonator and the modes of the cavity-short type loaded cavity.

2.3 Mode-Matching and Cavity-Open Type Solutions

Mode-matching derives its name from the method it describes of satisfying electromagnetic boundary conditions at junction surfaces between two regions. The fields in each region are expressed as infinite sums of modes, where each mode satisfies the boundary conditions in its own region. By equating appropriate field components from each region at the junction, the boundary conditions at the junction are met. Although this method has been used extensively in the past 50 years for waveguide junctions, it was originally conceived as the means of solving for the eigenfrequencies of a cavity. First suggested in 1936 by L. V. King for electrostatic applications, it was developed for microwave cavities in 1940 by W. C. Hahn of the General Electric Company.[32] Not having the computational ability we enjoy today in the age of the microcomputer, Hahn nevertheless showed the feasibility of using mode-matching to solve for the boundary conditions between two cylindrical cavity regions of differing diameters. Similar problems had been examined previous to Hahn's research, but all had relied on various approximations.[33]

---

[32]W. C. Hahn, "A New Method for the Calculation of Cavity Resonators," *J. App. Phy.* 12 (January 1941): 62-68. Hahn cites the work of L. V. King, *Phil. Mag.* 21 (1936): 128 ff.

[33]For example, W. W. Hansen's work on reentrant cavities, "On the Resonant Frequency of Closed Concentric Lines," *J. App. Phy.* 10 (Jan. 1939): 38-45.

Hahn's method was immediately taken up as a means of determining shunt impedances arising from discontinuities in waveguides, but it wasn't until 1961 that it was once again applied to resonant cavities. In that year D. M. Bolle used mode-matching to find the eigenvalues for the ϕ-symmetric TM modes of a cavity containing a conducting cylinder along its axis.[34] The center of the conducting cylinder was coincident with the center of the cavity so that in addition to being azimuthally symmetric, the configuration was axially symmetric across the transverse plane at the cavity center, i.e., cavity-image type. Bolle uses the axial symmetry plane as an electric wall where the transverse E-field is zero. His solutions may therefore be applied to the even (electric wall) modes of the centrally loaded cavity, or to the reentrant cavity.

He divides the imaged cavity into two regions separated by the plane containing one end surface of the conducting cylinder. The tangential and normal electric fields are expressed as series of modes in each region. In the region containing the cylinder, the modes are those of the coaxial waveguide with an axial dependence such that the tangential E-field is zero at the image plane. In the other region, the series is composed of empty waveguide modes with an axial dependence such that the tangential E-field is zero at the end of the cavity. Two infinite sums of modes are equated at the boundary for each boundary condition.

To simplify the resulting two equations, each containing an infinite sum on either side of the equals sign, the orthogonality of the modes is used to reduce one side of each equation to a single term and allow the equations to be put into matrix form. A key point in Bolle's approach is that he uses a mode from the empty waveguide region to orthogonalize one equation, and a mode from the coaxial waveguide to orthogonalize the other. In the work of Kobayashi, Fukuoka and

---

[34]Bolle.

Yoshida,[35] Zaki and Chen,[36] and Vigneron and Guillon,[37] which will be discussed below, they use only the empty waveguide mode to orthogonalize both equations. As will be shown in Chapter 9 of this dissertation, Bolle's method is preferable since the other yields an ill-conditioned characteristic matrix. The zeros of the determinant of the characteristic matrix are the resonant frequencies of the loaded cavity.

Bolle includes a full discussion of numerical errors and compares his results both to a perturbation solution and experiment. Unfortunately, his solution appears to work only for the TM_{010} mode. The perturbation technique proved to be better than Bolle's mode-matching method for the TM_{012} mode. This sad result is not due to imperfection in the mode-matching method, nor to numerical errors inherent in it. An oversight caused Bolle to neglect the TEM mode in his series for the coaxial waveguide region. The TEM mode is actually a ϕ-symmetric TM mode with a radial wavenumber equal to zero. It turns out that the TEM mode makes the dominant contribution to the field in the coaxial region for TM_{012}. Chapter 5 of this dissertation is devoted to reworking Bolle's solution by including the TEM mode. It is shown that by including the TEM mode, excellent agreement between theory and experiment is achieved for TM modes in the entire range of rod lengths from zero to cavity length.

An analysis of a cavity similar to Bolle's was carried out in 1969 by Bhartia and Hamid to model an Alvarez type linear accelerator.[38] Their configuration differs from Bolle's by the addition of a hole through the center along the axis of the

---

[35]Yoshio Kobayashi, Nobushige Fukuoka, and Sink-ichiro Yoshida, "Resonant Modes for a Shielded Dielectric Rod Resonator," *Elect. Comm. Jap.* 64-B (11) (trans. Scripta Publishing Co., 1983): 44-51, translated from *Denshi Tsushin Gakkai Ronbunshi* 64-B (5) (1981): 433-40.

[36]Kawthar A. Zaki and Chunming Chen, "New Results in Dielectric-Loaded Resonators," *IEEE Trans. Microwave Thry. Tech.* MTT-34 (7) (July 1986): 815-24.

[37]S. Vigneron and P. Guillon, "Mode-Matching Method for Determination of the Resonant Frequencies of a Dielectric Resonator Placed in a Metallic Box," *Proc. Inst. Elec. Eng.* 134, pt. H (2) (April 1987): 151-55.

[38]P. Bhartia and M. A. K. Hamid, "Field distribution in a Centrally Loaded Circular Cylindrical Cavity," *IEEE Trans. Nuc. Sci.* NS-16 (2) (April 1969): 27-34.

load. Their development of the characteristic equation is identical to Bolle's. This includes, apparently, neglecting the TEM mode since it is not included specifically in the equations provided. Since they present experimental data only for the TM_{010} mode, it is not discernable from their final results whether they did so or not.

The first application of mode-matching to resonant structures containing dielectrics was presented by Kobayashi, Fukuoka and Yoshida in 1981.[39] Their interest in cavities apparently arose from the necessity of shielding their dielectric resonators. They investigate mode similarities between parallel-plate-open dielectric rod resonator structures and cavity-open type configuration loaded cavities. The parallel-plate-open dielectric rod resonator is similar to the dielectric rod short-circuited at either end by parallel conducting plates, except the ends of the rod are detached from the plates such that a gap exists between the rod and the shorting plates. The terminology "cavity-open," "cavity-short," and "cavity-image" is derived from similar usage for dielectric rod resonators between parallel plates structures. Kobayashi, Fukuoka, and Yoshida introduce these terms for both the dielectric resonator between parallel plates and the loaded cavity.

Kobayashi, Fukuoka, and Yoshida are the first to apply the mode-matching method to the cavity coaxially-loaded with a lossless dielectric, anticipating by 5 years the work of Zaki and Chen. In their work they demonstrate numerically that the resonant frequency for TE_{01q} cavity-open type modes when the load is small and of high dielectric constant does not differ significantly from the case where the outer walls of the cavity are removed and the material behaves as a simple dielectric resonator. They present mode charts with drawings of the cavity field patterns for several modes. An apparently independent development of a solution for the parallel-plate-open dielectric resonator was published in 1983 by Maystre, Vincent, and Mage.[40] It is similar to the work of Kobayashi, Fukuoka, and Yoshida.

---

[39]Kobayashi, Fukuoka, and Yoshida.

[40]D. Maystre, P. Vincent, and J. C. Mage, "Theoretical and Experimental Study of the Resonant Frequency of a Cylindrical Dielectric Resonator," *IEEE Trans. Microwave Thry. Tech.* MTT-31 (10) (Oct. 1983): 844-48.

In 1983, Zaki and Atia presented a mode-matching solution for a lossless load, similar to that of Kobayashi, Fukuoka, and Yoshida, publishing with it some values of the radial wavenumbers in the coaxially-loaded waveguide region.[41] Although they derive a theoretical mode-matching matrix, their numerical solutions are an approximation based on truncating the matrix after the first element. This approximation was improved by Zaki and Chen in 1986 to include a sufficient number of matrix elements for eigenvalue convergence.[42] This model did not include complex coaxially-loaded waveguide modes which were added later.[43] The load configurations of Zaki and Chen and Kobayashi, et al., were actually of the cavity-image type, since their load was situated axially symmetrically in the cavity. A general cavity-open type solution for a load of varying height was published in 1987 by Vigneron and Guillon.[44]

The mode-matching solutions published thus far on the coaxially-loaded cavity have been aimed at discovering optimal cavity/load configurations for various microwave circuit components, primarily filters. Theoretical solutions provide essential information on mode spacing and sources of energy loss.[45] Since energy loss to the load and cavity is an undesirable effect in microwave circuitry, only lossless load materials have been considered. For materials processing, lossiness in the load is essential to being able to transfer energy from the fields to the material. Losses are also a feature of plasma loads. It is therefore desirable for materials processing or microwave plasma applications to understand the material/field interactions for the lossy case. It is the object of this dissertation to provide solutions for the fields of the coaxially-loaded cavity-open type configuration when the load material is lossy.

---

[41]Kawthar A. Zaki and Ali E. Atia, "Modes in Dielectric-Loaded Waveguides and Resonators," *IEEE Trans. Microwave Thry. Tech.* MTT-31 (12) (Dec. 1983): 1039-45.

[42]Zaki and Chen, "New Results."

[43]Chen and Zaki.

[44]S. Vigneron and P. Guillon, "Mode Matching Method for Determination of the Resonant Frequency of a Dielectric Resonator Placed in a Metallic Box," *IEE Proceedings* 134, pt. H (2) (April 1987): 151-55.

[45]Kawthar A. Zaki and Chunming Chen, "Loss Mechanisms in Dielectric-Loaded Resonators," *IEEE Trans. Microwave Thry. Tech.* MTT-33 (12) (December 1985): 1448-52.

Chapter 3
THEORY OF CYLINDRICAL WAVEGUIDES

3.1 Introduction

The theoretical formulation of field solutions to empty cylindrical waveguide and cavity systems is standard in advanced undergraduate and beginning graduate electromagnetics text books.[1] The treatment found here for empty waveguides is a digest of the conventional formulations and is provided for convenience and continuity. Standard text books also treat the coaxially loaded cylindrical waveguide,[2] although in less detail than is found here. In this Chapter the field solutions for the lossy coaxially loaded waveguide are delineated for all modes.

3.2 The Source-Free Time-Harmonic Maxwell Equations
3.2.1 Maxwell's Equations

The differential form of the Maxwell Equations, governing all well-behaved electromagnetic quantities, is given in general by

$$\nabla \times \mathbf{E} = -\frac{\partial \mathbf{B}}{\partial t}$$

$$\mathbf{D} = \epsilon \cdot \mathbf{E}$$

$$\nabla \cdot \mathbf{D} = \rho$$

$$\mathbf{J} = \sigma \cdot \mathbf{E} \tag{3-1}$$

$$\nabla \times \mathbf{H} = \frac{\partial \mathbf{D}}{\partial t} + \mathbf{J}$$

$$\mathbf{B} = \mu \cdot \mathbf{H}$$

$$\nabla \cdot \mathbf{B} = 0$$

where

---

[1] John R. Reitz, Frederick J. Milford, and Robert W. Christy, *Foundations of Electromagnetic Theory*, 3d ed. (Reading, Mass.: Addison-Wesley, 1979): 412-17; Harrington, 129-30, 198-216; Collin, 170-89, 195-98; J. D. Jackson, *Classical Electrodynamics* (New York: John Wiley & Sons, 1975): 339-56.

[2] Harrington, 219-223.

E is the electric field strength (Volts per meter)

D is the electric flux density (Coulombs per square meter)

H is the magnetic field strength (Amperes per meter)

B is the magnetic flux density (Volt-seconds per square meter)

J is the electric current density (Amperes per square meter)

ρ is the electric charge density (Coulombs per cubic meter)

ϵ is the electric permittivity of the medium (Coulombs per Volt-meter)

σ is the electric conductivity of the medium (Coulomb-meters per Volt-second)

μ is the magnetic permeability of the medium (Volt-seconds per Ampere-meter).

Taking the divergence of the third and using the second of Maxwell's equations above, the equation of continuity, expressing the law of the conservation of electrical charge, is given by

$$\nabla \cdot \mathbf{J} + \frac{\partial \rho}{\partial t} = 0. \tag{3-2}$$

Within this compact set of Equations (3-1) and (3-2) can be found the description of all macroscopic electromagnetic phenomena.

In the time harmonic domain, where time dependence can be described by a periodic sinusoid, Maxwell's equations become much simpler. In such a case, the time-dependence, including the time phase information, can be included in Maxwell's equations as a factor of the form $e^{j\omega t}$. If only source-free regions are considered, i.e., $\mathbf{J}=0$ and $\rho=0$, a further simplification can be achieved and the equations can be written as

$$\nabla \times \mathbf{E} = -j\omega \mathbf{B} \tag{3-3}$$

$$\nabla \cdot \mathbf{D} = 0 \tag{3-4}$$

$$\nabla \times \mathbf{H} = j\omega \mathbf{D} \tag{3-5}$$

$$\nabla \cdot \mathbf{B} = 0 \qquad \qquad (3\text{-}6)$$

where

$$\mathbf{D} = \hat{\epsilon} \cdot \mathbf{E} \qquad \qquad (3\text{-}7)$$

$$\mathbf{B} = \hat{\mu} \cdot \mathbf{H} \qquad \qquad (3\text{-}8)$$

The physical, time-dependent values of the electromagnetic fields are determined by multiplying the fields given in Equations (3-3) through (3-8) by $e^{j\omega t}$ and taking the real part.

It should be noted that the electric permittivity and magnetic permeability are complex quantities in the time-harmonic domain. This is indicated by the hat symbol ($\hat{\ }$) over ϵ and μ. In terms of their real and imaginary parts, they are expressed as

$$\hat{\epsilon} = \epsilon' - j\epsilon''$$
$$\hat{\mu} = \mu' - j\mu'' \ . \qquad \qquad (3\text{-}9)$$

where ϵ' is called the *dielectric constant*, ϵ'' the *dielectric loss factor*, μ' the *a-c inductivity*, and μ'' the *magnetic loss factor*. All materials, including free-space, have non-zero ϵ' and μ'. Materials with non-zero ϵ'' or μ'' are called "lossy" because they are capable of absorbing electromagnetic energy. Energy is absorbed directly from the electric field through ϵ'' and directly from the magnetic field through μ''.

Materials with finite, non-zero conductivities are also capable of absorbing electromagnetic energy directly from the electric field so that an effective dielectric loss factor can be defined which includes both dielectric relaxation and conductivity losses, i.e.,

$$\epsilon_e'' = \epsilon'' + \frac{\sigma}{\omega} \ . \qquad \qquad (3\text{-}10)$$

When ω is complex, a non-zero conductivity also contributes to the real part of the complex permittivity, making it useful to define an effective dielectric constant as well. However, unless it is necessary to separate the effects of dielectric relaxation

and capacitivity from free-electron conductivity, there is no need to complicate the notation. The notation of Equation (3-9) is sufficient to define the material properties for electromagnetic purposes, with the understanding that effects of free-electron conductivity are included in ϵ' and ϵ''. An important consequence of this understanding, from Equation (3-10), is that high values of ϵ'' are electromagnetically equivalent to to high values of σ. This principle will be used to explain field behavior in the presence of high ϵ'' materials in the Chapters that follow.

3.2.2 Magnetic and Electric Vector Potentials

The fields of the source-free Maxwell Equations can be represented by an alternate set of functions called potential functions.[3] Since $\nabla \cdot H = 0$, H can be represented as the curl of some other vector A. A is called the magnetic vector potential,

$$H = \nabla \times A .$$ (3-11)

Similarly, an electric vector potential can be defined such that

$$E = -\nabla \times F .$$ (3-12)

We remain free to choose values for $\nabla \cdot A$ and $\nabla \cdot F$. With appropriate choices, A and F may be found to satisfy the vector Helmholtz equations,

$$\nabla^2 F + k^2 F = 0$$
$$\nabla^2 A + k^2 A = 0,$$ (3-13)

where $k^2 = \omega^2 \hat{\epsilon} \hat{\mu}$.

The fields E and H can be represented exclusively in terms of A as in Equation (3-14),

---

[3]Harrington, 77, 129-130.

$$E = \frac{1}{j\omega\hat{\epsilon}} \nabla \times (\nabla \times A)$$

$$H = \nabla \times A,$$

(3-14)

or exclusively in terms of F as in Equation (3-15),

$$E = -\nabla \times F$$

$$H = \frac{1}{j\omega\hat{\mu}} \nabla \times (\nabla \times F).$$

(3-15)

Often it is convenient to express them as a superposition of solutions in terms of both A and F as in Equation (3-16),

$$E = -\nabla \times F + \frac{1}{j\omega\hat{\epsilon}} \nabla \times (\nabla \times A)$$

$$H = \nabla \times A + \frac{1}{j\omega\hat{\mu}} \nabla \times (\nabla \times F).$$

(3-16)

3.3 Electromagnetic Fields in Regions of Cylindrical Symmetry

3.3.1 Separation of Variables

Up to this point the formulation of the solution has been general to any coordinate system. Now we wish to restrict the discussion to problem geometries which can best be described using cylindrical coordinates. Taking solutions of the form given in Equation (3-14), solutions may be sought for E and H with $A = z\ \psi^m$, where z is the coordinate invariant z-directed unit vector and ψ^m is a scalar function of all coordinates. This choice for A allows us to solve a scalar Helmholtz equation, Equation (3-17), instead of the vector form, Equation (3-13). Whether or not this is a valid choice for A is determined by whether or not the fields given by Equation (3-14) meet the electromagnetic boundary conditions for the given configuration.

$$\nabla^2 \psi^m + k^2 \psi^m = 0$$

(3-17)

In cylindrical coordinates, Equation (3-17) becomes

$$\frac{1}{\rho}\frac{\partial}{\partial\rho}\left(\rho\frac{\partial\psi^m}{\partial\rho}\right) + \frac{1}{\rho^2}\frac{\partial^2\psi^m}{\partial\phi^2} + \frac{\partial^2\psi^m}{\partial z^2} + k^2\psi^m = 0. \qquad (3\text{-}18)$$

This equation can be solved by separation of variables, such that

$$\psi^m(\rho,\phi,z) = R(\rho)\ \Phi(\phi)\ Z(z). \qquad (3\text{-}19)$$

Ignoring the trivial solution $\psi^m = 0$, we divide both sides of Equation (3-18) by ψ^m to get

$$\frac{1}{\rho R(\rho)}\frac{\partial}{\partial\rho}\left(\rho\frac{\partial R(\rho)}{\partial\rho}\right) + \frac{1}{\rho^2\Phi(\phi)}\frac{\partial^2\Phi(\phi)}{\partial\phi^2} + \frac{1}{Z(z)}\frac{\partial^2 Z(z)}{\partial z^2} + k^2 = 0. \qquad (3\text{-}20)$$

The third term of Equation (3-20) is independent of ρ and ϕ. Since none of the other terms are z-dependent, yet all terms sum to zero for all z, it must not be dependent on z either. We set it equal to a constant,

$$\frac{1}{Z(z)}\frac{\partial^2 Z(z)}{\partial z^2} = -k_z^2. \qquad (3\text{-}21)$$

Multiplying both sides of Equation (3-20) by ρ^2 and substituting in the constant given in Equation (3-21) for the third term, we have

$$\frac{\rho}{R(\rho)}\frac{\partial}{\partial\rho}\left(\rho\frac{\partial R(\rho)}{\partial\rho}\right) + \frac{1}{\Phi(\phi)}\frac{\partial^2\Phi(\phi)}{\partial\phi^2} + (k^2 - k_z^2)\rho^2 = 0. \qquad (3\text{-}22)$$

An argument similar to the one leading to Equation (3-21) can be made for the second term of Equation (3-22) to get

$$\frac{1}{\Phi(\phi)}\frac{\partial^2\Phi(\phi)}{\partial\phi^2} = -n^2. \qquad (3\text{-}23)$$

This leaves an equation for ρ in terms of the separations constants k_z, n, and k. If we introduce a constant k_ρ, such that

$$k^2 = \omega^2 \hat{\mu}\hat{\epsilon} = k_\rho^2 + k_z^2, \tag{3-24}$$

then the equation for ρ can be written as follows,

$$\rho \frac{\partial}{\partial \rho}\left(\rho \frac{\partial R(\rho)}{\partial \rho}\right) + (\rho^2 k_\rho^2 - n^2) R(\rho) = 0. \tag{3-25}$$

Equation (3-25) is called Bessel's Equation with well-known tabulated solutions called Bessel's functions. With regard to these equations it should also be noted that if the configuration boundaries are symmetric in ϕ then n must be an integer; also if n is zero and the boundaries are symmetric in ϕ, $\Phi(\phi)$ must be a constant. The function space of the components of Equation (3-19), solving the differential equations in Equations (3-21) through (3-25), is given by

$$R(\rho) = B_n(k_\rho\rho) = \begin{Bmatrix} J_n(k_\rho\rho) \\ N_n(k_\rho\rho) \\ H_n^{(1)}(k_\rho\rho) \\ H_n^{(2)}(k_\rho\rho) \end{Bmatrix}, \quad \Phi(\phi) = \begin{Bmatrix} \text{a constant} \\ \text{or } \phi \quad (n=0) \\ \cos(n\phi) \\ \sin(n\phi) \\ e^{jn\phi} \\ e^{-jn\phi} \end{Bmatrix}, \tag{3-26}$$

$$Z(z) = \begin{Bmatrix} \cos(k_z z) \\ \sin(k_z z) \\ e^{jk_z z} \\ e^{-jk_z z} \end{Bmatrix}.$$

3.3.2 Electromagnetic Fields in Terms of the z-Directed Vector Potential

The electric field of Equation (3-14) can be reexpressed by using the Helmholtz equation for $\mathbf{A}$, given in Equation (3-13), as

$$E = \frac{1}{j\omega\hat{\epsilon}} \nabla \times (\nabla \times A) = -j\omega\hat{\mu}A + \frac{1}{j\omega\hat{\epsilon}} \nabla(\nabla \cdot A). \qquad (3\text{-}27)$$

With $A = z \, \psi^m$, where z is the unit normal in the z-direction and ψ^m in dimensions of Amperes, the electric and magnetic fields are given by

$$E = -j\omega\hat{\mu} \, z\psi^m + \frac{1}{j\omega\hat{\epsilon}} \nabla\left(\frac{\partial\psi^m}{\partial z}\right) \qquad (3\text{-}28)$$

$$H = \nabla \times (z\psi^m) = \nabla\psi^m \times z.$$

The cylindrical coordinate components can then be written in the following manner,

$$E_\rho = \frac{1}{j\omega\hat{\epsilon}} \frac{\partial^2\psi^m}{\partial\rho\,\partial z} \qquad\qquad H_\rho = \frac{1}{\rho}\frac{\partial\psi^m}{\partial\phi}$$

$$E_\phi = \frac{1}{j\omega\hat{\epsilon}} \frac{1}{\rho}\frac{\partial^2\psi^m}{\partial\phi\,\partial z} \qquad\qquad H_\phi = -\frac{\partial\psi^m}{\partial\rho} \qquad (3\text{-}29)$$

$$E_z = \frac{1}{j\omega\hat{\epsilon}} k_\rho^2 \, \psi^m \qquad\qquad H_z = 0.$$

The z-component of the magnetic field of Equation (3-29) is zero for any ψ^m. Therefore solutions of the form found in Equation (3-29) are referred to as *transverse magnetic*, abbreviated TM.

A similar set of equations can be found by beginning with Equations (3-15) and constraining F to be $z \, \psi^e$, with ψ^e in dimensions of Volts. The function space of ψ^e is the same as that of ψ^m given in Equation (3-26). The electric and magnetic fields are given by

$$E = -\nabla \times (z\psi^e) = -\nabla\psi^e \times z$$

$$H = -j\omega\hat{\epsilon} \, z\psi^e + \frac{1}{j\omega\hat{\mu}} \nabla\left(\frac{\partial\psi^e}{\partial z}\right), \qquad (3\text{-}30)$$

with the cylindrical coordinate components given by

$$E_\rho = -\frac{1}{\rho}\frac{\partial \psi^e}{\partial \phi} \qquad\qquad H_\rho = \frac{1}{j\omega\hat\mu}\frac{\partial^2 \psi^e}{\partial \rho \partial z}$$

$$E_\phi = \frac{\partial \psi^e}{\partial \rho} \qquad\qquad H_\phi = \frac{1}{j\omega\hat\mu}\frac{1}{\rho}\frac{\partial^2 \psi^e}{\partial \phi \partial z} \qquad\qquad (3\text{-}31)$$

$$E_z = 0 \qquad\qquad H_z = \frac{1}{j\omega\hat\mu}k_\rho^2\psi^e.$$

The set of fields given by Equation (3-31), due to the absence of the z-directed electric field, is referred to as *transverse electric*, or TE.

3.4 Homogeneously Filled Waveguides

The homogeneously filled cylindrical waveguide is shown below in Figure 3-1. It has an inside radius b and is filled with a homogeneous, isotropic material of complex dielectric constant $\hat\epsilon$ and complex magnetic permeability $\hat\mu$. The waveguide walls are perfectly conducting such that $E_{tan} = 0$ at the wall.

Beginning with appropriate choices for ψ^m and ψ^e from Equations (3-19) and (3-26), we seek field solutions using Equations (3-29) and (3-31). Since the region of
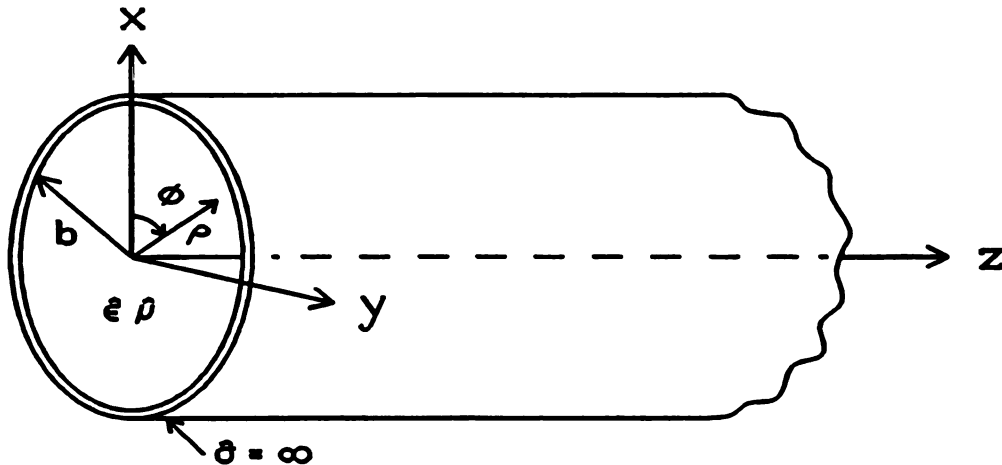
Figure 3-1 Homogeneously Filled Cylindrical Waveguide.

interest contains the origin, solutions for R(ρ) will be of the form $J_n(k_\rho \rho)$ rather than $N_n(k_\rho \rho)$, which is unbounded at $\rho = 0$.

The ϕ-dependence of the fields is determined primarily by the device used to couple electromagnetic energy into the waveguide. Although coupling is not considered here, it is practical to assure common ϕ-dependence for TE and TM field solutions since they will presumably be excited by the same coupling device for a given waveguide or cavity. If we choose $\Phi(\phi) = \cos(n\phi)$ for TM solutions and $\Phi(\phi) = \sin(n\phi)$ for TE solutions, the field components will have similar ϕ-dependence for both TE and TM solutions.

Finally, since the implicit time-dependence is represented by $e^{j\omega t}$, the direction of propagation may be chosen in the positive z-direction by allowing $Z(z) = e^{-jk_z z}$. ψ^m and ψ^e are then given by

$$\psi^m = A\, J_n(k_\rho^m \rho)\, \cos(n\phi)\, e^{-jk_z z}$$

$$\psi^e = B\, J_n(k_\rho^e \rho)\, \sin(n\phi)\, e^{-jk_z z}.$$

(3-32)

Using ψ^m from Equations (3-32) and plugging it into Equations (3-29), the TM field components, including the $n = 0$ case, are found to be

$$E_\rho = -A\, \frac{k_z k_\rho^m}{\omega \hat{\epsilon}}\, J_n'(k_\rho^m \rho)\, \cos(n\phi)\, e^{-jk_z z} \qquad (3\text{-}33)$$

$$E_\phi = A\, \frac{k_z n}{\omega \hat{\epsilon}}\, \frac{1}{\rho}\, J_n(k_\rho^m \rho)\, \sin(n\phi)\, e^{-jk_z z} \qquad (3\text{-}34)$$

$$E_z = A\, \frac{k_\rho^{m\,2}}{j\omega \hat{\epsilon}}\, J_n(k_\rho^m \rho)\, \cos(n\phi)\, e^{-jk_z z} \qquad (3\text{-}35)$$

$$H_\rho = -A\, \frac{n}{\rho}\, J_n(k_\rho^m \rho)\, \sin(n\phi)\, e^{-jk_z z} \qquad (3\text{-}36)$$

$$H_\phi = -A\, k_\rho^{\,m}\, J_n'(k_\rho^{\,m}\rho)\, \cos(n\phi)\, e^{-jk_z z} \qquad (3\text{-}37)$$

$$H_z = 0. \qquad (3\text{-}38)$$

TE field components, for $n \neq 0$, from Equations (3-31) with ψ^e from Equations (3-32) are given by

$$E_\rho = -B\, \frac{n}{\rho}\, J_n(k_\rho^{\,e}\rho)\, \cos(n\phi)\, e^{-jk_z z} \qquad (3\text{-}39)$$

$$E_\phi = B\, k_\rho^{\,e}\, J_n'(k_\rho^{\,e}\rho)\, \sin(n\phi)\, e^{-jk_z z} \qquad (3\text{-}40)$$

$$E_z = 0 \qquad (3\text{-}41)$$

$$H_\rho = -B\, \frac{k_z k_\rho^{\,e}}{\omega\hat{\mu}}\, J_n'(k_\rho^{\,e}\rho)\, \sin(n\phi)\, e^{-jk_z z} \qquad (3\text{-}42)$$

$$H_\phi = -B\, \frac{k_z n}{\omega\hat{\mu}}\, \frac{1}{\rho}\, J_n(k_\rho^{\,e}\rho)\, \cos(n\phi)\, e^{-jk_z z} \qquad (3\text{-}43)$$

$$H_z = B\, \frac{k_\rho^{\,e\,2}}{j\omega\hat{\mu}}\, J_n(k_\rho^{\,e}\rho)\, \sin(n\phi)\, e^{-jk_z z}. \qquad (3\text{-}44)$$

If $n = 0$, all TE field components are zero except E_ϕ, H_ρ, and H_z, which are given by

$$E_\phi = B\, k_\rho^{\,e}\, J_0'(k_\rho^{\,e}\rho)\, e^{-jk_z z} \qquad (3\text{-}45)$$

$$H_\rho = -B \frac{k_z k_\rho^e}{\omega \hat{\mu}} J_0'(k_\rho^e \rho) e^{-jk_z z} \tag{3-46}$$

$$H_z = B \frac{k_\rho^{e\,2}}{j\omega\hat{\mu}} J_0(k_\rho^e \rho) e^{-jk_z z}. \tag{3-47}$$

The boundary condition on E_{tan} at the waveguide wall, i.e., $\rho = b$, yields the following constraints on the radial wavenumbers $k_\rho^{m,e}$:

$$J_n(k_\rho^m b) = 0$$

$$J_n'(k_\rho^e b) = 0. \tag{3-48}$$

Equations (3-48) lead to the following definitions for $k_\rho^{e,m}$:

$$k_\rho^m = \frac{\lambda_{np}}{b}$$

$$k_\rho^e = \frac{\lambda_{np}'}{b} \tag{3-49}$$

where λ_{np} is p^{th} zero of J_n and λ_{np}' is the pth zero of J_n'.

3.5 The Coaxially-Loaded Waveguide

3.5.1 Description of the Coaxially-Loaded Waveguide

A diagram of the coaxially-loaded waveguide is shown in Figure 3-2. It consists of a cylindrical waveguide of radius b, and a homogeneous, isotropic material rod of radius a, dielectric constant $\hat{\epsilon}_1$, and magnetic permeability $\hat{\mu}_1$, located coaxially inside the waveguide. Between the load material and the waveguide walls is a homogeneous, isotropic filler of dielectric constant $\hat{\epsilon}_2$ and magnetic permeability $\hat{\mu}_2$. Often in practice the filler material consists of free space or a lossless dielectric used to support the load material.
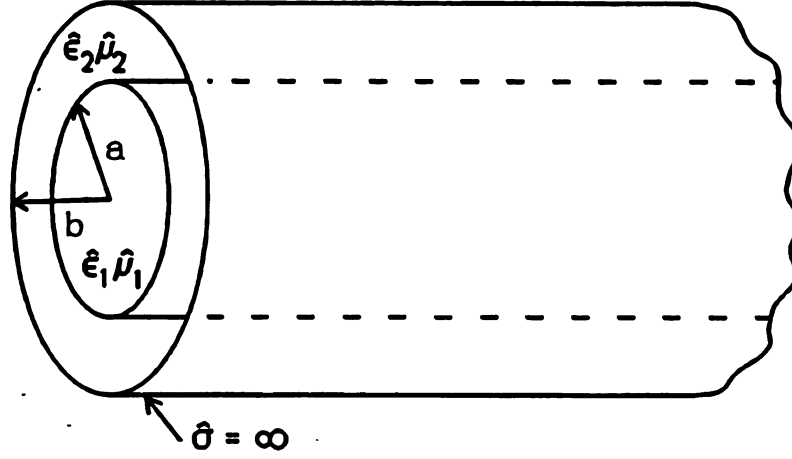
Figure 3-2 Coaxially-Loaded Waveguide.

3.5.2 Fields of the Coaxially-Loaded Waveguide

As shown in Figure 3-2, the coaxially-loaded waveguide is divided into two regions: region 1 for $\rho < a$ and region 2 for $a < \rho < b$. Fields in each of the regions may be obtained using the general solutions found in Section 3.3. Except for one special case, the case $n = 0$, the boundary conditions at the surface of the coaxial load cannot be met by fields that are exclusively TM or exclusively TE to z. Instead, a superposition of TM and TE solutions, as expressed by Equation (3-16), must be implemented.

We begin by writing down the potential function ψ's for the two waveguide regions. Field components from these potentials are found as before for the homogeneously loaded waveguide by substituting them into Equations (3-29) and (3-31). The superposition is achieved by adding the two resulting sets of equations together to get an expression for the total field. In region 1, the potential functions are given by

$$\psi^{ml} = A \, J_{n_{ml}}(k_{\rho 1}^m \rho) \, \cos(n_{ml}\phi) \, e^{-j\gamma_1^m z} \tag{3-50}$$

$$\psi^{el} = B \, J_{n_{el}}(k_{\rho 1}^e \rho) \, \sin(n_{el}\phi) \, e^{-j\gamma_1^e z} . \tag{3-51}$$

For $n = 0$ we replace the *sine* and *cosine* functions in the above equations by a constant. Note that the radial dependence in region 1, since it contains $\rho = 0$, consists only of Bessel's functions of the first kind.

In region 2 the radial dependence of the potential functions also includes Bessel's functions of the second kind. The potentials in region 2, with the same modification for the $n = 0$ case as for region 1, are given by

$$\psi^{m2} = C\,F_{n_{m2}}(k_{\rho 2}^m \rho)\,\cos(n_{m2}\phi)\,e^{-j\gamma_2^m z} \tag{3-52}$$

$$\psi^{e2} = D\,G_{n_{e2}}(k_{\rho 2}^e \rho)\,\sin(n_{e2}\phi)\,e^{-j\gamma_2^e z}, \tag{3-53}$$

where the boundary condition on $\mathbf{E}_{tan}$ at $\rho = b$ is met by requiring

$$F_{n_{m2}}(k_{\rho 2}^m \rho) = N_{n_{m2}}(k_{\rho 2}^m b)\,J_{n_{m2}}(k_{\rho 2}^m \rho) - J_{n_{m2}}(k_{\rho 2}^m b)\,N_{n_{m2}}(k_{\rho 2}^m \rho) \tag{3-54}$$

$$G_{n_{e2}}(k_{\rho 2}^e \rho) = N'_{n_{e2}}(k_{\rho 2}^e b)\,J_{n_{e2}}(k_{\rho 2}^e \rho) - J'_{n_{e2}}(k_{\rho 2}^e b)\,N_{n_{e2}}(k_{\rho 2}^e \rho). \tag{3-55}$$

The component wave numbers $k_{\rho 1}^m$, $k_{\rho 1}^e$, $k_{\rho 2}^m$, $k_{\rho 2}^e$, γ_1^m, γ_1^e, γ_2^m, and γ_2^e, and the azimuthal dependences n_{m1}, n_{e1}, n_{m2}, and n_{e2}, are found in terms of the frequency, ω, by applying the boundary conditions of continuous tangential electric and magnetic fields at the interface between regions 1 and 2. The application of these boundary conditions also reduces the number of component wave numbers such that

$$k_{\rho 1}^m = k_{\rho 1}^e \equiv k_{\rho 1}$$

$$k_{\rho 2}^m = k_{\rho 2}^e \equiv k_{\rho 2}$$

$$\gamma_1^m = \gamma_1^e = \gamma_2^m = \gamma_2^e \equiv \gamma$$

$$n_{m1} = n_{e1} = n_{m2} = n_{e2} \equiv n. \tag{3-56}$$

The separation equations for the two regions are

$$k_1^2 = \omega^2 \hat{\epsilon}_1 \hat{\mu}_1 = k_{\rho 1}^2 + \gamma^2$$

$$k_2^2 = \omega^2 \hat{\epsilon}_2 \hat{\mu}_2 = k_{\rho 2}^2 + \gamma^2 .$$

(3-57)

The radial wave numbers, $k_{\rho 1}$ and $k_{\rho 2}$, are coupled in Equation (3-57) through γ, the axial wave number common to both regions 1 and 2, and through ω.

We may now write down the field components for each region. In region 1 the fields for n $\neq$ 0 are given by

$$E_{\rho 1} = - \left[A \frac{\gamma k_{\rho 1}}{\omega \hat{\epsilon}_1} J_n'(k_{\rho 1} \rho) + B \frac{n}{\rho} J_n(k_{\rho 1} \rho) \right] \cos(n \phi) e^{-j\gamma z}$$

(3-58)

$$E_{\phi 1} = \left[A \frac{\gamma}{\omega \hat{\epsilon}_1} \frac{n}{\rho} J_n(k_{\rho 1} \rho) + B k_{\rho 1} J_n'(k_{\rho 1} \rho) \right] \sin(n \phi) e^{-j\gamma z}$$

(3-59)

$$E_{z1} = A \frac{k_{\rho 1}^2}{j \omega \hat{\epsilon}_1} J_n(k_{\rho 1} \rho) \cos(n \phi) e^{-j\gamma z}$$

(3-60)

$$H_{\rho 1} = - \left[A \frac{n}{\rho} J_n(k_{\rho 1} \rho) + B \frac{\gamma k_{\rho 1}}{\omega \hat{\mu}_1} J_n'(k_{\rho 1} \rho) \right] \sin(n \phi) e^{-j\gamma z}$$

(3-61)

$$H_{\phi 1} = - \left[A k_{\rho 1} J_n'(k_{\rho 1} \rho) + B \frac{\gamma}{\omega \hat{\mu}_1} \frac{n}{\rho} J_n(k_{\rho 1} \rho) \right] \cos(n \phi) e^{-j\gamma z}$$

(3-62)

$$H_{z1} = B \frac{k_{\rho 1}^2}{j \omega \hat{\mu}_1} J_n(k_{\rho 1} \rho) \sin(n \phi) e^{-j\gamma z} .$$

(3-63)

For $n = 0$ the above expressions remain valid except for E_ϕ, H_ρ, and H_z which become

$$E_{\phi 1} = B k_{\rho 1} J_0'(k_{\rho 1} \rho) e^{-j\gamma z} \qquad (3\text{-}64)$$

$$H_{\rho 1} = -B \frac{\gamma k_{\rho 1}}{\omega \hat{\mu}_1} J_0'(k_{\rho 1} \rho) e^{-j\gamma z} \qquad (3\text{-}65)$$

$$H_{z1} = B \frac{k_{\rho 1}^2}{j\omega \hat{\mu}_1} J_0(k_{\rho 1} \rho) e^{-j\gamma z}. \qquad (3\text{-}66)$$

The field equations in region 2 for n $\neq$ 0 are given by Equations (3-67) through (3-72),

$$E_{\rho 2} = -\left[C \frac{\gamma k_{\rho 2}}{\omega \hat{\epsilon}_2} F_n'(k_{\rho 2} \rho) + D \frac{n}{\rho} G_n(k_{\rho 2} \rho) \right] \cos(n\phi) e^{-j\gamma z} \qquad (3\text{-}67)$$

$$E_{\phi 2} = \left[C \frac{\gamma}{\omega \hat{\epsilon}_2} \frac{n}{\rho} F_n(k_{\rho 2} \rho) + D k_{\rho 2} G_n'(k_{\rho 2} \rho) \right] \sin(n\phi) e^{-j\gamma z} \qquad (3\text{-}68)$$

$$E_{z2} = C \frac{k_{\rho 2}^2}{j\omega \hat{\epsilon}_2} F_n(k_{\rho 2} \rho) \cos(n\phi) e^{-j\gamma z} \qquad (3\text{-}69)$$

$$H_{\rho 2} = -\left[C \frac{n}{\rho} F_n(k_{\rho 2} \rho) + D \frac{\gamma k_{\rho 2}}{\omega \hat{\mu}_2} G_n'(k_{\rho 2} \rho) \right] \sin(n\phi) e^{-j\gamma z} \qquad (3\text{-}70)$$

$$H_{\phi 2} = -\left[C k_{\rho 2} F_n'(k_{\rho 2} \rho) + D \frac{\gamma}{\omega \hat{\mu}_2} \frac{n}{\rho} G_n(k_{\rho 2} \rho) \right] \cos(n\phi) e^{-j\gamma z} \qquad (3\text{-}71)$$

$$H_{z2} = D \frac{k_{\rho 2}^2}{j\omega\hat{\mu}_2} G_n(k_{\rho 2}\rho) \sin(n\phi) e^{-j\gamma z}. \tag{3-72}$$

For $n = 0$, Equations (3-67) through (3-72) are correct except for E_ϕ, H_ρ, and H_z which are given by

$$E_{\phi 2} = D k_{\rho 2} G_0'(k_{\rho 2}\rho) e^{-j\gamma z} \tag{3-73}$$

$$H_{\rho 2} = - D \frac{\gamma k_{\rho 2}}{\omega\hat{\mu}_2} G_0'(k_{\rho 2}\rho) e^{-j\gamma z} \tag{3-74}$$

$$H_{z2} = D \frac{k_{\rho 2}^2}{j\omega\hat{\mu}_2} G_0(k_{\rho 2}\rho) e^{-j\gamma z}. \tag{3-75}$$

In Equations (3-67) through (3-75), the functions F_n, F_n', G_n, and G_n', from Equations (3-54) and (3-55), are given by

$$F_n(k_{\rho 2}\rho) = N_n(k_{\rho 2}b) J_n(k_{\rho 2}\rho) - J_n(k_{\rho 2}b) N_n(k_{\rho 2}\rho) \tag{3-76}$$

$$F_n'(k_{\rho 2}\rho) = N_n(k_{\rho 2}b) J_n'(k_{\rho 2}\rho) - J_n(k_{\rho 2}b) N_n'(k_{\rho 2}\rho) \tag{3-77}$$

$$G_n(k_{\rho 2}\rho) = N_n'(k_{\rho 2}b) J_n(k_{\rho 2}\rho) - J_n'(k_{\rho 2}b) N_n(k_{\rho 2}\rho) \tag{3-78}$$

$$G_n'(k_{\rho 2}\rho) = N_n'(k_{\rho 2}b) J_n'(k_{\rho 2}\rho) - J_n'(k_{\rho 2}b) N_n'(k_{\rho 2}\rho) \tag{3-79}$$

3.5.3 Characteristic Equation for the Coaxially-Loaded Waveguide

Application of the boundary conditions on E_{tan} and H_{tan} at the interface between regions 1 and 2, i.e., $\rho = a$, was mentioned in the previous Section with regard to reducing to four the number of component wave numbers. These were given by $k_{\rho 1}$, $k_{\rho 2}$, γ, and n. Application of these boundary conditions also provides sufficient information for calculation of all component wave numbers, for a given n, as a function of the excitation frequency, ω. In addition, the coefficients B, C, and D may be found in terms of A such that the fields for a given n may be calculated as a unique function of ω with A as an arbitrary amplitude coefficient.

The tangential field components at $\rho = a$ are E_ϕ, E_z, H_ϕ, and H_z. The boundary condition on tangential field components across an interface of finite conductivity is that they must be continuous. Enforcing continuity of E_ϕ at $\rho = a$ we have

$$A \frac{\gamma}{\omega \hat{\epsilon}_1} \frac{n}{a} J_n(k_{\rho 1} a) + B k_{\rho 1} J'_n(k_{\rho 1} a)$$

$$= C \frac{\gamma}{\omega \hat{\epsilon}_2} \frac{n}{a} F_n(k_{\rho 2} a) + D k_{\rho 2} G'_n(k_{\rho 2} a). \tag{3-80}$$

A similar equation results from the continuity of H_ϕ,

$$A k_{\rho 1} J'_n(k_{\rho 1} a) + B \frac{\gamma}{\omega \hat{\mu}_1} \frac{n}{a} J_n(k_{\rho 1} a)$$

$$= C k_{\rho 2} F'_n(k_{\rho 2} a) + D \frac{\gamma}{\omega \hat{\mu}_2} \frac{n}{a} G_n(k_{\rho 2} a). \tag{3-81}$$

From the continuity of E_z and of H_z,

$$A \frac{k_{\rho 1}^2}{\hat{\epsilon}_1} J_n(k_{\rho 1} a) - C \frac{k_{\rho 2}^2}{\hat{\epsilon}_2} F_n(k_{\rho 2} a) = 0 \tag{3-82}$$

$$B \frac{k_{\rho 1}^2}{\hat{\mu}_1} J_n(k_{\rho 1} a) - D \frac{k_{\rho 2}^2}{\hat{\mu}_2} G_n(k_{\rho 2} a) = 0. \qquad (3\text{-}83)$$

Equations (3-80) through (3-83) make it clear why it is not possible in general to excite a purely TM or TE mode in the coaxially loaded waveguide. For example, if B and D were both zero, i.e., the fields consist of the TM contribution only, Equation (3-82) would provide a value for C in terms of A. Then H_ϕ could be made continuous by some constraint on $k_{\rho 1}$ and $k_{\rho 2}$ in terms of ω, remembering that $k_{\rho 1}$ and $k_{\rho 2}$ are not both independent variables since they are linked by the separation equations. However, unless $n = 0$, that process leaves E_ϕ discontinuous. A similar argument can be used to demonstrate that TE solutions alone will not provide solutions which meet all of the boundary conditions unless $n = 0$.

It is convenient to make the following abbreviations:

$$J \equiv J_n(k_{\rho 1} a), \qquad J' \equiv J'_n(k_{\rho 1} a),$$

$$F \equiv F_n(k_{\rho 2} a), \qquad F' \equiv F'_n(k_{\rho 2} a), \qquad (3\text{-}84)$$

$$G \equiv G_n(k_{\rho 2} a), \qquad G' \equiv G'_n(k_{\rho 2} a).$$

Using these abbreviations, Equations (3-80) through (3-83) may be written in a single homogeneous matrix equation as

$$\begin{bmatrix} k_{\rho 1} J' & k_{\rho 2} F' & \dfrac{\gamma}{\omega \hat{\mu}_1} \dfrac{n}{a} J & \dfrac{\gamma}{\omega \hat{\mu}_2} \dfrac{n}{a} G \\[2mm] \hat{\epsilon}_2 k_{\rho 1}^2 J & \hat{\epsilon}_1 k_{\rho 2}^2 F & 0 & 0 \\[2mm] \dfrac{\gamma}{\omega \hat{\epsilon}_1} \dfrac{n}{a} J & \dfrac{\gamma}{\omega \hat{\epsilon}_2} \dfrac{n}{a} F & k_{\rho 1} J' & k_{\rho 2} G' \\[2mm] 0 & 0 & \hat{\mu}_2 k_{\rho 1}^2 J & \hat{\mu}_1 k_{\rho 2}^2 G \end{bmatrix} \begin{bmatrix} A \\[2mm] -C \\[2mm] B \\[2mm] -D \end{bmatrix} = \begin{bmatrix} 0 \\[2mm] 0 \\[2mm] 0 \\[2mm] 0 \end{bmatrix} \qquad (3\text{-}85)$$

The well-known solution to the homogeneous matrix equation is that the determinant of the matrix is equal to zero. Also the four field coefficients in the column vector are not independent. Three of them may be written in terms of the fourth. Calculation of the determinant of the matrix of Equation (3-85) yields the characteristic equation of the coaxially-loaded waveguide boundary value problem,

$$\tilde{V}_n \, \tilde{W}_n \; - \; n^2 \, \tilde{U}_n^2 \; = \; 0 \qquad (3\text{-}86)$$

where,

$$\tilde{V}_n \; = \; k_{\rho 1} k_{\rho 2} (\hat{\mu}_1 k_{\rho 2} J' \, G \; - \; \hat{\mu}_2 k_{\rho 1} J \, G') \qquad (3\text{-}87)$$

$$\tilde{W}_n \; = \; k_{\rho 1} k_{\rho 2} (\hat{\varepsilon}_1 k_{\rho 2} J' \, F \; - \; \hat{\varepsilon}_2 k_{\rho 1} J \, F') \qquad (3\text{-}88)$$

$$\tilde{U}_n \; = \; \frac{\gamma}{\omega a} (k_{\rho 1}^2 \; - \; k_{\rho 2}^2) \, J \sqrt{F \, G} \; . \qquad (3\text{-}89)$$

This equation is true regardless of the type of solutions chosen to represent the axial variation of the fields. However, as noted below, the mode coefficients do vary with the type of solutions chosen to represent the axial variation.

As these equations demonstrate, for the general $n \neq 0$ case the characteristic equation and field coefficient expressions are rather complicated. However, if $n = 0$ then the matrix of Equation (3-85), the characteristic equation, and the field coefficients are all greatly simplified.

The matrix equation for the case $n = 0$ is shown below in Equation (3-90). It should be noted that the matrix is resolved into two independent sub-matrices. If the determinant of either of the sub-matrices is zero then the determinant of the composite matrix is zero. The upper left sub-matrix corresponds to the field coefficients A and C which were assigned to the TM contribution in Equations (3-50) and (3-52). Similarly, the lower right sub-matrix corresponds to the field coefficients B and D which were assigned to the TE contribution in Equations (3-51) and (3-53).

$$\begin{bmatrix} k_{\rho1}J' & k_{\rho2}F' & 0 & 0 \\ \hat{\epsilon}_2 k_{\rho1}^2 J & \hat{\epsilon}_1 k_{\rho2}^2 F & 0 & 0 \\ 0 & 0 & k_{\rho1}J' & k_{\rho2}G' \\ 0 & 0 & \hat{\mu}_2 k_{\rho1}^2 J & \hat{\mu}_1 k_{\rho2}^2 G \end{bmatrix} \begin{bmatrix} A \\ -C \\ B \\ -D \end{bmatrix} = \begin{bmatrix} 0 \\ 0 \\ 0 \\ 0 \end{bmatrix} \qquad (3\text{-}90)$$

From Equation (3-90) the characteristic equation for $n = 0$ is given by,

$$\tilde{V}_0 \, \tilde{W}_0 = 0, \qquad (3\text{-}91)$$

where $\tilde{V}_0$ and $\tilde{W}_0$ are given by Equations (3-87) and (3-88) when $n = 0$. Equation (3-91) is consistent with the $n = 0$ special case of the general characteristic equation, Equation (3-86). Equation (3-91) is true for either $\tilde{V}_0 = 0$, or $\tilde{W}_0 = 0$. If $\tilde{V}_0 = 0$, then the solutions are TE; if $\tilde{W} = 0$, the solutions are TM.

For programming purposes it is best to write the characteristic equation in dimensionless form. This may be accomplished by multiplying Equation (3-86) by $\dfrac{\omega^2 a^2}{k_{\rho1}^2 k_{\rho2}^2 \epsilon_0 \mu_0}$. The characteristic equation becomes

$$V_n W_n - n^2 U_n^2 = 0, \qquad (3\text{-}92)$$

where

$$V_n = k_0 a \left(\frac{\hat{\mu}_1}{\mu_0} k_{\rho2} a J' G - \frac{\hat{\mu}_2}{\mu_0} k_{\rho1} a J G' \right) \qquad (3\text{-}93)$$

$$W_n = k_0 a \left(\frac{\hat{\epsilon}_1}{\epsilon_0} k_{\rho2} a J' F - \frac{\hat{\epsilon}_2}{\epsilon_0} k_{\rho1} a J F' \right) \qquad (3\text{-}94)$$

$$U_n = \gamma a \left(\frac{k_{\rho1}}{k_{\rho2}} - \frac{k_{\rho2}}{k_{\rho1}} \right) J \sqrt{F G}. \qquad (3\text{-}95)$$

If $n = 0$: TE solutions — $V_n = 0$, TM solutions — $W_n = 0$.

The field coefficients are not altered by writing the characteristic equation in dimensionless form. The coefficients B, C, and D are given in terms of A for traveling wave solutions as

$$B = A n \frac{k_0}{\omega \hat{\epsilon}_1} \frac{\hat{\mu}_1}{\mu_0} \sqrt{\frac{G}{F}} \frac{U_n}{V_n} \tag{3-96}$$

$$C = A \frac{\hat{\epsilon}_2 k_{\rho 1}^2 J}{\hat{\epsilon}_1 k_{\rho 2}^2 F} \tag{3-97}$$

$$D = A n \frac{k_0}{\omega \hat{\epsilon}_1} \frac{\hat{\mu}_2}{\mu_0} \frac{k_{\rho 1}^2}{k_{\rho 2}^2} \frac{J}{\sqrt{FG}} \frac{U_n}{V_n} \tag{3-98}$$

For axial standing waves the coefficients B and D as given above must be multiplied by $-j$, or by $+j$ if hyperbolic functions are used to represent the axial dependence. C is not affected by a change from traveling to standing waves.

In the case of TM solutions, the field coefficients B and D are set to zero and C is given in terms of A by Equation (3-97) above. For TE solutions A and C are set to zero with D given in terms of B, regardless of axial dependence, by

$$D = B \frac{\hat{\mu}_2 k_{\rho 1}^2 J}{\hat{\mu}_1 k_{\rho 2}^2 G} . \tag{3-99}$$

The field solutions and characteristic equation of the coaxially-loaded waveguide will be used extensively in the next Chapter for the coaxially-loaded cavity. As indicated above, the field coefficients will change slightly depending upon the eigenfunctions chosen to represent the axial dependence. Since it is often convenient to choose various axial dependences for the cavity solution, a field solution for generalized axial dependences will be developed. However, the characteristic equation, Equation (3-92), will be used without alteration.

Chapter 4
THE LOSSY-LOADED CYLINDRICAL CAVITY

4.1 Introduction

This Chapter is concerned with extending the waveguide solutions found in the last Chapter to cavities with cylindrical cross section. The axial boundaries imposed by the transformation to a cavity system discretizes the wavenumbers non-uniformly. The wavenumber can no longer be considered a continuous function of the axial wavenumber, i.e., the natural frequencies are discrete values which are determined by the cavity eigenvalue equation for an infinite set of discrete natural modes.

For the lossless case the natural frequencies are real and correspond to the sinusoidal steady-state resonant frequencies of the loaded cavity. The presence of loss in the cavity walls or in the material inside the cavity causes the natural frequencies to become complex. In the limit as losses approach zero, the complex natural frequencies approach the sinusoidal steady-state resonant frequencies of the lossless system, so that both lossless and lossy cavity solutions may be obtained from the solution for the lossy cavity. The solutions presented here will be for general lossy loads and may be specialized to the lossless condition simply by setting the imaginary part of the dielectric constant or magnetic permeability found in Equations (3-9) to zero.

In this Chapter three cavity/load configurations will be considered. First the modes of the cavity homogeneously filled with a lossy dielectric will be discussed. While homogeneously loaded cavities are commonly discussed in standard text books,[1] these discussions are for lossless loadings. A solution for a cavity homogeneously filled with a lossy dielectric, while not representing a standard practical application, provides a simple expression for the complex natural frequency which illustrates how losses affect cavity behavior. For simplicity, this solution is given for

---

[1] Harrington, 213-16; R. E. Collin, *Foundations for Microwave Engineering* (New York: McGraw-Hill, 1966), 326-29; Jackson, 354-56; C. G. Montgomery, *Technique of Microwave Measurements* (New York: McGraw-Hill, 1947), 297 ff.

a material with a real magnetic permeability and a complex dielectric constant, or vice-versa.

Secondly, a solution is given for a cavity coaxially loaded with a lossy cylindrical material which extends the entire axial length of the cavity. This is the cavity-short type configuration illustrated in Figure 1-3 of Chapter 1 and described more fully below. The solution for the cavity-short type configuration is a simple extension of the coaxially loaded waveguide solution, requiring only an additional restriction on the axial wavenumber, γ, as discussed below.

Finally, a solution is presented for a cavity coaxially loaded with a lossy cylindrical material of length less than the cavity length, i.e., cavity-open or cavity-image type solutions, shown in Figures 1-2 and 1-4 of Chapter 1. These solutions are much more complicated than either of the first two, requiring expression of the electromagnetic fields in the cavity as infinite modal expansions which are matched at the axial load-material boundaries. The method is called mode-matching and has been previously employed for the lossless case.[2]

The question of the relationship of the natural frequencies to the sinusoidal steady-state driven response of the cavity is reserved for Chaper 6. Since calculation of energy stored and dissipated at sinusoidal steady-state depends on this relationship, it will be discussed in Chapter 6 as well.

4.2 The Lossy Homogeneously Filled Cavity

The electromagnetic fields in the cylindrical cavity filled with a homogeneous, isotropic material are similar to those found in the similarly filled waveguide, but with standing waves instead of traveling waves in the axial direction. The cavity is constructed by placing shorting plates at either end of a section of waveguide. Fixing the origin of coordinates at one end of the cavity, as shown in Figure 4-1, the vector potential magnitudes ψ^m and ψ^e for the cavity are given by

---

[2]Kobayashi, Fukuoka, and Yoshida; Zaki and Chen, "New Results"; Vigneron and Guillon.
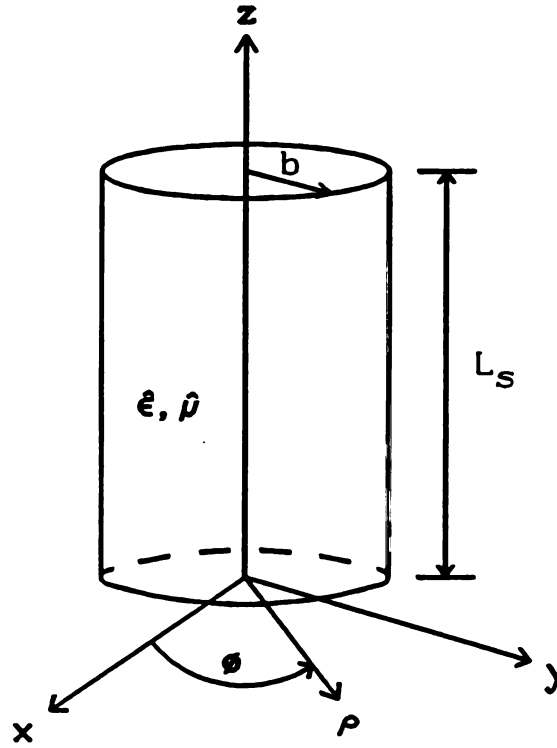
Figure 4-1 Homogeneously Filled Cylindrical Cavity.

$$\psi^m = A \, J_n(k_\rho^m \rho) \cos(n\phi) \cos(k_z z)$$

$$\psi^e = B \, J_n(k_\rho^e \rho) \sin(n\phi) \sin(k_z z) \, .$$

(4-1)

Equations (4-1), with Equations (3-29) and (3-31), provide field solutions similar to those for the waveguide in Equations (3-33) through (3-47). The TM field components, including the $n = 0$ case, are given explicitly as,

$$E_\rho = -A \, \frac{k_z}{j\hat{\omega}\hat{\epsilon}} \, \frac{\lambda_{np}}{b} \, J_n'(\lambda_{np} \frac{\rho}{b}) \cos(n\phi) \sin(k_z z)$$

(4-2)

$$E_\phi = A \, \frac{k_z}{j\hat{\omega}\hat{\epsilon}} \, \frac{n}{\rho} \, J_n(\lambda_{np} \frac{\rho}{b}) \sin(n\phi) \sin(k_z z)$$

(4-3)

$$E_z = A \frac{1}{j\hat{\omega}\hat{\epsilon}} \frac{\lambda_{np}^2}{b^2} J_n(\lambda_{np}\frac{\rho}{b}) \cos(n\phi) \cos(k_z z) \qquad (4\text{-}4)$$

$$H_\rho = -A \frac{n}{\rho} J_n(\lambda_{np}\frac{\rho}{b}) \sin(n\phi) \cos(k_z z) \qquad (4\text{-}5)$$

$$H_\phi = -A \frac{\lambda_{np}}{b} J_n'(\lambda_{np}\frac{\rho}{b}) \cos(n\phi) \cos(k_z z) \qquad (4\text{-}6)$$

$$H_z = 0. \qquad (4\text{-}7)$$

TE field components, for $n \neq 0$, are given by

$$E_\rho = -B \frac{n}{\rho} J_n(\lambda_{np}'\frac{\rho}{b}) \cos(n\phi) \sin(k_z z) \qquad (4\text{-}8)$$

$$E_\phi = B \frac{\lambda_{np}'}{b} J_n'(\lambda_{np}'\frac{\rho}{b}) \sin(n\phi) \sin(k_z z) \qquad (4\text{-}9)$$

$$E_z = 0 \qquad (4\text{-}10)$$

$$H_\rho = B \frac{k_z}{j\hat{\omega}\hat{\mu}} \frac{\lambda_{np}'}{b} J_n'(\lambda_{np}'\frac{\rho}{b}) \sin(n\phi) \cos(k_z z) \qquad (4\text{-}11)$$

$$H_\phi = B \frac{k_z}{j\hat{\omega}\hat{\mu}} \frac{n}{\rho} J_n(\lambda_{np}'\frac{\rho}{b}) \cos(n\phi) \cos(k_z z) \qquad (4\text{-}12)$$

$$H_z = B \frac{1}{j\hat{\omega}\hat{\mu}} \frac{\lambda_{np}'^2}{b^2} J_n(\lambda_{np}'\frac{\rho}{b}) \sin(n\phi) \sin(k_z z). \qquad (4\text{-}13)$$

If $n = 0$, all TE field components are zero except E_ϕ, H_ρ, and H_z, which are given by

$$E_\phi = B \frac{\lambda'_{op}}{b} J'_0(\lambda'_{op} \frac{\rho}{b}) \sin(k_z z) \qquad (4\text{-}14)$$

$$H_\rho = B \frac{k_z}{j \hat{\omega} \hat{\mu}} \frac{\lambda'_{op}}{b} J'_0(\lambda'_{op} \frac{\rho}{b}) \cos(k_z z) \qquad (4\text{-}15)$$

$$H_z = B \frac{1}{j \hat{\omega} \hat{\mu}} \frac{\lambda'^2_{op}}{b^2} J_0(\lambda'_{op} \frac{\rho}{b}) \sin(k_z z). \qquad (4\text{-}16)$$

These solutions meet the boundary condition on E_{tan} at the shorting plate located at the origin of coordinates. To meet the same boundary condition at the other end of the cavity, a constraint must be placed on k_z such that

$$k_z = \frac{q \pi}{L_s}, \qquad (4\text{-}17)$$

where q is an integer and L_s is the cavity length as shown in Figure 4-1.

Due to the constraints on k_ρ and k_z in Equations (3-49) and (4-17), k, hence the frequency $\hat{\omega}$, may take on only certain discrete values, defined for TM solutions by Equation (4-18) below. A similar equation exists for TE fields with λ_{np} replaced by λ'_{np}. At each discrete value of $\hat{\omega}$, electromagnetic energy may reside in the cavity in the standing wave patterns described above. Under these conditions the cavity is said to *resonate* in a certain *mode*. The fields may be either TM or TE to z, and their unique modal field patterns are prescribed by the integer values n, p, and q. The modes may then be designated in shorthand form by either TM_{npq} or TE_{npq}.

$$k = \hat{\omega} \sqrt{\hat{\mu} \hat{\epsilon}} = \sqrt{\left[\frac{\lambda_{np}}{b}\right]^2 + \left[\frac{q \pi}{L_s}\right]^2} \qquad (4\text{-}18)$$

The above results are valid whether the material inside the cavity is lossless or lossy. However, when the material is lossy, Equation (4-18) constrains $\hat{\omega}$ to be complex, signified by the hat symbol (^) over ω. This is evident since the right hand side of Equation (4-18) or its square is purely real. In order for the left hand side to

be purely real as well, the frequency must be complex such that

$$\text{Im}\,(\hat{\omega}^2\hat{\mu}\hat{\epsilon}) = 0,\qquad(4\text{-}19)$$

$$\text{Re}\,(\hat{\omega}^2\hat{\mu}\hat{\epsilon}) = \left[\frac{\lambda_{np}}{b}\right]^2 + \left[\frac{q\pi}{L_s}\right]^2.\qquad(4\text{-}20)$$

The complex radian frequency, $\hat{\omega}$, may be written as

$$\hat{\omega} = \omega' + j\omega'',\qquad(4\text{-}21)$$

where ω' is the real part and ω'' is the imaginary part of $\hat{\omega}$. Neglecting magnetic loss, i.e., setting $\mu'' = 0$, Equation (4-19) implies that ω'' is given in terms of ω' by

$$\omega'' = \omega'\,\frac{-\epsilon' \pm |\hat{\epsilon}|}{\epsilon''}.\qquad(4\text{-}22)$$

Either sign may be chosen as long as it is used consistently throughout. The same answer for $\hat{\omega}$ results. It is worth commenting that, from Equation (4-22), it is evident that values for $s = j\hat{\omega}$ do not fall into complex conjugate pairs. In order to consider the resonant cavity in terms of circuit analysis, it is necessary that the s's come in complex conjugate pairs. Equation (4-22) does not neccessarily present a contradiction, however, because the natural mode resonances do not individually form independent circuits; a sinusoidal steady-state resonance is composed of contributions from all the natural modes, dominated by the natural mode nearest in frequency.

Using Equations (4-20) and (4-22) an explicit expression for $\hat{\omega}$ for each integer value n, p, and q may be derived:

$$\hat{\omega} = \pm\sqrt{\left[\left[\frac{\lambda_{np}}{b}\right]^2 + \left[\frac{q\pi}{L_s}\right]^2\right]\frac{1}{2\mu|\hat{\epsilon}|^2}}\qquad(4\text{-}23)$$

$$\times\left(\sqrt{|\hat{\epsilon}|+\epsilon'} + j\sqrt{|\hat{\epsilon}|-\epsilon'}\right).$$

The choice of the positive sign in Equation (4-23) is the only physically realizable solution. Equation (4-23) may also be used to explore cavity resonances for magnetic loss with a lossless dielectric. Since $\hat{\epsilon}$ and $\hat{\mu}$ are symmetric in Equations (4-19) and (4-20), Equation (4-23) may be reconstructed for magnetic loss by replacing symbols ϵ with μ and vice-versa.

4.3 Coaxially loaded Cavity Configurations

The general configuration of the coaxially loaded cavity is shown below in Figure 4-2. As shown in Figure 4-2, the load of radius a and length ℓ is located coaxially in the cavity at a height h above the bottom. When the load length ℓ is less than the cavity length L_s, this configuration is referred to as cavity-open type.[†] Figure 4-2 shows the cavity divided into three regions. Regions I and III consist of homogeneously filled waveguide, while Region II consists of a section of coaxially loaded waveguide. Regions I and III are bounded by shorting plates at either end of the cavity.
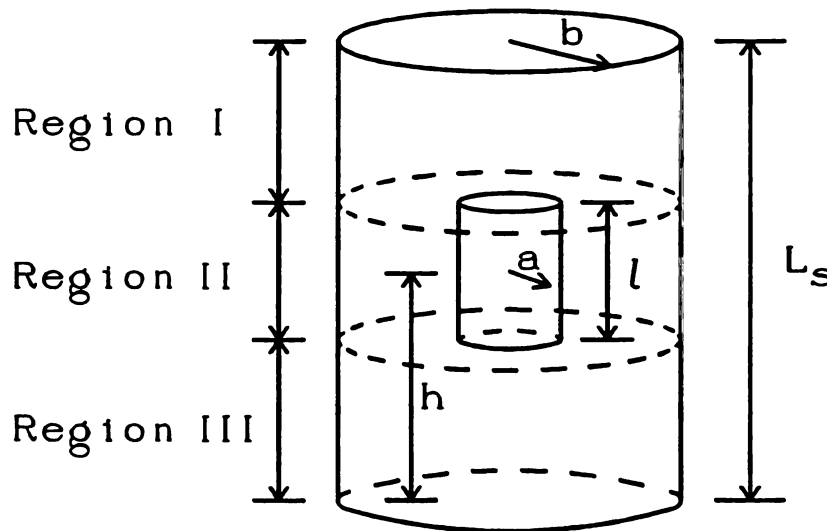
Figure 4-2 General Cavity-Open Type Configuration.

[†]The cavity configuration notation, as noted in Chapter 2, is that used by Kobayashi, Fukuoka, and Yoshida.

The general coaxially loaded configuration of Figure 4-2 may take on two special case configurations for variations in load length. The first special case, called the cavity-short type configuration, is for a load which extends the entire cavity length. The cavity-short type configuration consists of a section of coaxially loaded waveguide, as described in the previous Chapter in Section 3.5 and shown in Figure 3-2, with shorting plates on either end. An azimuthal cross sectional diagram of the cavity-short type cavity configuration is shown below in Figure 4-3.
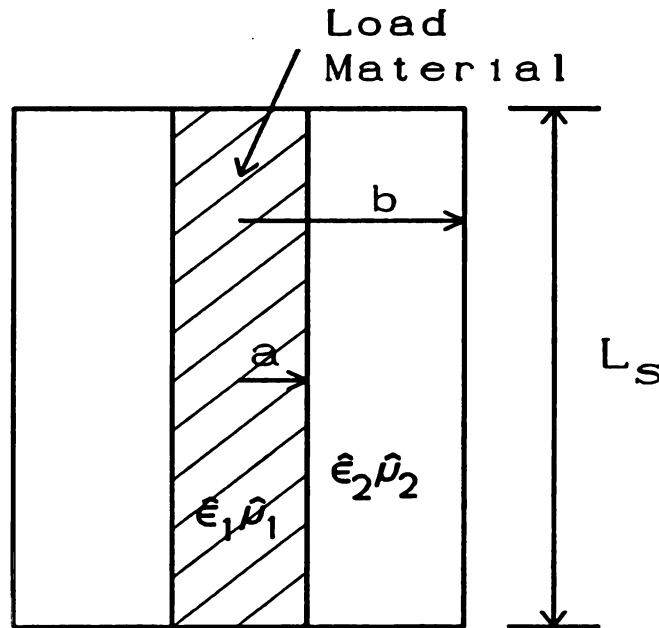
Figure 4-3 Cavity-Short Type Configuration.

A second special case is referred to as the cavity-image type configuration. In the cavity-image type configuration the load rests at one end of the cavity as shown in Figure 4-4. The cavity-image type configuration is composed of two regions. Region I consists of a homogeneously filled waveguide shorted at one end. Region II consists of a coaxially loaded waveguide region shorted at the end away from Region I.

The shorting plane which bounds Region II may be either a perfect electrical conductor, in which case the transverse electric field is shorted, or a perfect "magnetic conductor," in which case the transverse magnetic field is shorted. In the

first case, the Region II shorting plate a perfect electrical conductor, the cavity-image type configuration includes two cases. It includes the case where the load sits on one end of the cavity and the case for axially even modes where the load is located in the center of the cavity, referring to Figure 4-2, at $h = \frac{1}{2} L_s$. In the second case, the Region II shorting plate a perfect "magnetic conductor," the axially odd modes for a load in the center of the cavity may be found. Taking advantage of axial symmetry by formulating solutions to the cavity-open type configuration, when $h = \frac{1}{2} L_s$, as even or odd cavity-image type solutions greatly reduces the number of numerical operations required to solve the characteristic determinant.
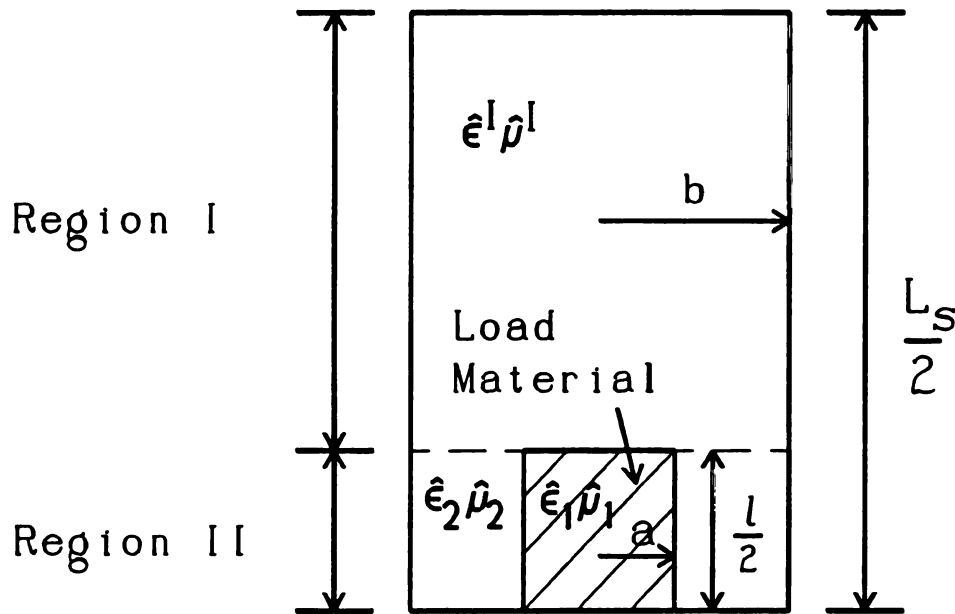
Figure 4-4 Cavity-Image Type Configuration.

4.4 The Cavity-Short Type Configuration

The characteristic equation for the cavity-short type configuration is found in a manner similar to that followed for the homogeneously-loaded cavity in Section 4.2. The eigenfrequencies of the homogeneously-loaded cavity were found by requiring the axial dependence of the fields for the homogeneously loaded waveguide to be represented by standing wave solutions instead of traveling wave solutions. Then the

axial wavenumber was constrained in order to meet the boundary conditions at the shorting plates.

For the cavity-short type configuration the same procedure is followed except now the radial wavenumbers are given by the coaxially loaded waveguide characteristic equation, Equation (3-92), instead of the homogeneously-loaded characteristic equation, Equation (3-48). With $z = 0$ at one end of the cavity, the field potential functions for the cavity-short type configuration in the loaded region, region 1, are given by

$$\psi^{m1} = A J_n(k_{\rho 1} \rho) \cos(n\phi) \cos(\gamma z) \qquad (4\text{-}24)$$

$$\psi^{e1} = B J_n(k_{\rho 1} \rho) \sin(n\phi) \sin(\gamma z) . \qquad (4\text{-}25)$$

For $n = 0$ we replace the ϕ-dependence in the above equations by a constant.
The potentials in region 2, with the same modification for the $n = 0$ case as for region 1, are given by

$$\psi^{m2} = C F_n(k_{\rho 2} \rho) \cos(n\phi) \cos(\gamma z) \qquad (4\text{-}26)$$

$$\psi^{e2} = D G_n(k_{\rho 2} \rho) \sin(n\phi) \sin(\gamma z) . \qquad (4\text{-}27)$$

As in the case of the homogeneously-loaded cavity, in order to meet the boundary condition at $z = L_s$, the axial wavenumber must be an integer number of half-wavelengths, i.e.,

$$\gamma = \frac{q \pi}{L_s} . \qquad (4\text{-}28)$$

The separation equations for each region, from Equations (3-57) for the coaxially loaded waveguide, are

$$k_1^2 = \hat{\omega}^2 \hat{\epsilon}_1 \hat{\mu}_1 = k_{\rho 1}^2 + (\frac{q\pi}{L_s})^2$$

$$k_2^2 = \hat{\omega}^2 \hat{\epsilon}_2 \hat{\mu}_2 = k_{\rho 2}^2 + (\frac{q\pi}{L_s})^2 .$$

(4-29)

The characteristic equation is given by Equation (3-92) with γ as given in Equation (4-28) and $k_{\rho 1}$ and $k_{\rho 2}$ linked by Equations (4-29).

The electric and magnetic fields given in Equations (3-58) through (3-75) are modified to reflect the standing waves in the z-direction. In region 1 the fields for $n \neq 0$ become,

$$E_{\rho 1} = - \left[A \frac{\gamma k_{\rho 1}}{j\omega\hat{\epsilon}_1} J_n'(k_{\rho 1}\rho) + B \frac{n}{\rho} J_n(k_{\rho 1}\rho) \right] \cos(n\phi)\sin(\gamma z)$$

(4-30)

$$E_{\phi 1} = \left[A \frac{\gamma}{j\omega\hat{\epsilon}_1} \frac{n}{\rho} J_n(k_{\rho 1}\rho) + B k_{\rho 1} J_n'(k_{\rho 1}\rho) \right] \sin(n\phi)\sin(\gamma z)$$

(4-31)

$$E_{z1} = A \frac{k_{\rho 1}^2}{j\omega\hat{\epsilon}_1} J_n(k_{\rho 1}\rho)\cos(n\phi)\cos(\gamma z)$$

(4-32)

$$H_{\rho 1} = \left[-A \frac{n}{\rho} J_n(k_{\rho 1}\rho) + B \frac{\gamma k_{\rho 1}}{j\omega\hat{\mu}_1} J_n'(k_{\rho 1}\rho) \right] \sin(n\phi)\cos(\gamma z)$$

(4-33)

$$H_{\phi 1} = \left[-A k_{\rho 1} J_n'(k_{\rho 1}\rho) + B \frac{\gamma}{j\omega\hat{\mu}_1} \frac{n}{\rho} J_n(k_{\rho 1}\rho) \right] \cos(n\phi)\cos(\gamma z)$$

(4-34)

$$H_{z1} = B \frac{k_{\rho 1}^2}{j\omega\hat{\mu}_1} J_n(k_{\rho 1}\rho)\sin(n\phi)\sin(\gamma z) .$$

(4-35)

For $n = 0$ the above expressions remain valid except for E_ϕ, H_ρ, and H_z which

become

$$E_{\phi 1} = B k_{\rho 1} J_0'(k_{\rho 1} \rho) \sin(\gamma z) \qquad (4\text{-}36)$$

$$H_{\rho 1} = B \frac{\gamma k_{\rho 1}}{j \omega \hat{\mu}_1} J_0'(k_{\rho 1} \rho) \cos(\gamma z) \qquad (4\text{-}37)$$

$$H_{z1} = B \frac{k_{\rho 1}^2}{j \omega \hat{\mu}_1} J_0(k_{\rho 1} \rho) \sin(\gamma z) \,. \qquad (4\text{-}38)$$

The field equations in region 2 for n $\neq$ 0 are given by Equations (4-39) through (4-44),

$$E_{\rho 2} = - \left[C \frac{\gamma k_{\rho 2}}{j \omega \hat{\epsilon}_2} F_n'(k_{\rho 2} \rho) + D \frac{n}{\rho} G_n(k_{\rho 2} \rho) \right] \cos(n \phi) \sin(\gamma z) \qquad (4\text{-}39)$$

$$E_{\phi 2} = \left[C \frac{\gamma}{j \omega \hat{\epsilon}_2} \frac{n}{\rho} F_n(k_{\rho 2} \rho) + D k_{\rho 2} G_n'(k_{\rho 2} \rho) \right] \sin(n \phi) \sin(\gamma z) \qquad (4\text{-}40)$$

$$E_{z2} = C \frac{k_{\rho 2}^2}{j \omega \hat{\epsilon}_2} F_n(k_{\rho 2} \rho) \cos(n \phi) \cos(\gamma z) \qquad (4\text{-}41)$$

$$H_{\rho 2} = \left[- C \frac{n}{\rho} F_n(k_{\rho 2} \rho) + D \frac{\gamma k_{\rho 2}}{j \omega \hat{\mu}_2} G_n'(k_{\rho 2} \rho) \right] \sin(n \phi) \cos(\gamma z) \qquad (4\text{-}42)$$

$$H_{\phi 2} = \left[- C k_{\rho 2} F_n'(k_{\rho 2} \rho) + D \frac{\gamma}{j \omega \hat{\mu}_2} \frac{n}{\rho} G_n(k_{\rho 2} \rho) \right] \cos(n \phi) \cos(\gamma z) \qquad (4\text{-}43)$$

$$H_{z2} = D \frac{k_{\rho 2}^2}{j \omega \hat{\mu}_2} G_n(k_{\rho 2} \rho) \sin(n \phi) \sin(\gamma z) \,. \tag{4-44}$$

For $n = 0$, Equations (4-39) through (4-44) are correct except for E_ϕ, H_ρ, and H_z which are given by

$$E_{\phi 2} = D k_{\rho 2} G_0'(k_{\rho 2} \rho) \sin(\gamma z) \tag{4-45}$$

$$H_{\rho 2} = D \frac{\gamma k_{\rho 2}}{j \omega \hat{\mu}_2} G_0'(k_{\rho 2} \rho) \cos(\gamma z) \tag{4-46}$$

$$H_{z2} = D \frac{k_{\rho 2}^2}{j \omega \hat{\mu}_2} G_0(k_{\rho 2} \rho) \sin(\gamma z) \,. \tag{4-47}$$

The coefficients B, C, and D are given in terms of A by

$$B = A \frac{n}{j} \frac{k_o}{\omega \epsilon_1} \frac{\hat{\mu}_1}{\mu_o} \sqrt{\frac{G}{F}} \frac{U_n}{V_n} \tag{4-48}$$

$$C = A \frac{\hat{\epsilon}_2 k_{\rho 1}^2 J}{\hat{\epsilon}_1 k_{\rho 2}^2 F} \tag{4-49}$$

$$D = A \frac{n}{j} \frac{k_o}{\omega \hat{\epsilon}_1} \frac{\hat{\mu}_2}{\mu_o} \frac{k_{\rho 1}^2}{k_{\rho 2}^2} \frac{J}{\sqrt{FG}} \frac{U_n}{V_n} \,. \tag{4-50}$$

4.5 The Cavity-Open Type Configuration

4.5.1 Mode-Matching Methods

The cavity-open and cavity-image type configurations require a much more complicated procedure for calculating the eigenvalues of the system than did the

special case of the cavity-short type configuration. This is due to the additional boundary conditions which must be met at $z = h - \frac{1}{2}L_s \pm \frac{1}{2}\ell$, referring to Figure 4-2 and placing the origin of coordinates at the cavity center half way between the shorting plates. In order to describe the electromagnetic fields in the cavity, the fields in each of regions I, II, and III, again referring to Figure 4-2, are represented as an infinite series modal expansion of the waveguide modes in each region. Boundary conditions are met by matching appropriate field components at

$z = h - \frac{1}{2}L_s \pm \frac{1}{2}\ell$ using the modal expansion representation of the fields. Hence the method is called "mode matching." This method was first applied to microwave resonators by W. C. Hahn[3] in 1940 and has since been used by several others to successfully calculate the characteristic values for lossless resonant cavities.[4]

There are two methods which may be used to resolve the mode matching boundary condition equations into one homogeneous matrix equation. Both involve orthogonalization of the modal field expansions by a single mode from one of the regions at the boundary where the fields are being matched. The first method uses a single mode from the homogeneous region, i.e., either region I or region III, to orthogonalize both of the boundary condition equations. This is the method used by Kobayashi, Fukuoka and Yohshida, Zaki and Atia, and Vigneron and Guillon for the lossless load.[5] The second method uses a mode from the homogeneous region to orthogonalize one of the boundary condition equations and a mode from the coaxially loaded waveguide region, region II, to orthogonalize the other equation. This method was used by Bolle in his work on the conducting load.[6]

The first method has the advantage of having fewer integrals to solve and results in simpler expressions for the elements of the characteristic matrix than the

---

[3]W. C. Hahn, "A New Method for the Calculation of Cavity Resonators," *J. App. Phs.* 12, no. 1 (Jan. 1941), 62-68.

[4]D. M. Bolle, "Eigenvalues for a Centrally Loaded Circular Cylindrical Cavity," *IRE Trans. Microwave Thry. Tech.* Mtt-10, no. 3 (March 1962), 133-138; Zaki and Atia; Vigneron and Guillon.

[5]Kobayashi, Fukuoka, and Yoshida; Zaki and Atia; Vigneron and Guillon.

[6]Bolle.

second method. However, the first method has the grave disadvantage of producing a highly ill-conditioned characteristic matrix. The characteristic matrix of the second method is much better conditioned than that of the first method and is the preferred method for numerical computation of the eigenfrequencies. Analytical expressions for both methods will be given here and numerical comparisons between them will be made in Chapter 9.

4.5.2 Field Equations for Generalized Axial Dependence

At the conclusion of the derivation of the characteristic equation for the coaxially loaded waveguide, it was briefly mentioned that the mode coefficients vary slightly depending upon which set of eigenfunctions are chosen to represent the axial dependence. Since it is convenient to use various representations for the axial dependence in constructing solutions for the cavity-open type configuration, a generalized form for the fields will be given here that allows for simple conversions between axial representations.

The potentials in regions I and III may be written as

$$\psi^m = T^{I, III} J_n(\lambda_{np}\rho) \cos(n\phi) Z_m^{I, III},$$

$$\psi^e = S^{I, III} J_n(\lambda'_{np}\rho) \sin(n\phi) Z_e^{I, III}.$$

$$(4\text{-}51)$$

Remembering that the origin of coordinates is located at the cavity center half way between the shorting plates, and applying the boundary conditions at the shorting plates, the axial dependences $Z_m^{I, III}$ and $Z_e^{I, III}$ may be written in any of the following pairs,

$$Z_m^{I, III} = e^{-jk_z^I z} + e^{jk_z^I (z \mp L_s)}$$

$$(4\text{-}52)$$

$$Z_e^{I, III} = e^{-jk_z^I z} - e^{jk_z^I (z \mp L_s)}$$

for traveling wave solutions,

$$Z_m^{I,III} = \cos\left[k_z\left(z \mp \frac{L_s}{2}\right)\right]$$

$$Z_e^{I,III} = \sin\left[k_z\left(z \mp \frac{L_s}{2}\right)\right]$$

(4-53)

for standing wave solutions, and

$$Z_m^{I,III} = \cosh\left[jk_z\left(z \mp \frac{L_s}{2}\right)\right]$$

$$Z_e^{I,III} = \sinh\left[jk_z\left(z \mp \frac{L_s}{2}\right)\right]$$

(4-54)

for hyperbolic solutions. We also introduce the constants $\xi_m^{I,III}$ and $\xi_e^{I,III}$, where

$\xi_m = -\xi_e = -1$	standing waves
$\xi_m = \xi_e = -j$	traveling waves
$\xi_m = \xi_e = j$	hyperbolic waves.

(4-55)

It may shown that

$$\frac{\partial Z_m}{\partial z} = \xi_m k_z Z_e \qquad \frac{\partial Z_e}{\partial z} = \xi_e k_z Z_m$$

(4-56)

where $\xi_m \xi_e = -1$.

The TM fields in regions I and III may then be written in the following form,

$$E_\rho^{I,III} = -T^{I,III} \frac{k_z \lambda_{nq}}{\hat\omega \epsilon^{I,III} b} J_n'(\lambda_{nq}\frac{\rho}{b}) \cos(n\phi) \, (j\xi_m^{I,III}) Z_e^{I,III},$$

(4-57)

$$E_\phi^{I,III} = T^{I,III} \frac{k_z}{\hat\omega \epsilon^{I,III}} \frac{n}{\rho} J_n(\lambda_{nq}\frac{\rho}{b}) \sin(n\phi) \, (j\xi_m^{I,III}) Z_e^{I,III},$$

(4-58)

$$E_z^{I, III} = T^{I, III} \frac{1}{j \hat{\omega} \epsilon^{I, III}} \frac{\lambda_{np}^2}{b^2} J_n(\lambda_{nq} \frac{\rho}{b}) \cos(n\phi) Z_m^{I, III}, \tag{4-59}$$

$$H_\rho^{I, III} = -T^{I, III} \frac{n}{\rho} J_n(\lambda_{nq} \frac{\rho}{b}) \sin(n\phi) Z_m^{I, III}, \tag{4-60}$$

$$H_\phi^{I, III} = -T^{I, III} \frac{\lambda_{nq}}{b} J_n'(\lambda_{nq} \frac{\rho}{b}) \cos(n\phi) Z_m^{I, III}, \tag{4-61}$$

$$H_z^{I, III} = 0. \tag{4-62}$$

The TE solutions for $n \neq 0$ may be written as

$$E_\rho^{I, III} = -S^{I, III} \frac{n}{\rho} J_n(\lambda_{nq}' \frac{\rho}{b}) \cos(n\phi) Z_e^{I, III}, \tag{4-63}$$

$$E_\phi^{I, III} = S^{I, III} \frac{\lambda_{nq}'}{b} J_n'(\lambda_{nq}' \frac{\rho}{b}) \sin(n\phi) Z_e^{I, III}, \tag{4-64}$$

$$E_z^{I, III} = 0, \tag{4-65}$$

$$H_\rho^{I, III} = -S^{I, III} \frac{k_z \lambda_{nq}'}{\hat{\omega} \mu^{I, III} b} J_n'(\lambda_{nq}' \frac{\rho}{b}) \sin(n\phi) (j\xi_e^{I, III}) Z_m^{I, III}, \tag{4-66}$$

$$H_\phi^{I, III} = -S^{I, III} \frac{k_z}{\hat{\omega} \mu^{I, III}} \frac{n}{\rho} J_n(\lambda_{nq}' \frac{\rho}{b}) \cos(n\phi) (j\xi_e^{I, III}) Z_m^{I, III}, \tag{4-67}$$

$$H_z^{I, III} = S^{I, III} \frac{1}{j \hat{\omega} \mu^{I, III}} \frac{\lambda_{np}'^2}{b^2} J_n(\lambda_{nq}' \frac{\rho}{b}) \sin(n\phi) Z_e^{I, III}. \tag{4-68}$$

If $n = 0$, all TE components are zero except for E_ϕ, H_ρ, and H_z, which are given by

$$E_\phi^{I,III} = S^{I,III} \frac{\lambda'_{oq}}{b} J'_0(\lambda'_{oq} \frac{\rho}{b}) Z_e^{I,III},$$ (4-69)

$$H_\rho^{I,III} = -S^{I,III} \frac{k_z \lambda'_{oq}}{\hat{\omega}\mu^{I,III} b} J'_0(\lambda'_{oq} \frac{\rho}{b}) (j\xi_e^{I,III}) Z_m^{I,III},$$ (4-70)

$$H_z^{I,III} = S^{I,III} \frac{1}{j\hat{\omega}\mu^{I,III}} \frac{\lambda'^2_{oq}}{b^2} J_0(\lambda'_{oq} \frac{\rho}{b}) Z_e^{I,III}.$$ (4-71)

In region II the generalized form is established by removing the coefficients A, B, C, and D from the radial dependence and investing the variations due to changes in axial dependence in the coefficients of the axial dependences themselves. We write the potentials in region 1 as

$$\psi^m = J_n(k_{\rho 1}\rho) \cos(n\phi) Z_m^A,$$

$$\psi^e = J_n(k_{\rho 1}\rho) \sin(n\phi) Z_e^B,$$ (4-72)

and those in region 2 as

$$\psi^m = \frac{C}{A} F_n(k_{\rho 2}\rho) \cos(n\phi) Z_m^A,$$

$$\psi^e = \frac{D}{B} G_n(k_{\rho 2}\rho) \sin(n\phi) Z_e^B.$$ (4-73)

The general axial dependences for region II, Z_m^A, Z_e^A, Z_m^B, and Z_e^B, are similar to those defined for regions I and III. The functions Z_m^A and Z_e^A are used for the TM formulation, i.e., a formulation which becomes TM for $n=0$. They are

$$Z_m^A = A e^{-j\gamma z} - P e^{j\gamma z}$$

$$Z_e^A = A e^{-j\gamma z} + P e^{j\gamma z}$$

(4-74)

for traveling waves,

$$Z_m^A = A \cos(\gamma z) - P \sin(\gamma z)$$

$$Z_e^A = A \sin(\gamma z) + P \cos(\gamma z)$$

(4-75)

for standing waves, and

$$Z_m^A = A \cosh(j\gamma z) + P \sinh(j\gamma z)$$

$$Z_e^A = A \sinh(j\gamma z) + P \cosh(j\gamma z)$$

(4-76)

for hyperbolic waves. For the TE formulation, i.e., the formulation which becomes TE for $n=0$, the axial functions are transformed by multiplying the TM formulation axial functions by $\dfrac{B}{A}$ to get Z_m^B and Z_e^B. We have

$$Z_m^B = B e^{-j\gamma z} - Q e^{j\gamma z}$$

$$Z_e^B = B e^{-j\gamma z} + Q e^{j\gamma z}$$

(4-77)

for traveling waves,

$$Z_m^B = B \cos(\gamma z) - Q \sin(\gamma z)$$

$$Z_e^B = B \sin(\gamma z) + Q \cos(\gamma z)$$

(4-78)

for standing waves, and

$$Z_m^B = B\cosh(j\gamma z) + Q\sinh(j\gamma z)$$

$$Z_e^B = B\sinh(j\gamma z) + Q\cosh(j\gamma z)$$

(4-79)

for hyperbolic waves, where $Q = \dfrac{BP}{A}$.

Using ξ_m and ξ_e defined above for regions I and III in Equation (4-55) we define the constants B_A, C_A, D_A, A_B, and C_B, which are independent of axial formulation:

$$B_A = \frac{B}{j\xi_m^{\text{II}}A} = n\frac{k_o}{\omega\hat\epsilon_1}\frac{\mu_1}{\mu_o}\sqrt{\frac{G}{F}}\frac{U_n}{V_n}$$

(4-80)

$$C_A = \frac{C}{A} = \frac{\epsilon_2 k_{\rho1}^2 J}{\hat\epsilon_1 k_{\rho2}^2 F}$$

(4-81)

$$D_A = \frac{D}{j\xi_m^{\text{II}}A} = n\frac{k_o}{\omega\hat\epsilon_1}\frac{\mu_2}{\mu_o}\frac{k_{\rho1}^2}{k_{\rho2}^2}\frac{J}{\sqrt{FG}}\frac{U_n}{V_n}$$

(4-82)

$$A_B = \frac{A}{j\xi_e^{\text{II}}B} = n\frac{k_o}{\omega\mu_1}\frac{\hat\epsilon_1}{\epsilon_o}\sqrt{\frac{F}{G}}\frac{U_n}{W_n}$$

(4-83)

$$C_B = \frac{C}{j\xi_e^{\text{II}}B} = n\frac{k_o}{\omega\mu_1}\frac{\epsilon_2}{\epsilon_o}\frac{k_{\rho1}^2}{k_{\rho2}^2}\frac{J}{\sqrt{FG}}\frac{U_n}{W_n}$$

(4-84)

$$D_B = \frac{D}{B} = \frac{\mu_2 k_{\rho1}^2 J}{\mu_1 k_{\rho2}^2 G}.$$

(4-85)

The following relationships may be shown to hold between the above defined constants,

$$B_A = \frac{1}{A_B}$$

$$C_B B_A = C_A \qquad D_B B_A = D_A \tag{4-86}$$

$$C_A A_B = C_B \qquad D_A A_B = D_B .$$

The TM formulation solutions in region 1 can then be written

$$E_{\rho 1} = - \left[\frac{\gamma k_{\rho 1}}{\hat{\omega} \hat{\epsilon}_1} J_n'(k_{\rho 1} \rho) + B_A \frac{n}{\rho} J_n(k_{\rho 1} \rho) \right] \cos(n\phi) \, (j \, \xi_m^{\text{II}}) \, Z_e^A \tag{4-87}$$

$$E_{\phi 1} = \left[\frac{\gamma}{\hat{\omega} \hat{\epsilon}_1} \frac{n}{\rho} J_n(k_{\rho 1} \rho) + B_A k_{\rho 1} J_n'(k_{\rho 1} \rho) \right] \sin(n\phi) \, (j \, \xi_m^{\text{II}}) \, Z_e^A \tag{4-88}$$

$$E_{z 1} = \frac{k_{\rho 1}^2}{j \hat{\omega} \hat{\epsilon}_1} J_n(k_{\rho 1} \rho) \cos(n\phi) \, Z_m^A \tag{4-89}$$

$$H_{\rho 1} = - \left[\frac{n}{\rho} J_n(k_{\rho 1} \rho) + B_A \frac{\gamma k_{\rho 1}}{\hat{\omega} \hat{\mu}_1} J_n'(k_{\rho 1} \rho) \right] \sin(n\phi) \, Z_m^A \tag{4-90}$$

$$H_{\phi 1} = - \left[k_{\rho 1} J_n'(k_{\rho 1} \rho) + B_A \frac{\gamma}{\hat{\omega} \hat{\mu}_1} \frac{n}{\rho} J_n(k_{\rho 1} \rho) \right] \cos(n\phi) \, Z_m^A \tag{4-91}$$

$$H_{z 1} = B_A \frac{k_{\rho 1}^2}{\hat{\omega} \hat{\mu}_1} J_n(k_{\rho 1} \rho) \sin(n\phi) \, \xi_m^{\text{II}} \, Z_e^A . \tag{4-92}$$

The field equations in region 2 are given by

$$E_{\rho 2} = - \left[C_A \frac{\gamma k_{\rho 2}}{\hat{\omega} \hat{\epsilon}_2} F_n'(k_{\rho 2} \rho) + D_A \frac{n}{\rho} G_n(k_{\rho 2} \rho) \right] \cos(n\phi) \, (j\xi_m^{II}) \, Z_e^A \qquad (4\text{-}93)$$

$$E_{\phi 2} = \left[C_A \frac{\gamma}{\hat{\omega} \hat{\epsilon}_2} \frac{n}{\rho} F_n(k_{\rho 2} \rho) + D_A k_{\rho 2} G_n'(k_{\rho 2} \rho) \right] \sin(n\phi) \, (j\xi_m^{II}) \, Z_e^A \qquad (4\text{-}94)$$

$$E_{z2} = C_A \frac{k_{\rho 2}^2}{j\hat{\omega} \hat{\epsilon}_2} F_n(k_{\rho 2} \rho) \cos(n\phi) \, Z_m^A \qquad (4\text{-}95)$$

$$H_{\rho 2} = - \left[C_A \frac{n}{\rho} F_n(k_{\rho 2} \rho) + D_A \frac{\gamma k_{\rho 2}}{\hat{\omega} \hat{\mu}_2} G_n'(k_{\rho 2} \rho) \right] \sin(n\phi) \, Z_m^A \qquad (4\text{-}96)$$

$$H_{\phi 2} = - \left[C_A k_{\rho 2} F_n'(k_{\rho 2} \rho) + D_A \frac{\gamma}{\hat{\omega} \hat{\mu}_2} \frac{n}{\rho} G_n(k_{\rho 2} \rho) \right] \cos(n\phi) \, Z_m^A \qquad (4\text{-}97)$$

$$H_{z2} = D_A \frac{k_{\rho 2}^2}{\hat{\omega} \hat{\mu}_2} G_n(k_{\rho 2} \rho) \sin(n\phi) \, \xi_m^{II} \, Z_e^A . \qquad (4\text{-}98)$$

For $n = 0$ the constants B_A and D_A are zero and these expressions become TM with E_ϕ, H_ρ, and H_z all being zero.

The TE formulation is a simple transformation of the TM formulation by multiplication of the TM formulation fields by $A_B \, B_A = 1$. The TE formulation fields in region 1 for $n \neq 0$ are

$$E_{\rho 1} = - \left[A_B \frac{\gamma k_{\rho 1}}{\hat{\omega} \hat{\epsilon}_1} J_n'(k_{\rho 1} \rho) + \frac{n}{\rho} J_n(k_{\rho 1} \rho) \right] \cos(n\phi) \, Z_e^B \qquad (4\text{-}99)$$

$$E_{\phi 1} = \left[A_B \frac{\gamma}{\hat{\omega}\hat{\epsilon}_1} \frac{n}{\rho} J_n(k_{\rho 1}\rho) + k_{\rho 1} J_n'(k_{\rho 1}\rho) \right] \sin(n\phi) Z_e^B \qquad (4\text{-}100)$$

$$E_{z1} = A_B \frac{k_{\rho 1}^2}{\hat{\omega}\hat{\epsilon}_1} J_n(k_{\rho 1}\rho) \cos(n\phi) \xi_e^{II} Z_m^B \qquad (4\text{-}101)$$

$$H_{\rho 1} = - \left[A_B \frac{n}{\rho} J_n(k_{\rho 1}\rho) + \frac{\gamma k_{\rho 1}}{\hat{\omega}\hat{\mu}_1} J_n'(k_{\rho 1}\rho) \right] \sin(n\phi) (j\xi_e^{II}) Z_m^B \qquad (4\text{-}102)$$

$$H_{\phi 1} = - \left[A_B k_{\rho 1} J_n'(k_{\rho 1}\rho) + \frac{\gamma}{\hat{\omega}\hat{\mu}_1} \frac{n}{\rho} J_n(k_{\rho 1}\rho) \right] \cos(n\phi) (j\xi_e^{II}) Z_m^B \qquad (4\text{-}103)$$

$$H_{z1} = \frac{k_{\rho 1}^2}{j\hat{\omega}\hat{\mu}_1} J_n(k_{\rho 1}\rho) \sin(n\phi) Z_e^B . \qquad (4\text{-}104)$$

For $n=0$ the constant A_B is zero and these expressions become TE with E_ρ, E_z, and H_ϕ all being zero. E_ϕ, H_ρ, and H_z are given by

$$E_{\phi 1} = k_{\rho 1} J_0'(k_{\rho 1}\rho) Z_e^B , \qquad (4\text{-}105)$$

$$H_{\rho 1} = - \frac{\gamma k_{\rho 1}}{\hat{\omega}\hat{\mu}_1} J_0'(k_{\rho 1}\rho) (j\xi_e^{II}) Z_m^B , \qquad (4\text{-}106)$$

$$H_{z1} = \frac{k_{\rho 1}^2}{j\hat{\omega}\hat{\mu}_1} J_0(k_{\rho 1}\rho) Z_e^B . \qquad (4\text{-}107)$$

The fields in region 2 for $n \neq 0$ may be written

$$E_{\rho 2} = -\left[C_B \frac{\gamma k_{\rho 2}}{\hat{\omega}\hat{\epsilon}_2} F_n'(k_{\rho 2}\rho) + D_B \frac{n}{\rho} G_n(k_{\rho 2}\rho) \right] \cos(n\phi)\, Z_e^B \qquad (4\text{-}108)$$

$$E_{\phi 2} = \left[C_B \frac{\gamma}{\hat{\omega}\hat{\epsilon}_2} \frac{n}{\rho} F_n(k_{\rho 2}\rho) + D_B k_{\rho 2} G_n'(k_{\rho 2}\rho) \right] \sin(n\phi)\, Z_e^B \qquad (4\text{-}109)$$

$$E_{z 2} = C_B \frac{k_{\rho 2}^2}{\hat{\omega}\hat{\epsilon}_2} F_n(k_{\rho 2}\rho) \cos(n\phi)\, \xi_e^{\Pi}\, Z_m^B \qquad (4\text{-}110)$$

$$H_{\rho 2} = -\left[C_B \frac{n}{\rho} F_n(k_{\rho 2}\rho) + D_B \frac{\gamma k_{\rho 2}}{\hat{\omega}\hat{\mu}_2} G_n'(k_{\rho 2}\rho) \right] \sin(n\phi)\, (j\xi_e^{\Pi})\, Z_m^B \qquad (4\text{-}111)$$

$$H_{\phi 2} = -\left[C_B k_{\rho 2} F_n'(k_{\rho 2}\rho) + D_B \frac{\gamma}{\hat{\omega}\hat{\mu}_2} \frac{n}{\rho} G_n(k_{\rho 2}\rho) \right] \cos(n\phi)\, (j\xi_e^{\Pi})\, Z_m^B \qquad (4\text{-}112)$$

$$H_{z 2} = D_B \frac{k_{\rho 2}^2}{j\hat{\omega}\hat{\mu}_2} G_n(k_{\rho 2}\rho) \sin(n\phi)\, Z_e^B \;. \qquad (4\text{-}113)$$

For $n = 0$ the constant C_B is zero and these expressions become TE with E_ρ, E_z, and H_ϕ all being zero. E_ϕ, H_ρ, and H_z are given by

$$E_{\phi 2} = D_B k_{\rho 2} G_o'(k_{\rho 2}\rho)\, Z_e^B \;, \qquad (4\text{-}114)$$

$$H_{\rho 2} = -D_B \frac{\gamma k_{\rho 2}}{\hat{\omega}\hat{\mu}_2} G_o'(k_{\rho 2}\rho)\, (j\xi_e^{\Pi})\, Z_m^B \;, \qquad (4\text{-}115)$$

$$H_{z 2} = D_B \frac{k_{\rho 2}^2}{j\omega\hat{\mu}_2} G_o(k_{\rho 2}\rho)\, Z_e^B \;. \qquad (4\text{-}116)$$

4.5.3 Characteristic Equation: Method I

In regions I and III, the homogeneously filled waveguide regions, the series expansion of the modal fields must be given by a series of both TM and TE modes. However, after the proper field components have been matched across the boundary at region II, both sides of the matching equation will be orthogonalized by one homogeneously filled waveguide mode, either a TM or a TE mode. If a TM mode is used to orthogonalize the equation, then the series of TE modes on the region I or III side of the equation will drop out according to Equation (4-117),[7]

$$\int \int \dot{E}_{t_i}^{TM} \cdot E_{t_j}^{TE} \, ds = 0 \, . \tag{4-117}$$

Similarly, if a TE mode is used to orthogonalize the equation, the series of TM modes on the region I or III side of the equation will drop out. Therefore, for matching purposes, the fields in the homogeneous regions of the cavity may be represented by a series of TM modes or a series of TE modes. However, when the fields are calculated, both the TM and TE solutions must be included.

The TM series for the electric field components in region I, tangential to the boundary at $z = h - \frac{1}{2}L_s + \frac{1}{2}\ell$, may be written as

$$E_\rho^{I} = \sum_m \sum_q -T_{mq}^{I} \frac{k_z \lambda_{mq}}{\hat{\omega} \epsilon^{I} b} J_m'(\lambda_{mq} \frac{\rho}{b}) \cos(m\phi) \, (j\xi_m^{I}) \, Z_e^{I} \tag{4-118}$$

$$E_\phi^{I} = \sum_m \sum_q T_{mq}^{I} \frac{k_z m}{\hat{\omega} \epsilon^{I} \rho} J_m(\lambda_{mq} \frac{\rho}{b}) \sin(m\phi) \, (j\xi_m^{I}) \, Z_e^{I} \, . \tag{4-119}$$

In region III, for the boundary at $z = h - \frac{1}{2}L_s - \frac{1}{2}\ell$, the equations are

$$E_\rho^{III} = \sum_m \sum_q -T_{mq}^{III} \frac{k_z \lambda_{mq}}{\hat{\omega} \epsilon^{III} b} J_m'(\lambda_{mq} \frac{\rho}{b}) \cos(m\phi) \, (j\xi_m^{III}) \, Z_e^{III} \tag{4-120}$$

---

[7]Harrington, 390.

$$E_\phi^{III} = \sum_m \sum_q T_{mq}^{III} \frac{k_z m}{\hat{\omega} \epsilon^{III} \rho} J_m(\lambda_{mq} \frac{\rho}{b}) \sin(m\phi) (j\xi_m^{III}) Z_e^{III} . \tag{4-121}$$

The tangential fields in region II, which consists of subregion 1 inside the load material ($\rho < a$), and subregion 2 outside the load material ($a < \rho < b$), are represented by modal series expansions as

$$E_{\rho 1}^{II} = \sum_m \sum_i - \left[\frac{\gamma_i k_{\rho 1}}{\hat{\omega} \hat{\epsilon}_1} J'_m(k_{\rho 1}\rho) + B_A \frac{m}{\rho} J_m(k_{\rho 1}\rho) \right] \tag{4-122}$$

$$\times \cos(m\phi) (j\xi_m^{II}) Z_e^A$$

$$E_{\phi 1}^{II} = \sum_m \sum_i \left[\frac{\gamma_i m}{\hat{\omega} \hat{\epsilon}_1 \rho} J_m(k_{\rho 1}\rho) + B_A k_{\rho 1} J'_m(k_{\rho 1}\rho) \right] \tag{4-123}$$

$$\times \sin(m\phi) (j\xi_m^{II}) Z_e^A$$

for subregion 1, and

$$E_{\rho 2}^{II} = \sum_m \sum_i - \left[C_A \frac{\gamma_i k_{\rho 2}}{\hat{\omega} \epsilon_2} F'_m(k_{\rho 2}\rho) + D_A \frac{m}{\rho} G_m(k_{\rho 2}\rho) \right] \tag{4-124}$$

$$\times \cos(m\phi) (j\xi_m^{II}) Z_e^A$$

$$E_{\phi 2}^{II} = \sum_m \sum_i \left[C_A \frac{\gamma_i m}{\hat{\omega} \epsilon_2 \rho} F_m(k_{\rho 2}\rho) + D_A k_{\rho 2} G'_m(k_{\rho 2}\rho) \right] \tag{4-125}$$

$$\times \sin(m\phi) (j\xi_m^{II}) Z_e^A$$

for subregion 2.

At the boundary between regions I and II, $z = h - \frac{1}{2} L_s + \frac{1}{2} \ell$, the fields may be expressed in abbreviated form as

$$E_\rho^I \Bigg|_{z = h - \frac{L_s}{2} + \frac{\ell}{2}} = \sum_m \sum_q E_{\rho m q}^I(\rho) \cos(m\phi) \tag{4-126}$$

$$E_\phi^I \Bigg|_{z = h - \frac{L_s}{2} + \frac{\ell}{2}} = \sum_m \sum_q E_{\phi m q}^I(\rho) \sin(m\phi) \tag{4-127}$$

in region I, and

$$E_\rho^{II} \Bigg|_{z = h - \frac{L_s}{2} + \frac{\ell}{2}} = \sum_m \sum_i E_{\rho m i}^{II^+}(\rho) \cos(m\phi) \tag{4-128}$$

$$E_\phi^{II} \Bigg|_{z = h - \frac{L_s}{2} + \frac{\ell}{2}} = \sum_m \sum_i E_{\phi m i}^{II^+}(\rho) \sin(m\phi) \tag{4-129}$$

in region II. Note that Equations (4-128) and (4-129) for the fields in region II implicitly include both subregions 1 and 2.

Using these abbreviated expressions for the field components, the tangential electric field in region I at the load boundary is given by

$$E_{tan}^I \Bigg|_{z = h - \frac{L_s}{2} + \frac{\ell}{2}} = \sum_m \sum_q \left[\hat{\rho} E_{\rho m q}^I(\rho) \cos(m\phi) + \hat{\phi} E_{\phi m q}^I(\rho) \sin(m\phi) \right]. \tag{4-130}$$

The tangential electric field in region II at the load boundary near region I is given by

$$E_{tan}^{II}\Bigg|_{z=h-\frac{L_s}{2}+\frac{\ell}{2}} = \sum_m \sum_i \left[\hat{\rho}\, E_{\rho mi}^{II^+}(\rho)\cos(m\phi) + \hat{\phi}\, E_{\phi mi}^{II^+}(\rho)\sin(m\phi)\right]. \qquad (4\text{-}131)$$

The boundary condition for continuity of the tangential electric field yields

$$\sum_m \sum_q \left[\hat{\rho}\, E_{\rho mq}^{I}(\rho)\cos(m\phi) + \hat{\phi}\, E_{\phi mq}^{I}(\rho)\sin(m\phi)\right]$$

$$= \sum_m \sum_i \left[\hat{\rho}\, E_{\rho mi}^{II^+}(\rho)\cos(m\phi) + \hat{\phi}\, E_{\phi mi}^{II^+}(\rho)\sin(m\phi)\right]. \qquad (4\text{-}132)$$

As Equation (4-132) demonstrates, equating two infinite series modal expansion representations for the electromagnetic fields results in a cumbersome and complicated expression. Equation (4-132) may be simplified by invoking the property of the orthogonality of the TM modes in region I. This property is expressed for both TM and TE modes by the following equations:[8]

$$\int \int E_{t_i}^{TM} \cdot E_{t_j}^{TM}\, ds = 0 \qquad i \neq j$$

$$\int \int E_{t_i}^{TE} \cdot E_{t_j}^{TE}\, ds = 0 \qquad i \neq j. \qquad (4\text{-}133)$$

It is important to remember that these equations hold only for modes in the homogeneous region of the cavity. Using these properties of the modes, the series expression for the fields in the homogeneous region may be reduced to a single term, making it possible to write the boundary condition equations in a more tractable form.

The transverse part of the electric field of the TM mode used for orthogonalization is

---

[8]Ibid.

$$E_{np}^{TM} = \hat{\rho}\, E_{\rho np}^{\,I}(\rho)\, \cos(n\phi) + \hat{\phi}\, E_{\phi np}^{\,I}(\rho)\, \sin(n\phi).$$ (4-134)

The orthogonalization is accomplished by dotting both sides of Equation (4-132) by the right hand side of Equation (4-134) and integrating over the cross section of the waveguide. The resulting equation is

$$\int_0^b \int_0^{2\pi} \sum_m \sum_q \left[E_{\rho mq}^{\,I}(\rho)\, E_{\rho np}^{\,I}(\rho)\, \cos(m\phi)\cos(n\phi) \right.$$
$$\left. + E_{\phi mq}^{\,I}(\rho)\, E_{\phi np}^{\,I}(\rho)\, \sin(m\phi)\sin(n\phi) \right] \rho\, d\phi\, d\rho$$ (4-135)
$$= \int_0^b \int_0^{2\pi} \sum_m \sum_i \left[E_{\rho mi}^{\,II^+}(\rho)\, E_{\rho np}^{\,I}(\rho)\, \cos(m\phi)\cos(n\phi) \right.$$
$$\left. + E_{\phi mi}^{\,II^+}(\rho)\, E_{\phi np}^{\,I}(\rho)\, \sin(m\phi)\sin(n\phi) \right] \rho\, d\phi\, d\rho.$$

The integration over ϕ eliminates all terms but those where $m = n$, therefore the summation over m disappears on both sides of Equation (4-135). This means that the ϕ-dependence is common to all regions and need no longer be explicitly declared. From now on the n subscripts will be left off in cases other than where it is necessary for correct Bessel function notation.

Furthermore, on the left hand side, the integration over ρ, according to Equations (4-133), eliminates all terms but those where $q = p$. Equation (4-135) may then be written

$$\frac{1}{2} T_p^I \frac{k_z^I}{\epsilon^I} \xi_m^I Z_e^{I^+} \lambda_{np}^2 J_n'^2(\lambda_{np}) = \sum_i \xi_m^{II} Z_e^{A^+} \frac{\gamma_i}{\bar{\epsilon}_1} \left\langle E, e^{TM} \right\rangle_{pi}$$ (4-136)

where $Z_e^{I^+}$ and $Z_e^{A^+}$ are the axial dependences evaluated at $z = z^+ = h - \dfrac{L_s}{2} + \dfrac{\ell}{2}$, and the dimensionless value $\left\langle E, e^{TM} \right\rangle_{pi}$ is found in Equation (C-2) of Appendix C.

The procedure leading to Equation (4-136) may be repeated for the electric field at the boundary between regions II and III and the magnetic fields at the two boundaries. This gives three more equations similar to Equation (4-136),

$$\frac{1}{2} T_p^{\mathrm{I}} Z_m^{\mathrm{I}^+} \lambda_{np}^2 J_n'^2(\lambda_{np}) = \sum_i Z_m^{A^+} \left\langle H, h^{\mathrm{TM}} \right\rangle_{pi}$$

(4-137)

$$\frac{1}{2} T_q^{\mathrm{III}} \frac{k_z^{\mathrm{III}}}{\epsilon^{\mathrm{III}}} \xi_m^{\mathrm{III}} Z_e^{\mathrm{III}^-} \lambda_{nq}^2 J_n'^2(\lambda_{nq}) = \sum_i \xi_m^{\mathrm{II}} Z_e^{A^-} \frac{\gamma_i}{\hat{\epsilon}_1} \left\langle E, e^{\mathrm{TM}} \right\rangle_{qi}$$

(4-138)

$$\frac{1}{2} T_q^{\mathrm{III}} Z_m^{\mathrm{III}^-} \lambda_{nq}^2 J_n'^2(\lambda_{nq}) = \sum_i Z_m^{A^-} \left\langle H, h^{\mathrm{TM}} \right\rangle_{qi}$$

(4-139)

where $Z_m^{\mathrm{I}^+}$ and $Z_m^{A^+}$ are the axial dependences evaluated at $z = z^+ = h - \dfrac{L_s}{2} + \dfrac{\ell}{2}$,

$Z_e^{\mathrm{III}^-}$, $Z_m^{\mathrm{III}^-}$, $Z_e^{A^-}$, and $Z_m^{A^-}$ are the axial dependences evaluated at $z = z^-$, i.e.,

$z = h - \dfrac{L_s}{2} - \dfrac{\ell}{2}$, and the dimensionless value $\left\langle H, h^{TM} \right\rangle_{pi}$ is found in Equation (C-3)

of Appendix C.

In abbreviated form Equations (4-136) through (4-139) may be written,

$$\left\langle e_p^{\mathrm{I}}, e_p^{\mathrm{I}} \right\rangle = \sum_i \left\langle E_i^{\mathrm{II}}, e_p^{\mathrm{I}} \right\rangle .$$

(4-140)

$$\left\langle h_p^{\mathrm{I}}, h_p^{\mathrm{I}} \right\rangle = \sum_i \left\langle H_i^{\mathrm{II}}, h_p^{\mathrm{I}} \right\rangle$$

(4-141)

$$\left\langle e_q^{\mathrm{III}}, e_q^{\mathrm{III}} \right\rangle = \sum_i \left\langle E_i^{\mathrm{II}}, e_q^{\mathrm{III}} \right\rangle$$

(4-142)

$$\left\langle h_q^{\mathrm{III}}, h_q^{\mathrm{III}} \right\rangle = \sum_i \left\langle H_i^{\mathrm{II}}, h_q^{\mathrm{III}} \right\rangle$$

(4-143)

These may be combined into two homogeneous equations which are given by

$$0 = \sum_i \left[\langle H_i^{\text{II}}, h_p^{\text{I}} \rangle \langle e_p^{\text{I}}, e_p^{\text{I}} \rangle - \langle E_i^{\text{II}}, e_p^{\text{I}} \rangle \langle h_p^{\text{I}}, h_p^{\text{I}} \rangle \right]$$

$$0 = \sum_i \left[\langle H_i^{\text{II}}, h_q^{\text{III}} \rangle \langle e_q^{\text{III}}, e_q^{\text{III}} \rangle - \langle E_i^{\text{II}}, e_q^{\text{III}} \rangle \langle h_q^{\text{III}}, h_q^{\text{III}} \rangle \right].$$

(4-144)

These equations actually represent a set of equations since they are true for any choice of the integer variables p and q.

This set of equations may be rewritten as

$$0 = \sum_i \left[A_i X_{pi}^{\text{I}} + P_i Y_{pi}^{\text{I}} \right]$$

$$0 = \sum_i \left[A_i X_{qi}^{\text{III}} + P_i Y_{qi}^{\text{III}} \right],$$

(4-145)

where A_i and P_i are the mode coefficients in region II found in the expressions for

Z_m^A and Z_e^A in Equations (4-74) through (4-76). Equations (4-145) may be expressed in matrix form as

$$\begin{bmatrix} X_{pi}^{\text{I}} & Y_{pi}^{\text{I}} \\ X_{qi}^{\text{III}} & Y_{qi}^{\text{III}} \end{bmatrix} \begin{bmatrix} A_i \\ P_i \end{bmatrix} = 0,$$

(4-146)

where the matrix indices run from 1 to infinity, i as the column index and p and q as row indices.

The characteristic equation for the cavity open-type configuration may now be written down as the zero determinant of the matrix of Equation (4-146):

$$Det \begin{bmatrix} X_{pi}^{\mathrm{I}} & Y_{pi}^{\mathrm{I}} \\ X_{qi}^{\mathrm{III}} & Y_{qi}^{\mathrm{III}} \end{bmatrix} = 0. \tag{4-147}$$

This determinant is a function of two variables, usually the real and imaginary parts of the complex frequency, $\hat{\omega}$. However, any two independent quantities or components of independent complex quantities may be used as the zero-finding variable, e.g., the real and imaginary parts of the complex dielectric constant when a complex value for $\hat{\omega}$ has been specified, or the imaginary part of the complex dielectric constant and the real part of the complex frequency when the real part of the dielectric constant and imaginary part of the frequency have been specified. The second of these examples may be useful in an instance when properties of a load material are being sought to produce a certain cavity quality factor for a given resonant frequency and mode.

For numerical computation of the eigenvalues the infinite matrix of Equations (4-146) and (4-147) must be truncated. This is equivalent to limiting the summations of Equation (4-145) to a finite number of terms. The number of terms or matrix elements is determined by the convergence of the eigenvalue for different matrix sizes. The procedure is to solve for the eigenvalue using a given matrix size. Then the matrix size is augmented and a new value for the eigenvalue is found. If after several iterations the eigenvalue is unaltered to a given precision, the eigenvalue is presumed determined to that precision.

It should be noted that the truncation process may eliminate selected modes and need not eliminate only those which are of highest order. In other words, referring to Equation (4-147), the truncation need not eliminate only terms for p and i greater than a certain value. Certain modes may be eliminated or included by choosing only selected values of p and i. As an example, suppose a solution were desired for ϕ-symmetric modes using TM_{01}, TM_{03}, and TM_{08} in region I, TM_{02}, TM_{04}, and TM_{05} in region III, and TM_{01}, TM_{02}, and TM_{09} in region II. With $n = 0$ implicit, the characteristic matrix would be

$$
\begin{bmatrix}
X_{11}^{I} & X_{12}^{I} & X_{19}^{I} & Y_{11}^{I} & Y_{12}^{I} & Y_{19}^{I} \\
X_{31}^{I} & X_{32}^{I} & X_{39}^{I} & Y_{31}^{I} & Y_{32}^{I} & Y_{39}^{I} \\
X_{81}^{I} & X_{82}^{I} & X_{89}^{I} & Y_{81}^{I} & Y_{82}^{I} & Y_{89}^{I} \\
X_{21}^{III} & X_{22}^{III} & X_{29}^{III} & Y_{21}^{III} & Y_{22}^{III} & Y_{29}^{III} \\
X_{41}^{III} & X_{42}^{III} & X_{49}^{III} & Y_{41}^{III} & Y_{42}^{III} & Y_{49}^{III} \\
X_{51}^{III} & X_{52}^{III} & X_{59}^{III} & Y_{51}^{III} & Y_{52}^{III} & Y_{59}^{III}
\end{bmatrix}
\qquad (4\text{-}148)
$$

It now remains to present the expressions for X_{pi}^{I}, Y_{pi}^{I}, X_{qi}^{III}, and Y_{qi}^{III}. In order to take advantage of the general axial formulations the axial representations must be expressed explicitly as

$$
Z_m^A = A\,\eta(\gamma z) + P\,\varphi(\gamma z)
$$

$$
Z_e^A = A\,\frac{\eta'(\gamma z)}{\xi_m^{II}} + P\,\frac{\varphi'(\gamma z)}{\xi_m^{II}}. \qquad (4\text{-}149)
$$

The expressions for X_{pi}^{I}, Y_{pi}^{I}, X_{qi}^{III}, and Y_{qi}^{III} are presented below in Equations (4-150) through (4-153). To arrive at these expressions, it is necessary to perform several non-standard integrations of products of Bessel's functions. Formulas for These integrals are found in Appendix A.

$$
X_{pi}^{I} = \eta'(\gamma_i z^{+})\frac{\gamma_i}{\bar{\epsilon}_1} Z_{m_p}^{I^+}\left\langle E, e^{TM}\right\rangle_{pi} - \eta(\gamma_i z^{+})\frac{k_{z_p}^{I}}{\epsilon^{I}}\xi_m^{I} Z_{e_p}^{I^+}\left\langle H, h^{TM}\right\rangle_{pi} \qquad (4\text{-}150)
$$

$$Y_{pi}^{I} = \varphi'(\gamma_i z^+) \frac{\gamma_i}{\hat{\epsilon}_1} Z_{m_p}^{I^+} \left\langle E, e^{TM} \right\rangle_{pi} - \varphi(\gamma_i z^+) \frac{k_{z_p}^{I}}{\epsilon^{I}} \xi_m^{I} Z_{e_p}^{I^+} \left\langle H, h^{TM} \right\rangle_{pi} \qquad (4\text{-}151)$$

$$X_{qi}^{III} = \eta'(\gamma_i z^-) \frac{\gamma_i}{\hat{\epsilon}_1} Z_{m_q}^{III^-} \left\langle E, e^{TM} \right\rangle_{qi} - \eta(\gamma_i z^-) \frac{k_{z_q}^{III}}{\epsilon^{III}} \xi_m^{III} Z_{e_q}^{III^-} \left\langle H, h^{TM} \right\rangle_{qi} \qquad (4\text{-}152)$$

$$Y_{qi}^{III} = \varphi'(\gamma_i z^-) \frac{\gamma_i}{\hat{\epsilon}_1} Z_{m_q}^{III^-} \left\langle E, e^{TM} \right\rangle_{qi} - \varphi(\gamma_i z^-) \frac{k_{z_q}^{III}}{\epsilon^{III}} \xi_m^{III} Z_{e_q}^{III^-} \left\langle H, h^{TM} \right\rangle_{qi} \qquad (4\text{-}153)$$

where z^-, z^+, $Z_{e_q}^{I^+}$, $Z_{m_q}^{I^+}$, $Z_{e_q}^{III^-}$, and $Z_{m_q}^{III^-}$ are defined on page 52 and $\left\langle E, e^{TM} \right\rangle_{pi}$

and $\left\langle H, h^{TM} \right\rangle_{pi}$ are defined in Appendix C in Equations (C-2) and (C-3).

ϵ^{I} and ϵ^{III} are the dielectric constants in regions I and III respectively; the

dielectric constants in region II are $\hat{\epsilon}_1$ and ϵ_2 in subregions 1 and 2 respectively.

The axial wavenumbers in regions I and III are given by

$$k_{z_p}^{I} = \sqrt{\hat{\omega}^2 \mu^{I} \epsilon^{I} - \frac{\lambda_{np}^2}{b^2}} \qquad (4\text{-}154)$$

and

$$k_{z_q}^{III} = \sqrt{\hat{\omega}^2 \mu^{III} \epsilon^{III} - \frac{\lambda_{nq}^2}{b^2}}\, , \qquad (4\text{-}155)$$

with the axial wavenumber in region II given by

$$\gamma_i = \sqrt{\hat{\omega}^2 \mu_2 \epsilon_2 - k_{\rho 2}^2}\, . \qquad (4\text{-}156)$$

Further, it should be remembered that the values of $k_{\rho 1}$, $k_{\rho 2}$, and γ are linked by

Equation (3-92) which ensures the matching of the boundary conditions at $\rho = a$ in region II.

It is of interest to note that for the ϕ-symmetric case, $n = 0$, the third terms of Equations (C-2) and (C-3) of Appendix C disappear. These terms are the contributions from the TE portions of the fields in region II. This implies that for the ϕ-symmetric case, TM modes in regions I and III match to purely TM modes in region II. Below it is shown that the same is true for ϕ-symmetric TE modes, i.e., ϕ-symmetric TE modes in regions I and III match to purely TE modes in region II.

In order to examine the effect of TE modes in regions I and III it is necessary to orthogonalize the mode-matching equation by a homogeneously filled waveguide TE mode. This provides an alternate set of equations for determining the eigenvalues of the non-ϕ-symmetric modes of the cavity-open type configuration. For the ϕ-symmetric case, TE orthogonalization provides the only means of obtaining TE eigenvalues. The procedure is the same as that outlined above for TM modes, but the matrix elements are different from those given in Equations (4-150) through (4-153). Also, the coefficient vector is written in terms of B_i and Q_i instead of A_i and P_i.

The TE-orthogonalized field matching equations, corresponding to Equations (4-136) through (4-139) for TM orthogonalization, are

$$\frac{1}{2} S_p^{I} Z_e^{I^{+}} (\lambda_{np}'^2 - n^2) J_n^2(\lambda_{np}') = \sum_i Z_e^{B^{+}} \left\langle E, e^{TE} \right\rangle_{pi} \tag{4-157}$$

$$\frac{1}{2} S_p^{I} \frac{k_z^{I}}{\mu^{I}} \xi_e^{I} Z_m^{I^{+}} (\lambda_{np}'^2 - n^2) J_n^2(\lambda_{np}') = \sum_i \xi_e^{II} Z_m^{B^{+}} \frac{\gamma_i}{\mu_1} \left\langle H, h^{TE} \right\rangle_{pi} \tag{4-158}$$

$$\frac{1}{2} S_q^{III} Z_e^{III^{-}} (\lambda_{nq}'^2 - n^2) J_n^2(\lambda_{nq}') = \sum_i Z_e^{B^{-}} \left\langle E, e^{TE} \right\rangle_{qi} \tag{4-159}$$

$$\frac{1}{2} S_q^{III} \frac{k_z^{III}}{\mu^{III}} \xi_e^{III} Z_m^{III^-} (\lambda_{nq}^{'2} - n^2) J_n^2(\lambda_{nq}') = \sum_i \xi_e^{II} Z_m^{B^-} \frac{\gamma_i}{\mu_1} \langle H, h^{TE} \rangle_{qi}. \quad (4\text{-}160)$$

The TE matrix elements are then written

$$X_{pi}^{I} = \eta'(\gamma z^+) \frac{k_{z_p}^{I}}{\mu^{I}} Z_{h_p}^{I} \langle E, e^{TE} \rangle_{pi} - \eta(\gamma z^+) \frac{\gamma_i}{\mu_1} \xi_m^{I} Z_{e_p}^{I} \langle H, h^{TE} \rangle_{pi} \quad (4\text{-}161)$$

$$Y_{pi}^{I} = \varphi'(\gamma z^+) \frac{k_{z_p}^{I}}{\mu^{I}} Z_{h_p}^{I} \langle E, e^{TE} \rangle_{pi} - \varphi(\gamma z^+) \frac{\gamma_i}{\mu_1} \xi_m^{I} Z_{e_p}^{I} \langle H, h^{TE} \rangle_{pi} \quad (4\text{-}162)$$

$$X_{qi}^{III} = \eta'(\gamma z^-) \frac{k_{z_q}^{III}}{\mu^{III}} Z_{h_q}^{III} \langle E, e^{TE} \rangle_{qi} - \eta(\gamma z^-) \frac{\gamma_i}{\mu_1} \xi_m^{III} Z_{e_q}^{III} \langle H, h^{TE} \rangle_{qi} \quad (4\text{-}163)$$

$$Y_{qi}^{III} = \varphi'(\gamma z^-) \frac{k_{z_q}^{III}}{\mu^{III}} Z_{h_q}^{III} \langle E, e^{TE} \rangle_{qi} - \varphi(\gamma z^-) \frac{\gamma_i}{\mu_1} \xi_m^{III} Z_{e_q}^{III} \langle H, h^{TE} \rangle_{qi} \quad (4\text{-}164)$$

where $\langle E, e^{TE} \rangle_{pi}$ and $\langle H, h^{TE} \rangle_{pi}$ are found in Equations (C-6) and (C-7) of Appendix C.

For TE orthogonalization the abbreviations used for TM orthogonalization remain valid except that the axial wavenumbers in regions I and III become

$$k_{z_p}^{I} = \sqrt{\hat{\omega}^2 \mu^{I} \epsilon^{I} - \frac{\lambda_{np}^{'2}}{b^2}} \quad (4\text{-}165)$$

and

$$k_{z_q}^{\mathrm{III}} = \sqrt{ \hat{\omega}^2 \, \mu^{\mathrm{III}} \, \epsilon^{\mathrm{III}} - \frac{\lambda_{nq}'^2}{b^2} } \; . \qquad (4\text{-}166)$$

Once the eigenvalues have been found, the field coefficients B_i and Q_i may be determined from the TE equation corresponding to Equation (4-146) and the fields may be calculated from Equations (4-99) through (4-116).

For the ϕ-symmetric case, $n = 0$, the third terms of Equations (C-6) and (C-7) of Appendix C disappear. These terms contain the contributions from the TM component of the fields in region II.

4.5.4 Characteristic Equation: Method II

As mentioned above, the matrix of the characteristic equation of Method I is highly ill-conditioned. This conditioning problem arises from the subtraction that takes place in arriving at Equation (4-144) from Equations (4-140) through (4-143). When one value is subtracted from another of much higher order, or if two values which are nearly equal are subtracted from one another, numerical information is lost unless calculations are carried out to high enough precision to track the operation. In the case of Method I, for certain cavity/load configurations and material properties, thirty-two decimal places is not enough to prevent loss of numerical information.

In order to avoid such numerical difficulties it is necessary to formulate a solution which does not require the same subtraction as that of Method I. The method used here, Method II, is similar to that of D. M. Bolle in his work on the cavity-open type problem when the load is a conductor.[9] Instead of using a mode from the homogeneous region of the cavity to orthogonalize both boundary condition equations for a given boundary, one boundary condition equation is orthogonalized by a mode from region II.

The resulting equation leaves coefficients T and S from the field expressions of the homogeneous region inside of a summation. Under Method I, T and S were

---

[9]Bolle.

always outside summations, as in Equations (4-136) and (4-157), and could be subtracted off. Instead of subtracting away the homogeneous field coefficients, explicit expressions for T and S are substituted into the first equation from the other boundary condition equations where T and S are outside summations. From this final equation, from which T and S have been eliminated by substitution, a characteristic matrix may be constructed whose roots are the desired natural frequencies of the system.

If we choose to orthogonalize the E_{tan} equation by a mode from region II, we may start from Equation (4-132) which expresses the continuity of the tangential electric field across the dielectric boundary between regions I and II. Mode orthogonality in non-homogeneous waveguides does not follow Equations (4-133) but must be expressed more generally as[10]

$$\int \int E_{tan_i} \times H_{tan_j} \cdot \hat{z} \, ds = 0 \qquad i \neq j, \qquad (4\text{-}167)$$

where $\hat{z}$ is the axial unit vector. The relationship between Equations (4-133) and Equation (4-167) is discussed further in Appendix B.

Equation (4-167) may be rewritten as

$$\int \int E_{tan_i} \cdot (H_{tan_j} \times \hat{z}) \, ds = 0 \qquad i \neq j. \qquad (4\text{-}168)$$

The orthogonalization vector, i.e., the tangential magnetic field crossed with the axial unit vector in abbreviated form is

$$H_{tan_j}^{II^+} \times \hat{z} = \hat{\rho} \, H_{\phi nj}^{II^+}(\rho) \cos(n\phi) - \hat{\phi} \, H_{\rho nj}^{II^+}(\rho) \sin(n\phi). \qquad (4\text{-}169)$$

Dotting both sides of Equation (4-132) by the right hand side of Equation (4-169) and integrating over the cross section of the cavity yields

---

[10]Collin, *Field Theory of Guided Waves*, 231.

$$\int\limits_{0}^{b} \int\limits_{0}^{2\pi} \sum_{m} \sum_{q} \left[E_{\rho m q}^{I}(\rho)\, H_{\phi n j}^{II^{+}}(\rho)\, \cos(m\phi)\cos(n\phi) \right.$$

$$\left. - E_{\phi m q}^{I}(\rho)\, H_{\rho n j}^{II^{+}}(\rho)\, \sin(m\phi)\sin(n\phi) \right] \rho\, d\phi\, d\rho$$

$$= \int\limits_{0}^{b} \int\limits_{0}^{2\pi} \sum_{m} \sum_{i} \left[E_{\rho m i}^{II^{+}}(\rho)\, H_{\phi n j}^{II^{+}}(\rho)\, \cos(m\phi)\cos(n\phi) \right.$$

(4-170)

$$\left. - E_{\phi m i}^{II^{+}}(\rho)\, H_{\rho n j}^{II^{+}}(\rho)\, \sin(m\phi)\sin(n\phi) \right] \rho\, d\phi\, d\rho \ .$$

The ϕ-dependence integrates away as before, leaving only terms with $m = n$. The integration over ρ, according to Equation (4-168), eliminates all terms on the left hand side but those where $i = j$.[†] The resulting equation is

$$\sum_{q} \left[Z_{e_q}^{I_{TM}^{+}} \xi_{m}^{I_{TM}} T_{q}^{I} \frac{k_{z_q}^{I_{TM}} \hat{\epsilon}_1}{\epsilon^{I}} \left\langle H, h^{TM} \right\rangle_{qj} - j Z_{e_q}^{I_{TE}^{+}} S_{q}^{I} B_{A_j} \frac{\gamma_j \hat{\epsilon}_1}{\mu_1} \left\langle H, h^{TE} \right\rangle_{qj} \right]$$

(4-171)

$$= \xi_{m}^{II} Z_{e_j}^{A^{+}} \gamma_j \left\langle E, H \times \hat{z} \right\rangle_{jj}^{TM}$$

where all notation has been defined previously except for the dimensionless $\left\langle E, H \times \hat{z} \right\rangle_{jj}^{TM}$, which is given in Equation (C-10) of Appendix C.

Equation (4-171) expresses the continuity of the tangential electric field at the boundary between regions I and II. To make use of information from the continuity of the tangential magnetic field, values for T_q^{I} and S_q^{I} are substituted into Equation (4-171) from Equations (4-137) and (4-158). The resulting equation is

---

[†] If the integration is performed with $i \neq j$, the left hand side of the equation contains factors of $V_n W_n - n^2 U_n^2$, referring to Equation (3-92). Equation (3-92) is the characteristic equation for the coaxially loaded region, i.e., $V_n W_n - n^2 U_n^2$ is equal to zero. Therefore only terms with $i = j$ are non-zero.

$$\sum_q \left[\xi_m^{I_{TM}} \frac{Z_{e_q}^{I_{TM}^+}}{Z_{m_q}^{I_{TM}^+}} \frac{k_{z_q}^{I_{TM}} \hat{\epsilon}_1}{\epsilon^I} \frac{\langle H, h^{TM} \rangle_{qj}}{\lambda_{nq}^2 J_n'^2(\lambda_{nq})} \sum_i Z_{m_i}^{A^+} \langle H, h^{TM} \rangle_{qi} \right.$$

$$\left. - \xi_m^{I_{TE}} \frac{Z_{e_q}^{I_{TE}^+}}{Z_{m_q}^{I_{TE}^+}} \frac{\mu^I \hat{\epsilon}_1}{k_{z_q}^{I_{TE}} \mu_1^2} \frac{\gamma_j B_{A_j} \langle H, h^{TE} \rangle_{qj}}{(\lambda_{nq}'^2 - n^2) J_n^2(\lambda_{nq}')} \sum_i B_{A_i} Z_{m_i}^{A^+} \gamma_i \langle H, h^{TE} \rangle_{qi} \right] \qquad (4\text{-}172)$$

$$= \frac{1}{2} \xi_m^{II} Z_{e_j}^{A^+} \gamma_j \langle E, H \times \hat{z} \rangle_{jj}^{TM} .$$

The summation over i is brought outside the summation over q and the equation is rearranged as follows,

$$\sum_i Z_{m_i}^{A^+} \sum_q \left[\xi_m^{I_{TM}} \frac{Z_{e_q}^{I_{TM}^+}}{Z_{m_q}^{I_{TM}^+}} \frac{k_{z_q}^{I_{TM}} \hat{\epsilon}_1}{\epsilon^I} \frac{\langle H, h^{TM} \rangle_{qj} \langle H, h^{TM} \rangle_{qi}}{\lambda_{nq}^2 J_n'^2(\lambda_{nq})} \right.$$

$$\left. - \xi_m^{I_{TE}} \frac{Z_{e_q}^{I_{TE}^+}}{Z_{m_q}^{I_{TE}^+}} \frac{\mu^I \hat{\epsilon}_1}{k_{z_q}^{I_{TE}} \mu_1^2} \frac{\gamma_j \gamma_i B_{A_j} B_{A_i} \langle H, h^{TE} \rangle_{qj} \langle H, h^{TE} \rangle_{qi}}{(\lambda_{nq}'^2 - n^2) J_n^2(\lambda_{nq}')} \right] \qquad (4\text{-}173)$$

$$= \frac{1}{2} \xi_m^{II} Z_{e_j}^{A^+} \gamma_j \langle E, H \times \hat{z} \rangle_{jj}^{TM} .$$

Using a shortened form notation, and taking advantage of the axial representation form given in Equation (4-149) we may write Equation (4-173) as

$$\sum_i (A_i \eta_i + P_i \varphi_i) K_{ji} = \delta_j (A_j \eta_j' + P_j \varphi_j'), \qquad (4\text{-}174)$$

where

$$\delta_j = \frac{1}{2} \gamma_j \langle E, H \times \hat{z} \rangle_{jj}^{TM} \qquad (4\text{-}175)$$

and

$$K_{ji} = K_{ij} = \sum_q \left[\xi_m^{I_{TM}} \frac{Z_{e_q}^{I_{TM}^+}}{Z_{m_q}^{I_{TM}^+}} \frac{k_{z_q}^{I_{TM}} \hat{\epsilon}_1}{\epsilon^I} \frac{\left\langle H,h^{TM}\right\rangle_{qj} \left\langle H,h^{TM}\right\rangle_{qi}}{\lambda_{nq}^2 J_n'^2(\lambda_{nq})} \right.$$

$$\left. - \xi_m^{I_{TE}} \frac{Z_{e_q}^{I_{TE}^+}}{Z_{m_q}^{I_{TE}^+}} \frac{\mu^I \hat{\epsilon}_1}{k_{z_q}^{I_{TE}} \mu_1^2} \frac{\gamma_j \gamma_i B_{A_j} B_{A_i} \left\langle H,h^{TE}\right\rangle_{qj} \left\langle H,h^{TE}\right\rangle_{qi}}{(\lambda_{nq}'^2 - n^2) J_n^2(\lambda_{nq}')} \right] . \tag{4-176}$$

Equation (4-174) represents a set of equations over the integer variable j and can be expressed in matrix form as

$$
\begin{bmatrix}
\dfrac{\delta_1 \eta_1'}{\eta_1} & 0 & 0 & \cdots & \vline & \dfrac{\delta_1 \varphi_1'}{\varphi_1} & 0 & 0 & \cdots \\
0 & \dfrac{\delta_2 \eta_2'}{\eta_2} & 0 & \cdots & \vline & 0 & \dfrac{\delta_2 \varphi_2'}{\varphi_2} & 0 & \cdots \\
0 & 0 & \dfrac{\delta_3 \eta_3'}{\eta_3} & \cdots & \vline & 0 & 0 & \dfrac{\delta_3 \varphi_3'}{\varphi_3} & \cdots \\
\vdots & \vdots & \vdots & \ddots & \vline & \vdots & \vdots & \vdots & \ddots
\end{bmatrix}
\begin{bmatrix}
A_1 \eta_1 \\
A_2 \eta_2 \\
\vdots \\
P_1 \varphi_1 \\
P_2 \varphi_2 \\
\vdots
\end{bmatrix}
$$

$$\tag{4-177}$$

$$
=
\begin{bmatrix}
K_{11} & K_{12} & K_{13} & \cdots & \vline & K_{11} & K_{12} & K_{13} & \cdots \\
K_{21} & K_{22} & K_{23} & \cdots & \vline & K_{21} & K_{22} & K_{23} & \cdots \\
K_{31} & K_{32} & K_{33} & \cdots & \vline & K_{31} & K_{32} & K_{33} & \cdots \\
\vdots & \vdots & \vdots & \ddots & \vline & \vdots & \vdots & \vdots & \ddots
\end{bmatrix}
\begin{bmatrix}
A_1 \eta_1 \\
A_2 \eta_2 \\
\vdots \\
P_1 \varphi_1 \\
P_2 \varphi_2 \\
\vdots
\end{bmatrix}
$$

This is reduced to homogeneous form by subtracting the left hand side from the right hand side. This subtraction is more numerically stable than the one used in the Method I solution. In abbreviated form the matrix equation becomes

$$\left[K_{ji} - I\, \frac{\delta_i \eta_i'}{\eta_i} \;\middle|\; K_{ji} - I\, \frac{\delta_i \varphi_i'}{\varphi_i} \right] \begin{bmatrix} A_i \eta_i \\ P_i \varphi_i \end{bmatrix} = 0, \qquad (4\text{-}178)$$

where I is the identity matrix.

In order to include the boundary conditions at the other end of the rod, it is convenient to write this Equation in slightly different form,

$$\left[K_{ji}\eta_i - I\,\delta_i\eta_i' \;\middle|\; K_{ji}\varphi_i - I\,\delta_i\varphi_i' \right] \begin{bmatrix} A_i \\ P_i \end{bmatrix} = 0. \qquad (4\text{-}179)$$

A similar set of equations is found for the boundary between regions II and III producing a second homogeneous matrix. Both boundaries are included in the same equation by vertical concatenation of the two homogeneous matrix equations to produce

$$\begin{bmatrix} K_{ji}^{I}\eta_i^{+} - I\,\delta_i^{I}\eta_i'^{+} & \bigg| & K_{ji}^{I}\varphi_i^{+} - I\,\delta_i^{I}\varphi_i'^{+} \\[2mm] K_{ji}^{III}\eta_i^{-} - I\,\delta_i^{III}\eta_i'^{-} & \bigg| & K_{ji}^{III}\varphi_i^{-} - I\,\delta_i^{III}\varphi_i'^{-} \end{bmatrix} \begin{bmatrix} A_i \\ P_i \end{bmatrix} = 0. \qquad (4\text{-}180)$$

When $h = \frac{1}{2}\, L_s$, P or A may be set to zero and only the upper left or right submatrix need be considered. In such a case Equation (4-178) should be used if possible since then the characteristic matrix is symmetric. The only reason to use one of the quadrants of the matrix of Equation (4-180) as the characteristic matrix when solving for an image-type configuration would be a singularity in the form found in Equation (4-178).

Equation (4-180) is for orthogonalization of the tangential electric field equation by region II modes, orthogonalization of the tangential magnetic field by region I/III modes. Similar equations may be derived for orthogonalization of the tangential magnetic field equation by region II modes, orthogonalization of the tangential electric field by region I/III modes. In that case the continuity of the tangential magnetic field may be expressed by

$$
\sum_q \left[Z_{m_q}^{I_{TM}^+} T_q^I \gamma_j \left\langle E, e^{TM} \right\rangle_{qj} + j Z_{m_q}^{I_{TE}^+} \xi_e^{I_{TE}} S_q^I B_{A_j} \frac{k_{z_q}^{I_{TE}} \hat{\epsilon}_1}{\mu^I} \left\langle E, e^{TE} \right\rangle_{qj} \right]
$$

$$
= Z_{m_j}^{A^+} \gamma_j \left\langle E, H \times \hat{z} \right\rangle_{jj}^{TM} . \tag{4-181}
$$

Using expressions for T^I and S^I from Equations (4-136) and (4-157), which express the continuity of the tangential electric field, we get the following characteristic equation,

$$
\sum_i Z_{e_i}^{A^+} \sum_q \left[\frac{Z_{m_q}^{I_{TM}^+}}{\xi_m^{I_{TM}} Z_{e_q}^{I_{TM}^+}} \frac{\epsilon^I}{\hat{\epsilon}_1 k_{z_q}^{I_{TM}}} \frac{\gamma_j \gamma_i \left\langle E, e^{TM} \right\rangle_{qj} \left\langle E, e^{TM} \right\rangle_{qi}}{\lambda_{nq}^2 J_n'^2(\lambda_{nq})} \right.
$$

$$
\left. + \frac{Z_{m_q}^{I_{TE}^+}}{Z_{e_q}^{I_{TE}^+}} \frac{\hat{\epsilon}_1 k_{z_q}^{I_{TE}}}{\xi_m^{I_{TE}} \mu^I} \frac{B_{A_j} B_{A_i} \left\langle E, e^{TE} \right\rangle_{qj} \left\langle E, e^{TE} \right\rangle_{qi}}{(\lambda_{nq}'^2 - n^2) J_n^2(\lambda_{nq}')} \right] \tag{4-182}
$$

$$
= \frac{1}{2 \xi_m^{II}} Z_{m_j}^{A^+} \gamma_j \left\langle E, H \times \hat{z} \right\rangle_{jj}^{TM} .
$$

In homogeneous matrix form this set of equations is written as

$$
\left[L_{ji} - I \frac{\delta_i \eta_i}{\eta_i'} \middle| L_{ji} - I \frac{\delta_i \varphi_i}{\varphi_i'} \right] \begin{bmatrix} A_i \eta_i' \\ P_i \varphi_i' \end{bmatrix} = 0, \tag{4-183}
$$

where

$$
L_{ji} = L_{ij} = \sum_q \left[\frac{Z_{m_q}^{I_{TM}^+}}{Z_{e_q}^{I_{TM}^+} \xi_m^{I_{TM}}} \frac{\epsilon^I}{\hat{\epsilon}_1 k_{z_q}^{I_{TM}}} \frac{\gamma_j \gamma_i \left\langle E, e^{TM} \right\rangle_{qj} \left\langle E, e^{TM} \right\rangle_{qi}}{\lambda_{nq}^2 J_n'^2(\lambda_{nq})} \right.
$$

$$
\left. + \frac{Z_{m_q}^{I_{TE}^+}}{Z_{e_q}^{I_{TE}^+} \xi_m^{I_{TE}}} \frac{\hat{\epsilon}_1 k_{z_q}^{I_{TE}}}{\mu^I} \frac{B_{A_j} B_{A_i} \left\langle E, e^{TE} \right\rangle_{qj} \left\langle E, e^{TE} \right\rangle_{qi}}{(\lambda_{nq}'^2 - n^2) J_n^2(\lambda_{nq}')} \right],
$$

(4-184)

and δ_i is given by Equation (4-175). The boundary condition between regions II and III is included in the same manner as before.

When $h = \frac{1}{2} L_s$, P or A may be set to zero and only one partition of the matrix of Equation (4-183) need be considered. If such is the case, solutions may be constructed as even and odd about the cavity center. For even solutions ($P = 0$) it is best to use Equation (4-178) since then the matrix elements will be written in terms of $\tan(\gamma \ell / 2)$ instead of $\cot(\gamma \ell / 2)$. For small sample lengths the cotangent function tends to blow up. The $\tan(\gamma \ell / 2)$ formulation also has the appealing property of creating a diagonal characteristic matrix for small sample lengths. For odd solutions ($A = 0$), it is best to use Equation (4-183) for the same reason.

Finally, it is necessary to consider the $n = 0$ cases. As formulated in Equations (4-173) and (4-182), the solutions become TM by simply setting $n = 0$ in the equations. There are no difficulties with indeterminant forms for $n = 0$ as long as TM solutions are being sought, i.e., $W_0 = 0$, referring to Equation (3-94). However, Equations (4-173) and (4-182) may also be used to find TE solutions for $n = 0$. These solutions may be found by resolving the indeterminant forms which arise when $V_0 = 0$, referring to Equation (3-93). The indeterminant forms are resolved by substituting appropriate values for n, W_n, V_n, and U_n from Equation (3-92) into

Equations (4-173) and (4-182) when indeterminacy arises.[†]

This may appear to be a formidable task, noting the complexity of the equations under consideration. However, there is a simple way of making all necessary substitutions by rewriting Equations (4-173) and (4-182) such that they become TE for $n = 0$ with no indeterminant forms. First, the region II axial dependences are rewritten in TE form, i.e., in terms of coefficients B and Q, using the notation defined in Equations (4-80) through (4-86),

$$Z^A = \frac{A}{B} Z^B = j \xi_e^{II} A_B Z^B . \tag{4-185}$$

Second, both sides of Equations (4-173) and (4-182) are multiplied by A_{B_j}. Equation (4-173) becomes

$$\sum_i Z_{m_i}^{B^+} \sum_q \left[\xi_m^{I_{TM}} \frac{Z_{e_q}^{I_{TM}^+}}{Z_{m_q}^{I_{TM}^+}} \frac{k_{z_q}^{I_{TM}} \hat{\epsilon}_1}{\epsilon^I} \frac{A_{B_j} A_{B_i} \left\langle H, h^{TM} \right\rangle_{qj} \left\langle H, h^{TM} \right\rangle_{qi}}{\lambda_{nq}^2 J_n'^2 (\lambda_{nq})} \right.$$

$$\left. - \xi_m^{I_{TE}} \frac{Z_{e_q}^{I_{TE}^+}}{Z_{m_q}^{I_{TE}^+}} \frac{\mu^I \hat{\epsilon}_1}{k_{z_q}^{I_{TE}} \mu_1^2} \frac{\gamma_j \gamma_i \left\langle H, h^{TE} \right\rangle_{qj} \left\langle H, h^{TE} \right\rangle_{qi}}{(\lambda_{nq}'^2 - n^2) J_n^2 (\lambda_{nq}')} \right] \tag{4-186}$$

$$= \frac{1}{2} \xi_m^{II} Z_{e_j}^{B^+} \gamma_j A_{B_j}^2 \left\langle E, H \times \hat{z} \right\rangle_{jj}^{TM} .$$

It is useful to define the dimensionless constant, $\left\langle E, H \times \hat{z} \right\rangle_{jj}^{TE}$, such that

$$\left\langle E, H \times \hat{z} \right\rangle_{jj}^{TE} = \frac{\mu_1}{\hat{\epsilon}_1} A_{B_j}^2 \left\langle E, H \times \hat{z} \right\rangle_{jj}^{TM} . \tag{4-187}$$

This constant is given explicitly in Equation (C-11) of Appendix C.

[†]The TE formulation for Method I could not be accomplished by simply rewriting the equations according to TE notation in region II. This was because all orthogonalization was performed using eigenvectors from regions I and III.

In matrix form, using this constant, Equation (4-186) is written,

$$\left[M_{ji} - I\, \frac{\theta_i \eta_i'}{\eta_i} \;\middle|\; M_{ji} - I\, \frac{\theta_i \varphi_i'}{\varphi_i} \right] \begin{bmatrix} A_i \eta_i \\ P_i \varphi_i \end{bmatrix} = 0, \qquad (4\text{-}188)$$

where

$$M_{ji} = M_{ij} = \sum_q \left[\xi_m^{\mathrm{I\,TM}} \frac{Z_{e_q}^{\mathrm{I^+_{TM}}}}{Z_{m_q}^{\mathrm{I^+_{TM}}}} \frac{k_{z_q}^{\mathrm{I\,TM}} \mu_1}{\epsilon^{\mathrm{I}}} \frac{A_{B_j} A_{B_i} \left\langle H, h^{\mathrm{TM}} \right\rangle_{qj} \left\langle H, h^{\mathrm{TM}} \right\rangle_{qi}}{\lambda_{nq}^2 J_n'^2(\lambda_{nq})} \right.$$
$$\left. - \xi_m^{\mathrm{I\,TE}} \frac{Z_{e_q}^{\mathrm{I^+_{TE}}}}{Z_{m_q}^{\mathrm{I^+_{TE}}}} \frac{\mu^{\mathrm{I}}}{k_{z_q}^{\mathrm{I\,TE}} \mu_1} \frac{\gamma_j \gamma_i \left\langle H, h^{\mathrm{TE}} \right\rangle_{qj} \left\langle H, h^{\mathrm{TE}} \right\rangle_{qi}}{(\lambda_{nq}'^2 - n^2) J_n^2(\lambda_{nq}')} \right], \qquad (4\text{-}189)$$

and

$$\theta_i = \frac{1}{2}\, \gamma_i \left\langle E, H \times \hat{z} \right\rangle_{ii}^{\mathrm{TE}}. \qquad (4\text{-}190)$$

In a similar manner the matrix form of Equation (4-182) may be written in TE form as

$$\left[N_{ji} - I\, \frac{\theta_i \eta_i}{\eta_i'} \;\middle|\; N_{ji} - I\, \frac{\theta_i \varphi_i}{\varphi_i'} \right] \begin{bmatrix} A_i \eta_i' \\ P_i \varphi_i' \end{bmatrix} = 0, \qquad (4\text{-}191)$$

where

$$N_{ji} = N_{ij} = \sum_q \left[\frac{Z_{m_q}^{I_{TM}^+}}{Z_{e_q}^{I_{TM}^+} \xi_m^{I_{TM}}} \frac{\epsilon^I \mu_1}{\hat{\epsilon}_1^2 k_{z_q}^{I_{TM}}} \frac{\gamma_j \gamma_i A_{B_j} A_{B_i} \left\langle E, e^{TM} \right\rangle_{qj} \left\langle E, e^{TM} \right\rangle_{qi}}{\lambda_{nq}^2 J_n'^2(\lambda_{nq})} \right.$$

$$\left. + \frac{Z_{m_q}^{I_{TE}^+}}{Z_{e_q}^{I_{TE}^+} \xi_m^{I_{TE}}} \frac{\mu_1 k_{z_q}^{I_{TE}}}{\mu^I} \frac{\left\langle E, e^{TE} \right\rangle_{qj} \left\langle E, e^{TE} \right\rangle_{qi}}{(\lambda_{nq}'^2 - n^2) J_n^2(\lambda_{nq}')} \right] \cdot \quad (4\text{-}192)$$

These analytical expressions for the complex natural frequencies will be used and tested in the numerical computations in the Chapters that follow. Method I and Method II expressions will be numerically compared, and as previously mentioned, it will be shown that Method II produces a well-conditioned characteristic matrix whose roots compare well with experimental measurements of the resonant frequency and cavity quality factor for a variety of load types and sizes.

Chapter 5

TM MODE SOLUTION FOR A PERFECTLY CONDUCTING ROD LOAD

5.1 Introduction

The solutions presented in Chapters 3 and 4 have been for dielectric or semi-conducting loads in a perfectly conducting cavity. Presumably, these solutions can be specialized to the case when the load is a perfect conductor by taking the limit as ϵ'' goes to infinity. Solutions for a perfectly conducting rod load would be useful since the cavity-image type configuration with an electric wall would represent a reentrant cavity. No attempt is made here to offer expressions for this limiting case except to say that fields in region 1, referring to Figure 3-2, of the loaded waveguide region must disappear, and that the solutions must become purely TE or purely TM, even for non-ϕ-symmetric modes. Furthermore, care must be taken that matching for H_ϕ has been carried out only in the region for $\rho > a$, where a is the radius of the conducting rod. This is because the currents on the top of the conducting rod are unknown prior to solving for the frequency and the relative contribution of each of the modes.

Examining the characteristic matrices at the end of Chapter 4, and the constants in Appendix C used to define the matrix elements, it must be admitted that it is not immediately obvious how the limiting case appears from the general expressions. That is not to say that the limiting case cannot be extracted from the general case, only that it is probably safer to derive the conducting rod solution from first principles. Since the modes are either TE or TM and the boundary conditions are simpler, solutions for the conducting rod load are much less complicated than for the dielectric load. Furthermore, since there are no losses present, the frequencies are real and all calculations can be carried out using real math.

In fact, a mode-matching solution for the ϕ-symmetric TM modes for the cavity-image type configuration with a conducting rod load was presented as early as 1962. In that year, D. M. Bolle's paper, "Eigenvalues for a Centrally Loaded Circular Cylindrical Cavity," was published in *IRE Transactions on Microwave*

Theory and Techniques.[1] As was discussed in Chapter 2, and mentioned in Chapter 4, Bolle's formulation of the characteristic matrix equation provides the basis for Chapter 4's Method II formulation of the characteristic matrix equation for the dielectric loaded cavity. Unfortunately, for the conducting load which he was analyzing, Bolle erred by omitting the TEM mode contribution in the loaded region of the cavity. This omission caused his numerical solutions to fail in predicting the resonant frequencies for loads in excess of 10% of the cavity length. This Chapter is a reworking of Bolle's solution with the TEM modes included. It is shown that his method actually provides highly accurate solutions for all load lengths from zero to cavity length.

5.2 Field Equations

The cavity is divided into homogeneously-loaded and coaxial waveguide regions, similar to the homogeneously-loaded and coaxially-loaded waveguide regions shown in Figures 4-2, 4-3, and 4-4 of the last Chapter. Figure 5-1 is a drawing of an azimuthal cross section of the cavity-image type configuration with a conducting load. As shown in the Figure, the dielectric constant and magnetic permeability in the homogeneously-loaded waveguide region are ϵ^I and μ^I respectively. The dielectric constant and magnetic permeability of the material between the inner conductor and the cavity wall in the coaxial waveguide region are ϵ^{II} and μ^{II} respectively.

The empty waveguide field equations are given by Equations (4-57) through (4-71). For a coaxial waveguide of inner radius b with a center conductor of radius a, TM mode solutions are given by

$$E_\rho^{II} = -\frac{\gamma}{\omega \epsilon^{II}} \frac{\nu_{np}}{b} F_n'(\frac{\nu_{np}}{b} \rho) \cos(n\phi) j \xi_m^{II} Z_e^A , \qquad (5\text{-}1)$$

---

[1]Bolle.
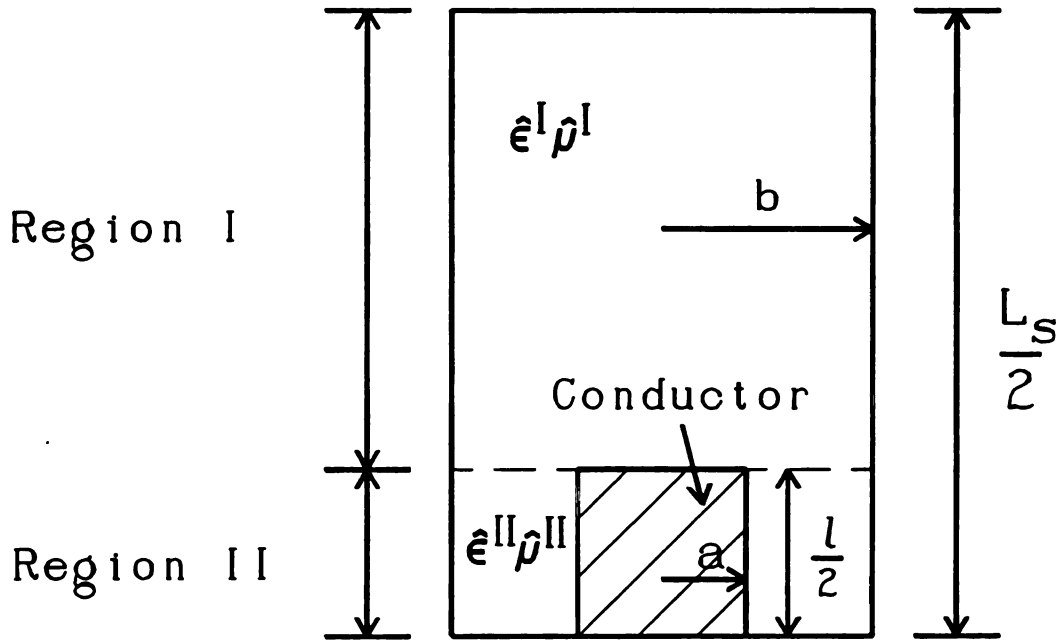
Figure 5-1 Cavity-image type configuration with conducting load.

$$E_\phi^{\rm II} = \frac{\gamma}{\omega\,\epsilon^{\rm II}}\,\frac{n}{\rho}\,{\rm F}_n(\frac{\nu_{np}}{b}\rho)\,\sin(n\phi)\,j\,\xi_m^{\rm II}\,Z_e^A\,, \qquad (5\text{-}2)$$

$$E_z^{\rm II} = \frac{1}{j\,\omega\,\epsilon^{\rm II}}\,\frac{\nu_{np}^2}{b^2}\,{\rm F}_n(\frac{\nu_{np}}{b}\rho)\,\cos(n\phi)\,Z_m^A\,, \qquad (5\text{-}3)$$

$$H_\rho^{\rm II} = -\frac{n}{\rho}\,{\rm F}_n(\frac{\nu_{np}}{b}\rho)\,\sin(n\phi)\,Z_m^A\,, \qquad (5\text{-}4)$$

$$H_\phi^{\rm II} = -\frac{\nu_{np}}{b}\,{\rm F}_n'(\frac{\nu_{np}}{b}\rho)\,\cos(n\phi)\,Z_m^A\,, \qquad (5\text{-}5)$$

$$H_z^{\rm II} = 0\,, \qquad (5\text{-}6)$$

where the axial dependence Z functions are defined by Equations (4-74) through (4-76) and the ξ constants are defined by Equation (4-55). The function F_n is defined by Equation (3-76) of Chapter 3. The constants ν_{np} are the radial wavenumber constants defined by the TM mode characteristic equation,

$$F_n(\frac{\nu_{np}}{b} a) = 0 .$$
(5-7)

These values are independent of frequency and the dielectric properties of the material between the inner conductor and the waveguide wall. They depend only on the ratio of a to b. Since they do not depend on frequency, they are defined in a manner analogous to the Bessel function zeros, λ_{np}.

When $n = 0$, a zero solution exists for ν_{0p}, i.e., $\nu_{00} = 0$. This solution corresponds to the TEM mode. The TEM field expressions may be found as limiting cases of the solutions given above for the TM modes with $n = 0$, $\nu_{00} \rightarrow 0$. The limiting values of the radial dependences are given by

$$\lim_{\nu_{00} \rightarrow 0} \nu_{00}^2 \, F_0(\frac{\nu_{00}}{b} \rho) = 0 ,$$
(5-8)

and

$$\lim_{\nu_{00} \rightarrow 0} \nu_{00} \, F_0'(\frac{\nu_{00}}{b} \rho) = - \frac{2b}{\pi \rho} .$$
(5-9)

Applying these limits to the TM equations above, all field components of the TEM modes disappear except E_ρ and H_ϕ which are given by

$$E_\rho^{II} = \frac{2}{\pi} \sqrt{\frac{\mu^{II}}{\epsilon^{II}}} \, \frac{1}{\rho} j \xi_m^{II} Z_e^A ,$$
(5-10)

$$H_\phi^{II} = \frac{2}{\pi \rho} Z_m^A .$$
(5-11)

The TE solutions are defined for $n \neq 0$ by

$$E_\rho^{\text{II}} = -\frac{n}{\rho} \, G_n(\frac{\zeta_{np}}{b}\rho) \cos(n\phi) \, j \, \xi_m^{\text{II}} \, Z_e^B \,, \tag{5-12}$$

$$E_\phi^{\text{II}} = \frac{\zeta_{np}}{b} \, G_n'(\frac{\zeta_{np}}{b}\rho) \sin(n\phi) \, j \, \xi_m^{\text{II}} \, Z_e^B \,, \tag{5-13}$$

$$E_z^{\text{II}} = 0 \,, \tag{5-14}$$

$$H_\rho^{\text{II}} = -\frac{\gamma}{\omega \mu^{\text{II}}} \, \frac{\zeta_{np}}{b} \, G_n'(\frac{\zeta_{np}}{b}\rho) \sin(n\phi) \, Z_m^B \,, \tag{5-15}$$

$$H_\phi^{\text{II}} = -\frac{\gamma}{\omega \mu^{\text{II}}} \, \frac{n}{\rho} \, G_n(\frac{\zeta_{np}}{b}\rho) \cos(n\phi) \, Z_m^B \,, \tag{5-16}$$

$$H_z^{\text{II}} = \frac{1}{\omega \mu^{\text{II}}} \, \frac{\zeta_{np}^2}{b^2} \, G_n(\frac{\zeta_{np}}{b}\rho) \sin(n\phi) \, \xi_m^{\text{II}} \, Z_e^B \,, \tag{5-17}$$

where the axial dependence Z functions are defined by Equations (4-77) through (4-79) and the function G_n is defined by Equation (3-78) of Chapter 3. The constants ζ_{np} are the radial wavenumber constants defined by the TE mode characteristic equation,

$$G_n'(\frac{\zeta_{np}}{b} a) = 0 \,. \tag{5-18}$$

For $n = 0$, E_ρ, E_z, and H_ϕ are zero with

$$E_\phi^{\text{II}} = \frac{\zeta_{0p}}{b} \, G_0'(\frac{\zeta_{0p}}{b}\rho) \, j \, \xi_m^{\text{II}} \, Z_e^B \,, \tag{5-19}$$

$$H_\rho^{\text{II}} = -\frac{\gamma}{\omega \mu^{\text{II}}} \, \frac{\zeta_{0p}}{b} \, G_0'(\frac{\zeta_{0p}}{b}\rho) \, Z_m^B \,, \tag{5-20}$$

$$H_z^{II} = \frac{1}{\omega \mu^{II}} \frac{\zeta_{0p}^2}{b^2} G_0(\frac{\zeta_{0p}}{b} \rho) \xi_m^{II} Z_e^B .$$

(5-21)

There is no $\zeta_{00} = 0$ solution for the TE modes.

5.3 Mode-Matching Equations for Bolle's Problem

In order to follow Bolle's solution, we consider only the ϕ-symmetric TM modes in a cavity-image type configuration with an electric wall. The field components Bolle used to match at the boundary between region I, the empty waveguide region, and region II, the coaxial waveguide region, were the tangential and normal electric fields, E_ρ and E_z. There is a difficulty with this choice of field components since the TEM mode has no E_z. It is possible to use the E_z component to find the appropriate expression for the non-TEM modes, but it is necessary to consider H_ϕ to get the amplitude coefficient for the TEM mode. The initial choice of these field matching components may be the reason Bolle overlooked the TEM mode contribution. In this analysis the field components used in the matching equations will be E_ρ and H_ϕ.

Using the coordinate system defined by Figure 5-1 with $z = 0$ at the cavity bottom, these field components are expressed in notation similar to Bolle's as

$$E_\rho^I = \sum_{m=1}^{\infty} A_m \beta_m \frac{b}{\lambda_{0m}} J_0'(\frac{\lambda_{0m}}{b} \rho) \frac{\sin[\beta_m(\frac{L_s}{2} - z)]}{\cos[\beta_m(\frac{L_s}{2} - \frac{\ell}{2})]} ,$$

(5-22)

$$H_\phi^I = \sum_{m=1}^{\infty} -A_m j \frac{\omega \epsilon^I b}{\lambda_{0m}} J_0'(\frac{\lambda_{0m}}{b} \rho) \frac{\cos[\beta_m(\frac{L_s}{2} - z)]}{\cos[\beta_m(\frac{L_s}{2} - \frac{\ell}{2})]} ,$$

(5-23)

Bolle	Chapter 5
P_{0m}	λ_{0m}
B_n	$B_n \, \nu_{0n}^2$
Γ_n	γ_n
$Z_0(\alpha x)$	$F_0(\alpha x)$
$Z_1(\alpha x)$	$- F_0'(\alpha x)$
L	$\ell/2$
H	$L_s/2$

Table 5-1 Notation differences between Bolle and Chapter 5.

in region I, where β takes the place of k_z in the notation of Chapters 3 and 4, and L_s and ℓ, as defined in Figure 5-1, are the cavity and load lengths respectively. In region II the fields are

$$E_\rho^{\text{II}} = \sum_{n=0}^{\infty} - B_n \, \gamma_n \, b \, \nu_{0n} \, F_0'(\frac{\nu_{0n}}{b} \rho) \, \frac{\sin(\gamma_n z)}{\cos(\gamma_n \frac{\ell}{2})}, \tag{5-24}$$

$$H_\phi^{\text{II}} = \sum_{n=0}^{\infty} - B_n \, j \, \omega \, \epsilon^{\text{II}} \, b \, \nu_{0n} \, F_0'(\frac{\nu_{0n}}{b} \rho) \, \frac{\cos(\gamma_n z)}{\cos(\gamma_n \frac{\ell}{2})}. \tag{5-25}$$

Table 5-1 provides a list of the minor differences in notation between Chapter 5 and Bolle's paper.

Matching E_ρ equations at $z = \ell/2$, and multiplying by $\rho \, J_0'(\frac{\lambda_{0q}}{b} \rho)$, the following integration may be carried out to simplify the matching equation,

$$\sum_{m=1}^{\infty} A_m \frac{\beta_m b}{\lambda_{0m}} \tan[\frac{\beta_m}{2}(L_s - \ell)] \int_0^b J_0'(\frac{\lambda_{0m}}{b}\rho) J_0'(\frac{\lambda_{0q}}{b}\rho)\rho\, d\rho$$

$$= \sum_{n=0}^{\infty} -B_n \gamma_n b \, \nu_{0n} \tan(\gamma_n \frac{\ell}{2}) \int_a^b F_0'(\frac{\nu_{0n}}{b}\rho) J_0'(\frac{\lambda_{0q}}{b}\rho)\rho\, d\rho \,. \tag{5-26}$$

Since the integral on the left hand side of Equation (5-26) is orthogonal, all terms except the $m = q$ term are zero. The integration for the $m = q$ term is given in Appendix A in Equation (A-30). Similarly, the integration on the right hand side of Equation (5-26) is given by integral identity (A-2) in Appendix A. The resulting equation is

$$-A_q \frac{\beta_q b}{2 a \lambda_{0q}} \tan[\frac{\beta_q}{2}(L_s - \ell)] \frac{J_0'^2(\lambda_{0q})}{J_0(\lambda_{0q}\frac{a}{b})}$$

$$= \sum_{n=0}^{\infty} B_n \gamma_n \tan(\gamma_n \frac{\ell}{2}) \frac{\nu_{0n}\lambda_{0q}}{\nu_{0n}^2 - \lambda_{0q}^2} F_0'(\nu_{0n}\frac{a}{b}) \,. \tag{5-27}$$

The TEM mode is included as the $n = 0$ term. Since $\nu_{00} = 0$, the limit of Equation (5-9) must be used in the calculation of the TEM term. For $n \neq 0$, Equation (5-27) is identical to Bolle's equation (16) with the exception of a minus sign. Bolle carries this sign through the rest of his equations, so it is unlikely to be a misprint. It turns out that if the sign is as written in Equation (5-27) and the TEM mode is left out, the frequency will increase with increasing load length instead of decreasing as expected.

The H_ϕ equations may now be used to provide an expression for the B_n coefficients. For $n = 0$, B_0 may be obtained simply by integrating the mode-matching equation for H_ϕ over ρ from a to b. The integration limits in region I must also be from a to b instead of the usual 0 to b since the currents on the top of the conducting rod are unknown,

$$\int\limits_a^b \left[\sum_{m=1}^{\infty} A_m \frac{\epsilon^I}{\lambda_{0m}} J_0'(\frac{\lambda_{0m}}{b}\rho) \right] d\rho$$

$$\tag{5-28}$$

$$= \int\limits_a^b \left[B_0 \, \epsilon^{II} \left[\frac{-2\,b}{\pi\,\rho} \right] + \sum_{n=1}^{\infty} B_n \, \epsilon^{II} \, \nu_{0n} \, F_0'(\frac{\nu_{0n}}{b}\rho) \right] d\rho \, .$$

The integral in the summation term on the right hand side is zero since

$$F_0(\frac{\nu_{0n}}{b}a) = F_0(\frac{\nu_{0n}}{b}b) = 0. \quad B_0 \text{ is then given by}$$

$$B_0 = \frac{\pi \, \epsilon^I}{2 \, \epsilon^{II}} \frac{1}{\ln \left[\frac{b}{a} \right]} \sum_{m=1}^{\infty} A_m \frac{J_0(\frac{\lambda_{0m}}{b} a)}{\lambda_{0m}^2} \, . \tag{5-29}$$

B_n for $n \neq 0$ is found by equating the H_ϕ field equations from each region at $z = \ell/2$, multiplying by $\rho \, \nu_{0p} \, F_0'(\frac{\nu_{0p}}{b}\rho)$, and integrating over ρ from a to b, i.e.,

$$\sum_{m=1}^{\infty} A_m \frac{\epsilon^I \nu_{0p}}{\lambda_{0m}} \int\limits_a^b J_0'(\frac{\lambda_{0m}}{b}\rho) F_0'(\frac{\nu_{0p}}{b}\rho) \rho \, d\rho$$

$$\tag{5-30}$$

$$= \sum_{n=0}^{\infty} B_n \, \epsilon^{II} \, \nu_{0n} \, \nu_{0p} \int\limits_a^b F_0'(\frac{\nu_{0n}}{b}\rho) F_0'(\frac{\nu_{0p}}{b}\rho) \rho \, d\rho \, .$$

For $p \neq 0$ this reduces to

$$B_p = \frac{\dfrac{2 \, \epsilon^I b}{\nu_{0p} \, \epsilon^{II} a} F_0'(\frac{\nu_{0p}}{b} a)}{\left[\dfrac{b^2}{a^2} F_0'^2(\frac{\nu_{0p}}{b} b) - F_0'^2(\frac{\nu_{0p}}{b} a) \right]} \sum_{m=1}^{\infty} A_m \frac{J_0(\frac{\lambda_{0m}}{b} a)}{\nu_{0p}^2 - \lambda_{0m}^2} \, . \tag{5-31}$$

With $\epsilon^I = \epsilon^{II}$, Equation (5-31) is an identical expression to Bolle's equation (15).

Substituting B_p from Equations (5-29) and (5-31) into Equation (5-27), the characteristic equation is found to be

$$- \frac{1}{4} \frac{\epsilon^{II}}{\epsilon^{I}} A_q \beta_q \tan\left[\frac{\beta_q}{2} (L_s - \ell)\right] \frac{J_0'^2(\lambda_{0q})}{\lambda_{0q}^2}$$

(5-32)

$$= \sum_{n=0}^{\infty} \gamma_n \tan\left(\gamma_n \frac{\ell}{2}\right) Z_n \cdot \sum_{m=1}^{\infty} A_m \frac{J_0(\lambda_{0m}\frac{a}{b}) J_0(\lambda_{0q}\frac{a}{b})}{(\nu_{0n}^2 - \lambda_{0m}^2)(\nu_{0n}^2 - \lambda_{0q}^2)},$$

where

$$Z_n = \begin{cases} \dfrac{1}{2 \ln\left[\dfrac{b}{a}\right]} & n = 0 \\[20pt] \dfrac{F_0'^2(\frac{\nu_{0n}}{b} a)}{\left[\dfrac{b^2}{a^2} F_0'^2(\frac{\nu_{0n}}{b} b) - F_0'^2(\frac{\nu_{0n}}{b} a)\right]} & n \neq 0. \end{cases}$$

(5-33)

For $\epsilon^{I} = \epsilon^{II}$, with the exception of a minus sign and the inclusion of the TEM mode through the $n = 0$ term, Equation (5-32) is Bolle's equation (19).

In a manner similar to that used to derive Equation (4-178) from (4-174), Equation (5-32) may be put into matrix form

$$\lim_{q \to \infty} \begin{bmatrix} (h_{11} - x_1) & h_{12} & \cdots & h_{1q} \\ h_{21} & (h_{22} - x_2) & \cdots & h_{2q} \\ \vdots & \vdots & \ddots & \vdots \\ h_{q1} & h_{q2} & \cdots & (h_{qq} - x_q) \end{bmatrix} \begin{bmatrix} A_1 \\ A_2 \\ \vdots \\ A_q \end{bmatrix} = 0,$$

(5-34)

where

$$x_q = -\frac{1}{4}\frac{\epsilon^{II}}{\epsilon^{I}} \beta_q \tan[\frac{\beta_q}{2}(L_s - \ell)] \frac{J_0'^2(\lambda_{0q})}{\lambda_{0q}^2},$$ (5-35)

$$C_{nmq} = \frac{J_0(\lambda_{0m}\frac{a}{b})J_0(\lambda_{0q}\frac{a}{b})}{(\nu_{0n}^2 - \lambda_{0m}^2)(\nu_{0n}^2 - \lambda_{0q}^2)} = C_{nqm},$$ (5-36)

$$h_{mq} = \sum_{n=0}^{\infty} \gamma_n \tan(\gamma_n \frac{\ell}{2}) Z_n C_{nmq} = h_{qm}.$$ (5-37)

The solutions to Equation (5-34) are the roots of the determinant of the matrix. The matrix of Equation (5-34) is symmetric and becomes diagonal for load lengths approaching zero. For $\ell = 0$ the solutions become

$$\tan(\frac{\beta_q}{2}L_s) = 0,$$ (5-38)

or

$$f_{0qm} = \frac{1}{2\pi\sqrt{\mu\epsilon^{I}}}\sqrt{\left[\frac{2m\pi}{L_s}\right]^2 + \left[\frac{\lambda_{0q}}{b}\right]^2},$$ (5-39)

which are the well-known frequencies of the homogeneously-loaded cavity axially even $TM_{0q(2m)}$ modes.

Bolle demonstrates that the higher order terms in the summation of Equation (5-37) for h_{mq} can be approximated, making numerical calculation of the sum more accurate without requiring a large number of terms in the sum. The higher order terms can be summed using the approximation and added as an error term to the explicit summation of the lower order terms. The error term is calculated by noting that for large n, γ_n is given by

$$\gamma_n = \sqrt{\omega^2 \mu \epsilon^{\text{II}} - \left[\frac{\nu_{0n}}{b}\right]^2} \approx j \frac{\nu_{0n}}{b} . \tag{5-40}$$

Using limiting forms for large arguments of the Bessel functions it may be shown that

$$\nu_{0n} \approx \frac{n \pi b}{b - a} , \tag{5-41}$$

and

$$Z_n \approx \frac{a}{b - a} . \tag{5-42}$$

For large n it is also true that

$$\nu_{0n}^2 - \lambda_{0q}^2 \approx \nu_{0n}^2 . \tag{5-43}$$

Therefore h_{mq} may be written as

$$h_{mq} = \sum_{n=0}^{p} \left[\gamma_n \tan(\gamma_n \frac{\ell}{2}) Z_n C_{nmq} \right] + E_p , \tag{5-44}$$

where

$$E_p \approx \frac{a(b-a)^2}{\pi b^4} J_0(\lambda_{0m} \frac{a}{b}) J_0(\lambda_{0q} \frac{a}{b}) \sum_{n=p+1}^{\infty} \frac{1}{n^3} \tanh \left[\frac{n \pi \ell}{2(a-b)} \right] . \tag{5-45}$$

E_p is independent of the frequency and may be calculated for each load length and matrix element prior to execution of the root-finding algorithm.

5.4 Numerical Solutions

Equation (5-34) was solved numerically for the resonant frequency as a function of load length for 0.5" diameter rods in a 6" diameter cavity. One such solution, with experimental measurement points included, is plotted in Figure 5-2.
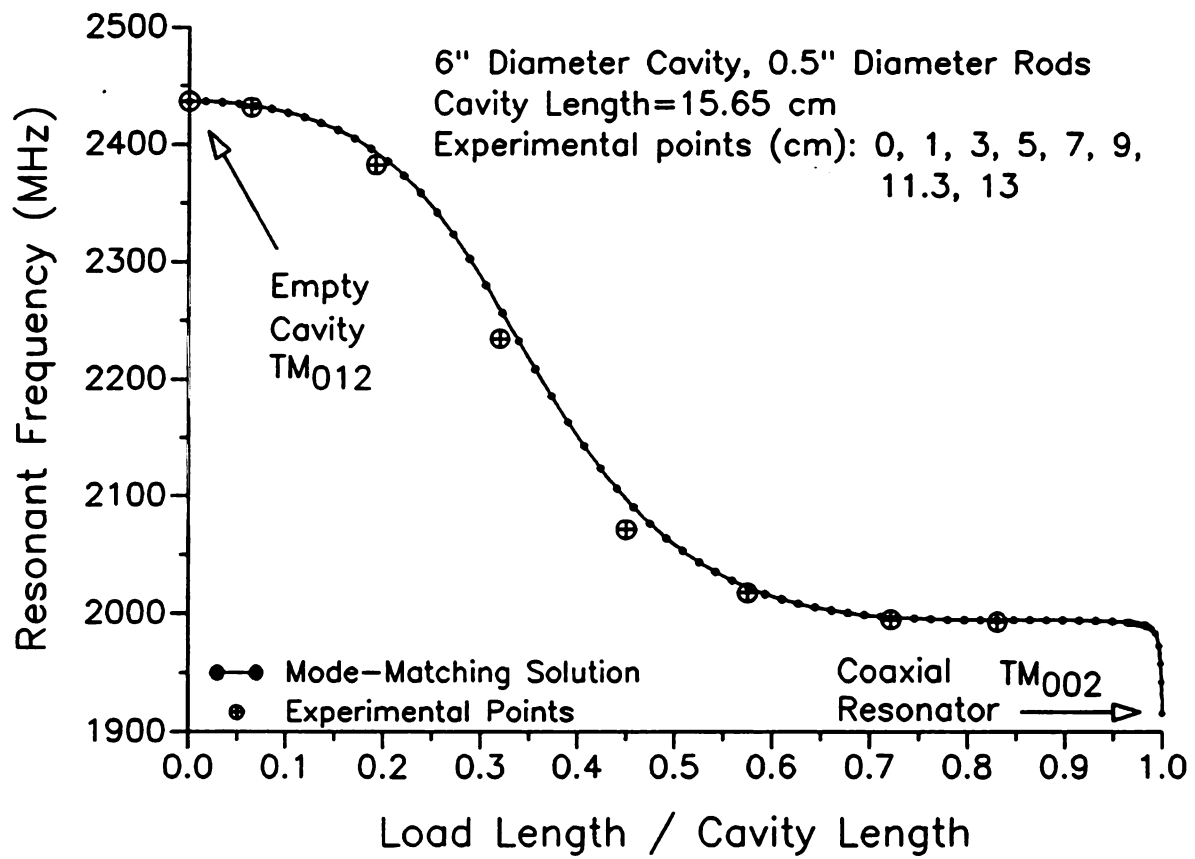
Figure 5-2 f_0 vs. ℓ for $L_s = 15.65\,\text{cm}$ from the empty cavity TM_{012} mode.

Figure 5-2 shows the resonant frequency variation versus load length beginning with the empty cavity TM_{012} mode for $L_s = 15.65$ cm. As the load length increases from zero, the resonant frequency drops from 2.44 GHz, slowly at first, then increasingly as the load length approaches 25% of the cavity length until it is nearly half of the cavity length. As the load length passes 60% of the cavity length, the resonant frequency versus load length becomes nearly level at around 2.0 GHz until the load almost touches the top of the cavity. Just before contact is made, the resonant frequency drops very sharply to 1.916 GHz which corresponds to the coaxial resonator TM_{002} mode. TM_{002} is a TEM mode with an axial dependence similar to that of the empty cavity TM_{012} mode.

As shown in Figure 5-2, the theoretical solution agrees very well with experimental measurements for all load lengths measured, the best agreement being in regions where the resonant frequency changes slowly with load length. The measurements were taken in the 6" diameter cavity shown in Figure 5-3.[2] This cavity is described in detail by Frasch,[3] but its main features are outlined here. The cavity has a sliding top shorting plate with a 1" diameter hole in the center so that materials may be introduced into the cavity. The hole may be plugged or fitted with collars with smaller holes in them. For the measurements shown in Figure 5-2, a collar with a 0.531" diameter hole through the center was used. Also shown in Figure 5-3 are small 2 mm diameter holes in the cavity walls. Small probes, also described by Frasch,[4] may be inserted through the holes so that diagnostic measurements can be taken of the fields near the walls. These holes do not significantly alter the microwave properties of the cavity since their diameter is much smaller than the wavelength of the excitation.

Figure 5-3 also shows the mechanism for coupling power into the cavity. The coupler consists of an adjustable length coaxial probe. For this 6" cavity, the probe

---

[2]The drawing is by Leonard Mahoney.

[3]Frasch, 137-52.

[4]Ibid., 155-57.
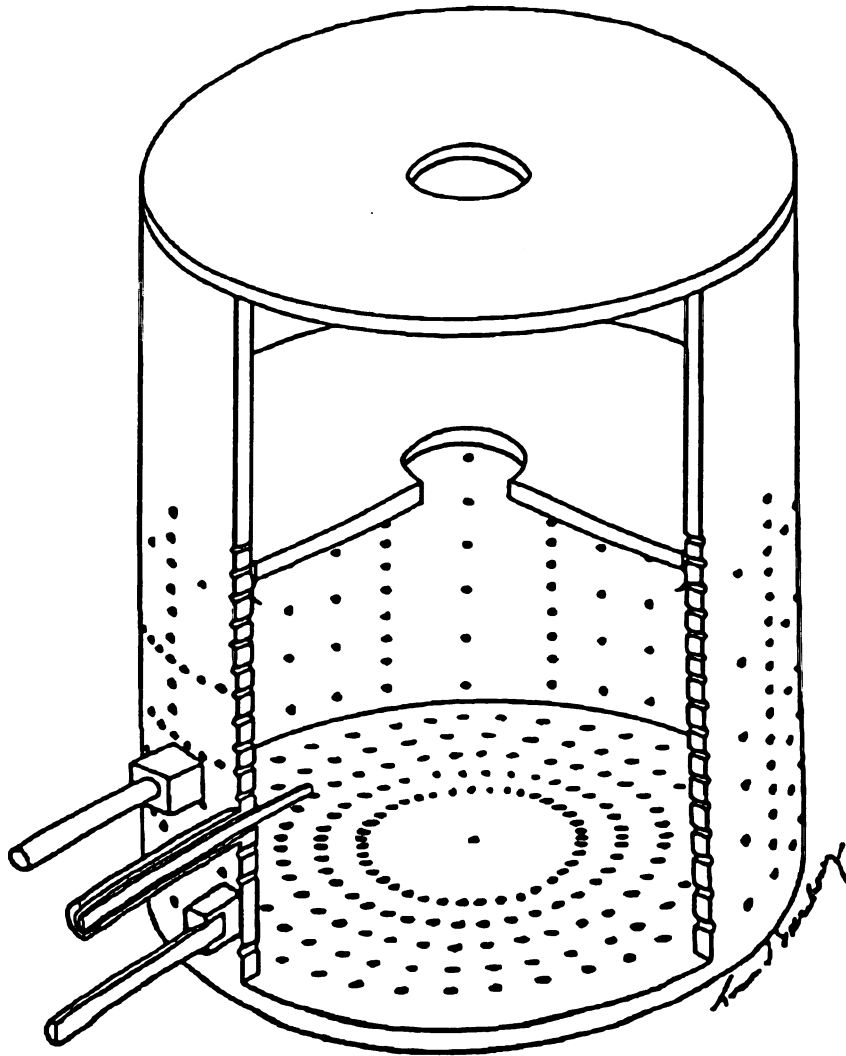
Figure 5-3 Cut-away drawing of the 6" cavity.
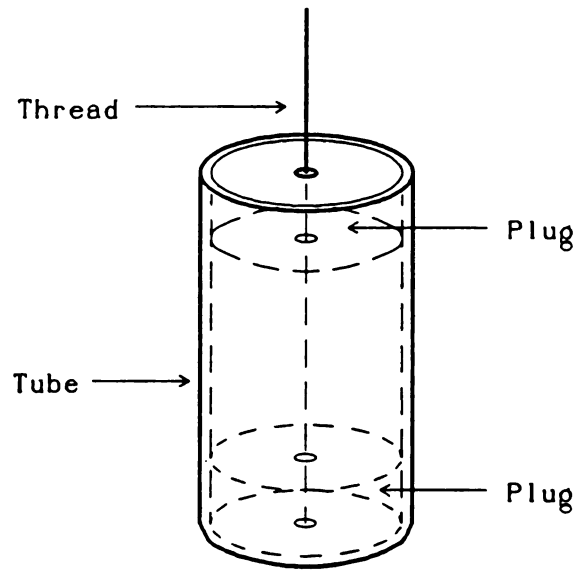
Figure 5-4 Conducting load sample construction.

is relatively small in order not to disturb the fields. The port diameter is 0.67 cm and the diameter of the inner conductor/probe is 0.2 cm. For a given load the probe is adjusted for impedance match at the port so that incident power is coupled into the cavity instead of being reflected at the cavity interface.

Experimental measurements were taken for load lengths of 0 (empty cavity), 1, 3, 5, 7, 9, 11.3, and 13 cm. The loads consisted of 0.5" diameter copper tubes with brass plugs on either end. A schematic drawing of a sample load is shown in Figure 5-4. Tiny holes were drilled through the plugs to allow a thread to be inserted through the entire tube. The threads were tied off on one end so that the tubes could be lowered into the cavity and suspended at the desired location along the cavity axis, in this case the cavity center. Figure 5-5 illustrates how the conducting rods are suspended inside the cavity. Resonant frequencies were measured using a Hewlett Packard 8350-B sweep oscillator with a 2 − 4 GHz plug in unit for the four highest frequency points. The lower frequency resonances were measured using a Hewlett Packard 8720-B network analyzer. The markers on the sweep oscillator are able to measure frequencies to 0.1 MHz, while the network analyzer is capable of measuring frequencies to even greater precision.
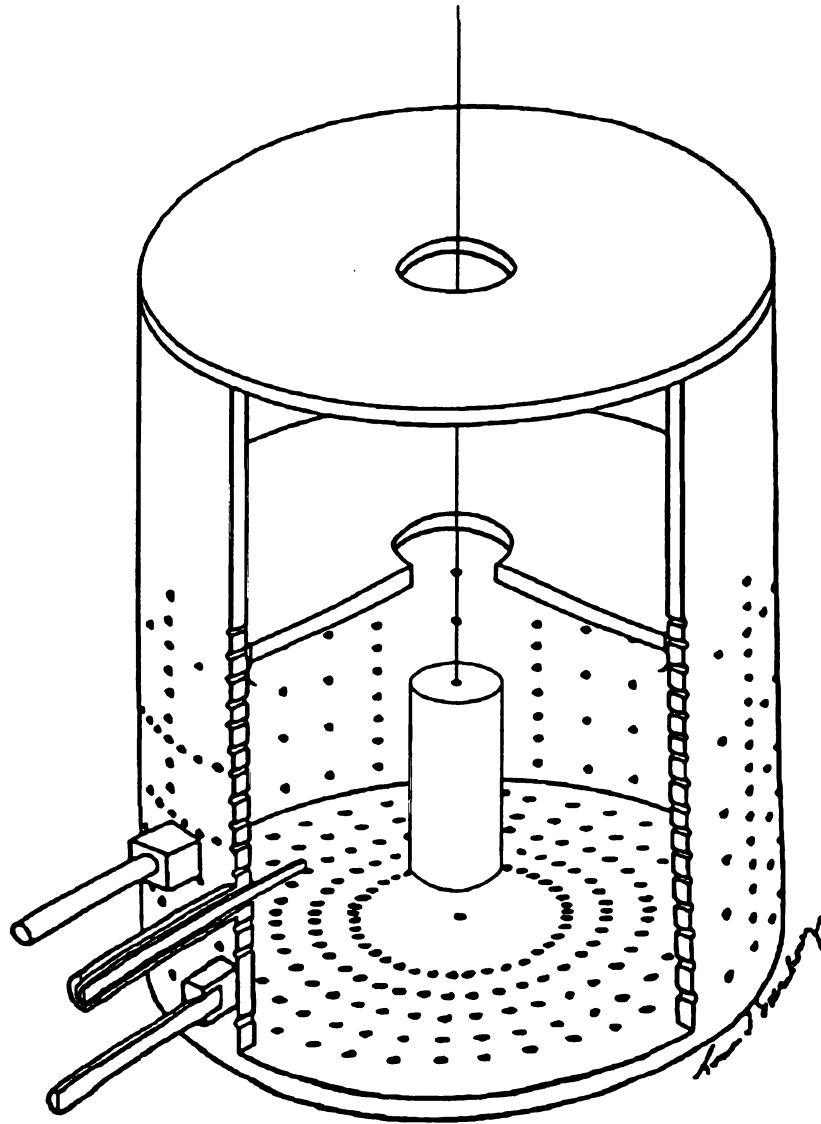
Figure 5-5 6" Cavity loaded with a suspended conducting rod.

Imperfections in the cavity cause its empty cavity resonant frequency to differ slightly from the theoretical value for a given cavity length. In this case the resonant frequency was measured at 2.450 GHz for a cavity length of 15.65 cm. The theoretical value is 2.437 GHz. In order to account for the perturbation due to the non-ideal cavity features, all of the measured values were shifted by -0.013 GHz. That is why the empty cavity measurement matches the theory perfectly in Figure 5-2. It was assumed that a similar shift applies to the other measurements as well.

The number of modes necessary to provide an accurate value of the resonant frequency is determined by convergence. The minimum number of modes such that the addition of more modes does not alter the frequency to a given accuracy is considered the number necessary for convergence to that accuracy. This concept is demonstrated in Figure 5-6 where solutions for the mode of Figure 5-2 are presented for matrix sizes of 1×1, 2×2, 3×3, 5×5, and 25×25. As shown in the Figure, the solution is clearly converging to the one represented by the 25×25 determinant for larger and larger matrices. Eventually, increasing the dimension of the matrix has no effect on the calculated resonant frequency. At that point it may be concluded that convergence has occurred.

It should be remembered that the dimension of the matrix corresponds to the number of modes in the empty waveguide region. The number of terms in the summation in each matrix element corresponds to the number of modes in the coaxial waveguide region. Since it is possible to accurately approximate the higher order terms in the sums, and account for them by adding an error term to the explicitly summation of the lower order terms, the number of terms in the summation is not very important in determining convergence. For all Figures shown, 30 lower order summation terms were calculated explicitly, with an error term added for the higher order terms. It is necessary, therefore, only to consider the number of modes in the empty waveguide region, i.e., the matrix dimensions, when determining convergence. The solution shown in Figure 5-2 is the 25×25 solution of Figure 5-6.

The behavior of the mode shown in Figure 5-2 when the load length is near that of the cavity is shown in a magnified view in Figure 5-7. Figure 5-7 shows that
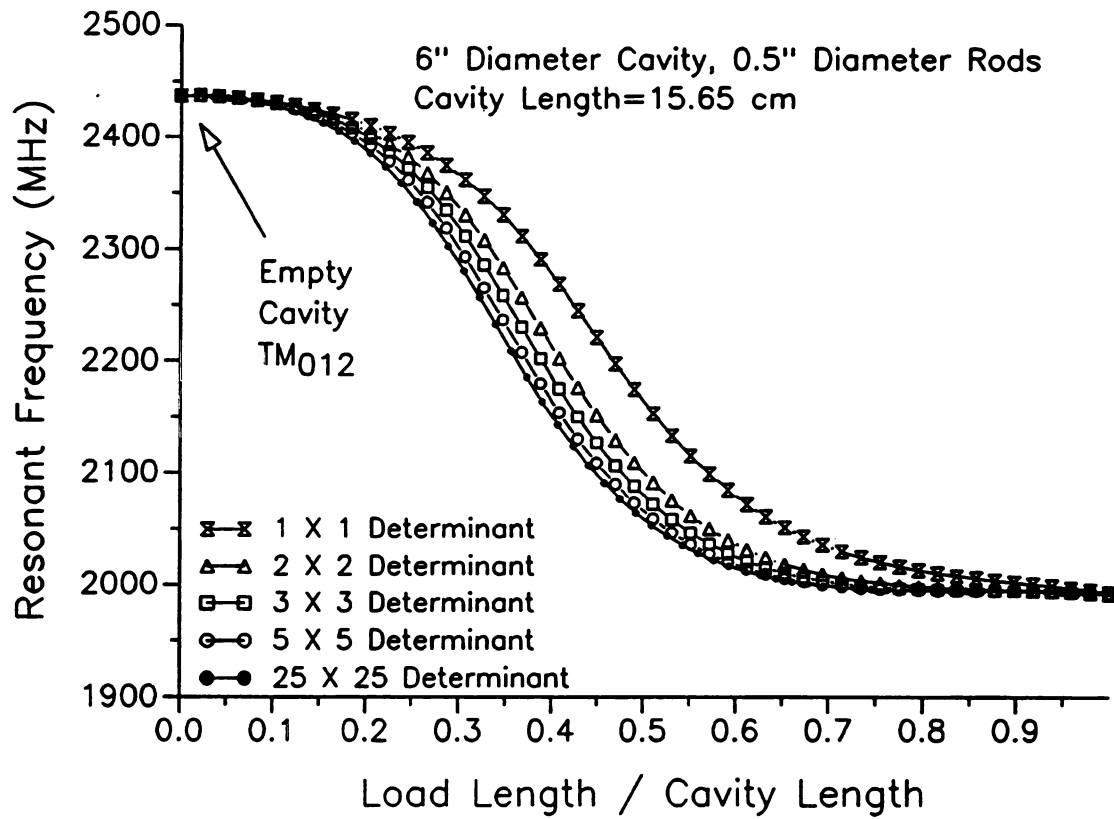
Figure 5-6 Convergence of solutions with matrix size.
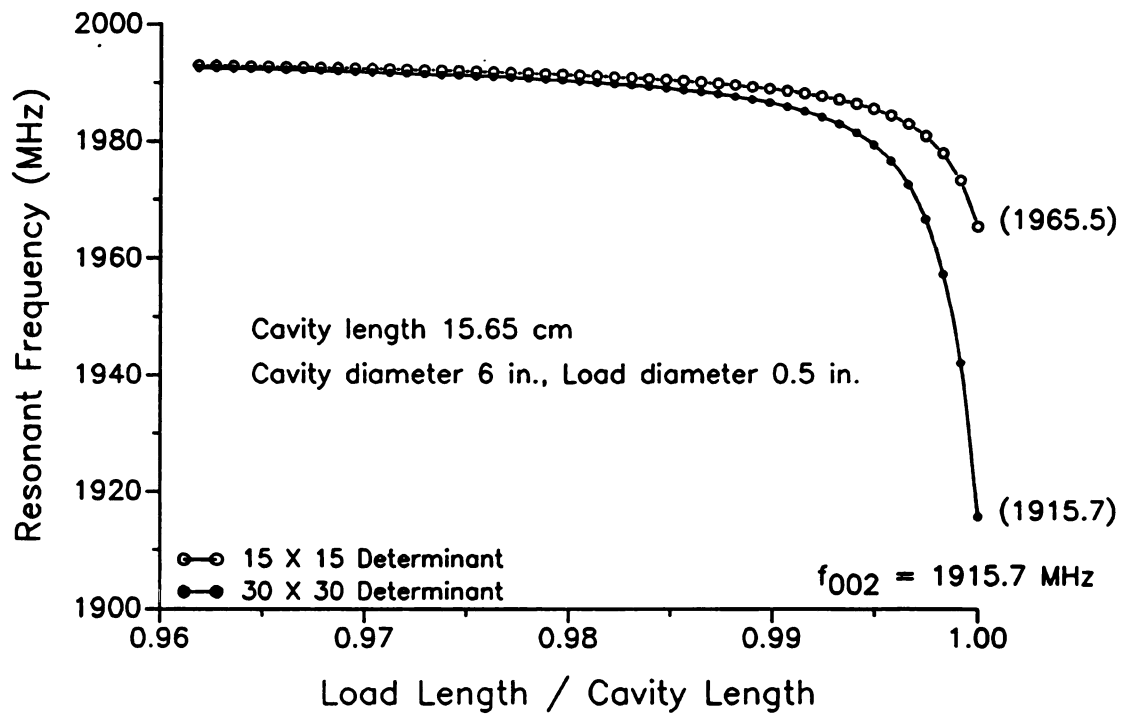
Figure 5-7 Resonant frequency behavior for load lengths near the cavity length.

in this region it is necessary to use a larger matrix size in order to achieve convergence. The 15 x 15 determinant provides nearly the same resonant frequency value as the 30 x 30 determinant when the load length is 97% of the cavity length, but when the load is 99% to 100% of the cavity length, the 15 x 15 determinant embodies too few modes for an accurate solution. The sudden drop in the frequency as the ends of the rod approach the end plates of the cavity, although not always as dramatic as shown in Figures 5-2 and 5-7, is a common feature of the ϕ-symmetric TM modes. This indicates that the capacitance between the ends of the rod and the cavity end plates, thinking of the cavity in terms of its equivalent circuit, becomes large enough to dominate resonant behavior in this region. As the gap between the rod and the end plates shrinks, this effect is enhanced, demonstrated by the increasingly steep slope of the resonant frequency curve as the rod ends approach the cavity shorting plates. Since the resonant frequency of a series or parallel *RLC* circuit is given by

$$\omega_0 = \frac{1}{\sqrt{LC}} ,$$
(5-46)

increasing the capacitance without significantly affecting L will cause a decrease in resonant frequency.

Thinking of the end of the rod and the shorting plate as a parallel plate capacitor, the capacitance is given by

$$C \propto \frac{a^2 \epsilon^1}{L_s - l} .$$
(5-47)

If the explanation given above for the resonant frequency behavior is valid, the frequency drop should occur earlier, i.e., for greater gap lengths, or drop faster when the rod radius is larger. Figure 5-8 shows how the resonant frequency changes when the load radius is increased from 0.635 cm (0.5" diameter) to 0.700 cm. The drop in resonant frequency when the ends of the load approach the shorting plates occurs slightly earlier for the larger load diameter. Also, the fall in resonant frequency is greater overall. Figure 5-9, a magnified view of the high load length region of Figure 5-8, shows this more clearly.
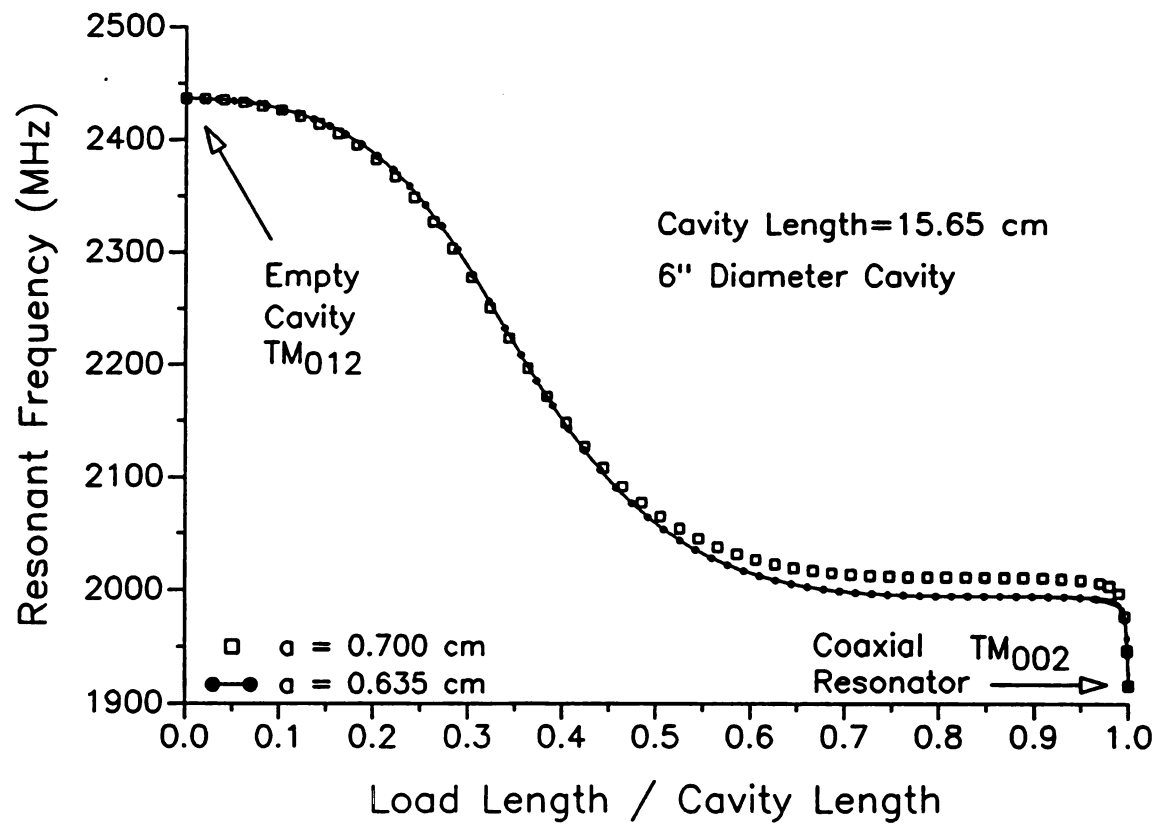
Figure 5-8 Comparison of solutions for $a = 0.635$ and 0.700 cm.
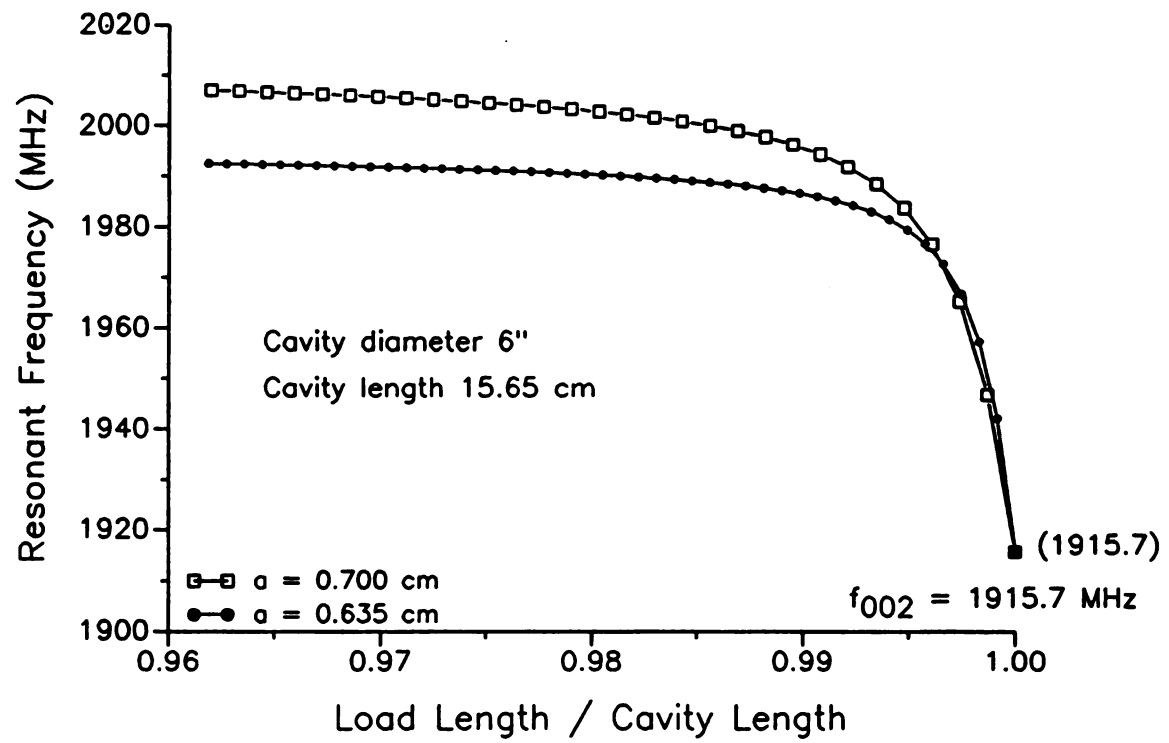
Figure 5-9 High load length region of Figure 5-8.

The reason that resonant frequency in Figure 5-9 is generally higher for the larger diameter load is due to the influence of the H-field in the region. When a perturbation is imposed on the space in which the fields exist, a loss of space in a high H-field region will raise the resonant frequency. A loss of space in a high E-field region will cause the resonant frequency to drop.[5] In the flat region of the curve in Figure 5-8, as the load gets longer, an equivalent amount of field space is blocked out for both the E-field and the H-field. However, an increase in the load diameter diminishes the region in which the H-field is higher than the E-field, causing the resonant frequency to rise.

Application of this principle also indicates that when the load is nearly as long as the cavity, the region between the load and the cavity shorting plate is a region of high E-field, since the frequency drops as the load length increases in that region. We may also infer that it is axial since a transverse E-field would be tangential to the end of the rod and the cavity shorting plate. The existence of an axial E-field between the end of the conducting rod and the cavity shorting plate accords well with the notion of a parallel plate capacitance effect.

Before passing on to the next Figure, it is worthwhile to notice an interesting feature of the coaxial resonator TEM modes demonstrated in Figure 5-9, viz., the resonant frequency is independent of the diameter of the inner conductor. Although it is not demonstrated in the Figure, it may be inferred, and is in fact the case, that the resonant frequency for the TEM modes is independent of the cavity diameter as well.

Other modes also exist in the 6" diameter cavity loaded with 0.5" diameter conducting rods. One of them is shown in Figure 5-10 along side the mode of Figures 5-2 through 5-9. The cavity length remains at 15.65 cm, but the frequency range has been extended up to 3500 MHz. Mode designations are provided for the empty cavity and coaxial resonator limits. The upper mode in the Figure begins as the length-independent empty cavity TM_{020} mode. As the length of load increases from zero, the mode eventually becomes the coaxial resonator TM_{010} mode, also length independent. Since the frequency at both load length limits is cavity/load

---

[5]Harrington, 319-20.
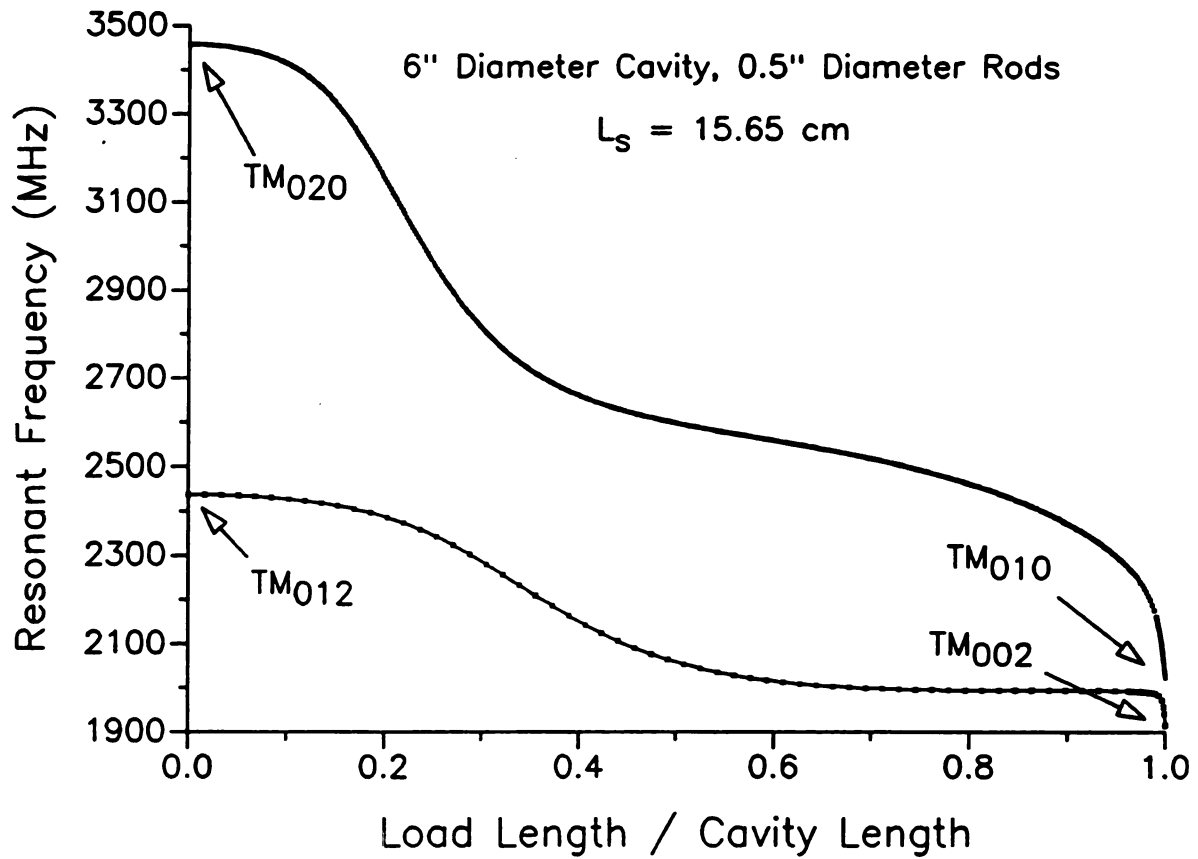
Figure 5-10 TM_{020} empty cavity to TM_{010} coaxial cavity mode for L_s = 15.65 cm.

length independent, it might be asked if the shape of the curve between the limits is affected by a change in cavity length.

For large changes in cavity length, this question is answered by the plot shown in Figure 5-11. Figure 5-11 is a plot of two modes each for cavity lengths of 10 cm and 25 cm. For each cavity length one plot is drawn as emanating from the empty cavity TM_{020} mode and another from the coaxial resonator TM_{010} mode. As shown in the Figure, neither the 10 cm cavity nor the 25 cm cavity have a mode which goes from the empty cavity TM_{020} mode to the coaxial cavity TM_{010} mode, not even to speak of the shape of the curve between the limits. For the 10 cm cavity, the empty TM_{020} mode goes to the coaxial TM_{002} mode, while the coaxial TM_{010} mode goes to the empty TM_{012} mode. For the 25 cm cavity, the empty TM_{020} mode goes to the coaxial TM_{012} mode, while the coaxial TM_{010} mode goes to the empty TM_{014} mode. All of these modes demonstrate a sharp drop in resonant frequency just as the cavity becomes coaxial.

Finally, it is shown that there exist conducting rod-loaded cavity modes which correspond to no coaxial cavity mode in the limit as the load length approaches the cavity length. Figure 5-12 shows that the resonant frequency of the mode which includes the empty cavity TM_{010} mode for $\ell = 0$ heads toward zero as the load length increases. The Figure shows this for $L_s = 5$ and 10 cm. For cavity lengths greater than 20 cm, the axially even TEM mode resonant frequencies drop below the empty cavity TM_{010} frequency. In such cases it is possible that the empty cavity TM_{010} mode would approach a coaxial cavity TEM mode as the length of the rod approached the cavity length. It is also possible that for certain load radii and cavity lengths higher order modes would exhibit the behavior shown in Figure 5-12, with the resonant frequency heading toward zero as the load increases in length.

5.5 Conclusion

This Chapter has demonstrated the application of mode-matching to solving for the resonant frequencies of a cavity loaded with a conducting rod, showing excellent agreement with experiment for a wide range of load lengths. The solution has
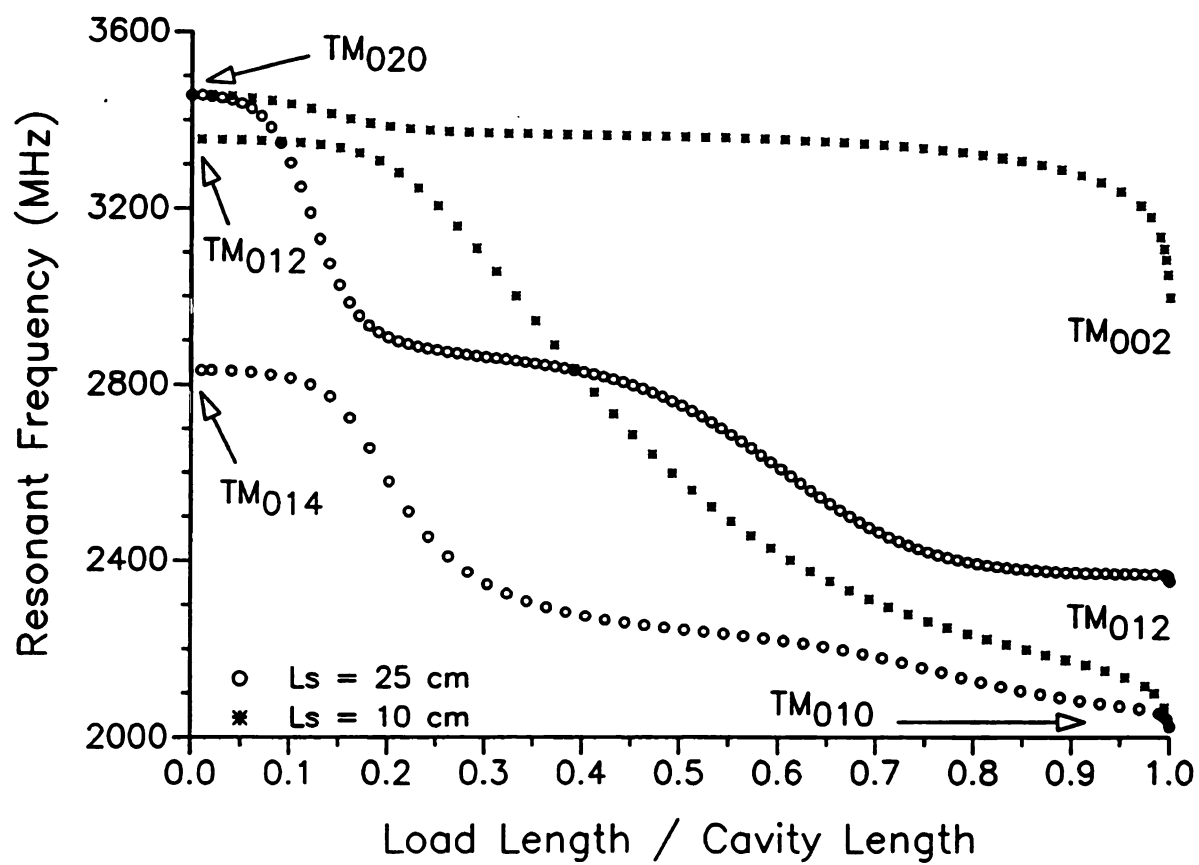
Figure 5-11 Several modes for L_s = 10 and 25 cm.
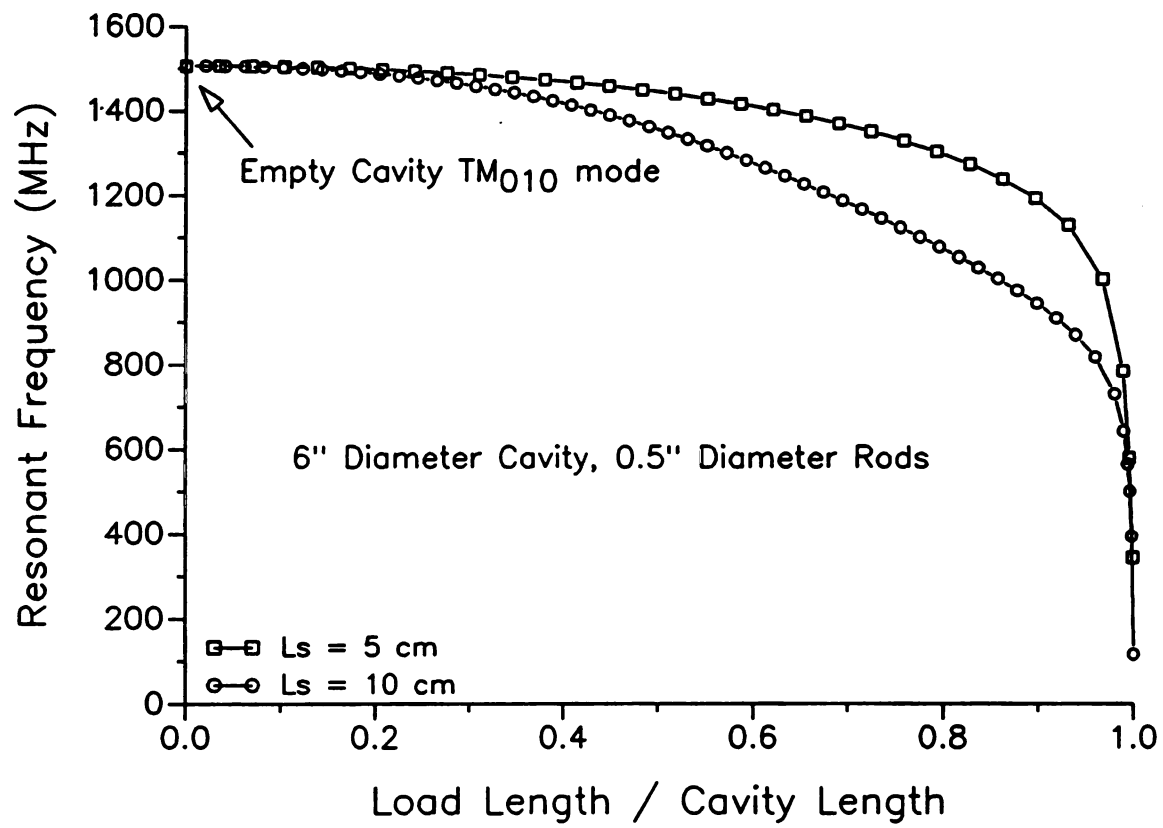
Figure 5-12 Empty cavity TM_{010} has no coaxial cavity companion mode.

provided special insight in predicting the sharp drop in resonant frequency for the TM modes which occurs just as the load length nears the cavity length.

Although no field calculations were made, resonant frequency behavior provides indications of the field structure. A rising resonant frequency indicates a high H-field in the direction of load expansion while a falling resonant frequency indicates a high E-field in the direction of load expansion. Modes exhibiting especially sharp resonant frequency declines as the load length approaches that of the cavity may be useful in focusing E-field energy into a material by placing the material between the end of the conducting rod and a cavity end plate. The theory provides the means for explicit field calculations if desired.

Finally, the solution presented here provides an example of the utility of the mode-matching method. It demonstrates that Bolle's approach to constructing the characteristic equation works very well in spite of the poor results reported in his paper. Last of all, it points to the necessity in mode-matching solutions of including all of the lower order modes in the field expansion expressions.

Chapter 6
NATURAL FREQUENCY AND THE SINUSOIDAL
STEADY-STATE RESPONSE

6.1 Introduction

The last three Chapters have provided analytical solutions for the
wavenumbers of the coaxially-loaded waveguide and various configurations of the
coaxially-loaded cavity. The waveguide solutions are for γ, the axial wavenumber,
$k_{\rho 1}$, the radial wavenumber inside the inner dielectric, and $k_{\rho 2}$, the radial
wavenumber in the region between the inner dielectric and the waveguide wall.
When the excitation frequency is specified these wavenumbers are found as roots of
the characteristic equation (3-92) of Chapter 3. For the waveguide, the excitation
frequency specified is a real value, therefore the solution extracted may be directly
associated with the sinusoidal steady-state driven response. Losses are accounted for
in space, i.e., wave attenuation as a function of distance from the source. This is the
response obtained experimentally with a continuous wave (CW) generator or sweep
oscillator source with a sweep rate much less than the excitation frequency.

In solving for the wavenumbers of the cavity, the frequency is not usually an
input value, but one of the values being sought. Frequency, through the wavenumber
k_0, is one of the variables determined by the characteristic equation. When losses are
present the frequency is complex.[†] This corresponds to wave attenuation in time,
i.e., in the absence of additional input energy, the magnitude of the electromagnetic
field within the cavity decreases with time. The complex frequency, also called the
natural frequency, describes the transient response of the cavity to a pulse or to
having a CW source instantaneously shut off or turned on. The real part of the
natural frequency describes the time period of field oscillation while the imaginary

---

[†]It is possible to input a complex frequency and search for other system eigenvalues. If there are
losses present, both the real and imaginary parts of the complex frequency must be known.

126

part of the natural frequency is the exponential decay constant.[†] The electromagnetic fields under such conditions are said to resonate in their *natural modes*.

This Chapter is a discussion of the relationship between the natural frequency and the sinusoidal steady-state response which is observed when the cavity system is driven by a CW source. Since nearly all microwave processing of materials employs continuous wave energy or relatively long (compared to one frequency cycle) pulses of continuous wave energy, the relationship between the natural frequency and the sinusoidal steady-state response must be understood in order to interpret natural mode solutions as descriptive of continuous wave applications.

6.2 Equivalent Circuit Description of the Lossy Cavity

The sinusoidal stead-state response is a term commonly used in lumped parameter circuit analysis. For an ordinary circuit, sinusoidal steady-state refers to the behavior of the circuit when it is driven by a current or voltage source which varies sinusoidally in time at a continuous frequency. Since microwave devices may be approximately represented by equivalent lumped circuits, the sinusoidal steady-state description is applied to microwave devices when the device is excited by a CW source. The sinusoidal steady-state response is contrasted with the transient response exhibited when the microwave energy source is instantaneously turned on or off.

Another concept borrowed from circuit theory and applied to microwave devices is the idea of resonant circuit *quality factor*, commonly abbreviated Q. The Q of a resonant circuit is a measure of the ratio of energy stored in the circuit at resonance to the amount of energy dissipated in the circuit every cycle. Q is conventionally defined in units of inverse radians such that,

$$Q = \frac{\text{Time average energy stored in circuit}}{\text{Time average energy dissipated in circuit per radian}}. \qquad (6\text{-}1)$$

[†]To speak more precisely, in the presence of losses, the electric and magnetic fields do not simply oscillate as they decay. Rather they rotate as described in Appendix D. The real part of the complex frequency corresponds to the rate of rotation in space.
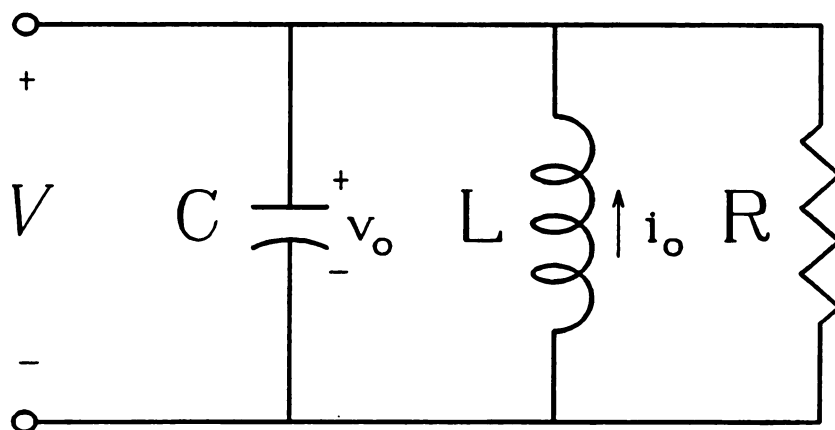
Figure 6-1 Parallel *RLC* Circuit.

We now examine the resonant characteristics of a lumped circuit, deriving the quality factor and resonant frequency. Given a parallel *RLC* circuit such as the one shown in Figure 6-1, it may be shown that the voltage *V* satisfies the following differential equation,[1]

$$\frac{d^2V}{dt^2} + \frac{1}{RC}\frac{dV}{dt} + \frac{V}{LC} = 0.$$ (6-2)

The underdamped solution (the one that is oscillatory) results in an expression for the voltage

$$V = A_1 e^{s_1 t} + A_2 e^{s_2 t} = A_1 e^{j\hat{\omega}_1 t} + A_2 e^{j\hat{\omega}_2 t},$$ (6-3)

where A_1 and A_2 are arbitrary coefficients dependent on the initial voltage on the capacitor, v_0, and the initial current in the inductor, i_0. The complex values s_1 and s_2 are the Laplace transform frequencies. The Laplace transform frequency is related to the natural frequency $\hat{\omega}$ by $s = j\hat{\omega}$. The underdamped Laplace transform frequencies are given by

---

[1]James W. Nilsson, *Electric Circuits* (Reading, Mass.: Addison-Wesley, 1983), 207.
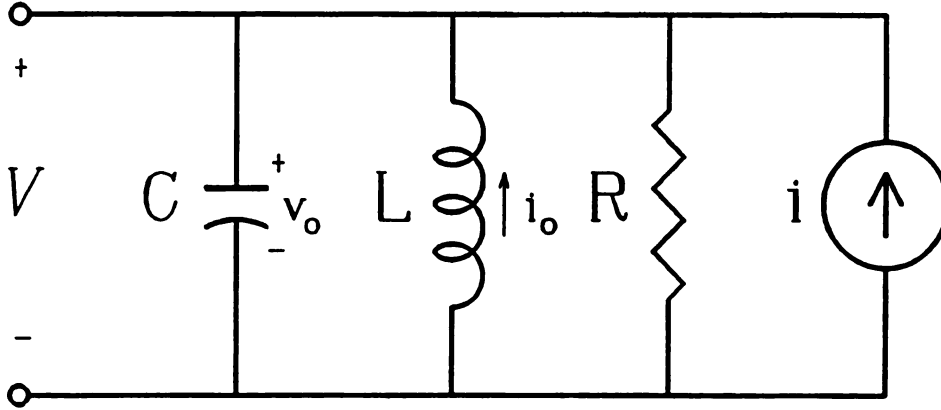
Figure 6-2 *RLC* circuit driven by a current source.

$$s_{1,2} = -\omega'' \pm j\sqrt{\omega_0^2 - \omega''^2}, \tag{6-4}$$

where

$$\omega'' = \frac{1}{2RC}, \qquad \omega_0 = \frac{1}{\sqrt{LC}}, \tag{6-5}$$

and $\omega_0 > \omega''$. It is evident that s_1 and s_2 are complex conjugate pairs.

When the circuit is driven by a time-harmonic current source as shown in Figure 6-2, it is found that ω_0 is the frequency at which the output voltage is maximized. If the current source is varying sinusoidally at a constant frequency such that $i = I_s \cos(\omega t)$, the phasor representation of the output voltage V is related to the phasor current of the source I by

$$V = \frac{I}{\frac{1}{R} + j\left[\omega C - \frac{1}{\omega L}\right]}. \tag{6-6}$$

The magnitude of V is given by

$$|V| = \frac{I_s}{\sqrt{\dfrac{1}{R^2} + \left[\omega C - \dfrac{1}{\omega L}\right]^2}} \qquad (6\text{-}7)$$

so that the magnitude of V is maximum for the frequency $\omega = \omega_0$, where ω_0 is given above in Equation (6-5). ω_0, or $f_0 = \omega_0 / 2\pi$, is called the *resonant frequency* of the driven circuit.

The Q of the circuit is found by determining the ratio of the stored energy in the inductor and the capacitor to the energy dissipated in the resistor per cycle at resonance. These two values may be put into Equation (6-1) to give a value for the circuit Q. Since the stored energy is transferred between the inductor and the capacitor $90°$ out of phase, the peak value of energy stored in one of them will provide an expression for the total. At resonance, the total and the time-average stored energies are the same. The peak value of energy stored in the capacitor is given by

$$U_s = \frac{1}{2} C V_{max}^2 . \qquad (6\text{-}8)$$

The time-average energy dissipated in the resistor over one cycle is

$$U_d = \frac{1}{2} \frac{V_{max}^2}{R} \frac{1}{\omega_0} . \qquad (6\text{-}9)$$

Therefore the quality factor is given by

$$Q = \frac{U_s}{U_d} = \omega_0 R C . \qquad (6\text{-}10)$$

Using Equations (6-5) we may write ω'' in terms of ω_0 and Q such that

$$\omega'' = \frac{1}{2RC} = \frac{\omega_0}{2Q} , \qquad (6\text{-}11)$$

and

$$s_{1,2} = \omega_o \left[-\frac{1}{2Q} \pm j \sqrt{1 - \left(\frac{1}{2Q}\right)^2} \right], \qquad (6\text{-}12)$$

or

$$\hat{\omega}_{1,2} = \pm \omega_o \sqrt{1 - \left(\frac{1}{2Q}\right)^2} + j \frac{\omega_o}{2Q}. \qquad (6\text{-}13)$$

These are the natural frequencies of the circuit.

Treating the cavity in terms of its equivalent circuit, Equation (6-13) shows that the complex natural frequency of the cavity, $\hat{\omega}$, contains within it information on both resonant frequency and Q. Recalling that the natural frequency of the cavity from Equation (4-21) of Chapter 4 is given by

$$\hat{\omega} = \omega' + j\omega'', \qquad (6\text{-}14)$$

the equivalent circuit description gives

$$\omega' = \omega_o \sqrt{1 - \left(\frac{1}{2Q}\right)^2} \qquad (6\text{-}15)$$

and

$$\omega'' = j \frac{\omega_o}{2Q}. \qquad (6\text{-}16)$$

For a high Q (≥ 50), the real part of $\hat{\omega}$ provides a close approximation to the resonant frequency ω_o, i.e.,

$$\omega_o \approx \omega'. \qquad (6\text{-}17)$$

and Q is given by

$$Q \approx \frac{\omega'}{2\omega''}. \qquad (6\text{-}18)$$

Having qualified these approximations by requiring Q's in excess of 50 or so, it needs to be said that, for a microwave cavity, Q's for a good resonance are commonly in the range of several thousand. The restriction is therefore not usually problematic.

6.3 Quality Factor and the Natural Frequencies of the Microwave Cavity

The cavity quality factor may be derived in terms of the real and imaginary parts of the natural frequency directly from the definition of Equation (6-1).[2] In the absence of input energy the power dissipated is related to the energy stored by the conservation of energy such that

$$P_d = - \frac{\partial U}{\partial t},\qquad\text{(6-19)}$$

where P_d is the power dissipated and U is the stored energy. The natural mode cavity quality factor may then be written

$$Q = \omega' \; \frac{U}{-\dfrac{\partial U}{\partial t}},\qquad\text{(6-20)}$$

where ω' is the real part of the natural frequency. This may be rewritten as

$$\frac{\partial U}{\partial t} + \frac{\omega'}{Q} U = 0.\qquad\text{(6-21)}$$

The solution to this differential equation is given by

$$U = U_0 \, e^{-\frac{\omega'}{Q} t}.\qquad\text{(6-22)}$$

Since energy stored is proportional to the square of the magnitude of the electric field, i.e., $E \cdot E^*$, the electric field is given by

$$E(t) = E_0 e^{-\frac{\omega'}{2Q} t} \, e^{j\omega' t},\qquad\text{(6-23)}$$

---

[2]Jackson, 357.

where $E_o = \sqrt{U_o}$. Since the electric field is also given by

$$E(t) = E_o \, e^{j\hat{\omega}t} = E_o \, e^{-\omega''t} \, e^{j\omega't},\tag{6-24}$$

where $\hat{\omega} = \omega' + j\omega''$, it is clear that this analysis yields the same value for the cavity Q as did the equivalent circuit approach, viz.,

$$Q = \frac{\omega'}{2\,\omega''}.\tag{6-25}$$

6.4 S-Plane Representation of Natural Frequencies

It is customary to present the complex Laplace transform frequencies $s_{1,2}$ as points on a Cartesian coordinate system plane where the y-axis represents the imaginary part of s while the x-axis represents the real part of s. Figure 6-3 is an
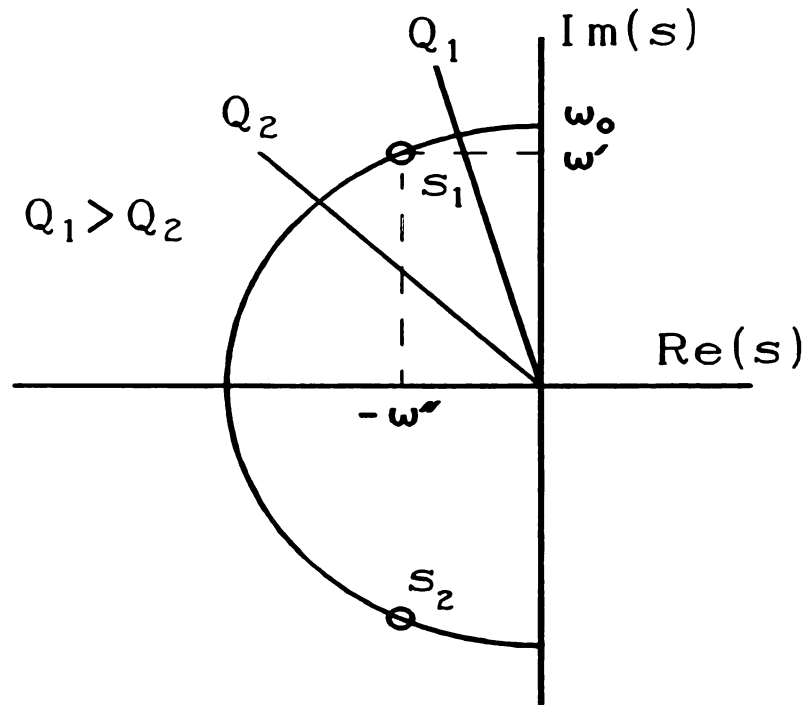
Figure 6-3 S-Plane presentation of the complex Laplace transform frequencies.

example of the s-plane representation of the location of the complex Laplace transform frequencies for an RLC circuit. As shown in Figure 6-3 the two frequencies s_1 and s_2 are complex conjugate pairs in the locus of points which form a circle of radius ω_0 centered at the origin. The real part of each of the two frequencies is located at $-\omega''$ while the imaginary parts are found at $\pm\omega'$. Q's are constant along lines through the origin with higher Q's along lines closer to the Re(s)-axis, lower Q's along lines closer to the Im(s)-axis

One of the useful features of Figure 6-3 is that it may be used to graphically represent the behavior of the impedance of the circuit shown in Figure 6-2. From Equation (6-6) the impedance seen by the current source of Figure 6-2 is given by

$$Z = \frac{V}{I} = \frac{1}{\frac{1}{R} + j\left[\omega C - \frac{1}{\omega L}\right]} . \tag{6-26}$$

Using Equations (6-4) and (6-5), the impedance may be rewritten as

$$Z = \frac{1}{C}\left[\frac{j\omega}{(j\omega - s_1)(j\omega - s_2)}\right] . \tag{6-27}$$

The magnitude of the impedance is simply the product of the magnitudes of the factors so that

$$|Z| = \frac{\frac{\omega}{C}}{\left|(j\omega - s_1)\right|\left|(j\omega - s_2)\right|} . \tag{6-28}$$

Equation (6-28) is the basis for representing the impedance graphically on the s-plane shown in Figure 6-3. At a point on the Im(s)-axis, i.e., $s = j\omega$, the impedance is inversely proportional to the product of the magnitudes of the vectors from s_1 and s_2 to s. These vectors are shown in Figure 6-4. It is apparent that when $j\omega$ is near s_1 or s_2 the impedance and the output voltage are large, especially if ω'' is small.
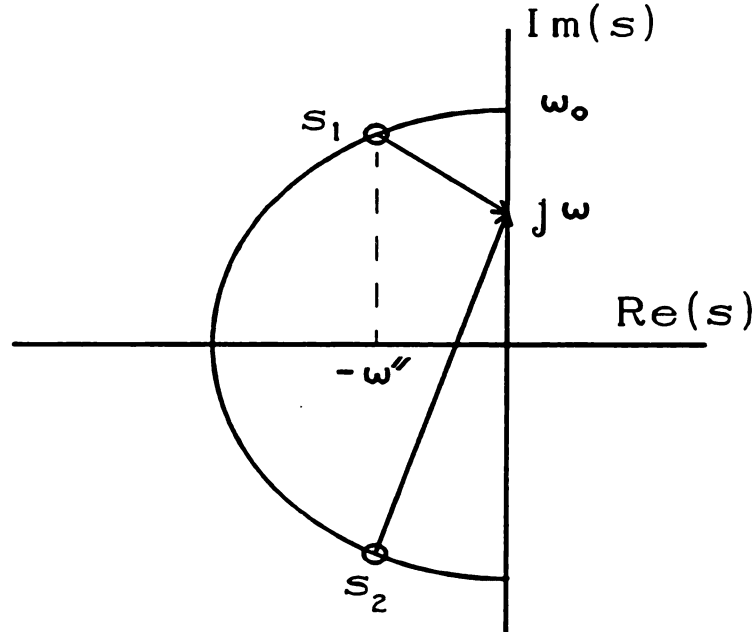
Figure 6-4 S-Plane representation of the magnitude of the impedance.

Because of the ω in the numerator, the impedance is not quite maximum at

$\omega = \text{Im}(s_{1,2})$, but reaches its peak at $\omega = \omega_0$.

Although the current source in the circuit of Figure 6-2 is driven at a real frequency ω, it is common to consider the impedance as a function of the complex Laplace transform frequency s. The generalized impedance function is given by Equation (6-27) except that $j\omega$ is replaced by s such that

$$Z = \frac{1}{C} \left[\frac{s}{(s - s_1)(s - s_2)} \right].$$ (6-29)

The complex Laplace transform frequencies s_1 and s_2 are seen to be poles of the generalized impedance.[†] The impedance also has a zero at the origin.

[†]The complex Laplace transform frequencies are often identified with the *zeros* of the impedance function and the *poles* of the admittance. It is the other way around here because a parallel rather than a series circuit is used to model the cavity.
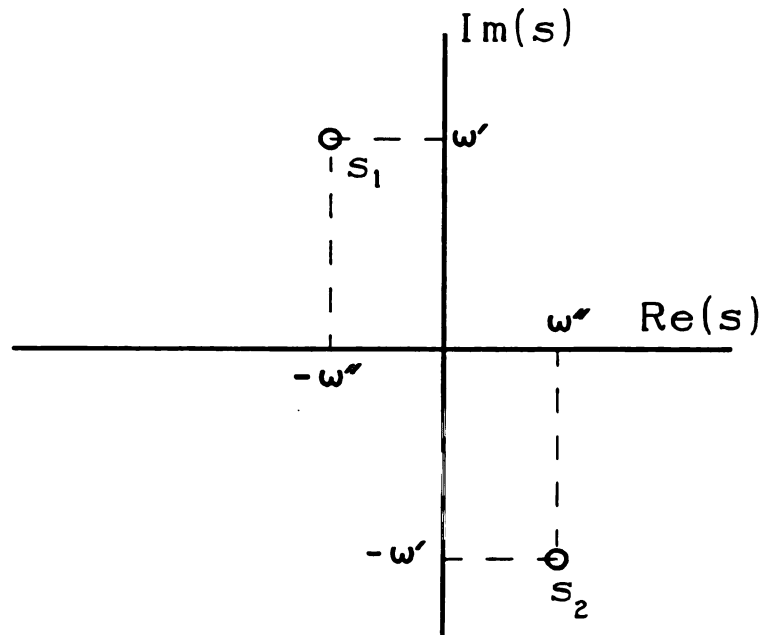
Figure 6-5 S-Plane frequencies of the lossy homogeneously filled cavity.

It is possible to plot the complex frequencies of the microwave cavity in an s-plane representation. Such a plot is shown in Figure 6-5 for the lossy homogeneously filled cavity whose complex frequencies are given by Equation (4-23). The relative positions of the two poles shown, both of which correspond to one mode, i.e., referring to Equation (4-23), the same value of n, p, and q, indicate that they are not complex conjugate pairs.[†] Furthermore, s_2 is a non-physically realizable frequency since it corresponds to exponential growth of energy in time. s_2 is neglected when using the natural frequencies to approximate sinusoidal steady state conditions. While Equation (4-23) is specific to the cylindrical cavity, Equation (4-22) with the "+" sign is true for any homogeneously filled cavity with perfectly conducting walls. Since the relative positions of the poles in Figure 6-5 may be

---

[†]An explanation was offered in Chapter 4 to the effect that individual modes do not form independent circuit elements and therefore natural mode frequencies do not have to conform individually to the complex conjugate pair requirement.

determined by Equation (4-22), Figure 6-5 may represent the natural frequencies of a general homogeneously filled cavity.

Although coupling has not been considered in the natural frequency solutions of Chapter 4, it is necessary to make a few general observations regarding the effect of coupling on sinusoidal steady-state resonances and their relation to the natural frequencies of the cavity alone. This necessarily involves the impedance of the system. However, without a detailed analysis of the coupling mechanism which transfers power from the source into the cavity, a full description of the impedance function is not possible. Nevertheless, the natural frequencies of the cavity constitute certain of the poles so that a partial knowledge of the impedance is known without considering the coupling. In fact, a well designed coupling mechanism should not introduce any new poles into the impedance, at least none that are near the $\text{Im}(s)$-axis. Such a pole would correspond to an undesirable resonance inside the coupler.

At the same time it must be noted that the coupling will slightly perturb the poles corresponding to the natural frequencies due only to the cavity. It is also possible that it may quash some of them by impressing a zero on top of the cavity pole. This would be the case, for example, if coupling were accomplished by means of an infinitesimal probe located in the center of one of the shorting plates of a cylindrical cavity. Such a probe would not be able to couple energy into any cavity mode which had no axial electric field in the center of the cavity cross section. This would include all TE modes and all non-ϕ-symmetric TM modes. Another coupling mechanism, whose impedance zeros were located elsewhere, would have to be used to excite these modes.

Finally, it is necessary that the s-plane frequencies of the cavity with coupling included should fall into complex conjugate pairs as do the frequencies for the RLC circuit. This is accomplished approximately by a reflection of the cavity pole s_1 across the $\text{Re}(s)$-axis. This is necessary because a negative excitation frequency in real time corresponds to a simple change in the direction of the propagation of the waves in the cavity, which in turn may be represented by a 180° phase delay and a positive frequency. Since the mode resonance is insensitive to a delay in the initial

excitation, both positive and negative driving frequencies should excite the same mode with the same losses.

With these considerations in mind, we now dismiss them by concentrating on a particular natural cavity frequency, assuming a coupling structure which imposes no poles or zeros near the natural cavity frequency pole. Other poles arising from the natural frequencies of the cavity should be far away as well. Then the magnitude of the impedance in the neighborhood of the natural cavity frequency s_0 may be written as

$$|Z| \approx A \frac{1}{|j\omega - s_0|}, \tag{6-30}$$

where A is a proportionality constant. The magnitude of the impedance may be plotted as a function of s along the $j\omega$-axis to show how the impedance and the input power vary as a function of the driving frequency.

An example of such a plot is shown below in Figure 6-6. The natural cavity frequency is $\hat{f} = 2 + j\,0.001$ GHz while the pole is located at $s_0 = j\hat{\omega} = j2\pi\hat{f}$. Figure 6-6 displays a plot of the normalized impedance in the vicinity of this pole. It is useful to note that the cavity Q may be determined from the resonant frequency and the band width at the half-power points. The half-power points refer to the frequency at which half of the power delivered at resonance is coupled into the cavity. The half power points occur for $|Z| = |Z|_{max} \div \sqrt{2}$, or, for the normalized impedance, $|Z| = .707$. If the half-power bandwidth, i.e., the frequency distance between the two half-power points, is denoted by $\Delta\omega$, then Q is given by

$$Q = \frac{\omega_0}{\Delta\omega}. \tag{6-31}$$

From Figure 6-6 we can see that $\Delta\omega = 2\pi\,(2.001 - 1.999)$ GHz. The resonant frequency is $\omega_0 = 2\pi\,(2.0)$ GHz. From Equation (6-31) Q is equal to 1,000. This is the same value found by using Equation (6-25).
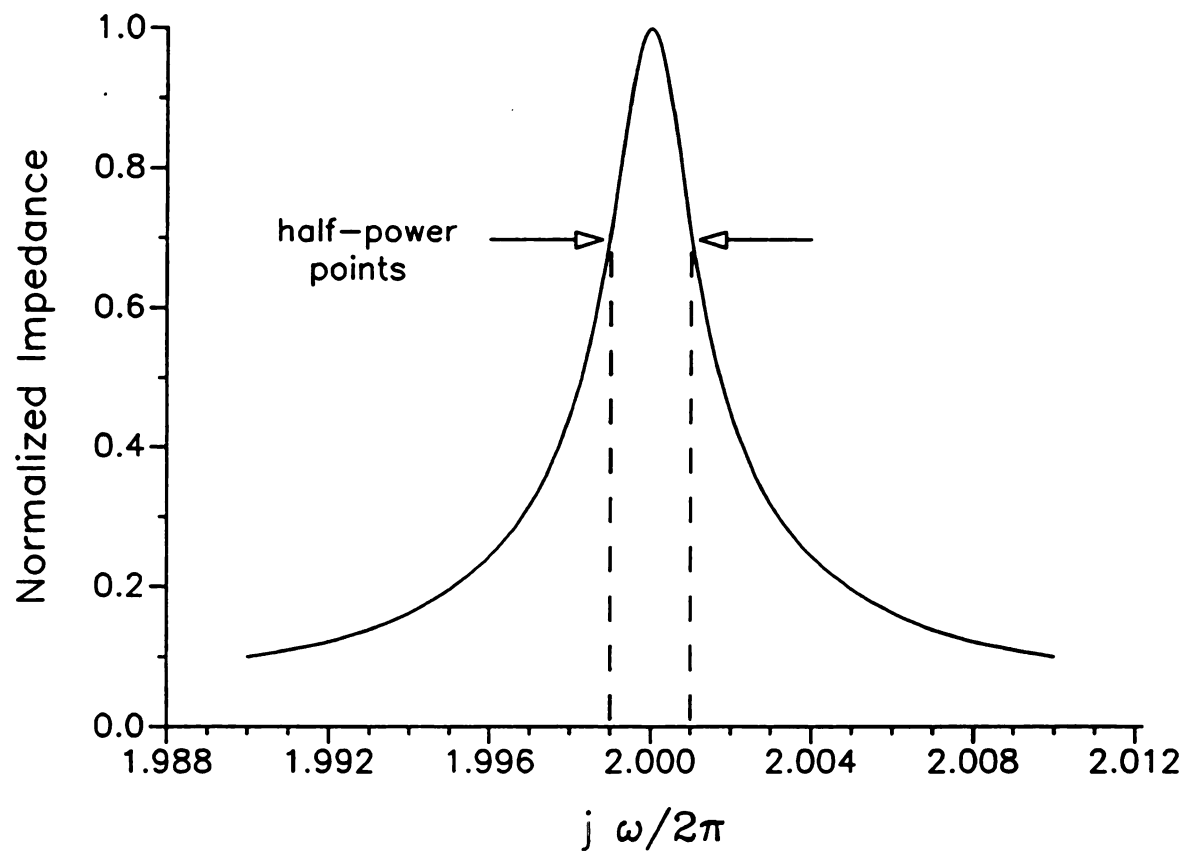
Figure 6-6 Impedance as a function of sinusoidal steady-state driving frequency ω.

6.5 S-Plane Frequencies vs. Loss Factor for Cavity-Short Type Modes

As examples of s-plane frequency charts and their uses, we demonstrate how the complex frequencies of two cavity-short type modes appear as plotted on the s-plane. The cavity-short type configuration is shown in Figure 4-3 of Chapter 4. It consists of a cylindrical cavity coaxially loaded with a dielectric rod of length equal to the cavity length. Figure 6-7 is a plot of a series of frequencies for the cavity-short type TE_{011} mode for a variety of load material loss factors, while the cavity length, cavity radius, load length, load radius and load dielectric constant are kept constant. The frequencies are found as roots of the characteristic equation (3-92) with $n = 0$ and TE solutions specified. The axial wavenumber, γ, is equal to π / L_s where L_s is the cavity length. The plot is for a 6" diameter cavity and 1" diameter load, with a cavity and load length both equal to 6.5 cm. All frequency values are in giga-radians per second.

The dielectric constant of the load material is $\epsilon_r' = 3$, where the subscript r indicates a *relative* dielectric constant, i.e., relative to the permittivity of free-space,

$$ \epsilon_r = \frac{\epsilon}{\epsilon_o} . \tag{6-32} $$

Material permittivities in the Figures of this and the following Chapters are given in terms of the relative dielectric constant.

As shown in Figure 6-7, s is purely imaginary when the loss factor is zero, but moves into the negative-real half of the plane as ϵ'' increases from zero. The magnitude of the real part is maximum when ϵ_r'' is near 5. Then, as ϵ'' continues to increase, the real part of s decreases until the frequency is nearly back at the $Im(s)$-axis for $\epsilon_r'' = 10,000$. At the same time, the imaginary part of s steadily increases with ϵ'' so that the frequency curve on the s-plane is oval shaped.

Also included in Figure 6-7 are lines of constant Q. Since the origin of the coordinate system is far away from the origin of the plot, the constant Q lines appear nearly vertical. Lines for $Q = 50$ and $Q = 30$ are shown. These lines provide a quick reference from which to estimate what the Q is at different points in the plane. The cavity/load system is shown to be high Q for both very low and very high loss
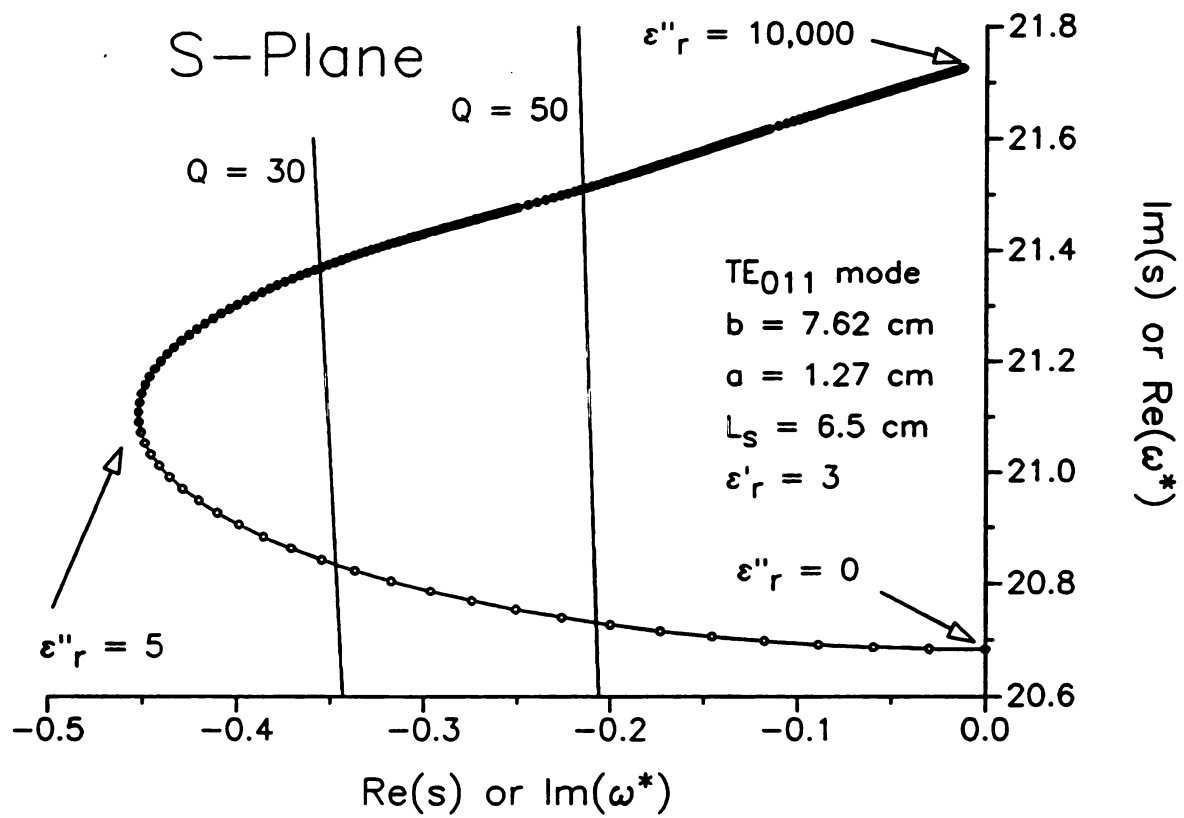
Figure 6-7 Cavity-short type TE_{011} mode frequencies as a function of loss factor.

S–Plane

$\varepsilon''_r = 10,000$

$Q = 100$

$Q = 30$

$Q = 15$

$\varepsilon''_r = 100$

$a = 0.2''$

16.8

16.4

$a = 0.1''$

TM_{011} mode

b = 7.62 cm

L_s = 7.76 cm

$\varepsilon'_r = 3$

$\varepsilon''_r = 0$

16.0

15.6

15.2

Im(s) or Re(ω^*)

−0.9   −0.7   −0.5   −0.3   −0.1

Re(s) or Im(ω^*)
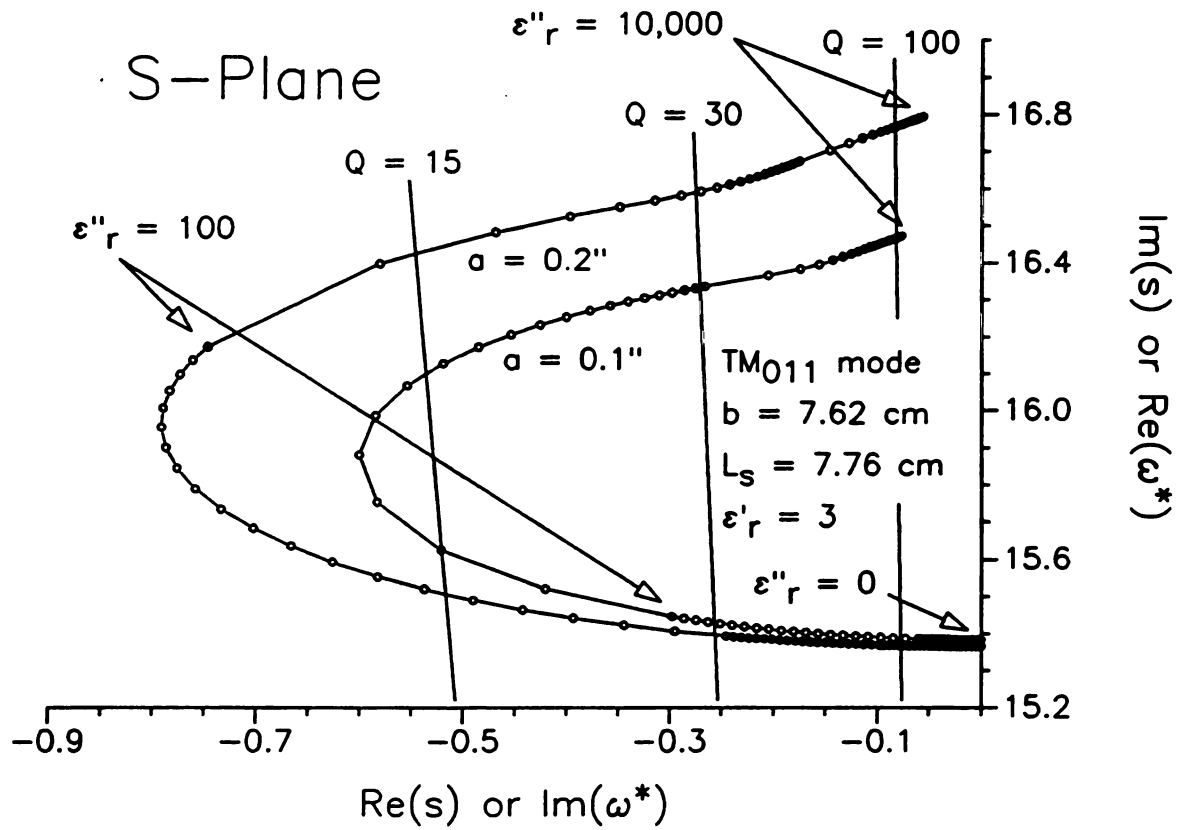
Figure 6-8 Cavity-short type TM_{011} mode frequencies as a function of loss factor: $a = 0.1''$ and $0.2''$.

factors. The Q is high for low loss factor loads because the load is a nearly lossless dielectric and there is little energy dissipated in the material. For very high loss factors the load behaves more like a conductor than a lossy dielectric—again little energy is dissipated in the load material.

A similar plot is shown in Figure 6-8 for the cavity-short type TM_{011} mode in a 6" diameter cavity. The cavity and load length is 7.76 cm and the load material dielectric constant is again given by $\epsilon_r' = 3$. Figure 6-8 contains two plots, one for a load radius of 0.1", one for a load radius of 0.2". As shown in the Figure, the larger load produces a greater effect on both the real and imaginary parts of the frequency as the load material loss factor changes. Comparing Figures 6-7 and 6-8, it is evident that even though the load material is much smaller for the TM modes of Figure 6-8, the Q is generally lower than that of the TE mode of Figure 6-7. The reason for this is because the electric fields couple more effectively to the load material when they are tangential to it. This implies more energy dissipation, and lower Q values, for TM modes when the greater dimension of the load is aligned axially in the cavity.

Field and material interaction will be discussed further in the Chapters that follow. The results of this Chapter, viz., how the complex natural frequencies are related to experimentally measured values of resonant frequency and cavity Q, will be used to show that the analysis presented accords with experiment.

Chapter 7

WAVENUMBER RELATIONSHIPS IN THE
COAXIALLY-LOADED WAVEGUIDE

7.1 Introduction

The theory of the coaxially-loaded waveguide is discussed in Section 3.5 of Chapter 3. A drawing of a coaxially-loaded waveguide of radius b with a load of complex dielectric constant $\hat{\epsilon}_1$, magnetic permeability μ_1, and radius a is shown in Figure 3-2. The material between the waveguide wall and the load boundary is composed of a material of dielectric constant $\hat{\epsilon}_2$ and magnetic permeability μ_2. The electric and magnetic fields are given by Equations (3-58) through (3-75). Numerical solution is required in order to find the wavenumbers γ, $k_{\rho 1}$, and $k_{\rho 2}$ defined by Equations (3-50) through (3-57). When ω is given (a real number), these are found as solutions to the characteristic equation, Equation (3-92), with the separation equations, Equations (3-57), linking them.

This Chapter concerns these numerical solutions and graphical presentation of the relationships that the wavenumbers sustain to the driving frequency, ω. Since the load material is allowed to be lossy, γ, $k_{\rho 1}$, and $k_{\rho 2}$ are complex. In the case of the axial wavenumber, γ, the existence of an imaginary part indicates that the wave is attenuated in the direction of energy propagation.[†] It is customary to express complex values of γ in terms of a real part β, and an imaginary part α. The same convention is followed here such that

$$\gamma = \beta - j\,\alpha. \qquad (7\text{-}1)$$

[†]Since it is possible to excite backward modes, i.e., modes in which the energy propagation moves in a direction opposite to the wave front, attenuation is not always in the direction that the wave front travels.

144

The numerical root-finding technique used to solve Equation (3-92) for the solutions presented in this Chapter was an implementation of Müller's method for complex functions of a complex variable, the FORTRAN code of which is given in Appendix E. The program was implemented on an IBM compatible 80386 (25 MHz) personal computer with a math coprocessor. Even without a good initial guess, solutions to Equation (3-92) could usually be found in under 2 seconds. In producing the curves presented in the Figures below, two adjacent points were located initially on each curve. Initial guesses for successive points were calculated by a linear approximation using the two points immediately behind the point being sought. All the points in a typical curve could usually be located within 10 seconds.

It is not the purpose here to present an exhaustive examination of the phenomena associated with the coaxially-loaded waveguide. One of the reasons for this is the extensive range of such phenomena. Even when the load material is lossless, there exist a number of interesting propagation characteristics, including backward and complex mode propagation.[1] When the load becomes lossy the range of solutions is even more multifarious, since the propagation characteristics are a function of two degrees of freedom in the dielectric constant, i.e., ϵ_r' and ϵ_r''. The motivation for this study is to examine wavenumber behavior to know how best to find wavenumbers for use in the coaxially-loaded region of the cavity-open type or cavity-image type loaded cavity. The primary aim is to understand how the wavenumbers and mode spacing are affected by the dielectric properties and radius of the load.

7.2 Naming of the Modes

As mentioned in Chapter 3, the modes of the coaxially-loaded waveguide do not divide into classifications TE and TM to z except for the case $n = 0$. Several schemes have been proposed for classifying hybrid modes of dielectric waveguides according to which field, the E-field or the H-field, has the dominant axial

---

[1]Clarricoats and Taylor, 1951.

component.[†] Most of them use the two designations HE and EH to distinguish between the two classes, but unfortunately, the schemes do not agree on whether EH is TE-like or whether it is TM-like, and similarly for the HE designation. The scheme favoring EH as TE-like seems to be in the ascendancy for non-shielded dielectric waveguides, being that of Snitzer, Kobayashi and Tanaka, and Bruno and Bridges.[2] On the other hand, the reverse designations have been chosen by several who have recently treated shielded dielectric waveguides, Chou and Lee, Sphicopoulos et. al., and Lin.[3] Zaki and Atia, and Zaki and Chen have simply referred to all hybrid coaxially-loaded waveguide modes as HE.[4] Vigneron and Guillon have called them all HEM.[5] Still another scheme has been adopted by those treating plasma columns in waveguides and cavities. Following Agdur and Enander[6] TE-like hybrid modes have been called TE^* modes with TM-like hybrid modes called TM^* modes.

The shielded waveguide group also their designations on a different principle than the non-shielded group. While most of the non-shielded group has concentrated on the ratios of E_z to H_z in the core region, those studying shielded waveguides have based their designations on the TE or TM limiting cases when the dielectric constant approaches unity or when the core material grows very small. The homogeneous waveguide mode remaining at end of the limiting procedure provides the designation

---

[†]While the coaxially-loaded waveguide is different from a circular dielectric waveguide, they are similar in many respects, especially in the necessity of hybrid modes when $n \neq 0$. Depending on one's perspective, the coaxially-loaded waveguide may just as easily be called a shielded dielectric waveguide, which it often is.

[2]Snitzer, "Cylindrical Dielectric Waveguide Modes," 494; Kobayashi and Tanaka, 1078-79; Bruno and Bridges, 884-85.

[3]Ri-Chee Chou and Shung-Wu Lee, 1168; T. Sphicopoulos, L. G. Bernier, and F. Gardiol, 97; Lin, 38.

[4]Zaki and Atia; Zaki and Chen, "Intensity and Distribution of Hybrid-Mode Fields."

[5]Vigneron and Guillon.

[6]Agdur and Enander, 576.

EH if the mode is TM or HE if the mode is TE. The name association of HE with TE modes and EH with TM modes appears to be arbitrary.

If there is to be a distinction in the hybrid modes based upon the TM-likeness or TE-likeness of the modes, the principles behind Snitzer's and Bruno and Bridges's schemes are more trustworthy than those of Chou and Lee, and Lin. It is possible to show that limiting cases do not provide unique labels for all coaxially-loaded waveguide modes. Sometimes, for example, a coaxially-loaded waveguide mode will approach a homogeneous waveguide TM mode for small load radii and a homogeneous waveguide TE mode as the load radius approaches that of the waveguide. Sometimes a low order coaxially-loaded mode will approach a homogeneous waveguide mode of much greater order making it very difficult to locate what kind of homogeneous waveguide mode is being approached. For highly lossy materials or plasmas with high conductivities, modes exist which are related to the coaxial waveguide TEM modes. These are not related to homogeneously filled waveguide or cavity modes. Although the limiting case method might be useful in some instances, particularly when the dielectric constant and loss factor of the load in the waveguide is low, it cannot provide a general means of distinguishing the modes.

While Snitzer's method of distinguishing between HE and EH modes has been associated with comparisons between the relative magnitudes of E_z and H_z, Snitzer himself does not refer to the relative magnitudes of E_z and H_z. Instead, Snitzer points out that the physical difference between the HE and EH modes is that "for the EH modes the peaks in the Poynting flux are located further from the center of the guide than the peaks in E_z and H_z; the reverse is the case for the HE modes."[7] It may be that this is a more fundamental physical distinction than the relative magnitudes of E_z and H_z and bears more detailed study. Nonetheless, Snitzer's distinctions appear also to differentiate between modes with greater and lesser relative magnitudes of the ratios of E_z to H_z. Bruno and Bridges, whose method involves a direct calculation of the ratio of E_z to H_z, claim that their method is identical to Snitzer's when their three region guide is reduced to a two region guide.

---

[7]Snitzer, 497.

148

Another feature of Snitzer's method that needs addressing is that it depends upon a certain factorization of the characteristic equation. That the factorization employed always provides a physically significant distinction in the shielded dielectric waveguide modes is not clear. On the other hand, Bruno and Bridges's method involves a simple direct calculation of the absolute value of the ratio of E_z to H_z (suppressing the ϕ-dependence). This ratio is compared to the wave impedance of a plane wave traveling at the same phase velocity, i.e.,

$$Z = \frac{\sqrt{\dfrac{\mu_0}{\epsilon_0}}}{\dfrac{\beta}{k_0}} . \tag{7-2}$$

If the ratio is greater than the plane wave impedance the mode is called HE (TM-like), otherwise it is labeled EH (TE-like). The method therefore has simplicity and a physically intuitive quality to recommend it.[†] For this reason, the method developed by Bruno and Bridges is preferable to Snitzer's if the relative magnitudes of the axial electric and magnetic fields are to be the distinguishing traits of the two mode types.

Given that the hybrid modes are to be distinguished by the relative contributions of the axial electric and magnetic fields, the only matter left to settle is what to call the TE/TM-like modes. Although it seems to be the most popular, from the point of view of this author, the EH/HE mode naming convention is not well-conceived. Since one type of mode is distinguished from another by a simple transposition of letters, it is difficult to remember which is which. Furthermore, it is not clear that there is a fundamental physical distinction between the EH and HE modes, especially when E_z and H_z are approximately equal in the wave impedance sense. It may be best to refer to hybrid modes simply as HEM in general and to distinguish them according to the method of Bruno and Bridges when such distinction

---

[†]It needs to be mentioned, however, that the intuitive appeal of this method suffers somewhat when losses are present, or when examining modes in the non-propagating region, i.e., when γ is complex or purely imaginary. In the present work, $|\gamma|$ has been used in place of β in Equation (7-2). It should also be noted that the field ratio is taken in the load material. In cases where the field resides primarily outside the load, the field ratio inside the load may not be physically significant.

lends significant physical insight to the description. At any rate, a more transparent naming scheme is necessary when hybrid modes are distinguished as being TM-like or TE-like.

It is proposed here that the label HE be retained for the TM-like modes and that TE-like modes be called HH modes. In addition to removing confusion due to transposition of the characters, there are at least four other good reasons for adopting this scheme: 1) as Bruno and Bridges point out, it is conventional to refer to the fundamental mode of the dielectric waveguide, which is TM-like, as HE_{11}, 2) the first letter of this mode designation may be understood to stand for "hybrid," and is thus descriptive of both types of modes, 3) in the older literature TM modes are referred to as "E modes" and TE modes are called "H modes." Thus the hybrid modes would use a similar naming scheme in calling the TM-like modes "H(ybrid)E" and the TE-like modes "H(ybrid)H", 4) the letters in mode labels stand for actual words and may be considered abbreviations in the same way that "TM" stands for "transverse magnetic" and "TE" stands for "transverse electric."

This is the labelling scheme adopted here to distinguish between TM-like and TE-like hybrid modes when it is useful to do so. Otherwise the hybrid modes will simply be called HEM. TE and TM labels will be retained for the ϕ-symmetric modes. Particular modes within each class will be distinguished by the conventional method of double subscripting the labels. The first subscript refers to the integer order of the azimuthal dependence. The second subscript refers to the relative order of the real part of the radial wavenumber in the core region. The following examples serve to illustrate the use of the subscripts: the TM mode whose radial wavenumber (real part) is the lowest for a particular frequency is called TM_{01} for that frequency. The hybrid TE-like mode with $n = 2$ and the lowest core radial wavenumber (real part) at a given frequency is called HH_{21} at that frequency. If the real part of the core radial wavenumber for an HE mode exists below that of the HH_{21} mode, the generic HEM label for HH_{21} would be HEM_{22}, etc.

7.3 Lossless Load: $\epsilon_r = 37.6$

As was demonstrated in Chapter 3, the coaxially-loaded waveguide is capable of sustaining TM or TE modes only when the fields are azimuthally (ϕ) symmetric, i.e., referring to Equations (3-58) through (3-75), $n = 0$. When the load material is lossless, the cutoff frequency is merely the frequency at which β and α are both zero. This is the simplest case and provides a foundation for understanding wave propagation in the coaxially-loaded waveguide. This Section presents the behavior of several different modes in a waveguide of radius $b = 1.27$ cm with a load radius $a = 1.00$ cm and lossless dielectric constant $\epsilon_r = 37.6$. The dielectric constant, load radius, and waveguide radius in Figures 7-1 through 7-8 below are the same as those found in the results presented by Zaki and Atia[8] and Zaki and Chen[9] so that comparisons might be made with their study.

Figure 7-1 is a plot of the radial wavenumber in region 1 versus frequency for the ϕ-symmetric TE and TM modes. The radial wavenumber is normalized by the load radius, a, while the frequency is given in terms of k_0 and is also normalized by a. For reference, the horizontal axis running from $k_0 a = 0$ to $k_0 a = 2$ corresponds to a frequency range of 0 to 9.5 GHz. A plot of k_ρ versus k_0, such as the one shown in Figure 7-1, is equivalent to the familiar ω-β diagram for representing the mode. It is sometimes more convenient or lends more insight to view the mode diagrams in k_ρ rather than β. k_ρ-k_0 type mode diagrams are especially useful if k_ρ is the independent variable in the root-finding algorithm of the characteristic equation solution. At other times an ω-β diagram makes it easier to understand the behavior of the mode. Both types of mode diagrams will be used in this Chapter.

The solid dots in Figure 7-1, as indicated, outline the TM modes, while the open circles are for the TE modes. The diagonal line drawn from the origin to the upper right corner distinguishes the propagation region, i.e., γ real, from the cutoff region, i.e., γ imaginary. A real value of $k_{\rho 1}$ to the right of the propagation line

---

[8]Zaki and Atia, 1043.

[9]Zaki and Chen, "Intensity and Distribution of Hybrid-Mode Fields," 1446.
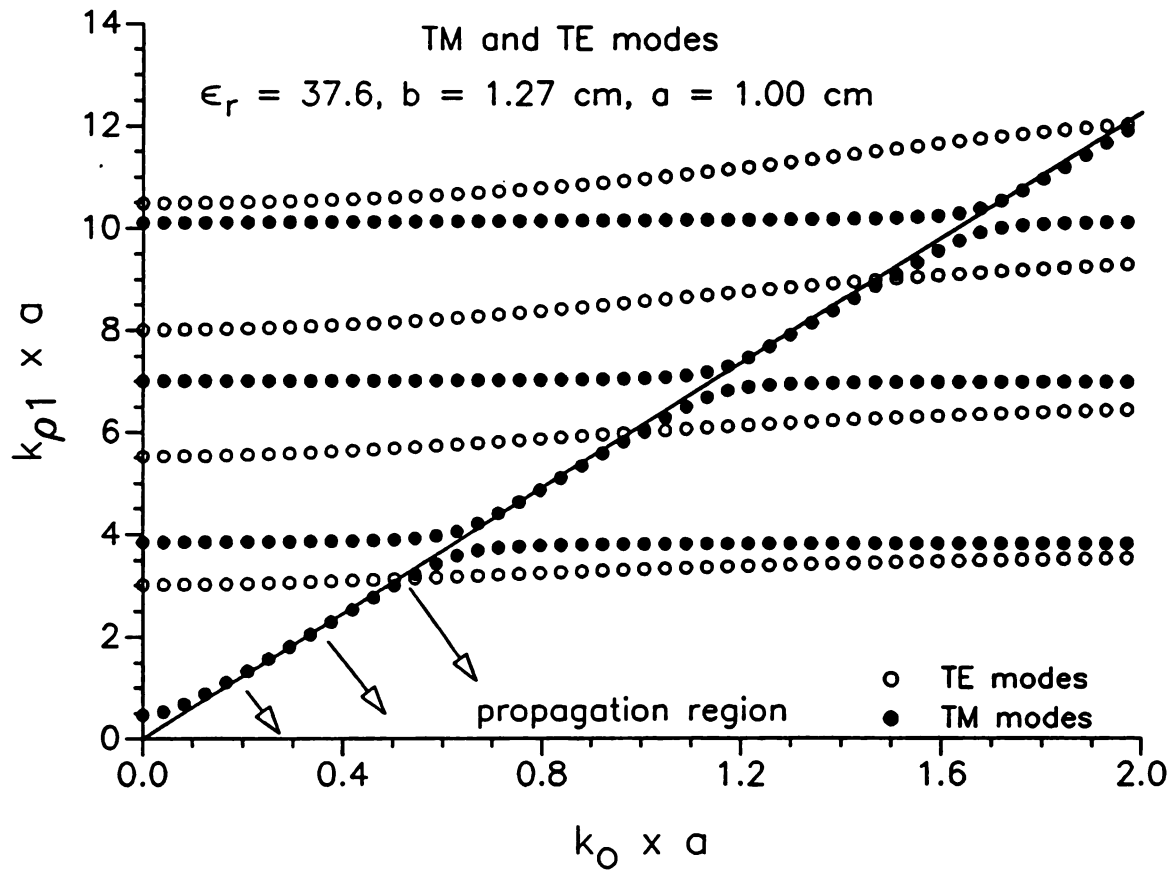
Figure 7-1 $k_{p1} a$ vs. $k_o a$ for TE and TM modes, $\epsilon_r = 37.6$, $a = 1$ cm, $b = 1.27$ cm.

means that the waves propagate axially down the waveguide unattenuated. If k_{p1} is real and to the left of the line, the waves do not propagate, but decay exponentially in z. When there is no azimuthal dependence, as is the case for the TE and TM modes, there is no possibility of exciting complex modes.[10] Therefore, all values of k_{p1} in Figure 7-1 are purely real and cutoff for each mode is clearly marked by a simple propagation line. A final remark on the general characteristics of Figure 7-1 is that far from cutoff the modes are interlaced TM-TE-TM-TE, etc. Although it is not proven here that this is always the case, this Figure and Figures 7-2 and 7-5 below show the interlacing of the TE and TM modes far from cutoff for the first several modes with $\epsilon_r = 37.6$, $a = 1$ cm, $b = 1.27$ cm.

For $k_o a = 0.8384$, Zaki and Atia report $k_{p1} a$ values of 3.4542, 5.8988, and 8.4158 for the first three TM modes, and 3.7863 and 7.0296 for the first two TE modes. Actually, in their paper they have mistakenly reversed the TE and TM mode designations so that their TE modes should be understood to be TM modes and vice versa. The results presented in Figure 7-1 at $k_o a = 0.8384$ give values of 3.7864, 5.0961, and 7.0294 for the first three TM modes and 3.2535, 5.8970, and 8.4117 for the first three TE modes. Small differences in the parameter values due to unit conversion (Zaki and Atia use inch units while the present calculations are in cm, and they may be using $f = 4$ GHz instead of $k_o a = 0.8384$) probably account for the discrepancies in the final two digits. They miss the second TM mode and give 3.4542 for the first TE mode. It is probably a typographic error and should read 3.2542. With these minor discrepancies, the results presented here match those of Zaki and Atia.

Figure 7-2 is similar to Figure 7-1, except that the azimuthal dependence is specified by $n = 1$. When $n \neq 0$ some regions are characterized by complex mode behavior, therefore the vertical axis indicates that Figure 7-2 presents the real part of $k_{p1} a$. In fact, $k_{p1} a$ is real in most of the region covered by Figure 7-2. There are two regions, indicated by arrows in the Figure, where the radial and axial

---

[10]Omar and Schünemann, 271-72. Complex modes have complex wavenumbers even in the absence of losses. They will be discussed in the description of Figure 7-2 below.
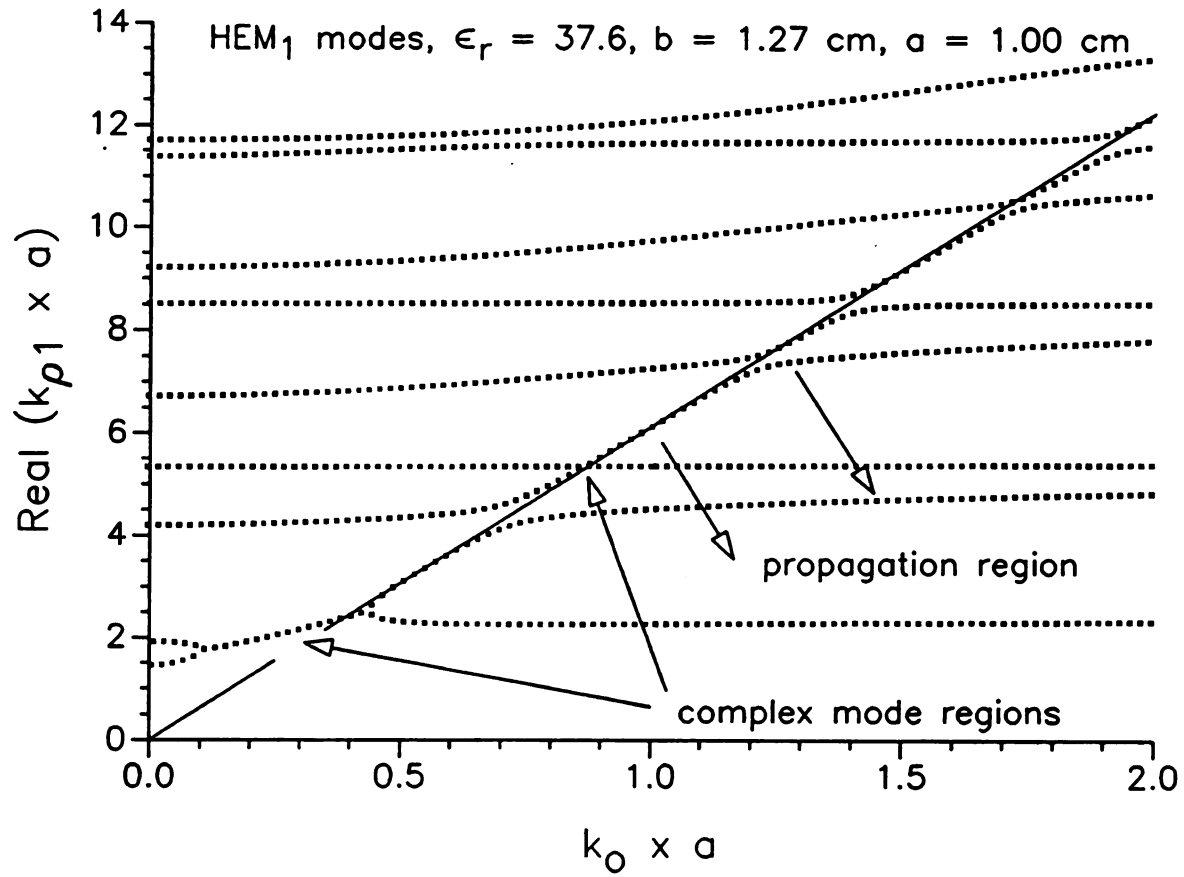
Figure 7-2 Real $k_{p1} a$ vs. $k_o a$ for HEM_1 modes, $\epsilon_r = 37.6$, $a = 1$ cm, $b = 1.27$ cm.

wavenumbers are complex. These two regions occur near the propagation line and extend behind it for the first two pairs of modes. They may be identified as the region where two complex modes exist together. The complex region begins where the two modes join and ends where they split back apart. In this region the two modes have complex conjugate propagation constants.

The complex modes must be understood as existing in pairs. The electric field of one of the complex modes couples to the magnetic field of the other instead of to its own magnetic field.[11] One of them cannot exist without the other. Individually, one is a decaying, forward propagating mode, the other is a decaying, backward propagating mode. The net power propagation is zero, so that together, the complex mode pair is non-propagating. Since there is no loss in the system, the power carried by the complex mode pair is purely reactive.[12] It may observed that the lower ordered pair complex modes in Figure 7-2 extends slightly beyond the propagation line, indicating that these modes do not begin to propagate until the frequency is slightly higher than necessary for normal, non-complex mode propagation.

Hand-drawn labels in Figure 7-2 indicate the TE/TM-like characteristics of the modes, whether the mode is HE or HH. These designations are based on the criteria of Bruno and Bridges discussed above. The point at which HH regions become HE modes and vice versa is indicated by a small vertical line drawn on the mode path. In the complex mode regions, these vertical lines cannot be drawn with great certainty since there are actually two modes present. Since the electric field of one of the complex modes couples to the magnetic field of the other instead of to its own magnetic field, it is likely that one of the complex modes is HH and the other HE. Again, as for the $n = 0$ case, and except for the first two modes below cutoff, the modes alternate between being HH and HE away from cutoff. It is interesting to note that in the non-ϕ-symmetric case it is the TE-like HH modes which follow the propagation line near cutoff. In the ϕ-symmetric case it was the TM modes which followed the propagation line near cutoff.

---

[11]Omar and Schünemann, 268.

[12]Ibid.

Comparing results with Zaki and Chen[13] we find good agreement with a slight discrepancy in the 4th and 5th digits, due again to unit differences and conversions in setting the waveguide and load parameters. For $f = 4$ GHz Zaki and Chen give $k_{\rho 1} a$ values of 2.2607, 4.4052, 5.2145, and 5.3523. Values found on the curves of Figure 7-2 are 2.2605, 4.4044, 5.2134, and 5.3525.

Figure 7-3 is a plot of the imaginary part of $k_{\rho 1} a$ for the lower order complex mode of Figure 7-2. The imaginary part rises from 0 at the edges of the band to a maximum just above the frequency midpoint. This plot serves to characterize both of the coupled complex modes, since the imaginary part of the one is simply the negative of the imaginary part of the other. The axial wavenumber, γ, in this region is plotted in Figure 7-4 where both the real and imaginary parts are shown. The scale for the imaginary part is given by the vertical axis on the right side while the scale for the real part is shown on the left. The Figure demonstrates that α drops toward zero as the frequency increases toward the point where the two complex modes divide near $k_0 a = 0.45$, while β increases from zero from the point where the two modes join near $k_0 a = 0.1$.

Figure 7-5 is similar to Figure 7-2 except that the azimuthal dependence is given by $n = 2$. Again there exist complex mode regions where two modes join. Now there are 3 of these regions instead of two. Also note that there are blank spaces in certain of the lower mode path lines. In these regions the roots could not be located accurately by the Müller's method technique used to solve the characteristic equation. It is not clear why this is so, but that roots do exist in those regions is confirmed by Zaki and Chen who locate a root at $f = 8$ GHz, $k_{\rho 1} a = 5.9195$.[14] The imaginary part of $k_{\rho 1} a$ for the complex modes is plotted in Figure 7-6, showing a similar pattern to that plotted in Figure 7-3 for the HEM_1 modes. Figure 7-6 demonstrates two additional features of the complex modes: 1) the imaginary part of the radial wavenumber is smaller for the higher order complex

[13]Zaki and Chen, "Intensity and Distribution of Hybrid-Mode Fields," 1446.

[14]Ibid.
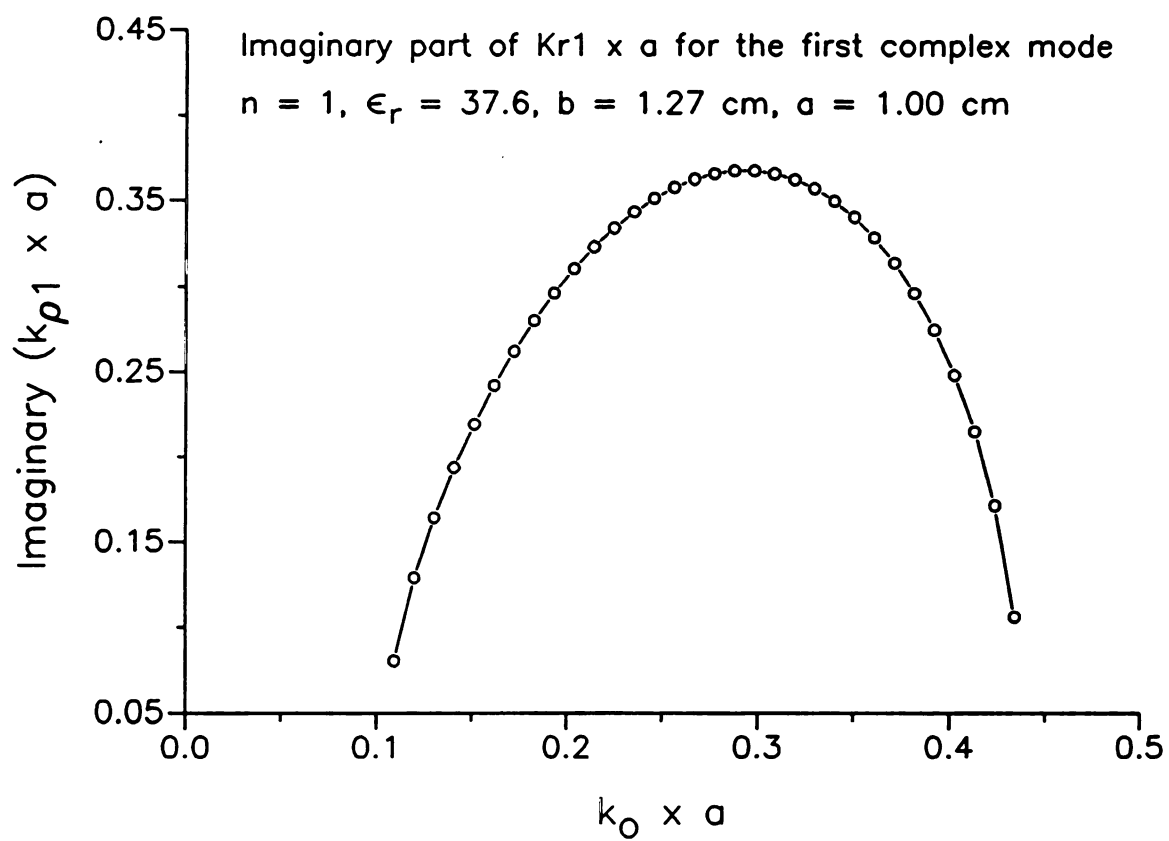
Figure 7-3 Imaginary $k_{\rho 1}\, a$ vs. $k_o a$ for HEM$_1$ modes, $\epsilon_r = 37.6$, $a = 1$ cm, $b = 1.27$ cm.
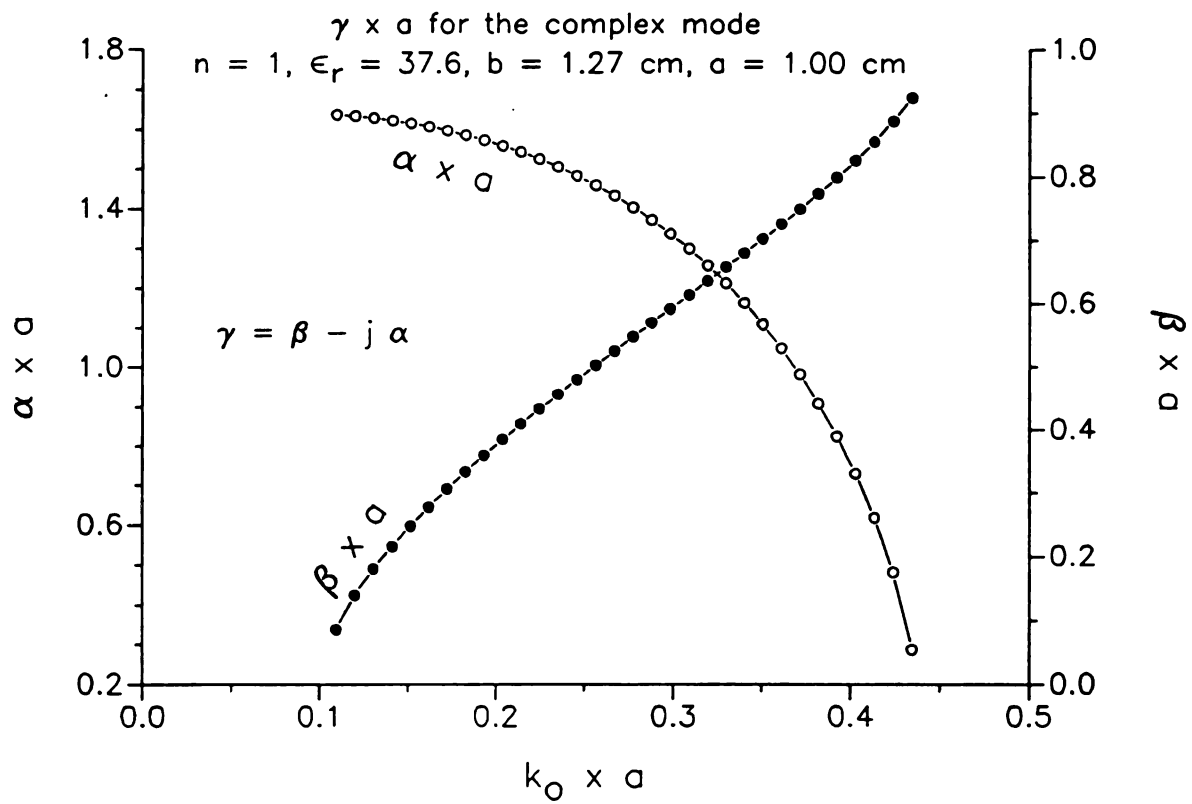
Figure 7-4 γa vs. $k_o a$ for HEM_1 modes, $\epsilon_r = 37.6$, $a = 1$ cm, $b = 1.27$ cm.
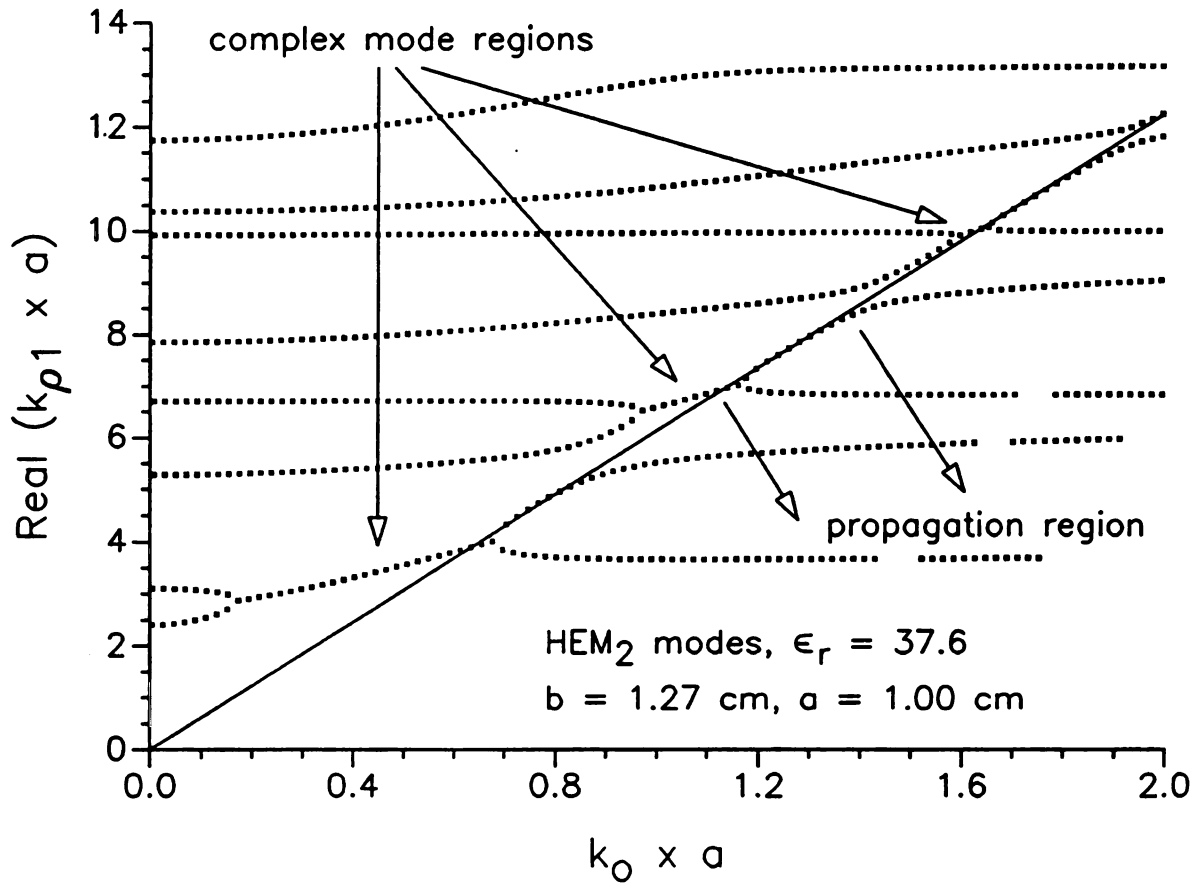
Figure 7-5 Real $k_{\rho 1} a$ vs. $k_o a$ for HEM$_2$ modes, $\epsilon_r = 37.6$, $a = 1$ cm, $b = 1.27$ cm.
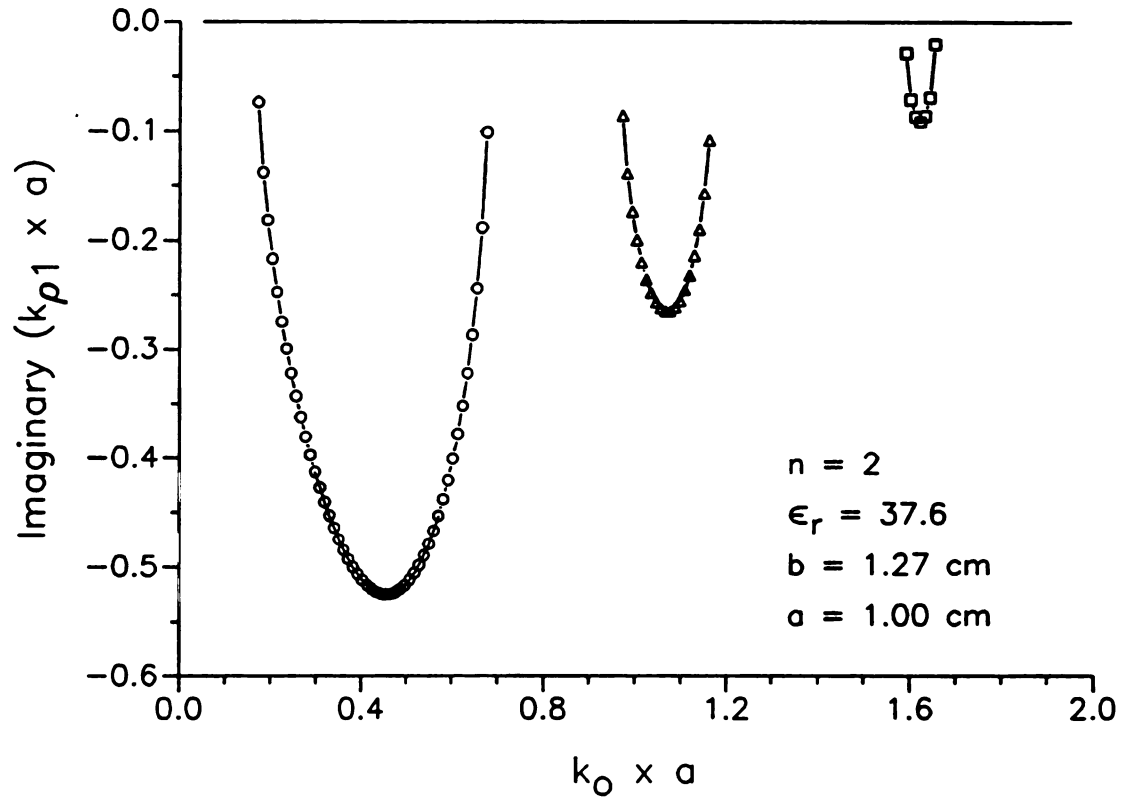
Figure 7-6 Imaginary $k_{\rho 1} a$ vs. $k_o a$ for HEM_2 modes, $\epsilon_r = 37.6$, $a = 1$ cm, $b = 1.27$ cm.

modes, and 2) at a given frequency not more than one pair of complex modes may be excited.

Figures 7-7 and 7-8 are similar to Figures 7-5 and 7-6, except that the azimuthal order has been increased to $n = 3$. Comparing Figures 7-2, 7-5, and 7-7, it is evident that $k_{\rho 1}$ for the lowest order mode rises for increasing azimuthal order. Comparing Figures 7-3, 7-6, and 7-8, it becomes apparent that the imaginary part of $k_{\rho 1}$ for the complex modes increases with increasing azimuthal order. In addition, for $n = 3$, the propagation line has become nearly coincident with the points at which the complex modes split into two propagating modes.

Zaki and Chen supply the following $k_{\rho 1} a$ values for the HEM_2 modes at 4 GHz: 3.6865, 5.0922, 5.8560 and 6.6960. The corresponding values in Figure 7-5 are 3.6860, 5.0919, 5.8537, and 6.6963. For the HEM_3 modes at 4 GHz Zaki and Chen give 6.7953, calling it HE_{31}. Since they were searching only for evanescent and propagating modes, their calculations were all in real math and they did not locate the complex mode at $k_{\rho 1} a = 5.25 - j0.33$. In a later paper they corrected this deficiency and also were able to locate complex modes, although they do not report any specific values of $k_{\rho 1} a$ with which we may make comparison.[15] For HEM_3 modes at 4 GHz Figure 7-7 contains $k_{\rho 1} a$ values of $5.2450 - j0.33310$, 6.7924, and 8.0240.

7.4 Lossless Loads: $\epsilon_r = 3.0$

Many of the experimental results presented in this dissertation involve loads made of nylon 66 which has a complex dielectric constant of $\hat{\epsilon}_r = 3.03 - j0.039$. In addition, the diameter of the experimental cavity in which most of the experiments were performed was 6". In order to compare the results for nylon loads under the experimental conditions presented here with a similar lossless load material, several mode path charts were made for a 6" diameter waveguide with coaxial loads of dielectric constant $\epsilon_r = 3.0$. Since the load diameter was varied while the waveguide

---

[15]Chen and Zaki, 1455.
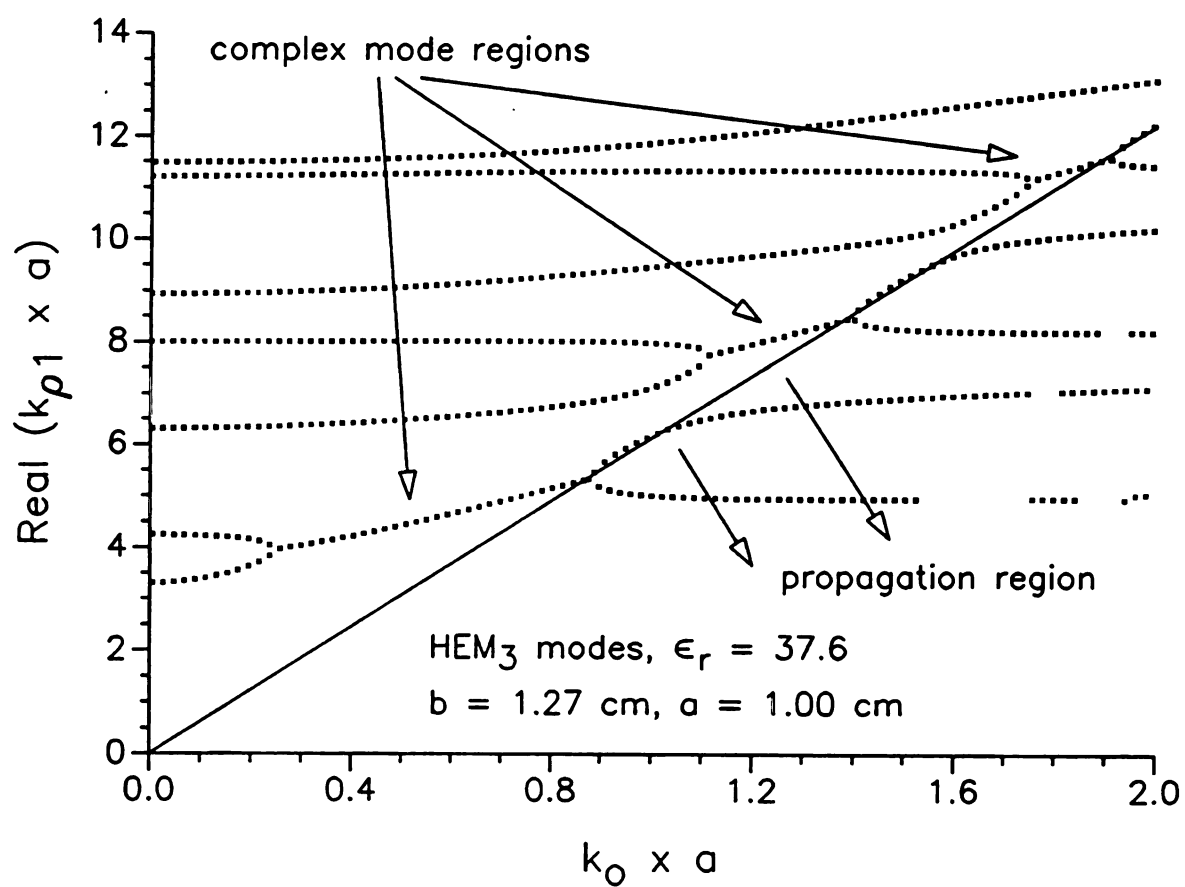
Figure 7-7 Real $k_{\rho 1} a$ vs. $k_o a$ for HEM$_3$ modes, $\epsilon_r = 37.6$, $a = 1$ cm, $b = 1.27$ cm.
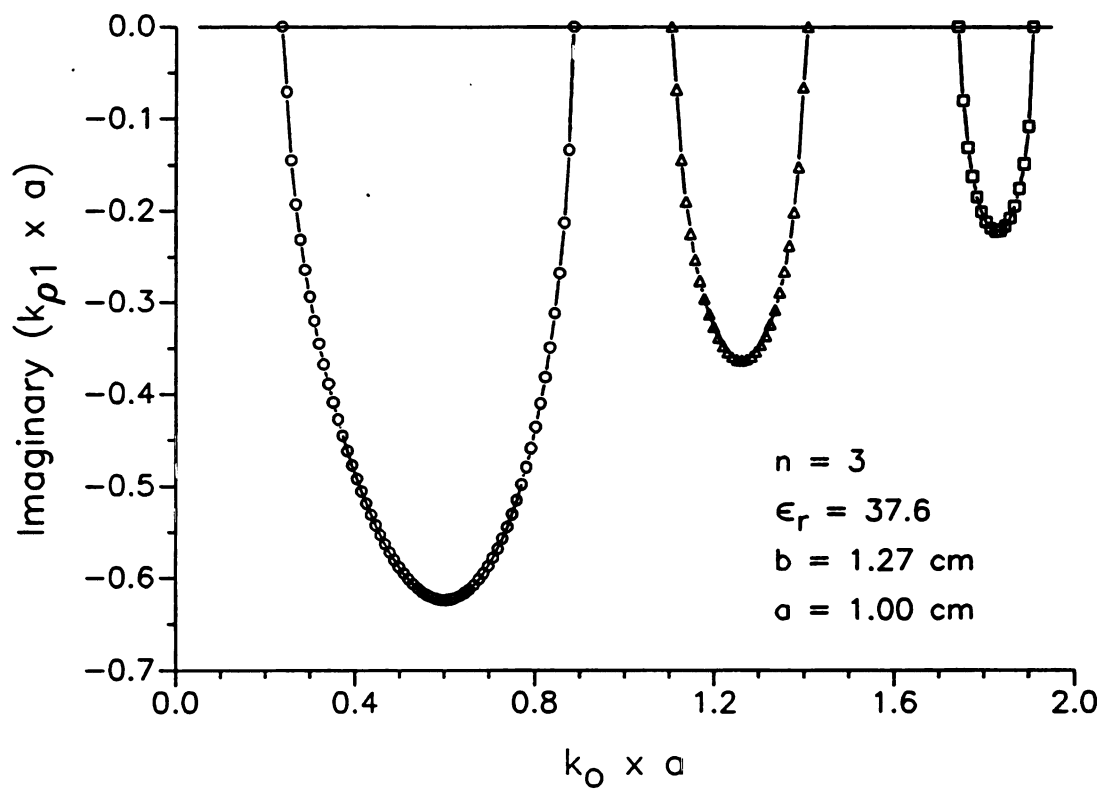
Figure 7-8 Imaginary $k_{\rho 1} a$ vs. $k_o a$ for HEM$_3$ modes, $\epsilon_r = 37.6$, $a = 1$ cm, $b = 1.27$ cm.

diameter remained constant, the radial wavenumber is normalized by b instead of a. Frequency is plotted directly rather than in terms of $k_0 a$.

Figures 7-9 through 7-12 show how the radial wavenumber for TE and TM modes changes as the load radius increases from 16.7% to 99.7% of the waveguide radius. As the load radius increases, the radial wavenumber becomes less dependent on frequency until, for all frequencies, $k_{\rho 1} b$ is equal to the zeros of $J_0(x)$ for TM modes and $J_0'(x)$ for TE modes when the load completely fills the waveguide. Values of $k_{\rho 1} b$ in Figure 7-12 are nearly identical to the Bessel function zeros for the TM modes, and to the zeros of the first derivative of the Bessel function for the TE modes. It may be observed that the cutoff frequency of these modes drops with increasing load radius. If the dielectric constant of the load were higher, the slope of the propagation line would also be greater. For large load diameters, at least, this means that the cutoff frequency drops for both an increase in load diameter and dielectric constant.

In terms of mode spacing, Figures 7-9 through 7-12 show that for lower dielectric constants the modes are more evenly spaced than for the high dielectric constant loads of Figure 7-1. Depending on the frequency, the radial wavenumbers of the TM modes in Figure 7-1 might be separated by 0.5 cm^{-1} between two modes and then 3 cm^{-1} until the next one. In Figures 7-9 through 7-12 the modes do not fall in into a perfectly uniform pattern, but one which is far more uniform than that of Figure 7-1. Although it is not shown here, as the order of the modes grows higher they become more uniform in their separation. This uniformity is similar to that of the Bessel function zeros which become linearly separated as their order increases. The separation characteristics of the modes are important to understand in order that no modes be left out and no spurious modes be included in constructing solutions to the cavity-open or cavity-image type solutions which were discussed in Chapter 4.

Both real and imaginary parts of the axial propagation constant, γ, are plotted as a function of frequency for the TM$_{01}$ mode with $a = 1.27$ cm in Figure 7-13. Above the cutoff frequency, approximately 1.3 GHz, the imaginary part is zero and γ is purely real, i.e., $\gamma = \beta$. Below cutoff γ is purely imaginary, being equal to $-j\alpha$.
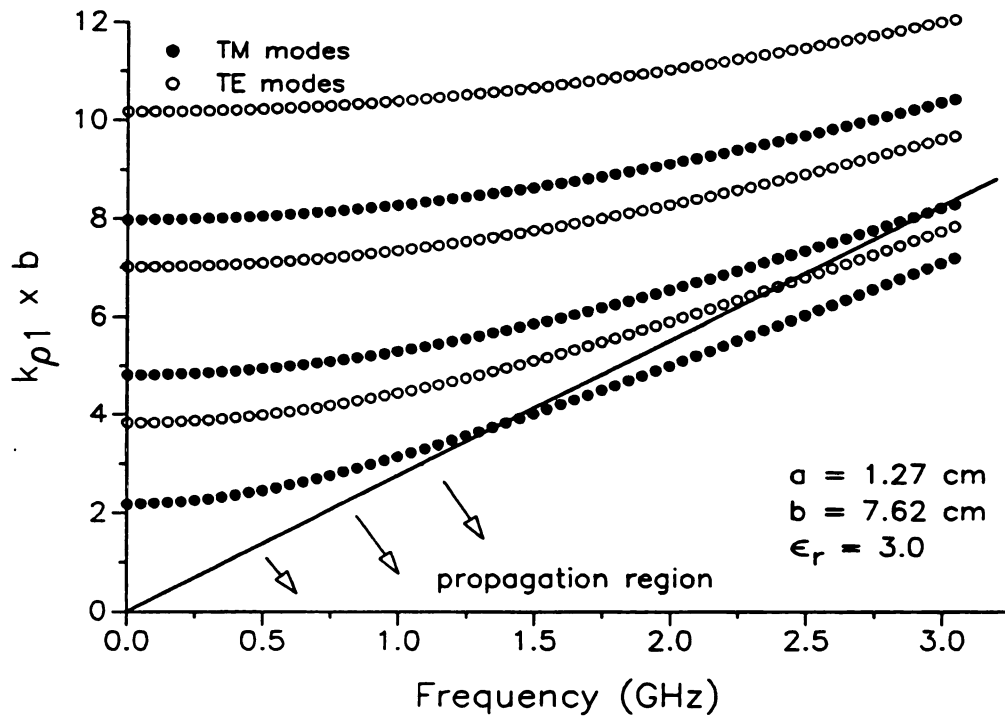
Figure 7-9 $k_{\rho 1} b$ vs. f for TE and TM modes, $\epsilon_r = 3.0$, $a = 1.27$ cm, $b = 7.62$ cm.
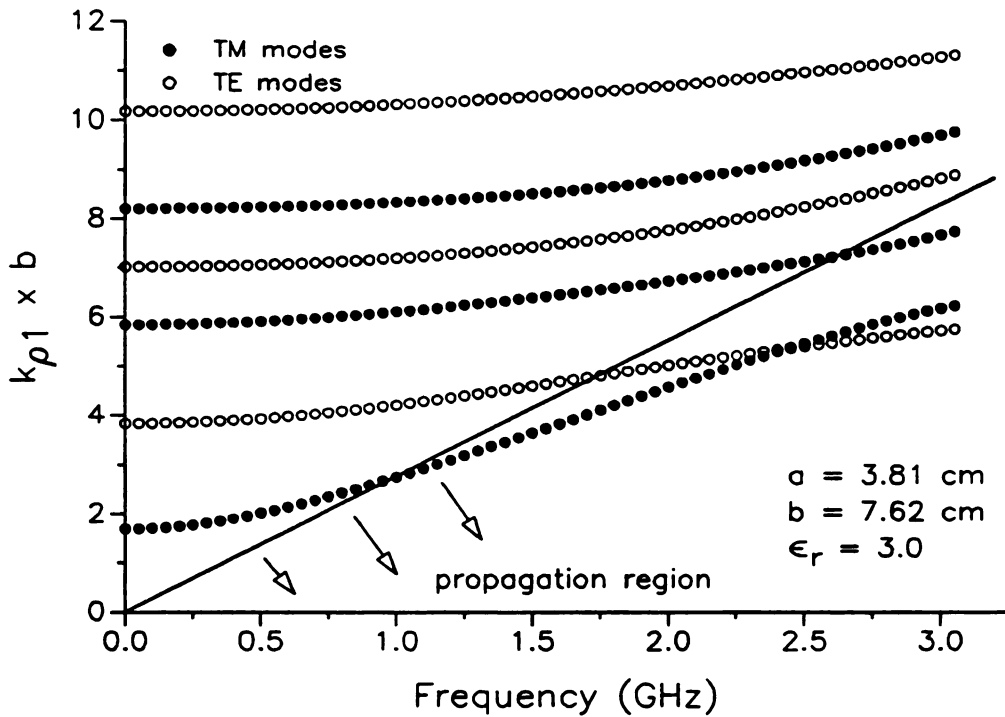
Figure 7-10 $k_{\rho 1} b$ vs. f for TE and TM modes, $\epsilon_r = 3.0$, $a = 3.81$ cm, $b = 7.62$ cm.
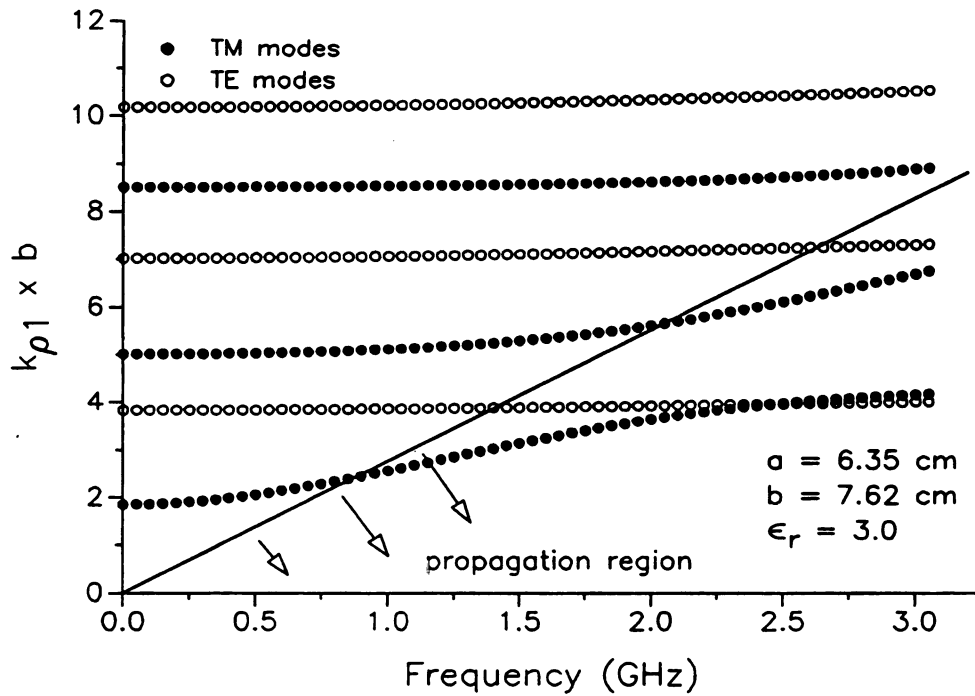
Figure 7-11 $k_{\rho 1} b$ vs. f for TE and TM modes, $\epsilon_r = 3.0$, $a = 6.35$ cm, $b = 7.62$ cm.
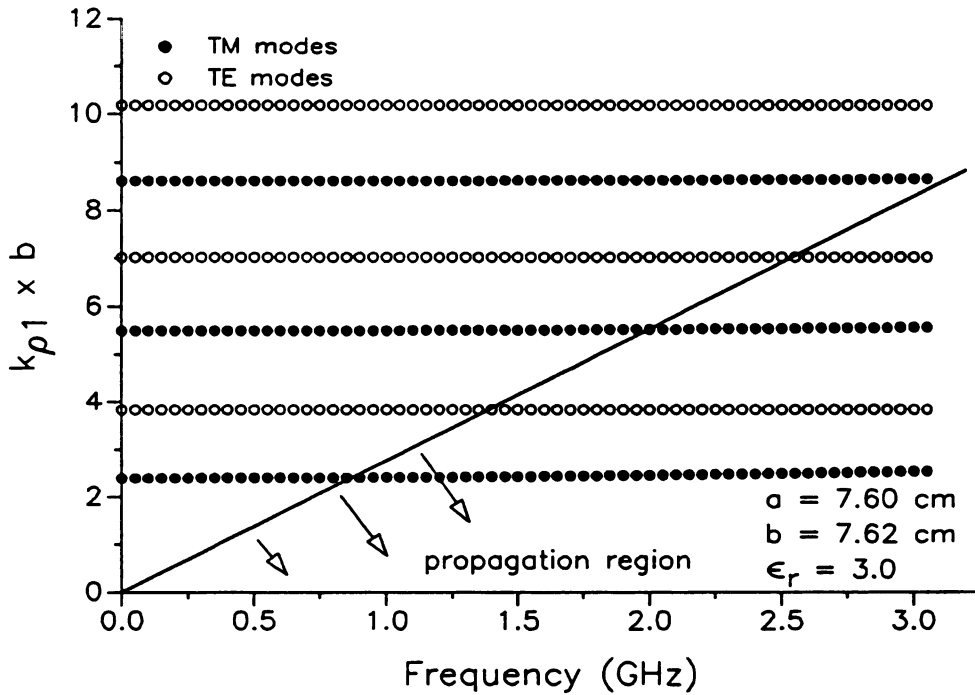
Figure 7-12 $k_{\rho 1} b$ vs. f for TE and TM modes, $\epsilon_r = 3.0$, $a = 7.60$ cm, $b = 7.62$ cm.
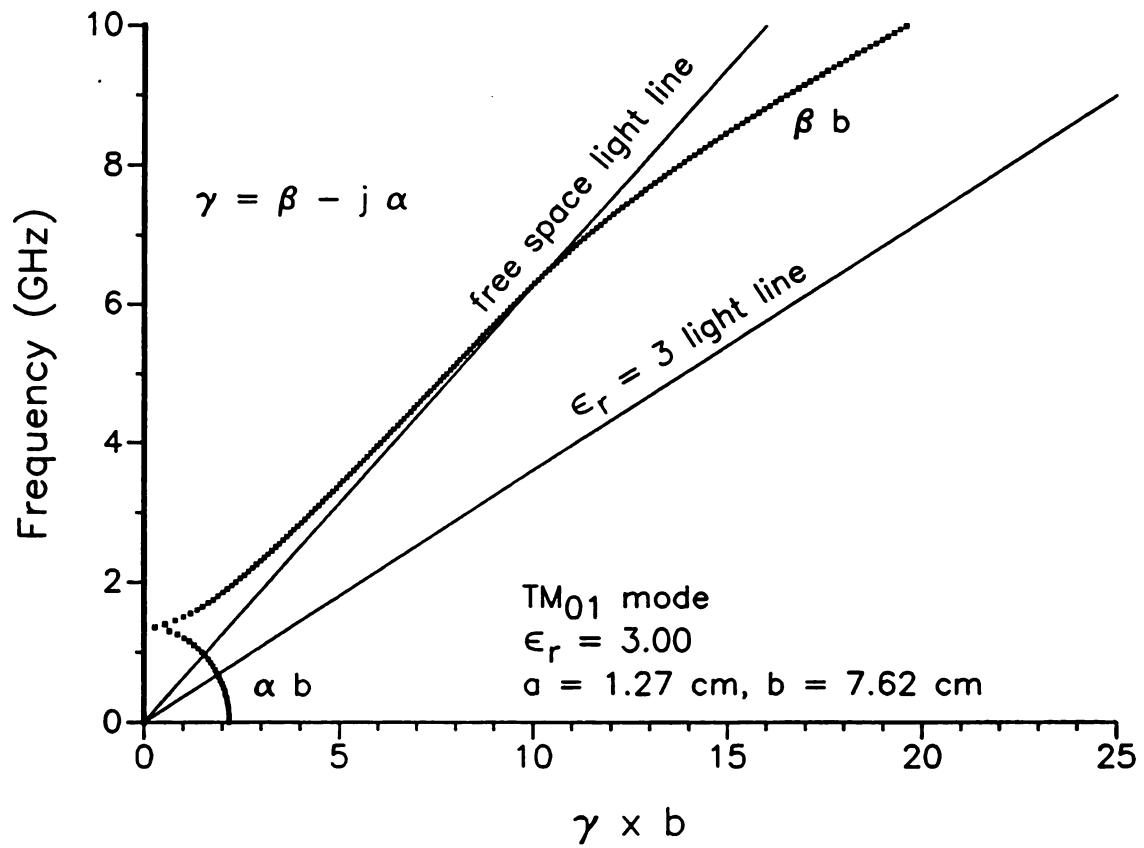
Figure 7-13 f vs. γ for the TM_{01} mode, $\epsilon_r = 3.0$, $a = 7.60$ cm, $b = 7.62$ cm.
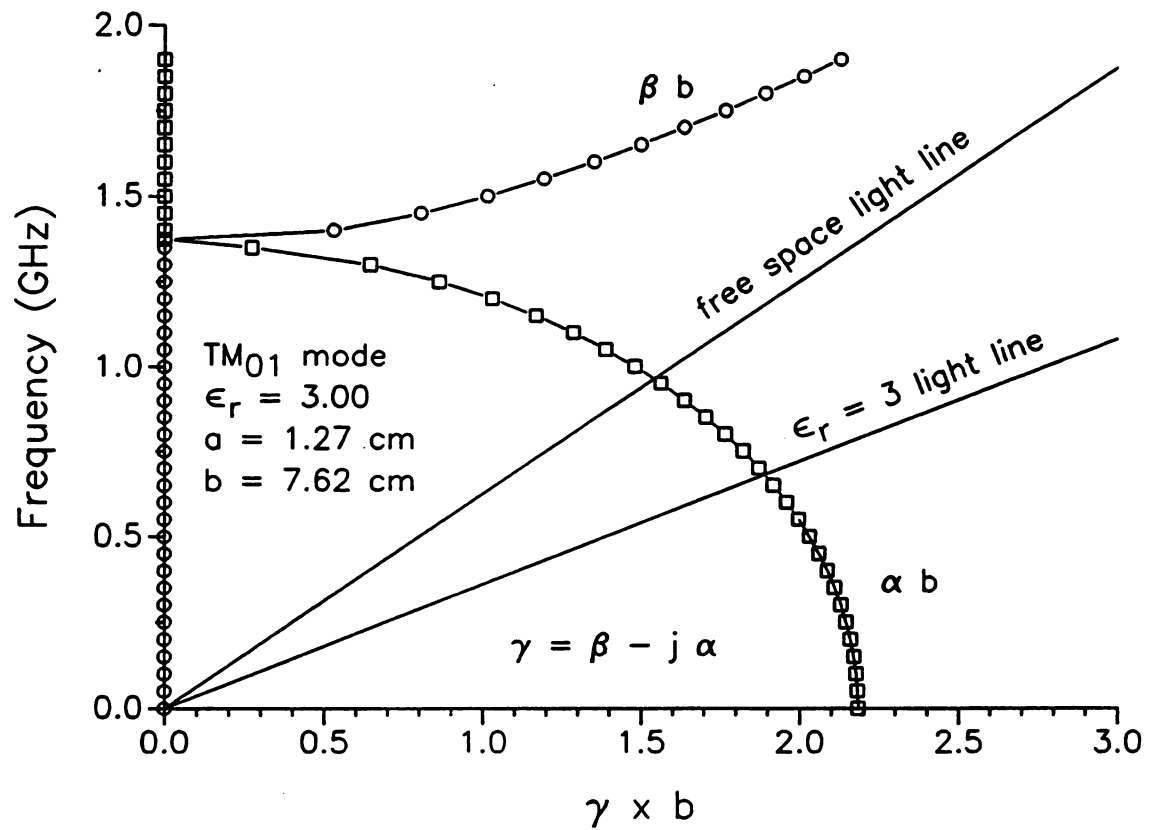
Figure 7-14 Low frequency, low γ region of Figure 7-13.

In the propagating region just above 6 GHz the mode crosses the free-space light line into the free-space slow wave region. As the frequency increases the propagation curve approaches the $\epsilon_r = 3$ light line from the left. Figure 7-14 is an enlarged view of the cutoff region showing that $\beta = 0$ below cutoff and $\alpha = 0$ above cutoff. Points on the plot are shown as open squares for α and as open circles for β.

7.5 Nylon Loads: $\hat{\epsilon}_r = 3.03 - j0.039$

Adding a small amount of loss to a material does not substantially affect the real part of $k_{\rho 1}$. As an example, Figure 7-15 contains a plot of $k_{\rho 1} b$ as a function of frequency for a nylon load of complex dielectric constant $\hat{\epsilon}_r = 3.03 - j0.039$ over the same range as that shown above in Figure 7-9 for a lossless load with $\epsilon_r = 3.0$. Apart from the inclusion of a decisive cutoff line in Figure 7-9, the two Figures are nearly indistinguishable. The imaginary part of $k_{\rho 1}$, on the other hand, is very different when losses are included. In the absence of losses, for non-complex modes the imaginary part of $k_{\rho 1}$ is always zero. Figure 7-16 shows how the imaginary part of $k_{\rho 1} b$ behaves as a function of frequency for nylon. In the frequency range below 3 GHz the imaginary part decreases negatively with frequency for all modes shown. If the frequency range is increased to include frequencies up to 20 GHz, it may be seen that eventually the imaginary part reaches a minimum and begins to rise. This is shown in Figure 7-17 for the TM_{01} and TE_{01} modes.

The frequency at which the imaginary part of $k_{\rho 1}$ bottoms out in Figure 7-17 is near the point at which β crosses the free-space light line. Figure 7-18 shows that β crosses the free-space light line just above 6 GHz for the TM_{01} mode. The minimum of the imaginary part of $k_{\rho 1}$ is at 7 GHz. There is also a slight bulge in α in this frequency region which is more visible with materials that have a higher loss factor. The bulge in α corresponds not so much to the light line crossing as to the change in the slope of β, which happens to occur near the crossing point in this case. In the high frequency range, Figure 7-18 shows that the slope of β changes to become nearly parallel with the nylon light line. In the low frequency range it is somewhat parallel with the free-space light line indicating that the group velocity of the wave is
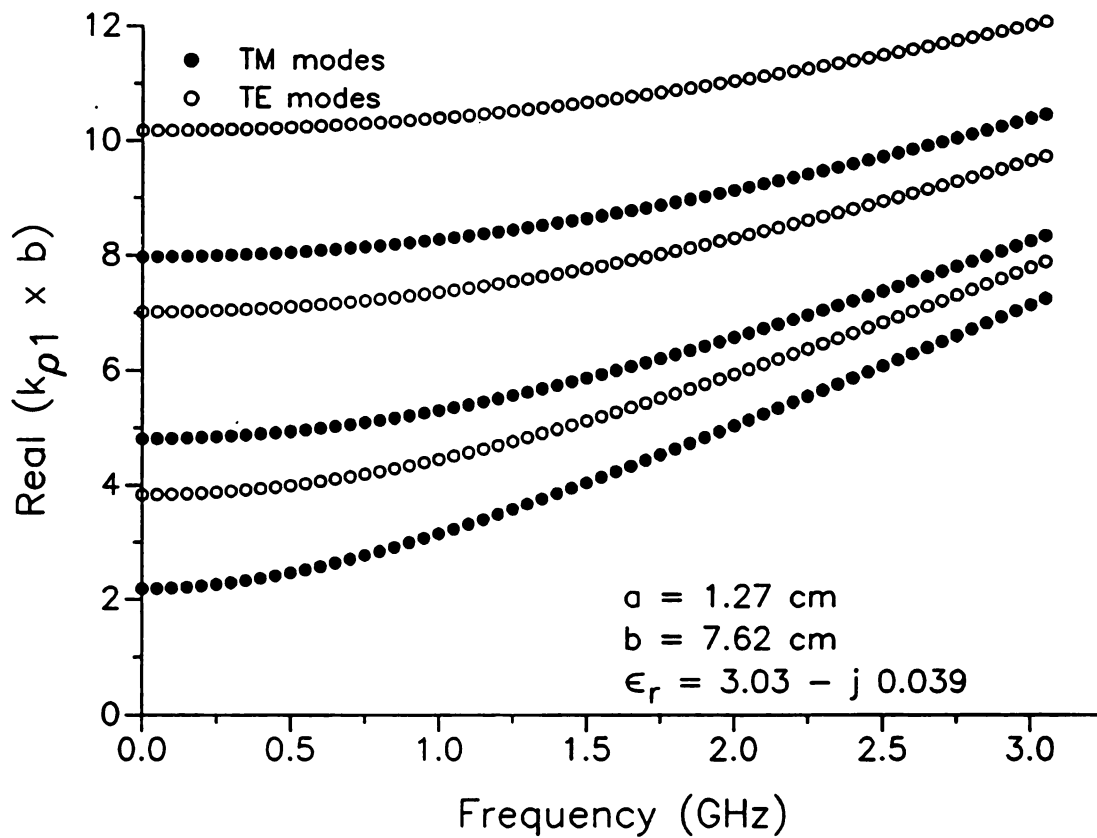
Figure 7-15 Real $k_{\rho 1} b$ vs. f for TE and TM modes: nylon, $a = 1.27$ cm, $b = 7.62$ cm.
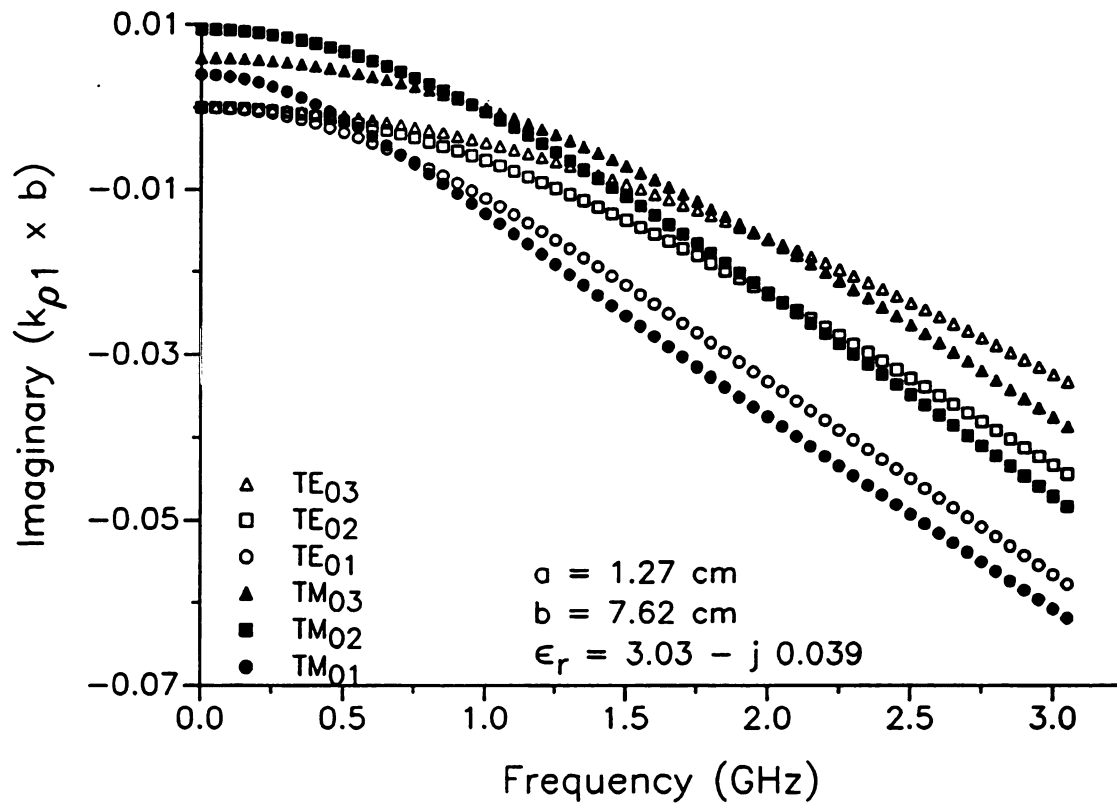
Figure 7-16 Imaginary $k_{\rho 1} b$ vs. f for TE and TM modes: nylon, $a = 1.27$ cm, $b = 7.62$ cm.
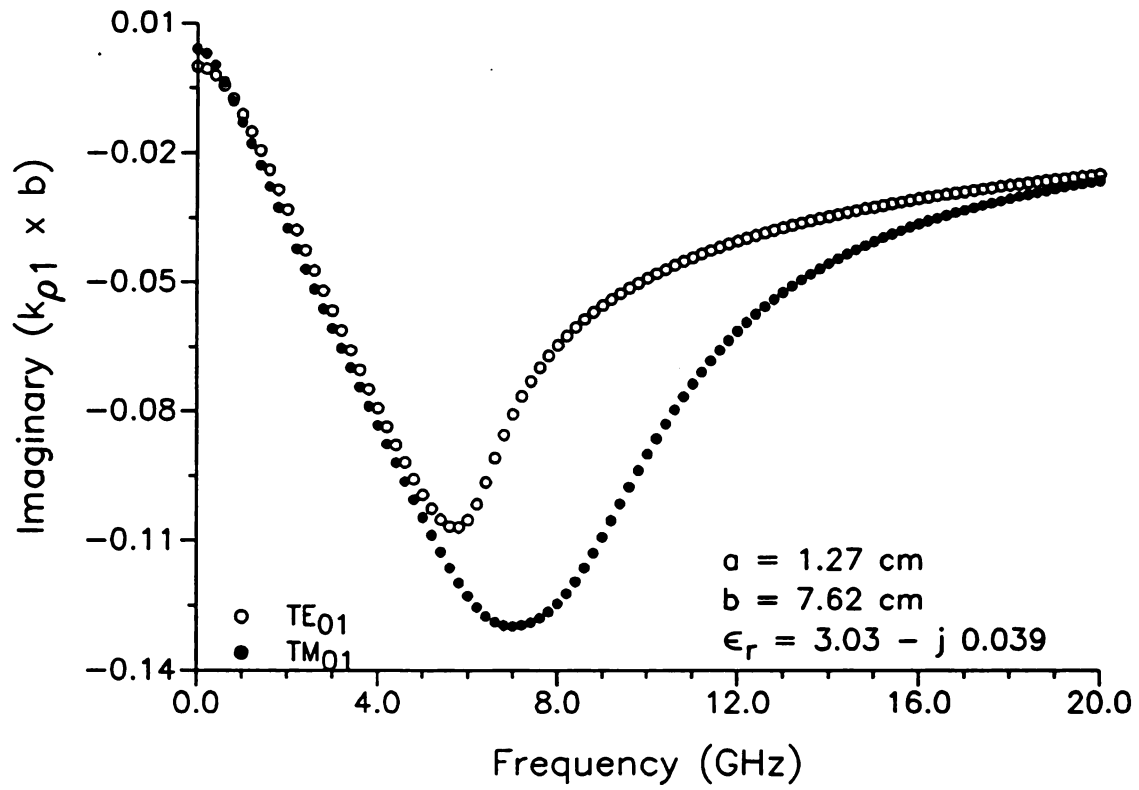
Figure 7-17 Imaginary $k_{\rho 1}\, b$ vs. f for TE_{01} and TM_{01} up to 20 GHz.
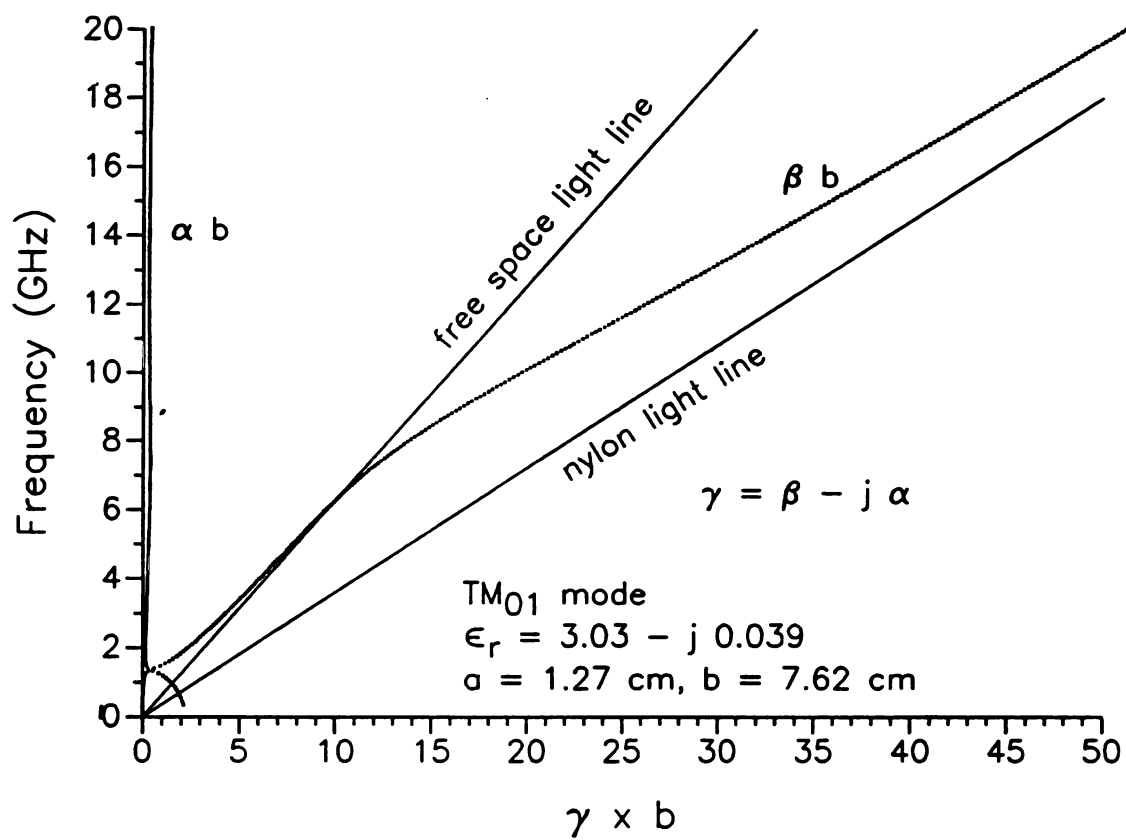
Figure 7-18 f vs. γ for the TM_{01} mode: nylon, $a = 7.60$ cm, $b = 7.62$ cm.

approximately that of a plane wave propagating in free space. At higher frequencies the group velocity is that of a plane wave traveling in a nylon medium.

Figures 7-19 and 7-20 show an enlarged view of the lower frequency range of the mode shown in Figure 7-18. In Figure 7-19 the frequency range is 0 to 10 GHz while Figure 7-20 is primarily a picture of the cut off region. These two Figures should be compared with the similar plots for the lossless, $\epsilon_r = 3.0$ load shown in Figures 7-13 and 7-14.

Figures 7-18, 7-19, and 7-20 exhibit another interesting feature of TM mode propagation in the lossy, coaxially-loaded waveguide. In the very low frequency range, below 450 MHz, α is negative. These negative values are not shown in Figure 7-20 but may be seen outside the coordinate space in the lower left hand corner of Figures 7-18 and 7-19. Ordinarily, negative values of α would present a difficulty in that they would represent energy growth in the direction of energy propagation. However, a further magnification of β in the low frequency region reveals that for frequencies where α is negative, the TM_{01} mode is backward. This is demonstrated in Figure 7-21. A backward mode is one in which the slope of the ω-β diagram is negative, meaning that energy is propagating in a direction opposite to that of the wave front. For a lossy backward mode it is necessary that α be negative in order that the fields decay in the direction of energy propagation. Figure 7-21 shows that α changes sign at the exact point that the mode becomes backward, at approximately 420 MHz.

It should be pointed out that this region is very highly damped, the magnitude of α being near .26 cm^{-1}. Any wave excited in this frequency range would be damped by a factor of $1/e$ within 3.8 cm. The shortest wavelength in the backward region shown in Figure 7-21 is approximately 1.2×10^4 cm. The damping length is therefore but a tiny fraction of the wavelength. Backward wave regions will be pointed out below in TM modes for loads with higher loss factor—it is not observed here in any other but the ϕ-symmetric TM modes.
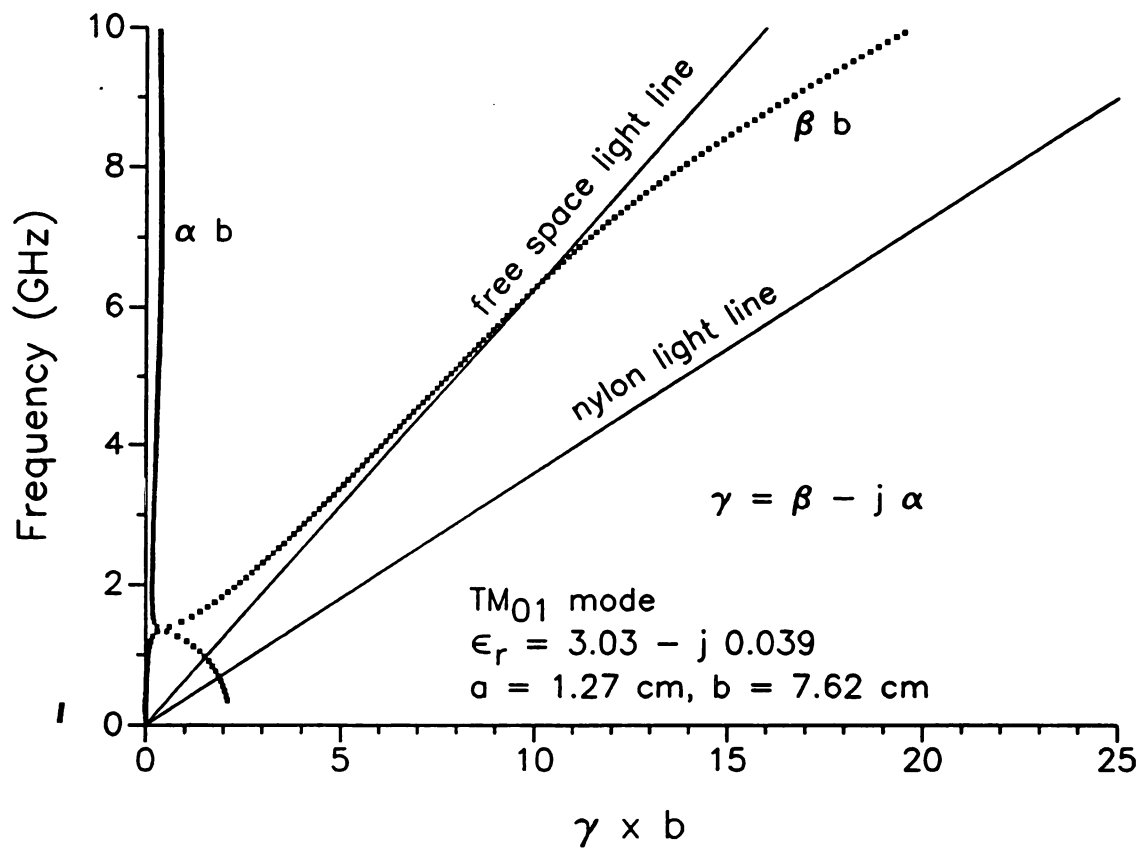
Figure 7-19 f vs. γ for the TM_{01} mode for frequencies up to 10 GHz.
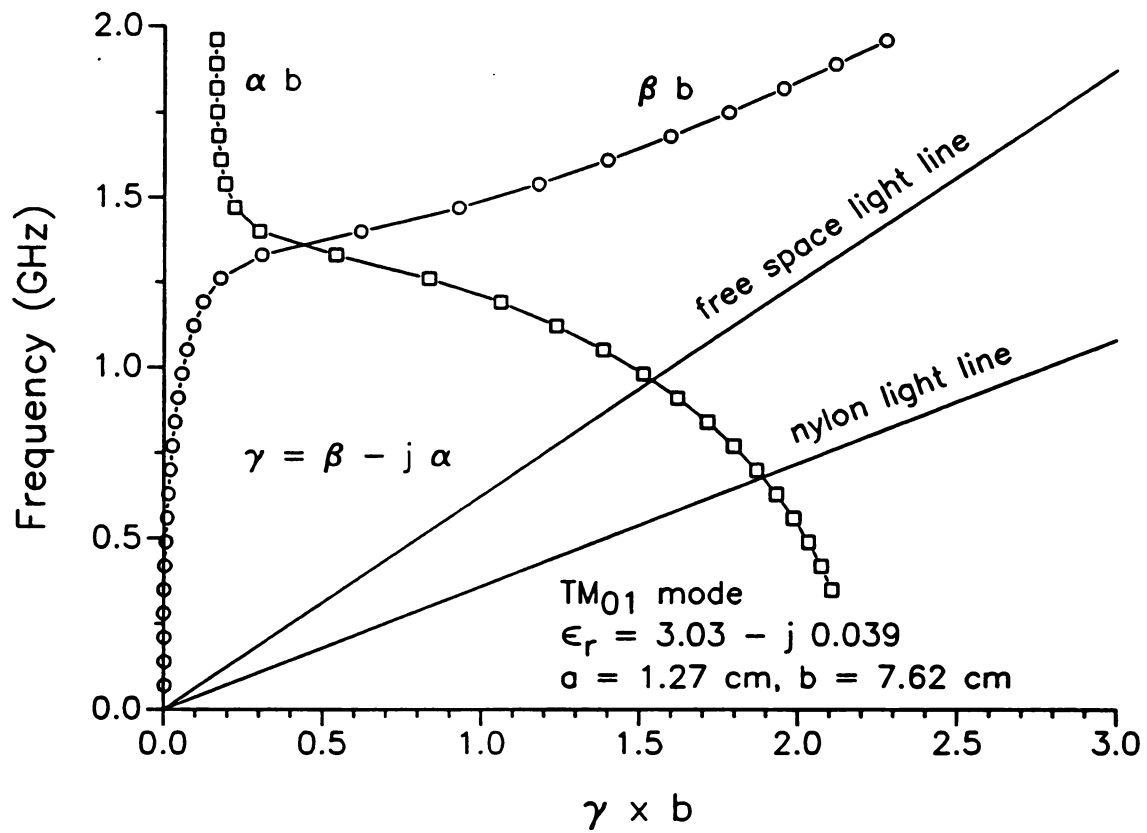
Figure 7-20 Cut off region of Figures 7-18 and 7-19.
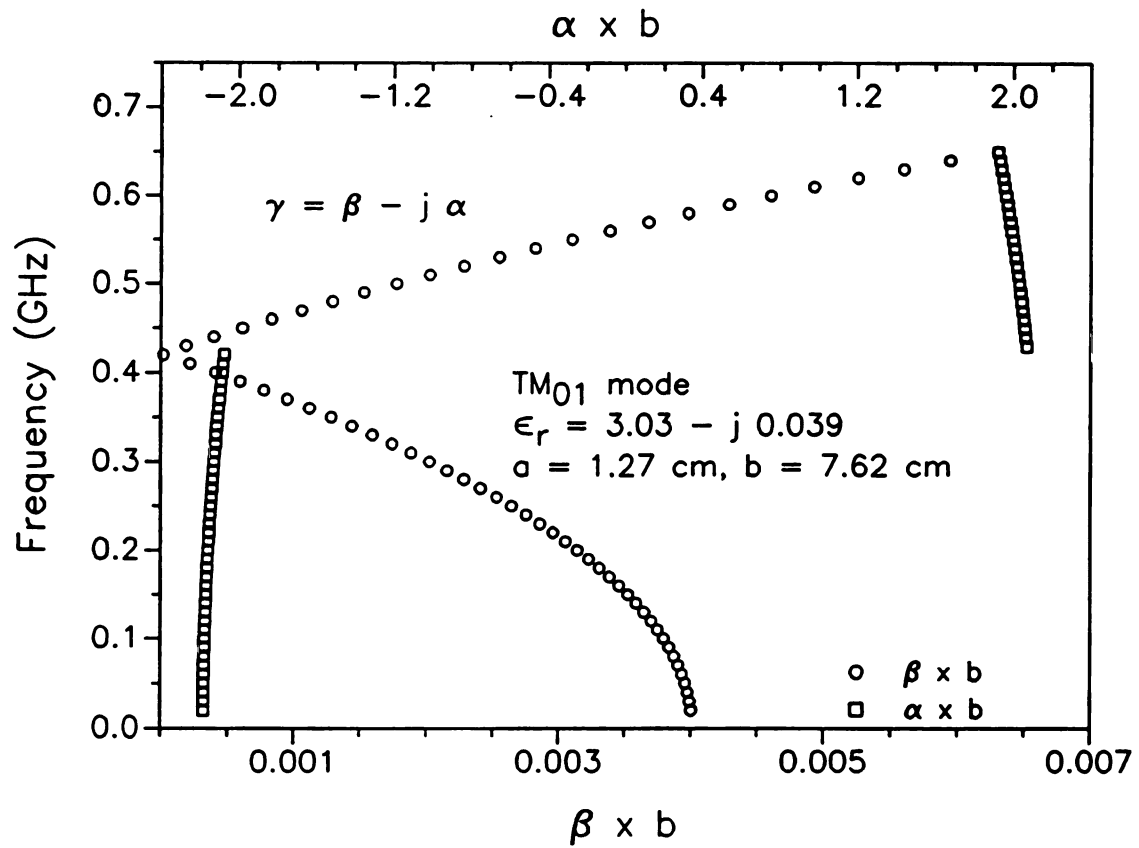
Figure 7-21 f vs. γ for the TM_{01} mode, exhibiting low frequency backward mode behavior.

7.6 Higher Loss Factor Loads

It is to be expected that the degree of damping rise with an increase in the loss factor of the load material. That is, as long as the loss factor is small enough that the load does not appear to be a good conductor. Figures 7-22 and 7-23 are plots of γ for TM modes in a waveguide of radius 7.62 cm, a load radius of 1.27 cm, and a complex dielectric constant of $\hat{\epsilon}_r = 3 - j\,1$. The real part of the dielectric constant, ϵ_r', is nearly the same as that of nylon, but the loss factor, ϵ_r'', is larger by a factor of more than 20. The high loss factor affects not only α, but also β, as can be seen by comparing Figure 7-22 with 7-18. In Figure 7-18, β crosses the free-space light line just above 6 GHz; in Figure 7-22 the crossing point is at less than 2 GHz. In Figure 7-22 there is an obvious increase in α over that of nylon in Figure 7-18: For the nylon load at 10 GHz, αb is 0.34. For TM_{01} in Figure 7-22 it is nearly 40 times as great at 13.3. The relationship between ϵ_r'' and α is clearly non-linear.

With such high damping coefficients, neither of the modes in Figure 7-22 can be considered to be truly propagating. With αb at 13.3, the mode is damped by a factor of $1/e$ within 6 mm. Using Lin's criteria for complex cutoff,[16] i.e., cutoff occurs when $\alpha \lambda_o = 1$ where λ_o is the free-space wavelength, the modes in both Figures 7-22 and 7-23 are everywhere cutoff. A general observation can also be made that, for low frequencies, the higher order modes, TM_{03} and TM_{04}, are more highly damped than the lower order modes, TM_{01} and TM_{02}. The high damping of these modes over all frequency ranges suggests a possible use for appropriately matched lossy coaxially-loaded waveguide sections as non-reflective termination microwave circuit components.

Figure 7-22 exhibits a bulge in α for the TM_{02} mode in the region where β changes slope. This was noted earlier in the TM_{01} mode for the nylon load. This bulge is also a feature of the TM_{04} mode in Figure 7-23 where it is especially pronounced. Two more characteristics of these mode should be noted. First is that the high frequency range of TM_{01} in Figure 7-22 is nearly coincident with the high frequency range of TM_{03} in Figure 7-23. It is possible, although it is not shown

---

[16]Lin, 101.
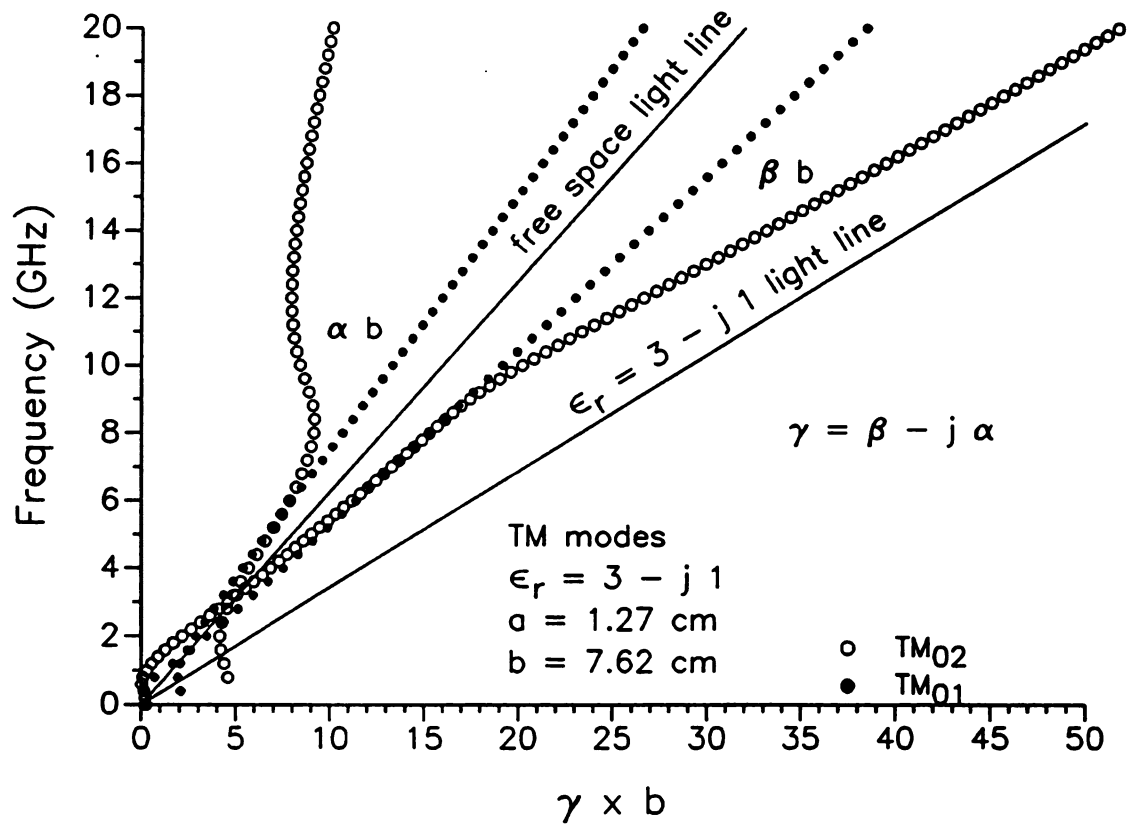
Figure 7-22 f vs. γ for TM_{01} and TM_{02} modes: $\hat{\epsilon}_r = 3 - j1$.
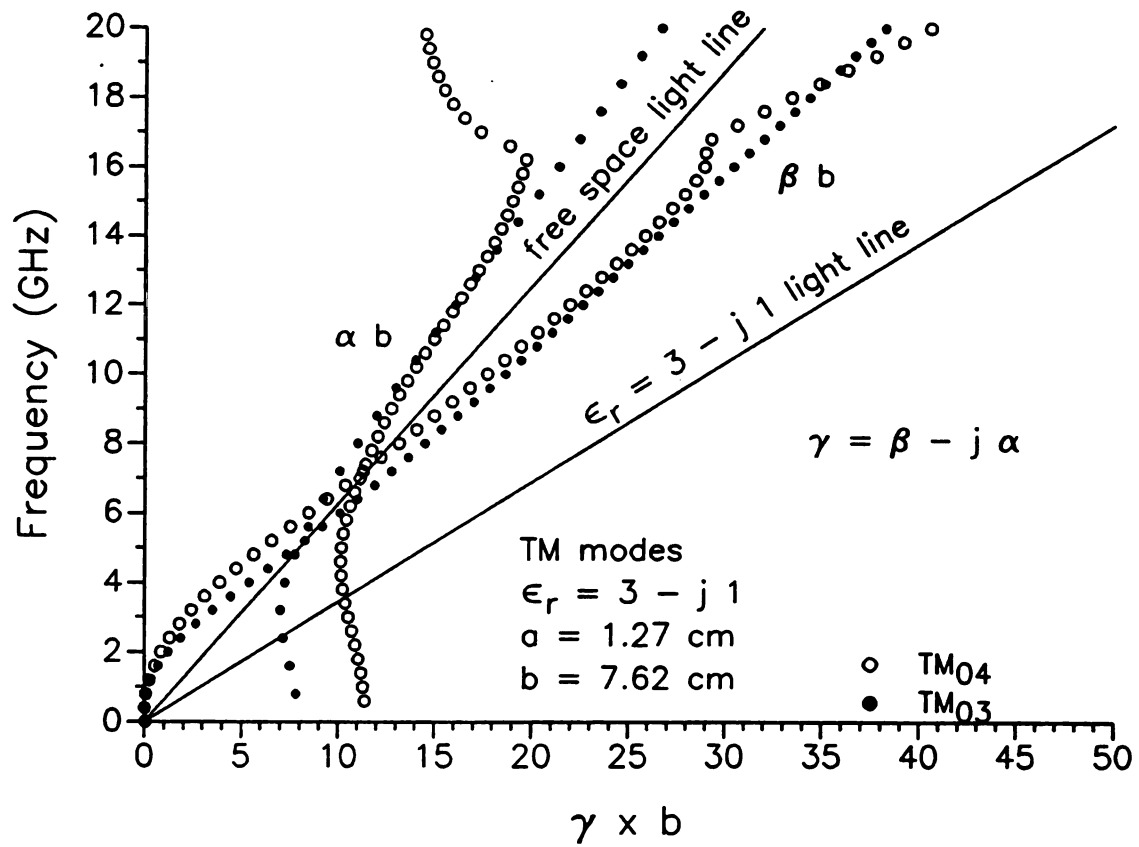
Figure 7-23 f vs. γ for TM_{03} and TM_{04} modes: $\hat{\epsilon}_r = 3 - j\,1$.

here, that the odd ordered modes behave similarly for high frequencies. The same is not true of the evenly ordered modes. Secondly, all of these TM modes exhibit backward wave behavior in the low frequency range. For the TM_{02} mode in Figure 7-22 it is especially obvious and may be observed in the region just below 1 GHz without magnification of the plot. That the other modes exhibit backward behavior may be ascertained by the negative α regions which are indicated by the initiation points of the α curves which are located above $f = 0$.

A plot similar to those shown in Figures 7-22 and 7-23 for TM modes is given by Figure 7-24 for the TE_{01}, TE_{02}, and TE_{03} modes. The physical properties of the waveguide and the load for Figure 7-24 are the same as those for Figures 7-22 and 7-23. The same general observations might be made concerning the TE modes as were mentioned for the TM modes except that there is no backward wave behavior in the low frequency range. The oddly ordered modes behave almost identically for high frequencies and the TE_{02} mode exhibits a definite bulge in α near the frequency where β makes a change in slope, in this case, near the free-space light line crossing point. The TE modes, just like the TM modes, are very highly damped.

As a final example of coaxially-loaded waveguide propagation, the propagation characteristics of the non-ϕ-symmetric HEM_1 modes are plotted in Figures 7-25 and 7-26. The waveguide and load radii are still 7.62 cm and 1.27 cm respectively, ϵ_r' is still 3.0, but ϵ_r'' has been reduced to 0.5. Although α has been reduced from the case for TM and TE modes with $\epsilon_r'' = 1$, Figure 7-25 indicates that these modes are still cutoff for all frequencies using Lin's criteria. It is not indicated in the Figures whether the modes are HE or HH, but both HEM_{11} and HEM_{12} are HE above 3.5 GHz, while below 3.5 GHz HEM_{11} is HH and HEM_{12} is HE. An enlarged view of the region below 5 GHz is shown in Figure 7-26. There does not appear to be anything remarkable in the propagation constant behavior at 3.5 GHz for either mode. Once again, as for the TE modes, the HEM_1 modes exhibit no backward wave behavior in the low frequency region.
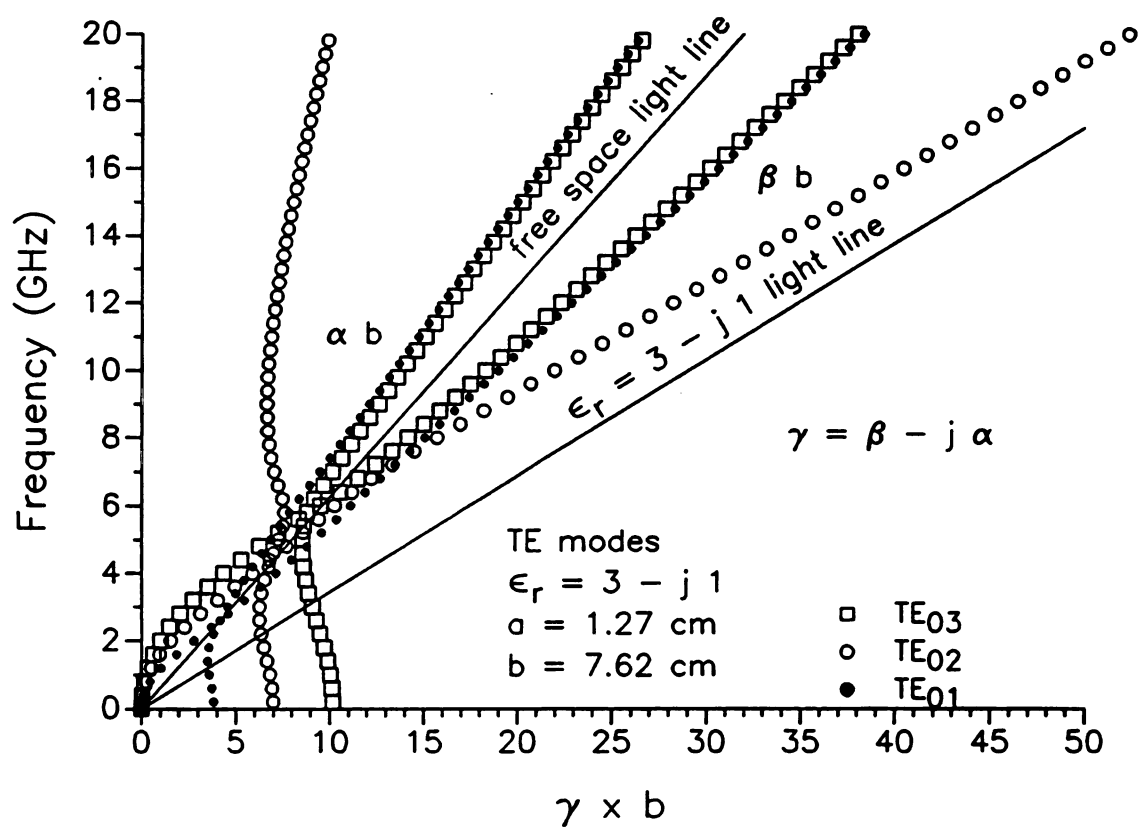
Figure 7-24 f vs. γ for TE_{01}, TE_{02}, and TE_{03} modes: $\hat{\epsilon}_r = 3 - j1$.
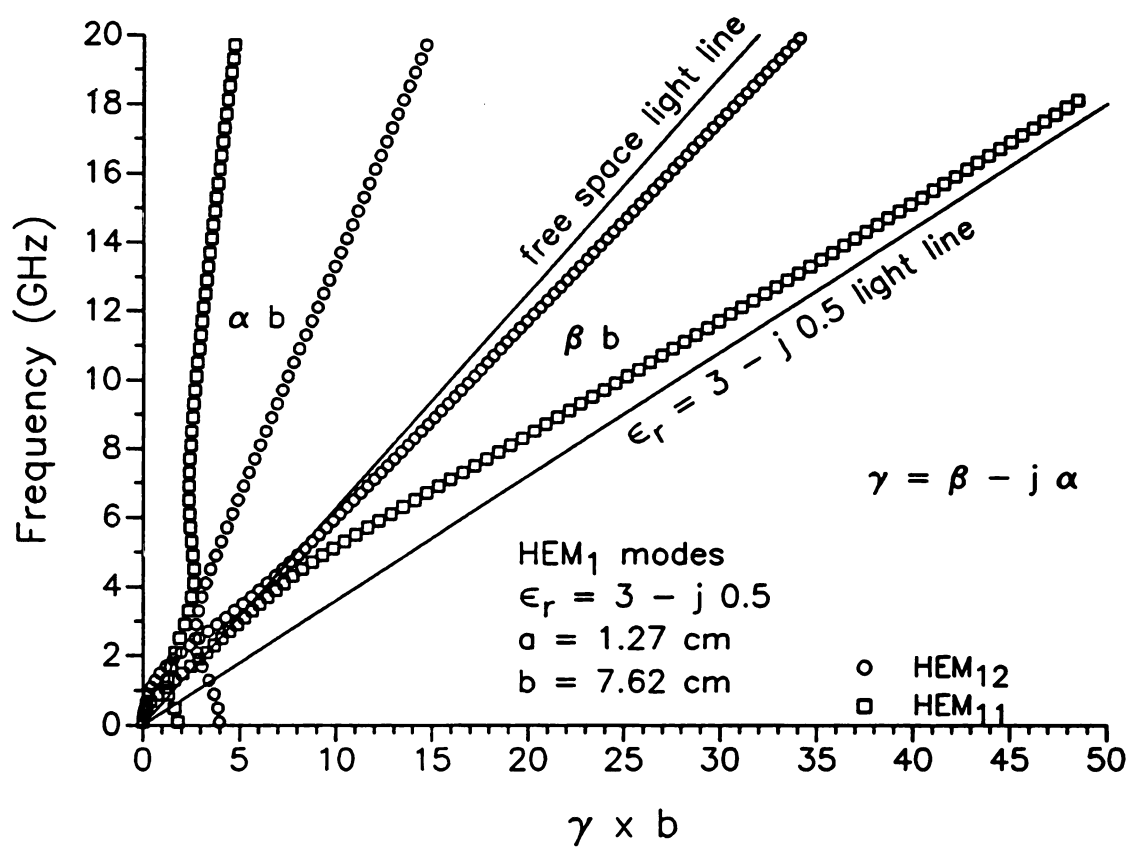
Figure 7-25 f vs. γ for HEM_{11} and HEM_{12} modes: $\hat{\epsilon}_r = 3 - j0.5$.
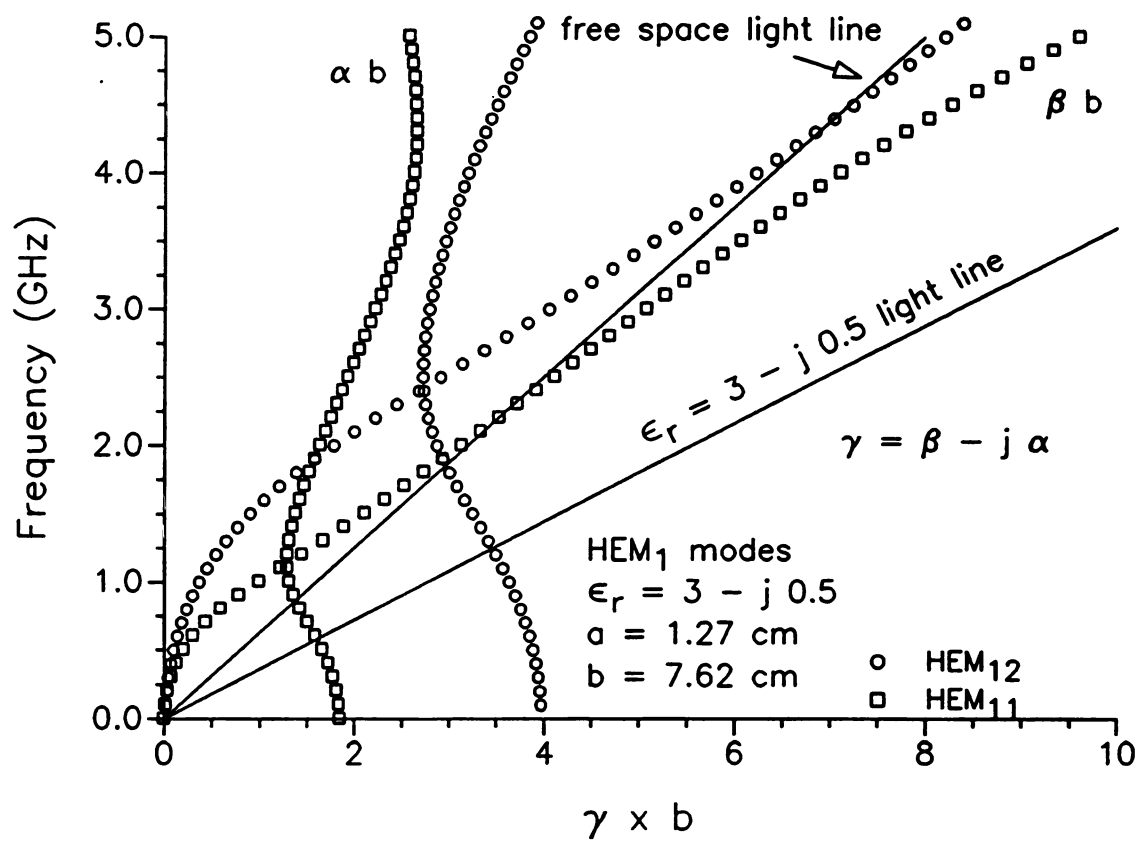
Figure 7-26 f vs. γ for HEM_{11} and HEM_{12} modes in the lower frequency region.

7.7 Conclusion

Solutions to Equation (3-92) of Chapter 3 have been presented as a function of real frequency values. These solutions correspond to various modes and propagation behavior in coaxially-loaded waveguides. A mode naming scheme has been developed, based on the criteria of Bruno and Bridges, which makes it easier to remember which hybrid modes are TE-like and which are TM-like, labeling TE-like modes HH and TM-like modes HE. It was also pointed out that these distinctions do not always provide physical insight and that they might all be labeled HEM modes in such cases.

Graphical solutions were presented for both lossless and lossy loaded waveguides. Lossless solutions for $\epsilon_r = 37.6$ with $a = 1$ cm and $b = 1.27$ cm were compared to results published by Zaki and Atia and Zaki and Chen and were shown to match within a small uncertainty related to unit conversion. Complex modes were identified for these load and waveguide parameters and both real and imaginary parts of the wavenumbers were plotted. TE and TM modes propagating in a waveguide of radius 7.62 cm coaxially loaded with lossless loads of varying radii and a dielectric constant of $\epsilon_r = 3.0$ were examined in the region from 0 to 3 GHz. It was shown that for large load radii the radial wavenumber in region 1 is not dependent on frequency. Additionally, the cutoff frequency falls with increasing load radius and, at least for the larger load radii, load dielectric constant.

Small losses were considered by exploring the propagation characteristics of the TE and TM modes for a 1.27 cm radius nylon load in a 7.62 cm radius waveguide. It was shown that the real parts of the TM_{01} wavenumbers were not greatly changed from the lossless case, but that the modes were attenuated. The losses also introduced a highly damped backward wave region in the TM_{01} mode below 420 MHz. When larger losses were included, the TM modes continued to display the backward wave region which was not observed in the TE or HEM_1 modes. It was shown that for complex dielectric constants of $3 - j1$ for TE and TM modes, and $3 - j0.5$ for HEM_1 modes, all of the lower order modes were highly damped for all frequencies below 20 GHz with $a = 1.27$ cm and $b = 7.62$ cm.

The chief benefit of this Chapter regarding its relation to the solutions for the coaxially-loaded cavity is the presentation of the location of the radial wavenumbers for a variety of loads and frequencies. For high dielectric constant materials more care is needed in searching out the wavenumbers for lower order modes. Since they are not evenly spaced, it easy to miss one of them, as Zaki and Atia do in an early paper. Plotting the wavenumbers versus frequency, as in Figures 7-1, etc., is the safest means of assuring that all modes are located when constructing solutions for the coaxially-loaded cavity.
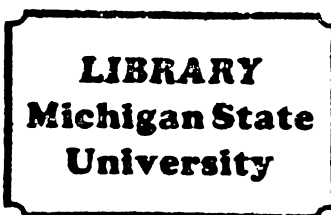
PLACE IN RETURN BOX to remove this checkout from your record.
TO AVOID FINES return on or before date due.

DATE DUE	DATE DUE	DATE DUE
MAY 1994 365556		
SEP 2 5 1995 FEB 0 6 1995		
JUN 1 1 1997		

MSU Is An Affirmative Action/Equal Opportunity Institution

ELECTROMAGNETIC FIELD SOLUTIONS
FOR THE NATURAL MODES OF A CYLINDRICAL CAVITY
LOADED WITH LOSSY MATERIALS

Volume II

By

Edward Benjamin Manring

A DISSERTATION

Submitted to
Michigan State University
in partial fulfillment of the requirements
for the degree of

DOCTOR OF PHILOSOPHY

Department of Electrical Engineering

1992

Chapter 8
NUMERICAL SOLUTIONS FOR THE
CAVITY-SHORT TYPE CONFIGURATION

8.1 Introduction

The purpose of the present Chapter is to present numerical frequency solutions to Equation (3-92) of Chapter 3 with γ defined by the cavity-short type constraint given in Equation (4-28) of Chapter 4. Plots of the real and imaginary parts of the frequency versus system parameters are referred to in general as *mode charts*. These mode charts are useful in investigating resonant frequency and quality factor behavior as a function of such parameters as load radius, cavity length, load dielectric constant, and load loss factor. They demonstrate sensitivity or indifference of the modes to changes in cavity and load parameters, and predict, through the quality factor, which modes are best for heating purposes. Once the frequency is known, the fields may be directly calculated and plotted. Many of these plots are included in this Chapter. Plots of the field magnitudes versus spacial coordinates show where the energy is concentrated in the cavity, and the primary direction of the fields. This information is useful for determining which modes are best used to couple energy into materials of a given size and shape. Field plots also help to explain resonant frequency and cavity quality factor behavior.

The cavity-short type configuration, described in Section 4.3 and shown in Figure 4-3, consists of a section of coaxially loaded waveguide, shown in Figure 3-2, of length L_s with shorting plates on either end. The radius of the cavity is b; the radius of the coaxial load is a. As given in Chapter 3 by Equation (3-9), and defined relative to the free-space permittivity by Equation (6-32) of Chapter 6, the relative complex permittivity of the load is defined by

$$\hat{\epsilon}_r = \epsilon_r' - j\epsilon_r'', \qquad (8\text{-}1)$$

where ϵ_r' is the relative dielectric constant and ϵ_r'' is the relative loss factor. For the computations presented here, the dielectric constant outside the load is that of free space, ϵ_0.

This Chapter will include a brief discussion of the naming of the modes followed by several mode charts for resonant frequency versus L_s, a, ϵ_r', and ϵ_r''. Calculations of cavity Q will be presented for several modes as a function of loss factor and rod radius, a, for a variety of dielectric constants, ϵ_r'. It will be shown how coaxially loaded modes approach the TE and TM modes of the homogeneously filled cavity, both as $a \to 0$ and $a \to b$.

8.2 Naming of Modes

The naming of modes for the cavity-short type configuration involves the same considerations encountered in naming the modes in the coaxially loaded waveguide. The difference between the cavity and the waveguide is that the axial wavenumber, γ, in the cavity is constrained to be a real number as defined by Equation (4-28), and the frequency is complex when the load is lossy. It was vice-versa in the lossy, coaxially-loaded waveguide. This exchange of complex properties between the propagation wavenumber and the frequency presents no fundamental difficulties in retaining the same mode naming scheme for the cavity-short type cavity modes as for the coaxially-loaded waveguide modes. The ϕ-symmetric modes are called TM or TE depending on the characteristic equation solved to find the wavenumbers, while the hybrid modes may be labeled HEM in general, or when it lends insight, labeled according to the HE/HH system developed for the coaxially-loaded waveguide.

The HE/HH system of mode naming discussed in Chapter 7 involves comparing the ratio of E_z to H_z in the load material with the wave impedance of a plane wave traveling at the same phase velocity, defined by Equation (7-2). If the ratio is greater than the wave impedance, the mode is called HE (TM-like). Otherwise it is called HH (TE-like). For the coaxially-loaded waveguide, the plane

wave phase velocity was defined according to the absolute value of the axial wavenumber, γ, where $\gamma = \beta - j\,\alpha$. For the cavity-short type configuration cavity, γ is always real, but the frequency is not. In this case, the real part of the frequency is used in Equation (7-2). The plane wave whose impedance is compared with the ratio of E_z to H_z is decaying in time at the same rate the natural mode fields decay in the cavity.

The labels are subscripted with three integers n, p, and q. The orders of the ϕ and z dependences are pre-specified by the integers n and q in Equations (4-24) through (4-50). p is used to indicate the order of the radial dependence and is determined the same way that the radial order subscript is determined in the coaxially-loaded waveguide, using the real part of the frequency. For a given n and q, the mode with the lowest frequency (real part) is assigned a p value of 1. The mode with the next lowest frequency is identified with p equal to 2, etc.

The complex frequencies plotted in the Figures in this Chapter are related to the sinusoidal steady-state as described in Chapter 6. They are actually the real and imaginary parts of the complex natural frequency. Since the real part of the natural frequency differs slightly from the sinusoidal steady-state resonant frequency, it is not appropriate to call it the resonant frequency. At the same time, it is cumbersome to use the full description "real part of the natural frequency" every time reference is made to it. The abbreviated terms *"real frequency"* and *"imaginary frequency"* will be used to refer to the real and imaginary parts respectively, of the complex natural frequency.

8.3 Mode Charts and Field Patterns: TM Modes

8.3.1 Low Dielectric Constant Loads with Various Loss Factors

Changes in resonant frequency with cavity length provide a convenient means of comparing coaxially loaded modes with empty cavity modes, since both configurations allow for variation in cavity length. It is also simple to measure the frequency as the cavity length is varied when experimenting with a variable length

single-mode cavity.[1] Figures 8-1 and 8-2 below are cavity length mode charts for TM_{012} and TM_{011} modes for dielectric constant loads of $\epsilon_r' = 3.03$. ϵ_r'' in Figure 8-1 is that of nylon, while Figure 8-2 contains plots for a variety of loss factors.

For a material such as nylon, with a low dielectric constant and loss factor, $(\hat{\epsilon}_r = 3.03 - j\ 0.039$ at 2.45 GHz) the TM_{01q} modes of the empty cavity and coaxially loaded cavity are closely related, particularly for rod radii much less than the cavity radius. Figure 8-1 is a comparison of the real frequencies of the empty cavity TM_{012} mode and the coaxially loaded TM_{012} mode for a 1" diameter nylon rod inside a 6" diameter cavity. Experimental frequency measurements are included for both the empty and loaded configurations, showing excellent agreement between theory and experiment for both.[†] The slopes of the two curves are nearly the same, with the real frequency of the loaded cavity is shifted down from the empty cavity by approximately 100 MHz. The shift is slightly less for the lower cavity lengths, increasing slowly as the cavity and load grow longer.

Figure 8-2 demonstrates the effect of a hypothetically rising loss factor for the nylon load of Figure 8-1, this time in the TM_{011} mode. The upper curve for a relative loss factor of 1.0 is essentially the same as that for actual nylon which has a relative loss factor of 0.039. As the relative loss factor increases from 1 to 30 the resonant frequency drops dramatically, approximately 500 MHz for a cavity length of 7 cm. As the relative loss factor continues to increase from 30 to 1000 the resonant frequency stops falling and rises approximately 100 MHz at the 7 cm eigenlength. As shown in Figure 8-2, resonant frequencies for $\epsilon_r'' = 1000$ are close to those of the TM_{001} (TEM) mode of the coaxial cavity of the same dimensions.[‡]

Figure 8-3 contains plots of the imaginary frequency versus load length corresponding to the real frequency plots of Figure 8-2. Figure 8-3 demonstrates that

---

[1]Asmussen, Lin, Manring, and Fritz.

[†]The experimental points were all shifted as described in Section 5.4 of Chapter 5, using the empty cavity measurement at $L_s = 11$ cm as reference. Loaded cavity measurements agree with theory to within 7 MHz.

[‡]The term "coaxial cavity" is used to refer to the cavity produced by terminating a length of perfectly conducting coaxial line on either end by a shorting plate.
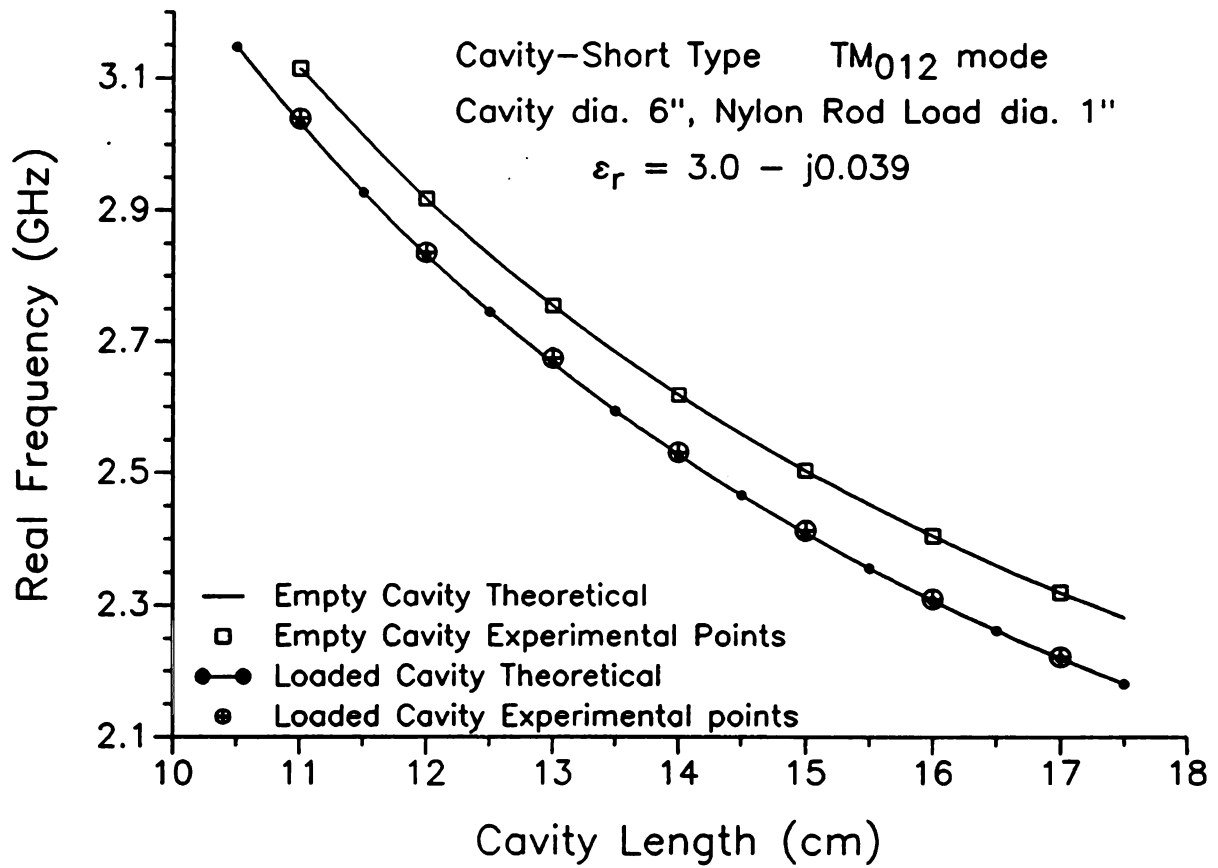
Figure 8-1 Resonant frequency vs. eigenlength for 1" diameter nylon rod in 6" diameter cavity.
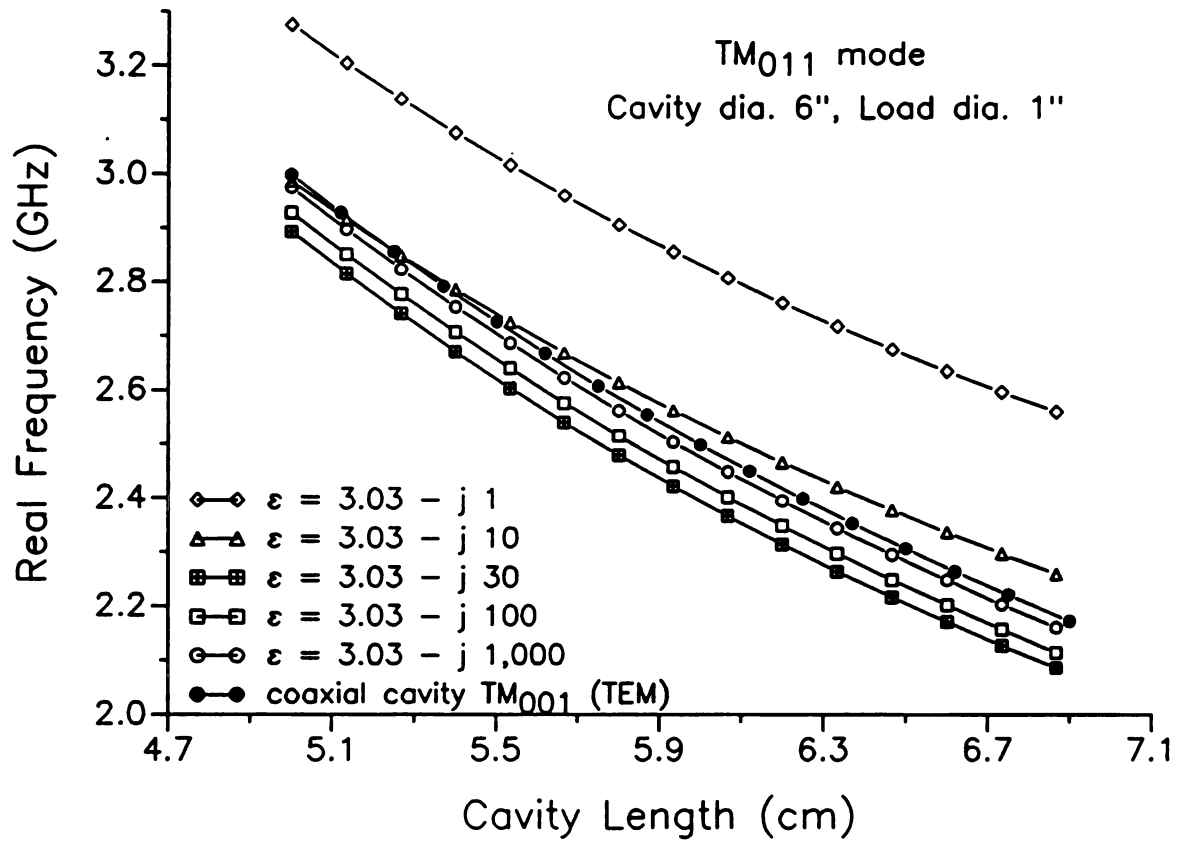
Figure 8-2 Resonant frequency vs. cavity length for nylon load with hypothetical loss factors.
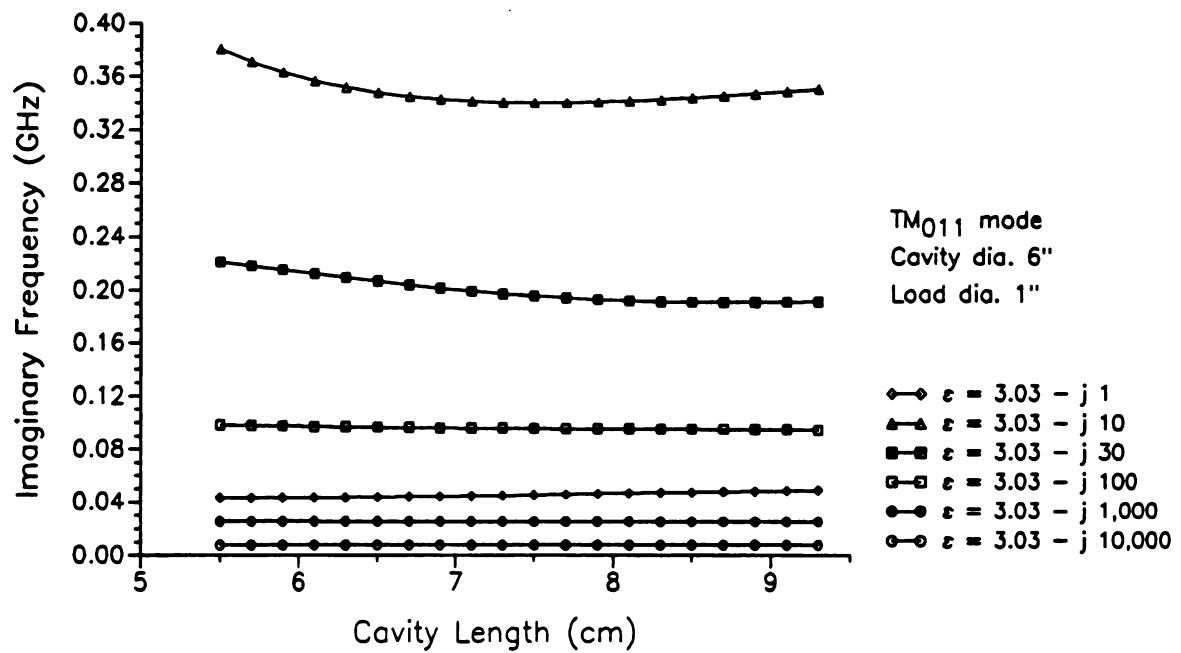
Figure 8-3 Imaginary frequency vs. cavity length for nylon load with hypothetical loss factors.

for the TM_{011} mode with $a = 0.5"$, $b = 3"$, and a low dielectric constant material, the imaginary frequency, hence the quality factor, does not change much with cavity length. Although there are exceptions for some modes and load materials, this is the general rule. Figure 8-3 shows that the quality factor changes a great deal with material loss factor.

For a loss factor of 1 the imaginary frequency is approximately 45 MHz for $L_s = 7$ cm. For $\epsilon_r'' = 10$ the imaginary frequency rises nearly an order of magnitude to approximately 350 MHz. From there it falls steadily for increasing loss factors, approaching zero for $\epsilon_r'' = 10,000$. From Equation (6-18) of Chapter 6, the cavity Q is given by

$$Q = \frac{\text{Re}(f)}{2\,\text{Im}(f)}, \tag{8-2}$$

where f is the complex frequency. It is evident then that the quality factor is lowest for $\epsilon_r'' = 10$, being approximately $3.5^\dagger$ at $L_s = 6$ cm. At $\epsilon_r'' = 1$ the quality factor is approximately 31. For an actual nylon load, $\hat{\epsilon}_r = 3.03 - j\,0.039$ (not shown in the Figure), the quality factor from Equation (8-2) is 840.

8.3.2 Electric Field Magnitudes for Increasing Loss Factors[‡]

It is of interest to question what causes the frequency to fall for increasing loss factor in the lower loss factor range, and what causes it to rise as the loss factor becomes very large? In fact, it is easier to explain the rise in the resonant frequency with increasing large loss factors than it is to explain the decrease in the frequency for the lower values of increasing loss factor. As pointed out in Chapter 3, Equation (3-10), the complex dielectric constant $\hat{\epsilon}$ may be considered to include a free electron

---

[†]The approximation of Equation (7-3) is not strictly true for this low Q value, but provides a rough estimate.

[‡]While the field magnitudes provide useful information and demonstrate beneficial qualitative similarities between various modes, the phase information is necessary to fully characterize the fields. This is especially true in the presence of losses as discussed in Appendix D.

conductivity, σ, as well as the dielectric constant ϵ' and loss factor ϵ'' such that, for a general material,

$$\hat{\epsilon} = \epsilon' - j\left(\epsilon'' + \frac{\sigma}{\omega}\right). \tag{8-3}$$

This means that a large loss factor has the same electromagnetic effect as a high conductivity.

The increasing resonant frequency may be understood as resulting from the shielding of the load from the fields as the material appears more and more like a good conductor. As the fields are blocked out of the load material they exist primarily in the free space region of the cavity instead of the higher dielectric constant region of the load, causing the resonant frequency to rise. Therefore, for very large loss factors it is safe to say that an increase in loss factor will produce an increase in resonant frequency.

This shielding effect is demonstrated in Figures 8-4 and 8-5. Figure 8-4 is a plot of the magnitude[†] of the axial electric field along a cavity radius for the TM_{011} mode of Figure 8-2 with $\epsilon_r'' = 100$. The vertical line at the radial coordinate 1.27 cm indicates the load boundary. Figure 8-5 is a similar plot for $\epsilon_r'' = 1000$. It may be seen by comparing Figures 8-4 and 8-5 that the axial electric field is nearly squeezed out of the load region for $\epsilon_r'' = 1000$.

However, comparisons between field magnitudes in the loaded region cannot provide a general answer to the question of why the frequency drops for increasing ϵ'' in one ϵ'' range and rises in another. This is evident by examination of Figures 8-6 and 8-7 which are plots of the axial electric field along a radius similar to the plots of Figures 8-4 and 8-5, except with ϵ_r'' equal to 10 and 30. Even though the field in the load region is relatively smaller for $\epsilon_r'' = 30$ than for $\epsilon_r'' = 10$, Figure 8-2

[†]There are difficulties in defining time average values of decaying fields, not only because of the universal decay factor, but also because of arbitrary phase differences between field components. The field magnitudes used in this chapter and those that follow are relative time-average values as defined in Equation (D-19) of Appendix D.
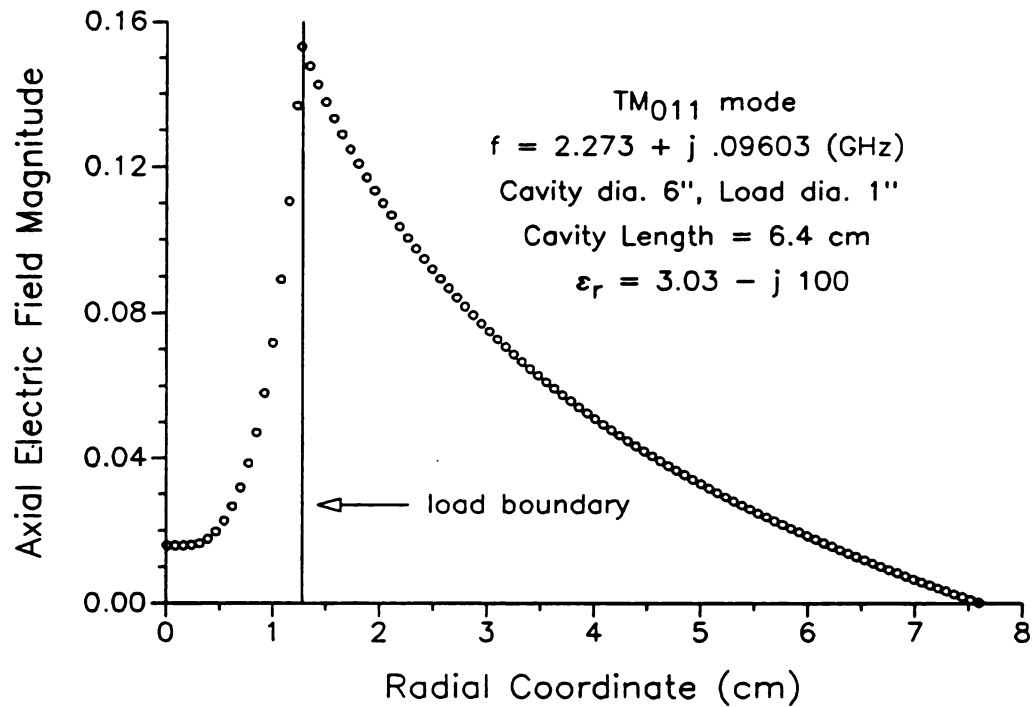
Figure 8-4 Axial electric field magnitude along a radius, TM_{011} mode, $\epsilon_r'' = 100$.

Figure 8-5 Axial electric field magnitude along a radius, TM_{011} mode, $\epsilon_r'' = 1000$.

Figure 8-6 Axial electric field magnitude along a radius, TM_{011} mode, $\epsilon_r'' = 10$.
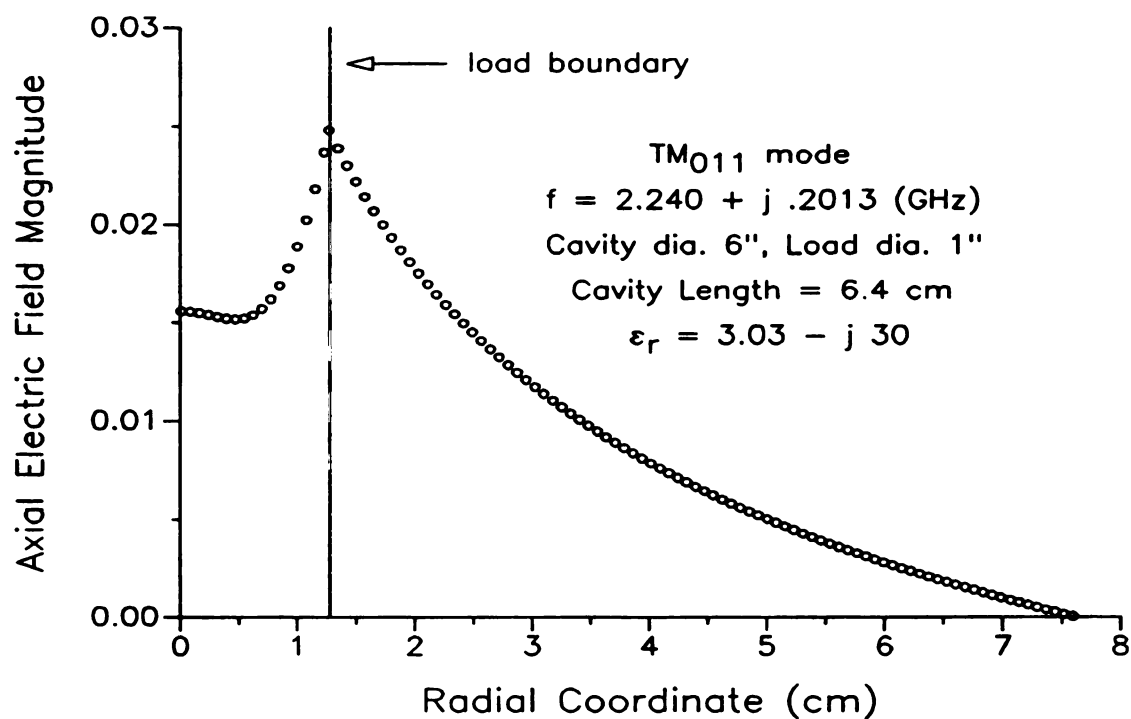
Figure 8-7 Axial electric field magnitude along a radius, TM_{011} mode, $\epsilon_r'' = 30$.

demonstrates that the resonant frequency drops as the relative loss factor goes from 10 to 30.

The field plots in Figures 8-4 through 8-7 are for the axial component of the electric field. Since the total electric field for a TM mode consists of both axial and radial components both must be considered in order know the total field magnitude. Concerning the question of the cause of the fall or rise in the resonant frequency with increasing loss factor, the behavior of the radial component is clearly a necessary consideration. According to Figures 8-4 through 8-7, the axial component of the field is reduced for increasing loss factor whether the frequency rises or falls. Is that also true for the radial component? Figures 8-8 through 8-11 show that it is. These Figures contain plots of the magnitude of the radial component of the electric field for relative loss factors of 10, 30, 100, and 1000 respectively. As shown, the radial component of the field inside the load diminishes as the loss factor of the load increases.

Since a decrease in field magnitude inside the load cannot be associated generally with a rising real frequency, how is it possible to say that the rising real frequency for $\epsilon_r'' = 100$ to $\epsilon_r'' = 1,000$ in Figure 8-2 is due to the decrease in field magnitude inside the load material? The argument is based upon perturbation considerations. It is well known that the resonant frequency of a cavity with perfectly conducting walls drops when the walls are perturbed to reflect a finite conductivity.[2] A high loss factor material which allows field penetration only to a given skin-depth is similar to a finitely conducting cavity wall. The higher the loss factor, the smaller the skin-depth and the higher the frequency. When the loss factor is low enough that a substantial field exists in the material, the analogy between loss factor and conductivity breaks down and the perturbation assumptions are no longer valid.

Returning to Figures 8-4 through 8-11, it may be observed how the field direction changes with increasing loss factor. At a given point along the radial coordinate of the cavity, the field direction may be found by vectorially adding radial

---

[2]Harrington, 372 (Problem 7-4).
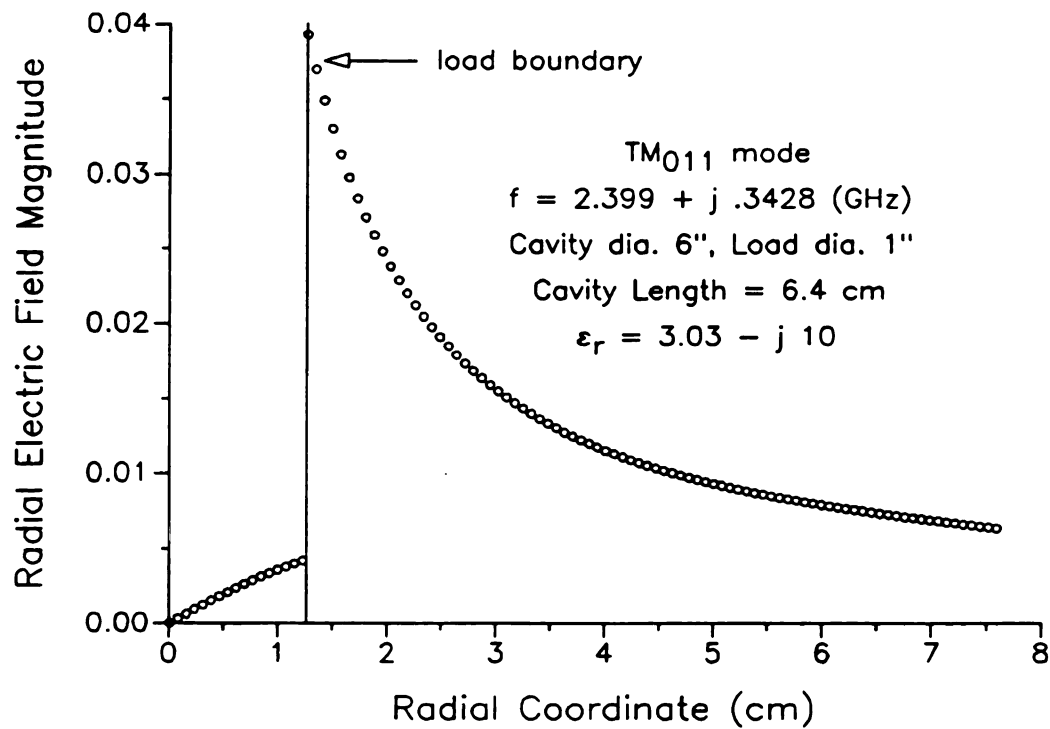
Figure 8-8 Radial electric field magnitude along a radius, TM_{011} mode, $\epsilon_r'' = 10$.
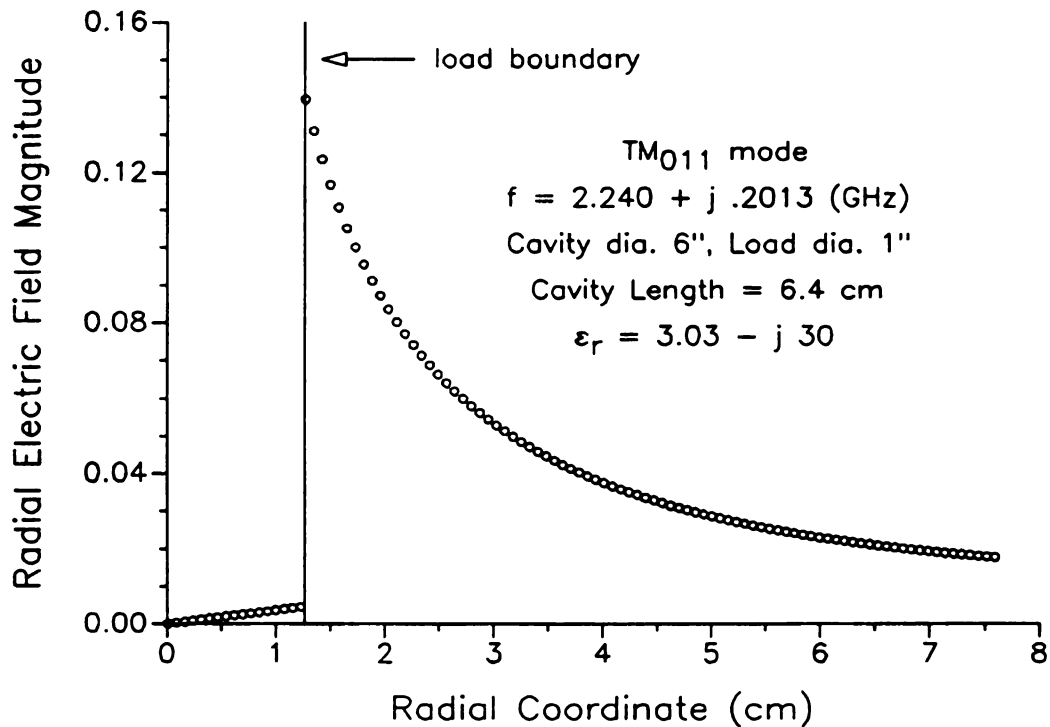
Figure 8-9 Radial electric field magnitude along a radius, TM_{011} mode, $\epsilon_r'' = 30$.
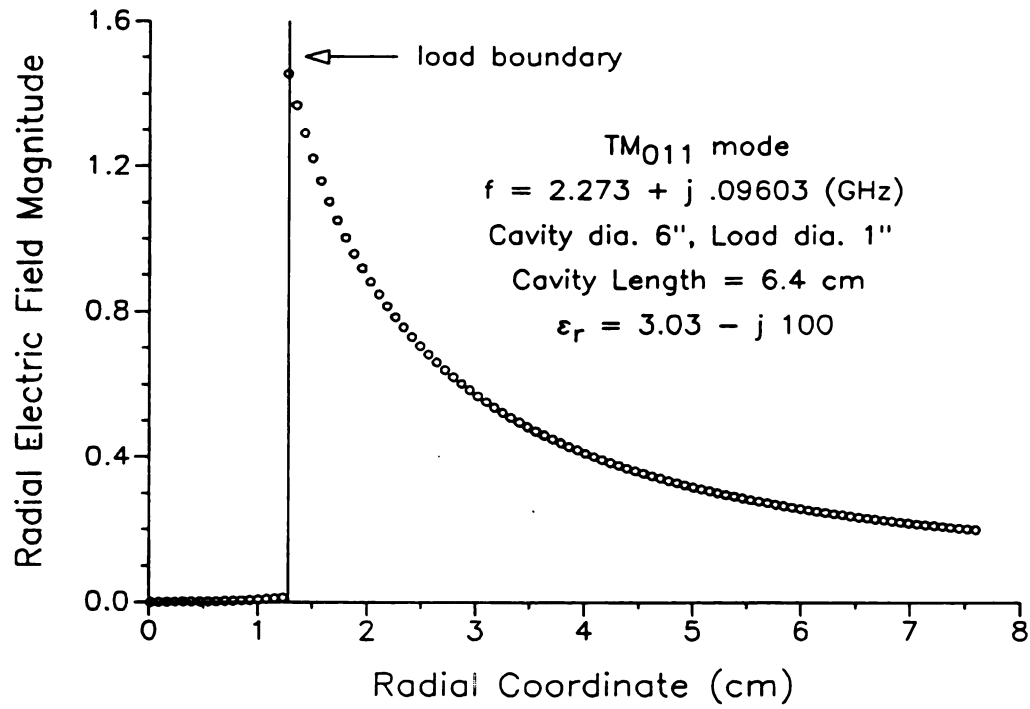
Figure 8-10 Radial electric field magnitude along a radius, TM_{011} mode, $\epsilon_r'' = 100$.
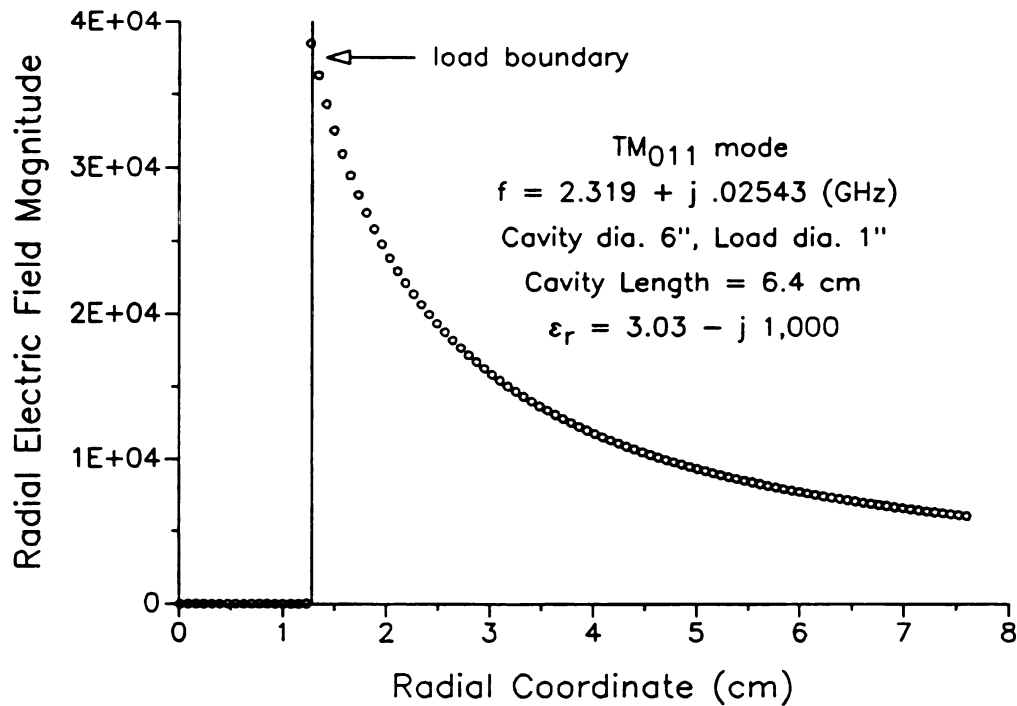
Figure 8-11 Radial electric field magnitude along a radius, TM_{011} mode, $\epsilon_r'' = 1000$.

and axial components. The axial position of the point must also be considered since E_r is proportional to $\sin(k_z z)$ while E_z is proportional to $\cos(k_z z)$.

As an example we choose a point at $z = L_s/4$ where the axial dependence factor is the same for both radial and axial components. A point on the load boundary provides a convenient radial position at which to examine the field direction. From Figures 8-6 and 8-8 the ratio of the radial field magnitude to the axial field magnitude is approximately 2.9 for $\epsilon_r'' = 10$. For $\epsilon_r'' = 30$ from Figures 8-7 and 8-9 the ratio is 5.8. Similarly, for $\epsilon_r'' = 100$ the ratio is 9.5 and for $\epsilon_r'' = 1000$ the ratio is 32. This indicates that the field at the load boundary becomes predominantly radial, or normal to the load boundary, as the losses increase. This observation is in accordance with associating a high loss factor load with a conducting material.

8.3.3 High Loss Factor Modes Associated with Coaxial Cavity TM Modes

Further confirmation of associating a high loss factor material with a conductor is demonstrated by the similarity in the radial electric fields for the $\epsilon_r'' = 1000$ load of Figure 8-11 and the coaxial cavity TM_{001} mode, which is TEM. Figure 8-12 is a normalized plot of the field magnitude for a half-wavelength TEM mode in a 6" diameter coaxial cavity with a 1" diameter inner conductor. For the TEM mode the axial components of both the electric and magnetic fields are zero; the only two field components are the radial electric field and the azimuthal magnetic field, each with a radial dependence of $1/\rho$. The similarity is demonstrated by comparing Figure 8-12 with Figure 8-11.

Likewise, an examination of the TM_{021} mode for different loss factors shows that for increasing loss factors the mode approaches that of the TM_{011} mode of the coaxial cavity. Figure 8-13 contains a mode chart for the TM_{021} mode similar to that of Figure 8-2 for TM_{011}. The same general behavior is demonstrated in Figure 8-13 as was shown in Figure 8-2, with real frequency at first falling with increased loss factor, then rising again as the loss factor becomes large. For large loss factor, the
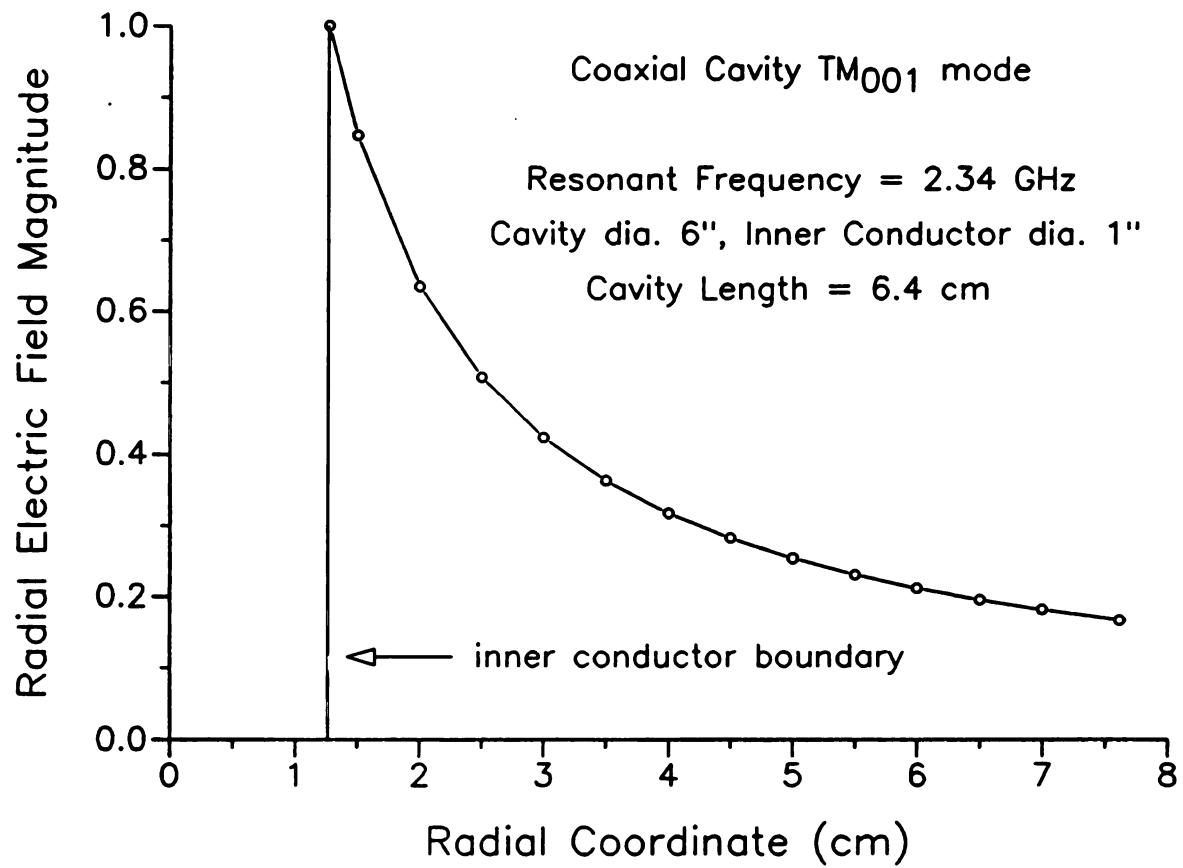
Figure 8-12 Radial electric field magnitude along a radius, coaxial cavity TEM mode.
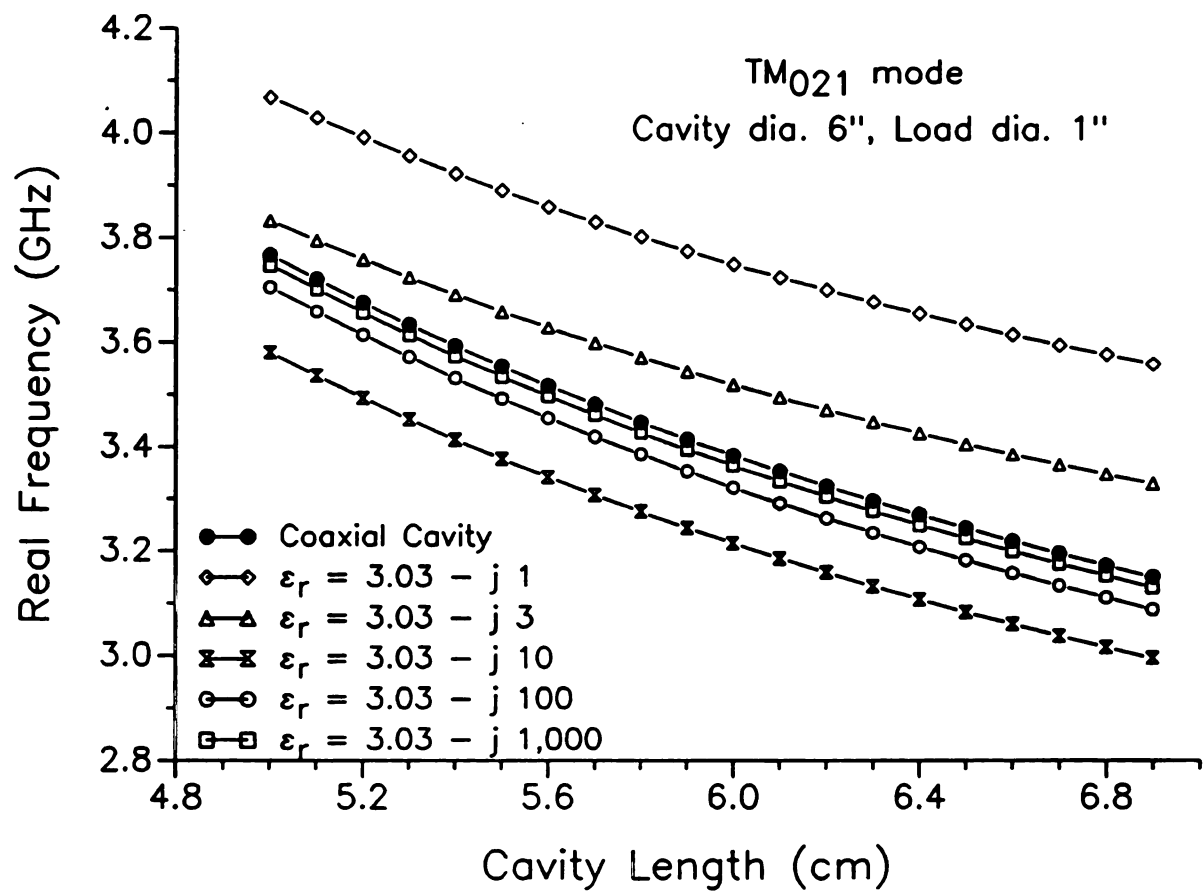
Figure 8-13 Resonant frequency vs. cavity length: 1" diameter rod in 6" diameter cavity, TM_{021}.

frequencies approach those of the coaxial cavity TM_{011} mode. In this case the coaxial cavity TM mode is not TEM but has an axial electric field component.

It is difficult to determine from Figure 8-13 the precise loss factor value for which the real frequency is a minimum, being somewhere between 3 and 100. For $L_s = 6.5$ cm, Figure 8-14 shows that the minimum occurs near $\epsilon_r'' = 9$. Figure 8-14 also demonstrates that the separate curves in Figure 8-13 belong to the same mode. As shown in the Figure, the real frequency changes most dramatically from $\epsilon_r'' = 0$ to $\epsilon_r'' = 9$, undergoing a change of nearly 600 MHz. In the same loss factor region, the imaginary frequency is also undergoing considerable variation, as shown by Figure 8-15. As the loss factor increases from zero, the imaginary frequency quickly rises to a peak near $\epsilon_r'' = 4$, then drops almost as fast until $\epsilon_r'' = 10$ where it continues to fall, but not as dramatically. The rapid changes in resonant frequency and quality factor represented by these Figures show that low loss materials that become lossy during microwave processing may very quickly detune the system for certain modes.

Figures 8-16 and 8-17 are plots of the electric field magnitudes along a radius for the TM_{021} mode for $\epsilon_r'' = 1000$. Figures 8-18 and 8-19 are similar plots for the TM_{011} mode in a coaxial cavity of the same dimensions. The two sets of plots have similar shapes and the relative magnitudes of the axial and radial components are the same, the maximum of the radial component being roughly twice that of the axial component.

8.3.4 TM_{011} Mode Frequency Variation with Dielectric Constant and Loss Factor

The plots in Figures 8-14 and 8-15 above demonstrate the usefulness of plotting the frequencies as functions of the load material loss factor. During materials processing, it is chiefly the dielectric properties of the load material that undergo change rather than their physical dimensions. Plots like the ones shown in Figures 8-14 and 8-15 describe the frequency and energy coupling cycle of materials, like alumina, whose loss factors increase with temperature. In this Section, the real and imaginary frequencies of the TM_{011} mode will be examined as functions of the
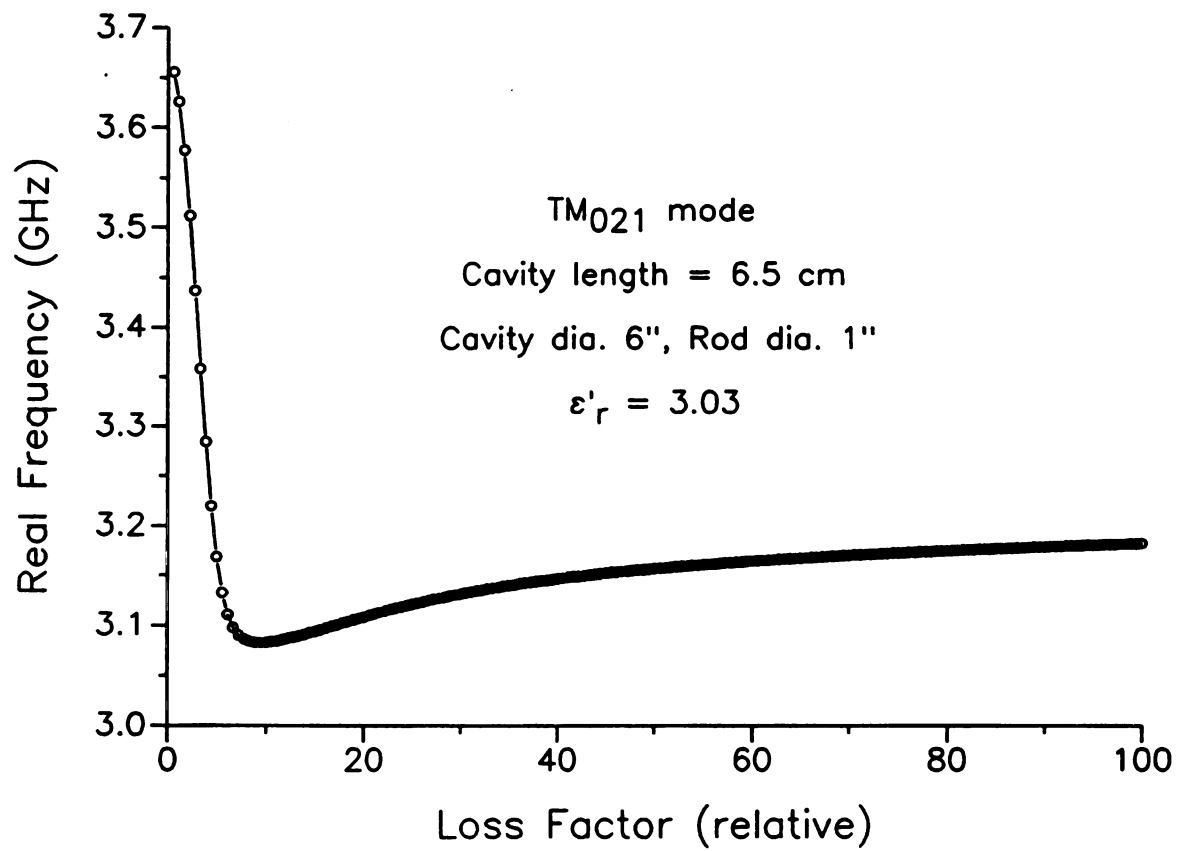
Figure 8-14 Real frequency versus loss factor: TM_{021} mode.
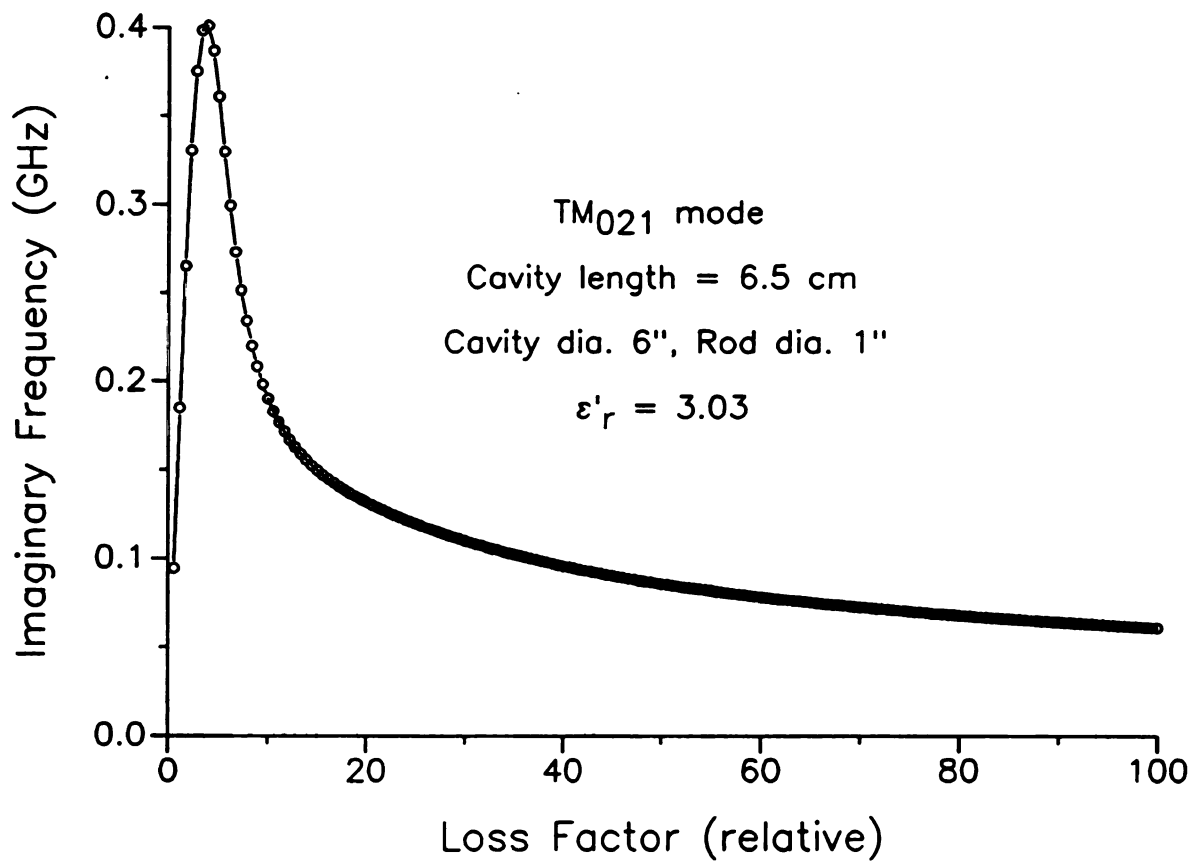
**Figure 8-15** Imaginary frequency versus loss factor: TM_{021} mode.

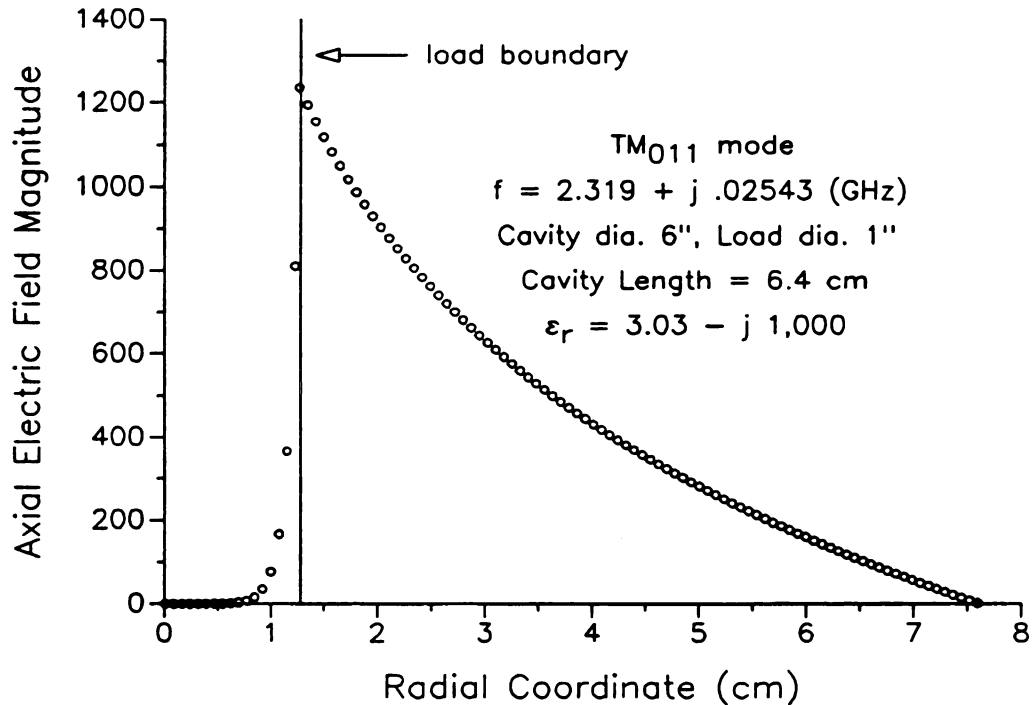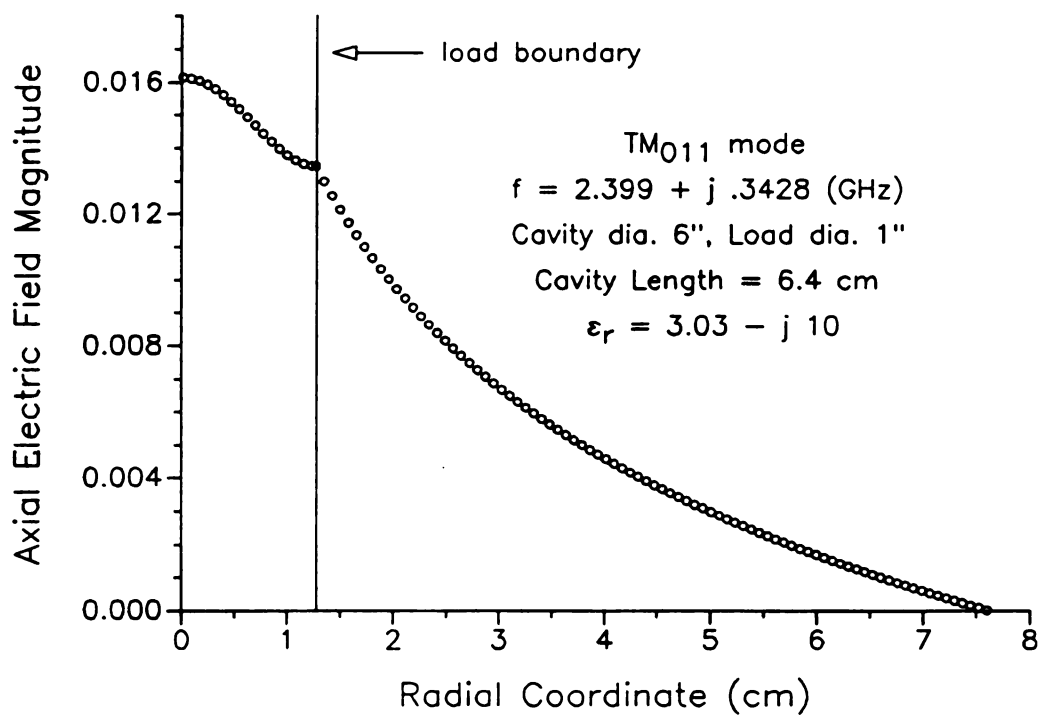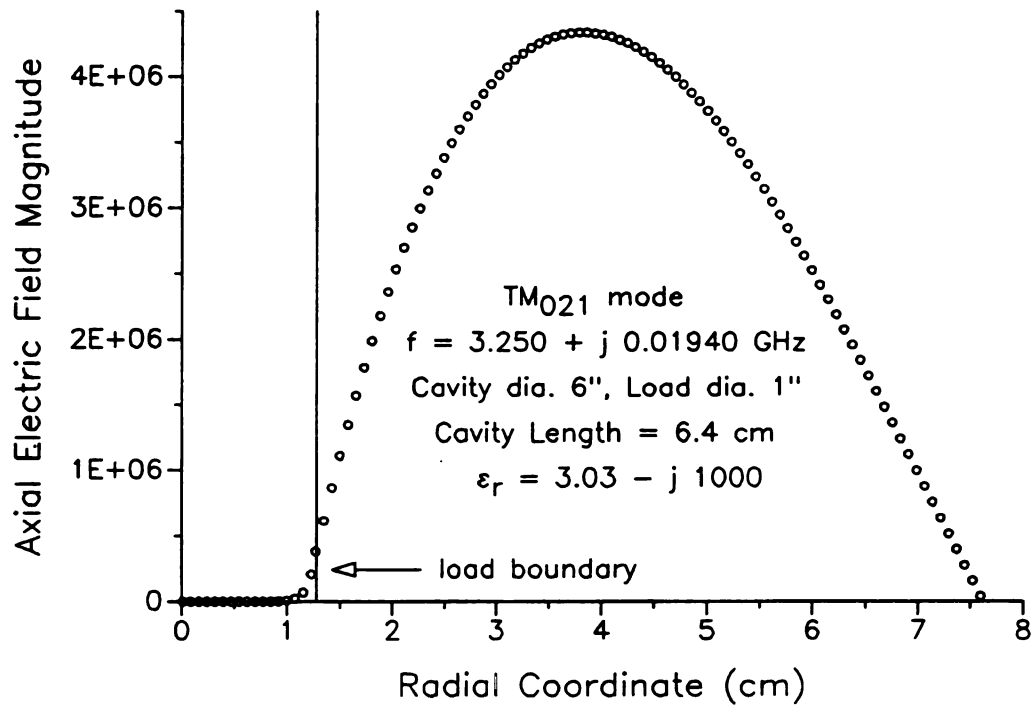**Figure 8-16** Axial electric field magnitude along a radius, TM_{021} mode, $\epsilon' = 1000$.
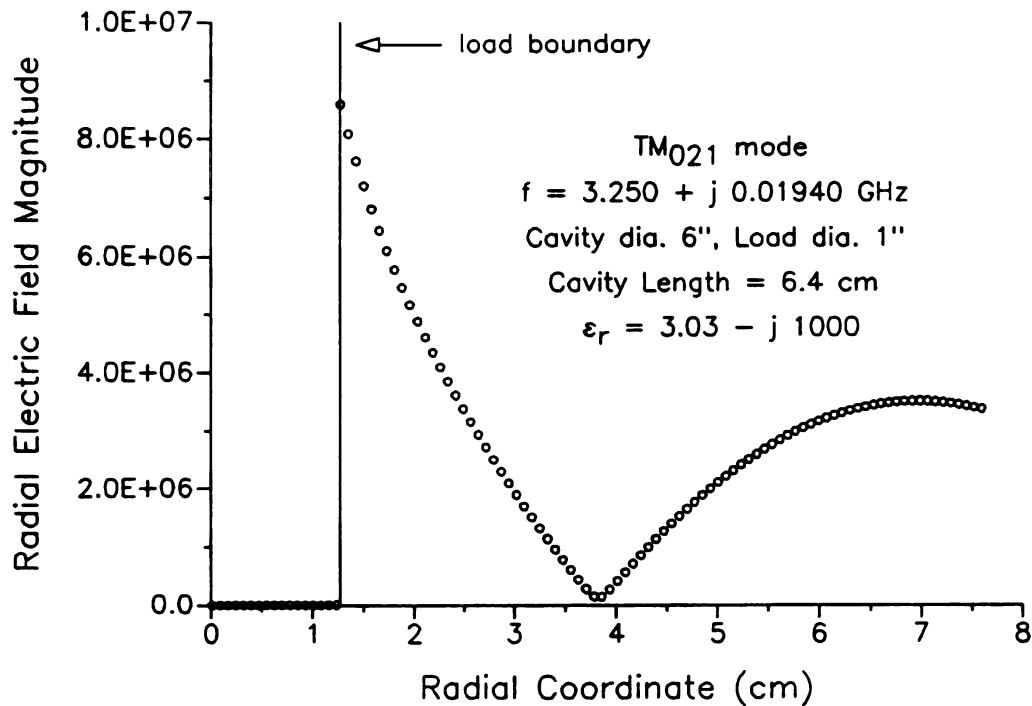
Figure 8-17 Radial electric field magnitude along a radius, TM_{021} mode, $\epsilon'' = 1000$.

Coaxial Cavity TM$_{011}$ mode

Resonant Frequency = 3.27 GHz
Cavity dia. 6", Inner Cond. dia. 1"
Cavity Length = 6.4 cm

◁—— inner conductor boundary

Axial Electric Field Magnitude

0.48
0.40
0.32
0.24
0.16
0.08
0.00

Radial Coordinate (cm)

0 1 2 3 4 5 6 7 8
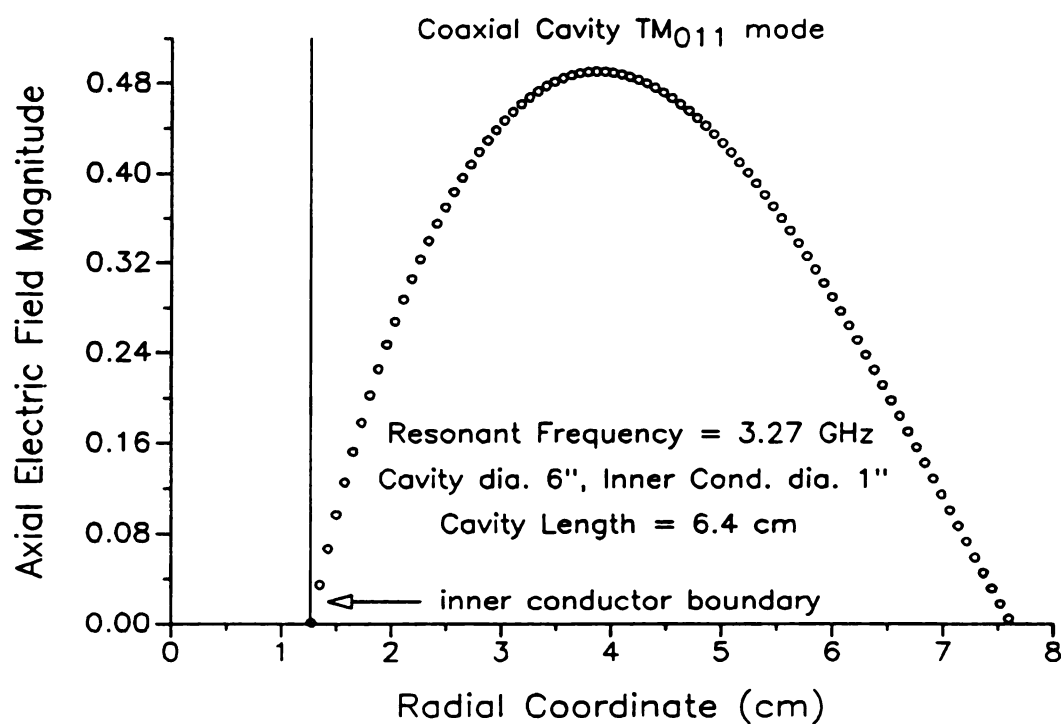
Figure 8-18 Axial electric field magnitude for the coaxial cavity TM$_{021}$ mode.

◁—— inner conductor boundary

Coaxial Cavity TM$_{011}$ mode

Resonant Frequency = 3.27 GHz
Cavity dia. 6", Inner Conductor dia. 1"
Cavity Length = 6.4 cm

Radial Electric Field Magnitude

1.0
0.8
0.6
0.4
0.2
0.0

Radial Coordinate (cm)

0 1 2 3 4 5 6 7 8
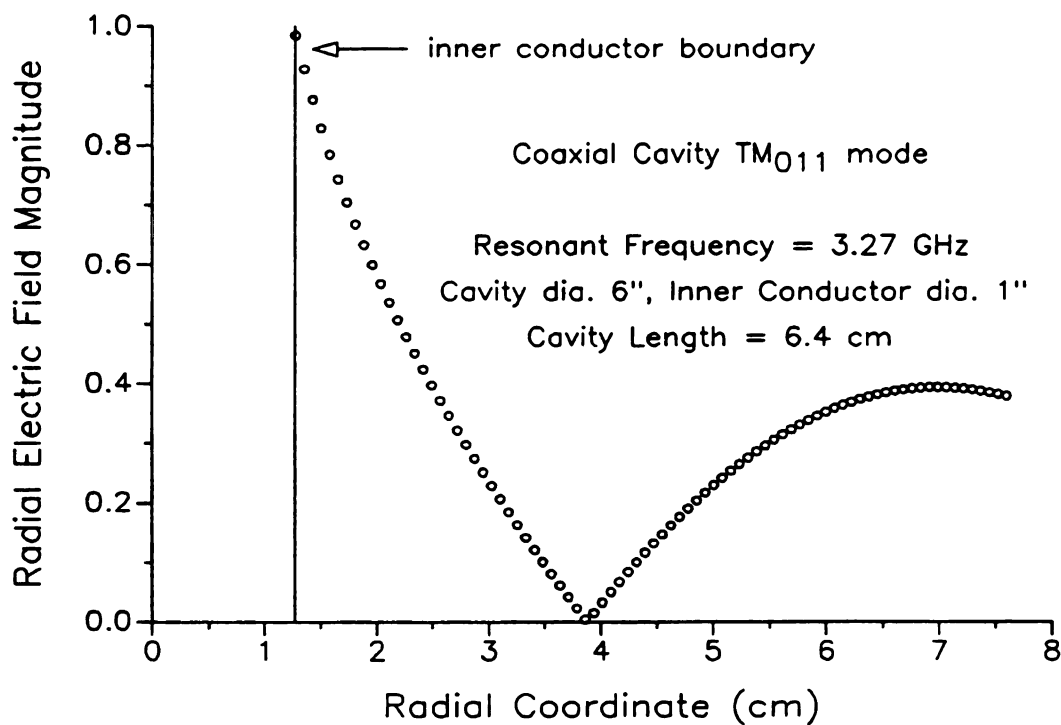
Figure 8-19 Radial electric field magnitude for the coaxial cavity TM$_{021}$ mode.

dielectric properties of the load, where the load is 1" in diameter and the cavity is 6" in diameter.

Figure 8-20 contains a plot of the real frequency versus relative loss factor over the range of 0 to 50 for loads with relative dielectric constants of 1.5, 5.0, and 10.0. The Figure demonstrates that the real frequencies for loads with different ϵ_r' values converge as the loss factor grows large. For low loss factors, the real frequency for small ϵ_r' values is higher than for greater ϵ_r' values; the relative positions are reversed for higher loss factors, with real frequency being higher for the larger values of ϵ_r'. Figure 8-21 shows the imaginary frequency variation of the resonances of Figure 8-20. As shown Figure 8-21, the imaginary frequency rises from 0 for a load with no losses to a peak, which occurs near $\epsilon_r'' = 10$ for a dielectric constant of 5. The peak is higher and sharper and occurs for a slightly lower ϵ_r'' when the dielectric constant is lower at $\epsilon_r' = 1.5$. For $\epsilon_r' = 10$, the imaginary frequency variation with ϵ_r'' is more moderate than for either of the other two curves, but it demonstrates the same rise for low loss factors followed by a gentle decline. As the relative loss factor increases beyond 40, the imaginary frequencies for the various dielectric constants converge so that the imaginary frequency becomes independent of ϵ_r' for large values of ϵ_r''.

The real frequency plot for $\epsilon_r' = 1.5$ in Figure 8-20 shows that there is no variation in the real frequency with increasing loss factor in the low loss factor region. This region is examined in more detail in Figure 8-22, which is a magnified view of the low dielectric constant zone for relative loss factors less than 8. Plots are shown for $\epsilon_r' = 1$, 1.25, 1.5, 1.75, and 2.0. The plots show that for extremely low dielectric constant materials there is actually slight rise in real frequency as the loss factor increases from zero. This rise is most evident in the "lossy vacuum," i.e., a hypothetical material with a dielectric constant of 1 and a loss factor greater than 1. A rise is also evident in materials with ϵ_r' values of 1.25 and 1.5. For low dielectric constant loads with $\epsilon_r' \geq 2$, adding loss causes the real frequency to decrease.
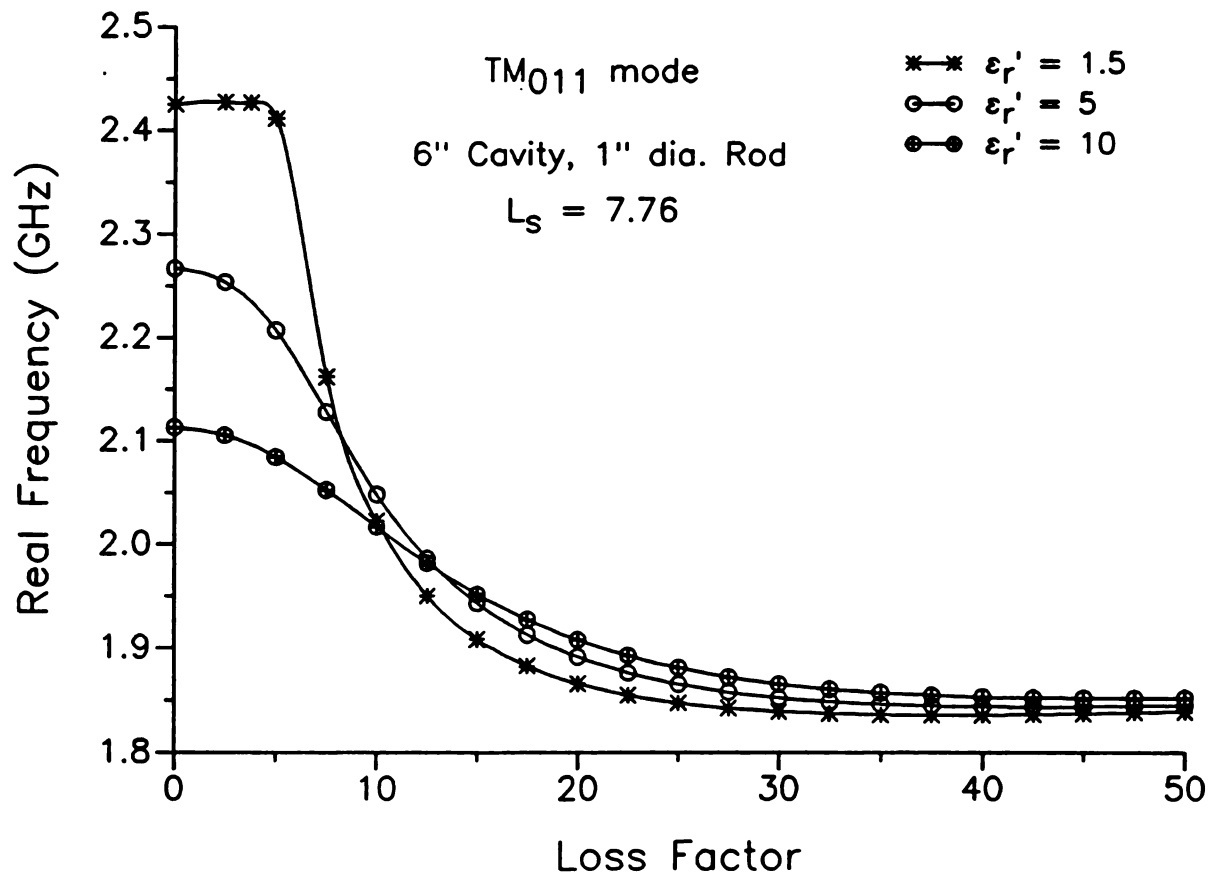
Figure 8-20 Real frequency versus loss factor for $\epsilon_r'' = 0$ to 50.
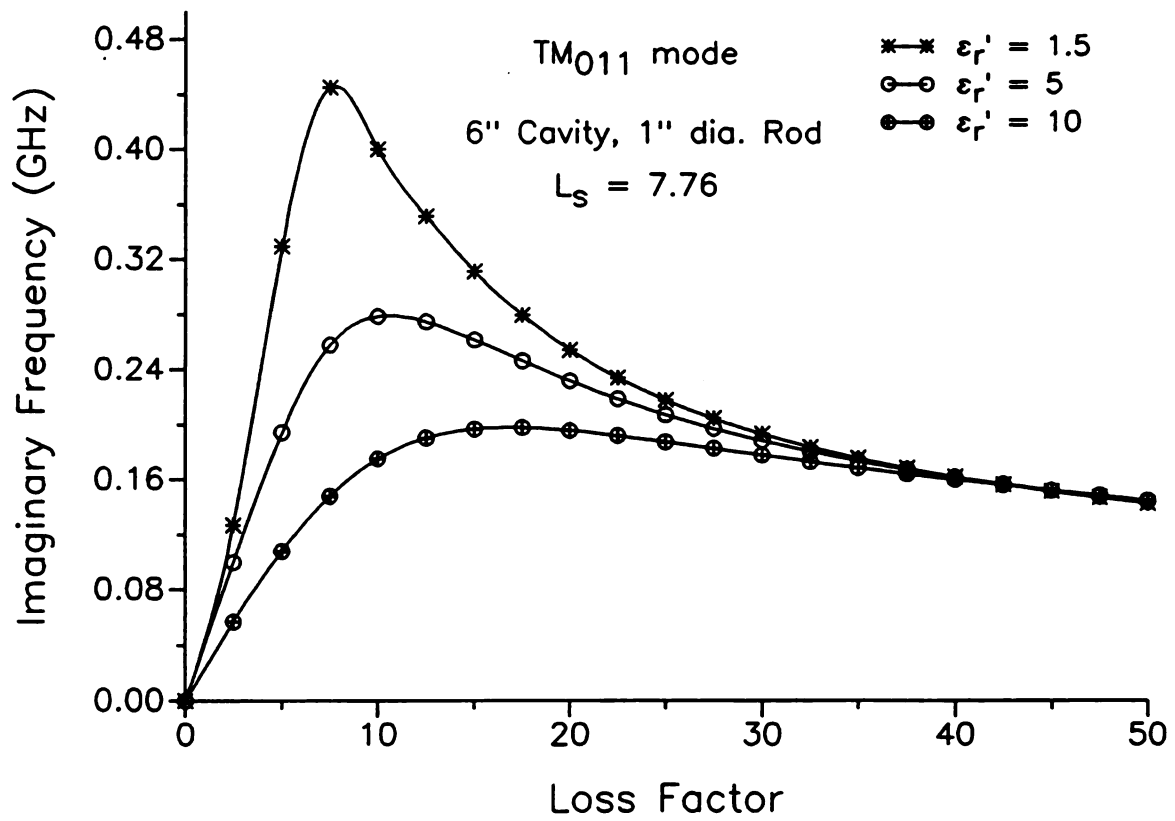
Figure 8-21 Imaginary frequency vs. loss factor for TM_{011} mode, $\epsilon_r'' = 0$ to 50.
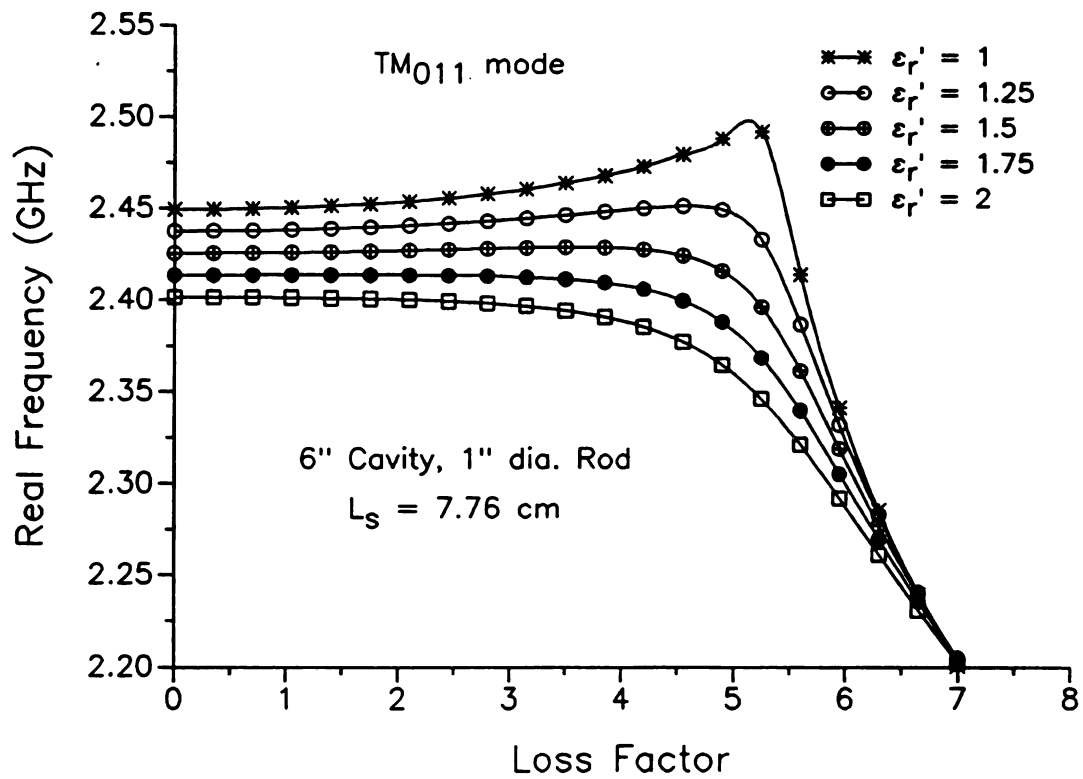
Figure 8-22 Real frequency vs. loss factor for materials with low values of ϵ_r'.

For a lossless cavity and load it may be shown that an increase in dielectric constant may produce only a decrease in the cavity resonant frequency.[3] When losses are present, however, that is not the case. This was shown in the high loss factor region of Figure 8-20 as ϵ_r' increased from 1.5 to 10. It can also be seen in Figure 8-23, which contains plots of the real frequency versus dielectric constant for values of ϵ_r'' equal to 0, 1, 5, 7, 10, and 20. As shown in the Figure, the real frequency is strictly decreasing with increasing dielectric constant for the lossless case, as expected. The real frequency for $\epsilon_r'' = 1$ is indistinguishable from the lossless case.

The real frequency is also strictly decreasing for loss factors 5, and 7. For the higher loss factors of 10 and 20, however, the real frequency increases with dielectric constant in certain ranges. For $\epsilon_r'' = 10$ the real frequency increase with increasing dielectric constant in the range of $\epsilon_r' = 1$ to approximately 5. For $\epsilon_r'' = 20$ this range extends from 1 to nearly 15, but the slope is gentler. In the higher dielectric constant range, i.e., $\epsilon_r' \geq 35$, Figure 8-23 shows that increasing the loss factor from 10 to 20 causes an increase in real frequency. Although the Figure is not clear enough to distinguish what happens as the loss factor is increased from 0 to 10 for these higher dielectric constants, the data for the dielectric constant value $\epsilon_r' = 40.2$ indicates that the real frequency rises uniformly with increasing loss factor throughout the range from 0 to 20.

Finally, Figure 8-23 demonstrates that for dielectric constants in the range of 33 to 35 the loss factor plays no part in determining the real frequency for this mode and load configuration. While that may be true of the real frequency, the same cannot be said of the imaginary frequency. Figure 8-24 shows that there is no dielectric constant range for which a change in loss factor does not produce a change in imaginary frequency or cavity Q.

Figure 8-24 is of much interest in itself. The best means of understanding it as a whole is to view each separate ϵ_r'' curve in succession. For the lossless case, $\epsilon_r'' = 0$, the imaginary frequency is zero for all values of the dielectric constant ϵ_r'.

---

[3]Harrington, 323.
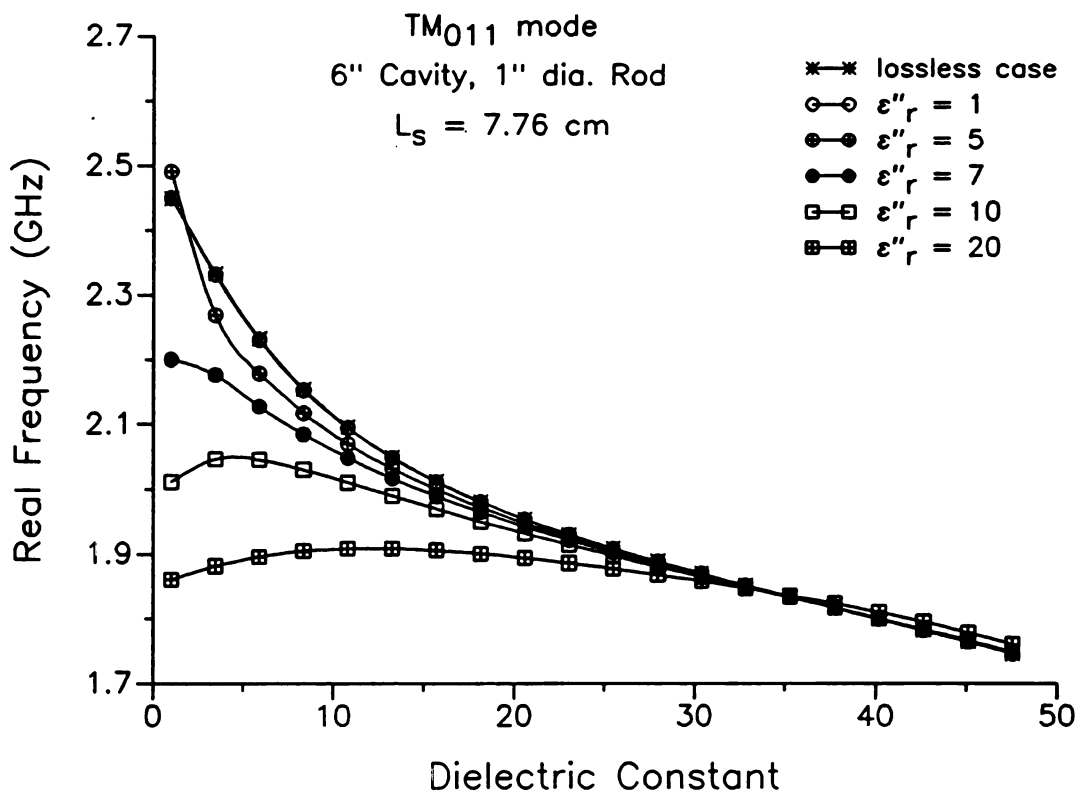
Figure 8-23 Real frequency vs. dielectric constant for TM_{011} mode, $\epsilon_r' = 1$ to 50.
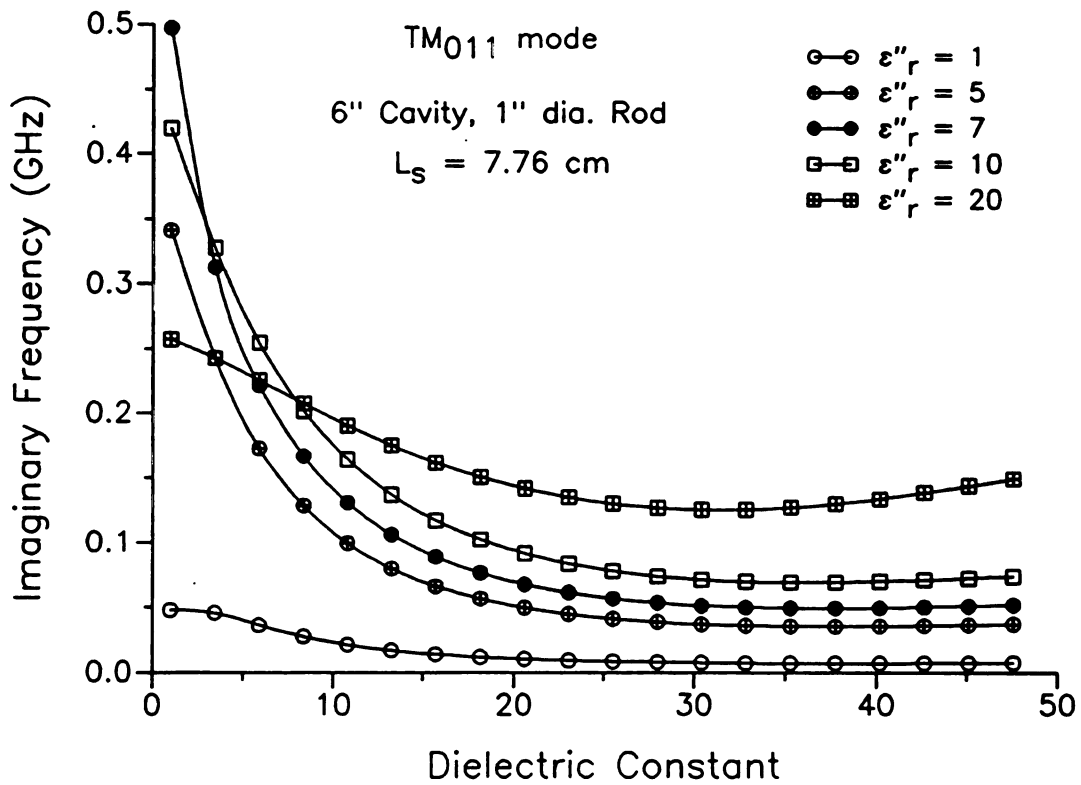
Figure 8-24 Imaginary frequency vs. dielectric constant for TM_{011} mode, $\epsilon_r' = 1$ to 50.

The curve for this case, were it shown in the Figure, would like along the ϵ_r'-axis. As ϵ_r'' increases from zero the curve begins to rise up off of the ϵ_r'-axis as shown in the Figure for $\epsilon_r'' = 1$. As loss factor continues to increase, the imaginary frequency increases, especially for lower values of ϵ_r' as the curves for $\epsilon_r'' = 5$ and 7 demonstrate. If the loss factor continues to increase to 10 or 20 the imaginary frequency continues to increase for loads with higher dielectric constants, but for low dielectric constant loads the imaginary frequency comes down, i.e., Q rises.

What this means as far as material heating is concerned is that high dielectric constant materials absorb increasing amounts of energy with increasing loss factor. It is true that Q is lower for materials with lower ϵ_r' than for those with higher ϵ_r', at least for those with ϵ_r'' less than 20, but as the loss factor of the material increases, Q values begin to rise in the lower dielectric constant materials whereas they continue to decrease for materials with higher dielectric constant.

8.3.5 Frequency and Field Pattern Variation with Load Radius

In order to understand mode behavior in relation to cavity and load parameters it is useful to explore frequency variation as a function of the load radius. For lossless and low loss materials it is often possible to trace coaxially loaded cavity modes back to nearby empty cavity modes as the load radius vanishes. Similarly, as the load radius increases and approaches the cavity radius, coaxially loaded cavity modes approach homogeneously loaded, or *material filled*, cavity modes. The complex frequencies of the homogeneously loaded cavity are given in Chapter 4 by Equation (4-23).

It might seem reasonable that coaxially loaded cavity modes would approach the same empty cavity mode for vanishingly small load radii as they would homogeneously filled cavity mode for load radii approaching the cavity radius. It is shown here that this is not always the case. Where the same mode is approached in either limit it seems safe to name the coaxially loaded cavity mode with the name of the empty or homogeneously filled cavity modes which it approaches. This characteristic of certain modes for a particular load material, where the empty cavity

modes may be traced through the coaxially loaded modes to the same homogeneously filled cavity modes by increasing the load radius from zero until the load fills the cavity, will appear in several of the examples that follow. It is therefore convenient to assign to such modes a designation by which to identify them. We will refer to modes which exhibit this behavior as *radially traceable*. Radial traceability is a characteristic of a mode only for a particular load material, and possibly only for a particular cavity size.

Figure 8-25 contains an example of radial traceability for the first three TM modes of the 6" diameter coaxially loaded cavity for a lossless load with $\epsilon_r = 9$. The cavity length is 13.87 cm. In the Figure the modes are labeled TM_{012}, TM_{022}, and TM_{032} since at the limits of vanishing load radius and cavity dimension load radius the modes become empty and material filled TM_{012}, TM_{022}, and TM_{032} modes.

For the lossless case, the material filled cavity frequency differs from that of the empty cavity by a factor of $1/\sqrt{\epsilon_r}$. With $\epsilon_r = 9$ the empty cavity mode frequency is three times that of the corresponding material filled mode. The empty and material filled mode frequencies for the modes of Figure 8-25 are in this ratio. For the TM_{012} mode shown in Figure 8-25, the resonant frequency when the load radius is zero is 2.634 GHz; this is the empty cavity TM_{012} eigenfrequency for a 6" diameter cavity with length 13.87 cm. For a load radius of 7.62 cm the coaxially loaded mode frequency is 0.8781 GHz, the same as that of a cavity of the same dimensions filled with a lossless dielectric of $\epsilon_r = 9$. The TM_{022} mode has frequencies of 4.077 GHz and 1.359 GHz at either limit and the TM_{032} mode has frequencies of 5.834 GHz and 1.945 GHz.

Adding loss to the load makes the natural frequency complex. Both the real and imaginary parts may then be plotted as a function of load radius. Figures 8-26 and 8-27 show the real and imaginary frequencies versus load radius for the modes of Figure 8-25 when the complex permittivity of the load is $\hat{\epsilon}_r = 3 - j\,0.039$. In this case, as for the lossless case with $\epsilon_r = 9$, the modes shown are radially traceable. Since the natural frequencies of the modes are complex, both the real and imaginary parts of the frequency must match the appropriate components of the complex
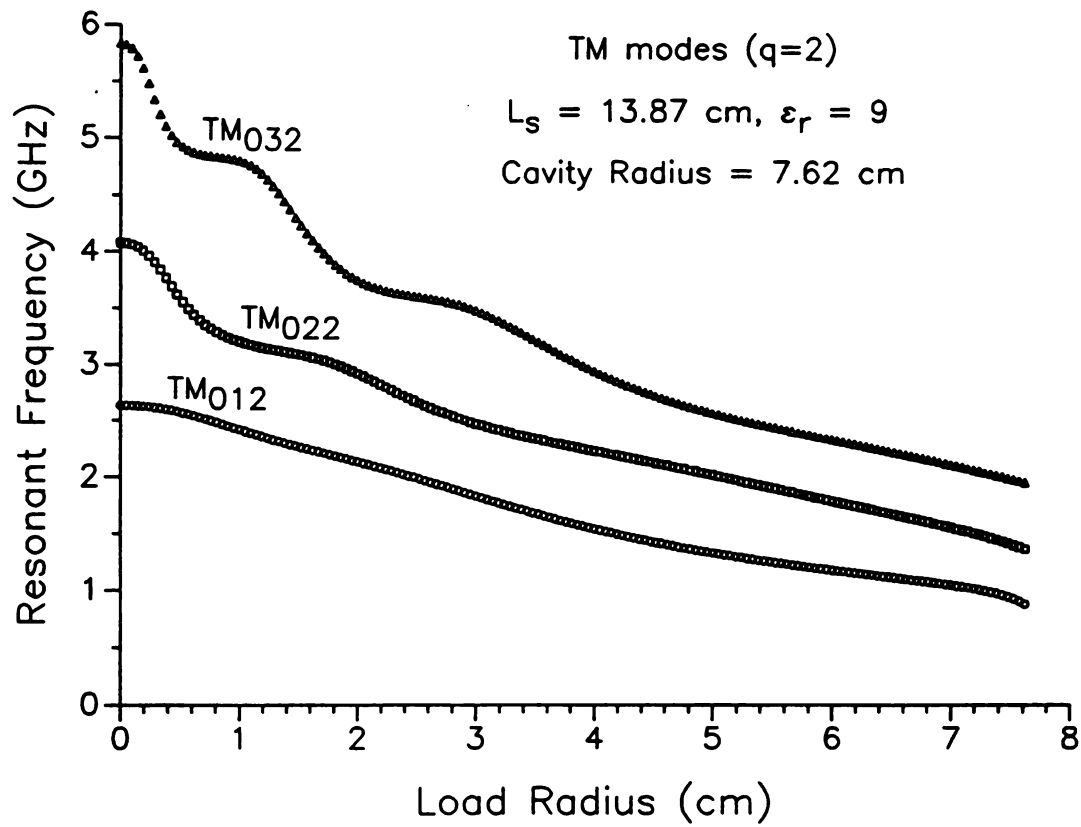
Figure 8-25 Resonant frequency vs. load radius for lossless load, $\epsilon_r = 9$.
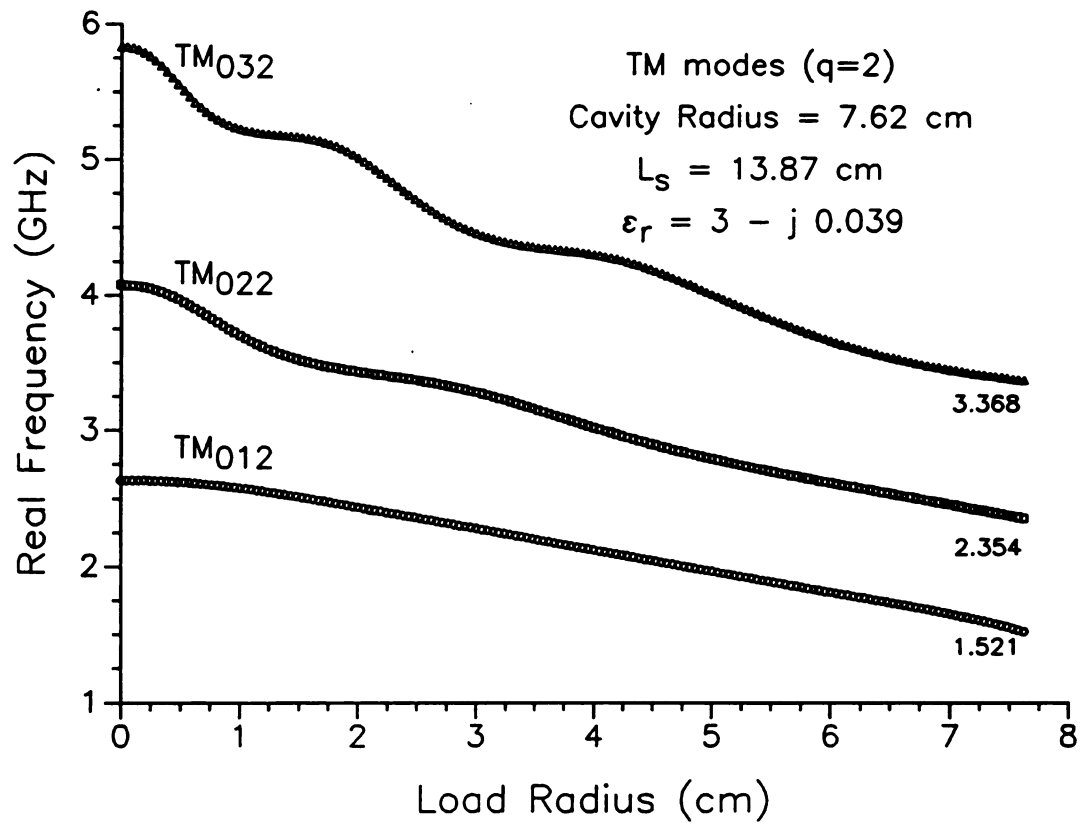
Figure 8-26 Real frequency vs. load radius for nylon load, $\hat{\epsilon} = 3 - j\,0.039$.
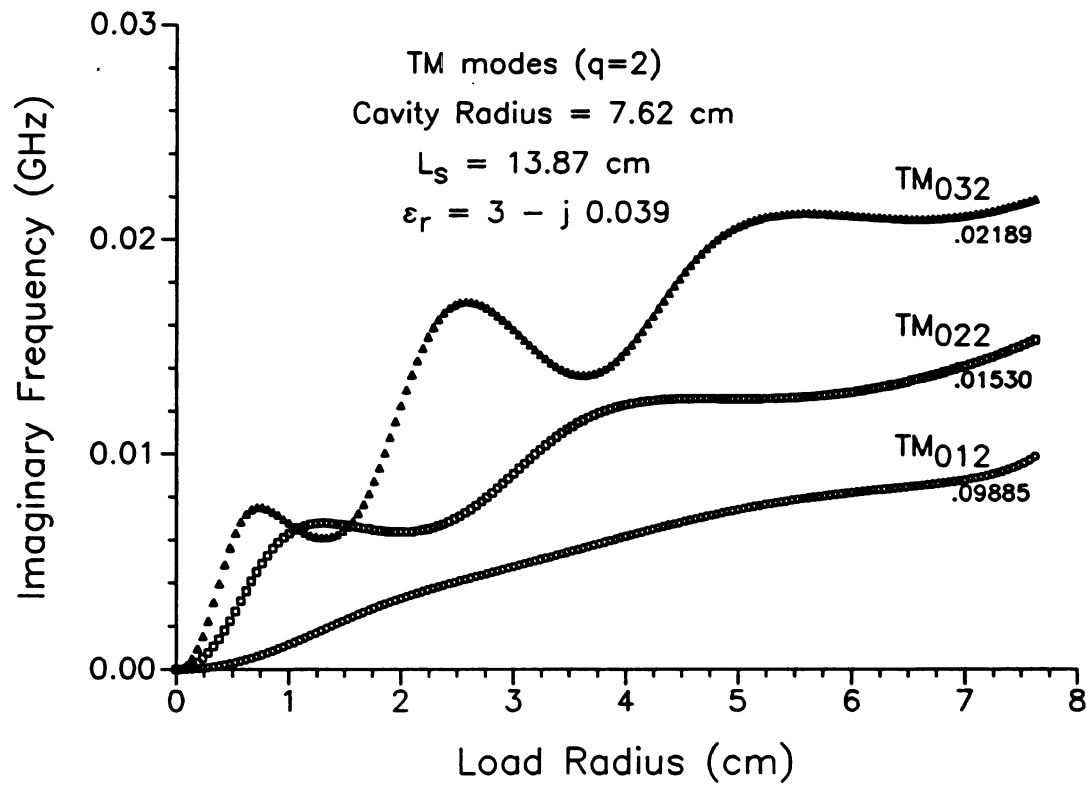
Figure 8-27 Imaginary frequency vs. load radius for nylon load, $\hat{\epsilon} = 3 - j\,0.039$.

frequency of the material filled cavity in order for the modes to be considered radially traceable. From Equation (4-23), the complex natural frequency of the material filled cavity TM_{012} mode for a 6" diameter cavity of length 13.87 cm is $1.521 + j\,0.009885$ GHz. For the TM_{022} and TM_{032} modes the frequencies are $2.354 + j\,0.01530$ GHz and $3.368 + j\,0.02189$ GHz respectively. As shown in Figures 8-26 and 8-27, both the real and imaginary parts of the frequencies of the coaxially loaded cavity modes approach those of the material filled modes as the load radius approaches the cavity radius. The empty cavity frequencies are consistent with those given above under the description of Figure 8-25.

Another feature of Figure 8-27 is that the radial order of the modes is revealed in the oscillations of the imaginary frequency as a function of load radius. It may be roughly observed that there are three undulations in the TM_{032} plot, two in the TM_{022} plot, and one in the TM_{012} plot. This sort of variation is also observable in the real frequency plots where there occur regions in which there is little variation with radius or "flats" in the plot. The radial order is seen more clearly in higher order modes or with loads of higher dielectric constant and loss factor, as is shown in the next Figure.

Increasing both the load loss factor and the dielectric constant to $\hat{\epsilon}_r = 20 - j\,8$ the lower order TM modes remain radially traceable as shown in Figures 8-28 and 8-29. For this higher complex permittivity load the frequency varies more strongly with load radius, especially the imaginary part. Here is a good example to show how the complex nature of the frequency is useful for correctly tracing the mode. If it appears that one component of the frequency has jumped to another mode as the mode is traced out with load radius, the plot of the other component may be consulted to see if it has also changed drastically at the same point. If so then it is likely that the trace has jumped from the original mode to another. On the other hand, if one component of the frequency demonstrates good continuity even though the other may appear to be discontinuous, it is likely that the mode is being traced correctly. In order to accurately trace the modes even for lossless materials, it may prove useful in
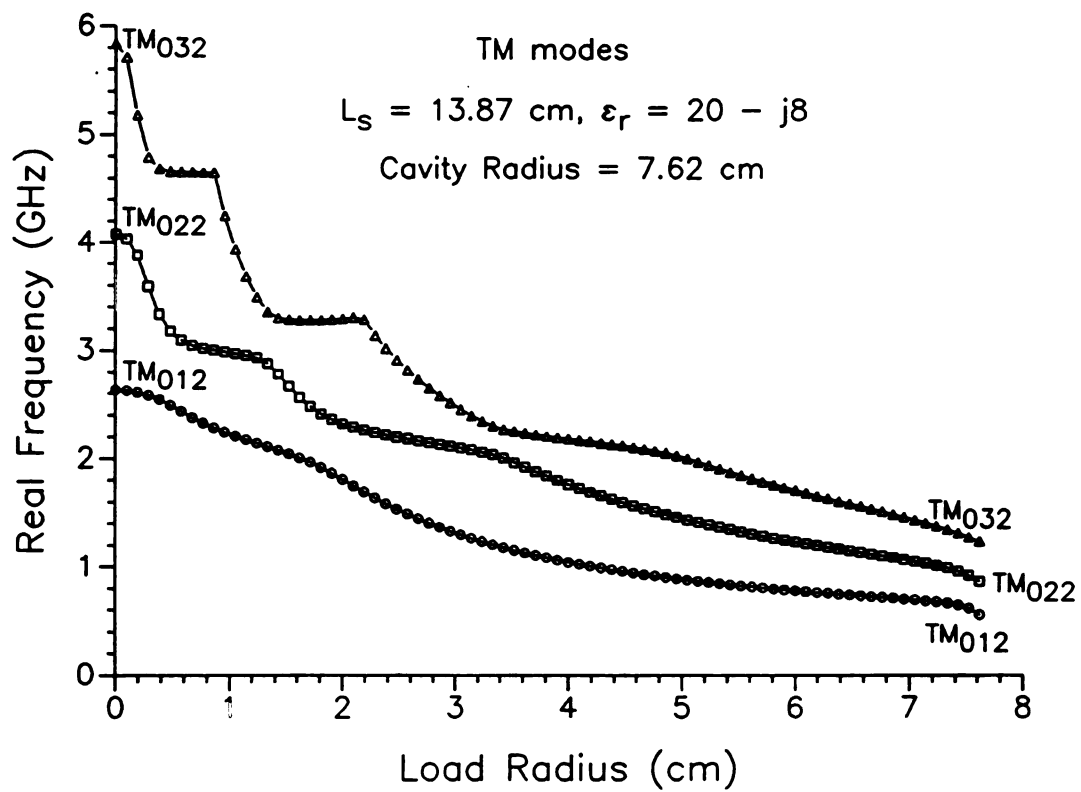
Figure 8-28 Real frequency vs. load radius for moderately lossy load, $\hat{\varepsilon} = 20 - j\,8$.
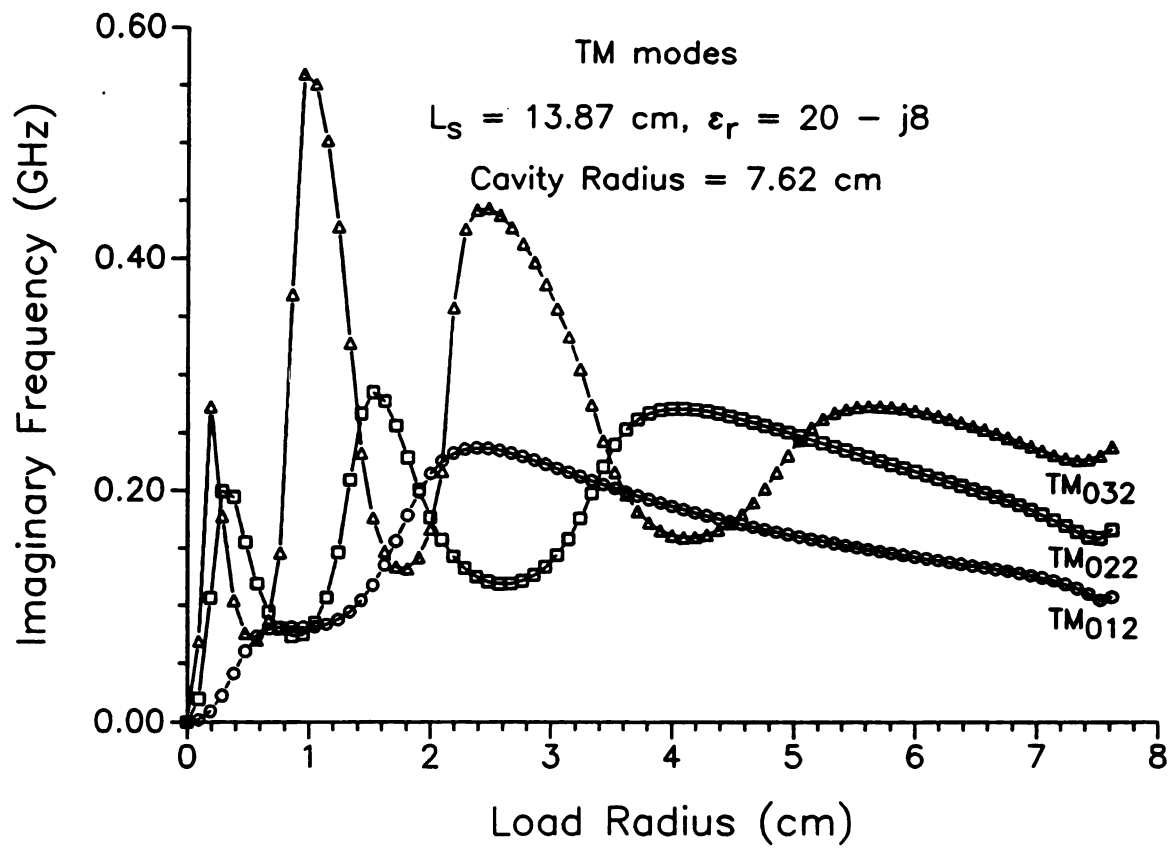
Figure 8-29 Imaginary frequency vs. load radius for moderately lossy load, $\hat{\varepsilon} = 20 - \text{j}\,8$.

certain cases to add a tiny amount of loss to insure that the trace belongs to a single mode.

The high load radius range in Figure 8-28 displays similar real frequency behavior to that of the resonant frequency of the conducting rod loaded cavity discussed in Chapter 5. Recall that the conducting rod solution demonstrated a sharp drop in resonant frequency with increasing rod length just as the rod length reached the length of the cavity. This was attributed to the increased capacitance between the end of the rod and the cavity shorting plate. A similar, although less dramatic, drop in real frequency is shown in Figure 8-28 as the material radius nears the cavity radius. It is more pronounced in the lower order modes. Comparing Figure 8-28 with Figure 8-26, this phenomenon appears only for the higher loss material.

Figure 8-29 is a good example to point out that even radially traceable coaxially loaded cavity modes may not be consistently ordered radially with the imaginary frequency. In other words, the magnitude of the imaginary frequency is not always higher for a higher order coaxially loaded cavity mode. In Figure 8-29, for example, at a load radius of 4 cm the imaginary frequency of the TM_{032} mode is lower than that of both the TM_{022} and the TM_{012} modes. This is in contrast to the material filled cavity where both the real and imaginary parts of the frequency are higher for higher order modes.

8.3.6 Dielectric Confinement and Exclusion

Figures 8-30 and 8-31 reveal some of the more unusual behaviors of the mode frequencies as a function of load radius. Figures 8-30 and 8-31 show the frequency mode paths which emanate from the empty and material filled cavity natural frequencies of the TM_{012} mode for a load material of complex relative permittivity $\hat{\epsilon}_r = 10 - j\, 30$. The arrows in Figure 8-30 indicate the empty and material filled modes to which the real frequencies correspond for load radii of zero and 7.62 cm (the cavity radius). As shown in Figure 8-30 the mode emanating from the empty cavity TM_{012} mode, mode B, exhibits a frequency rise from the empty cavity resonant frequency as the load radius increases from zero, growing faster as the load
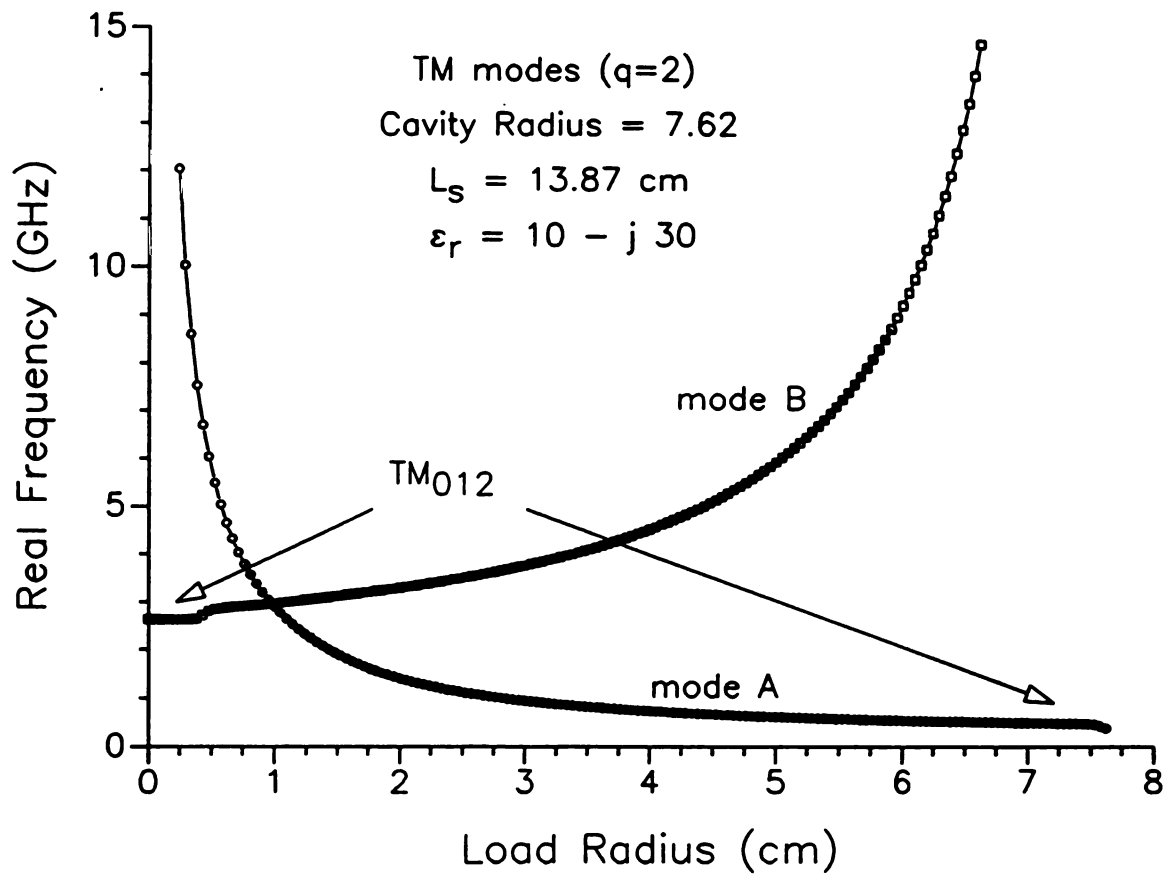
Figure 8-30 Real frequency vs. load radius for highly lossy load, $\hat{\varepsilon} = 10 - j\,30$.
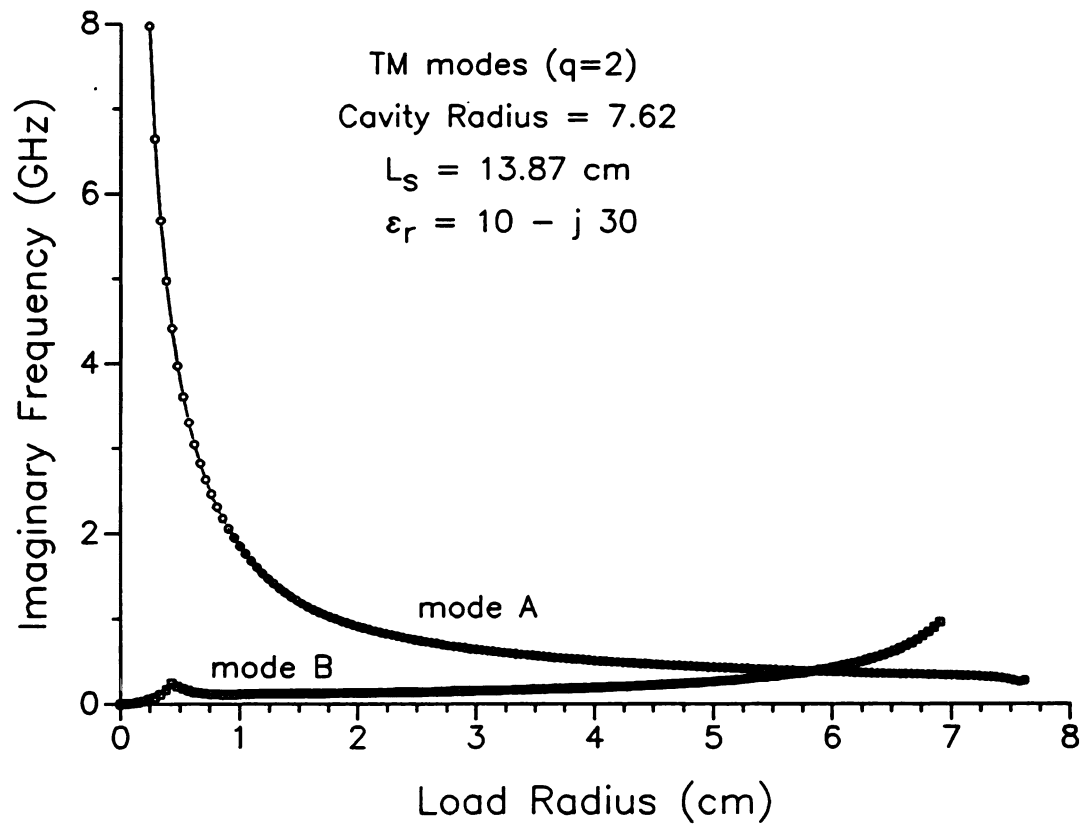
Figure 8-31 Imaginary frequency vs. load radius for highly lossy load, $\hat{\epsilon} = 10 - j\,30$.

radius draws near that of the cavity. At the same time mode A, which approaches the material filled TM_{012} mode for load radius approaching cavity radius, is traced back with decreasing load radius to a much higher order empty cavity mode.

Clearly, these modes are not radially traceable as defined above. The frequency behavior of modes A and B will be seen later on in the TE and HEM modes, so it is convenient to attach a name to these sorts of modes in order to refer to them more concisely. The rapidly rising frequency behavior of mode A for decreasing load radius in the low radius range will be referred to as *dielectric confinement*. The rapidly rising real and imaginary frequency behavior of mode B for increasing load radius in the high radius range will be referred to as *dielectric exclusion*. As will be shown below, these names refer to the distribution of the fields relative to the load material. The fields of the dielectric confined modes tend to be concentrated in and around the load material in the high frequency range of the mode. Conversely, the fields of the dielectric excluded modes in the high frequency range tend to be excluded from the load, being concentrated in the region between the load and the cavity walls. In the low frequency range of the modes these qualitative descriptions may not characterize the existing field distribution, but the names dielectric confined and dielectric excluded will be applied to the mode for all values of load radius.

It is important to realize that the Q's of these modes are extremely low. Using the formula of Equation (8-2), although it is not strictly applicable for such low Q values, yields a Q of approximately 1 for mode A at a load radius of 2 cm, and not much higher for any other load radius. Mode B has higher Q's, especially for very small load radii, but it rapidly decreases as the load radius goes up, being approximately 13 for a load radius of 2 cm. For large load radii, the real frequency of Mode B begins to outstrip the imaginary frequency so that the Q rises, but it is still quite low.

In order to understand the nature of these modes it is helpful to examine their field distributions. Figures 8-32 through 8-42 contain plots of the magnitudes of the axial and radial components of the electric field at several different load radii for

Figure 8-32 Axial electric field magnitude: TM_{0p2} mode A, load radius 7.57 cm.

Figure 8-33 Radial electric field magnitude: TM_{0p2} mode A, load radius 7.57 cm.
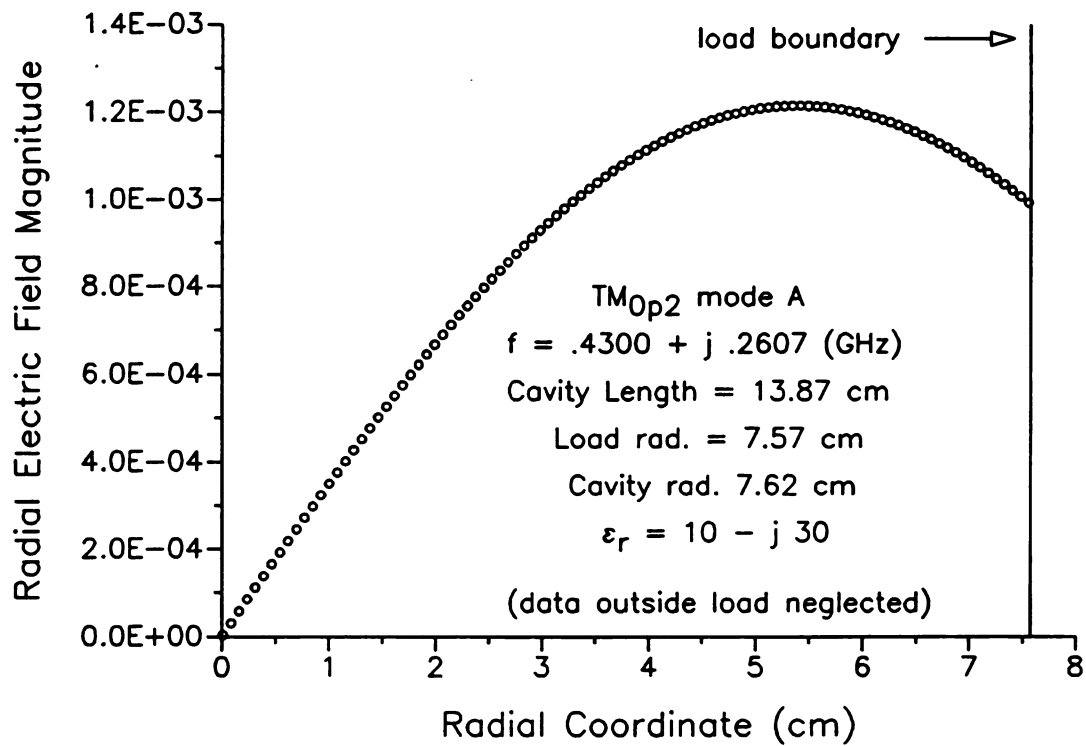
Figure 8-34 Radial electric field magnitude (load only): TM_{0p2} mode A, load radius 7.57 cm.
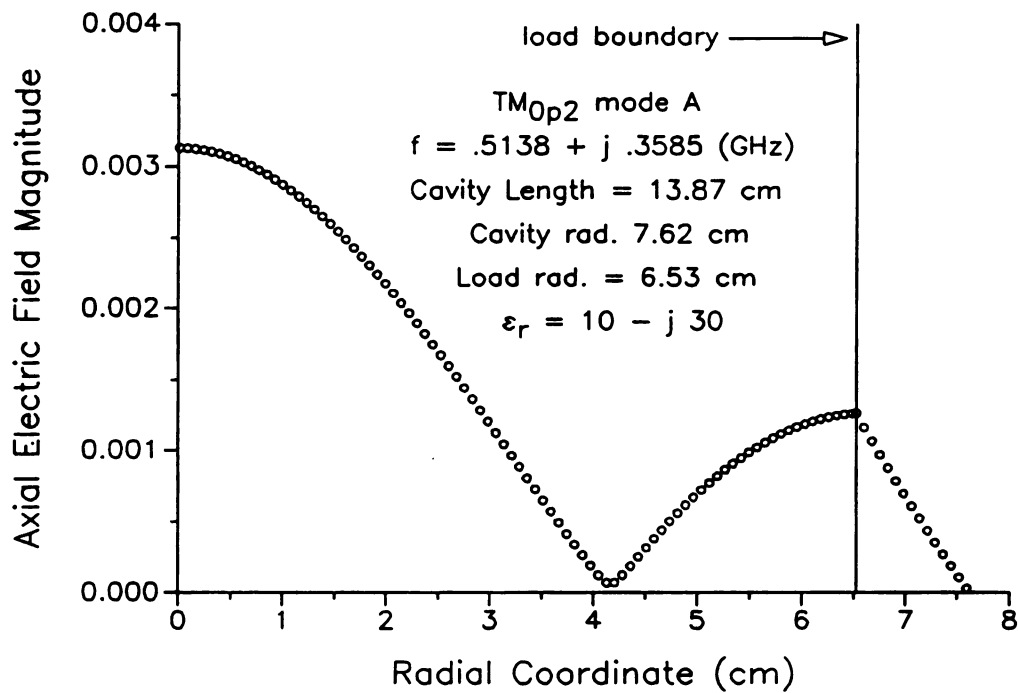
Figure 8-35 Axial electric field magnitude: TM_{0p2} mode A, load radius 6.53 cm.
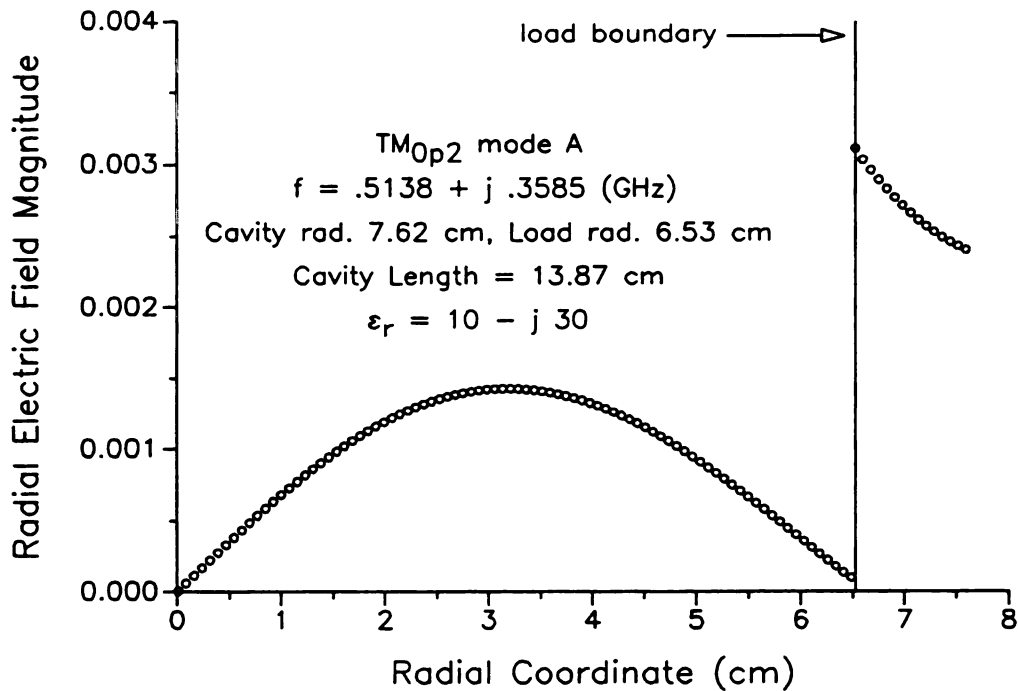
Figure 8-36 Radial electric field magnitude: TM_{0p2} mode A, load radius 6.53 cm.
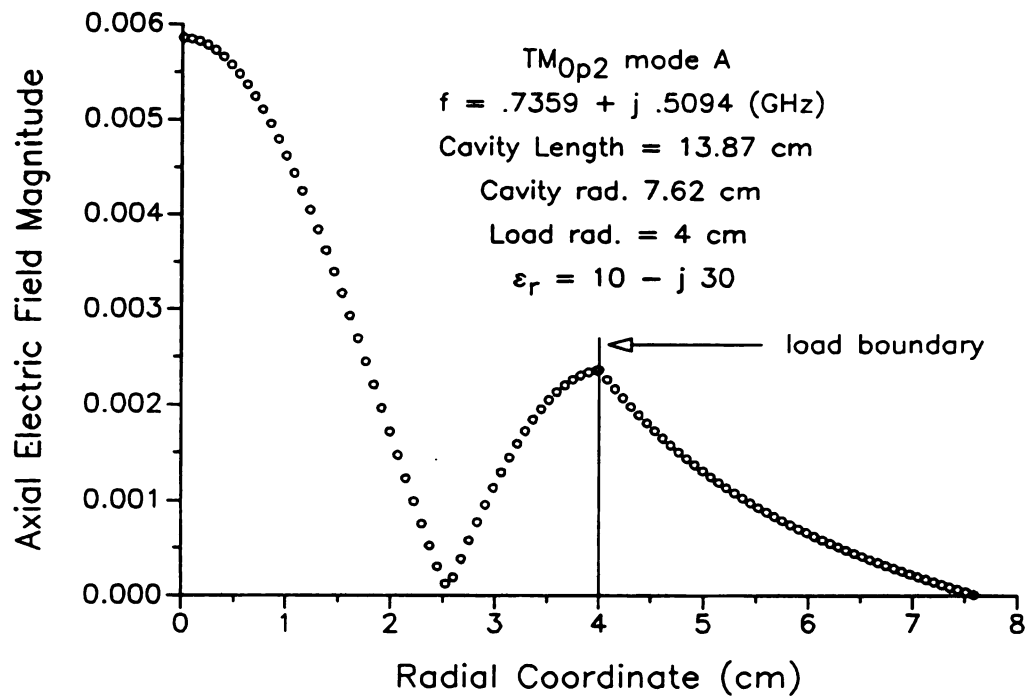
Figure 8-37 Axial electric field magnitude: TM_{0p2} mode A, load radius 4 cm.
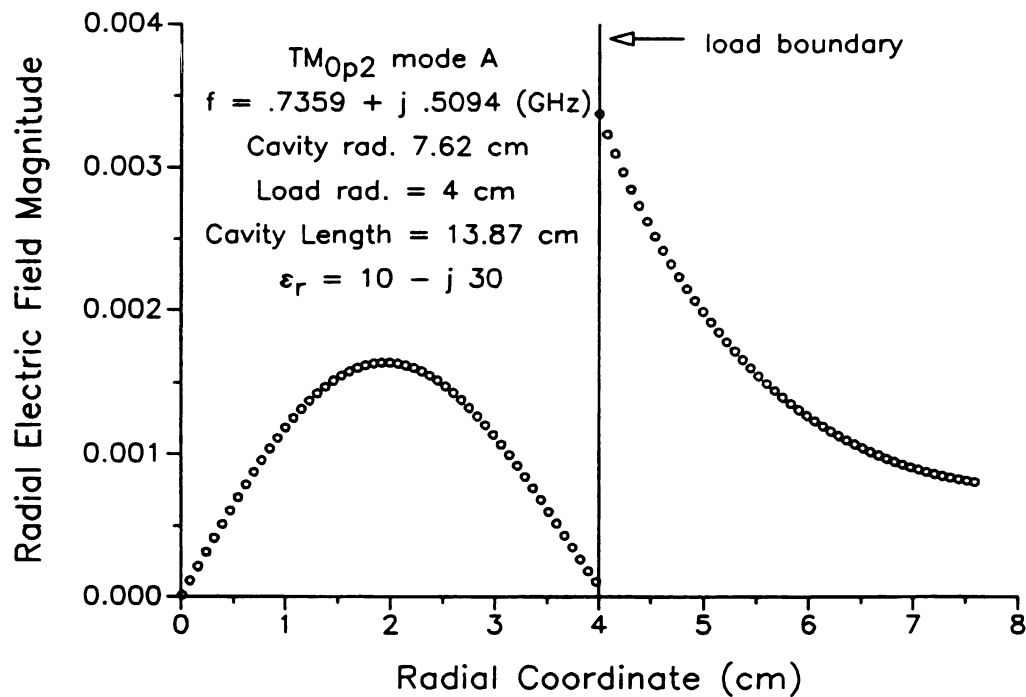
Figure 8-38 Radial electric field magnitude: TM_{0p2} mode A, load radius 4 cm.
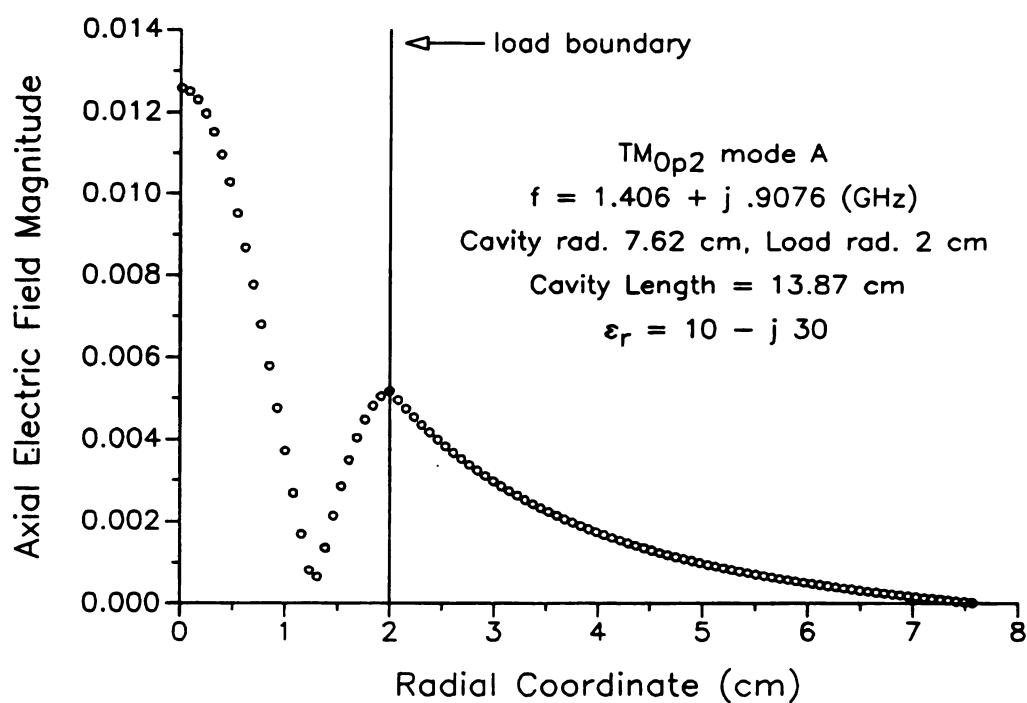
Figure 8-39 Axial electric field magnitude: TM_{0p2} mode A, load radius 2 cm.
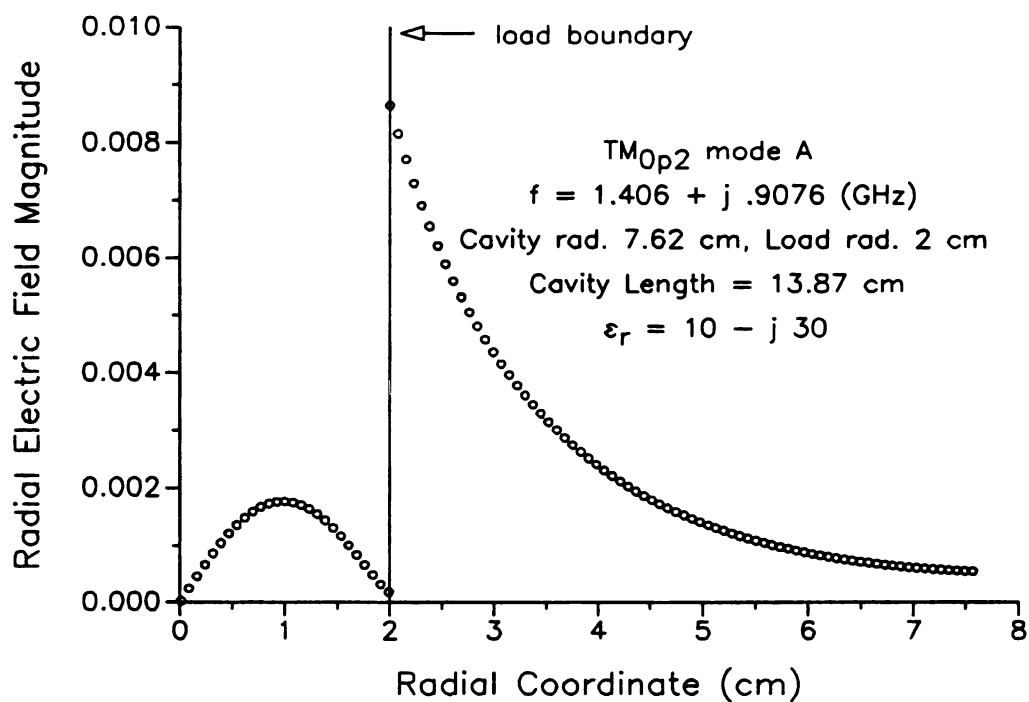
Figure 8-40 Radial electric field magnitude: TM_{0p2} mode A, load radius 2 cm.
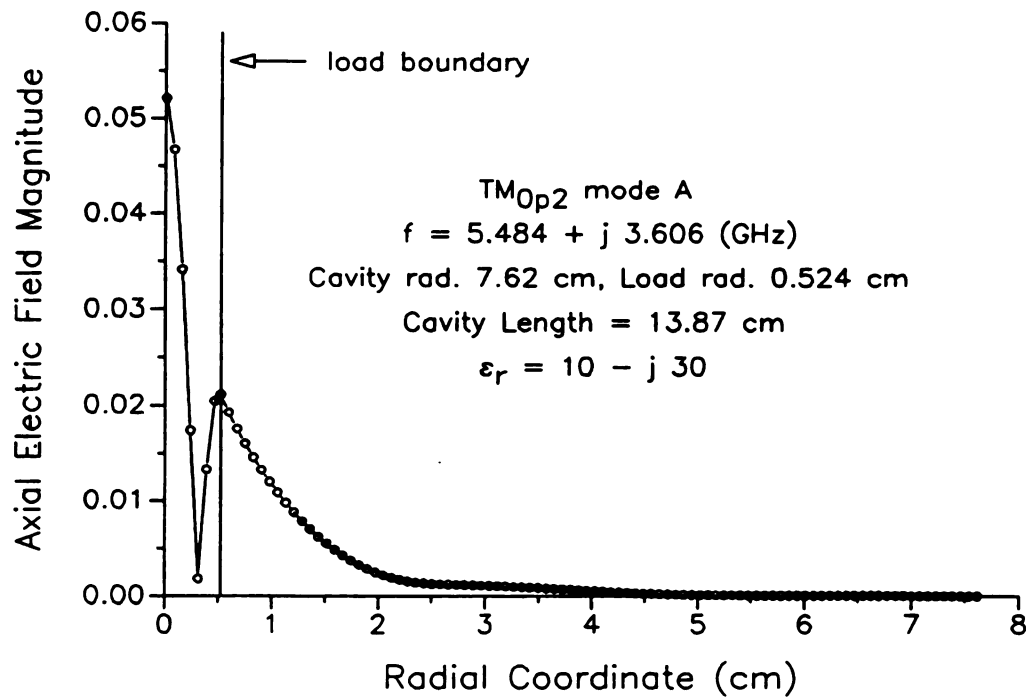
Figure 8-41 Axial electric field magnitude: TM_{0p2} mode A, load radius 0.524 cm.
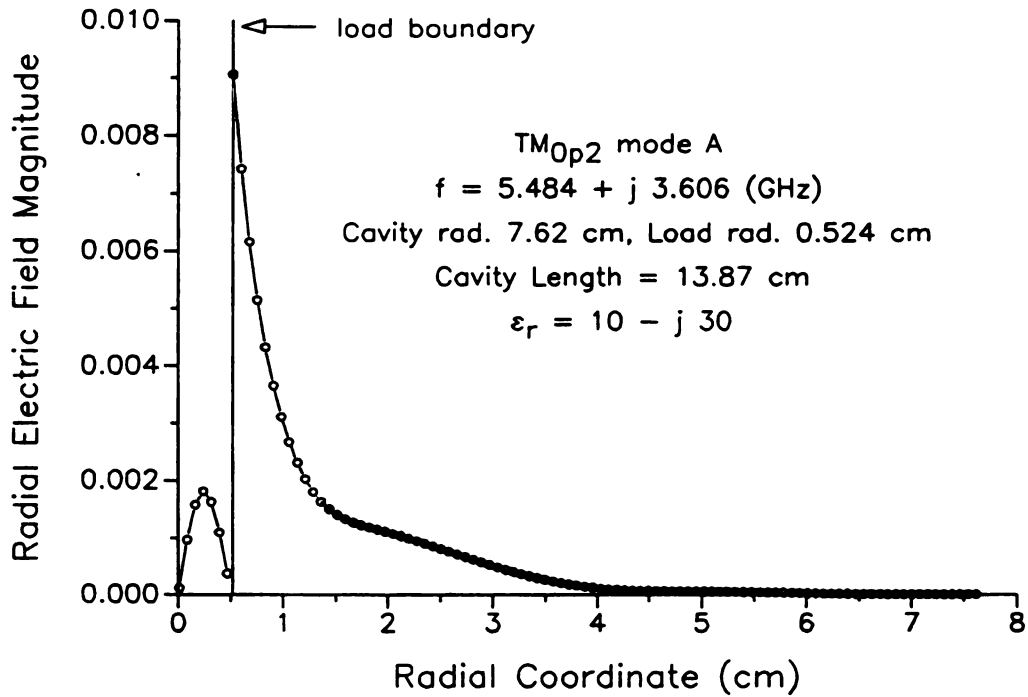
Figure 8-42 Radial electric field magnitude: TM_{0p2} mode A, load radius 0.524 cm.

mode A, referring to Figure 8-30. Figures 8-43 through 8-54 are similar plots for mode B. Examining the field structure in a progressive order with increasing or decreasing load radius provides insight into frequency behavior as a function of load radius.

Referring to Figure 8-30, mode A becomes the material filled cavity TM_{012} mode when the load radius is equal to that of the cavity radius. Figure 8-32 shows the axial field magnitude for the coaxially loaded cavity when the load nearly fills the cavity, being 0.5 mm from the 6" diameter cavity wall. Even for this slight perturbation from the material filled case it is evident that the axial field pattern is somewhat different from the familiar TM_{012} pattern where the axial field magnitude falls uniformly with the radial coordinate to zero, forming a quarter-period Bessel function pattern (compare Figure 8-43). The field pattern of Figure 8-32 is similar to the material filled TM_{012} pattern near the cavity center, but near the wall the magnitude turns up just inside the load boundary. Since the axial field is continuous and is also zero at the cavity wall there is a very sharp drop in the axial field in the short distance between the load and the wall.

Figures 8-33 and 8-34 show the radial electric field magnitude for the same mode. Due to the sharp rise in the discontinuous radial field at the load boundary Figure 8-33 is difficult to recognize as a close relative of the radial field of the TM_{012} mode. However, the radial field inside the load alone, shown in Figure 8-34, shows that the coaxially loaded radial field appears almost identical to the radial field of the material filled TM_{012} mode with a maximum approximately 2/3 along the radius from the center to the cavity wall.

These Figures, 8-32 through 8-34, are presented to demonstrate that the field structure of mode A is in fact similar to that of the material filled TM_{012} mode. This is necessary because as the load radius becomes smaller, pulling the load material farther away from the cavity wall, the field patterns begin to look very different from the material filled TM_{012} mode field patterns. Figures 8-35 through 8-42 show the field magnitudes for load radii of 6.53 cm, 4 cm, 2 cm, and 0.524 cm successively. In these Figures the axial field magnitude is seen to display a double half-lobed

appearance which is normally associated with modes of second radial order. These plots demonstrate three things.

First of all, they show by their similar shapes that there is good reason to classify all of these resonances as belonging to a common mode, mode A as it is referred to in Figure 8-30. Second, they demonstrate that an appreciable amount of the field remains inside the load material as the load grows smaller in radius. Furthermore the double half-lobe pattern of the axial field exists within the load material, even for small load radii. This field oscillation within the load material accounts for the high frequency of this mode for small load radii since the load boundary behaves as a reflector for the fields inside the material. Third, the Figures show that the field becomes more and more axial for mode A as the load radius decreases. When the load nearly fills the cavity the average radial and axial contributions to the field are comparable. When the load radius is .524 cm the axial contribution is approximately twice the radial contribution in the region outside the load. Inside the load the average value of the axial electric field is approximately 18 times that of the radial electric field.

Incidentally, it should be noted that it would be difficult to couple to mode A through the side of the cavity when the load radius is small. The coupling probe would have to extend quite far into the cavity. A probe inserted through the end of the cavity near the load would be best. This is true for two reasons: 1) the field magnitude is low outside and away from the load, 2) the direction of the field is primarily axial.

Similar kinds of information may be gathered from the field pattern plots for mode B. Figures 8-43 and 8-44 contain plots of the axial and radial electric field magnitudes for a load radius of 0.04772 cm, a filament of less than 1 mm diameter. It might be expected that the introduction of this filament would produce more of a change in the pattern of the axial field than in the radial field since the loss factor is fairly large, $\epsilon_r'' = 30$, and the load lies parallel to the axial field. In fact, Figures 8-43 and 8-44 show that this is not the case. The axial field pattern is essentially that of the empty cavity TM_{012} axial field. Moreover, the overall magnitude of the axial
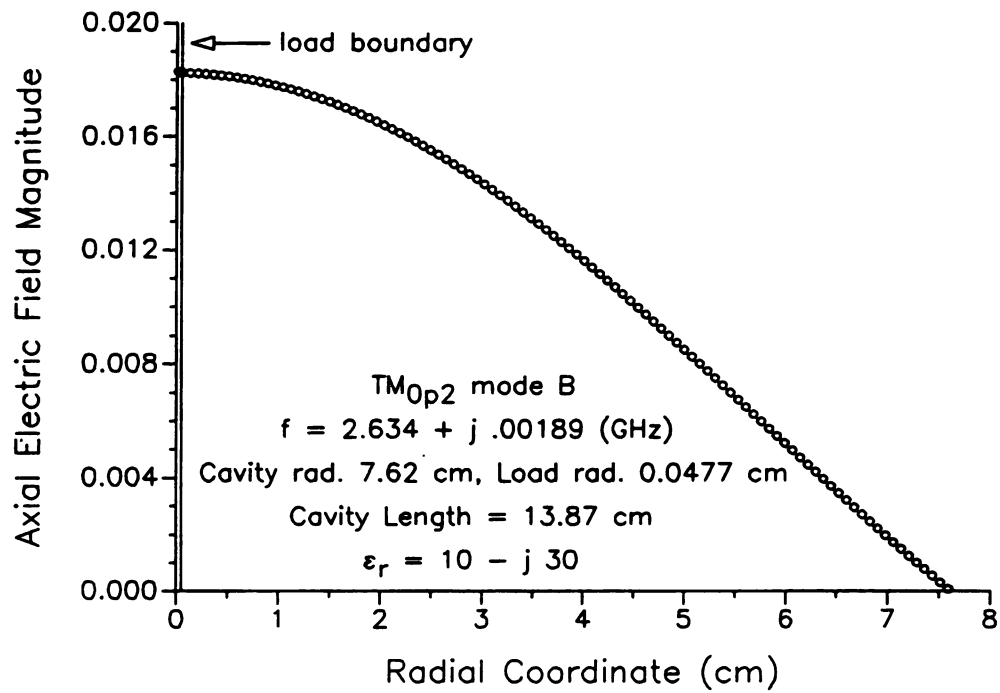
Figure 8-43 Axial electric field magnitude: TM_{0p2} mode B, load radius 0.0477 cm.
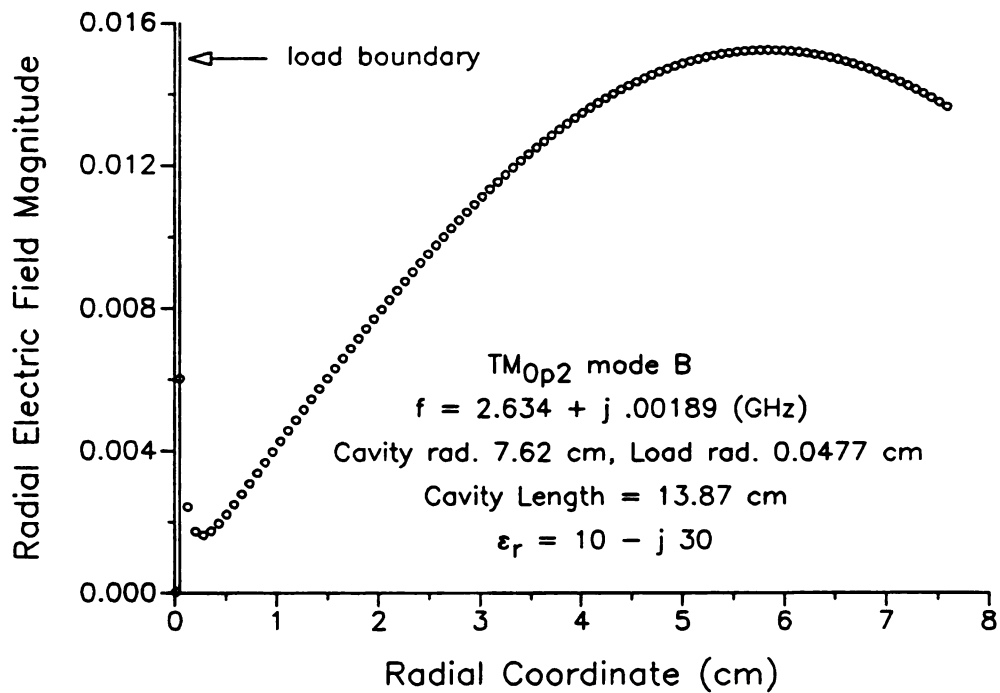
Figure 8-44 Radial electric field magnitude: TM_{0p2} mode B, load radius 0.0477 cm.
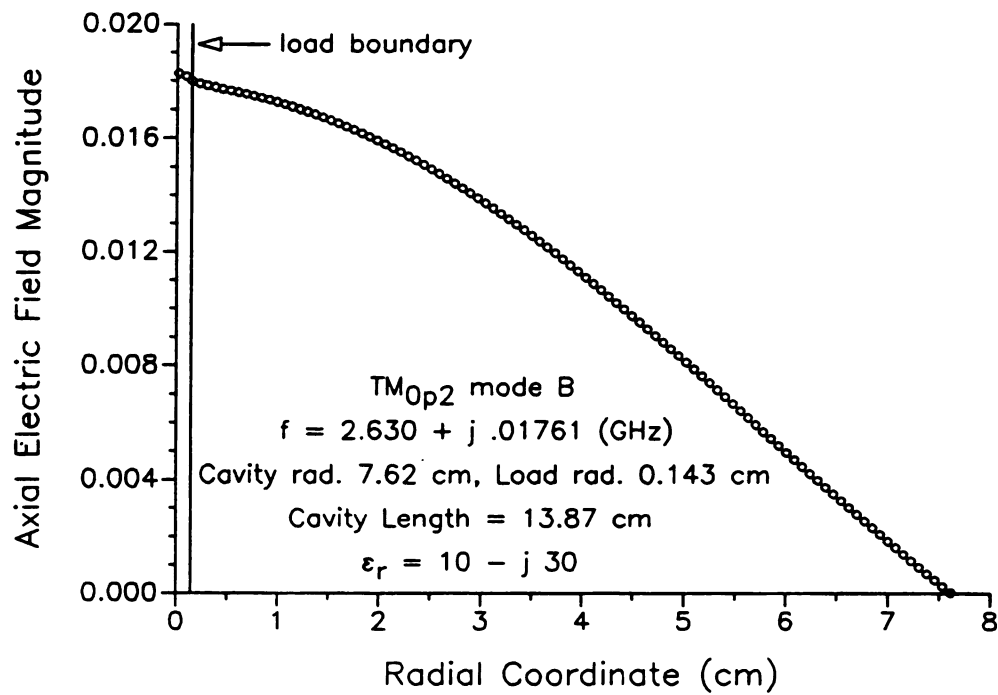
Figure 8-45 Axial electric field magnitude: TM_{0p2} mode B, load radius 0.143 cm.
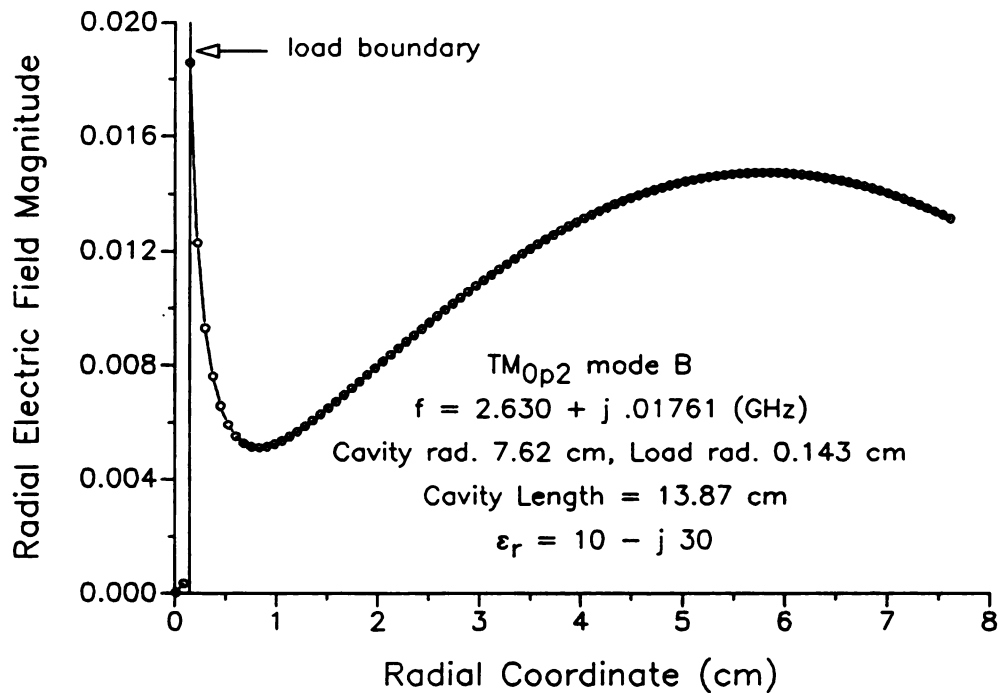
Figure 8-46 Radial electric field magnitude: TM_{0p2} mode B, load radius 0.143 cm.
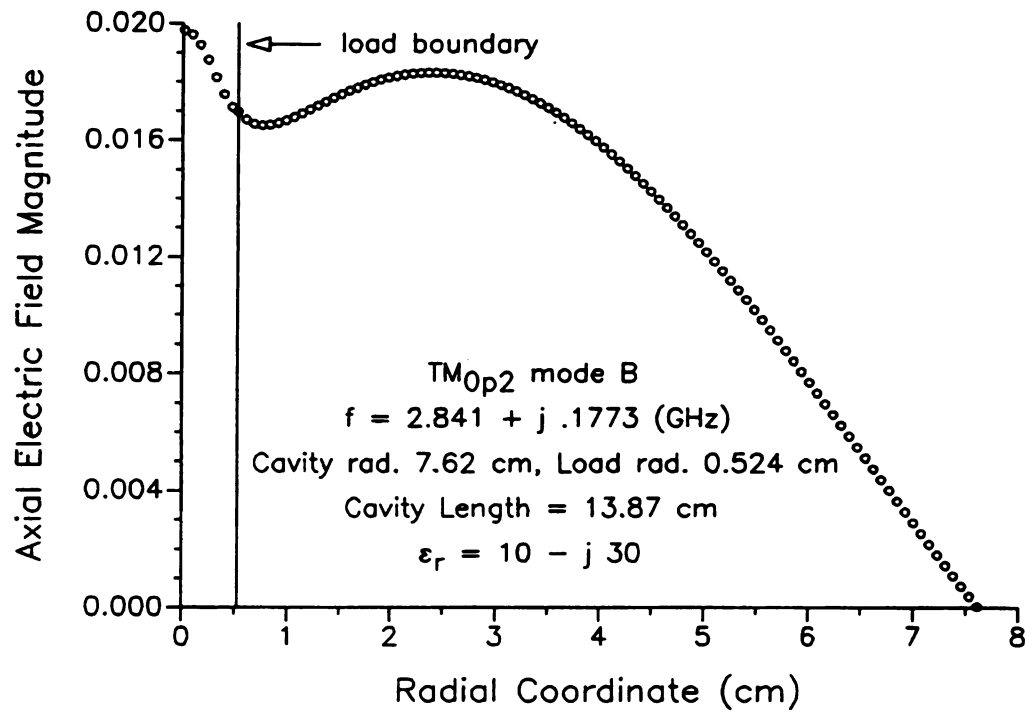
Figure 8-47 Axial electric field magnitude: TM_{0p2} mode B, load radius 0.524 cm.
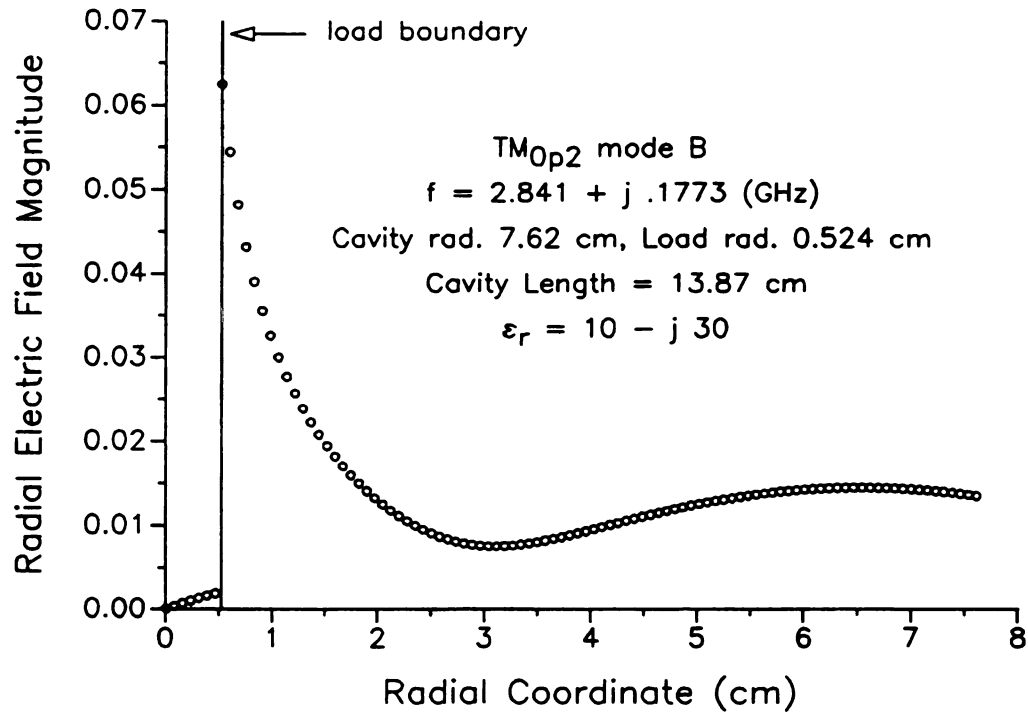
Figure 8-48 Radial electric field magnitude: TM_{0p2} mode B, load radius 0.524 cm.
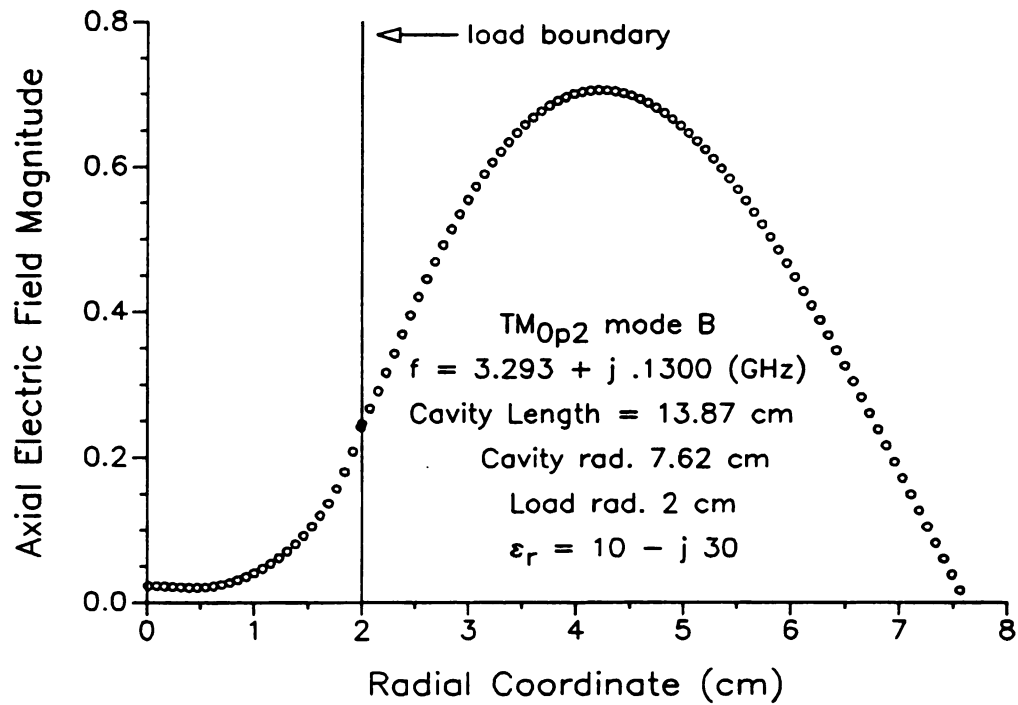
Figure 8-49 Axial electric field magnitude: TM_{0p2} mode B, load radius 2 cm.
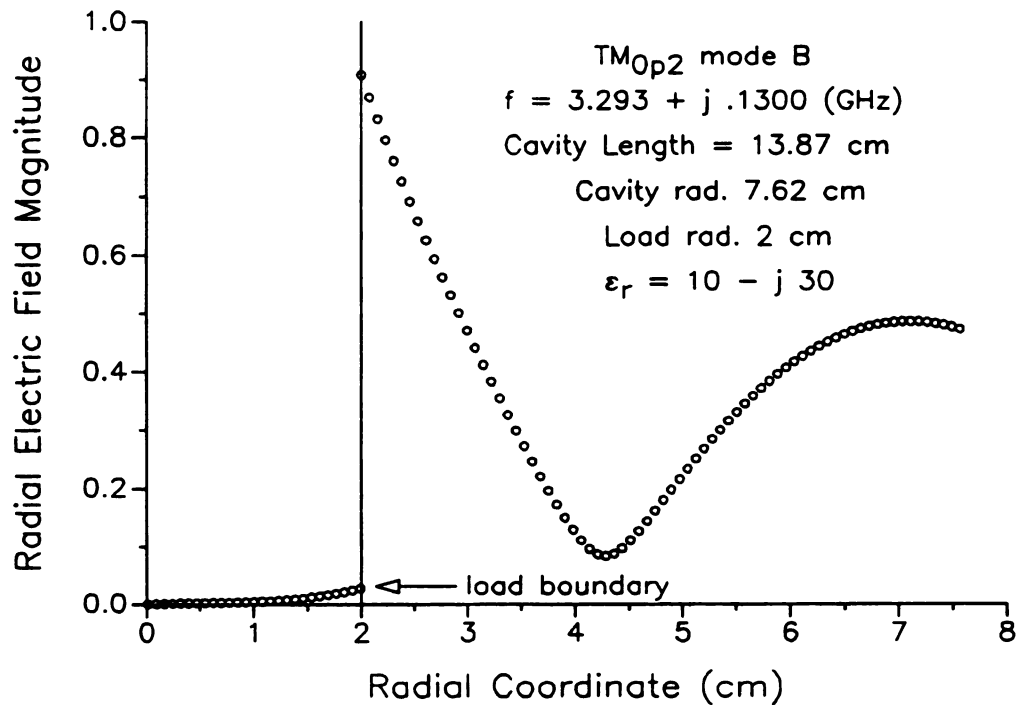
Figure 8-50 Radial electric field magnitude: TM_{0p2} mode B, load radius 2 cm.
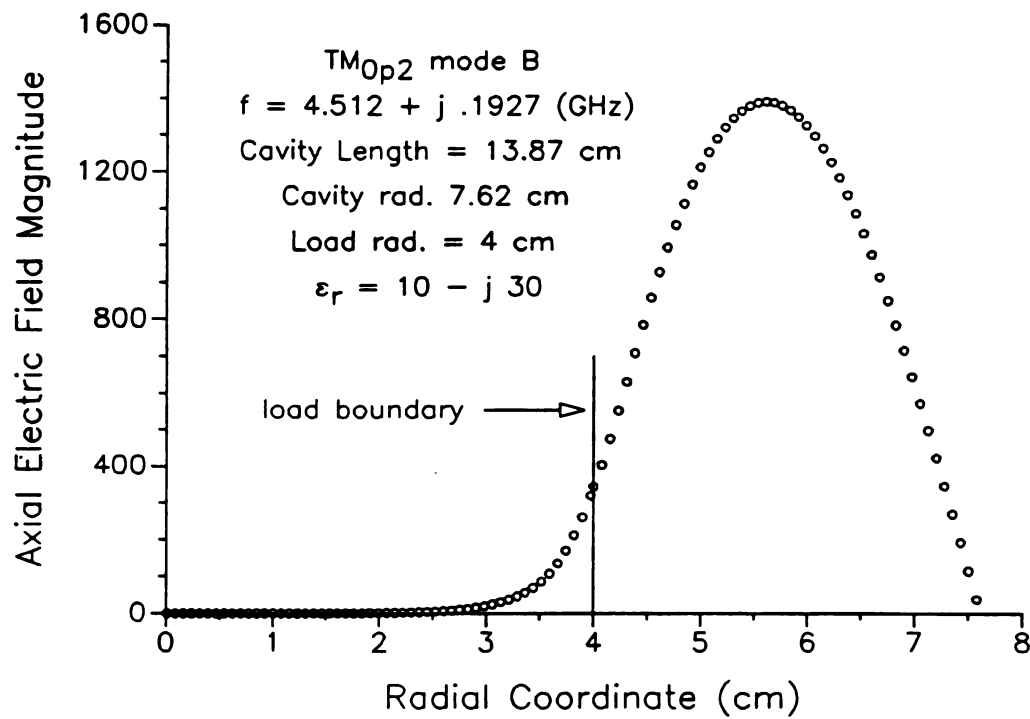
Figure 8-51 Axial electric field magnitude: TM_{0p2} mode B, load radius 4 cm.
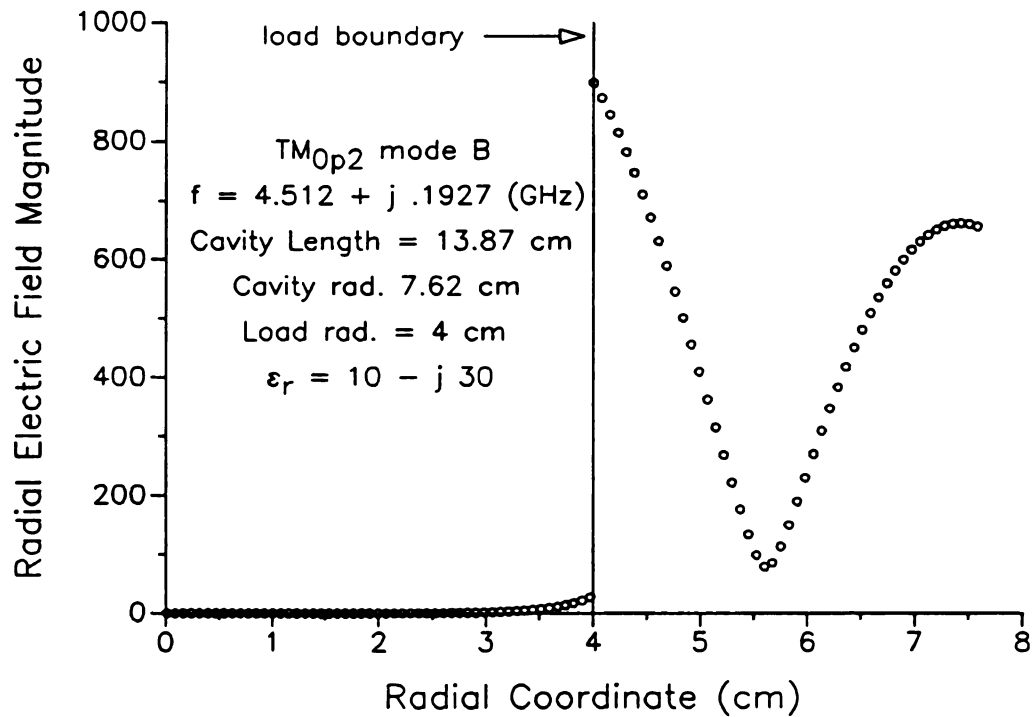
Figure 8-52 Radial electric field magnitude: TM_{0p2} mode B, load radius 4 cm.
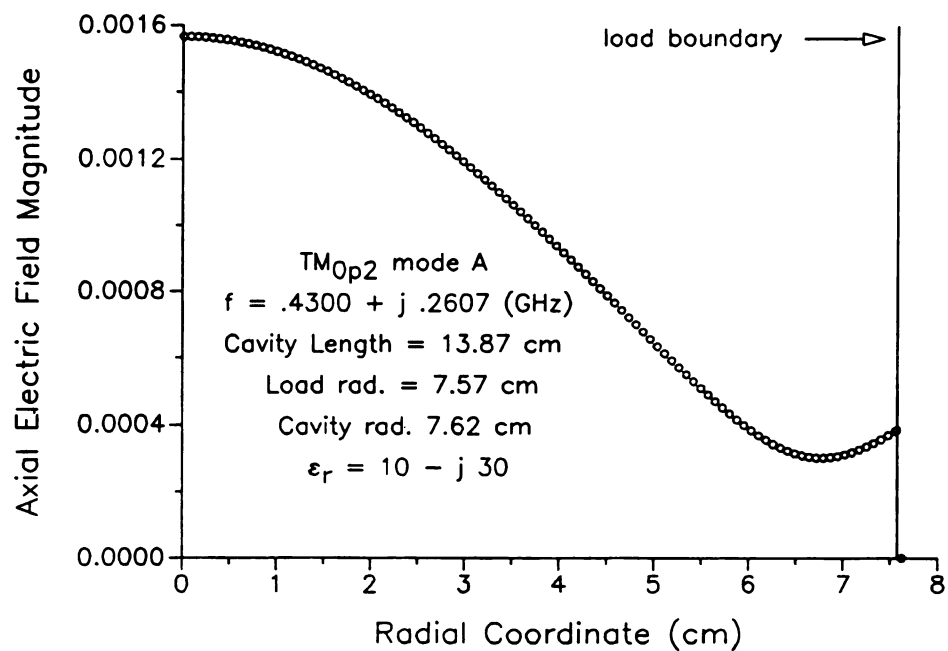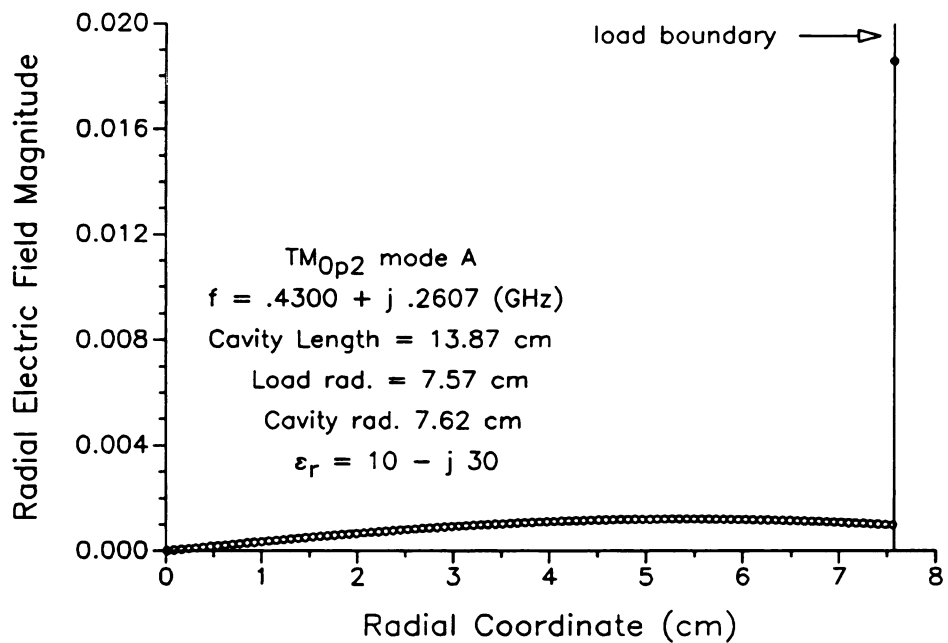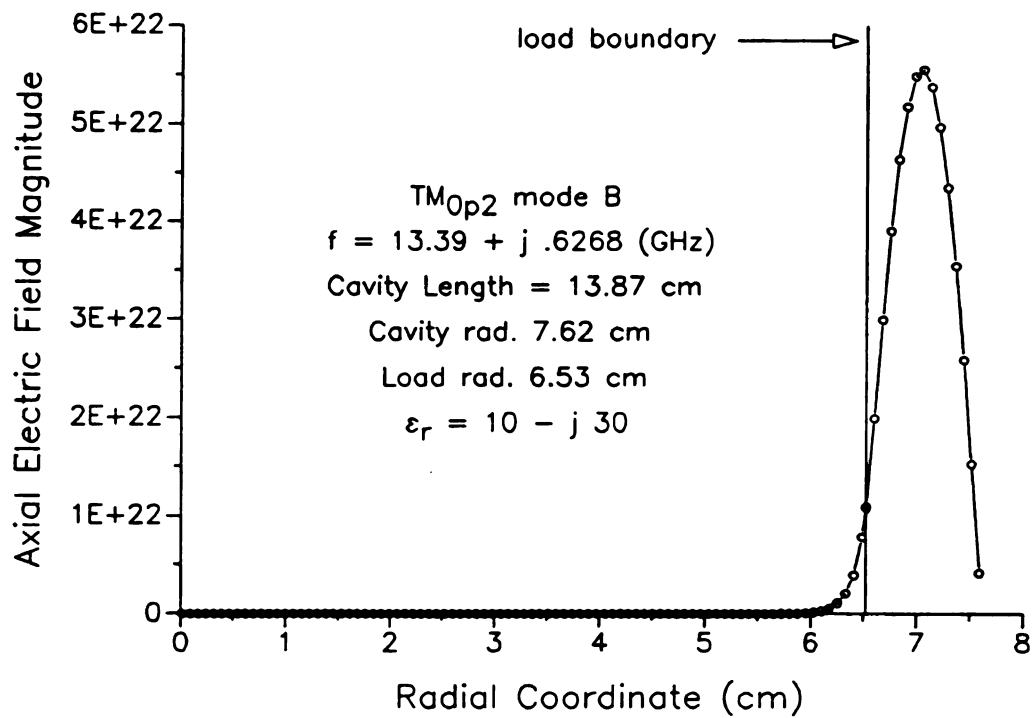
Figure 8-53 Axial electric field magnitude: TM_{0p2} mode B, load radius 6.53 cm.
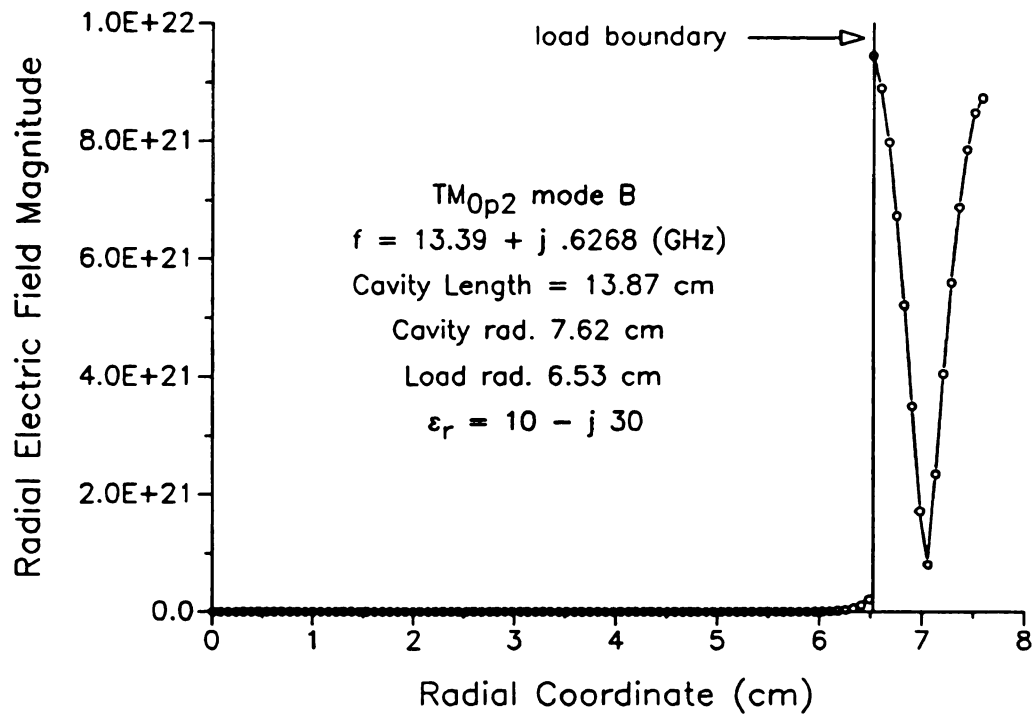
Figure 8-54 Radial electric field magnitude: TM_{0p2} mode B, load radius 6.53 cm.

field is not diminished relative to the radial field magnitude but remains in approximately the same average proportion to the radial field as for the empty cavity case. The radial field magnitude for the mode does exhibit a somewhat different shape than the empty cavity TM_{012} mode radial field in the vicinity of the load. This is due to the boundary condition on the radial electric field which mandates that the radial field be discontinuous at the load boundary in a proportion related to the complex permittivity, which is substantial in this case. Nevertheless, in the greater portion of the cavity the shape of the radial field is essentially that of the empty cavity TM_{012} mode.

Even though the field patterns are not greatly perturbed from the empty cavity field patterns, and although the resonant frequency (closely approximated by the real part of the natural frequency) is nearly the same as the empty cavity resonant frequency, the imaginary frequency indicates that the material is absorbing a large percentage of the input energy. The imaginary frequency, as indicated in Figures 8-43 and 8-44, is 0.00189 GHz. With the real frequency at 2.634 GHz this translates into a Q factor value of 697. We refer to this Q, derived from material losses alone, as Q_m.

Of course, when the cavity walls are modeled as perfect conductors, all of the input energy must be dissipated in the lossy load material. However, by including a finite wall conductivity in the model as a perturbation losses in the cavity walls may be computed. It is possible to show that an empty brass cavity of the same dimensions as the coaxial cavity of Figures 8-43 and 8-44 has a quality factor, called Q_0 for the empty cavity, of 14,700. Since the electric fields for the coaxially loaded cavity of Figures 8-43 and 8-44 are essentially the same at the cavity wall as the empty cavity fields the contribution to the cavity Q from the wall losses, Q_w, is given by $Q_w \approx 14,700$. The Q of the cavity system, Q_u, including both wall losses and losses in the load material, is given by

$$\frac{1}{Q_u} = \frac{1}{Q_w} + \frac{1}{Q_m} . \tag{8-4}$$

With $Q_m = 697$ and $Q_w = 14,700$ the contribution to Q_u from the wall losses is almost negligible giving $Q_u = 665$. For this value of the system quality factor, and using the fact that the fields at the cavity walls are similar to the empty cavity fields, the material coupling efficiency may be determined by the following equation[4]

$$Eff = 100 \left[1 - \frac{Q_u}{Q_o} \right] \% . \tag{8-5}$$

The coupling efficiency to the filament load as given by Equation (8-5) is 95 %. This example demonstrates that it is possible to couple energy very efficiently to certain materials without altering the resonant frequency or substantially changing the field patterns from the empty cavity conditions.

As the radius of the load increases the axial electric field retains a resemblance to the empty cavity axial field until the load is more than 1 cm in diameter. The radial field pattern begins to change immediately. Figures 8-45 through 8-54 contain plots of the axial and radial fields of mode B of Figure 8-30 for load radii of 0.143 cm, 0.524 cm, 2 cm, 4 cm, and 6.53 cm. The axial field as depicted in Figure 8-45 for a load radius of 0.143 cm is not much different from the axial field for 0.0477 cm shown in Figure 8-43, but the radial field of Figure 8-46 is altered significantly from the empty cavity radial field and from that of Figure 8-44 for load radius 0.0477 cm. As the load radius continues to increase both the axial and radial field patterns are altered significantly. It becomes evident when the load has reached 2 cm in radius, Figures 8-49 and 8-50, that the fields of mode B are being excluded from the load, existing primarily in the region between the load and the cavity wall. This helps to explain why the Q is higher in general for mode B than for mode A.

In fact, the field patterns begin to resemble those of the coaxial cavity TM_{01q} modes where the fields reside exclusively outside the inner conductor. This is seen

---

[4]Asmussen, Lin, Manring, and Fritz, 1482.

by comparing Figures 8-51 and 8-52 for the coaxially-loaded cavity with a load radius of 4 cm and material complex permittivity of $\hat{\epsilon}_r = 10 - j\,30$ with Figures 8-55 and 8-56 for the coaxial cavity TM_{012} mode with a 4 cm radius inner conductor. Not only are the field patterns similar, but the real frequency of the coaxially loaded mode is 4.512 GHz, very near the coaxial cavity resonant frequency of 4.657 GHz. It is interesting to note that although the real frequency in Figures 8-51 and 8-52 is close to that of the coaxial cavity TM_{012} mode, the Q of Figures 8-51 and 8-52 is only 12.

The fields of mode B do not resemble coaxial cavity modes for small load radius, yet when the load radius is larger they do. At the same time it is apparent that there is a smooth transition in the field patterns as the load radius is increased so that all of the resonances can be thought of as members of a single mode in the load radius variable.

Two final comments on mode B of Figure 8-30 will conclude our discussion of this mode. First, as with mode A, a higher resonant frequency is associated with the region of the mode where fluctuation of the field occurs within a smaller space. For mode A this occurred in the small load radius region with the field fluctuating inside the load. For mode B the high frequency region is where the load radius approaches the cavity radius with the fields confined to the region between the load and the cavity wall. Second, the field pattern Figures 8-43 through 8-54 show that the electric field becomes more axial as the load radius increases. Again, this is similar to the behavior of mode A in that the high frequency regions of both modes are regions of higher axial electric field.

The final mode chart for cavity-short type TM modes presented here is found in Figure 8-57 for the real part of the frequency and in Figure 8-58 for the imaginary part of the frequency where it is shown that the mode behavior demonstrated in Figure 8-30 depends not only upon the material loss factor but also the dielectric constant. Figures 8-57 and 8-58 are plots of the real and imaginary frequencies for TM_{0p2} modes for the same cavity dimensions and material loss factor as for the modes of Figure 8-30, but with the dielectric constant doubled from 10 to 20.
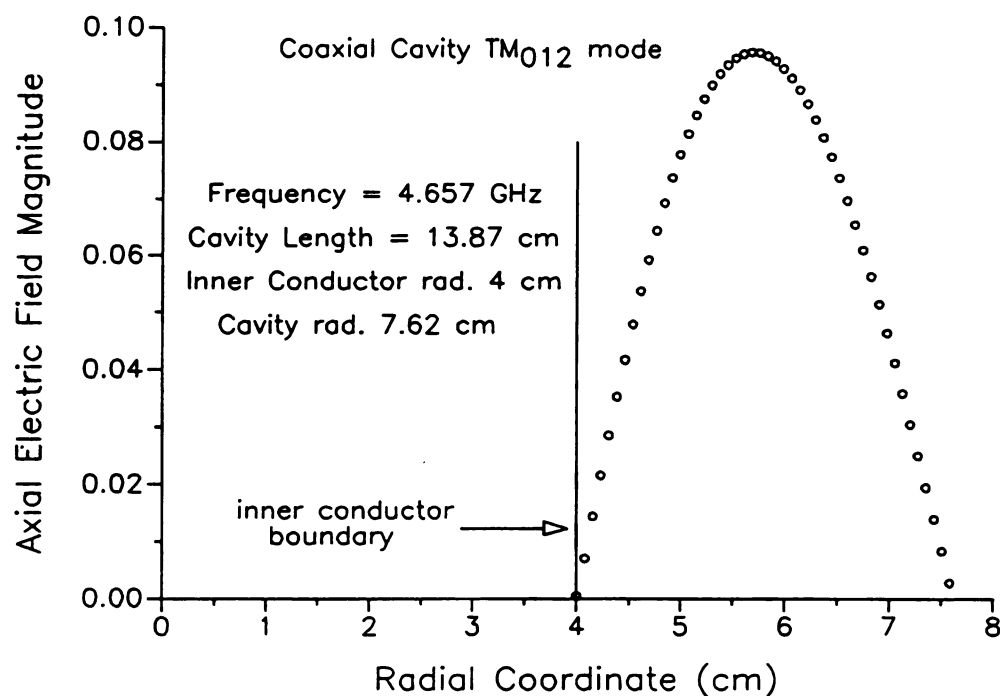
Figure 8-55 Axial electric field magnitude for the coaxial cavity TM_{022} mode.
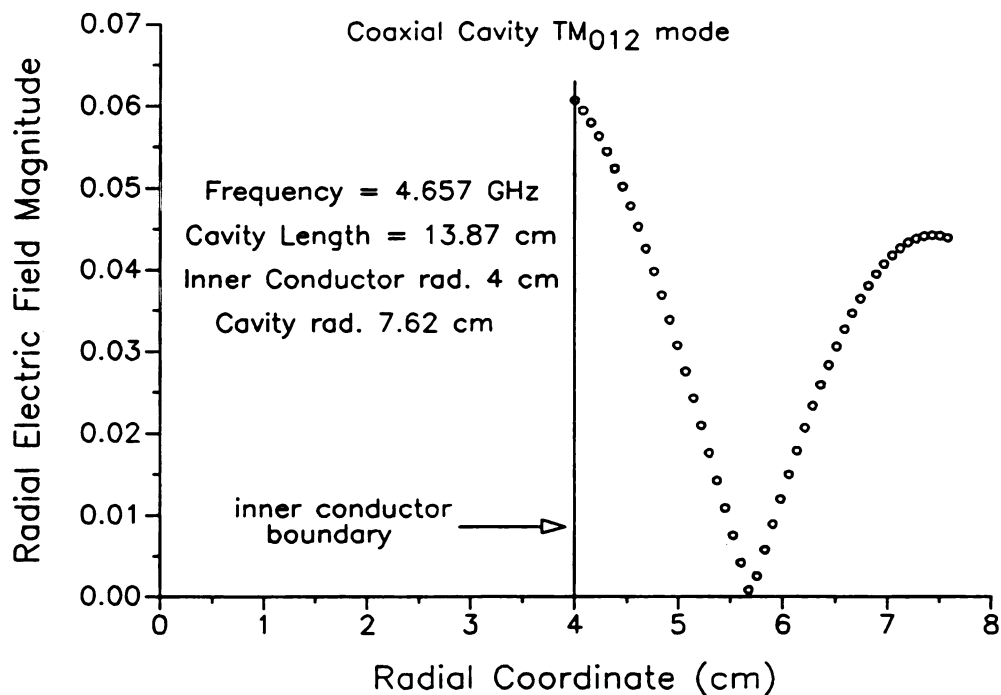
Figure 8-56 Radial electric field magnitude for the coaxial cavity TM_{022} mode.

Figure 8-57 Real frequency vs. load radius: $\hat{\varepsilon}_r = 20 - j\,30$, TM_{0p2}.
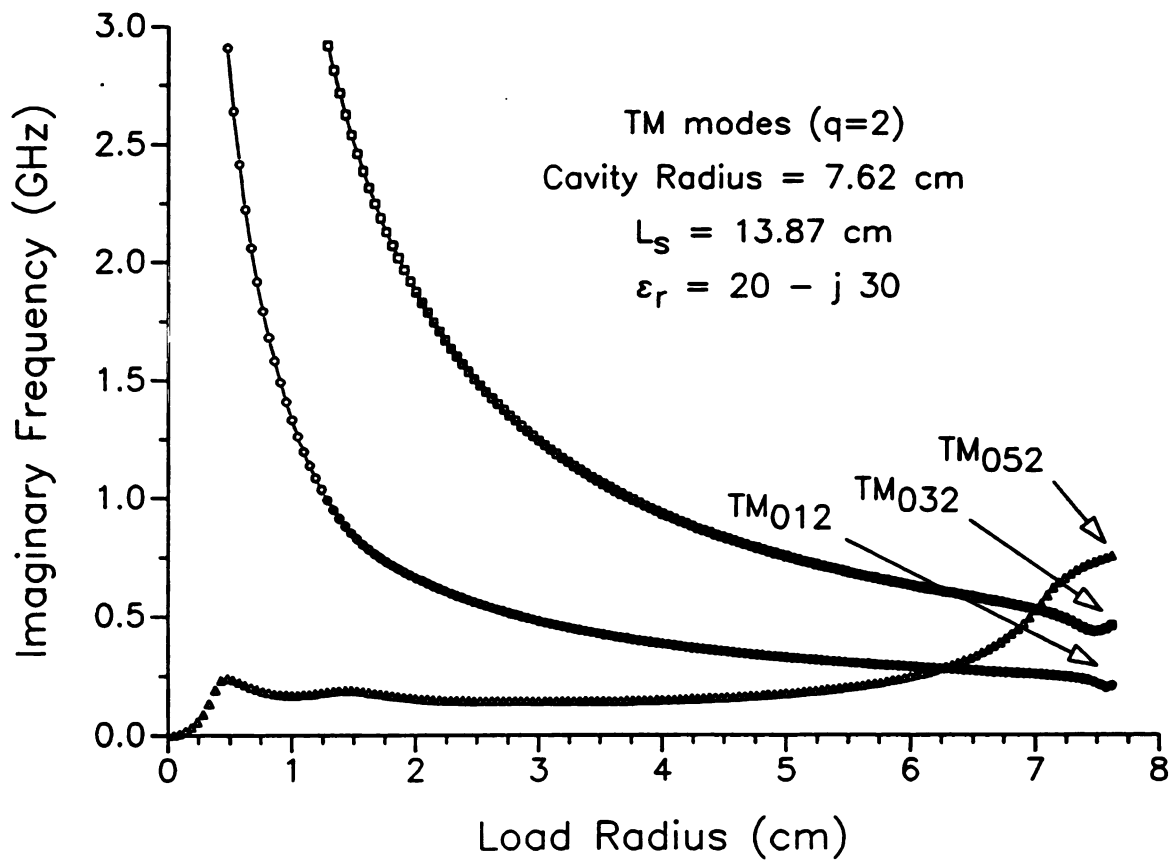
Figure 8-58 Imaginary frequency vs. load radius: $\hat{\epsilon}_r = 20 - j\,30$, TM_{0p2}.

The mode which includes the material filled cavity TM_{012} mode at the limit of load radius approaching the cavity radius behaves similarly to mode A of Figures 8-30 and 8-31. However, the mode which includes the empty cavity TM_{012} resonance for zero load radius is quite different from mode B. Instead of the real frequency increasing with load radius there is almost no variation in the real frequency for this mode except near the load radius limits. The frequency stability of this mode suggests a use for it in processing non-uniformly shaped materials, if the mode exists for the dielectric properties of the material in question. If the Q of the mode can be raised it might also be useful as a lossy filter for a precisely centered frequency band.

Figure 8-57 suggests that the behavior exhibited by mode A of Figure 8-30 is confined to the lower ordered modes. While the frequencies become large for small load radii for the coaxially loaded cavity modes which include material filled TM_{012} and TM_{032} modes, such is not the case for the mode which includes the material filled TM_{052} mode.

In this Section we have developed explanations for various mode behaviors which will be utilized in the following Sections for TE and HEM modes. These have included demonstrating the close relationship between modes for high loss factor materials and the coaxial cavity modes. Additionally, high frequency behavior for modes emanating from lower order empty or material filled cavity modes has been associated with the confinement of field fluctuation into a small region, the material boundary behaving as a reflector of either or both the radial (normal) and the axial (parallel) fields. Other interesting features of particular TM modes have been examined which may or may not appear in TE and HEM mode behavior.

8.4 Mode Charts and Field Patterns: TE Modes

8.4.1 Variations in the TE_{011} Mode with Increasing Loss Factor

Referring back to Figure 8-2, several mode charts of real frequency versus cavity length were shown for the TM_{011} mode with $\epsilon_r' = 3.03$, $a = 0.5"$, and $b = 3"$. Each curve in Figure 8-2 represents the mode for a different loss factor, ϵ_r'', in the

range from 1 to 1,000. The frequency versus cavity length mode chart of the coaxial cavity TM_{001} mode is included in Figure 8-2 for comparison with coaxially loaded TM_{011} modes for high loss factor loads. Now we wish to examine a TE mode for the same load materials and sizes. The mode charts of Figure 8-59 are for the same loads as those of Figure 8-2, but for the TE_{011} mode. The coaxial cavity TE_{011} mode is included in Figure 8-59 to demonstrate that the real frequencies of the TE_{011} coaxially loaded mode approach those of the coaxial cavity for high loss factors.

In contrast to the TM_{011} mode of Figure 8-2 and the TM_{021} mode of Figure 8-13, Figure 8-59 shows that the frequency of the TE_{011} mode rises uniformly with increasing loss factor. This is shown more clearly in Figure 8-60 where the real frequency is plotted against the load material loss factor for a constant cavity length of 6.5 cm. Figure 8-60 shows that the real frequency rises rapidly as ϵ_r'' goes from zero to near 10. For higher loss factors it continues to increase, but much more slowly.

The imaginary frequency is plotted as a function of loss factor in Figure 8-61. For a lossless dielectric the imaginary frequency is zero. As the loss factor increases from zero the imaginary frequency rises rapidly to a peak of approximately 73 MHz near $\epsilon_r'' = 5$. The real frequency at the same point is 3.354 GHz. Taken together this translates into a Q factor of approximately 23, where the Q as a function of material loss factor is a minimum. Further increasing of the loss factor causes the imaginary frequency to fall and Q to rise. The imaginary frequency peak occurs at a lower loss factor for TE_{011}, i.e., $\epsilon_r'' = 5$, than for TM_{011} where the peak occurs near $\epsilon_r'' = 10$. However, the imaginary frequency peak for the TM_{021} occurs at approximately $\epsilon_r'' = 5$, the same as for the TE_{011} mode.

For large loss factors, e.g., $\epsilon_r'' = 1,000$, the eigenfrequency of the coaxially loaded TE_{011} mode is nearly equal to that of the coaxial cavity TE_{011} mode, as shown in Figure 8-59. It is also true that the field patterns appear more like the coaxial cavity field patterns as loss factor is increased. Figures 8-62 through 8-66 show how the azimuthal electric field magnitude of the coaxially loaded cavity changes with increasing loss factor. Notice that the electric field inside the load, i.e.,
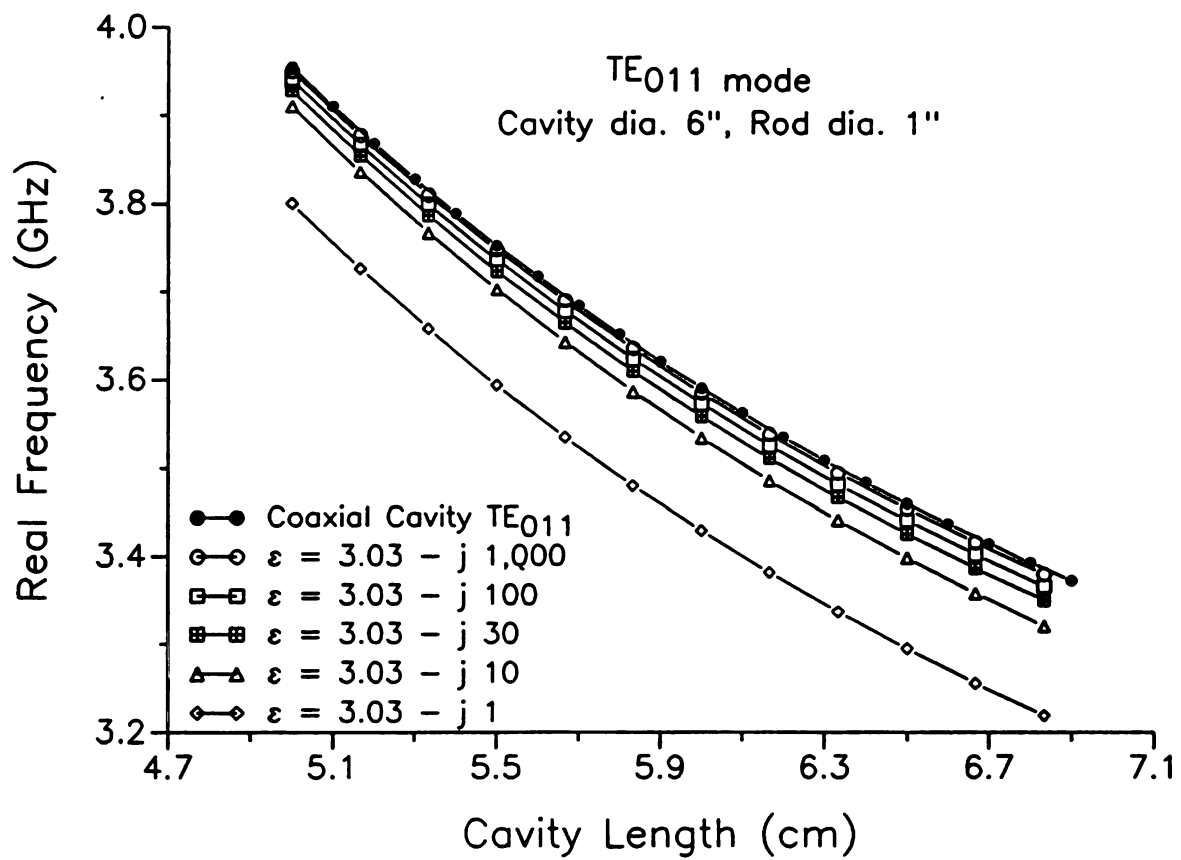
Figure 8-59 TE_{011} Real frequency vs. cavity length for $\epsilon_r' = 3.03$ with hypothetical loss factors.
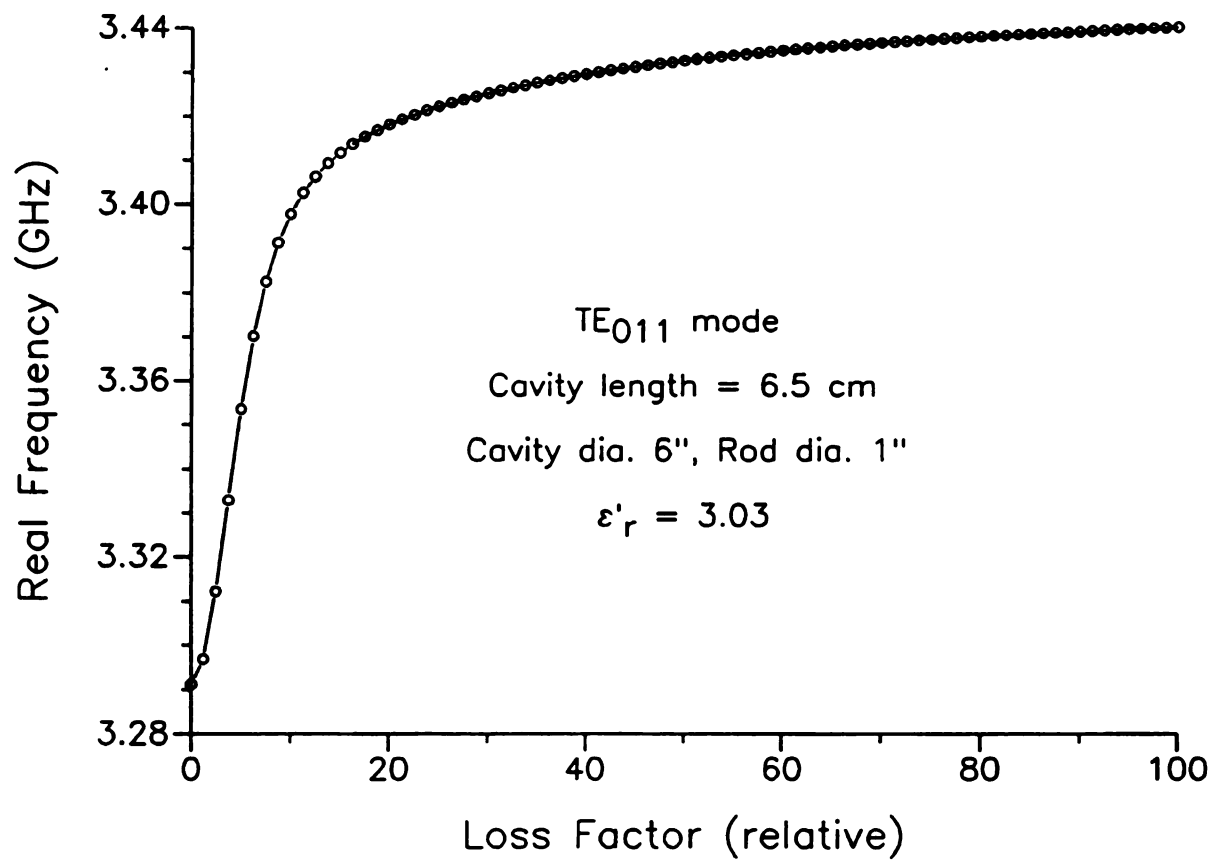
Figure 8-60 Real frequency vs. loss factor for $\epsilon_r' = 3.03$ in the TE_{011} mode.
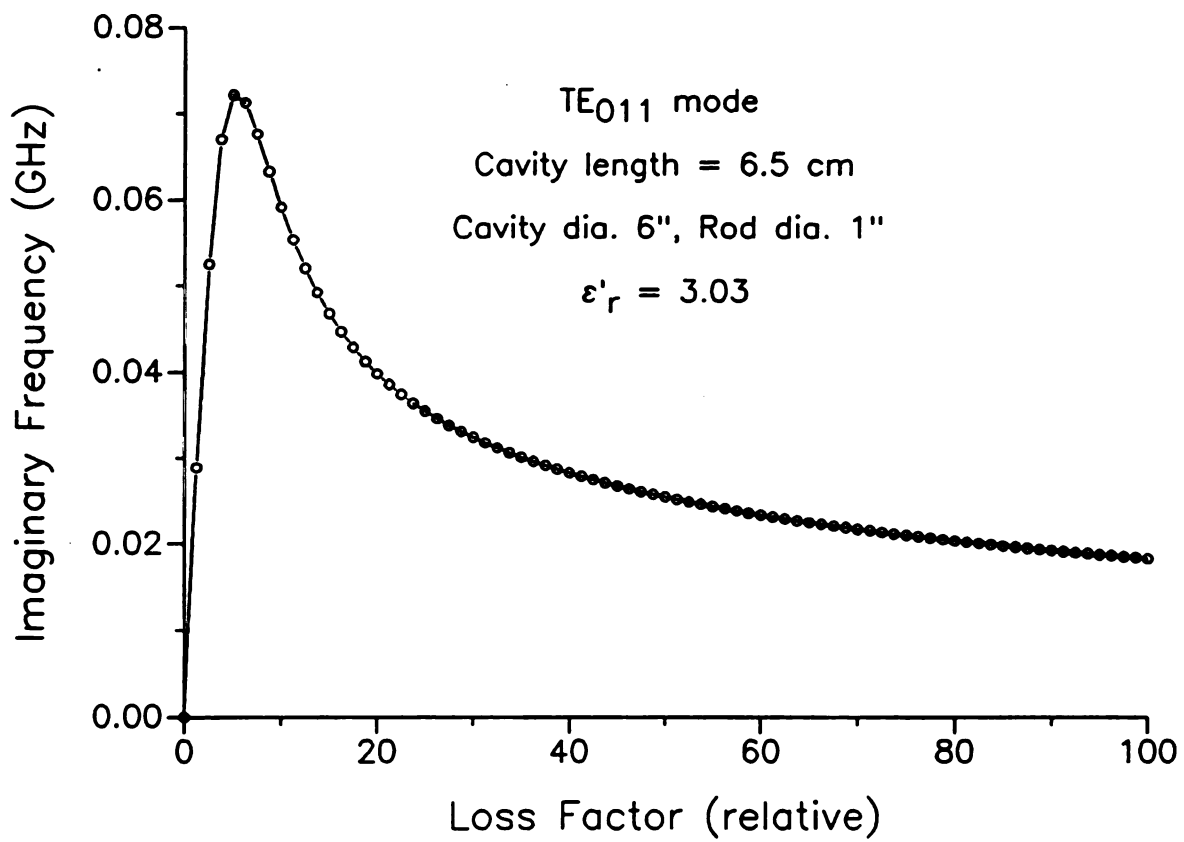
Figure 8-61 Imaginary frequency vs. loss factor for $\epsilon'_r = 3.03$ in the TE_{011} mode.
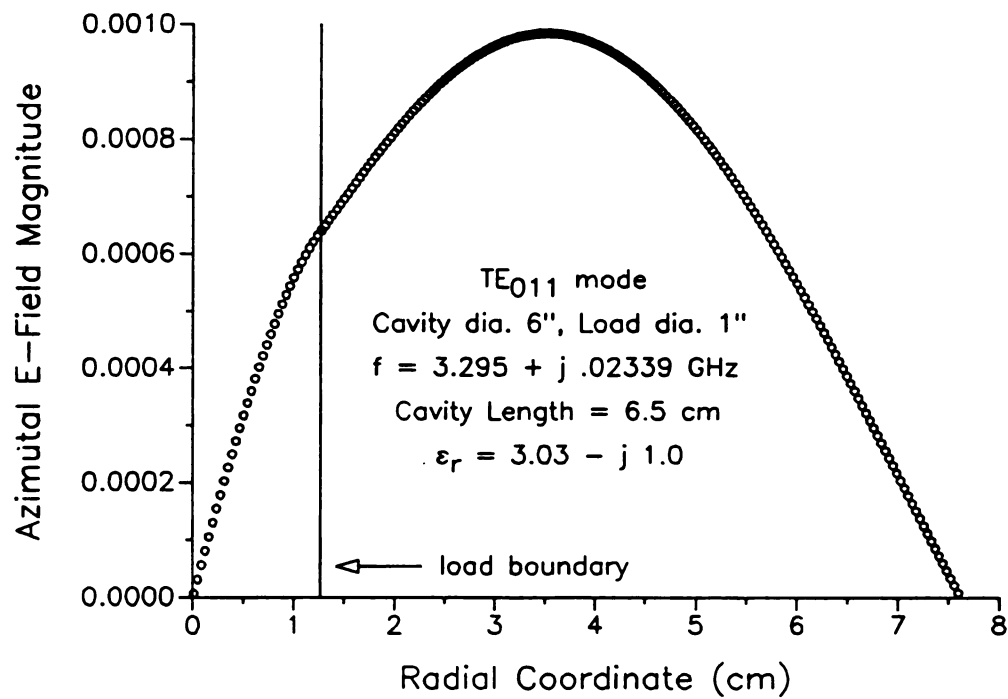
Figure 8-62 Azimuthal E-field magnitude along a radius, TE_{011} mode, $\epsilon_r'' = 1$.
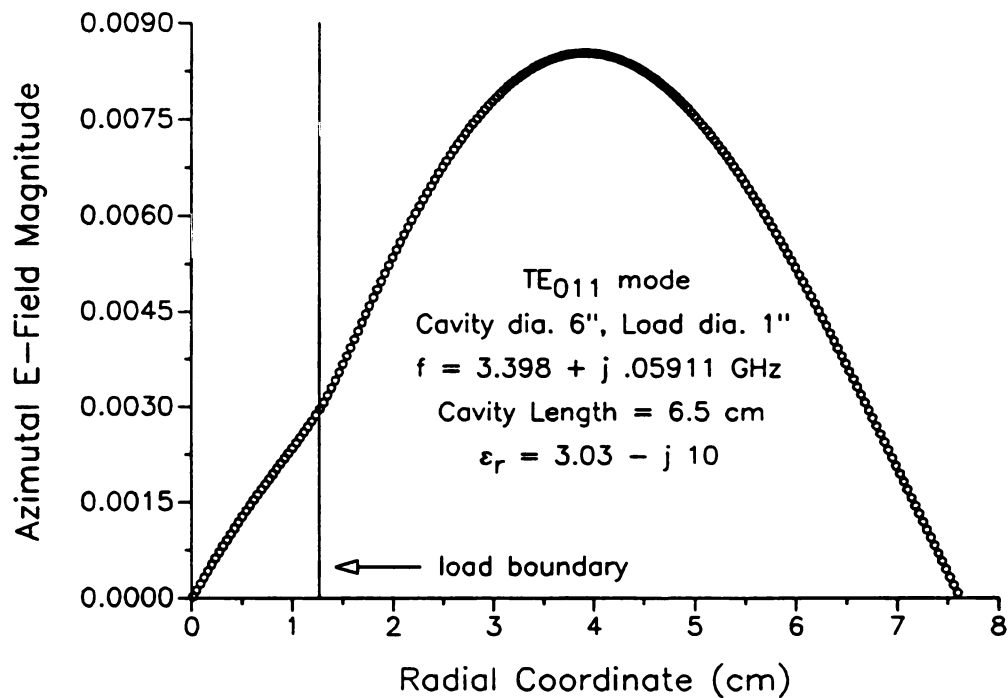
Figure 8-63 Azimuthal E-field magnitude along a radius, TE_{011} mode, $\epsilon_r'' = 10$.
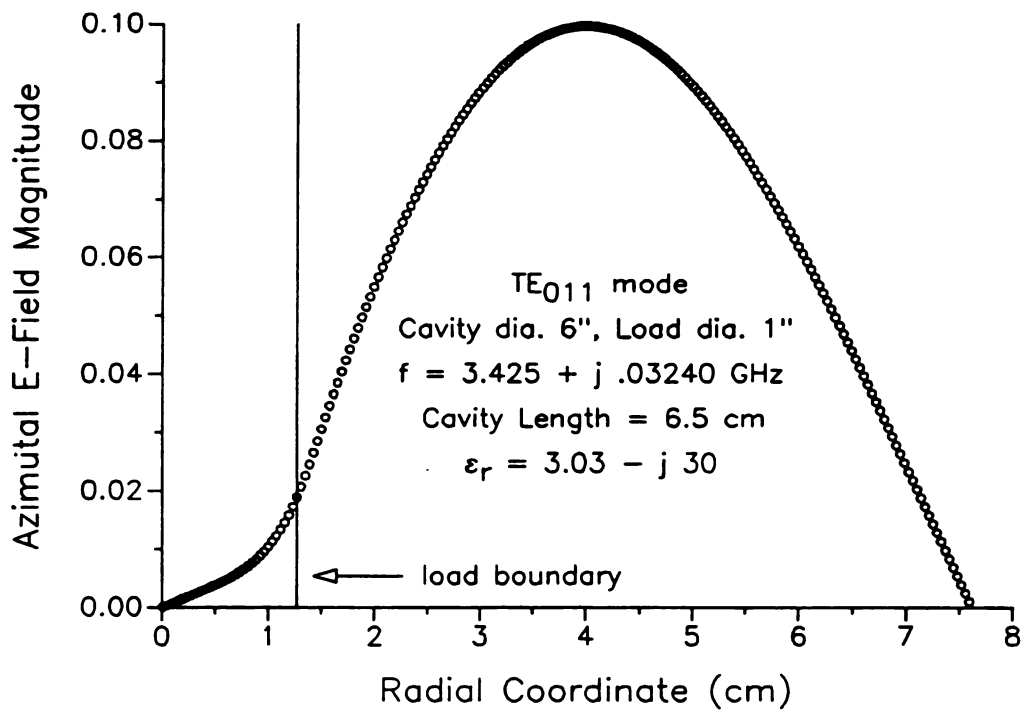
Figure 8-64 Azimuthal E-field magnitude along a radius, TE_{011} mode, $\epsilon_r'' = 30$.
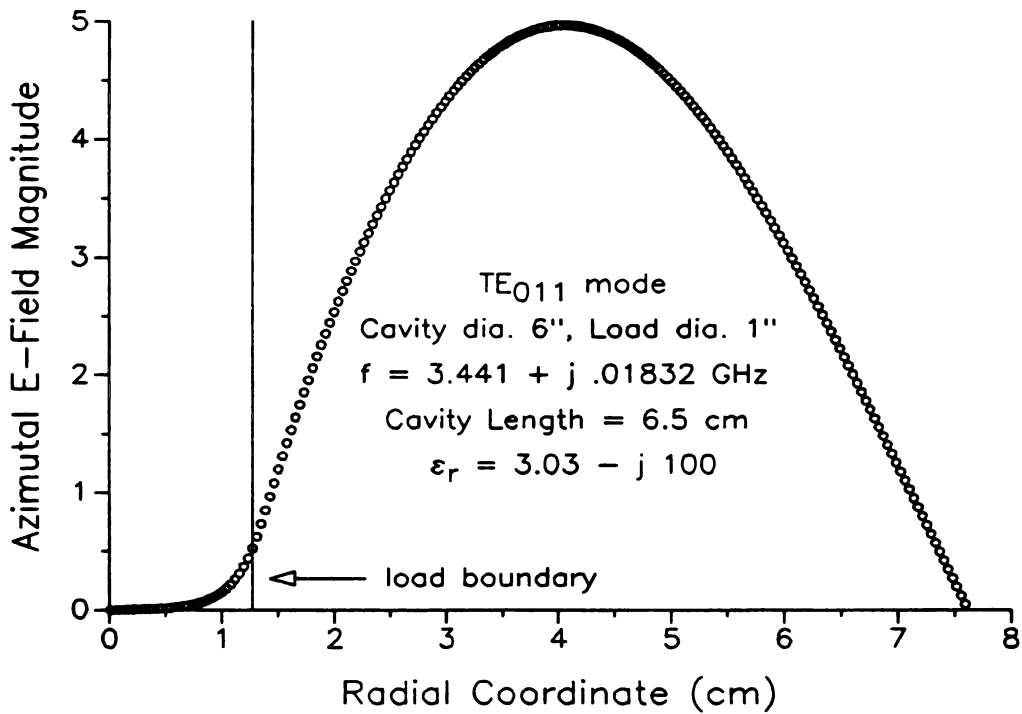
Figure 8-65 Azimuthal E-field magnitude along a radius, TE_{011} mode, $\epsilon_r'' = 100$.

TE$_{011}$ mode
Cavity dia. 6", Load dia. 1"
f = 3.454 + j .005997 GHz
Cavity Length = 6.5 cm
ε_r = 3.03 - j 1,000

load boundary
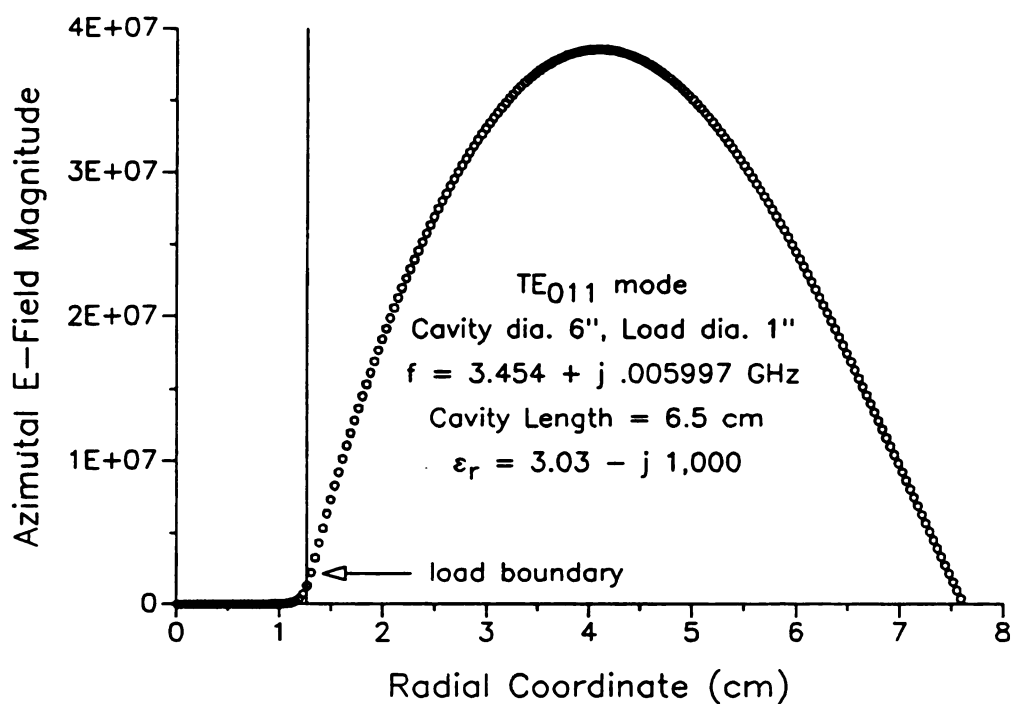
Figure 8-66 Azimuthal E-field magnitude along a radius, TE$_{011}$ mode, $\epsilon_r'' = 1,000$.

Coaxial Cavity TE$_{011}$ mode

Cavity dia. 6"
Inner conductor dia. 1"
Frequency = 3.460 GHz
Cavity Length = 6.5 cm

load boundary
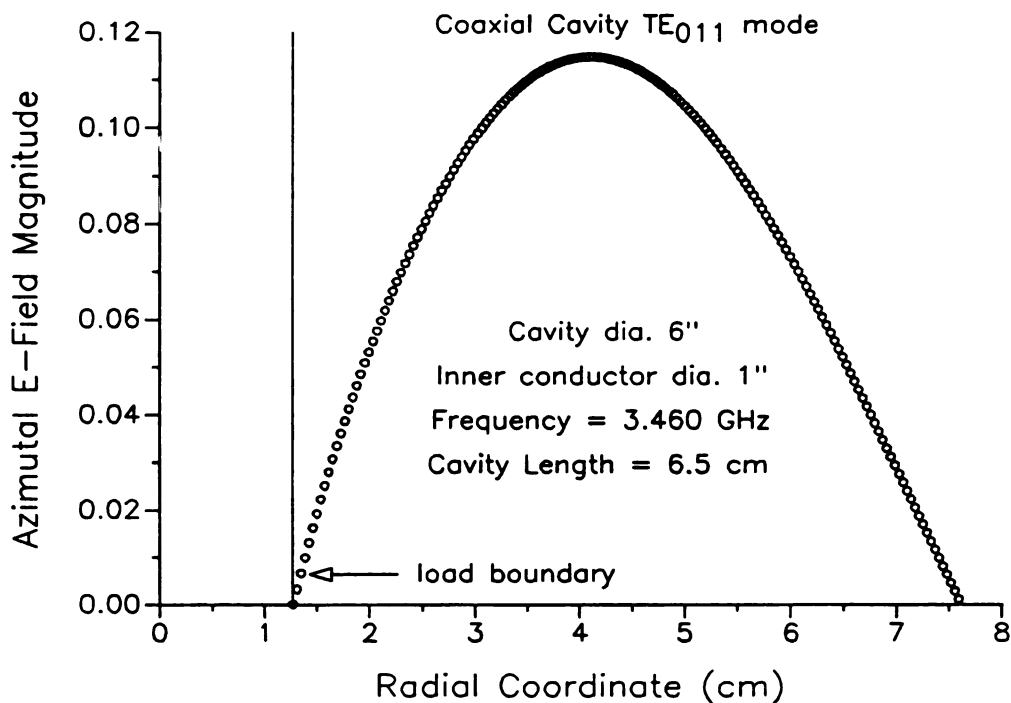
Figure 8-67 Azimuthal E-field magnitude along a radius, coaxial cavity TE$_{011}$ mode.

$\rho < 1.27$ cm, steadily diminishes until the field for $\epsilon_r'' = 1,000$, shown in Figure 8-66, is nearly zero, identical to the coaxial cavity field shown in Figure 8-67.

8.4.2 Radial Order Exhibited in Frequency Variation with Load Radius

The TE modes exhibit frequency behavior similar to the TM modes as the load radius is varied. This includes radial traceability[†] under certain conditions. It is also possible to see in the real frequency mode charts a correlation between the radial order of the modes and the number of "flats" in the plot, i.e., regions where frequency is not greatly dependent on load radius. Both of these features, radial traceability and radial order correspondence, are seen in Figures 8-68 and 8-69 which are mode charts of real frequency versus rod radius for the first few TE_{0p2} modes. Figure 8-68 is plotted for a lossless load material with $\epsilon_r = 9$, while Figure 8-69 is for a low loss material of $\hat{\epsilon}_r = 3 - j\, 0.039$, similar to nylon. Since the modes are radially traceable they have been named according to the modes they become at either radial limit, which are the TE_{012} mode, TE_{022} mode, and TE_{032} mode in both Figures.

Comparing Figures 8-68 and 8-69 with Figures 8-25 and 8-26, which contain similar plots for the TM modes, it appears that the radial dependence is even more visible in the real frequency behavior for the TE modes than for the TM modes. Taking the TE_{012} mode of Figure 8-68, a single flat exists from $\rho = 0$ to $\rho = 0.8$ cm. For the TE_{022} mode there are two flats which go from $\rho = 0$ to $\rho = 0.5$ cm and from $\rho = 1.4$ cm to $\rho = 2.2$ cm. Three flats are distinguishable in the TE_{032} mode plot: the first extends from $\rho = 0$ to $\rho = 0.15$ cm, the second from $\rho = 1$ cm to $\rho = 1.2$ cm, the third from $\rho = 2.6$ cm to $\rho = 3.2$ cm.

The flat regions of the plots in Figure 8-69 for $\hat{\epsilon}_r = 3 - j\, 0.039$ are not quite as pronounced as those in Figure 8-68 where the dielectric constant is higher, but the radial order correlation is still distinguishable. In addition, since the load is lossy, the imaginary frequency also provides a radial order correlation by the number of local minima in the imaginary frequency versus load radius chart. Comparing the radial coordinates of imaginary frequency local minima in Figure 8-70 with the location of

---

[†]This term is defined above on page 215.
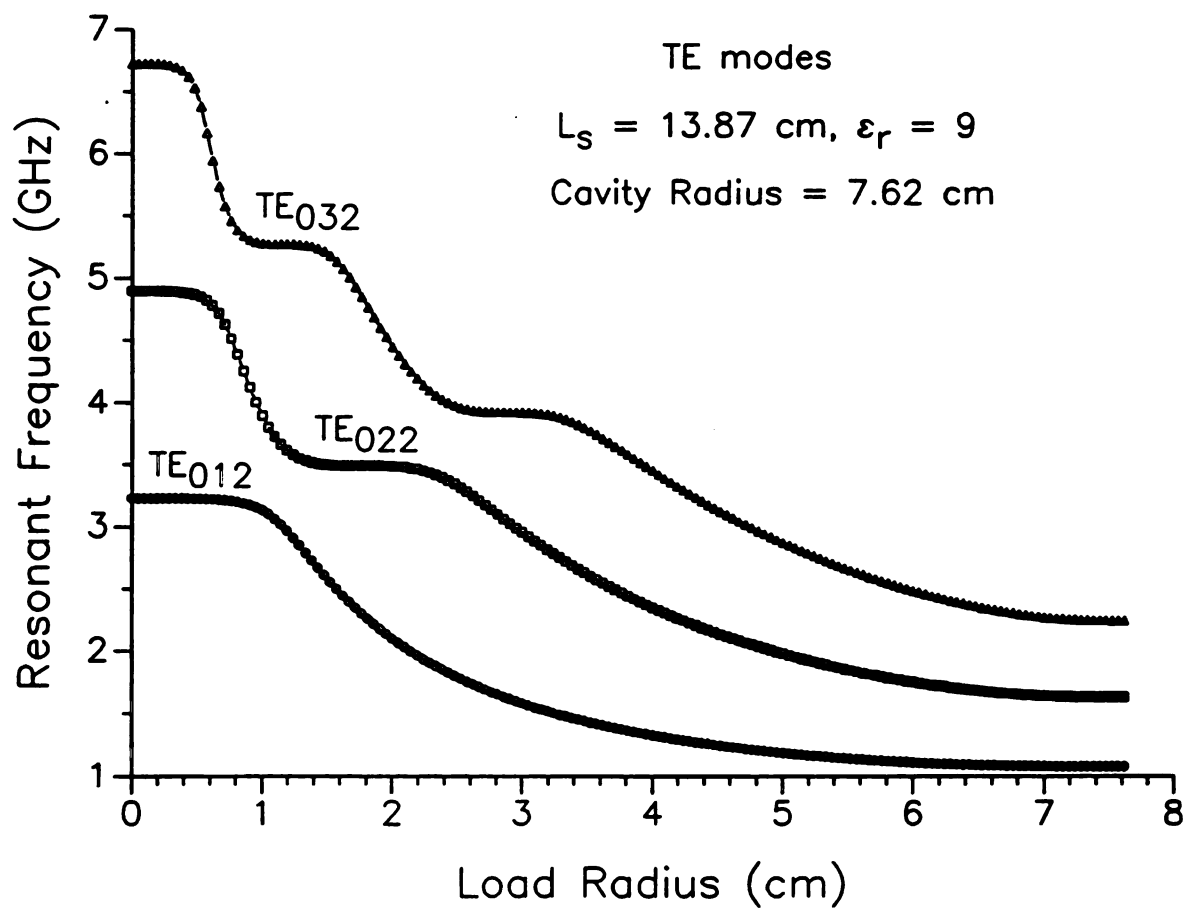
Figure 8-68 Resonant frequency vs. load radius: lossless load, $\epsilon_r = 9$, TE_{0p2} modes.
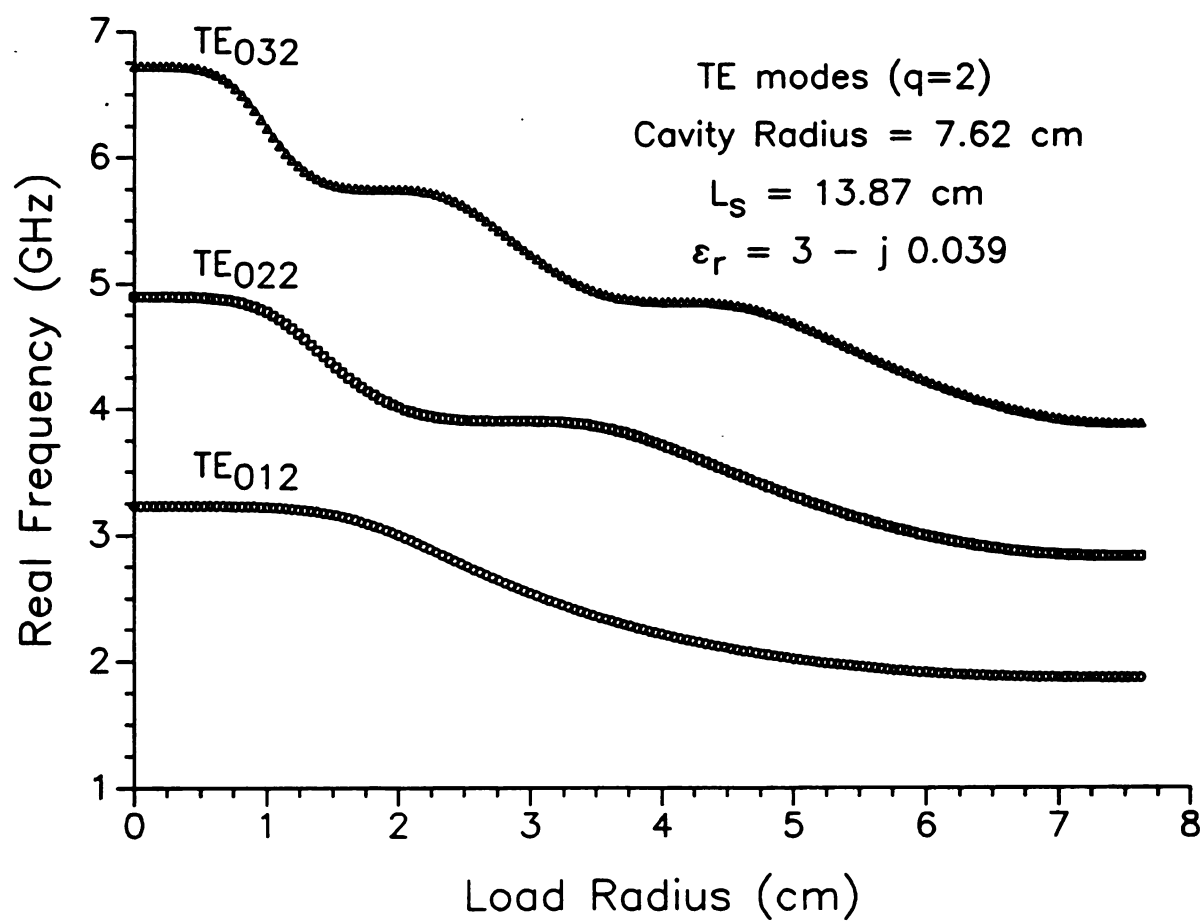
Figure 8-69 Real frequency vs. load radius: $\hat{\epsilon}_r = 3 - j\,0.039$, TE_{0p2} modes.
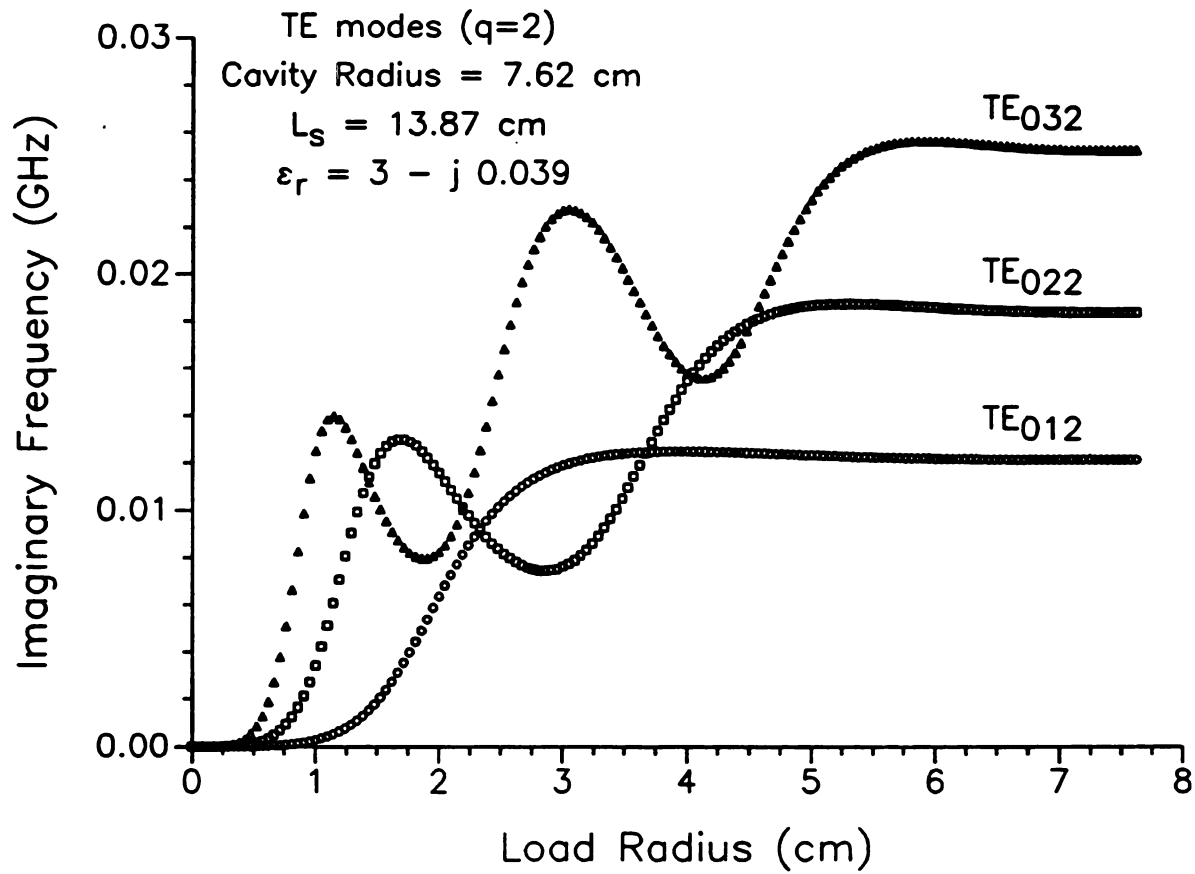
Figure 8-70 Imaginary frequency vs. load radius: $\hat{\varepsilon}_r = 3 - j\,0.039$, TE_{0p2} modes.

the real frequency flats in Figure 8-69, it may be seen that local imaginary frequency minima occur toward the end of each real frequency flat region. (Local maxima in the imaginary frequency occur near the end of regions of maximal slope in the real frequency plots.) Glancing back at Figures 8-26 and 8-27, the real frequency flats and imaginary frequency local minima are similarly related for TM modes.

8.4.3 Dielectric Confined and Dielectric Excluded TE Modes

The behavior of the two TM modes presented previously in Figure 8-30 was shown to be consistent with the mode descriptions *dielectric confined* for mode A and *dielectric excluded* for mode B, as described above in Section 8.3.6. Similar behavior occurs for TE modes. This is demonstrated in Figures 8-71 and 8-72 where dielectric confined and dielectric excluded modes labeled A and B respectively are shown to exist in a 6" diameter cavity for a complex permitivitty of $\hat{\varepsilon}_r = 20 - j\,8$. The cavity length is 13.87 cm and the axial order is given by $q = 2$.

The real and imaginary frequencies of mode A, for load radii approaching the cavity radius, become the real and imaginary frequencies of the material filled cavity TE_{012} mode. Likewise, the resonant frequency of mode B for zero load radius is that of the empty cavity TE_{012} mode. These empty and material filled modes are indicated by the arrows in the Figures. For small load radii the real frequency of the dielectric confined mode, mode A, rises rapidly, as does the real frequency of the dielectric excluded mode, mode B, for load radii approaching the cavity radius.

It is interesting to note that the imaginary frequency of mode A shown in Figure 8-72 makes an abrupt drop close to the imaginary frequency axis. At the same time the real frequency continues to rise smoothly. Although it might appear that there has been some error in the root finding, it is unlikely for two reasons: 1) the real frequency curve is smooth in the neighborhood of the apparent discontinuity in the imaginary frequency, and 2) it is necessary for the imaginary frequency to drop at some point near the imaginary frequency axis so that the imaginary frequency is zero for zero loss inside the cavity. The resonant frequencies of the empty cavity TE_{0p2} modes in the neighborhood of the low radius endpoint of mode A, near 55 GHz in
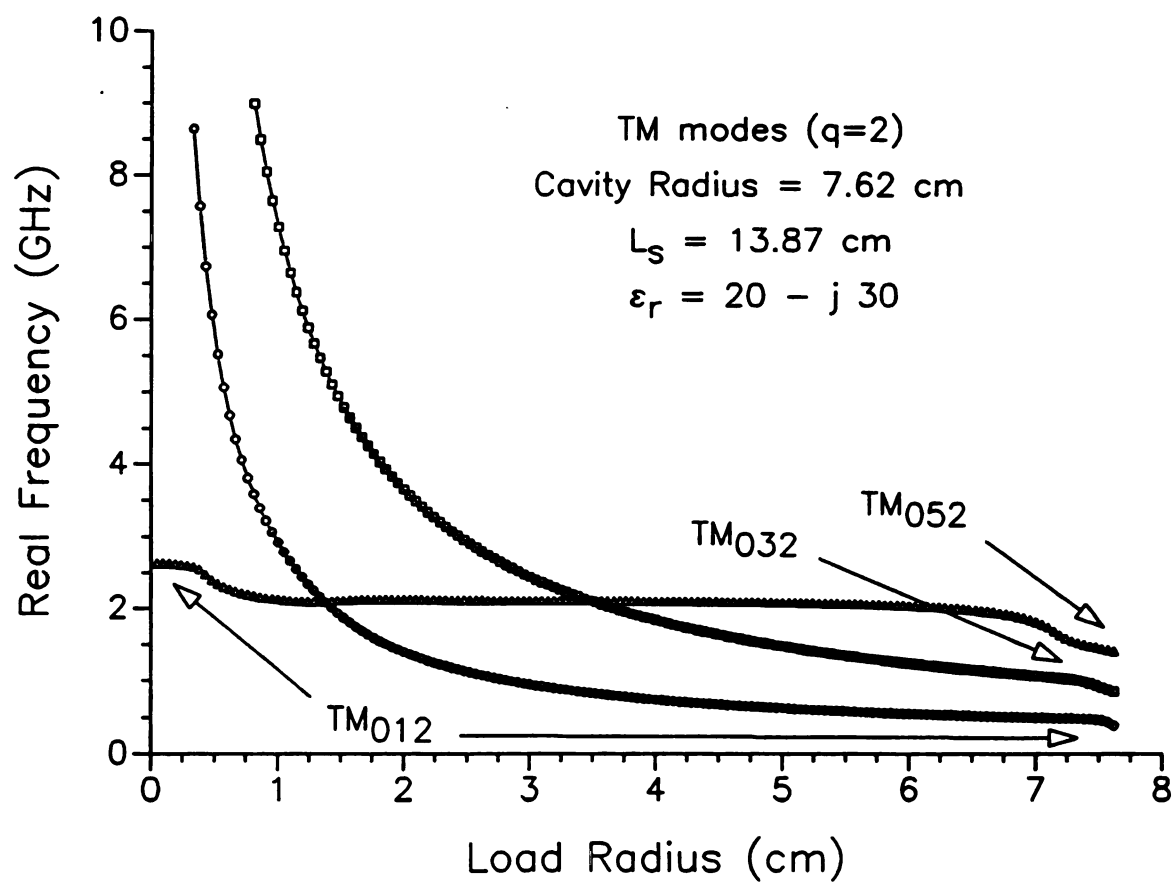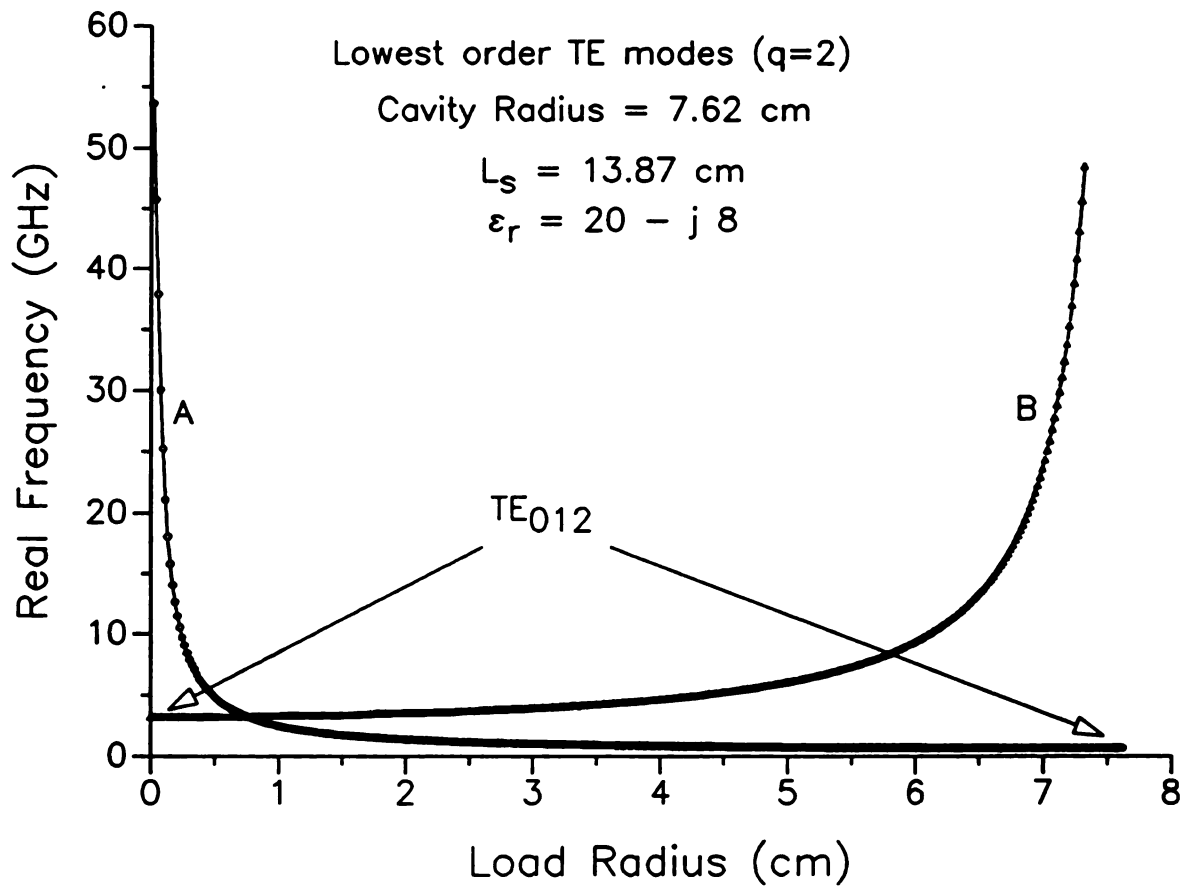
Figure 8-71 Real frequency vs. load radius: $\hat{\varepsilon}_r = 20 - j\,8$, TE_{0p2} modes.
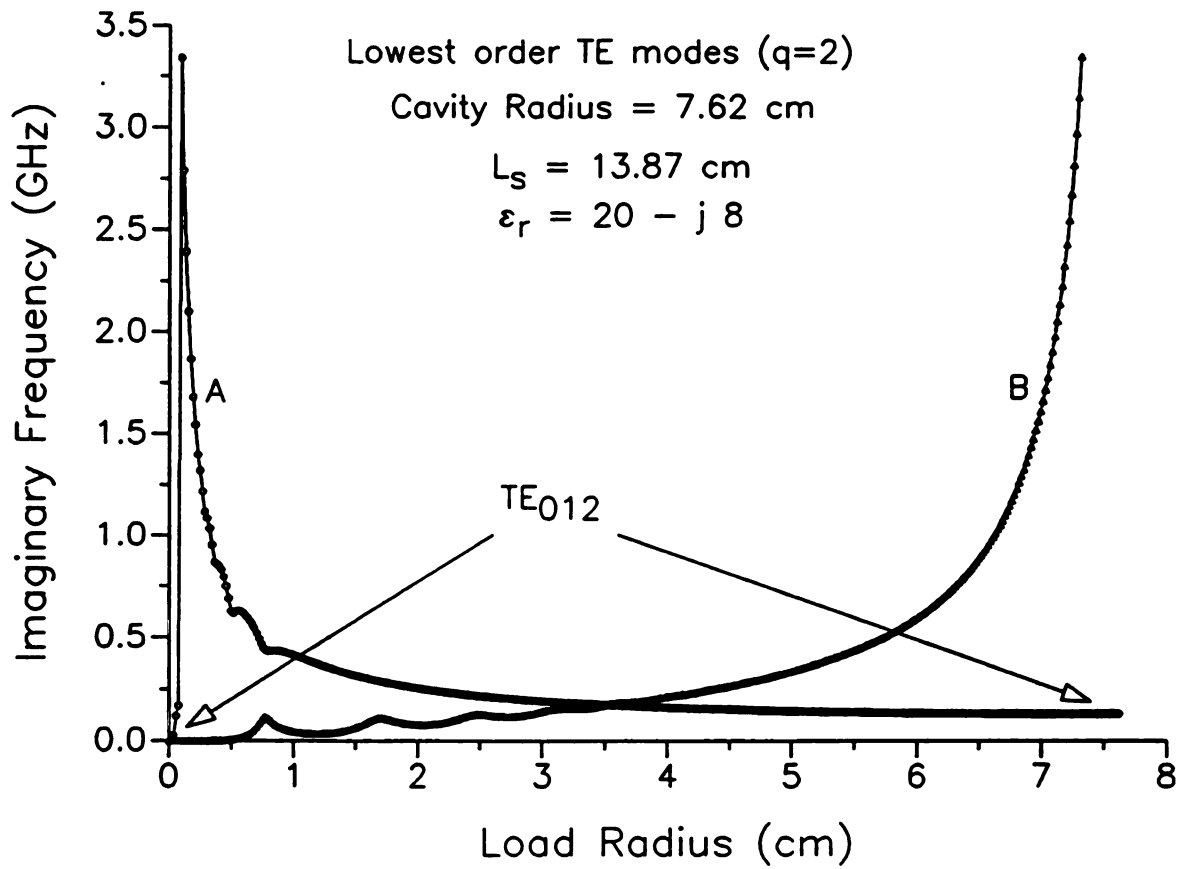
Figure 8-72 Imaginary frequency vs. load radius: $\hat{\varepsilon}_r = 20 - j\,8$, TE_{0p2} modes.

Figure 8-71, are 55.61 GHz for $TE_{0(29)2}$, 57.58 GHz for $TE_{0(30)2}$, and 59.54 GHz for $TE_{0(31)2}$. Mode A appears to approach one of these empty cavity modes in the limit as the load radius goes to zero.

Modes A and B also exhibit behavior that indicates interaction between the two modes. There are several localized fluctuations in the imaginary frequencies of both modes. The sharpest fluctuation in the imaginary frequency of mode B is the first one encountered as the load radius increases from zero. There is a fluctuation in the imaginary frequency of mode A for the same load radius. It may be seen by comparing Figures 8-71 and 8-72 that these two fluctuations correspond to the point where the real frequency curves of modes A and B cross one another. Figure 8-73 is an enlarged view of the region with both real and imaginary parts of the frequency plotted for both modes. The real frequency crossing is at a load radius of 0.76 cm. The imaginary frequency fluctuation maximum of mode B and the minimum of mode A both occur at 0.78 cm, just after the real frequency crossing.

Since the crossing shown in Figure 8-73 takes place between the lowest ordered dielectric excluded and dielectric confined modes it is referred to as the primary crossing. The other imaginary frequency fluctuations in Figure 8-72, as is shown in Figures 8-74 through 8-76, correspond to real frequency crossings between modes A and B and higher order modes. Figure 8-74 is similar to Figure 8-71 except the modes which have radial endpoints at the empty and material filled TE_{022} and TE_{032} modes have been plotted with those of Figure 8-71. Figure 8-75 contains the imaginary frequencies of the modes of Figure 8-74. Fluctuations are visible in each of the imaginary frequency plots. An enlarged view of the small load radius region of the imaginary frequencies is shown in Figure 8-76 where it may be more clearly observed that the place at which the imaginary frequencies of a dielectric confined mode and a dielectric excluded mode are pinched together corresponds to the point at which their real frequencies cross.
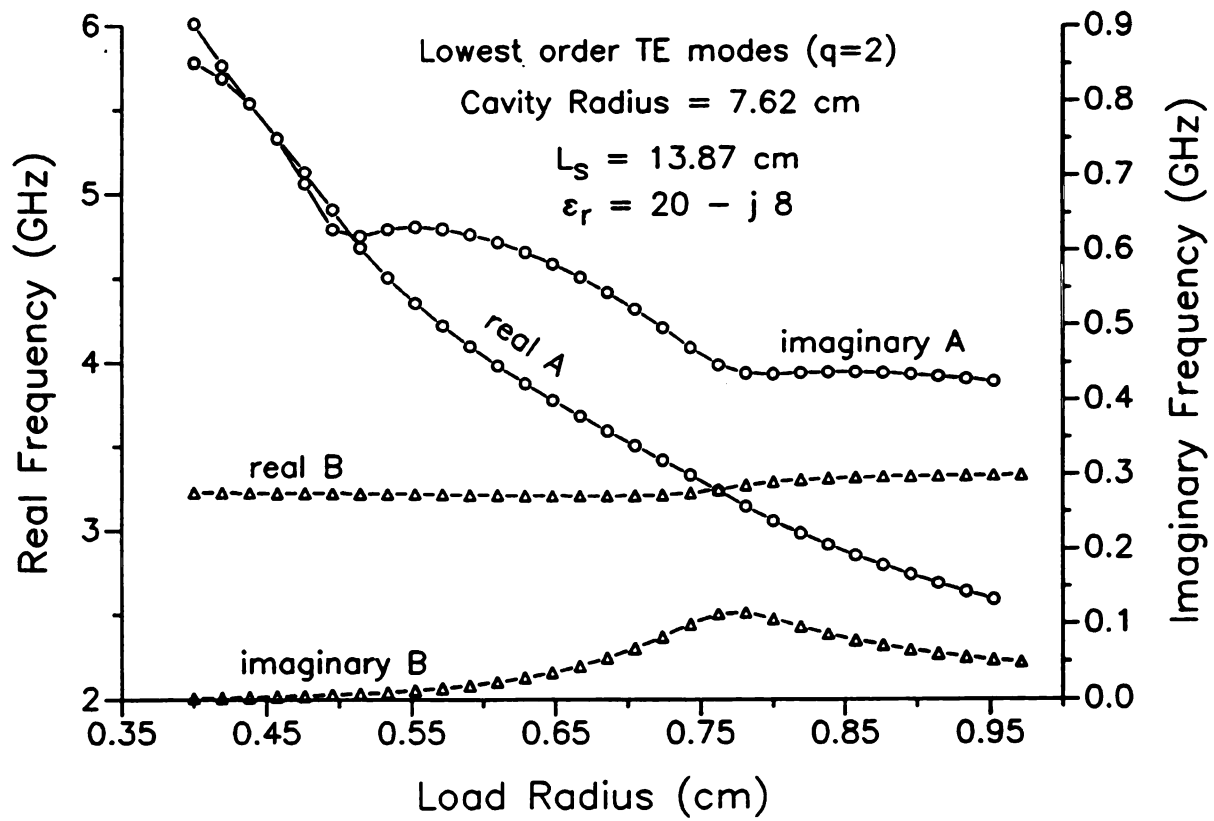
Figure 8-73 Enlarged view of primary mode crossing: $\hat{\varepsilon}_r = 20 - j\,8$, TE_{0p2} modes.
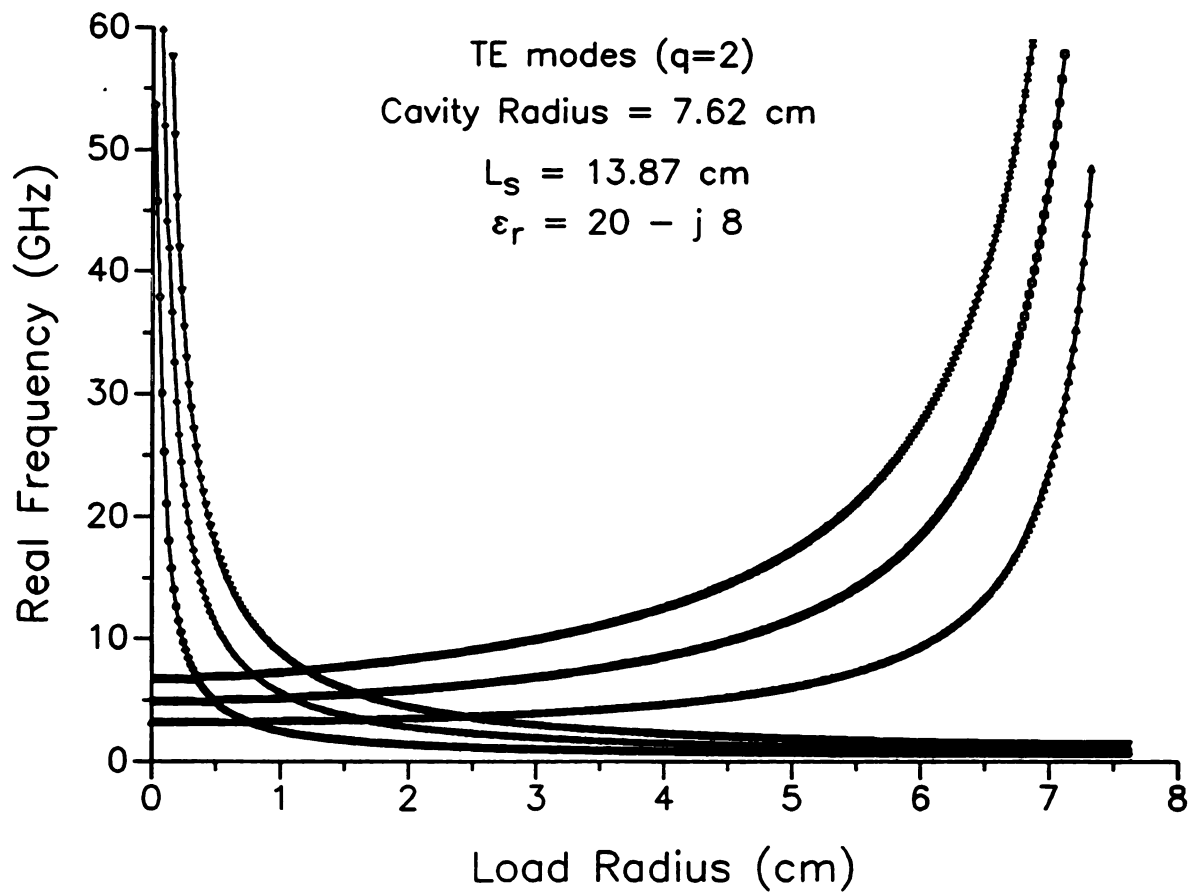
Figure 8-74 Real frequency vs. load radius for higher order TE_{0p2} modes.
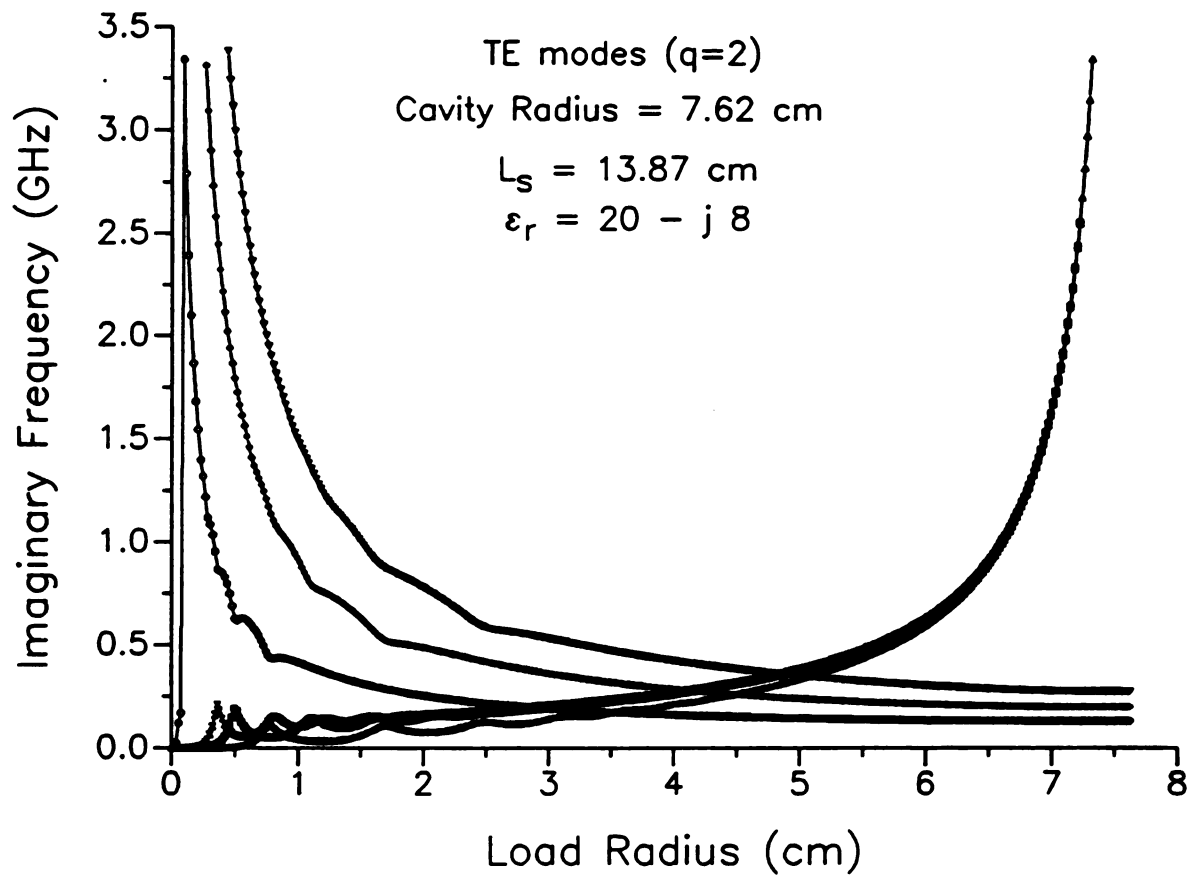
Figure 8-75 Imaginary frequency vs. load radius for higher order TE_{0p2} modes.
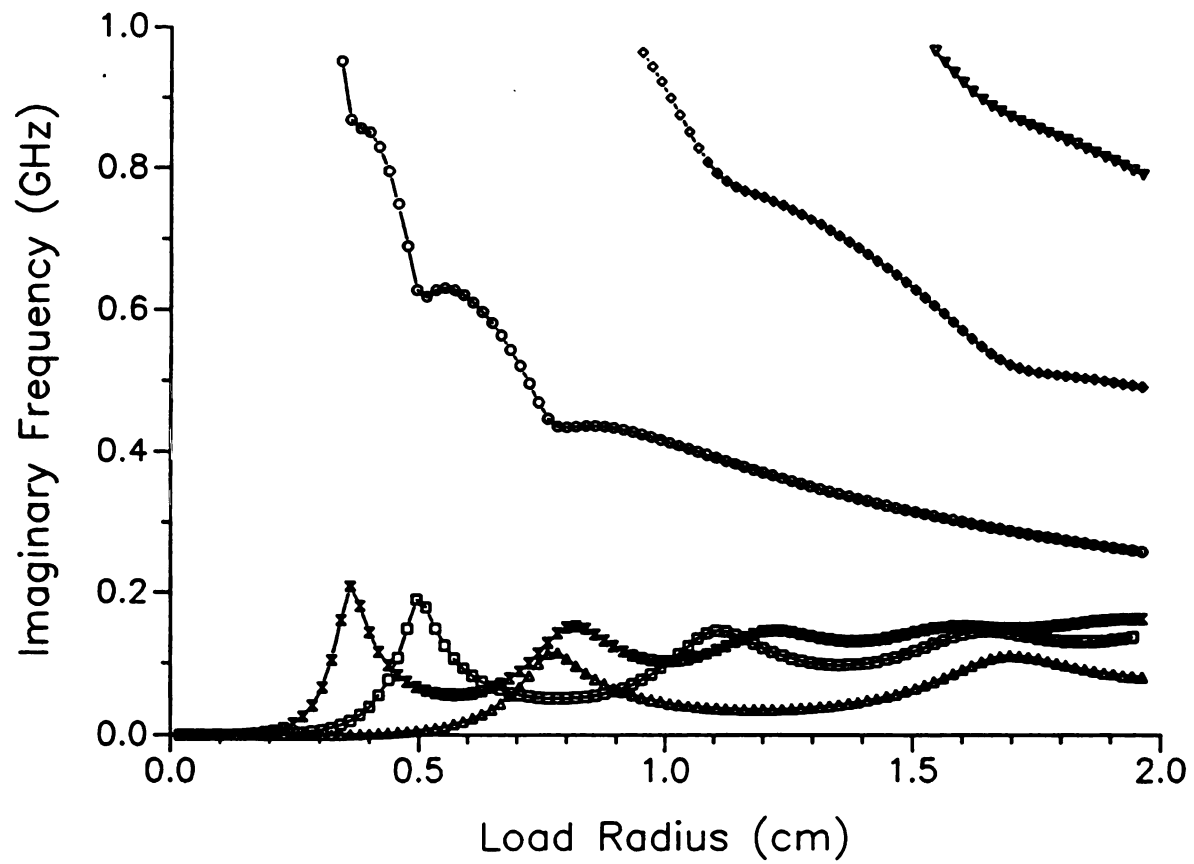
Figure 8-76 Enlarged view of imaginary frequencies in mode crossing region.

8.4.4 Dielectric Excluded and Coaxial Cavity TE Modes

Examination of the H-field of Mode B of Figure 8-71 demonstrates that dielectric excluded TE modes approximate coaxial cavity TE modes for large load radii. This was shown above for TM modes in Figures 8-51, 8-52, 8-55, and 8-56. The H-field distribution of the TE_{012} mode in a 6" diameter coaxial cavity with an inner conductor radius of 4 cm is shown in Figures 8-77 and 8-78, where the axial and radial magnitudes are plotted as functions of the radial coordinate. Figures 8-79 and 8-80 show the corresponding axial and radial magnitudes of the H-field of mode B in Figure 8-71.

It may be observed that the field patterns outside the load region are similar to those of the coaxial cavity TE_{012} mode; however, the axial H-field inside the load is still rather substantial, proportionally greater than the electric field inside the load for the TM mode in Figures 8-51 and 8-52. This may be explained by the fact that the loss factor in Figures 8-79 and 8-80, where $\epsilon_r'' = 8$, is much less than that of Figures 8-51 and 8-52, where $\epsilon_r'' = 30$. Even so, the field patterns bear resemblance to the coaxial cavity fields and the real frequency, 4.679 GHz, is near the resonant frequency of the coaxial cavity mode, 4.727 GHz. By adding 2 cm to the load radius the resemblance between mode B and the coaxial cavity TE_{012} mode becomes even more apparent. The axial and radial H-field magnitudes for mode B of Figure 8-71 are shown in Figures 8-81 and 8-82 for a load radius of 6 cm. Notice that the axial H-field inside the load is reduced in comparison to that of the 4 cm load radius plot of Figure 8-79.

8.5 Mode Charts and Field Patterns: HEM Modes

8.5.1 Lossless Loads

It was mentioned at the beginning of this Chapter under the question of naming the cavity-short type modes that a mode defined in certain mode variables, e.g., the load radius, may be traced through the mode variable to a homogeneously loaded cavity mode. In the case of the mode variable being the load radius a, the homogeneously loaded cavity may be either the empty cavity, for $a = 0$, or the
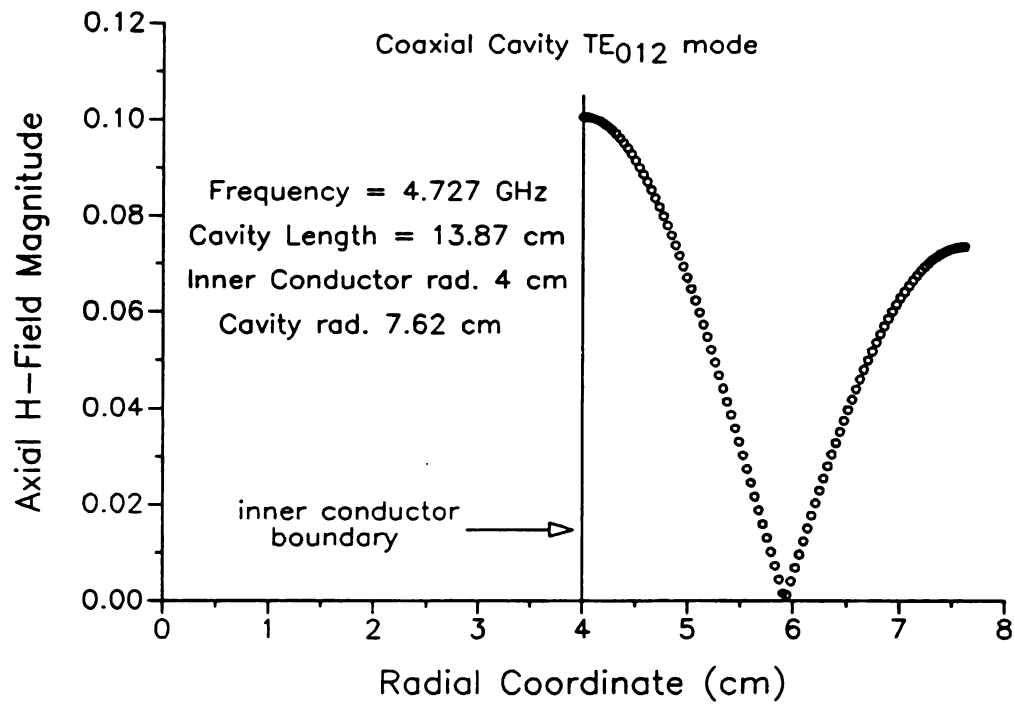
Figure 8-77 Axial H-field magnitude for the coaxial cavity TE_{012} mode.
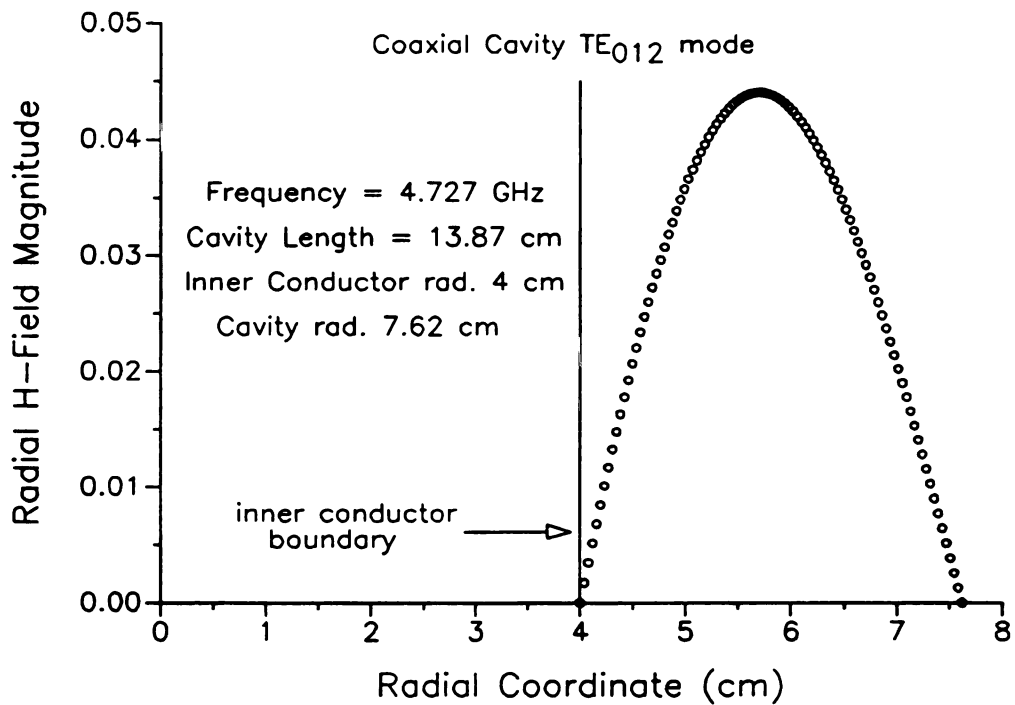
Figure 8-78 Radial H-field magnitude for the coaxial cavity TE_{012} mode.
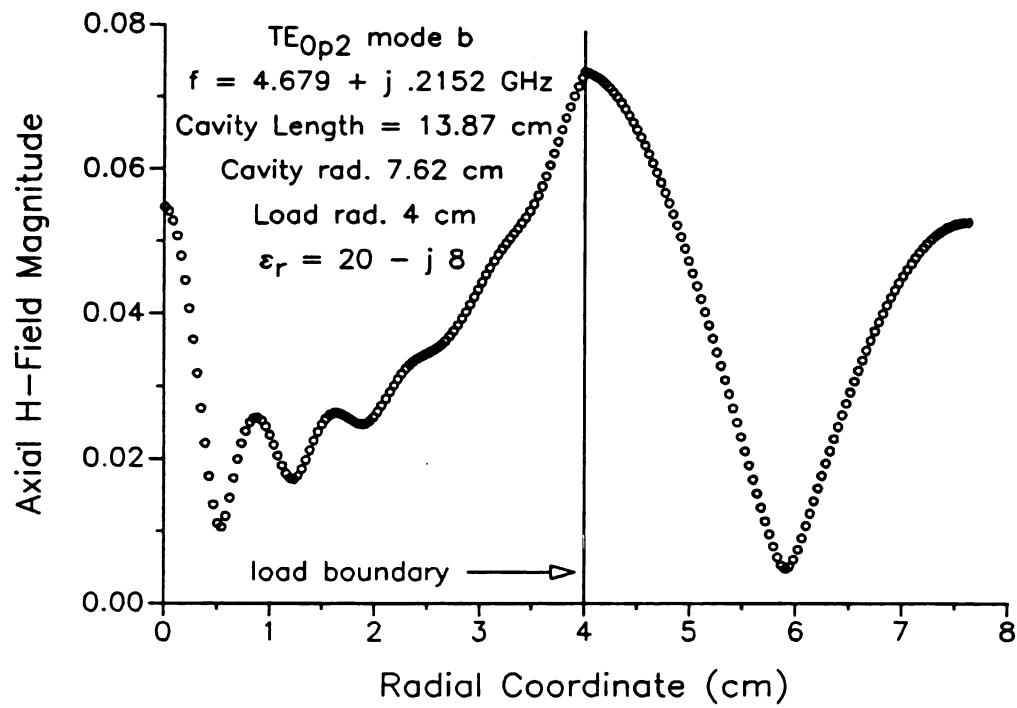
Figure 8-79 Axial H-field magnitude: TE_{0p2} mode B, load radius 4 cm.
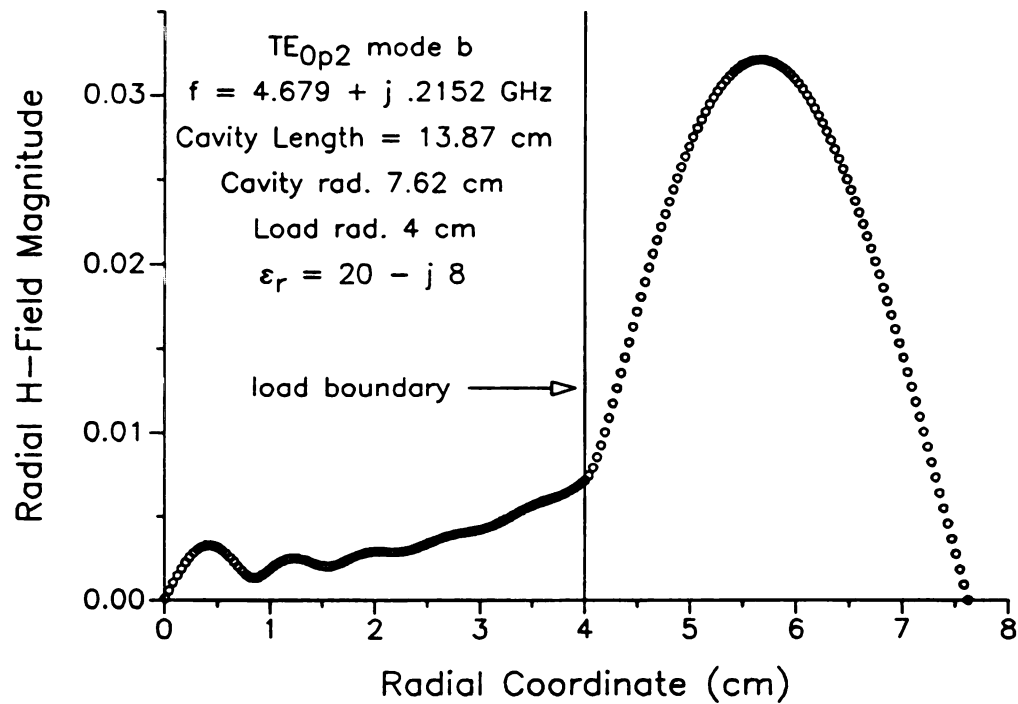
Figure 8-80 Radial H-field magnitude: TE_{0p2} mode B, load radius 4 cm.
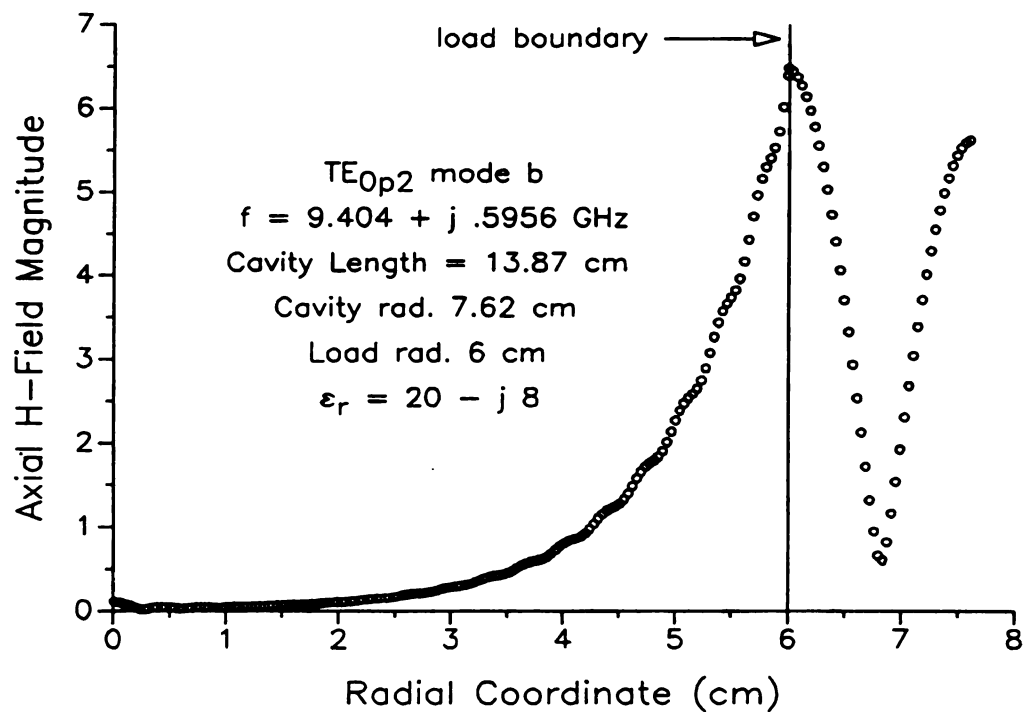
Figure 8-81 Axial H-field magnitude: TE_{0p2} mode B, load radius 6 cm.
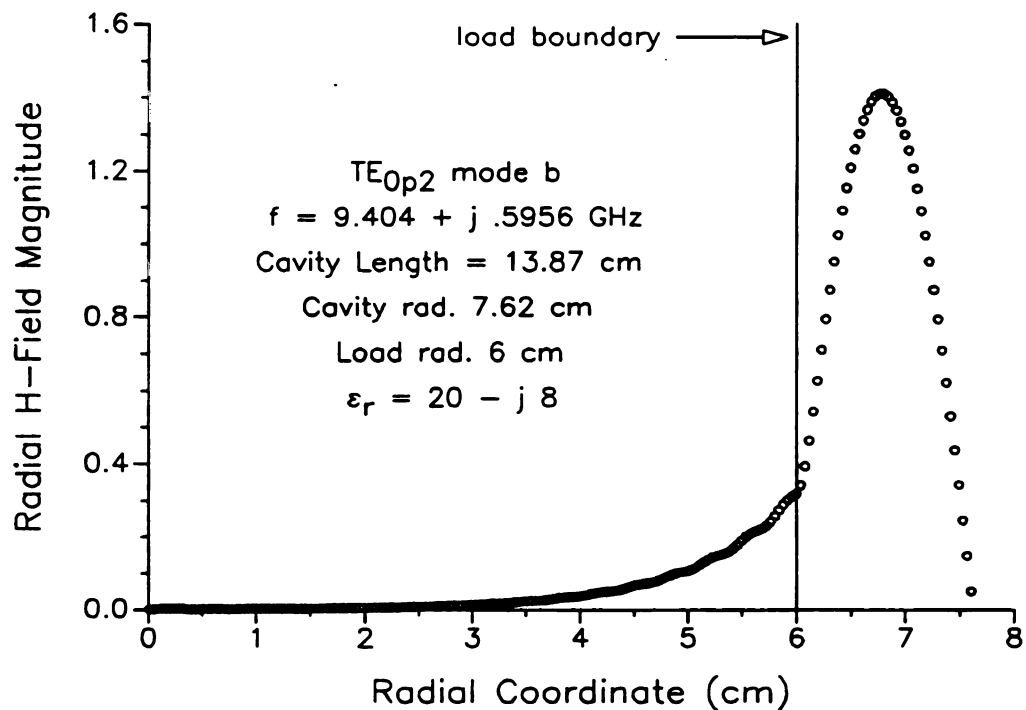
Figure 8-82 Radial H-field magnitude: TE_{0p2} mode B, load radius 6 cm.

material filled cavity, for $a = b$, where b is the cavity radius. If the mode variable is the dielectric constant ϵ' and the load material is lossless, the cavity-short type mode may be traced to an empty cavity mode as ϵ' approaches zero. There are, of course, other possibilities of this sort.[†] Additionally, as has been shown above for the cases of the TE and TM modes, it is possible to trace cavity-short type modes to coaxial cavity modes as the loss factor ϵ'' becomes large, independent of the value of ϵ'.

It was also mentioned that the names of the material filled cavity modes to which the cavity-short type modes are traced cannot always be used to name the cavity-short type modes. This is because in general cavity-short type modes are traced by different mode variables to different material filled cavity modes. In the case of the load radius as mode variable there are certain load materials for which a trace may lead to a differently named empty cavity mode for $a = 0$ than that of the material filled mode for $a = b$. This phenomenon was demonstrated most clearly in Figure 8-57 where one of the modes shown became the empty cavity TM_{012} mode at $a = 0$ and the TM_{052} mode at $a = b$. Modes defined in the load radius mode variable where both radial endpoint empty cavity and material filled cavity modes bear the same designation were called *radially traceable*, as discussed above in Section 8.3.5.

The hybrid or HEM modes may be represented in a similar manner to the TM and TE modes through mode charts for a number of different mode variables. However, the characteristic equation for hybrid modes is more complicated than for either the TE or the TM modes, as can be seen by comparing Equations (3-86) and (3-91) of Chapter 3. In addition to the added numerical difficulty, the hybrid modes cannot be classified according to their axial fields, as can the TE modes (no axial E-field) or the TM modes (no axial H-field), because the hybrid modes have both an axial E-field and an axial H-field. This makes naming them more difficult. In general they must be named according to the scheme introduced in Section 8.2 of

---

[†]Clearly this procedure is not valid for all mode variables, e.g., the cavity length, since there is no value for the cavity length, except for zero, at which the cavity-short type configuration and the homogeneously filled configuration are indistinguishable.

calling the hybrid modes HEM modes, indexing them according to their azimuthal, radial, and axial order.

As discussed in Section 8.2, it is possible to distinguish the HEM modes into two classes based on the ratio of E_z to H_z, calling TM-like modes HE and TE-like mode HH. However, these distinctions are not always meaningful, especially when E_z and H_z are both substantial. As will be shown in this Section, even in cases where HEM modes are radially traceable, they may be HH in one load radius region and HE in another. Yet there do appear to be two classes of modes within the HEM modes which bear a strong relationship to the HE/HH distinction described in Section 8.2.

Figures 8-83 and 8-84 demonstrate both the usefulness of the HE/HH division and the difficulty associated with it. Figure 8-83 shows two radially traceable HEM_{1p2} modes for a lossless load with $\epsilon_r' = 9$ in a cavity of radius 7.62 cm and length 13.87 cm. One of the modes, labeled HH_{192} in the Figure, is traceable to the homogeneously loaded TE_{192} modes. The other, labeled HE_{192}, is traceable to the homogeneously loaded TM_{192} modes. That there is a physical significance to the radial index of these modes, i.e., 9, is demonstrated by the 9 flat regions on each curve. Although it appears from the Figure that the HH mode has only 8 "flats" it is evident from the enlarged view shown in Figure 8-84 that it actually has 9. Were these modes named according to the HEM convention, they would be called $HEM_{1(17)2}$ and $HEM_{1(18)2}$. The axial field information and radial order would not be represented in the names.

At the same time, Figure 8-84 shows that there is a region of the HE_{192} mode which is not HE but is HH. Most of the HE_{192} curve is indeed HE, and therefore it has been labeled as such, but the small HH region from $\rho = 0.24$ cm to $\rho = 0.33$ cm shows that this labeling method is not perfectly consistent for mode charts of frequency versus load radius. Although no other Figures are presented to demonstrate that this occurs for other modes and load parameters, it has been frequently observed by the author. Sometimes, though, a mode is purely HH or purely HE for all values of load radius. The HH_{192} mode is HH for all points shown in Figure 8-83.
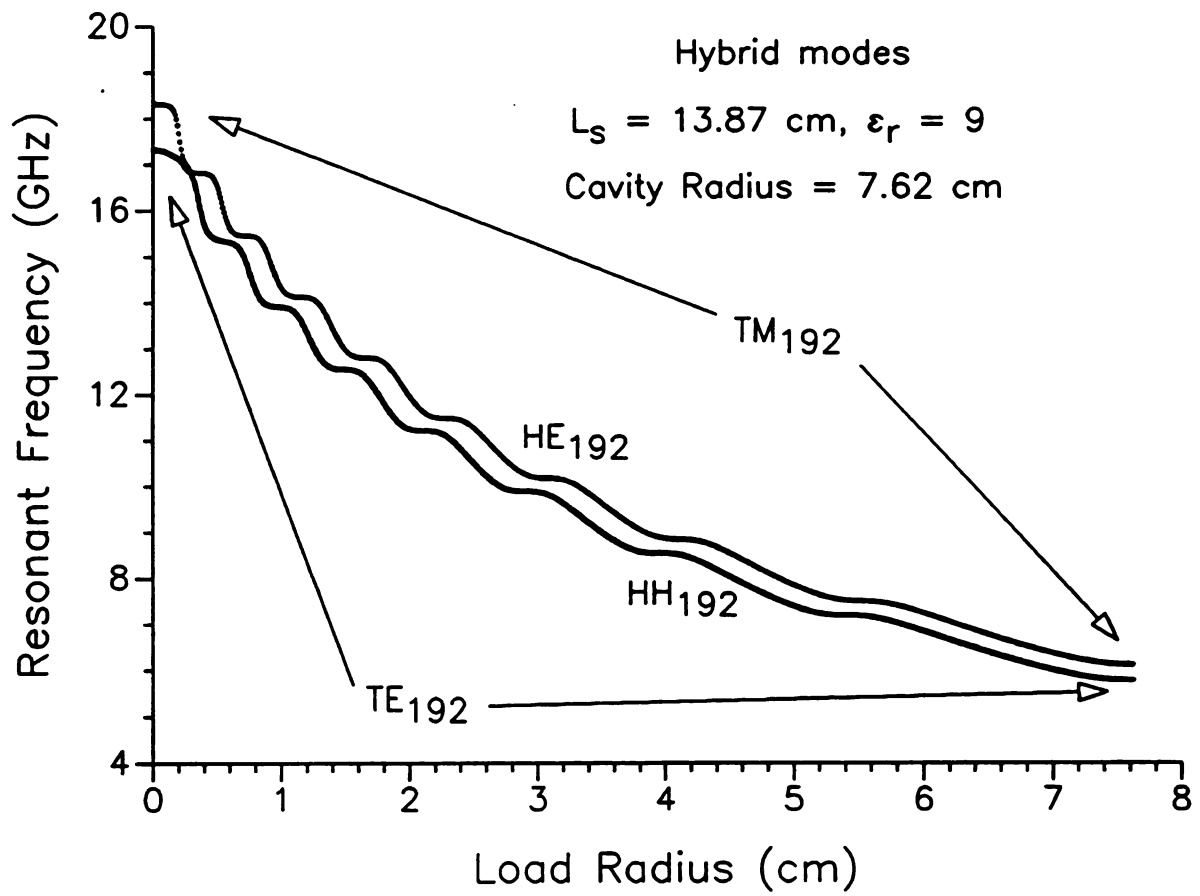
Figure 8-83 Resonant frequency vs. load radius: HE_{192} and EH_{192}, $\epsilon_r = 9$.
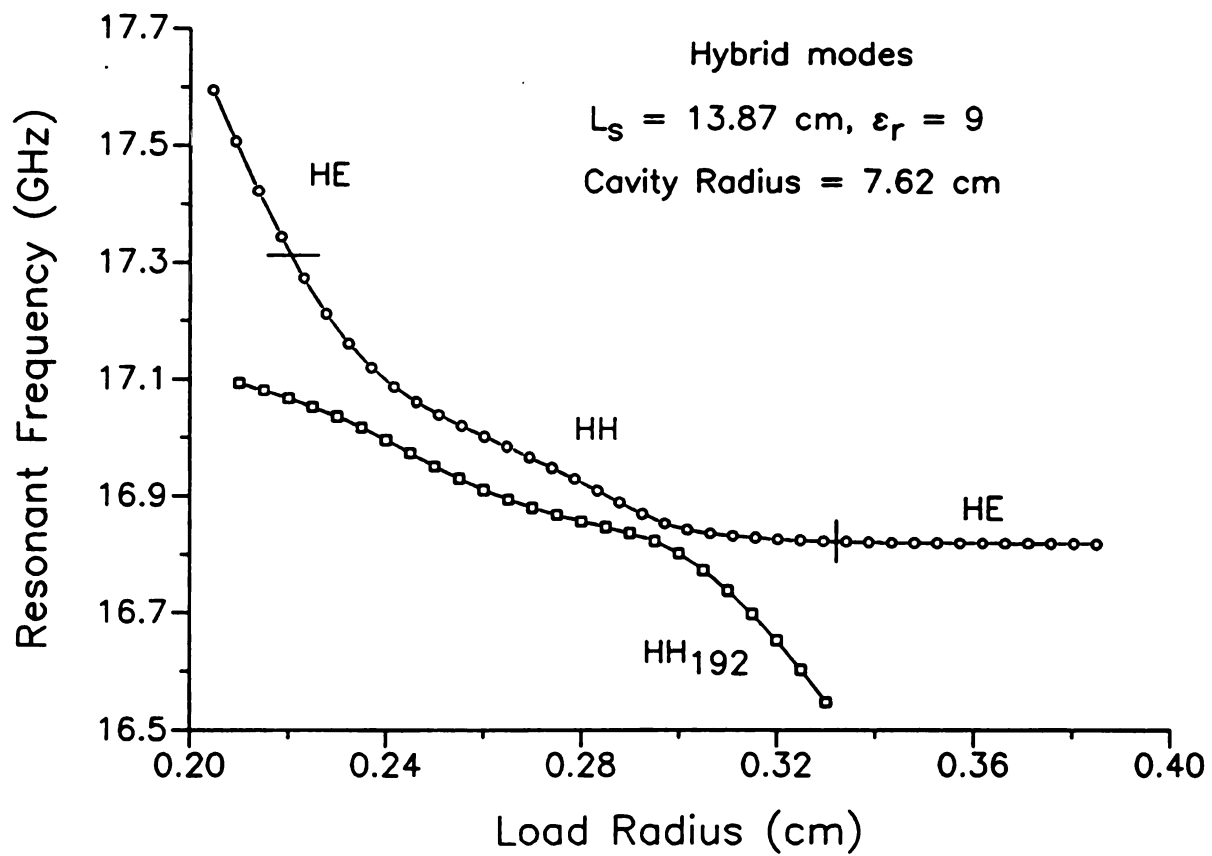
Figure 8-84 Blow up view of small load radius region.

In all Figures presented for the TM and TE cases, the modes showed radial traceability when the load was lossless. Figure 8-85 shows that even for lossless loads the hybrid modes are not always radially traceable and may demonstrate dielectric confined behavior. Figure 8-85 is a plot of the mode which includes the material filled TM_{712} mode when the load radius is equal to the cavity radius. The lossless load has a relative dielectric constant of 9. As shown, the material filled TM_{712} mode is traced back through the load radius mode variable to a much higher order empty cavity mode. The frequency behavior of this mode for small load radii is similar to that displayed by TM and TE confined modes identified earlier.

8.5.2 Tracing HEM Modes Through Permittivity and Load Radius Variables

HEM modes introduce another facet into the discussion of how modes are traced from the empty cavity through the load radius mode variable to the material filled cavity: whereas with TM or TE cavity-short type modes, the modes at either radial endpoint were either TM for TM cavity-short type modes or TE for TE cavity-short type modes, now it is possible that at one endpoint a mode may be TM and at the other it may be TE. It is probably also possible, although it is not shown here, that a non-ϕ-symmetric coaxial cavity TE mode may be traced through the loss factor mode variable to an empty cavity TM mode, etc.

Because it is useful to understand the relationship between cavity-short type modes and material filled or coaxial cavity modes, an effort will be made in this Section to examine two cavity-short type HEM modes as they may be traced to material filled cavity modes. The two modes are shown in Figure 8-86 where their real frequencies are plotted against the relative dielectric constant of the load, ϵ_r'. These modes exist in a 6" diameter cavity for a 1" diameter load and a cavity length of 13.87 cm. The loss factor of the material is given by $\epsilon_r'' = 8$. As shown in the Figure, the modes are labeled as mode 1 and mode 2.

The question might arise as to whether these modes are properly identified as being connected as shown. Figure 8-86 shows them crossing near $\epsilon_r' = 10$. How do we know that the points identified with mode 1 for $\epsilon_r' < 10$ should not be grouped
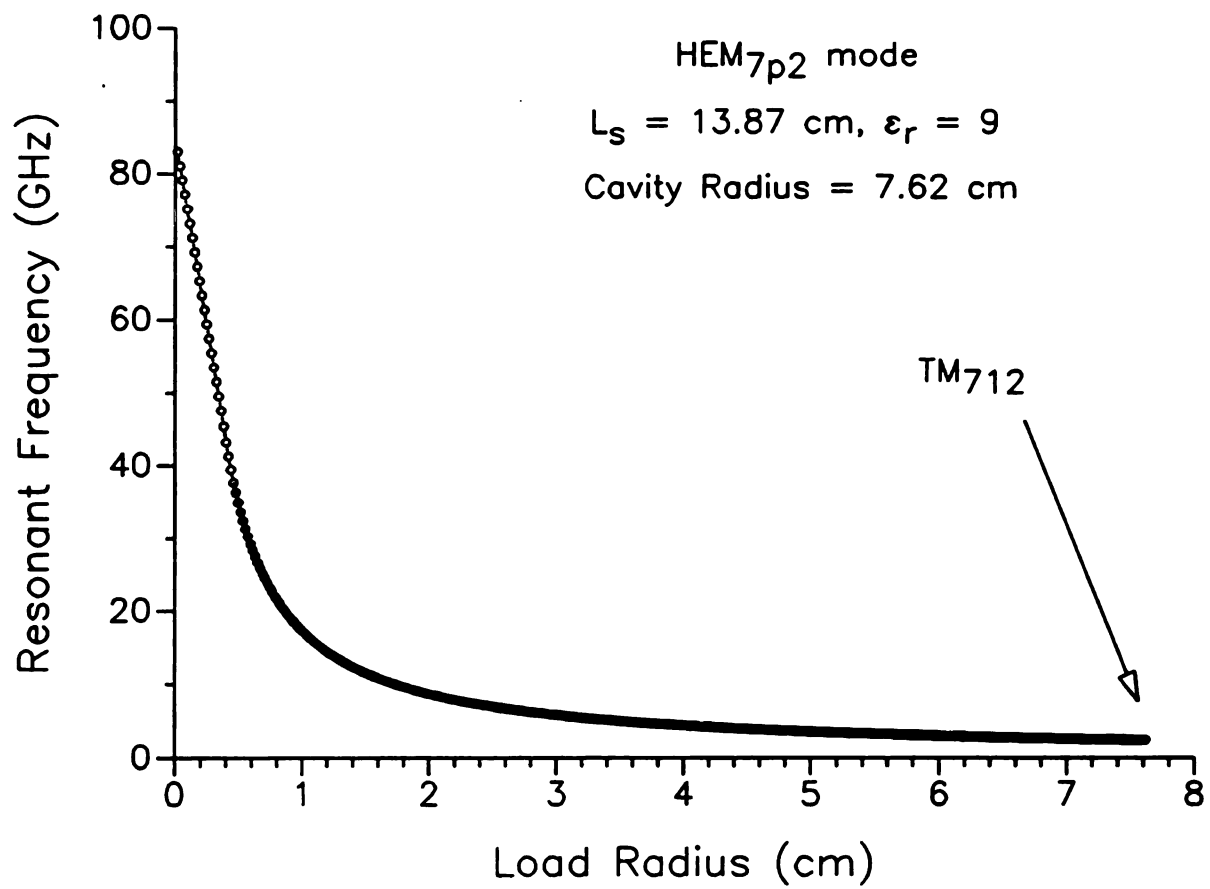
Figure 8-85 Resonant frequency vs. load radius: HEM_{7p2}, $\epsilon_r = 9$.
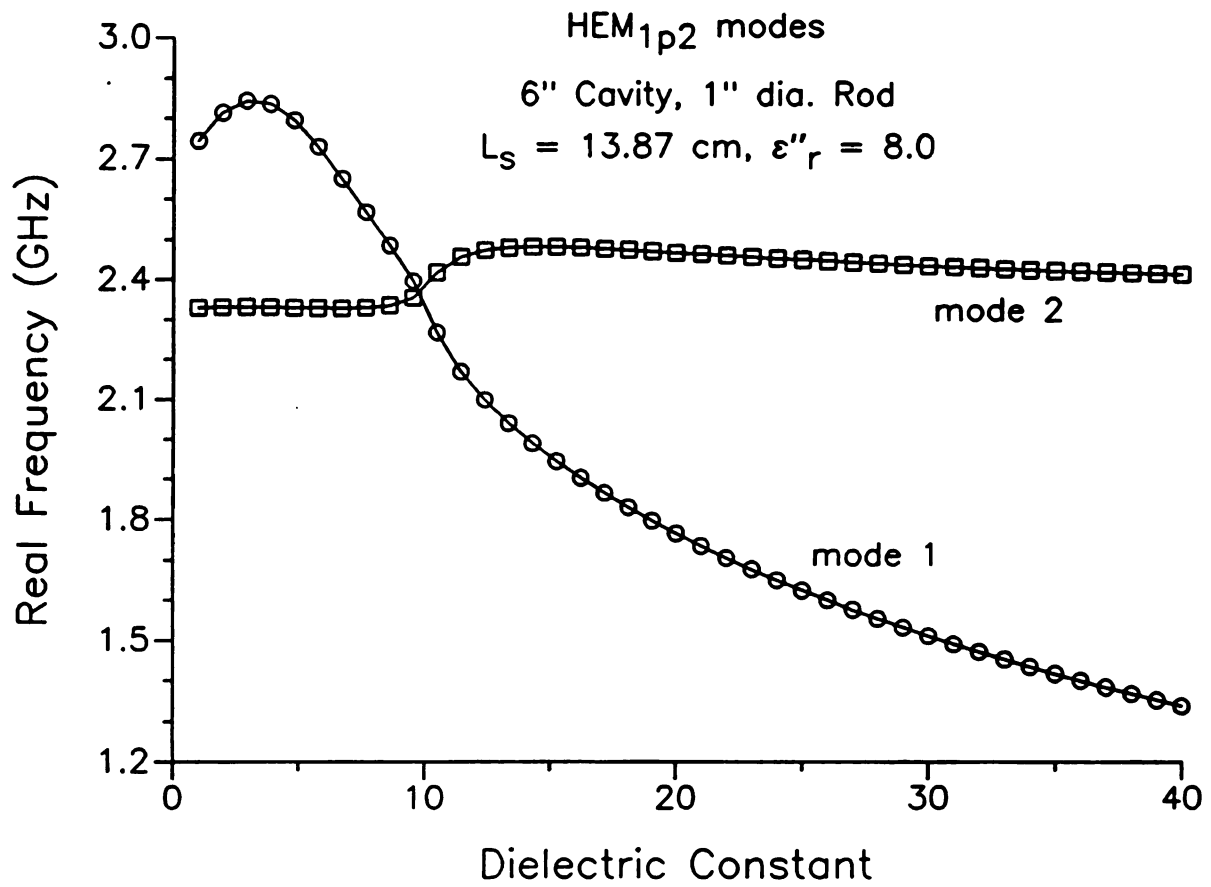
Figure 8-86 Real frequency vs. dielectric constant ϵ_r': HEM_{1p2}, $\epsilon_r'' = 8$.

with those of mode 2 for $\epsilon_r' > 10$ to form one mode, and vice-versa to form the other mode? One indication that the points are properly grouped is that the slopes of the modes are continuous as identified in the Figure, whereas they would not be continuous the other way. This is only an indication because it has not been shown that their slopes must be continuous.[†] However, even if the slopes are not required to be always continuous, is it likely that two different modes would have discontinuous slopes at precisely the same value for the mode variable? The continuity of the slope at the crossing point is therefore a good indication of how the points ought to be grouped into a mode.

A better indication, and in fact a conclusive reason, is given by the plots of the imaginary frequencies in Figure 8-87. There it is shown that the modes are distinguishable by their imaginary frequencies, whose plots do not cross in this case. There is no question, then, which points belong to which mode. As an aside, this demonstration points out that if a mode chart is being constructed for a lossless system and it is difficult to determine how discrete points are to be grouped into modes, adding a small amount of loss may provide the answer through the imaginary frequency.

It is now shown how these modes are traced to material filled cavity modes. First, a trace through the load radius is shown in Figures 8-88 and 8-89. In Figures 8-88 and 8-89 the modes are labeled 1 and 2, corresponding to the modes in Figures 8-86 and 8-87. The two sets of Figures contain common natural resonance points: The points at $\epsilon_r' = 20$ in Figures 8-86 and 8-87 are for the same natural resonances as the points at $a = 1.27$ cm in Figures 8-88 and 8-89. The common resonance points are the basis for the labels 1 and 2 in Figures 8-88 and 8-89.

From Figures 8-88 and 8-89 it may be observed that mode 1 for $\epsilon_r' = 20$ may be traced back through diminishing load radius to the empty cavity TE_{112} mode. It may also be traced with increasing load radius to the material filled cavity TE_{112}

[†] It must also be recognized that continuity, especially in the slope, is difficult to judge when the curve is composed of discrete points. A sharp bend may appear discontinuous at low resolution, i.e., for a curve composed of only a few points. Adding more points may demonstrate that the curve is actually continuous.
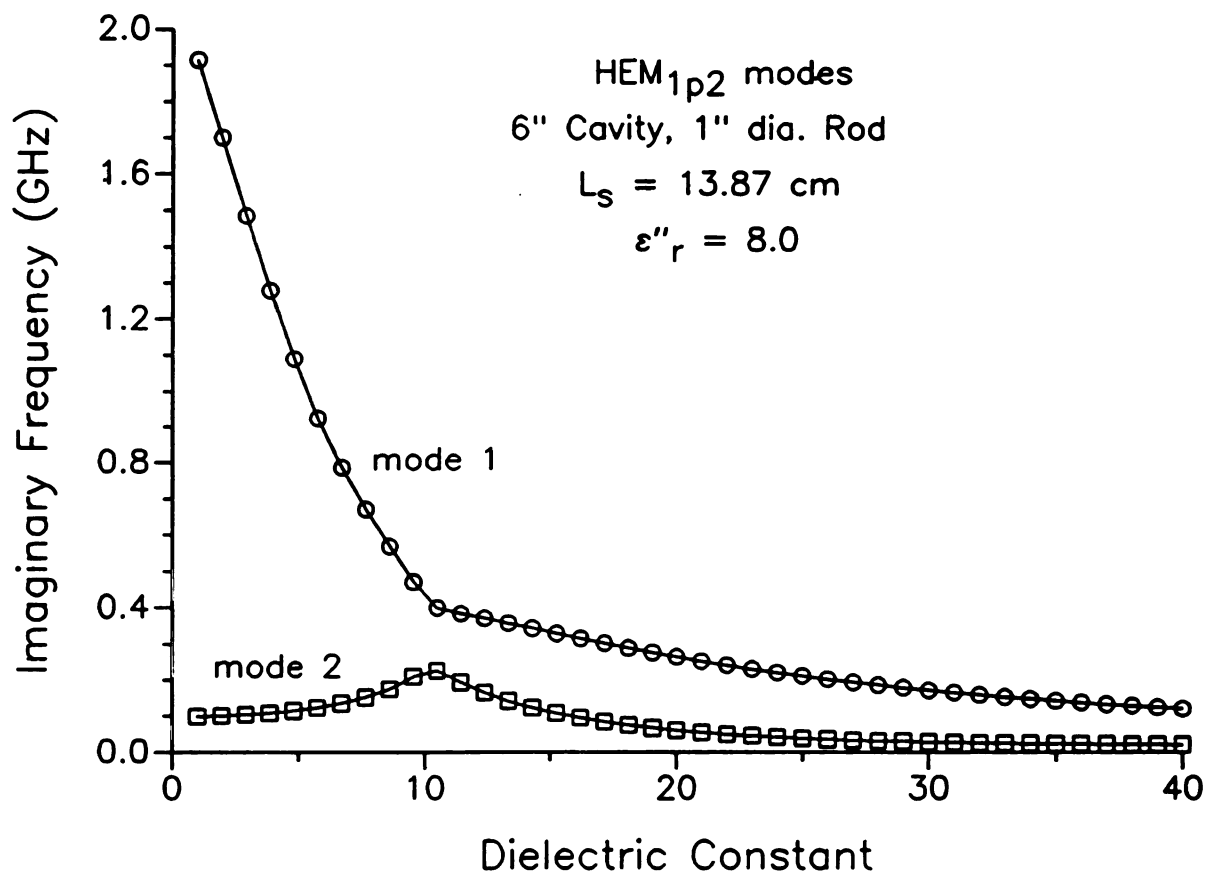
Figure 8-87 Imaginary frequency vs. dielectric constant ϵ_r': HEM_{1p2}, $\epsilon_r'' = 8$.
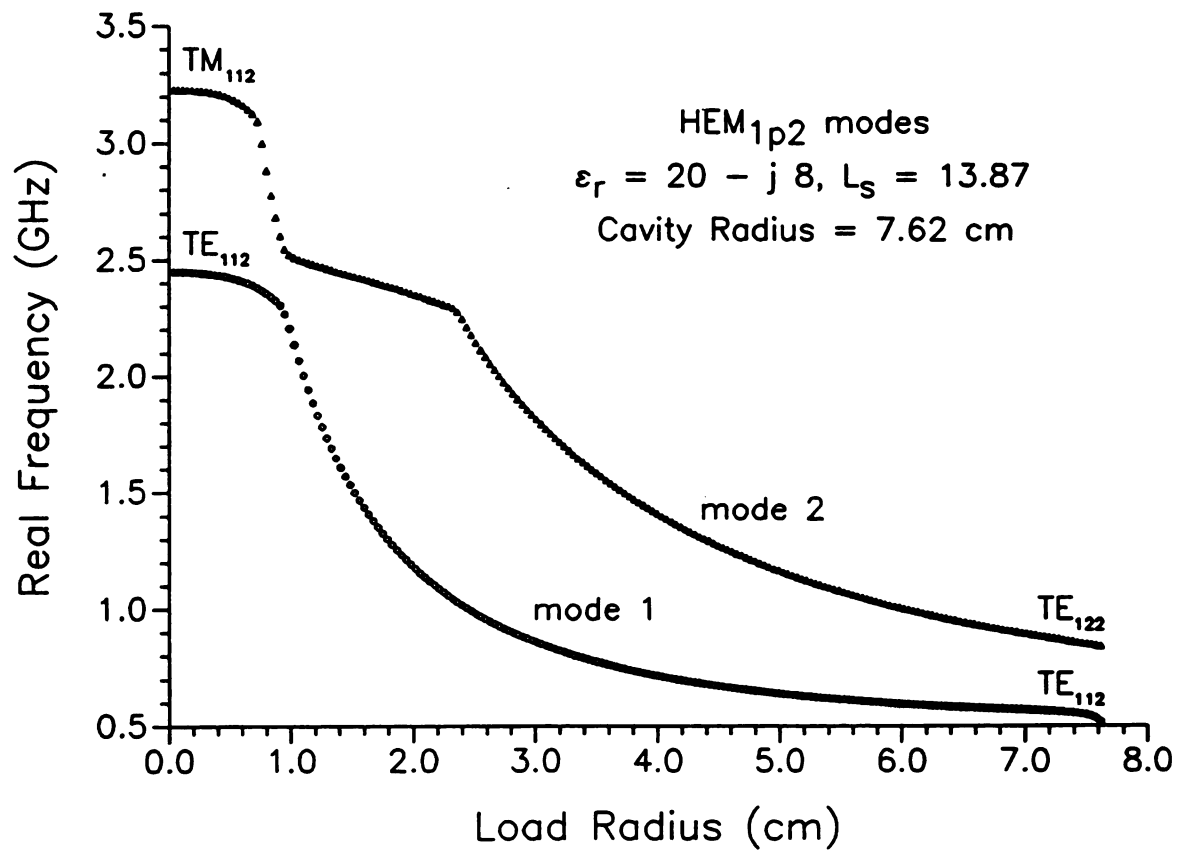
Figure 8-88 Real frequency vs. load radius: HEM_{1p2}, $\hat{\epsilon}_r = 20 - j\,8$.
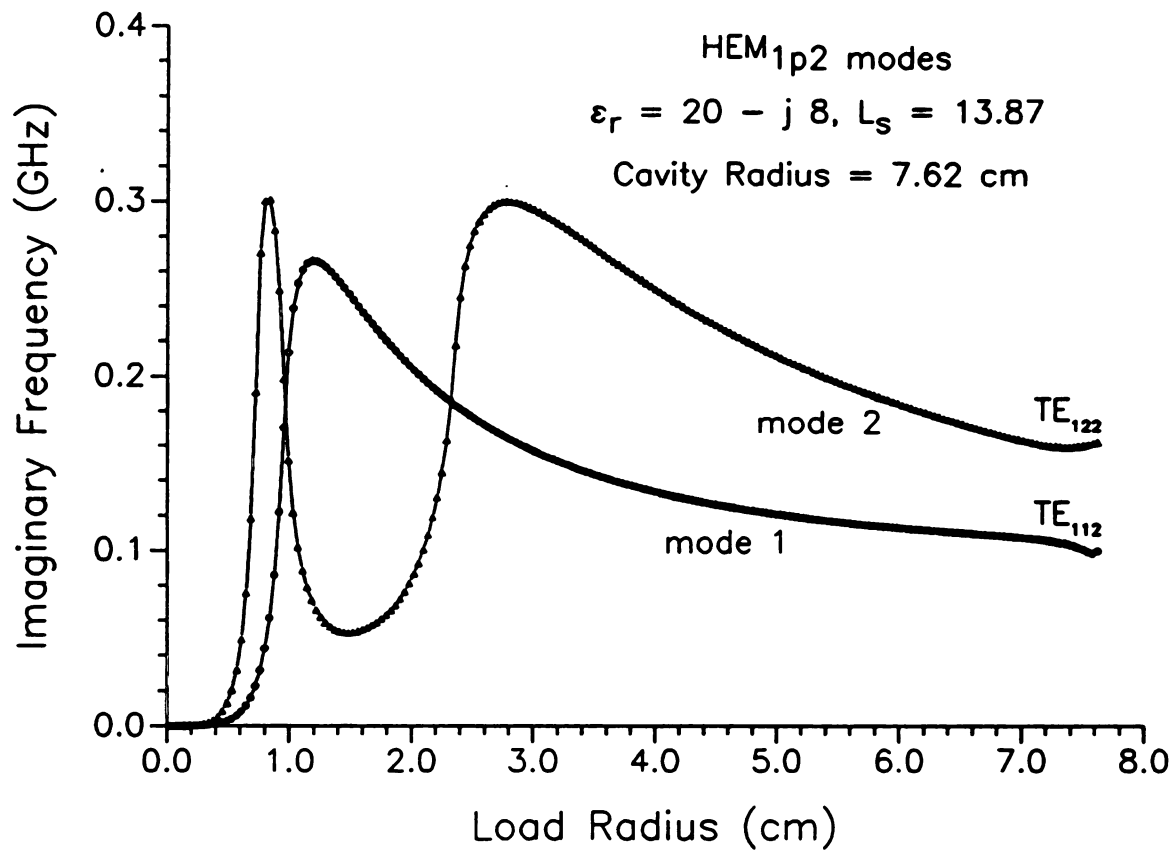
Figure 8-89 Imaginary frequency vs. load radius: HEM_{1p2}, $\hat{\epsilon}_r = 20 - j\,8$.

mode. Since the empty cavity and material filled cavity modes are the same this resonance is radially traceable. That does not mean that all points on mode 1 in Figure 8-86 are radially traceable. Radial traceability has only been shown for the $\epsilon'_r = 20$ natural resonance.

The resonance at $\epsilon'_r = 20$ for mode 2 is not radially traceable. As the load radius decreases toward zero the mode approaches the empty cavity TM_{112} mode. As the load radius increases near the cavity radius the mode approaches the material filled TE_{122} mode. This is an example of how an empty cavity TM mode may be transformed into a material filled TE mode through the load radius mode variable.

Something else to notice about Figures 8-88 and 8-89 is that the display of the radial order of the modes by the number of "flats" in the real frequency plot, or the number of local minima in the imaginary frequency, corresponds to the radial order of the material filled mode rather than the empty cavity mode. Mode 2 contains two "flats" in the real frequency and two local minima in the imaginary frequency. These numbers correspond to the radial order of the material filled TE_{122} mode rather than the empty cavity TM_{112} mode.

Returning to Figures 8-86 and 8-87, we now wish to trace modes 1 and 2 back to the empty cavity through the loss factor. In order to reach the empty cavity by reducing the loss factor to zero, the dielectric constant must be that of a vacuum, i.e., $\epsilon'_r = 1$. Beginning with the natural resonance for $\epsilon'_r = 1$ in Figures 8-86 and 8-87, the modes are traced in Figures 8-90 and 8-91, starting at the far right for $\epsilon''_r = 8$, back to the lossless empty cavity modes at $\epsilon''_r = 0$. Mode 1 is traced back to the empty cavity TM_{142} mode while mode 2 is traced back to TE_{112}. It is interesting that it was mode 1 which was traced back to the empty cavity TE_{112} mode through the load radius mode variable in Figures 8-88 and 8-89.

It must now appear as indisputable that tracing a mode through an arbitrary mode variable back to a material filled cavity mode, while providing some fascinating pictures of the paths of the modes, cannot be used to uniquely associate material filled cavity modes with cavity-short type modes. This is the basis for the discussion in Section 8.2 on the naming of the cavity-short type modes by the general HEM
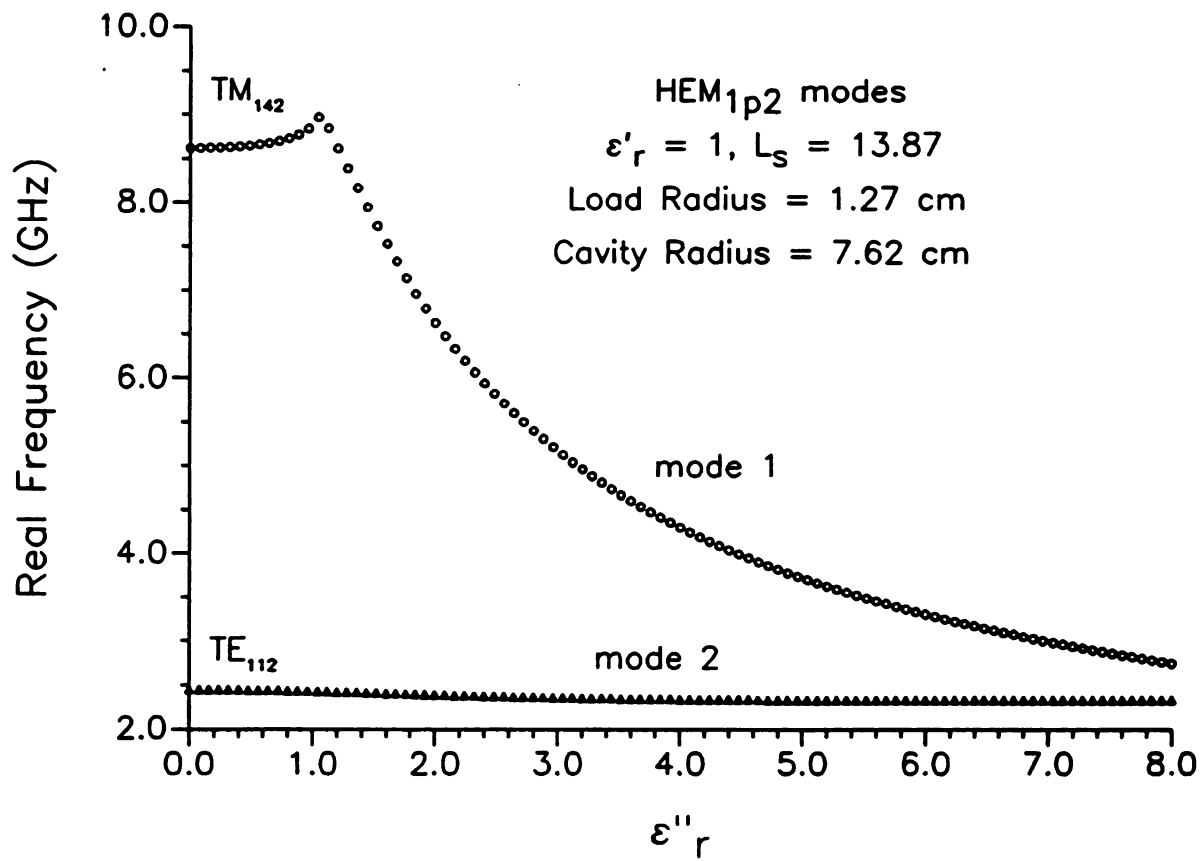
Figure 8-90 Real frequency vs. loss factor: HEM_{1p2}, $\epsilon_r' = 1$, $a = 1.27$ cm.
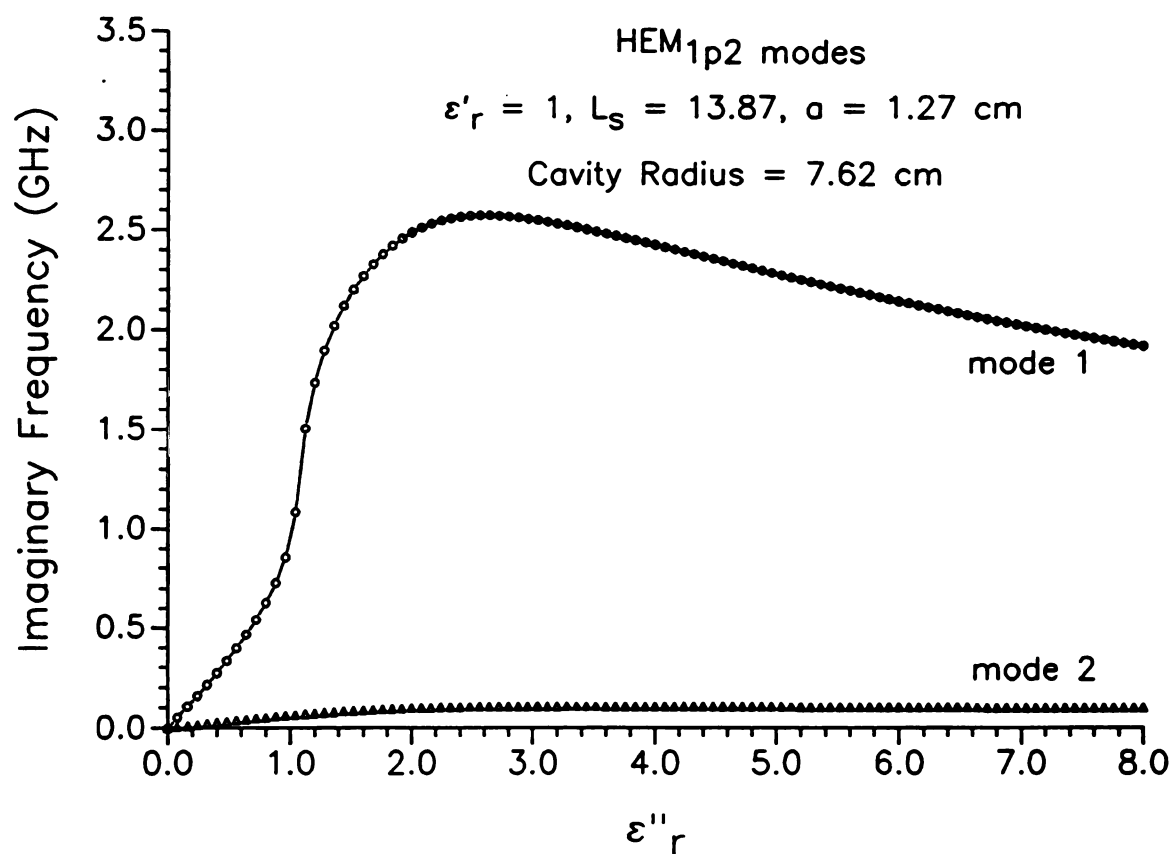
Figure 8-91 Imaginary frequency vs. loss factor: HEM_{1p2}, $\epsilon'_r = 1$, $a = 1.27$ cm.

convention. Although some of the radially traceable modes have been named in this Chapter according to the HE/HH convention, even they cannot be unambiguously labeled so in every instance. It is important to bear this in mind when discussing these modes.

8.5.3 Modal Ordering and Loss Factor

In Figures 8-86 and 8-87 two modes are shown for the dielectric constant, ϵ_r', as the mode variable. The modes in the Figures were defined for a loss factor of $\epsilon_r'' = 8$. It is interesting to examine the behavior of these two modes for a variety of loss factors. The Figures on the following several pages, numbered 8-92 through 8-109 show how the modes of Figures 8-86 and 8-87 are related to one another for loss factors $\epsilon_r'' = 4, 5, 6, 7, 7.5, 9, 10, 12,$ and 15. What makes this rather extended series of Figures interesting is the way the modes seem to trade positions as the loss factor rises.

Figures 8-92 and 8-93 show two independent modes defined by frequency as a function of dielectric constant. The loss factor is held constant at $\epsilon_r'' = 4$. Figures 8-94 and 8-95 show the same modes, but for $\epsilon_r'' = 5$, and so on. As ϵ_r'' increases the two modes begin to draw near to one another in real frequency for dielectric constants near $\epsilon_r' = 10$. Their imaginary frequencies, which are intertwined and cross near $\epsilon_r' = 10$ for loss factors less than 8, begin to pull apart as the loss factor rises. When the loss factor is near 7, a neck is clearly visible in the real frequency plot of Figure 8-98. Increasing the loss factor slightly to 7.5 the modes nearly touch as shown in Figure 8-100.

Adding another 0.5 to the relative loss factor, the modes appear as shown in Figures 8-86 and 8-87, which were discussed above. At this point the imaginary frequency plots are no longer intertwined, but the real frequency plots of the two modes now cross. The way in which this crossing and uncrossing has occurred has been for the modes at some critical juncture between $\epsilon_r'' = 7.5$ and $\epsilon_r'' = 8$ to trade places for points in the range $\epsilon_r' > 10$.
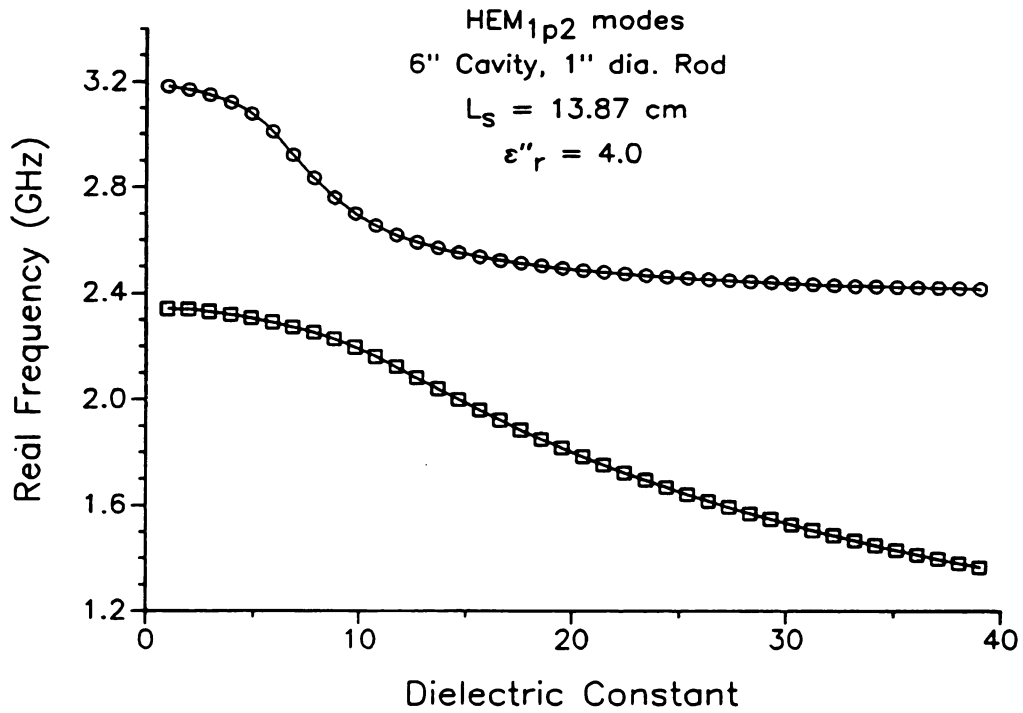
Figure 8-92 Real frequency vs. ϵ_r': HEM_{1p2}, $\epsilon_r'' = 4$.
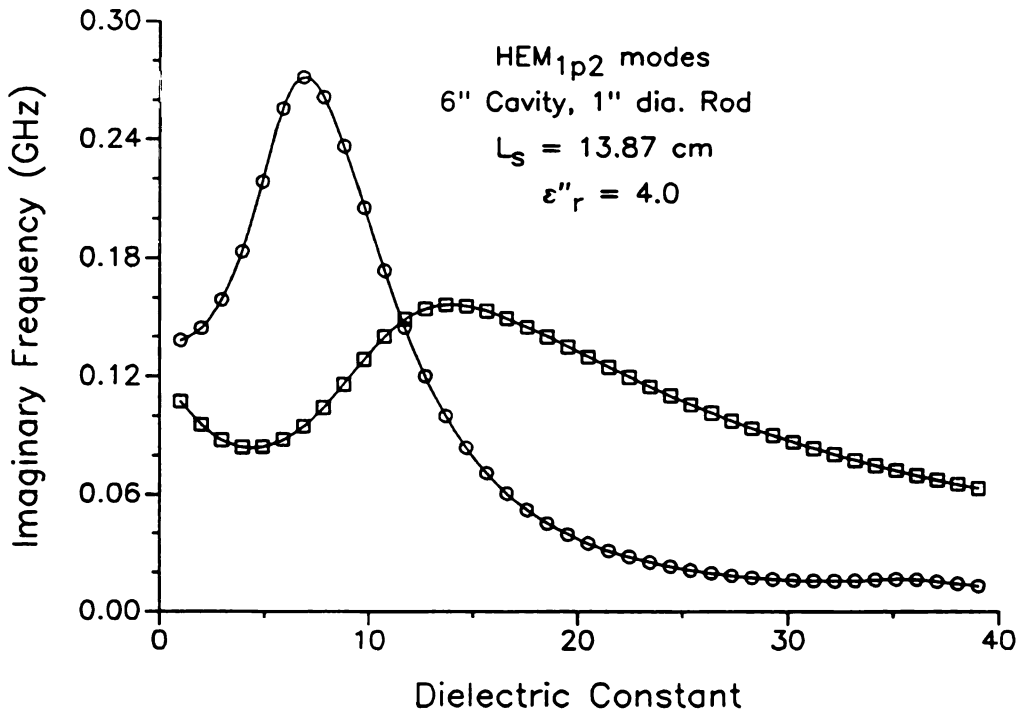
Figure 8-93 Imaginary frequency vs. ϵ_r': HEM_{1p2}, $\epsilon_r'' = 4$.
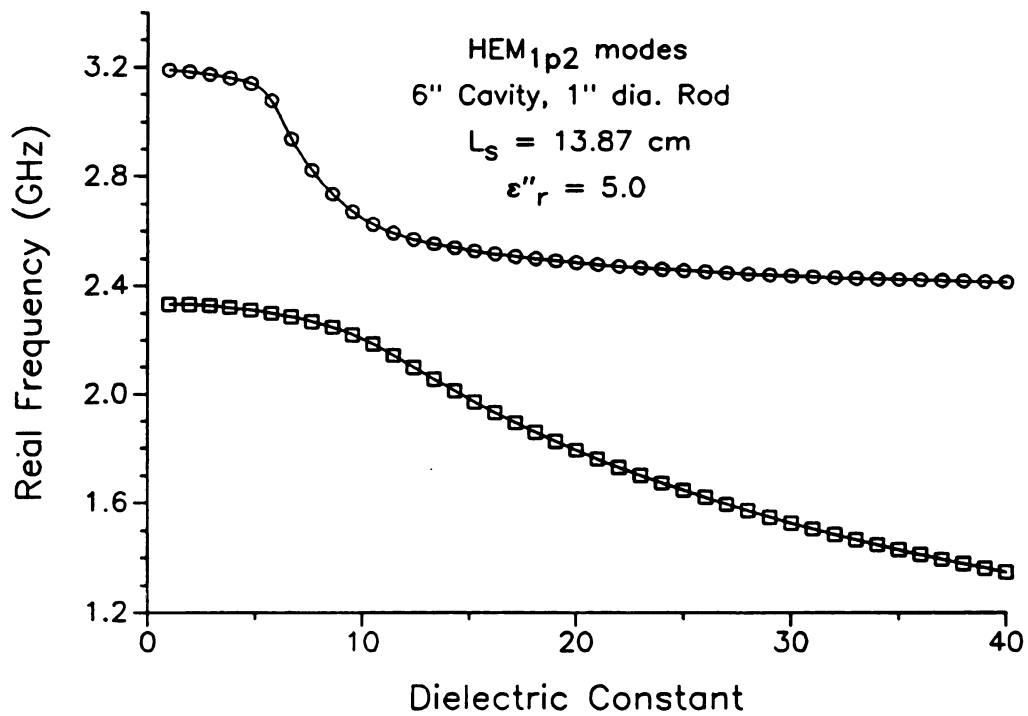
Figure 8-94 Real frequency vs. ϵ_r': HEM_{1p2}, $\epsilon_r'' = 5$.
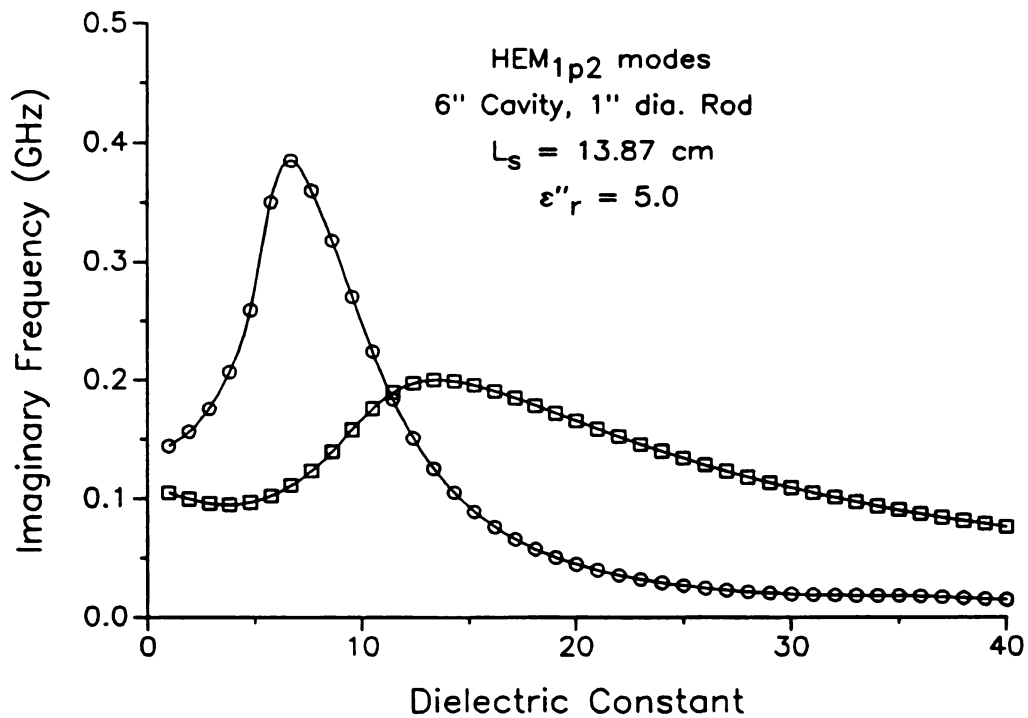
Figure 8-95 Imaginary frequency vs. ϵ_r': HEM_{1p2}, $\epsilon_r'' = 5$.
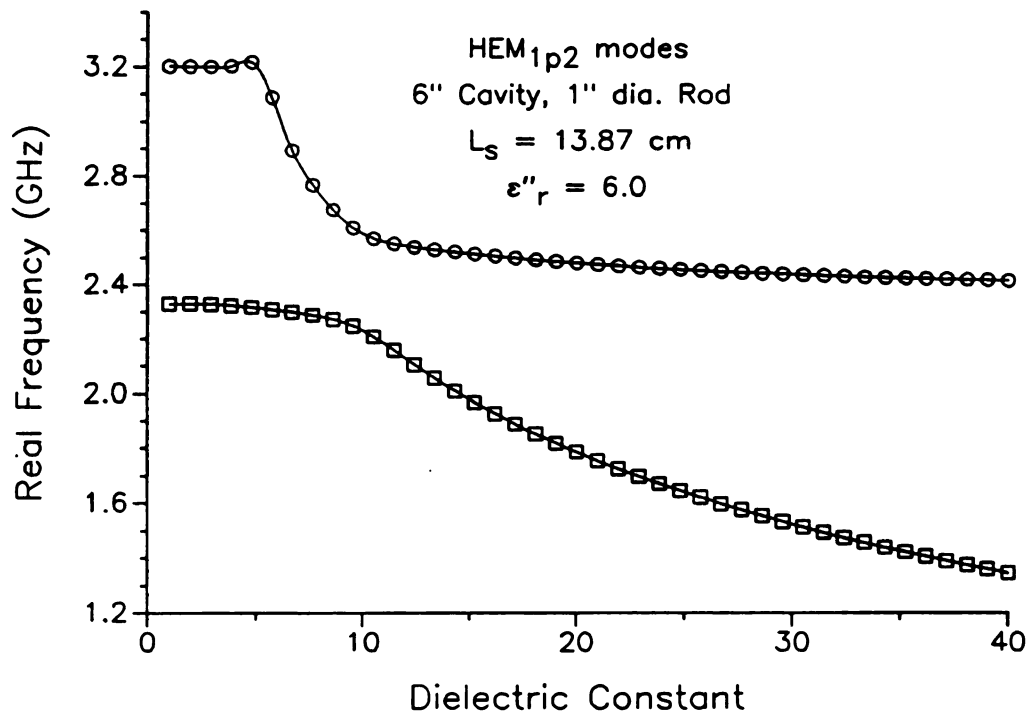
Figure 8-96 Real frequency vs. ϵ_r': HEM_{1p2}, $\epsilon_r'' = 6$.
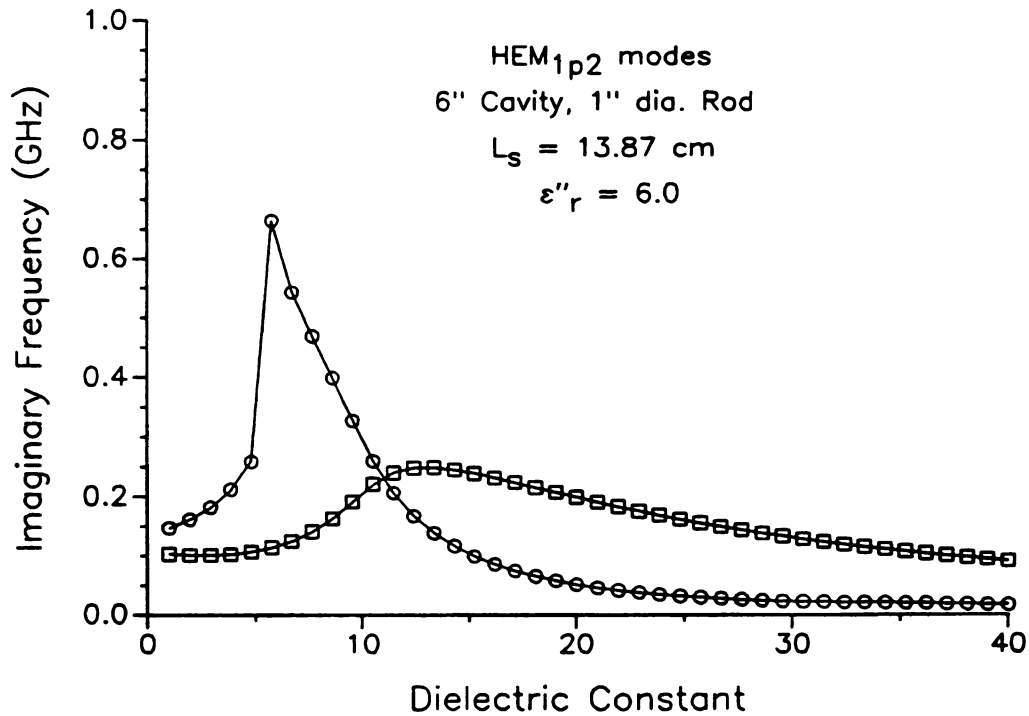
Figure 8-97 Imaginary frequency vs. ϵ_r': HEM_{1p2}, $\epsilon_r'' = 6$.
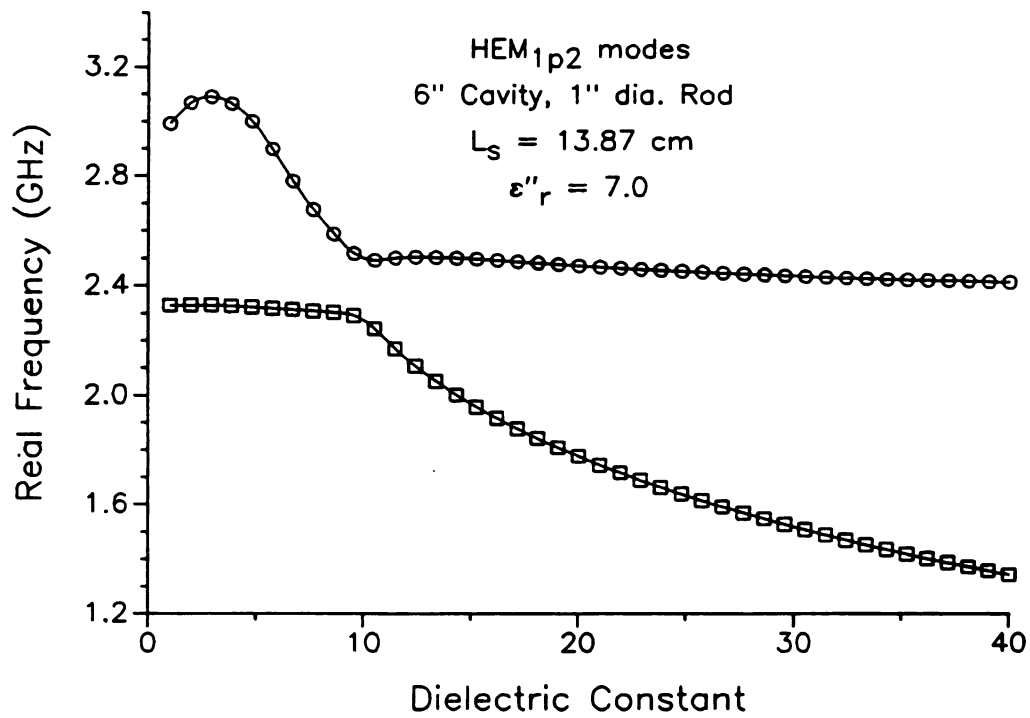
Figure 8-98 Real frequency vs. ϵ_r': HEM_{1p2}, $\epsilon_r'' = 7$.
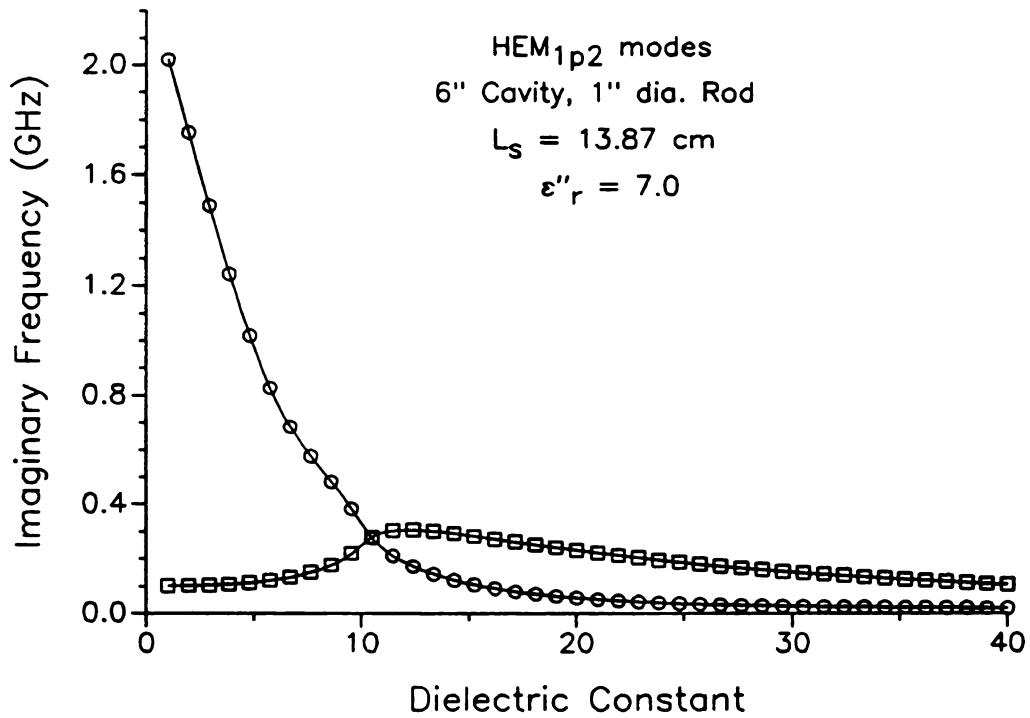
Figure 8-99 Imaginary frequency vs. ϵ_r': HEM_{1p2}, $\epsilon_r'' = 7$.
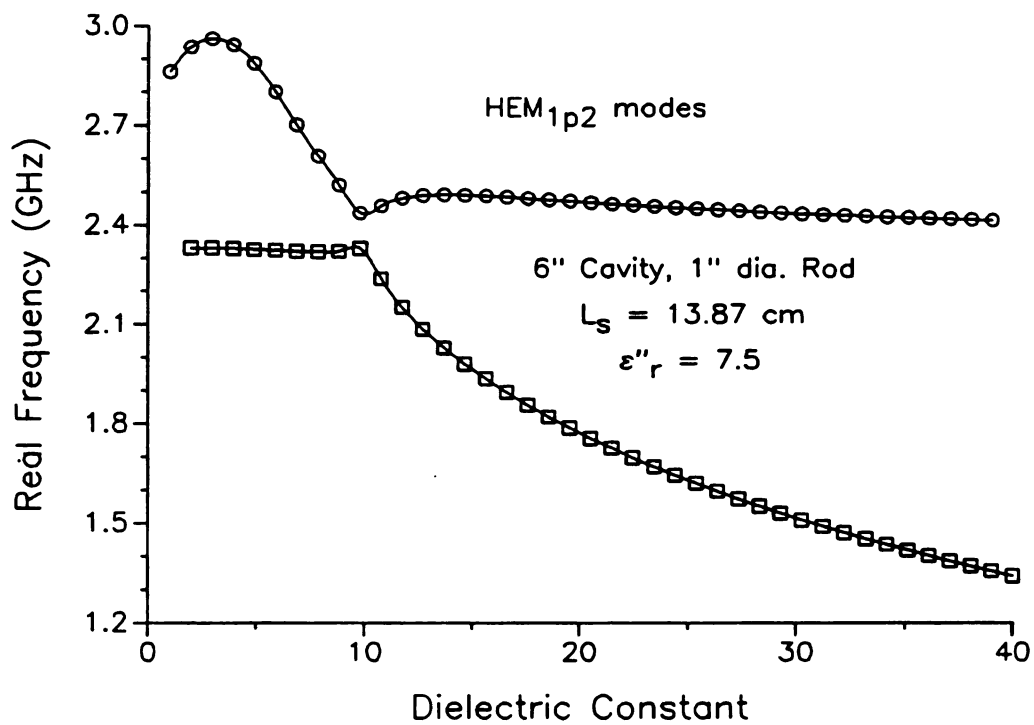
Figure 8-100 Real frequency vs. ϵ_r': HEM_{1p2}, $\epsilon_r'' = 7.5$.
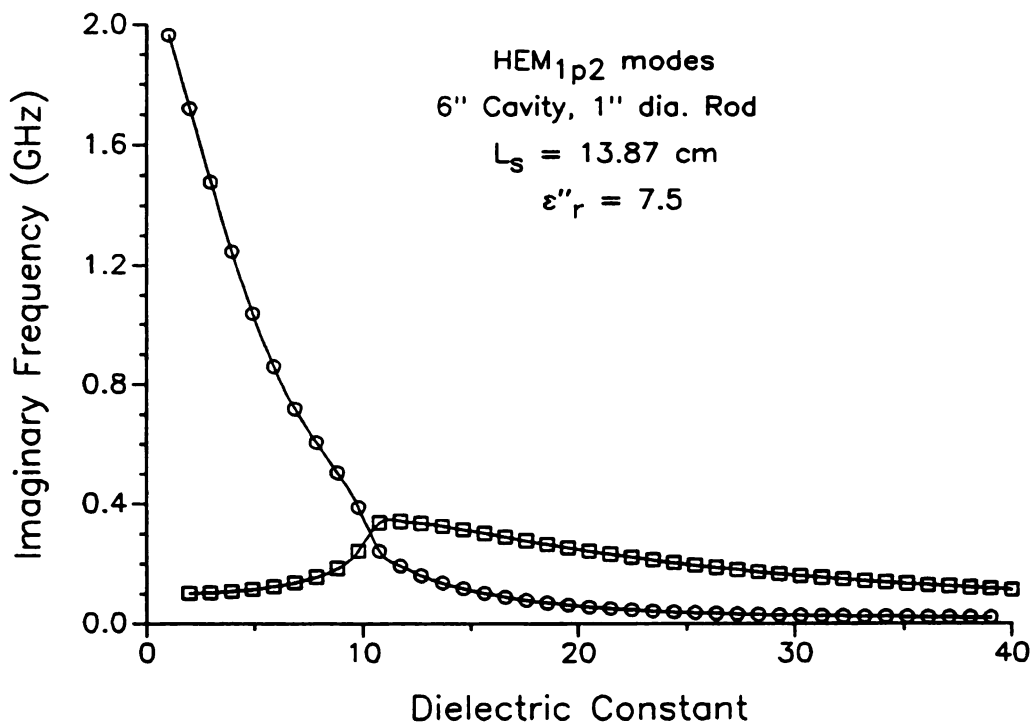
Figure 8-101 Imaginary frequency vs. ϵ_r': HEM_{1p2}, $\epsilon_r'' = 7.5$.
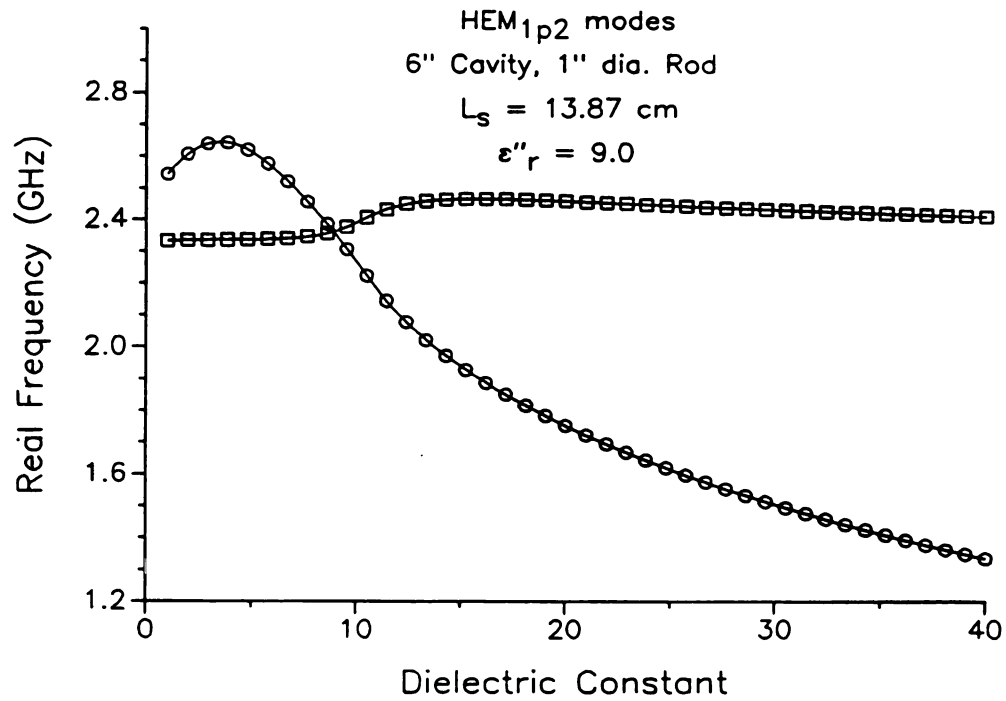
Figure 8-102 Real frequency vs. ϵ_r': HEM_{1p2}, $\epsilon_r'' = 9$.
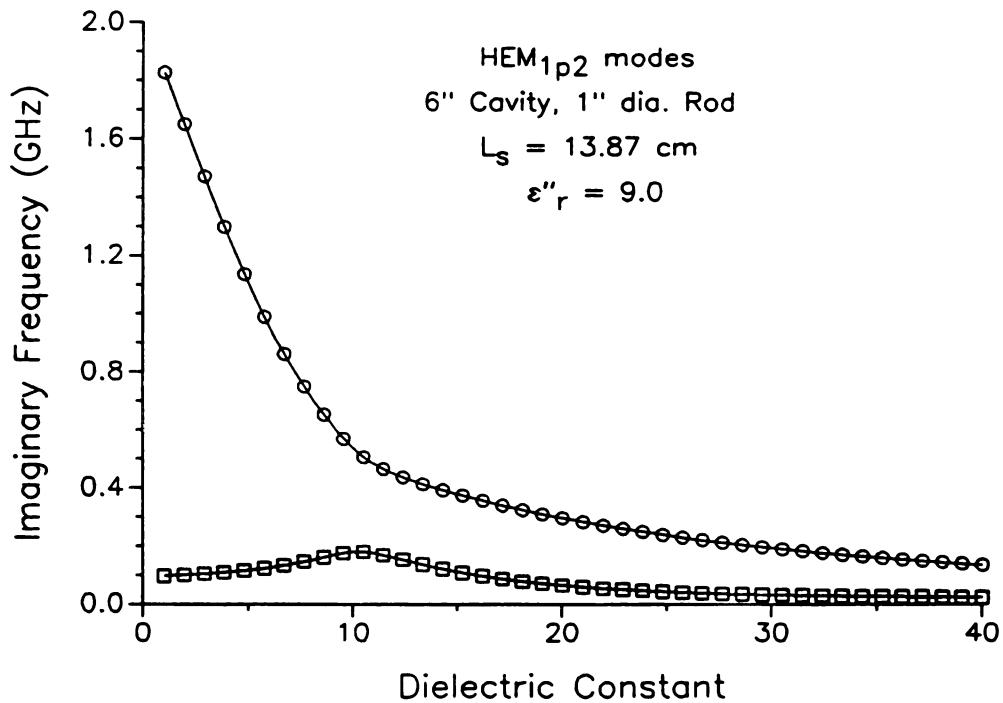
Figure 8-103 Imaginary frequency vs. ϵ_r': HEM_{1p2}, $\epsilon_r'' = 9$.
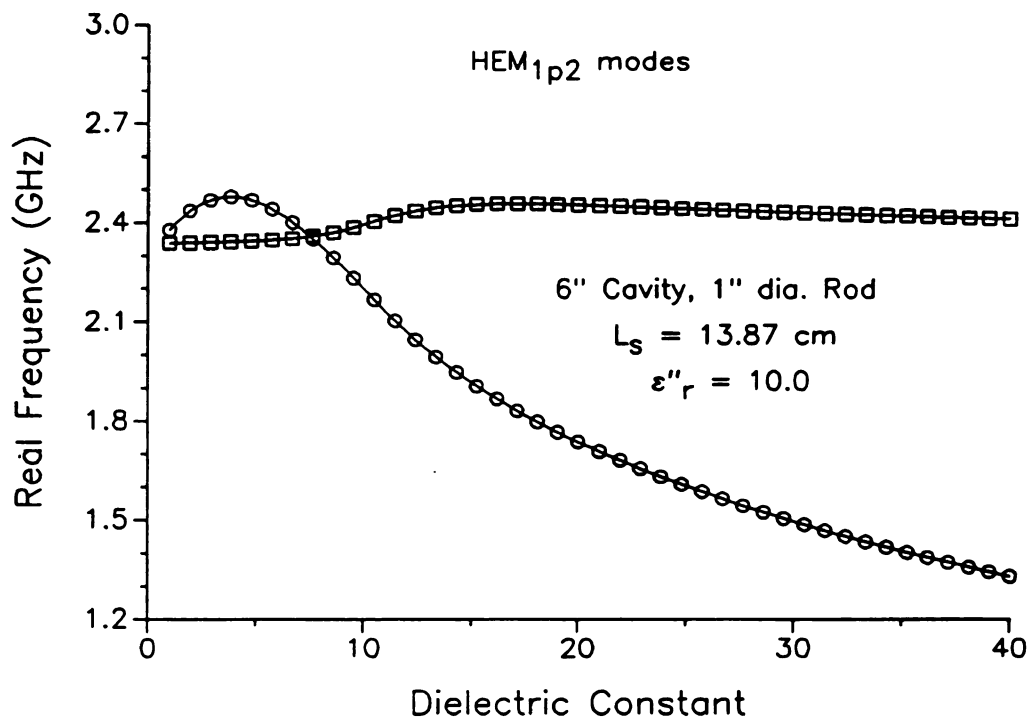
Figure 8-104 Real frequency vs. ϵ_r': HEM_{1p2}, $\epsilon_r'' = 10$.
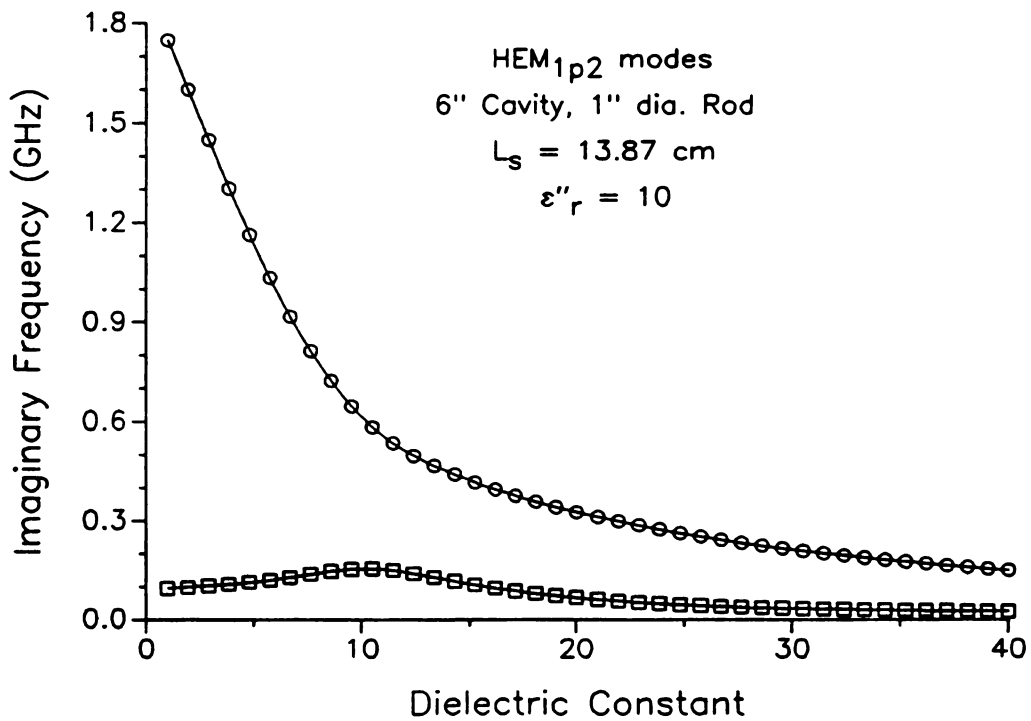
Figure 8-105 Imaginary frequency vs. ϵ_r': HEM_{1p2}, $\epsilon_r'' = 10$.
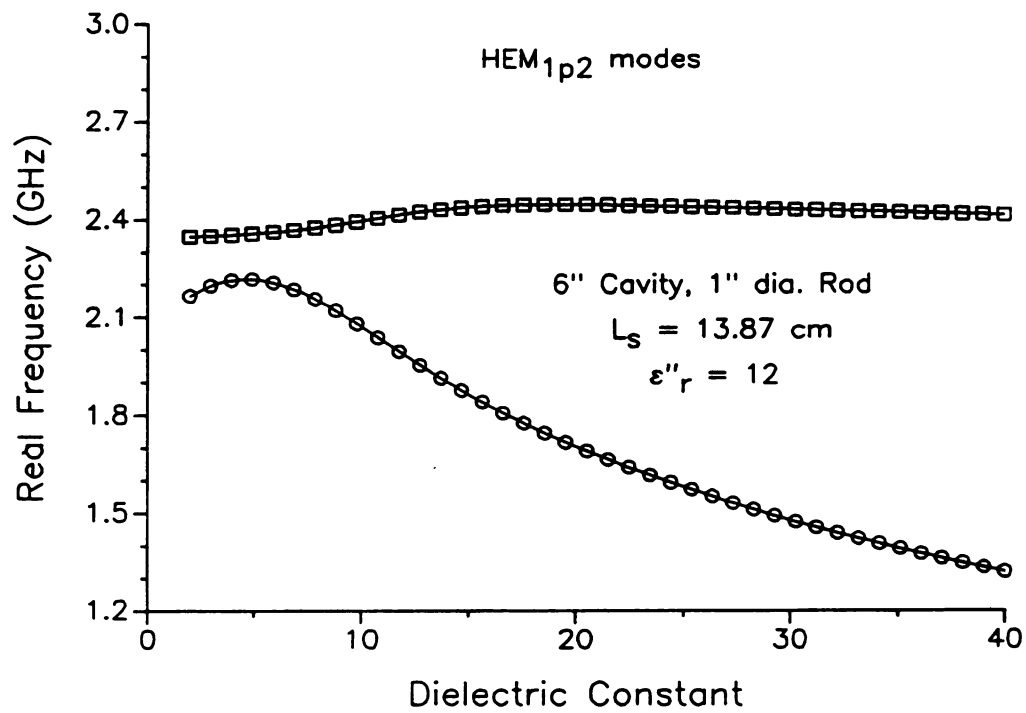
Figure 8-106 Real frequency vs. ϵ_r': HEM_{1p2}, $\epsilon_r'' = 12$.
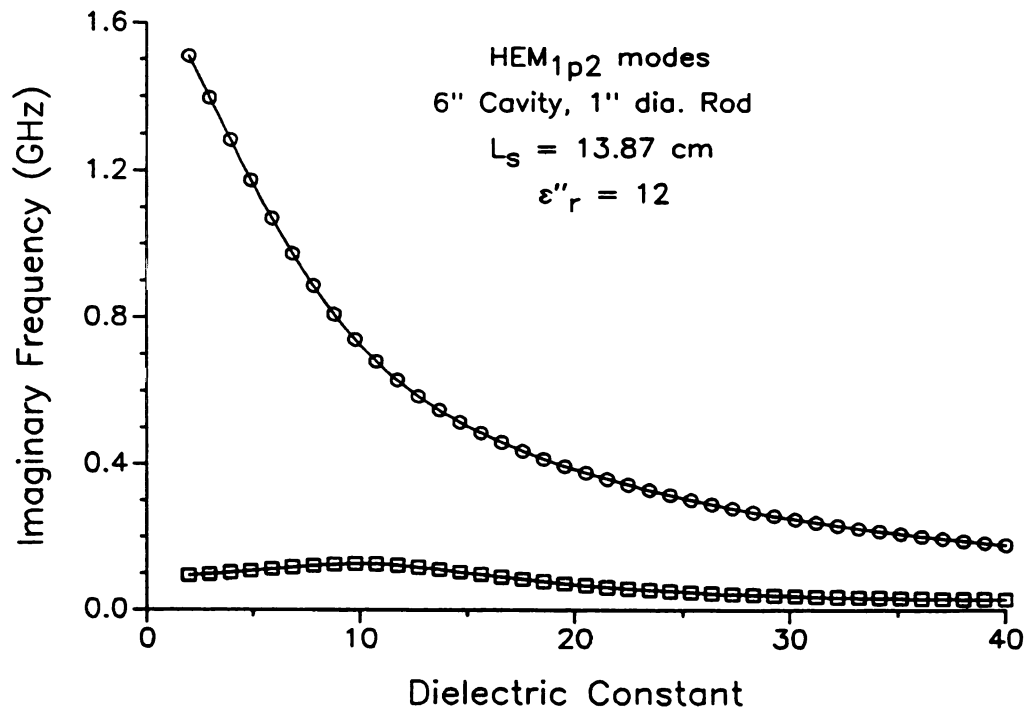
Figure 8-107 Imaginary frequency vs. ϵ_r': HEM_{1p2}, $\epsilon_r'' = 12$.
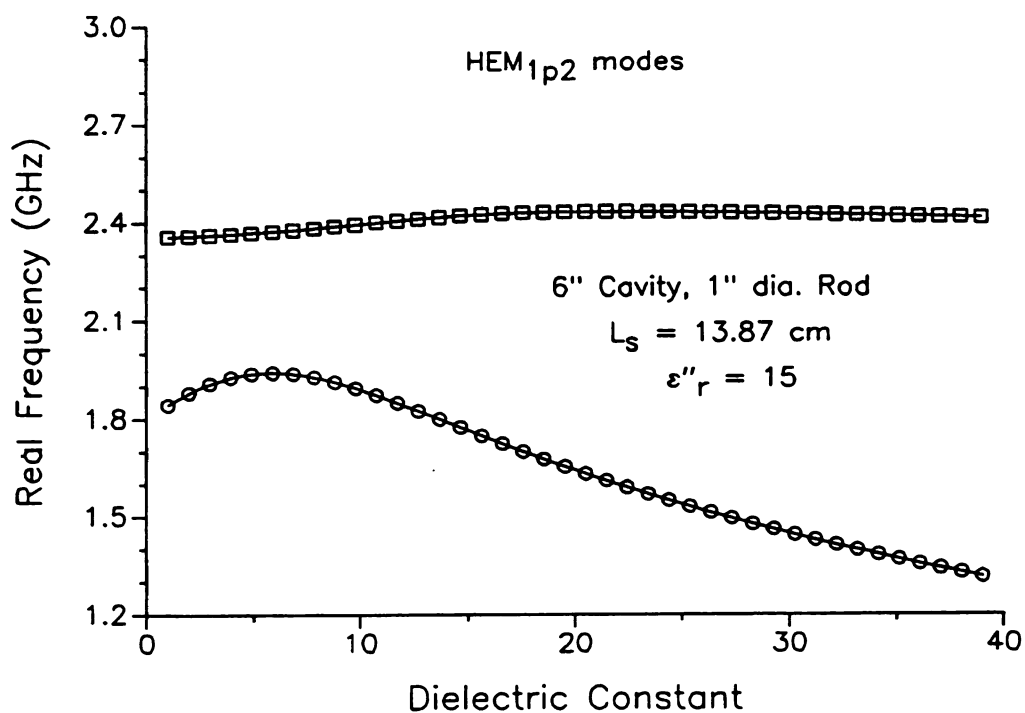
Figure 8-108 Real frequency vs. ϵ'_r: HEM_{1p2}, $\epsilon''_r = 15$.
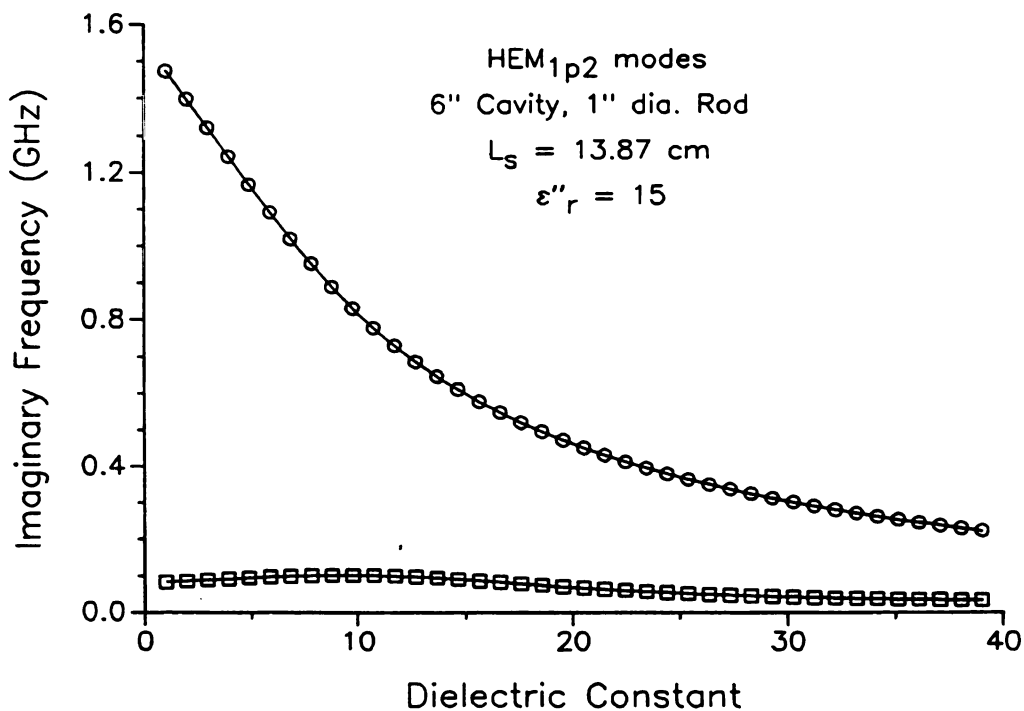
Figure 8-109 Imaginary frequency vs. ϵ'_r: HEM_{1p2}, $\epsilon''_r = 15$.

As the relative loss factor continues to rise beyond 8, the low dielectric constant range of the mode called mode 1 in Figures 8-86 and 8-87 drops in real frequency, while mode 2 remains relatively stable. By the time $\epsilon_r'' = 12$ the real frequency of mode 1 has fallen completely below mode 2, as shown in Figure 8-106. The modes separate even farther, in both real and imaginary frequency, as the loss factor rises beyond 12 to 15, shown in Figures 8-108 and 8-109.

These Figures demonstrate the complicated nature of the relationship of lossy cavity-short type modes to one another. They demonstrate that a slight change in dielectric constant or loss factor can switch a heating process from one mode over to another with no immediately noticeable change in resonant frequency or quality factor. For instance, suppose that a certain heating process using the modes described by Figures 8-92 through 8-109 causes the relative dielectric constant of a material to increase from 5 to 15. If the relative loss factor is between 7.5 and 8, a very slight change in the loss factor at $\epsilon_r' = 10$ will cause a switch in the excited mode which heats the material. While the resonant frequency is not disturbed at the point where the mode is switched, further processing will require different tuning in the resonant frequency as ϵ_r' increases from 10 to 15. In the one case the frequency will need to be tuned higher and will then remain stable, in the other it will have to be continuously tuned downward.

8.6 Conclusion

The plots presented in the Figures of this Chapter demonstrate some of the characteristics of the wide variety of mode behavior displayed by the cavity-short type loaded cavity. It has been shown that for low dielectric constants and loss factors, and for small load radii, the cavity-short type modes are similar to empty cavity modes, both in frequency and field patterns. For small load radii, even when the loss factor and dielectric constant are high, and the material absorbs most of the microwave energy, resonant frequency and field patterns can be similar to empty cavity conditions, as shown in Figures 8-43 and 8-44.

High loss factor materials can be viewed as perturbations of the coaxial cavity, both in frequency and field structure. It has been shown that increasing loss factor in the high loss factor range causes an increase in resonant frequency, but that an increasing loss factor in a moderately lossy material can cause a reduction in resonant frequency, particularly for TM modes. It has been demonstrated that changes in cavity length affect the resonant frequency, while the cavity Q is relatively insensitive to such changes.

While a few generalizations are possible, on the whole, the Figures demonstrate that the cavity-short type modes display diverse and sometimes unusual behavior, especially when the dielectric properties of the load material are altered. For this reason it is worthwhile, when designing a heating process, to determine how changes in dielectric properties will affect cavity tuning and coupling of energy into the material. Cavity tuning may be partially understood by resonant frequency behavior, while energy coupling to the material involves consideration of both quality factor and field structure. For simple configurations like the coaxially-loaded cavity, numerical solutions like those presented in this Chapter may prove invaluable for understanding the process. For materials of arbitrary shape, careful analogies to the simple configuration may lend insight as well.

Chapter 9
NUMERICAL SOLUTIONS FOR THE
CAVITY-OPEN TYPE CONFIGURATION

9.1 Introduction

The cavity-open type loading configuration is shown in its most general form in Figure 4-2 of Chapter 4. It consists of a cylindrical cavity of radius b and length L_s with a cylindrically shaped, homogeneous, isotropic dielectric load placed coaxially inside the cavity with its center at height h above the cavity floor. The load is of radius a and length ℓ. The essential characteristic of the cavity-open type configuration which distinguishes it from the waveguide or cavity-short type configuration is that the load length is less than the waveguide or cavity length. The ends of the load become additional boundaries at which the electromagnetic fields must be appropriately matched.

A special case of the cavity-open type configuration exists for $h = \frac{1}{2} L_s$. This special case, as discussed in Section 4.3 of Chapter 4, is called the cavity-image type configuration. The discussion in Section 4.3 points out that, by taking advantage of the geometrical symmetry of the cavity-image type configuration, calculations of resonant characteristics are greatly simplified over the general cavity-open type case. The cavity-image type configuration is shown in Figure 4-4 of the same Section.

This Chapter is intended to demonstrate that the analytic solutions presented in Chapter 4 for the cavity-open type configurations may be implemented numerically. Due to their complexity, however, comparatively few solutions are presented relative to the number of solutions presented in the previous Chapter for the cavity-short type configuration. Furthermore, the simpler, ϕ-symmetric TM modes have been chosen to represent the technique for obtaining numerical solutions for the general case. Section 9.2 contains a TM ($n = 0$) specialization of the general characteristic equations found in Chapter 4. No special naming scheme is proposed for the modes examined in this Chapter. They are simply called by their nearest empty cavity

relative. In general this is an insufficient means of identifying cavity-open type modes, but it will serve for the few cases presented here.

Next will be presented an outline of the method of the numerical procedure. The aim of the procedure is to find the solutions to the cavity-open type characteristic equation, Equation (4-147) or Equation (4-180). The complexity of Equations (4-147) and (4-180) require that they be solved in a number of steps. These steps consist of input of cavity and load parameters, reading in the radial wavenumbers for the modes in the empty waveguide regions, solving for radial wavenumbers in the loaded waveguide regions, constructing the characteristic matrix, finding its determinant, finding the determinant zeros, and solving for the mode coefficients. A detailed description of this procedure is given in Section 9.3.

Following the discussion of the numerical procedure, numerical solutions will be presented for selected modes and material loads. Solutions for Methods I and II of Chapter 4 for the cavity-image type configuration will be compared with each other and with experiment. The convergence criteria, regarding the number of matrix elements necessary to provide accurate results, will also be examined. The Chapter concludes with numerical and experimental results for the general cavity-open type configuration when the height h of the load is allowed to vary.

9.2 TM Specialization of the Cavity-Open Type Characteristic Equation

9.2.1 Coaxially-Loaded Waveguide TM Characteristic Equation

The equations governing cavity-open type resonances are much simplified when the modes have no ϕ-dependence, i.e., $n = 0$. As demonstrated in Chapters 3 and 4, under such conditions the cavity modes may be construed as either TM or TE. For TM modes the characteristic equation for the wavenumbers in the coaxially-loaded waveguide region of the cavity are found as the solution to

$$W_n \bigg|_{n=0} = 0, \tag{9-1}$$

where W_n is defined by Equation (3-94) of Chapter 3.

9.2.2 Method I

The Method I characteristic equation for the loaded cavity is given by Equation (4-147) of Chapter 4 with the matrix elements as given in Equations (4-150) through (4-153). The subordinate expressions from Appendix C, found in Equations (C-2) and (C-3), are simplified to become

$$\left\langle E, e^{TM} \right\rangle_{pi} = R_o(k_{\rho 1} a) - \frac{k_{\rho 1}^2}{k_{\rho 2}^2} \frac{J_o(k_{\rho 1} a) S_o(k_{\rho 2} a)}{F_o(k_{\rho 2} a)}, \qquad (9\text{-}2)$$

and

$$\left\langle H, h^{TM} \right\rangle_{pi} = R_o(k_{\rho 1} a) - \frac{\epsilon_2 k_{\rho 1}^2}{\hat{\epsilon}_1 k_{\rho 2}^2} \frac{J_o(k_{\rho 1} a) S_o(k_{\rho 2} a)}{F_o(k_{\rho 2} a)}, \qquad (9\text{-}3)$$

where $R_o(k_{\rho 1} a)$ and $S_o(k_{\rho 2} a)$ are given by Equations (C-4) and (C-5), $J_o(k_{\rho 1} a)$ is an ordinary Bessel function of the first kind, and $F_o(k_{\rho 2} a)$ is defined by Equation (3-76) of Chapter 3.

If the load is located at the center of the cavity, i.e., $h = \frac{1}{2} L_s$, and standing wave solutions are used for the axial dependence in both Region I and in Region II, the matrix elements for Method I are given by

$$X_{pi} = \frac{\gamma_i}{\hat{\epsilon}_1} \sin(\gamma_i \frac{\ell}{2}) \cos \left[k_z \left[\frac{L_s - \ell}{2} \right] \right] \left\langle E, e^{TM} \right\rangle_{pi}$$

$$+ \frac{k_z}{\epsilon^I} \cos(\gamma_i \frac{\ell}{2}) \sin \left[k_z \left[\frac{L_s - \ell}{2} \right] \right] \left\langle H, h^{TM} \right\rangle_{pi}. \qquad (9\text{-}4)$$

This matrix, as will be shown below, is highly ill-conditioned and, despite its relative simplicity, is not suitable for calculating the complex frequencies of the TM modes.

9.2.3 Method II

A more numerically stable matrix is found on the left hand side of Equation (4-180). When $n = 0$, the TM mode off-diagonal matrix elements defined by

Equation (4-176) are simplified such that K_{ij} is given by

$$K_{ij} = K_{ji} = \sum_q \frac{Z_{e_q}^{I^+} \xi_m^I}{Z_{m_q}^{I^+}} \frac{k_{z_q}^I \hat{\epsilon}_1}{\epsilon^I} \frac{\langle H, h^{TM} \rangle_{qj} \langle H, h^{TM} \rangle_{qi}}{\lambda_{oq}^2 J_o'^2 (\lambda_{oq})}.$$ (9-5)

The diagonal elements are also simplified. With K_{ii} given by Equation (9-5) when $i = j$, δ_i is given by Equation (4-175) where $\langle E, H \times \hat{z} \rangle_{ii}^{TM}$ has been simplified to become

$$\langle E, H \times \hat{z} \rangle_{ii}^{TM} = \frac{(k_{\rho 1} a)^2}{2} \left\{ \langle J, J' \rangle + \frac{\epsilon_2 J^2 k_{\rho 2}^2}{\hat{\epsilon}_1 F^2 k_{\rho 2}^2} \left[\frac{b^2}{a^2} F_o'^2 (k_{\rho 2} b) - \langle F, F' \rangle \right] \right\},$$ (9-6)

with

$$\langle J, J' \rangle = \left[J'^2 + J^2 + \frac{2}{k_{\rho 1} a} J J' \right],$$ (9-7)

and

$$\langle F, F' \rangle = \left[F'^2 + F^2 + \frac{2}{k_{\rho 2} a} F F' \right].$$ (9-8)

J, F, J', and F' are defined by Equations (3-84) of Chapter 3.

9.3 Outline of Numerical Procedure Used to Solve Equations (4-147) and (4-180)

It is possible to solve the characteristic equations for a variety of system parameters, e.g., given the geometrical dimensions, resonant frequency and cavity Q, the complex dielectric constant may be determined as a zero of the determinant of the characteristic matrix. Similarly, given resonant frequency, cavity Q, and complex dielectric constant, any two geometrical parameters might be found as solutions.[†] The eigenvalues for which the characteristic equation is solved in this discussion are

---

[†]Of course, it is possible in this case that a solution does not exist. However, if a solution does exist for the input variables, it may be found as a solution to the characteristic equation.

the real and imaginary parts of the complex frequency. The geometrical parameters of the cavity and load, i.e., a, b, ℓ, L_s, and h, and the complex dielectric constant of the load, $\hat{\epsilon}$, are pre-specified. The roots of the characteristic equation are then values for complex frequency, i.e., $\hat{\omega} = \omega' + j\omega''$.

There are common steps in the numerical solution process for the characteristic equations of both Methods I and II. The first of these is the input of data describing the cavity and load dimensions, and the real and imaginary parts of the complex dielectric constant of the load material. For the general case, the height of the sample above the cavity floor is also specified. It is convenient to include such data in an editable file which the computer program reads automatically at the beginning of execution. Accessing the parameters from a file saves time in typing them in each time, and makes them independent of the program itself. If parameters are made a part of the program code, the program must be recompiled each time the parameters change. For the parameters which change with each execution, e.g., if it is desired to find the complex frequency for a number of different sample lengths, it is convenient to input them at a program prompt such that the input value overrides the value read from the parameter file.

Other variable program information may be treated the same way. Such information as the matrix dimensions, the accuracy of the roots desired, maximum number of iterations, etc., may be included in the parameter file or placed in its own file. It is useful to place comments in these external files to indicate what each numeric field corresponds to.

In order to construct the matrix elements it is necessary that the radial and axial wavenumbers be known for each mode in each region. All of these values, except for the radial wavenumbers in the empty waveguide region, are frequency dependent. The frequency dependent wavenumbers must be calculated during the root-finding process as the frequency changes. However, the empty waveguide region radial wavenumbers are given simply in terms of the zeros of Bessel functions and may be read into an array at the start of the program. Since these Bessel function zeros may be calculated independently, or may be found in reference tables, it is best

to store them in a file, subroutine, or external function program block. The axial wavenumbers are linked to the radial wavenumbers through the frequency according to Equation (3-24) of Chapter 3.

The radial wavenumbers in the coaxially-loaded waveguide region of the cavity must be calculated during the root-finding process, as mentioned above. However, these wavenumbers are themselves determined by a root-finding procedure. They, along with the axial wavenumbers, are found as the solution of Equation (9-1). In order to solve for them, an initial guess for the radial wavenumber of each mode must be entered. It is possible, during the process of finding the roots of the matrix determinant, to give a zero initial guess for each radial wavenumber every time the frequency is adjusted and then increment the initial guesses until they are close enough that the radial wavenumber root is found. The problem with this approach is that it often results in spurious roots. It is also extremely slow and the wavenumbers are not found in order so that they must be sorted afterwards.

A better alternative is to read in a list of initial guesses for the coaxially-loaded waveguide radial wavenumbers at the beginning of program execution. These initial guesses may be calculated independently as roots of Equation (9-1) for a specified complex frequency. As long as the frequency during the zero finding for the matrix determinant does not change drastically from the frequency used to calculate the guesses, the list will contain good initial guesses for the wavenumbers in the coaxially-loaded region. This list of guesses, or "seeds," may be entered at the beginning of program execution in the same way as the Bessel function zeros.

The body of the program is concerned with the actual finding of the zeros of the determinant of the characteristic matrix. For the implementation here, the zeros are the complex frequencies of the loaded cavity. Complex root-finding is a much more difficult task than finding the roots of a real function with real arguments. For smoothly varying complex functions there are fairly reliable techniques which may be used, among them the secant method and Müller's method. These are useful only for single-ordered roots, i.e., no functions like $f(z) = (z - z_0)^2$. Newton's method is also

available for complex roots of a complex function, but requires a smoothly varying function, a good guess for the root, and computation of the function derivative.

The characteristic equation zeros for the coaxially-loaded waveguide, i.e., Equations (3-91), (3-92), and (9-1), have been found, for the results presented here, using Traub's recension of Müller's method. This method was also used to find the complex frequencies for the cavity-short type cavity in Chapter 8 and the coaxially-loaded waveguide in Chapter 7. It is briefly discussed and the FORTRAN source code provided in Appendix E. Although this method works well for the waveguide characteristic equation, it does not work for finding the zeros of the cavity-open type matrix determinant. The zeros of the determinants of the matrices in Equations (4-147) and (4-180) could not be found by this technique because neither Method I nor Method II matrix determinants are smoothly varying complex functions. Both the real and imaginary parts of the matrix determinants are step functions in both the real and imaginary parts of the arguments. The zeros may be pictured as "pin-holes" in the determinant magnitude surface over the complex plane.

In order to find the zeros of the matrix determinants it was necessary to invoke a technique based upon mapping the zeros of the real and imaginary parts separately on the complex argument plane. Since the real and imaginary parts of the determinant are step functions, bisection is necessary to find their zeros. The procedure is as follows: 1) The zeros of the real part of the determinant are plotted in the complex plane, forming a curve, 2) the zeros of the imaginary part are plotted in a separate curve, 3) the point where the two curves cross is the zero of the complex determinant. In actuality, physical plots are not necessary and the crossing points may be determined without graphical output. A FORTRAN program called COMBIS was developed to solve for the roots in this manner. The code for COMBIS is found in Appendix E.

Whatever root-finding routine is used, the general procedure for finding roots is the same. The root-finder must be given a function whose zeros are being sought, an initial guess or two for the zero, the accuracy to which the zero is desired, and the

maximum number of iterations to discharge before giving up. The output of the root-finder is, of course, the root.

In the case at hand, after calling the root-finder from the main program, the root-finding routine specifies the initial guesses as frequencies for which the matrix elements are calculated. Control is then transferred to a subroutine which calculates the matrix for the given frequency. The first thing the matrix calculation subroutine does is to call another subroutine that calculates the coaxially-loaded waveguide wavenumbers γ, $k_{\rho 1}$, and $k_{\rho 2}$, and returns them to the matrix calculator in an indexed array. This wavenumber calculation subroutine uses the "seed" values for $k_{\rho 1}$ that were initially specified in the main program. Having calculated all of the wavenumbers and knowing the frequency, the matrix elements may then be calculated according to Equations (4-150) or (9-4) for Method I, or (4-175) and (4-176) or (9-5) and (9-6) for Method II.

With the matrix elements calculated, the determinant of the matrix is computed and the answer returned to the root-finder.[†] The root-finder evaluates the answer and suggests another frequency for which the matrix determinant is to be calculated. The process of matrix calculation followed by computation of the determinant continues for each new frequency specified by the root-finder until the root-finder is satisfied that the root has been found. If all that is wanted is the complex frequency, the problem is solved at this point.

If the field values are needed, it is necessary to compute the characteristic matrix for the complex frequency and solve Equation (4-146) or Equation (4-180) for the mode coefficients in Region II. The mode coefficients in Regions I or III are calculated using the Region II mode coefficients in Equations (4-136) through (4-139) and Equations (4-157) through (4-160). All coefficients, and their corresponding wavenumbers, are then put back into the summed field equations, Equations (4-118) through (4-125), etc. The fields are then known at any point within the cavity or load.

[†]For symmetric matrices, the determinant is calculated more simply and accurately by taking the symmetry into account in the determinant algorithm.

9.4 Numerical and Experimental Results

9.4.1 Experimental Measurement Techniques: Cavity-Image Type with Varying Load Length

Since the chief feature of the cavity-image type configuration is a load length different from the cavity length, measurements were made for a variety of load lengths to explore the effect of load length on resonant frequency and cavity Q. Load samples of a common material were prepared in a number of different lengths and fitted with tiny holes to accommodate the thread used to suspend the samples in the cavity, similar to the load suspension shown in Figure 5-5. A typical sample is shown in Figure 9-1 with thread holes diagonally through the top and sides as indicated.

The measurements presented in this Chapter were made using the 6" diameter cavity described above in Chapter 5. Input power was provided by an unamplified signal from a sweep oscillator, on the order of 1 mW, so that the load material temperature would not be affected by the measurement apparatus. A circuit diagram for low power frequency and cavity Q measurements is shown in Figure 9-2.

The resonant frequency and cavity Q were measured in the following manner: Since any changes in the cavity parameters L_s, the cavity length, and L_p, the probe penetration length, affect the resonant frequency, these adjustments were held constant for all frequency measurements for a given experiment. The constant values of L_s and L_p were determined by first tuning and critically coupling the empty cavity to the desired empty cavity TM mode by adjusting L_s and L_p. These settings, along with the resonant frequency and cavity Q were recorded. Then an average sized sample was placed in the center of the cavity and L_p was adjusted for critical coupling. L_s was not adjusted from the empty cavity setting. L_s and L_p remained at these settings throughout the experiment for frequency measurement.

Samples of varying length were then placed inside the cavity by suspending them on thin cotton threads and lowering them until their centers coincided with the cavity center. The resonant frequency was measured. Then L_p was adjusted for critical coupling and Q was measured by the half-power bandwidth method using the
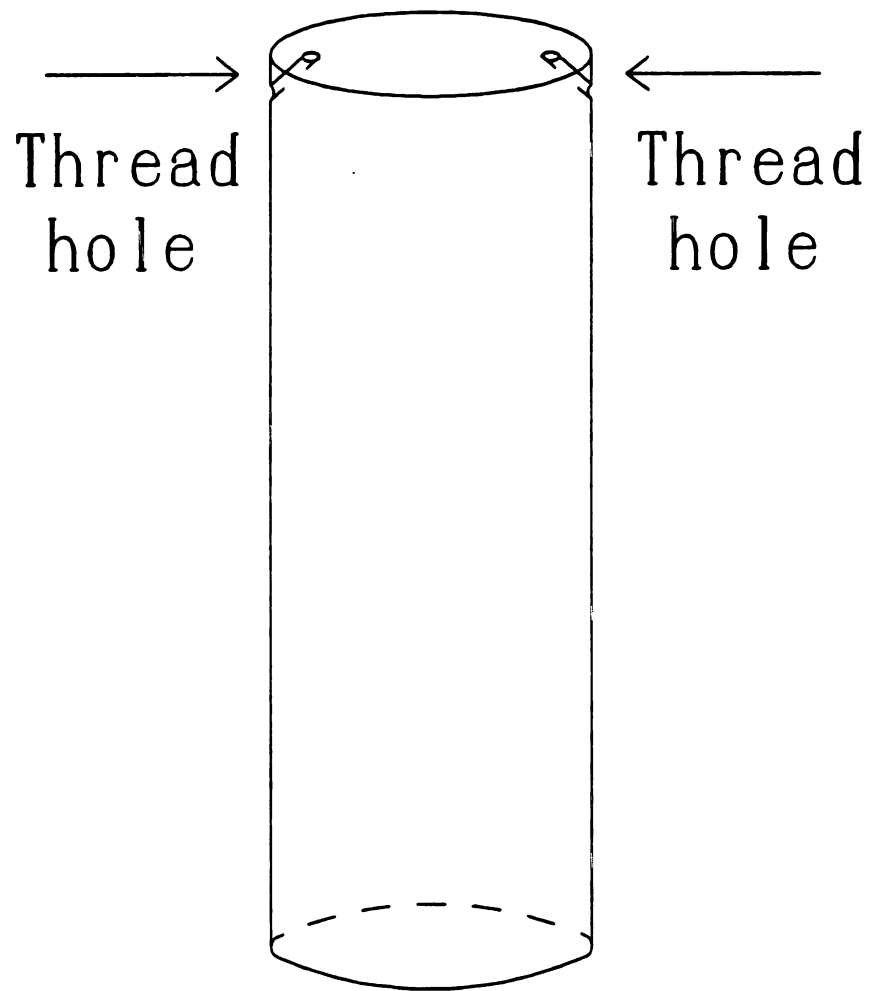
Figure 9-1 Load sample with holes for thread suspension.
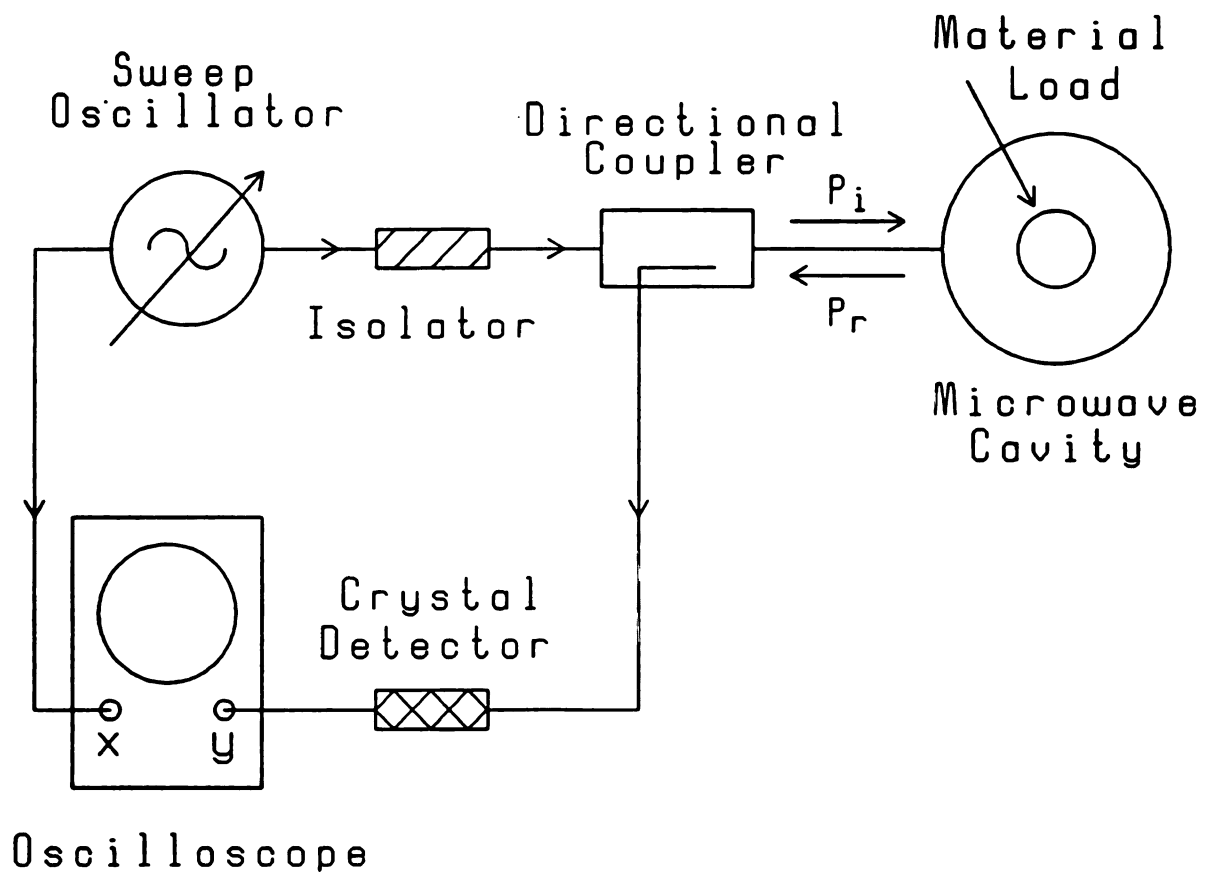
Figure 9-2 Microwave circuit for low power measurements of frequency and Q.

osc
Sin
exp

tak
exp
TN
in
obs
shi
wa
pla
pex
shi
5.
nov

sto
the
fre
dia
res
ep,
13
sa

se
co
sr

oscilloscope.[†] L_p was returned to its original setting and the sample was removed. Since the empty cavity resonant frequency tended to shift very slightly during the experiment, it was remeasured after each sample was removed.

Finally, it was necessary to shift the measured resonant frequencies and Q's to take into consideration non-idealities in the experimental cavity. For example, the experimental empty cavity eigenlength, L_s, is 15.648 cm at 2.45000 Ghz for the TM_{012} mode. For the same eigenlength the theoretical empty cavity should resonate in the TM_{012} mode at 2.43685 Ghz. In order for these to match, the experimentally obtained frequency must be shifted down by 13.15 Mhz. The justification for this shift is that non-idealities have been introduced into the experimental cavity, e.g., walls of finite conductivity, an excitation probe, finger stock around the top shorting plate, tiny holes in the cavity walls. The 13.15 Mhz shift accounts for the perturbation due to these non-ideal features of the experimental cavity. A similar shift was applied to the experimental measurements for the conducting load in Chapter 5. Since the degree of perturbation depends on the field patterns in the vicinity of the non-ideal features of the cavity, the shift is different for each mode.

If it can be assumed that the field patterns near the cavity walls, the finger stock, and the probe, etc., are not greatly altered by introducing the load sample into the cavity, then the same shift should be applied to the experimentally measured frequencies when the load sample is in place. For relatively small samples with low dielectric constants and loss factors this assumption is valid; in the experimental results that follow the experimental frequencies have been shifted down by approximately 13.15 Mhz for the TM_{012} mode. The precise shift, between 13.15 and 13.45 Mhz, was determined by the empty cavity resonant frequency measured after each successive sample was removed.

When the sample presents a large electromagnetic load, by virtue of large geometrical dimensions or dielectric properties, the above assumption regarding the continuity of the field pattern shapes is less legitimate. However, in such a case, the small perturbation of 13 or so MHz is insignificant in proportion to the overall

---

[†]See Section 8.2 of Chapter 8.

frequency shift due to the load itself. It may still be included or neglected without significantly affecting the accuracy of the measurement. Still, unless the field patterns are changed from the empty cavity fields so radically as to have switched regions of high H-field for regions of high E-field and vice-versa, a small frequency shift in the same direction as before is in order. Therefore, it is usually best to include the original frequency shift perturbation regardless of the load.

The same type of argument can be made for shifting the experimental measurements of cavity Q. The ideal empty cavity with perfectly conducting walls has a Q_o of ∞, where the subscript o indicates that the cavity is empty. Since the experimental cavity walls are made of brass, which has a finite conductivity, it's quality factor, Q_w, is finite. The subscript w indicates that the finiteness of this quality factor is due to the cavity *wall* conductivity. If the quantity E_s is defined as the energy stored in the empty cavity, and the quantity P_{dw} as the power dissipated in the cavity walls, Q_w is defined as

$$Q_w = \omega \frac{E_s}{P_{dw}}.$$ (9-9)

If P_{dm} is the power dissipated in the load material of the loaded cavity, the theoretical value for the quality factor in a perfectly conducting cavity, assuming that the stored energy is close to the energy stored in the empty cavity, may be approximated by

$$Q_m \approx \omega \frac{E_s}{P_{dm}}.$$ (9-10)

The actual measured value contains power losses in both the cavity walls and the load material, i.e.,

$$Q_e \approx \omega \frac{E_s}{P_{dw} + P_{do}},$$ (9-11)

where the subscript e refers to *experimentally* measured loaded cavity Q.

It is the quantity Q_m which we want to compare with the theoretical calculations. From Equations (9-9) through (9-11) it is evident that

$$\frac{1}{Q_m} \approx \frac{1}{Q_e} - \frac{1}{Q_w}, \tag{9-12}$$

or

$$Q_m \approx \frac{Q_w Q_e}{Q_w - Q_e}. \tag{9-13}$$

Having derived this expression, it is necessary to say that Equation (9-13) is a fairly rough approximation for Q_m since the energy dissipated in the cavity walls is less when the cavity contains a dielectric load which doesn't touch the walls than when the cavity is empty.[1] Subtracting off empty cavity wall losses is an over compensation for losses in the walls when the cavity is loaded. Therefore, the experimental Q_m as given by Equation (9-13) ought to be higher than the theoretical value of Q_m. It will be shown below that this is in fact the case.

9.4.2 Method I

The cavity-image type solution from the matrix defined by Equation (9-4) provides the theoretical curves in Figure 9-3. Experimental measurements were taken, as described above, for samples of lengths 1.03, 2.98, 4.07, 5.01, 7.61, 10.01, and 11.90 cm, cut from a 0.5" diameter rod of nylon 66. The cavity diameter was 6" and its length was 15.648 cm. The samples were inserted through a hole of diameter 0.531" in the top of the cavity and suspended at the cavity center by thin cotton thread. A measurement was also made for a sample which extended the entire cavity length, i.e., a cavity-short type configuration. The measurements on the shorter samples, the cavity-length sample, and the empty cavity all appear as crossed O's in Figure 9-3.

Figure 9-3 demonstrates that the theoretical solutions are very close to the measured values for sample lengths of 0 cm (empty cavity) and 15.648 cm (cavity-short type). Furthermore, the matrix determinant zero calculation method, i.e.,

---

[1] Zaki and Atia, 1040-41.
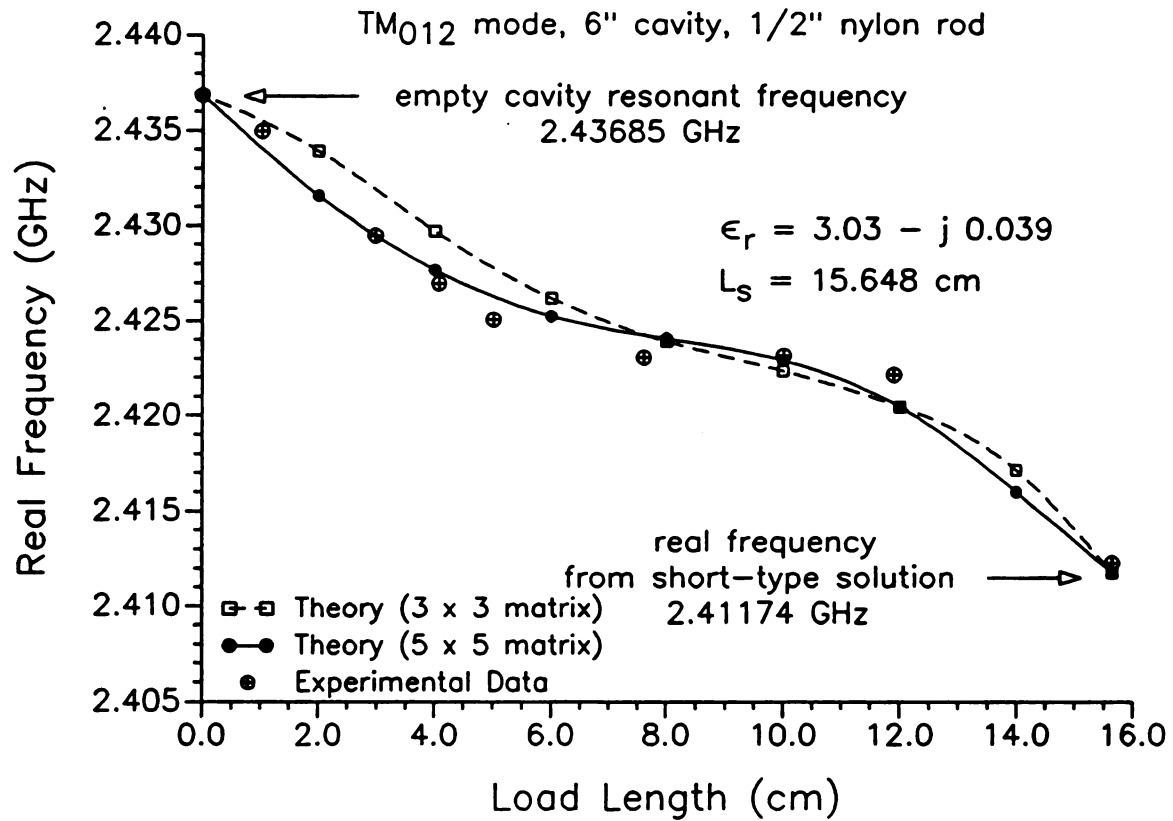
Figure 9-3 Real frequency vs. rod length: TM_{012} mode, 3×3 and 5×5 matrices.

cavity-image type solution, yields precisely the same theoretical value when $\ell = 0$ as the empty cavity theoretical solution, Equation (4-18). Similarly, for $\ell = L_s = 15.648$, the cavity-image type solution yields the same value as the cavity-short type solution, Equation (9-1) with the constraint of Equation (4-28). These values are given in Figure 9-3 to six significant digits.

As indicated in the Figure, the theoretical curves are for matrices truncated at 3×3 and 5×5. Since the actual theoretical solution requires a matrix of dimensions $\infty \times \infty$, if the determinant is uniformly convergent in the matrix dimension, the larger the matrix the better the solution should be. Examining only the 3×3 and 5×5 determinant zeros, initial indications are that that is the case here. The 5×5 solution appears to better fit the experimental data than the 3×3. In fact, if it could be shown that the larger matrix solutions converged to the solution shown here for the 5×5 matrix, we would say that the solution shows fair agreement with experiment. However, that is not the case.

Figure 9-4 shows what happens to the solution when the matrix size is increased to 7×7. The solutions match at both ends and at a point near $\ell = 9$ cm. As for points between, it is clear that the solution for the 7×7 matrix is straying away from the experimental data. This tendency becomes more pronounced as the matrix size increases. Figures 9-5 and 9-6 show what happens when the matrix size increases to 13×13. These Figures are for a 7" cavity which demonstrates nearly identical behavior to the 6" cavity of Figures 9-3 and 9-4. The larger the matrix, the more wild the curve becomes. This is typical behavior for a numerically unstable matrix.

Other factors indicate a problem with this solution as well. First of all, there are no determinant zeros in the vicinity of the true solution for evenly numbered matrix dimensions. Thence the odd-dimensioned matrices in Figures 9-3 through 9-6. There is no intrinsic reason why the truncation must occur only at odd dimensions for a solution to appear. This points to a numerical difficulty. Furthermore, the imaginary part of the frequency bears no semblance of correspondence to the experimental measurements. In fact, for small load lengths, the imaginary frequency
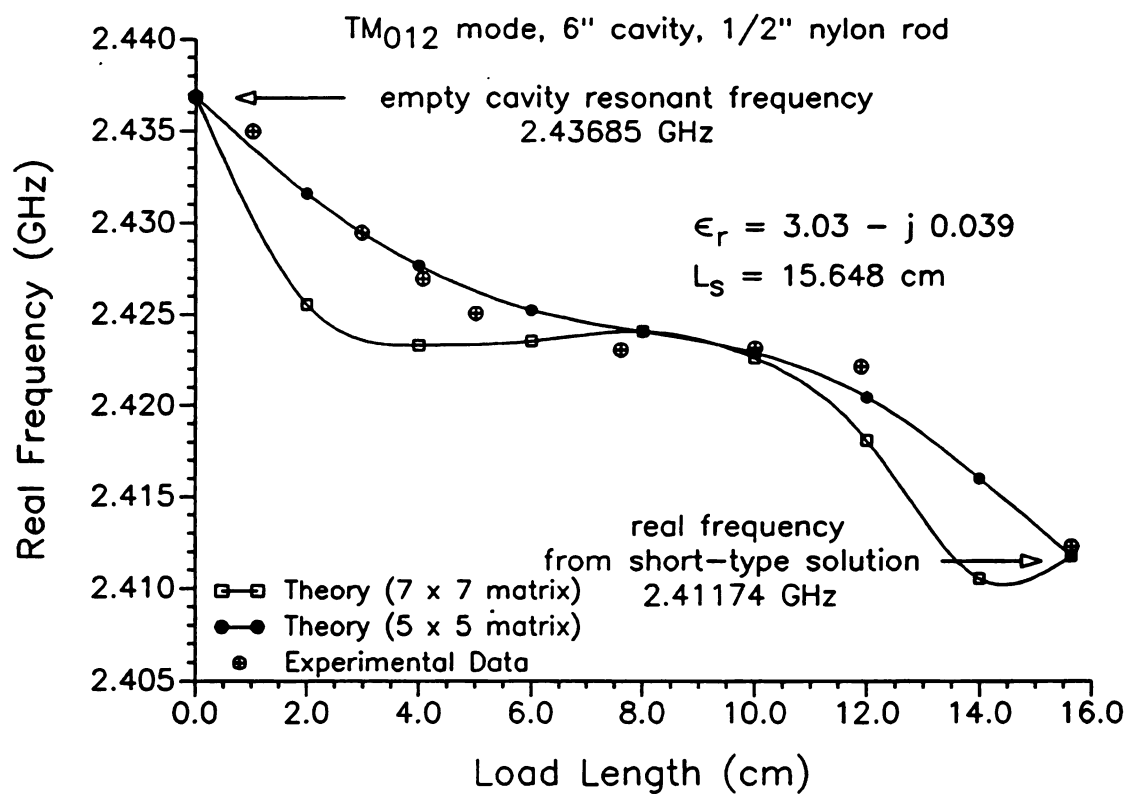
Figure 9-4 Real frequency vs. rod length: TM_{012} mode, 5 x 5 and 7 x 7 matrices.
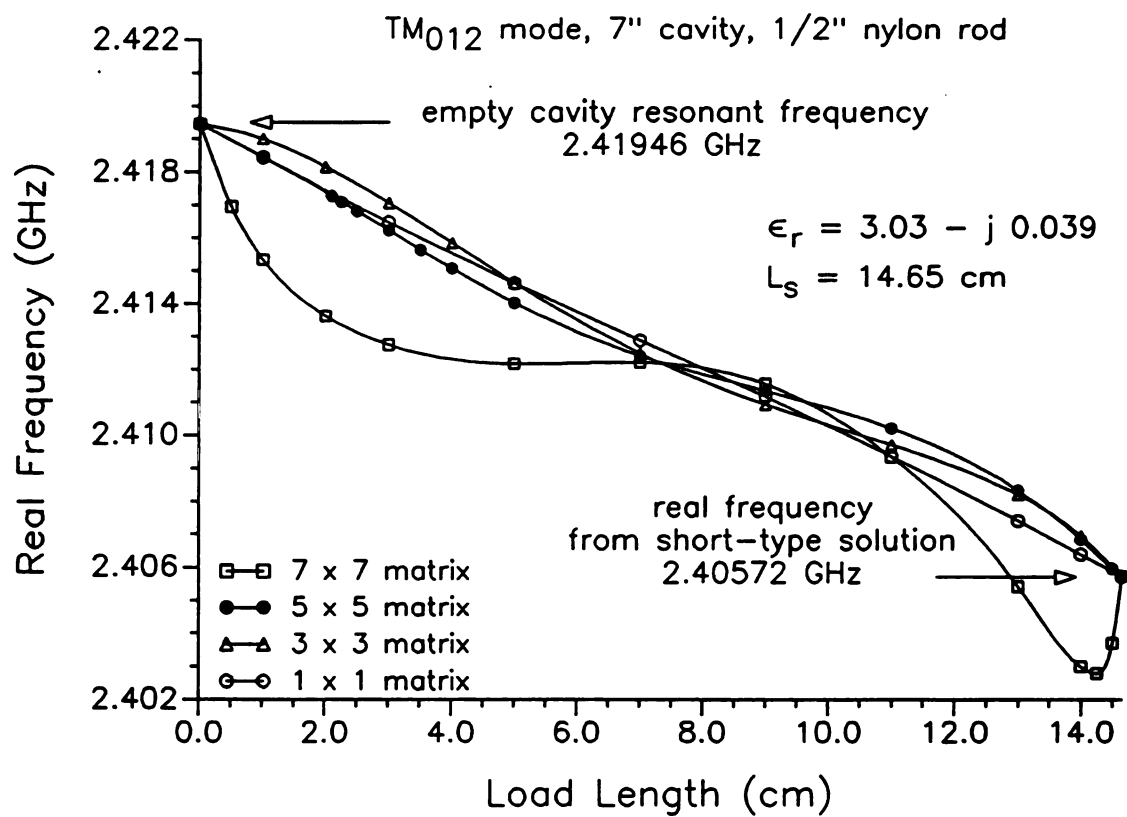
Figure 9-5 7" cavity, TM_{012} mode: 1 x 1, 3 x 3, 5 x 5, and 7 x 7 matrices.
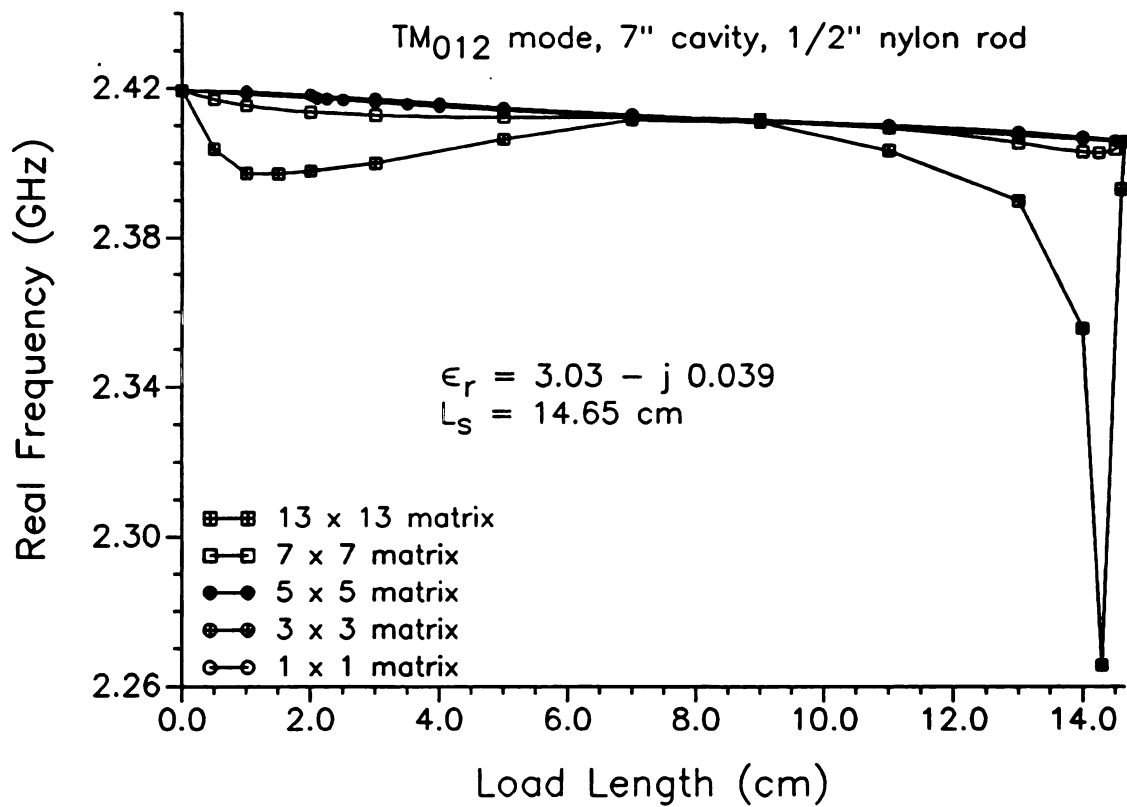
Figure 9-6 7" cavity, TM_{012} mode: 1 x 1, 3 x 3, 5 x 5, 7 x 7, and 13 x 13 matrices.

found by Method I is negative. As has been previously mentioned, negative imaginary frequency corresponds to non-physical, exponential growth of energy in time. That these problems are caused by insufficient numerical precision can be proved by examining the condition numbers of the matrices.

By definition, the condition number is the ratio of the largest to the smallest of the singular values of a matrix. It is a gauge by which to determine the numerical precision necessary to provide accurate results in calculations involving the matrix. A rough estimate of the necessary number of digits to carry is the order of magnitude of the condition number. A condition number of 10^6 indicates that at least 6 digits must be carried in the calculations. Therefore, the higher the condition number, the more digits necessary. Numerically unstable matrices have high condition numbers and are referred to as "ill-conditioned." Condition numbers were measured for 3×3, 5×5, and 7×7 matrices for the configuration of Figures 9-3 and 9-4 for a load length of 4 cm. The frequency was set to a real value of 2.43 GHz. Since an accurate measurement was desired from a presumably ill-conditioned matrix, 25 to 30 digits were carried in the calculations of the condition number. This was accomplished by using *Mathematica*,[2] a mathematical software package which, among its other capabilities, is able to perform arbitrary precision numerical calculations.

Looking at Figures 9-3 through 9-6, the point (4 cm, 2.43 GHz) does not coincide with a zero for any of the matrix sizes, yet is in the vicinity of zeros for all three. This is a good location at which to measure the condition number since the matrix is evaluated in this neighborhood during the zero-finding process. At the same time, a calculated zero is not chosen as a point at which to evaluate the condition number since the condition number is high, theoretically infinite, at a determinant zero. The condition number for the 3×3 matrix was 5.5×10^9. This is a remarkably high condition number for a 3×3 matrix, although manageable at 16 digits of precision. For the 5×5 matrix the condition number was 3.8×10^{16}, an increase of 7 orders of magnitude over the 3×3 case. Finally, the 7×7 matrix yielded a condition

---

number of 9.8×10^{25}. These numbers are rather amazing for such small matrices. They may provide outstanding examples of numerical instability to be referred to in the future by teachers of numerical mathematics, but in this context they indicate that the natural frequencies of the lossy, cavity-image type configuration are not to be found by Method I.

9.4.3 Method II

A solution based upon Method II was compared to the same experimental data presented above in Figures 9-3 and 9-4 for the Method I solution. For Method II, convergence to a solution involves not only the matrix size, as in the Method I solution, but also the number of terms to consider in the summations which make up each element. Three different cases are shown in Figure 9-7: The first is for a 5×5 matrix with 10 term summations, the second is for a 10×10 matrix with 20 term summations, and the third is for a 1×1 matrix considering only the first term of each summation. As shown in the Figure, the 5×5 and the 10×10 solutions are nearly the same. In addition, a 20×20 solution with 30 term summations, not shown in the Figure, was indistinguishable at the resolution of this plot from the 10×10 solution. This indicates that convergence has been achieved and a viable theoretical solution found for the cavity image-type configuration. The general convergence of these solutions is discussed more fully in the next section.

In Figure 9-7 all the solutions at $\ell = 0$ give the theoretical empty cavity resonant frequency value of 2.43685 GHz. For $\ell = L_s$, the solutions are near the real frequency result from the cavity-short type solution, but only the 10×10 solution matches it to the six digits indicated in the Figure. The 20×20 solution, not shown, also matches the cavity-short type solution to six digits.

The 1×1 matrix with one term per summation is plotted for comparison to demonstrate the effect of neglecting the higher order modes in the solution. Additionally, the 1×1 plot may be used to compare the Method II solution to the 5×5 matrix solution of Method I. It is a coincidence that, for the given cavity and
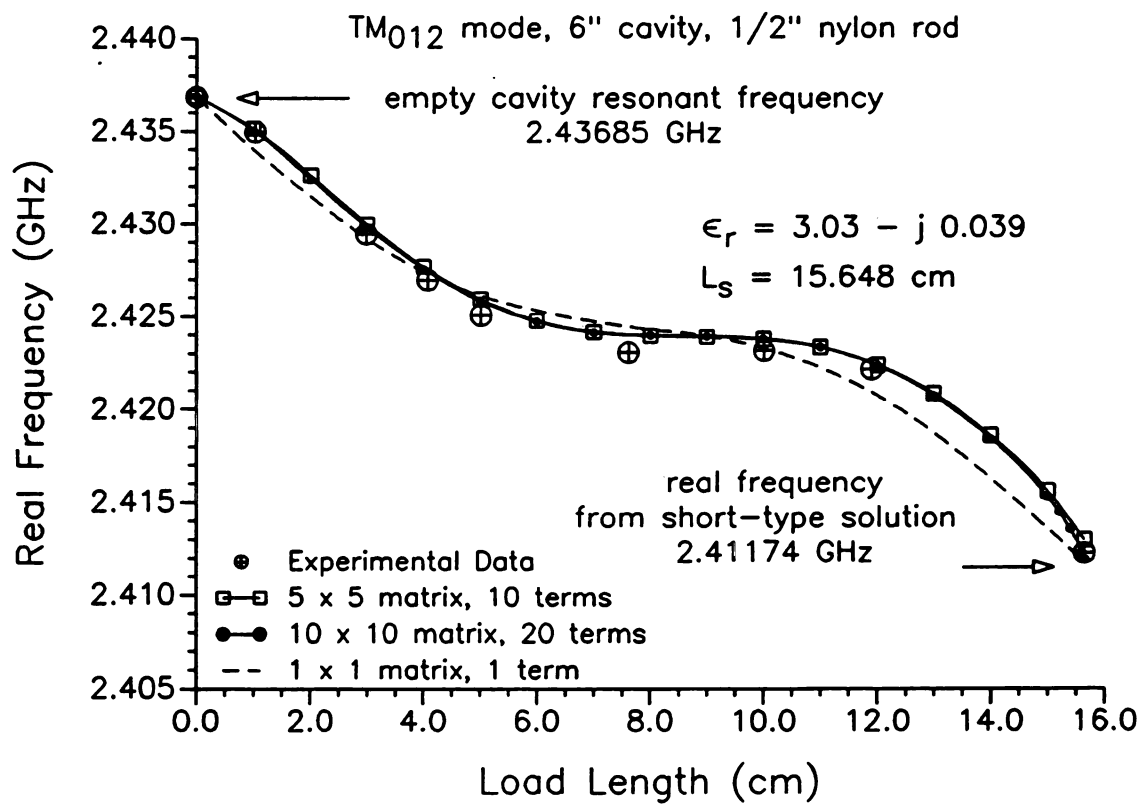
Figure 9-7 Real frequency vs. load length: Method II.

load parameters, the 1 x 1 matrix solution for Method II and the 5 x 5 matrix solution of Method I are practically identical.

The higher dimensioned solutions agree very well with the experimental data, especially for the smaller and the larger load lengths. In the range from 4 to 11 cm or so, the experimentally measured values are slightly below those calculated from the theory. The point farthest below its corresponding theoretical value was measured for a load length of 7.61 cm. There the experimental frequency is approximately 1.5 MHz below the theoretical value. It is possible that the 13 MHz downward shift in the experimental values, to account for cavity non-idealities, is not as good an approximation in this range of cavity load.

Figure 9-8 is a comparison between the Method II solution and a perturbation solution based upon a quasi-static approximation for the electric field inside the load. For this relatively small load the perturbation solution is not terribly different from the exact solution of Method II, even maintaining a reasonable degree of accuracy for the longer load lengths. This indicates that the assumptions of the perturbation solution, viz., that the fields inside the cavity and load are the closely approximated by the empty cavity fields, are valid.

Figure 9-9 demonstrates how the frequency changes when the load diameter is doubled from 0.5" to 1.0". Changes in the length of the load effect much greater changes in the real frequency for the 1.0" diameter load than for the 0.5" diameter load. A 20 x 20 matrix is used for the 1.0" load diameter solution since, in this load diameter range, larger load diameters require larger characteristic matrix sizes for convergence. Figure 9-10 shows the 1.0" diameter exact solution compared to a perturbation solution. While the agreement between perturbation and exact theories in Figures 9-8 and 9-10 may appear similar, the frequency scale in Figure 9-10 is broader and the discrepancies between perturbation theory and the exact solution are a great deal more in Figure 9-10 than in Figure 9-8. This indicates that the assumptions behind the perturbation theory are breaking down for the 1.0" diameter case.
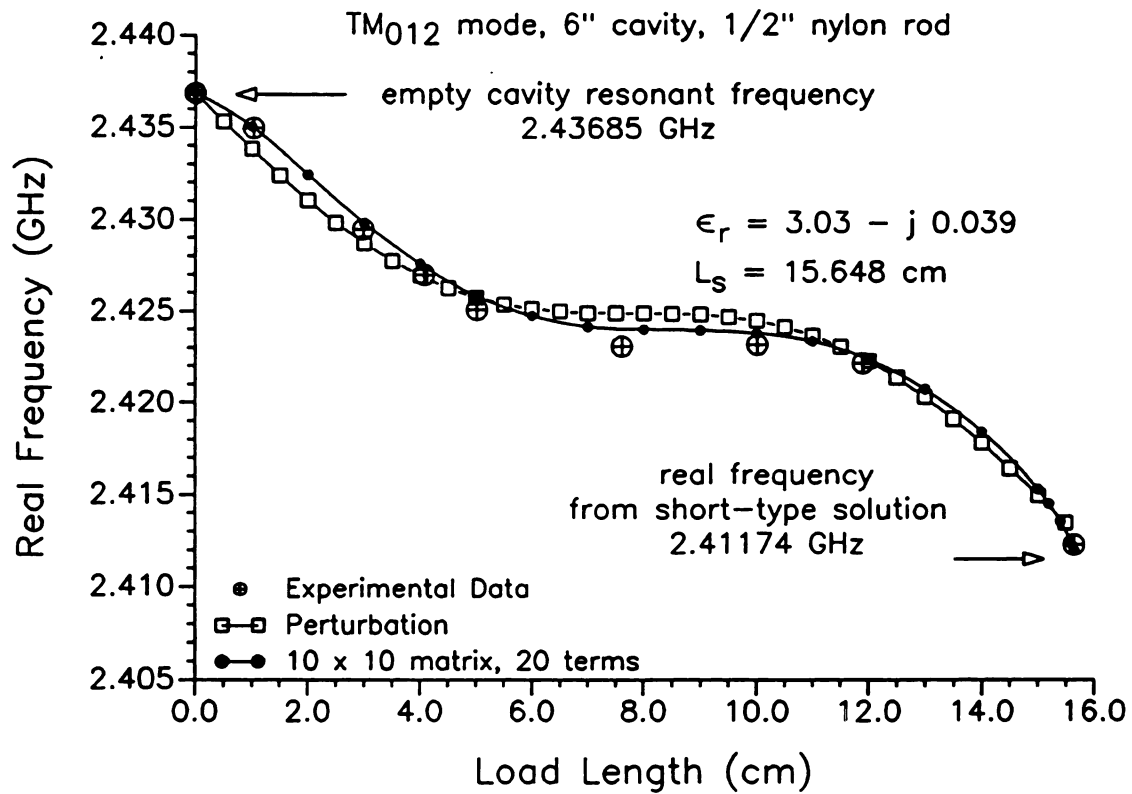
Figure 9-8 Method II compared with a perturbation solution.
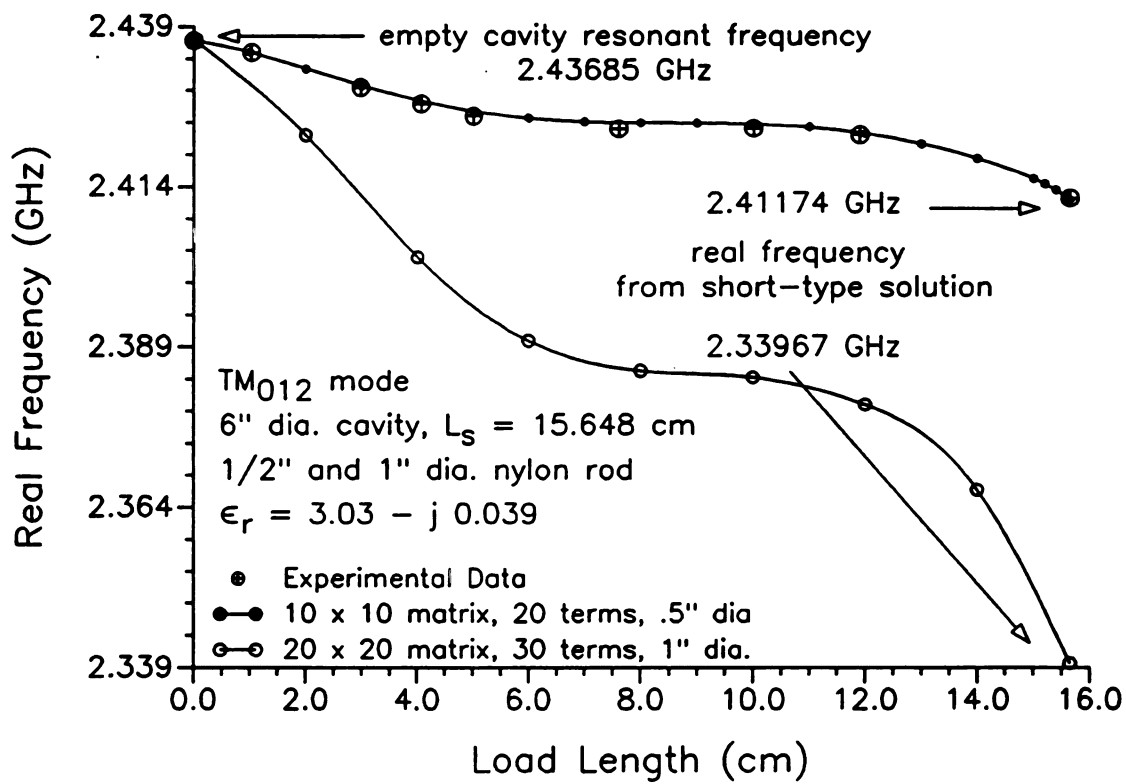
Figure 9-9 Real frequency vs. load length: $2a = 0.5''$ and $1.0''$.
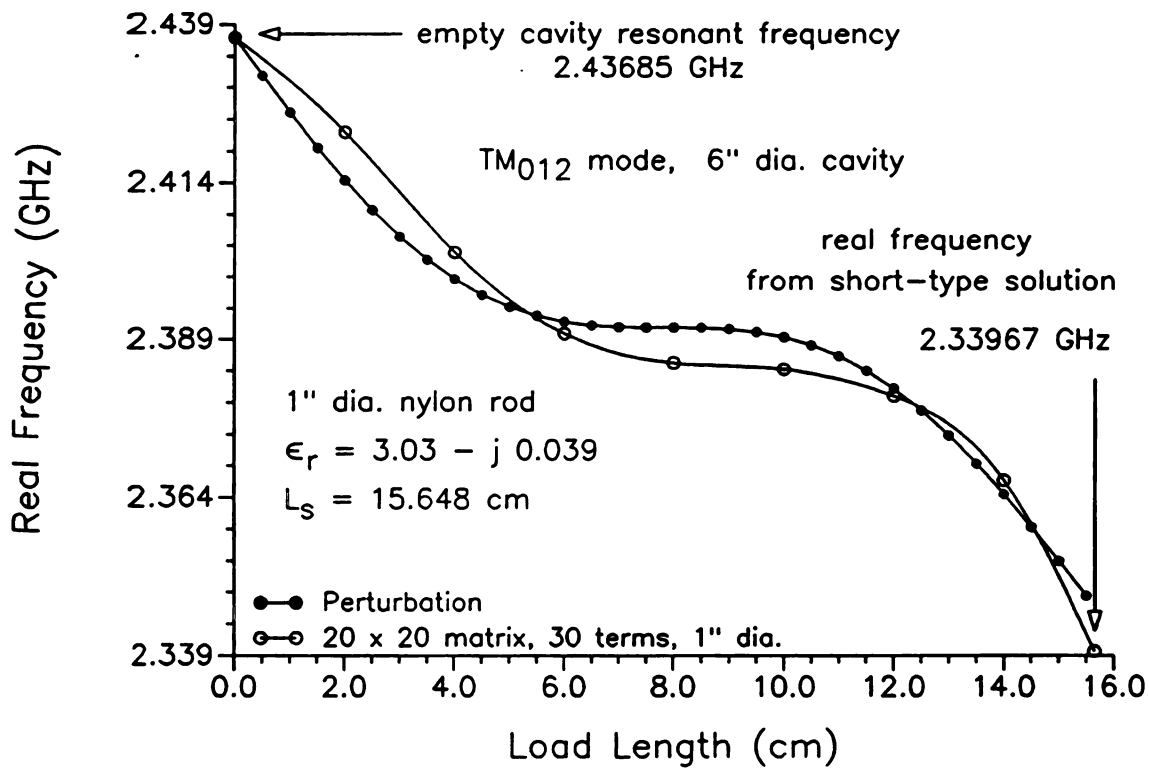
Figure 9-10 Real frequency vs. load length, $2a = 1.0$": Method II and perturbation.

exa

exac

the

solu

surf

is ro

norr

seen

load

cylin

here

devia

lesser

vary

All o

using

$a = 0$

the ca

comr

transc

charac

are giv

the cav

is simp

also be

cavity i

slab on

[3]Harr

It might be thought that the perturbation theory should at least agree with the exact solution when the load material is small, i.e., $\ell \approx 0$. This is true for $\ell = 0$ exactly, but for loads with small but non-zero ℓ, the perturbation solution strays from the exact solution. This is because one of the assumptions behind the perturbation solution shown in Figure 9-10 is that the electric field is primarily tangential to the surface of the load. This is a good assumption for longer load lengths when the load is rod-shaped, but for small load lengths the load is more like a disk with the fields normal to the flat surface. In fact, this explanation can be applied to the discrepancy seen in the 7 to 11 cm load length range of the plot. In this region the end of the load is passing through an area where the electric fields are perpendicular to the cylindrical surface of the load. The assumption of a tangential E-field breaks down here as well. Examining Figure 9-8 it may be observed that the same sort of deviations appear in the perturbation solution for the 0.5" diameter load, but on a lesser scale.

Figures 9-11 and 9-12 show how the real and imaginary parts of the frequency vary as a function of the load radius for a 4 cm long nylon load in the TM_{012} mode. All of the theoretical points shown, except those for $a = 0$ and $a = b$, were found using the Method II cavity image-type solutions. The empty cavity frequency for $a = 0$ is given by Equation (4-18) of Chapter 4. The $a = b$ solution corresponds to the case for a load filling the entire cross-section of the cavity. Such a load is commonly called a "slab." The characteristic equations for slab-loaded cavities are transcendental, but are fairly simple to solve numerically. Appendix F contains the characteristic equations for a slab-loaded cavity for both TE and TM modes. These are given for the general case where the slab is allowed to move up and down inside the cavity. When the slab lies on the bottom of the cavity the characteristic equation is simplified as shown in Appendix F. The simplified form for the special case may also be found in standard text books.[3] The point corresponding to the slab-loaded cavity in Figures 9-11 and 9-12 was found using the simple form for a 2 cm thick slab on the bottom of a 7.824 cm length cavity excited in the TM_{011} mode. The

---

[3]Harrington, 258.
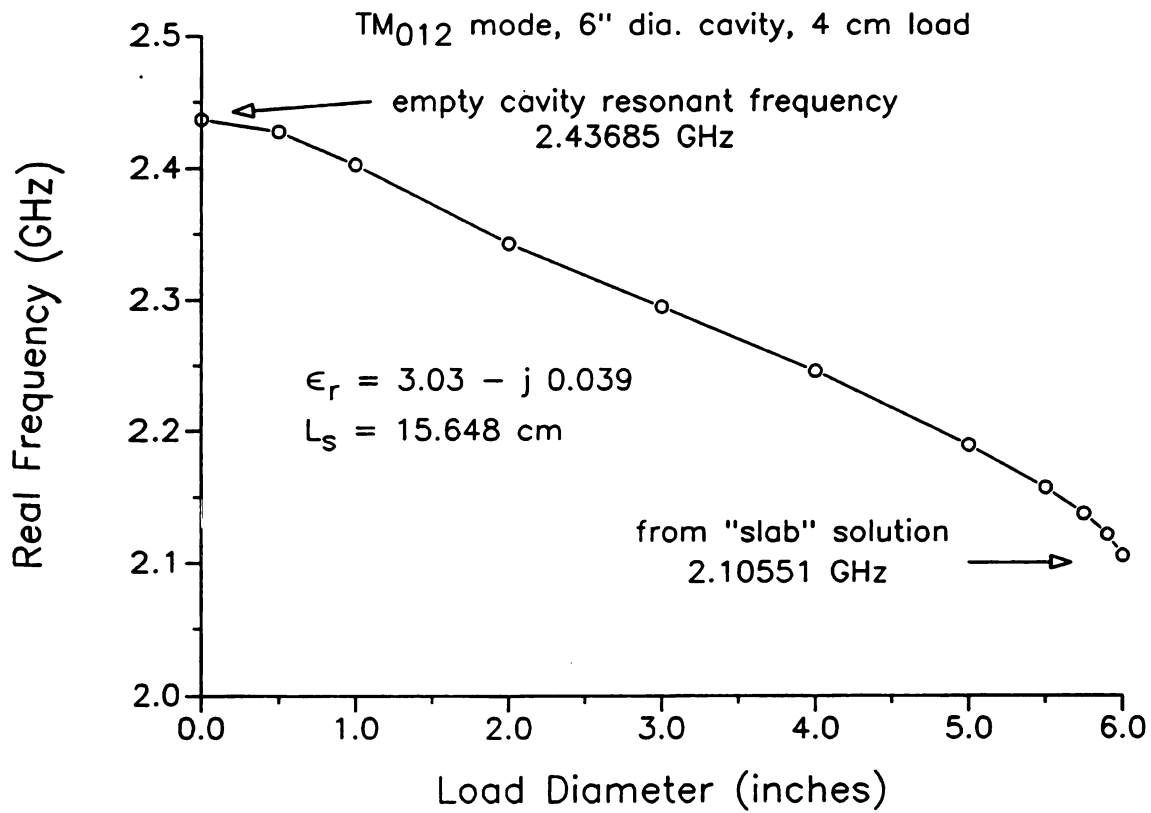
Real Frequency (GHz)

Figure 9-11 Real frequency vs. a for a nylon load: TM_{012}, $b = 3''$, $\ell = 4\,cm$.
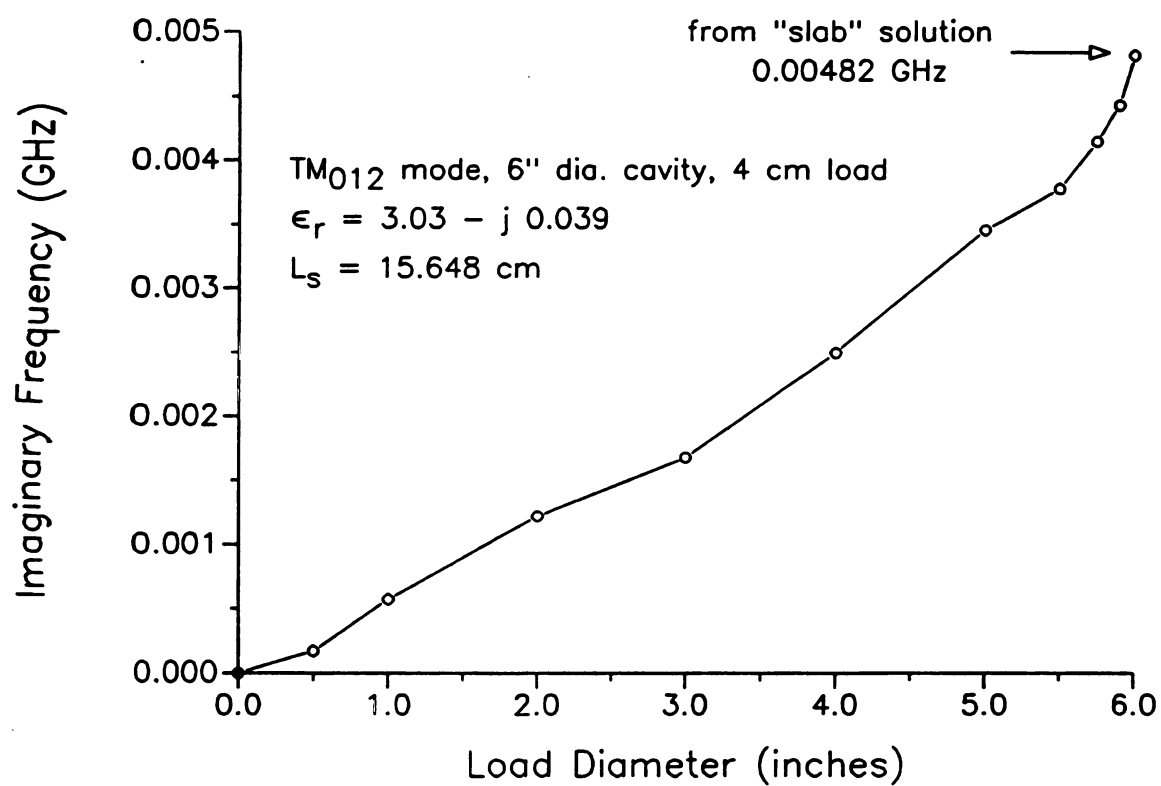
Figure 9-12 Imaginary frequency vs. a for a nylon load: TM_{012}, $b = 3"$, $\ell = 4$ cm.

resonant frequency is the same as that of a 15.648 cm length cavity centrally loaded with a slab 4 cm thick in the TM_{012} mode.

For the case shown, the real frequency drops almost linearly with load radius when the load radius is not near zero or is close to the cavity radius. The imaginary frequency is also nearly linear with the load radius until it approaches the cavity radius. Just as the load radius nears the cavity radius there is a drop in real frequency. This effect is reminiscent of the frequency drop which occurs in the conducting rod loaded cavity when the rod length nears the cavity length, referring to Figures 5-2 and 5-7. This affect, attributed to the increased capacitance between the load and the cavity wall, was also observed when the load material was a dielectric. This was discussed in Chapter 8 with regard to Figure 8-28.

9.4.4 Convergence

It is necessary at this point to answer the question of how many waveguide modes are needed to build a suitable representation of the actual electromagnetic field in the loaded cavity. Using Method II, the number of coaxially-loaded waveguide modes is equal to one of the dimensions of the square characteristic matrix. The number of empty waveguide modes is equal to the number of terms included in the summations. The same question may then be considered in terms of how large must the matrix be, and how many terms must be included in the summations. In framing the question in this way, i.e., in terms of number of modes instead of asking which particular modes, it is implied that the modes included begin at lowest order and are added successively according to their order.

The answer to the question depends upon how many significant digits are desired in the solution. If a crude approximation is all that is required, say two significant digits, only a few modes are needed. If it is necessary to have 4 or 5 significant digits, then more modes will have to be considered.

The minimum number of modes necessary to give the desired precision is not a number that may be easily predicted before numerical calculations are carried out. No attempt has been made to do so. Rather, the number is determined for a specific

α

m

n

si

n

th

ne

co

loa

the

lin

mi

N

c

a

w

ap

configuration by making several numerical calculations, each for different numbers of modes. The results are then compared to determine the point beyond which further numbers of modes do not change the answer to the desired precision.

Since there are two ways in which the number of modes may be varied, matrix size and number of terms in the summations, a study of the number of modes necessary for convergence could be complicated. It is further complicated by the fact that convergence also depends on the cavity and load parameters. A load which nearly extends to the ends of the cavity might require only a few modes from the coaxially-loaded region, but many modes from the empty regions. Similarly, a short load might require only a few modes from the empty regions, but many modes from the coaxially-loaded region. For the sake of simplicity, the brief study given here is limited to the case where an equal number of modes are taken from each region. The minimum number of modes necessary for convergence at a given precision is called N_{min}.

Figure 9-13 shows how N_{min} varies with load radius for the same cavity configuration as that shown in Figures 9-11 and 9-12. The load is composed of nylon and has a length of 4 cm. The cavity is 15.648 cm long, 6" in diameter, and is excited in the TM_{012} mode. The three curves in the Figure represent different numbers of significant digits in the convergence of the real part of the frequency. For example, a load diameter of 0.5" (0.0833 when normalized by the 6" cavity diameter) takes one mode in each region to give 3 significant digits in the real frequency, 2.43 GHz. For four significant digits, 2.427 GHz, three modes are required. Similarly, for five significant digits, 2.4275 GHz, it is necessary that nine modes be included.

Except for one point on the five significant digit curve, the general trend is for N_{min} to increase with load radius until the load nears the cavity wall. When the load radius approaches that of the cavity, N_{min} decreases. Qualitatively speaking, when the load is small the coaxially-loaded region is not much different from the empty waveguide region and the lowest order modes in each region provide a good approximation to the total field. The same is true when the load radius is near the
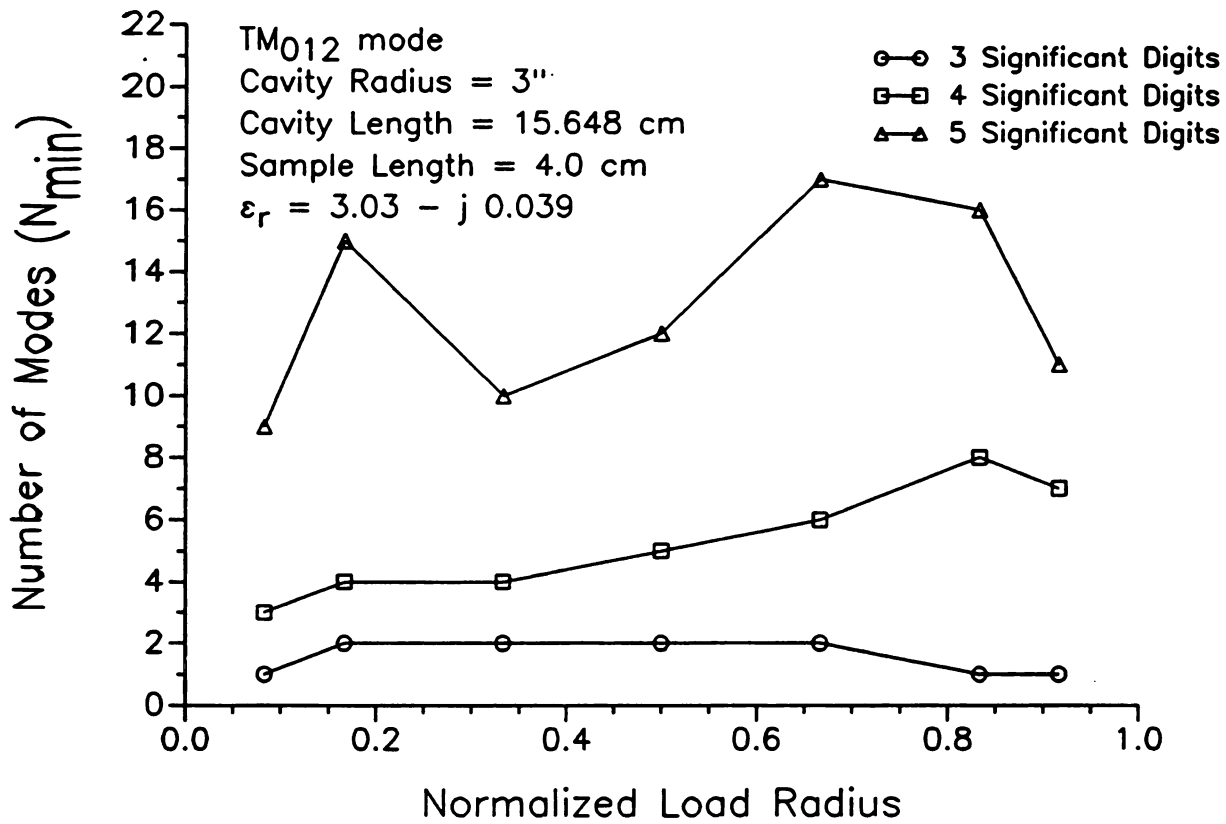
Figure 9-13 Imaginary frequency vs. a for a nylon load: TM_{012}, $b = 3''$, $\ell = 4$ cm.

cavity radius. In this case the cavity is approximately a slab-loaded cavity. For a slab-loaded cavity it may be shown that the modes from the empty and slab regions match by one-to-one correspondence. It would therefore be expected that N_{min} would decrease for a load radius near the cavity radius.

9.4.5 Cavity-Open Type Solutions: Varying h

As soon as the height of the load is allowed to vary from $L_s/2$, i.e., the sample moves up or down the cavity axis from the center, the cavity-image type configuration no longer describes the system. The general cavity-open type matrix must be used in the characteristic equation. For the TM modes ($n = 0$) the matrix is given by Equation (4-180) with the simplifications embodied in Equation (9-5). Numerically, the zeros of the determinant of this matrix are more elusive than those of the cavity-image type presented in Figures 9-7 through 9-10. Nevertheless, it is possible to find them and determine that convergence has been achieved.

A plot of the real frequency versus h is shown in Figure 9-14 for the TM_{012} mode in a 7" diameter cavity. The load is a 2 cm length piece of nylon rod 0.5" in diameter. The matrix size indicated in the Figure, 9×9, is the dimension of each quadrant, making the total matrix 18×18. Each matrix element was calculated using 20 terms in the summation. Since the TM_{012} mode is symmetric across the transverse plane which contains the cavity center, $z = L_s/2$, Figure 9-14 shows the frequency for only values of h in the upper region of the cavity. Frequencies are plotted for the load moving up the axis from the center of the cavity until the top of the load coincides with the top of the cavity. Since the load is 2 cm long, the final value of h is 1 cm less than L_s.

Included in the Figure are points representing experimental measurements taken in a 7" diameter cavity with a 2 cm long nylon load 0.5" in diameter. The 7" cavity, described by Manring,[4] contains more non-ideal features than the 6" cavity

---

[4]Edward B. Manring, "An Experimental Investigation of the Microwave Heating of Solid Non-Reactive Materials in a Circular Cylindrical Resonant Cavity" (M.S. thesis, Michigan State University, 1988), 23-27.
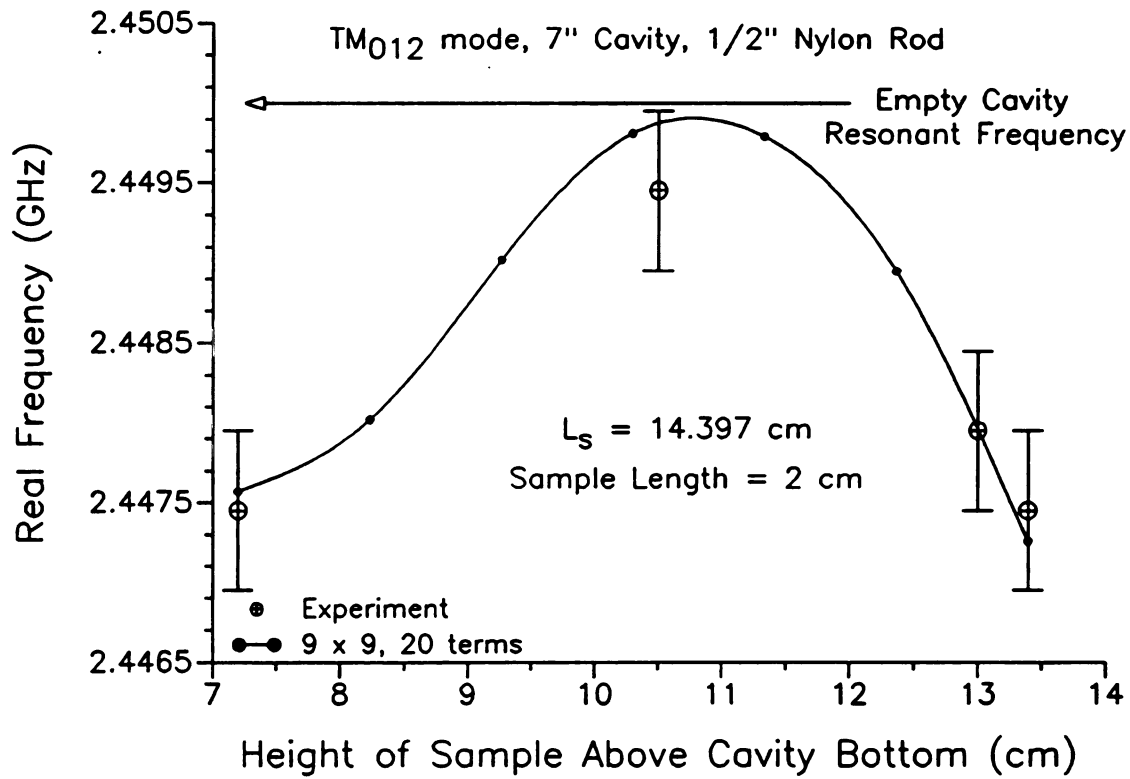
Figure 9-14 Real frequency vs. h: TM_{012}, $a = 0.25"$ (nylon), $b = 3.5"$, $\ell = 2\,cm$.

used to make measurements for the cavity-image type experiments presented above. These features are primarily a window in the side of cavity, a larger diameter excitation probe, and a larger hole in the moveable cavity short. For these reasons frequency error bars are placed on the data points to indicate an uncertainty for comparison with ideal cylindrical cavity calculations. Although the error bars appear large in the Figure, they are only ± 0.5 MHz in extent. The Figure demonstrates remarkable agreement between theory and experiment.

The horizontal arrow near the top Figure 9-14 indicates the value of the empty cavity resonant frequency for TM_{012} with the given L_s. As is evident by examining the curve, for h near 10.75 cm the loaded cavity real frequency is very near the empty cavity resonant frequency. This is due to the low electric field intensity of the TM_{012} mode in the vicinity of the load for this h. When the load is in a region of higher electric field intensity, e.g., at the center of the cavity or at either end, it affects the frequency much more than when it is in a region of low field intensity, e.g., half way between the cavity center and one end.

9.4.6 Quality Factor Calculations

The cavity Q may be calculated from the natural frequency in the same way as for the cavity-short type configuration, using Equation (6-18) or (8-2). The cavity Q's corresponding to the real frequencies of Figures 9-7 and 9-8 above are shown in Figure 9-15. The calculated Q's are for losses in the load material only and do not account for losses due to finite wall conductivity. Therefore the Q values become infinite as the volume of the material decreases to zero. Two sets of experimental points shown. One set, identified by crossed squares in the Figure, is calculated from measurements of Q_w and Q_e as described above and combined in Equation (9-13). As shown in the Figure, these values are higher than the theoretical values. The second set, identified by crossed circles in the Figure, are values of Q_e, direct experimental measurements of the Q of the loaded cavity. For this set of data no attempt has been made to compensate for the inclusion in the measurement of energy dissipation in the cavity walls, therefore they are lower than the theoretical values.
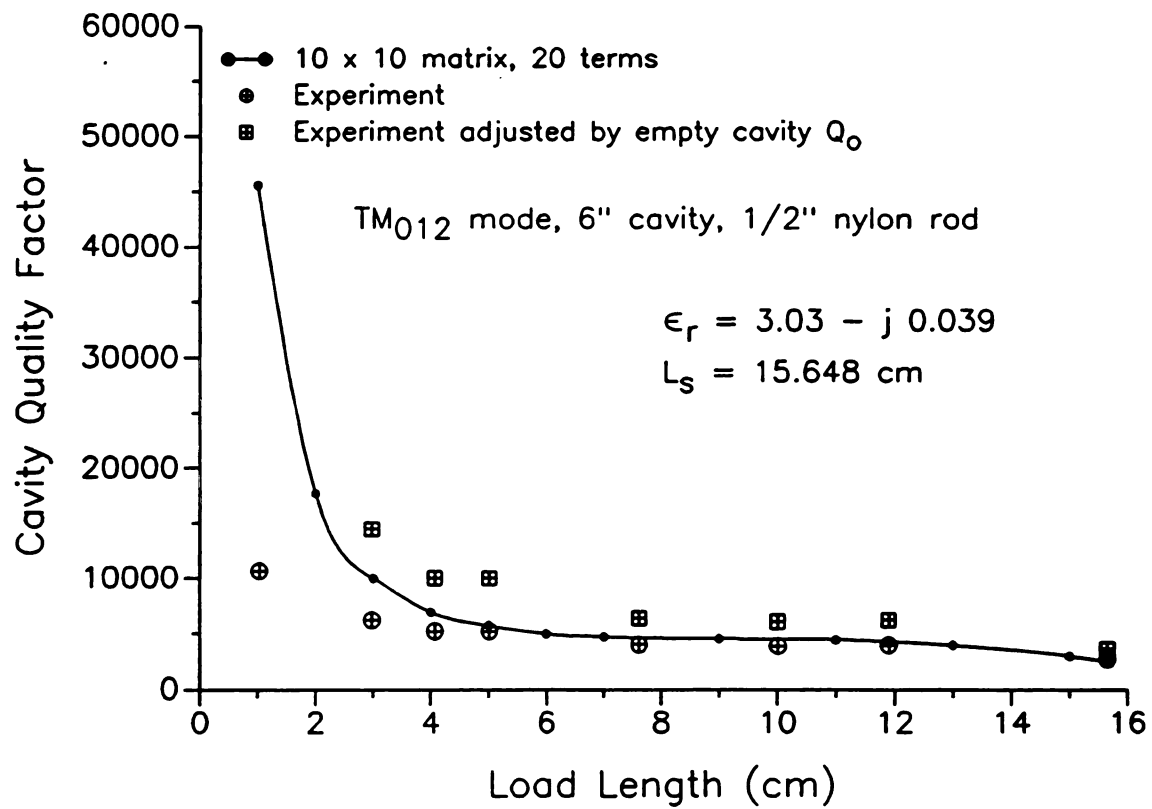
Figure 9-15 Quality factor vs. load length: TM_{012}, $a = 0.25"$ (nylon), $b = 3"$.

For the upper (adjusted) set of data, measured values are higher than the theoretical values by one to four thousand, the better agreement being for longer length loads. The discrepancy is significant, in the neighborhood of 25% to 40% of the theoretical value. Two reasons are put forth to explain the discrepancy. First of all, it is difficult to consistently measure cavity Q to within better than 10%.[†] This is especially true of high Q factors, e.g., for the empty cavity and small loads. Day to day changes in the conditions of the cavity, coupling probe, fit of the collars, and sliding short drive up the uncertainty in measurements of cavity Q. Since both the experimentally measured empty cavity quality factor, Q_w, and the experimentally measured material loaded quality factor, Q_e, are used to find Q_m, the contribution to Q due only to losses in the material with which our calculations are compared, the error in Q_m is compounded.

Secondly, the approximations and assumptions behind Equation (9-13), as mentioned above, are responsible for the greater part of the difference. There is no guarantee that the stored energy will be the same for the loaded and empty cavity; we know, in fact, that it will be somewhat different. Additionally, P_{dw}, the power dissipated in the walls, is different for the loaded cavity than for the empty cavity. Figure 9-15 demonstrates, at least in the case shown, that the adjustment procedure leading to Equation (9-13) actually makes the agreement between theory and experiment worse than if no adjustments were attempted. The unadjusted data, for load lengths greater than 4 cm, agrees reasonably well with the theory, to within less than 15%.

Although it may appear that Figure 9-15 paints a somewhat dismal picture of the ability of the theory to predict experimental Q values, in reality the opposite is true. The fact that the theoretical values fall between the adjusted and unadjusted measurement values is a pleasant verification of the validity of the theory. It has already been pointed out that subtracting empty cavity wall losses to account for loaded cavity wall losses is an over compensation and should result in an experimental

---

[†]The same is not true of frequency measurements which are consistently measurable to within a fraction of a percent.

Q that is too high. On the other hand, a measured Q that includes loaded cavity wall losses should be lower than a theoretical value which neglects wall losses. Both of these predictions are borne out in the Figure. Furthermore, when the load is larger and wall losses are proportionally less than material losses, the theory agrees very well with experimental values, adjusted or not. This is another verification of the validity of the theory since it only stands to reason that theoretical calculations which consider only material losses should agree better with experiments where material losses dominate than where wall losses dominate.

One way to improve on the theoretically calculated values of Q would be to include wall losses as a perturbation using the fields derived from the solution for lossless walls. The losses calculated from the perturbation of the loaded cavity solution, not the empty cavity wall losses, would then be used to calculate Q_w of Equation (9-9). This value would be substituted into Equation (9-13) to give a value of Q_m to be compared with the theoretical value given by Equation (6-18) or (8-2). Similarly, Q_m calculated from Equation (6-18) or (8-2) and the perturbation calculation of Q_w could be combined, as in Equation (9-12), to provide a theoretical value of Q_e. No attempt is made here to do this, but the suggestion is offered as a next step in improving on the theory.

As a final example of Q factor behavior, theoretical Q_m for the cavity and load configuration of Figure 9-14 is shown in Figure 9-16. The Q is lowest in regions of high electric field intensity, i.e., the center of the cavity and the ends. The peak value of Q is found in the region where the load passes through a region of low electric field. In this region the cavity hardly senses the presence of the load and accordingly its resonant frequency and Q are close to those of the empty cavity. Since the empty cavity for these calculations has an infinite Q, the high values are several orders of magnitude above the low values. The vertical axis of the plot in Figure 9-16 is therefore on a logarithmic scale.
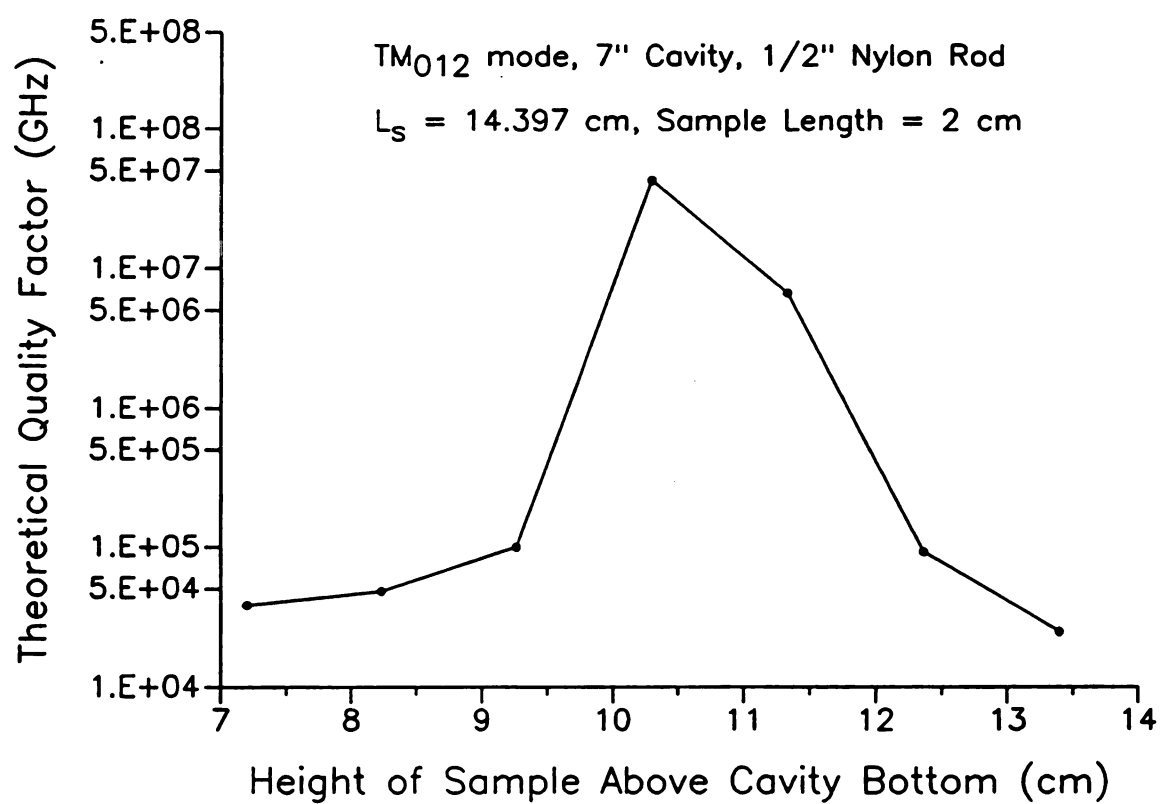
Figure 9-16 Quality factor vs. h: TM_{012}, $a = 0.25''$ (nylon), $b = 3.5''$, $l = 2$ cm.

9.5 Conclusion

Chapter 9 has demonstrated that the traditional mode-matching approach to solving for the eigenvalues of the cavity-open or cavity-image type loaded cavity configurations, called Method I in this dissertation, is numerically unstable. Method II, that chosen by Bolle for the conducting rod cavity-image type configuration, is numerically stable and has been shown to provide resonant frequency solutions which agree with experimental values to within 1.5 MHz (0.06%) or better for a 0.5" diameter nylon load in a 6" diameter cavity in the TM_{012} mode for load lengths of zero to cavity length. A cavity-open type solution was also presented for frequency as a function of the height of the load. Theory was compared with experiment for a 0.5" diameter nylon rod, 2 cm in length, in the TM_{012} mode of a 7" diameter cavity, agreeing to within less than 0.5 MHz.

Calculations of quality factor did not agree as well with experiment as frequency measurements due to losses in the cavity walls which were not accounted for by the theory. Nevertheless, it was shown that calculated values fall between the experimental values and experimental values adjusted by subtracting off wall losses approximated by the empty cavity case. Additionally, when the cavity was loaded with larger materials, and energy losses within the cavity were dominated by material losses, theoretically calculated Q's were very close to measured values.

In summary, a numerical solution for the cavity-open type and cavity-image type loaded cavity eigenvalues has been presented for lossy loads. This Chapter, in conjunction with Chapter 4, extends the scope of the current literature by a rigorous inclusion of losses in the load material.

Chapter 10
SUMMARY AND CONCLUSIONS

10.1 Introduction

As stated in Chapter 1, the purpose of the work presented here has been to present analytical and numerical solutions for the electromagnetic fields of coaxially-loaded cylindrical waveguides and cavities. These solutions were developed in order to provide fundamental information on waveguide and cavity fields, quality factors, and characteristic frequencies for application to microwave heating of lossy materials. The fields, quality factors, and resonant frequencies of a material loaded microwave cavity are highly dependent on both the shape and size of the confining boundary represented by the cavity walls, and the physical properties of the material inside. Therefore, a mathematical model is necessary to describe the electromagnetic behavior of the material loaded cavity or waveguide applicator.

Material loaded cavities have often been understood simply in terms of the empty cavity. Empty cavity solutions, since they have been known for many years, and since well-developed special functions, such as the Bessel functions, provide convenient means of expressing them, are simple. It is also true that inserting a material into an empty cavity does not always alter the field structure a great deal, or if it does, the alteration can be understood in terms of a perturbation from the empty cavity case. However, for materials of larger size and higher dielectric constant and loss factor (or conductivity), the fields and resonant frequency can be radically changed so that empty cavity analogies or perturbations are no longer meaningful. New models must be developed to describe these cases. To that end, natural mode solutions were developed for the cavity-short type, cavity-image type, and cavity-open type configurations, referring to Figures 1-2, 1-3, and 1-4, for homogeneous, isotropic, lossy dielectric loads.

337

10.2 The Coaxially-Loaded Waveguide

An element of all three cavity configurations was the coaxially-loaded waveguide, shown in Figure 1-1. A detailed analysis of field solutions in coaxially-loaded waveguides was presented in Chapter 3. It was demonstrated that boundary conditions at the surface of the load prevent the modes from being characterized as TE or TM except when there is no ϕ-dependence. In general, they are composed of a superposition of both TE and TM modes, thus acquiring the designation of hybrid. This analysis culminated in the characteristic equation for the wavenumbers, Equation (3-92), and expressions for the coefficients of the field components, Equations (3-96) through (3-99). These equations were used throughout the analysis and numerical solutions presented in the Chapters following.

For a pre-specified real frequency, numerical solutions to Equation (3-92) for complex values of the propagation wavenumber correspond to the modes of the coaxially-loaded waveguide. Chapter 7 was dedicated to presenting these types of numerical solutions. Also discussed in Chapter 7 was a method for labeling the hybrid modes. Several different methods for distinguishing the hybrid modes as TM-like or TE-like were discussed. The method of Bruno and Bridges, based upon a comparison of the ratio of E_z to H_z in the load region to the wave impedance of a plane wave traveling at the same phase velocity, was chosen, although it was recognized that the distinction is not always meaningful. When the distinction was employed, TM-like modes were called HE and TE-like modes were called HH. Otherwise the general label for the hybrid modes was HEM. The HE/HH system proposed in Chapter 7 to replace the HE/EH system makes it easier to remember which modes are TE-like and which are TM-like.

Numerical waveguide solutions were found by solving Equation (3-92) using a complex root-finding technique based on Müller's method. Even though the analytical expressions are fairly simple, at least compared to those for the cavity-image or cavity-open type configurations, this task required a great deal of effort and development of technique. Once the means of gathering solutions had been developed, however, it was possible to produce them quickly. With a good initial

guess, the points on a typical curve in the Figures of Chapter 7 could all be located within 10 seconds using an 80386 (25 MHz) based computer with a math coprocessor.

Numerical solutions for the coaxially-loaded waveguide were produced for TM, TE, and hybrid modes for both lossy and lossless materials. Complex mode regions were identified and examined for lossless loads with $\epsilon_r = 37.6$. These modes were discussed, explaining that although the wavenumbers of the complex modes are complex, they exist in coupled pairs such that no energy is propagated or dissipated by them. Radial wavenumbers for the same lossless loading were compared favorably with other published numerical results. For lossless loads it was shown that the cutoff frequency drops with increasing load radius, and that for large load diameters it also drops with increasing dielectric constant. For lossy materials, a highly damped backward wave region was discovered for the TM modes at very low frequencies. All modes appeared to be highly damped for low dielectric constant materials (~ 3) with relative loss factors of 0.5 or 1.0.

10.3 The Cavity-Short Type Configuration

Solutions for the cavity-short type configuration of Figure 1-3 were presented analytically in Chapter 4 and numerically in Chapter 8. Analytically, they are nearly identical to the waveguide solution, requiring only that γ, the axial wavenumber, be constrained to an integer multiple of π normalized by the cavity length, and that the field expressions be modified to reflect standing waves in the axial dependence. The characteristic equation is given by Equation (3-92) with a complex frequency.

The cavity-short type solution was compared with experimental frequency measurements of the TM_{012} mode with a 1" diameter nylon load in a 6" diameter cavity. Measurements were taken for a number of different cavity and load lengths. Resonant frequency measurements matched the real frequency of the theory to within 6 MHz (0.2%).

A large number of plots of cavity-short type numerical solutions were presented in Chapter 8 for TM, TE, and HEM modes, demonstrating the effects of varying load parameters. Increasing loss factors were shown to produce different

effects on the resonant frequency depending on the mode and range of the loss factor. For TM modes with loads of $\epsilon_r' = 3.03$ and low loss factors, an increase in loss factor produced a decrease in resonant frequency, while the frequency increased when the loss factor was greater than 30. For TE modes with $\epsilon_r' = 3.03$, an increasing loss factor always produced an increase in resonant frequency. It was shown that the cavity-short type configuration for very high loss factor loads approximates the perfectly conducting coaxial cavity both in resonant frequency and field structure. Plots of frequency and Q factor variations with load dielectric constant, ϵ', showed that a slight change in dielectric constant can shift a resonance from one mode to another without affecting the resonant frequency. It was also interesting to find that for certain dielectric constants, referring to Figure (8-23), loss factor plays no role in determining the real frequency.

Cavity-short type resonances were also studied as a function of load radius. It was shown that for low loss factors an empty cavity mode could be traced, as the load radius increased from zero, to the same material filled cavity mode in the limit as the load radius approached the cavity radius. These modes were called *radially traceable*. For lossless loads, all of the plots for TE and TM modes demonstrated radial traceability. For HEM modes, on the other hand, an example was presented to show that radial traceability was not assured even in the lossless case. Another example was presented to show that a non-ϕ-symmetric empty cavity TM mode may be traced to a material filled TE mode. Two other mode phenomena as a function of load radius were identified as *dielectric exclusion* and *dielectric confinement*. Both of these refer to high loss factor load modes which exhibit dramatic frequency increases as the load radius grows large (exclusion) or as it diminishes toward zero (confinement). Dielectric excluded modes are very low Q modes where, for larger load radii, the fields tend to be excluded from the dielectric and concentrated in the region between the load and the cavity walls. Dielectric confined modes are very low Q modes where, for smaller load radii, the fields tend to be confined to the load region.

10.4 The Cavity-Image and Cavity-Open Type Configurations

The chief contribution of the work presented here is the development of numerically stable analytical solutions for the fields of the cavity-image and cavity-open-type configurations, shown in Figures 1-2 and 1-4. Chapter 4 discusses two different approaches to constructing a characteristic equation for the complex natural frequencies of these configurations. The first approach follows the procedure found in the literature on the subject for lossless loads, using a mode expression from the empty waveguide region to orthogonalize both the E_{tan} and H_{tan} matching equations. In Chapter 9 this formulation is found to produce a highly ill-conditioned characteristic matrix and is unsuitable for numerical implementation. A second expression of the characteristic equation is developed using a mode from the empty waveguide region to orthogonalize one matching equation and a mode from the coaxially-loaded waveguide region to orthogonalize the other. This results in a very complicated expression for the characteristic matrix, which is, nonetheless, numerically stable.

Analytic solutions are presented for the general case. This includes HEM modes and variability in the height of the load above the cavity bottom. A specialization to the TM case, with numerical solutions for both characteristic equation approaches, is presented in Chapter 9. The numerical problem was much more complicated for the cavity-image and cavity-open type configurations than for either the cavity-short type configuration or the coaxially-loaded waveguide. The complex frequencies were roots of the determinant of an infinitely dimensioned characteristic matrix, which was truncated according to the number of elements necessary for convergence to a solution. These frequencies could not be located by conventional complex root-finding techniques so that a method based on separately mapping the roots of real and imaginary parts of the determinant had to be developed. This root-finding technique is described in Appendix E.

Plots of frequency versus load length were made using the characteristic equations from both analytical methods. Convergence could not be achieved with the first method due to numerical instability, i.e., round-off error. The second method,

however, demonstrated convergence for a 10×10 matrix in the TM_{012} mode when the load was composed of a 0.5" diameter nylon rod in a 6" diameter cavity. The numerical solution demonstrated excellent agreement with the experimental resonant frequency, showing a maximum difference of 1 MHz for a load length equal to half of the cavity length. For other load lengths the difference was even less. A cavity-open type solution was also plotted for a 0.5" diameter nylon load, 2 cm in length, for various heights within the cavity. Again, the empty cavity TM_{012} mode was used. Experimental frequency measurements were within 1.5 MHz of those calculated using the mode-matching theory.

Comparisons of the measured quality factor with the quality factor calculated from Equation (6-18) did not show as close agreement as the frequency comparisons. This was due to the finite conductivity of the cavity walls which was neglected in the model. The lossy material contribution to the experimentally measured Q could not be separated from the effect of the finite wall conductivity by a simple subtraction of the contribution that would be presented by the empty cavity walls. This is because the ratio of energy stored to power dissipated in the walls is higher in the loaded cavity than in the empty cavity, at least for low loss factor materials. In adjusting the experimentally measured values to account for wall losses, too much loss is subtracted if empty cavity wall losses are used to approximate the wall losses when the cavity is loaded. Using the empty cavity wall loss approximation, adjusted experimental values are much higher than calculated values. On the other hand, if wall losses are neglected altogether, experimental Q values are lower than those calculated considering material loss alone. Closer agreement for Q between theory and experiment is observed with larger loads since the material losses then dominate the wall losses.

10.5 Lossy, Material Filled Cavity and Conducting Rod Loaded Cavity Solutions

Solutions were also presented for two other cavity configurations. The first was for a simple, material-filled cavity, similar to the empty or free-space filled cavity. The difference between them is only that the dielectric filling the cavity was

allowed to be lossy, i.e., $\hat{\epsilon}$ is complex. This solution was provided as a simple example to show how the natural frequency of a cavity becomes complex in the presence of losses.

The second cavity configuration was similar to the cavity-image type configuration, except with a conducting rod for a load. An unsuccessful solution for TM modes in this configuration had been presented several years ago by D. M. Bolle. Chapter 5 presented a reworking of his solution which turned up the fact that the TEM mode contribution in the coaxial waveguide region had been neglected in Bolle's paper.[1] Reintroducing it produced solutions which showed excellent agreement with experiment for a complete range of load lengths from zero to cavity length. The solution showed that when the load length is very near the cavity length, the capacitance between the ends of the conducting rod and the cavity end plates dominates the frequency behavior, causing a sharp drop in resonant frequency just before the rod reaches the end of the cavity.

10.6 Relationship of Complex Natural Frequencies to Resonant Frequency and Q

Chapter 6 was devoted to explanation of the relationship between the complex natural frequencies, which were calculated as roots of the characteristic equations, and the resonant frequency and quality factor, Q, which are measured experimentally. Using an equivalent circuit analogy, it was shown that for Q's in excess of 50, the real part of the natural frequency could be identified with the resonant frequency and the Q could be determined by the ratio of the real part of the natural frequency to twice the imaginary part. Cavity-short type configuration solutions were plotted on the complex frequency plane, demonstrating the effect of varying loss factor on resonant frequency and Q.

10.7 Miscellaneous Theoretical Formulation Contributions

In the process of deriving various aspects of the models reviewed above, several formulations and procedures were developed or discovered which are worth

---

[1]Bolle.

mentioning in themselves. These are presented in some of the Appendices. One of these is the complex root-finding technique mentioned above. Another is found in Appendix A which contains a derivation of three previously unpublished indefinite Bessel function integrals and three Bessel function recurrence relationships. To make definite evaluation of the integrals simpler, expressions for limiting cases as the argument goes to zero or infinity were provided. Using these integrals in conjunction with other published indefinite integrals, two definite integrals displaying orthogonality were identified.

·Appendix B contains a discussion of mode orthogonality in isotropic, inhomogeneously loaded cylindrical waveguides of arbitrary cross section. It is well-known that the "energy orthogonality" relationships which are valid for homogeneously loaded waveguide modes do not hold in general for the inhomogeneous case, but that the "power orthogonality" relationships do. Appendix B showed that energy orthogonality is actually a special case of power orthogonality and that energy orthogonality expressions exist for purely TE or purely TM modes in an inhomogeneously loaded waveguide.

Appendix D is an attempt to define a time-average magnitude of the components of the natural fields. Since the natural fields decay with time, the time average over all time is zero. An additional difficulty is that the natural mode fields rotate in time in the presence of a lossy load boundary. A relative magnitude definition was given in Appendix D, based on the average magnitude during first half time period after the fields are excited. It was pointed out that the rotation of the natural mode fields may possibly be used to heat materials more uniformly or find applications in materials bonding. If this rotation is confined to the natural mode fields, i.e., it does not exist in the sinusoidal steady state, it could be exploited by rapidly pulsing energy into the cavity. The frequency of the pulse would have to be on the order of the frequency of the excitation in order to deliver an appreciable amount of energy to the load, prompting the designation of *extremely rapid pulse* (ERP) to the process.

A final contribution to the theory of loaded cylindrical cavities was included in Appendix F. A characteristic equation was derived for the slab-loaded cavity when the slab is not confined to one end of the cavity. The slab-loaded cavity can be considered to be the radial counterpart of the cavity-short type configuration. In the cavity-short type configuration the cavity and load have the same length. In the slab-loaded cavity the cavity and load have the same radius. Solutions for the slab-loaded cavity are useful for checking cavity-open type solutions for large load radii.

10.8 Application of Theory to Materials Heating Processes

At the end of Chapter 8 it was pointed out that material loaded cavities exhibit diverse behavior when the properties of the load change. Empty cavity fields or perturbations from the empty cavity solutions do not always provide good approximations of the material and field interaction. In such cases, solutions like the ones presented here are very useful in determining which modes are best for heating different kinds and shapes of materials. A mode that is useful for heating a low loss filament in the cavity-short type configuration may not be good for heating a short rod or wafer located in the center of the cavity. Given two loads of the same shape, one mode may be better than another depending on the dielectric constant or loss factor of the materials. The cavity-open type solution may be used to find the optimum height above the cavity bottom and the best mode for heating semi-conducting wafers or slabs of material.

Once the mode and position of the load are chosen, the theory may be used to predict resonant frequency and Q changes that occur as the material properties change during heating. Inversely, changes in resonant frequency and Q may be used to determine how dielectric properties and material shape are being modified by the heating process.[2] The theory may similarly be used to diagnose the properties of homogeneous, isotropic plasmas contained in the cavity.

Conducting rod solutions from Chapter 5 can be good approximations for semi-conducting loads or for loads with very high loss factors. They may also be

---

[2]Asmussen, Lin, Manring, and Fritz.

used to model reentrant cavity applications, including materials processing by placing materials between the end of the conducting rod and the cavity end plate. The high capacitance between the end of the rod and the cavity end plate for thin gaps may be exploited for uniform, localized heating of materials located in that region.

Whatever the application, whether it be heating of materials, plasma diagnosis, dielectric constant measurement, or reentrant cavity design, knowledge of the resonant frequency, quality factor, and field structure for the various modes is foundational. While a certain amount of this information may be gathered experimentally or by perturbation theory, a rigorous mathematical model explains behaviors, sheds new light, and demonstrates new possibilities that are not discernable otherwise.

10.9 Suggestions for Further Research

Despite the large amount of research that has been expended on coaxially-loaded waveguide and cavity systems, there is still much work to do even for homogeneous, isotropic load materials. Much effort could be put into finding solutions for new materials alone. Adding more layers to the load only increases the possibilities for finding interesting solutions. More specific to the solutions presented here is the need of a more detailed numerical study of the lossy load cavity-open type configuration, with more numerical solutions for the TM modes, and numerical solutions for the TE and HEM modes. Neither have solutions been reported for TE or non-ϕ-symmetric TM modes in the conducting rod loaded cavity.

To better represent experimental conditions, these solutions could be improved by including wall losses in the theory. The easiest way to do this would probably be to calculate wall losses as a perturbation from the perfectly conducting cavity case, using the fields calculated by the mode-matching theory. Closer approximation to experimental conditions would also be achieved by allowing for inhomogeneous and anisotropic material loads, and including sources, i.e., coupling probes, loops, or irises.

It would also be interesting to investigate whether or not the sinusoidal steady state fields rotate in the presence of a lossy material boundary as the natural mode

fields do. If not, plots of field rotation ellipses could be compared with ERP materials heating experiments to see if there is a correlation between the field rotation and more uniform heating of the materials.

More sophisticated numerical solutions would account for time-dependent changes in material temperature and its subsequent effect on material properties. This would involve a simultaneous solution of energy balance equations with Maxwell's equations. A solution of this type has already been presented for plasma loads in the TM_{010} mode in the cavity-short type configuration,[3] however, in practice many microwave cavity plasmas are excited by other modes and do not extend the entire cavity length. Both cavity-short and cavity-open type solutions, coupled with energy balance, would be useful in describing microwave plasma and ceramic sintering processes.

---

[3] Offermanns, "Electrodeless High-Pressure Microwave Discharges."

APPENDICES

Appendix A

INTEGRALS AND RECURRENCE RELATIONSHIPS USED IN CIRCULAR CYLINDRICAL ORTHOGONALITY INTEGRATION AND ENERGY CALCULATIONS

A.1 Introduction

Often in the solution of electromagnetics problems in cylindrical coordinates, combinations of Bessel functions are encountered in indefinite integrals or elsewhere. Examples are orthogonalization integrals of modal expansions for matching fields across discontinuities, calculation of power dissipated and energy stored in cylindrical waveguides and cavities, or similar calculations for cylindrical dielectric waveguides.[1] While there are tabulated solutions to certain of these integrals, some cannot be found in common references.[2] Three previously untabulated integrals are derived and presented here.

This appendix contains a tabulation of several of these uncommon integral and recurrence identities. While some of the identities below are not necessary for calculations involved in the solutions presented in this dissertation, particularly those involving modified Bessel functions, they are closely related to those which are. It was thought convenient to include them here for the benefit of those working on related problems.

A.2 Indefinite Integrals

Given F_ν and G_ν such that

---

[1]Darko Kajfez, "Indefinite Integrals Useful in the Analysis of Cylindrical Dielectric Resonators," *IEEE Trans. Microwave Thry. Tech.*, MTT-35 (9) (Sep. 1987): 873-74.

[2]Milton Abramowitz and Irene Stegun, *Handbook of Mathematical Functions* (New York: Dover Publications, n.d.): 479-94; I. S. Gradshteyn and I. M. Ryzhik, *Table of Integrals, Series, and Products* (San Diego: Academic Press, 1980): 633-34.

$$F_\nu(\alpha z) = A\,J_\nu(\alpha z) + B\,Y_\nu(\alpha z), \qquad F'_\nu(\alpha z) = A\,J'_\nu(\alpha z) + B\,Y'_\nu(\alpha z),$$

$$G_\nu(\beta z) = C\,J_\nu(\beta z) + D\,Y_\nu(\beta z), \qquad G'_\nu(\beta z) = C\,J'_\nu(\beta z) + D\,Y'_\nu(\beta z), \qquad \text{(A-1)}$$

where J_ν and Y_ν are ordinary Bessel functions with complex arguments and ν is an arbitrary complex constant, it is possible to show that

$$\int \left[F'_\nu(\alpha z)\,G'_\nu(\beta z) + \frac{\nu^2}{\alpha\beta z^2} F_\nu(\alpha z)\,G_\nu(\beta z) \right] z\,dz$$

$$\qquad\qquad\qquad\qquad\qquad\qquad\qquad\qquad \alpha \neq \beta \qquad \text{(A-2)}$$

$$= \frac{z}{\alpha^2 - \beta^2} \left[\alpha\,F_\nu(\alpha z)\,G'_\nu(\beta z) - \beta\,F'_\nu(\alpha z)\,G_\nu(\beta z) \right].$$

Since the Hankel functions $H_\nu^{(1)}$ and $H_\nu^{(2)}$ are linear combinations of J_ν and Y_ν, Equation (A-2) is also true if F_ν and G_ν contain linear combinations of Hankel functions. The integral may be checked by differentiating the right hand side and showing that it is equal to the integrand.

In order to perform the differentiation, it is necessary to have an expression for the second derivatives of F_ν and G_ν. These are found by examining the differential equation defining ordinary Bessel functions,

$$z^2 \frac{d^2 w}{dz^2} + z \frac{dw}{dz} + (z^2 - \nu^2) w = 0. \qquad \text{(A-3)}$$

The same integral relationship as is contained in Equation (A-2) may be derived for modified Bessel functions. Given L_ν and M_ν such that

$$L_\nu(\alpha z) = P\,I_\nu(\alpha z) + Q\,K_\nu(\alpha z), \qquad L'_\nu(\alpha z) = P\,I'_\nu(\alpha z) + Q\,K'_\nu(\alpha z),$$

$$M_\nu(\beta z) = R\,I_\nu(\beta z) + S\,K_\nu(\beta z), \qquad M'_\nu(\beta z) = R\,I'_\nu(\beta z) + S\,K'_\nu(\beta z), \qquad \text{(A-4)}$$

where I_ν and K_ν are modified Bessel functions, it may be shown that

$$\int [L_\nu'(\alpha z) M_\nu'(\beta z) + \frac{\nu^2}{\alpha\beta z^2} L_\nu(\alpha z) M_\nu(\beta z)] z\, dz$$

$$= \frac{z}{\alpha^2 - \beta^2} [\alpha L_\nu(\alpha z) M_\nu'(\beta z) - \beta L_\nu'(\alpha z) M_\nu(\beta z)].$$

$$\alpha \neq \beta \qquad \text{(A-5)}$$

Equation (A-5) is true for K_ν and $e^{j\pi\nu} K_\nu$ formulations of the modified Bessel function of the second kind, using the notation of Abramowitz and Stegun.[3] This integral is identical to the one given above for ordinary Bessel functions and can be checked by differentiation using the general differential equation for the modified Bessel functions,

$$z^2 \frac{d^2 w}{dz^2} + z \frac{dw}{dz} - (z^2 + \nu^2) w = 0. \qquad \text{(A-6)}$$

When ordinary and modified Bessel functions are combined in the form found in the integrals of Equations (A-2) and (A-5), the integral is different. Using the previously defined functions F_ν and M_ν, the following integral relationship may be established,

$$\int [F_\nu'(\alpha z) M_\nu'(\beta z) + \frac{\nu^2}{\alpha\beta z^2} F_\nu(\alpha z) M_\nu(\beta z)] z\, dz$$

$$= \frac{z}{\alpha^2 + \beta^2} [\alpha F_\nu(\alpha z) M_\nu'(\beta z) + \beta F_\nu'(\alpha z) M_\nu(\beta z)]. \qquad \text{(A-7)}$$

This relationship is true for linear combinations of the modified Bessel functions I_ν, K_ν, and $e^{j\pi\nu} K_\nu$, and for the ordinary Bessel functions including Hankel functions.

The integrals of Equations (A-2) and (A-5) are valid for $F_\nu = G_\nu$ and $L_\nu = M_\nu$, but in general it is necessary that α and β be different. For the case where $\alpha = \beta$, a

---

[3] Abramowitz and Stegun, 358.

solution does exist when the functions are identical. Integrals for the case $\alpha = \beta$ with $F_\nu = G_\nu$ for ordinary Bessel functions, and $\alpha = \beta$ with $L_\nu = M_\nu$ for modified Bessel functions, are given by Kajfez and are repeated here:[4]

$$\int \, [F_\nu'^2(\alpha z) \, + \, \frac{\nu^2}{\alpha^2 z^2} \, F_\nu^2(\alpha z)] \, z \, dz$$

$$= \frac{z^2}{2} \, [F_\nu'^2(\alpha z) \, + \, F_\nu^2(\alpha z) \, (1 \, - \, \frac{\nu^2}{\alpha^2 z^2}) \, + \, \frac{2}{\alpha z} \, F_\nu(\alpha z) \, F_\nu'(\alpha z)] \, ,$$

(A-8)

$$\int \, [L_\nu'^2(\alpha z) \, + \, \frac{\nu^2}{\alpha^2 z^2} \, L_\nu^2(\alpha z)] \, z \, dz$$

$$= \frac{z^2}{2} \, [L_\nu'^2(\alpha z) \, - \, L_\nu^2(\alpha z) \, (1 \, + \, \frac{\nu^2}{\alpha^2 z^2}) \, + \, \frac{2}{\alpha z} \, L_\nu(\alpha z) \, L_\nu'(\alpha z)] \, .$$

(A-9)

A.3 Recurrence Identities

The above integrals, as noted, may be checked by differentiation. However, derivation of them proceeds from the following identities,

$$F_\nu'(\alpha z) \, G_\nu'(\beta z) \, \pm \, \frac{\nu^2}{\alpha \beta z^2} \, F_\nu(\alpha z) \, G_\nu(\beta z)$$

$$= \pm \frac{1}{2} \, [F_{\nu-1}(\alpha z) \, G_{\nu \mp 1}(\beta z) \, + \, F_{\nu+1}(\alpha z) \, G_{\nu \pm 1}(\beta z)] \, ,$$

(A-10)

$$L_\nu'(\alpha z) \, M_\nu'(\beta z) \, \pm \, \frac{\nu^2}{\alpha \beta z^2} \, L_\nu(\alpha z) \, M_\nu(\beta z)$$

$$= \frac{1}{2} \, [L_{\nu-1}(\alpha z) \, M_{\nu \mp 1}(\beta z) \, + \, L_{\nu+1}(\alpha z) \, M_{\nu \pm 1}(\beta z)] \, ,$$

(A-11)

---

[4]Kajfez, 873-874.

$$F_{\nu}'(\alpha z)\, M_{\nu}'(\beta z) \;\pm\; \frac{\nu^2}{\alpha\beta z^2}\, F_{\nu}(\alpha z)\, M_{\nu}(\beta z)$$

$$= \frac{1}{2}\,[\,F_{\nu-1}(\alpha z)\, M_{\nu\mp 1}(\beta z) \;-\; F_{\nu+1}(\alpha z)\, M_{\nu\pm 1}(\beta z)\,]\,. \tag{A-12}$$

These identities may be derived from the recurrence relationships for ordinary and modified Bessel functions.[5] They are true only when the coefficients A, B, C, D, P, Q, R and S, are independent of ν and $Q \to e^{i\pi\nu}\, Q$, $S \to e^{i\pi\nu}\, S$. However, the integrals given above are not dependent upon such conditions as can be shown by the verification by differentiation.

Using integral 5.54.1 of Gradshteyn and Ryzhik[6] or 11.3.29 of Abramowitz and Stegun[7] with the identities of Equations (A-10) and (A-11) above, the integrals of Equations (A-2) and (A-5) may be found. The integral of Equation (A-7) was derived in this instance by trial and error differentiation. The integrals of Equations (A-8) and (A-9) may derived using the identities of Equations (A-10) and (A-11) with 5.54.2 of Gradshteyn and Ryzhik.

A.4 Evaluation of the Integral Expressions at Extremum

The indefinite integrals given above must often be evaluated at extremum values of 0 and ∞. The results vary depending upon the Bessel functions included in the linear combinations which make up F_{ν}, G_{ν}, L_{ν}, and M_{ν}. The simplest means of presenting the values of the integral expressions at extremum is in terms of the coefficients A, B, C, D, P, Q, R, and S.

---

[5]Abramowitz and Stegun, 361, 376.

[6]Gradshteyn and Ryzhik, 634. The 1980 edition contains an error in this integral which seems not to be present in earlier editions. The " + " sign in the numerator should be a "-".

[7]Abramowitz and Stegun, 484.

A.4.1 Evaluation at $z=0$.

At $z=0$ the right hand side of the integral of Equation (A-2), call it I1, is given by

$$\lim_{z \to 0} I1 \bigg|_{\nu=0} = \begin{cases} \lim_{z \to 0} \dfrac{BD}{\alpha\beta} \ln(z) & B, D \neq 0 \\[4mm] -\dfrac{2\beta}{\pi\alpha} \dfrac{BC}{(\alpha^2 - \beta^2)} & D = 0 \\[4mm] 0 & B, D = 0, \end{cases} \qquad \text{(A-13)}$$

for $\nu=0$, and in general ($Re\ \nu > 0$),

$$\lim_{z \to 0} I1 = \begin{cases} \lim_{z \to 0} \dfrac{-BD(\nu!)^2}{\nu (\alpha\beta)^{\nu+1} \left[\dfrac{z}{2}\right]^{2\nu}} & B, D \neq 0 \\[6mm] -\dfrac{(\alpha^2 + \beta^2)}{(\alpha^2 - \beta^2)} \dfrac{BC\beta^{\nu-1}}{\pi\alpha^{\nu+1}} & D = 0 \\[4mm] 0 & B, D = 0. \end{cases} \qquad \text{(A-14)}$$

For the integral of Equation (A-5), call it I2, the limit at $z=0$ is

$$\lim_{z \to 0} I2 \bigg|_{\nu=0} = \begin{cases} \lim_{z \to 0} \dfrac{QS}{\alpha\beta} \ln(z) & Q, S \neq 0 \\[4mm] \dfrac{\beta}{\alpha} \dfrac{QR}{(\alpha^2 - \beta^2)} & S = 0 \\[4mm] 0 & S, Q = 0, \end{cases} \qquad \text{(A-15)}$$

for $\nu=0$, and in general ($Re\ \nu > 0$),

$$\lim_{z \to 0} I2 = \begin{cases} \lim\limits_{z \to 0} \dfrac{-QS(\nu!)^2}{\nu\,(\alpha\beta)^{\nu+1}\left[\dfrac{z}{2}\right]^{2\nu}} & Q, S \neq 0 \\[4ex] \dfrac{(\alpha^2 + \beta^2)}{(\alpha^2 - \beta^2)}\dfrac{QR\,\beta^{\nu-1}}{2\,\alpha^{\nu+1}} & S = 0 \\[3ex] 0 & Q, S = 0 \,. \end{cases} \tag{A-16}$$

Considering the limit at $z=0$ for the integral of Equation (A-7), call it I3, for $\nu=0$ we have

$$\lim_{z \to 0} I3 \bigg|_{\nu=0} = \begin{cases} \lim\limits_{z \to 0} \dfrac{-BS}{\alpha\beta}\ln(z) & B, S \neq 0 \\[3ex] \dfrac{-2\beta}{\alpha\pi}\dfrac{BR}{(\alpha^2 - \beta^2)} & S = 0 \\[3ex] \dfrac{-\alpha}{\beta}\dfrac{AS}{(\alpha^2 - \beta^2)} & B = 0 \\[3ex] 0 & B, S = 0 \,, \end{cases} \tag{A-17}$$

and in general ($Re\ \nu > 0$),

$$\lim_{z \to 0} I3 = \begin{cases} \lim\limits_{z \to 0} \dfrac{BS(\nu!)^2}{\nu\,(\alpha\beta)^{\nu+1}\left[\dfrac{z}{2}\right]^{2\nu}} & B, S \neq 0 \\[4ex] -\dfrac{(\alpha^2 + \beta^2)}{(\alpha^2 - \beta^2)}\dfrac{BR\,\beta^{\nu-1}}{\pi\,\alpha^{\nu+1}} & S = 0 \\[3ex] -\dfrac{(\alpha^2 + \beta^2)}{(\alpha^2 - \beta^2)}\dfrac{AS\,\alpha^{\nu-1}}{2\,\beta^{\nu+1}} & B = 0 \\[3ex] 0 & B, S = 0 \,. \end{cases} \tag{A-18}$$

The limit at $z=0$ for the integral of Equation (A-8), call it I4, for $\nu=0$ is

$$\lim_{z \to 0} \text{I4} \Bigg|_{\nu=0} = \begin{cases} \lim\limits_{z \to 0} \dfrac{4B^2}{\pi^2 \alpha^2} \ln(z) & B \neq 0 \\[3em] 0 & B = 0, \end{cases} \qquad \text{(A-19)}$$

and in general ($Re\ \nu > 0$),

$$\lim_{z \to 0} \text{I4} = \begin{cases} \lim\limits_{z \to 0} B^2 \left[\dfrac{\nu!}{\pi \alpha}\right]^2 \dfrac{\left(\dfrac{1}{2} - \dfrac{1}{\nu}\right)}{\left(\dfrac{1}{2}\alpha z\right)^{2\nu}} & B \neq 0 \\[3em] 0 & B = 0. \end{cases} \qquad \text{(A-20)}$$

The limit at $z=0$ for the integral of Equation (A-9), call it I5, for $\nu=0$ is

$$\lim_{z \to 0} \text{I5} \Bigg|_{\nu=0} = \begin{cases} \lim\limits_{z \to 0} \dfrac{Q^2}{\alpha^2} \ln(z) & Q \neq 0 \\[3em] 0 & Q = 0, \end{cases} \qquad \text{(A-21)}$$

and in general ($Re\ \nu > 0$),

$$\lim_{z \to 0} \text{I5} = \begin{cases} \lim\limits_{z \to 0} Q^2 \left[\dfrac{\nu!}{\alpha}\right]^2 \dfrac{\left(1 + \dfrac{3}{4\nu}\right)}{\left(\dfrac{1}{2}\alpha z\right)^{2\nu}} & Q \neq 0 \\[3em] 0 & Q = 0. \end{cases} \qquad \text{(A-22)}$$

If a limit at zero is encountered with $Re\ \nu < 0$, the ordinary Bessel functions may be transformed by

$$F_{-\nu}(\alpha z) = [A \cos(\nu \pi) + B \sin(\nu \pi)] \, J_\nu(\alpha z)$$

$$+ \, [-A \sin(\nu \pi) + B \cos(\nu \pi)] \, Y_\nu(\alpha z) .$$

(A-23)

The modified Bessel functions may be transformed such that

$$L_{-\nu}(\alpha z) = P \, I_\nu(\alpha z) + [Q + P \frac{2}{\pi} \sin(\nu \pi)] \, K_\nu(\alpha z) .$$

(A-24)

A.4.2 Evaluation at $z = \infty$.

For the limits at $z = \infty$, there are no special case limits for $\nu = 0$. However, there are many possible results depending on the values of α, β, and the coefficients A, B, C, D, P, Q, R, and S. Due to the large number of possible results, the expressions are left in simplest general limit form.

For the integral of Equation (A-2) the limit at ∞ for $|\arg \beta z| < \pi$ and $|\arg \alpha z| < \pi$ is given by

$$\lim_{z \to \infty} I1 = \lim_{z \to \infty} \frac{2}{\pi \sqrt{\alpha \beta} \, (\alpha^2 - \beta^2)} \left\{ \alpha \left(A \cos \chi_\alpha + B \sin \chi_\alpha \right) \right.$$

$$\times \left(-C \sin \chi_\beta + D \cos \chi_\beta \right) - \beta \left(-A \sin \chi_\alpha + B \cos \chi_\alpha \right)$$

$$\left. \times \left(C \cos \chi_\beta + D \sin \chi_\beta \right) \right\} ,$$

(A-25)

where $\chi_\alpha = \alpha z - (\tfrac{1}{2}\nu + \tfrac{1}{4})\pi$ and $\chi_\beta = \beta z - (\tfrac{1}{2}\nu + \tfrac{1}{4})\pi$.

The limit at ∞ of the integral of Equation (A-5) for $|\arg \beta z| < \tfrac{1}{2}\pi$ and $|\arg \alpha z| < \tfrac{1}{2}\pi$ is

$$\lim_{z \to \infty} I2 = \lim_{z \to \infty} \frac{1}{2 \sqrt{\alpha \beta}} \left\{ \frac{1}{\alpha + \beta} \left[\frac{1}{\pi} P R e^{z(\alpha + \beta)} \right. \right.$$

$$\left. - \pi Q S e^{-z(\alpha + \beta)} \right] + \frac{1}{\alpha - \beta} \left[Q R e^{-z(\alpha - \beta)} - P S e^{z(\alpha - \beta)} \right] \right\} .$$

(A-26)

The limit at ∞ for the integral of Equation (A-7) for $|\arg \beta z| < \frac{1}{2}\pi$ and $|\arg \alpha z| < \pi$ is

$$\lim_{z \to \infty} I3 = \lim_{z \to \infty} \frac{1}{\sqrt{\pi \alpha \beta} (\alpha^2 + \beta^2)} \left\{ e^{z\beta} R \left[A \left(\alpha \cos\chi_\alpha - \beta \sin\chi_\alpha \right) \right. \right.$$

$$\left. + B \left(\alpha \sin\chi_\alpha + \beta \cos\chi_\alpha \right) \right] - \pi e^{-z\beta} S \left[A \left(\alpha \cos\chi_\alpha \right. \right. \tag{A-27}$$

$$\left. \left. + \beta \sin\chi_\alpha \right) + B \left(\alpha \sin\chi_\alpha - \beta \cos\chi_\alpha \right) \right] \right\}.$$

The limit at ∞ for the integral of Equation (A-8) for $|\arg \alpha z| < \pi$ is

$$\lim_{z \to \infty} I4 = \lim_{z \to \infty} \left\{ \frac{z}{\pi \alpha} (A^2 + B^2) + \frac{2}{\pi \alpha^2} \right.$$

$$\left. \times \left[\sin\chi_\alpha \cos\chi_\alpha (B^2 - A^2) + (1 - 2\sin^2\chi_\alpha) AB \right] \right\}. \tag{A-28}$$

The limit at ∞ for the integral of Equation (A-9) for $|\arg \alpha z| < \frac{1}{2}\pi$ is

$$\lim_{z \to \infty} I5 = \lim_{z \to \infty} \left[P^2 \frac{e^{2\alpha z}}{2\pi \alpha^2} + Q^2 \frac{\pi e^{-2\alpha z}}{2\alpha^2} - PQ \frac{z}{2\alpha} \right]. \tag{A-29}$$

A.5 Definite Integrals

Certain orthogonality properties of Bessel functions may be determined from the integral relationships found in Equations (A-2), (A-5), (A-8), and (A-9) with the limiting relationships (A-13) through (A-22). We give two of them here for ordinary Bessel functions of the first kind:

$$\int_0^b [J_n'(\frac{\lambda_{np}}{b}\rho)J_n'(\frac{\lambda_{nq}}{b}\rho) + n^2\frac{b^2}{\lambda_{np}\lambda_{nq}\rho^2}J_n(\frac{\lambda_{np}}{b}\rho)J_n(\frac{\lambda_{nq}}{b}\rho)]\rho\,d\rho$$

$$= \begin{cases} 0 & p \neq q \\ \frac{1}{2}[b\,J_n'(\lambda_{np})]^2 & p = q \end{cases},$$

(A-30)

$$\int_0^b [J_n'(\frac{\lambda'_{np}}{b}\rho)J_n'(\frac{\lambda'_{nq}}{b}\rho) + n^2\frac{b^2}{\lambda'_{np}\lambda'_{nq}\rho^2}J_n(\frac{\lambda'_{np}}{b}\rho)J_n(\frac{\lambda'_{nq}}{b}\rho)]\rho\,d\rho$$

(A-31)

$$= \begin{cases} 0 & p \neq q \\ \frac{b^2}{2}\left[1 - \frac{n^2}{\lambda'^2_{np}}\right]J_n^2(\lambda'_{np}) & p = q \end{cases},$$

where λ_{np} and λ'_{np} are the zeros of ordinary Bessel functions and their derivatives respectively. These integrals are used in orthogonalization of the fields in regions I and III by a region I/III mode, referring to Chapter 4, Section 4.5.3. Equation (A-30) occurs in the TM mode orthogonalization formulation and Equation (A-31) is used for TE mode orthogonalization.

Appendix B

MODE ORTHOGONALITY IN INHOMOGENEOUSLY
FILLED WAVEGUIDES

The well-known orthogonality conditions for modes in homogeneously loaded cylindrical waveguides of arbitrary cross section,

$$\int \int E_{t_i}^{TM} \cdot E_{t_j}^{TM} \, ds = 0 \qquad i \neq j$$

$$\int \int E_{t_i}^{TE} \cdot E_{t_j}^{TE} \, ds = 0 \qquad i \neq j \qquad\qquad \text{(B-1)}$$

$$\int \int E_{t_i}^{TM} \cdot E_{t_j}^{TE} \, ds = 0 \,,$$

do not hold for the inhomogeneous case. A more general expression for a cylindrical waveguide loaded with an inhomogeneous, isotropic material is given by Collin as[1]

$$\int \int E_{t_i} \times H_{t_j} \cdot \mathbf{a}_z \, ds = 0 \qquad i \neq j \,, \qquad\qquad \text{(B-2)}$$

where the integration is over the cross-section of the waveguide, $\mathbf{a}_z$ is the axial unit vector, and the t subscript indicates the transverse portion of the field. The orthogonality conditions of Equation (B-1) are called *energy orthogonality* while the conditions of Equation (B-2) are called *power orthogonality*.[2]

Under certain circumstances Equation (B-2) may assume a form similar to Equations (B-1). Given a cross-sectional region as shown in Figure 1, consisting of several adjacent subregions where each subregion consists of an isotropic, homogeneous dielectric, it is in general not possible to find solutions that are purely

---

[1]Collin, 231.

[2]R. B. Adler, "Waves on Inhomogeneous Cylindrical Structures," *Proceedings of the I.R.E.* (40) (March 1952): 339-48.
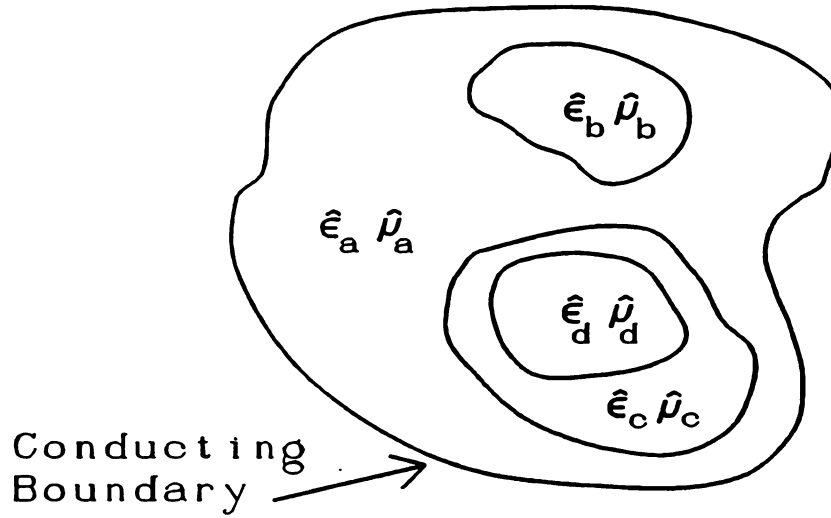
Figure B-1 Cross-section of an inhomogeneously filled cylindrical waveguide.

TM or purely TE to the waveguide axis. However, the fields may be constructed as a superposition of TM and TE modes.

In each homogeneous region TM and TE solutions may be written in terms of a scalar potential, $\varphi(u,v,z) = \psi(u,v)Z(z)$, where u and v are the cross-sectional coordinates, z is the axial coordinate, and

$$\nabla_t \psi + k_c^2 \psi = 0$$

$$k_c^2 + k_z^2 = k^2 = \omega^2 \hat{\mu}\hat{\epsilon} \qquad (B\text{-}3)$$

$$\frac{\partial^2 Z}{\partial z^2} + k_z^2 Z = 0,$$

where k_c is the transverse wave number, k_z is the axial wave number, and the *hat* over μ and ϵ indicates that they may assume complex values. The transverse fields are given in terms of the potentials as

$$H_t = (\nabla_t \psi^m \times a_z)Z^m + \frac{1}{j\omega\hat{\mu}}(\nabla_t \psi^e)\frac{\partial Z^e}{\partial z}$$

$$E_t = \frac{1}{j\omega\hat{\epsilon}}(\nabla_t \psi^m)\frac{\partial Z^m}{\partial z} - (\nabla_t \psi^e \times a_z)Z^e, \qquad (B\text{-}4)$$

where the superscripts m and e indicate a TM or a TE component respectively.

The axial fields are given simply by

$$E_z = \frac{k_c^2}{j\,\omega\,\hat{\epsilon}}\;\psi^m\,Z^m$$

$$H_z = \frac{k_c^2}{j\,\omega\,\hat{\mu}}\;\psi^e\,Z^e\,.$$

(B-5)

Applying boundary conditions of the continuity of E_z and H_z at the interface between homogeneous regions it is evident that Z^m, Z^e, and k_z must be the same in all regions of the waveguide. Otherwise the boundary condition equations are z-dependent. The two equations from the matching of tangential E and H fields in the transverse plane at boundaries between homogeneous regions are

$$\left[(\nabla_t \psi_i^m \times a_z)\,Z^m + \frac{1}{j\,\omega\,\hat{\mu}_i}\,(\nabla_t \psi_i^e)\frac{\partial Z^e}{\partial z} \right] \cdot t$$

$$= \left[(\nabla_t \psi_j^m \times a_z)\,Z^m + \frac{1}{j\,\omega\,\hat{\mu}_j}\,(\nabla_t \psi_j^e)\frac{\partial Z^e}{\partial z} \right] \cdot t\,,$$

(B-6)

and

$$\left[(\nabla_t \psi_i^e \times a_z)\,Z^e - \frac{1}{j\,\omega\,\hat{\epsilon}_i}\,(\nabla_t \psi_i^m)\frac{\partial Z^m}{\partial z} \right] \cdot t$$

$$= \left[(\nabla_t \psi_j^e \times a_z)\,Z^e - \frac{1}{j\,\omega\,\hat{\epsilon}_j}\,(\nabla_t \psi_j^m)\frac{\partial Z^m}{\partial z} \right] \cdot t\,,$$

(B-7)

where t is the unit tangent in the transverse plane to the interface between regions i and j. The only way for these equations to be z-independent is for Z^e to be proportional to $\partial Z^m / \partial z$, and for Z^m to be proportional to $\partial Z^e / \partial z$, i.e.,

$$\frac{\partial Z^m}{\partial z} = \alpha Z^e \qquad\qquad \frac{\partial Z^e}{\partial z} = \beta Z^m\,.$$

(B-8)

By the third of Equations (B-3), the constants α and β are related by $\alpha\beta = -k_z^2$.

Collin's expression may be rewritten as

$$\int \int E_{t_i} \cdot (H_{t_j} \times a_z) \, ds = 0 \qquad i \neq j. \tag{B-9}$$

Using Equations (B-4) and (B-8) it may be shown that

$$H_t \times a_z = \frac{Z^m}{Z^e} \frac{1}{j\omega\hat{\mu}\alpha} [k^2 E_t^{TM} + k_z^2 E_t^{TE}]. \tag{B-10}$$

Since k_z, ω, Z^m, Z^e, and α are not functions of the cross-sectional coordinates, the orthogonality condition may be rewritten as

$$\int \int E_{t_i} \cdot \frac{1}{\hat{\mu}} [k^2 E_{t_j}^{TM} + k_z^2 E_{t_j}^{TE}] \, ds = 0 \qquad i \neq j. \tag{B-11}$$

For certain waveguide configurations, non-hybrid modes, i.e., TM modes or TE modes, will propagate in an inhomogeneously filled waveguide. An example is ϕ-symmetric modes in a coaxially-loaded circular cylindrical waveguide. In such cases for TM modes Equation (B-11) becomes

$$\int \int \hat{\epsilon} \, E_{t_i}^{TM} \cdot E_{t_j}^{TM} \, ds = 0 \qquad i \neq j, \tag{B-12}$$

and for TE modes

$$\int \int \frac{1}{\hat{\mu}} E_{t_i}^{TE} \cdot E_{t_j}^{TE} \, ds = 0 \qquad i \neq j. \tag{B-13}$$

Similar equations can be written for the magnetic field,

$$\int \int H_{t_i} \cdot \frac{1}{\hat{\epsilon}} [k^2 H_{t_j}^{TE} + k_z^2 H_{t_j}^{TM}] \, ds = 0 \qquad i \neq j$$

$$\int \int \frac{1}{\hat{\epsilon}} H_{t_i}^{TM} \cdot H_{t_j}^{TM} = 0 \qquad i \neq j \tag{B-14}$$

$$\int \int \hat{\mu} \, H_{t_i}^{TE} \cdot H_{t_j}^{TE} = 0 \qquad i \neq j.$$

For a homogeneously filled waveguide, where only TM or TE modes exist, it is clear how these equations specialize to the first two of Equations (B-1).

It also should be noted on the basis of these equations that the cavity orthogonality conditions given by Harrington are not valid in general.[3] The equation given for the electric field is valid only for TM modes while the equation for the magnetic field is valid only for TE modes.

---

[3]Harrington, 432.

Appendix C

BRACKETED CONSTANTS USED IN THE
CAVITY-OPEN TYPE SOLUTIONS

Orthogonalization of the boundary condition equations at either end of the cavity load for the cavity-open type configuration produces complicated spacial constant expressions on the side of the equation for which the orthogonalization vector is not an orthogonal eigenfunction. These constants have been abbreviated in the text of Chapter 4 in angled brackets to indicate that they result from integrations. For example, the spacial constant arising from the integration over the cavity cross section of the tangential electric field in region II, referring to Figure 4-2, dotted with the tangential portion of the electric field of a TM mode in region I or III is abbreviated,

$$\left\langle E, e^{TM} \right\rangle_{pi} , \tag{C-1}$$

where the capital letter refers to a field in region II and the small letter refers to a field in region I or III. The superscript above the small letter indicates whether the region I/III mode is TM or TE. Outside the brackets the first subscript pertains to the radial wavenumber of the region I/III mode, the second subscript to the radial wavenumber of the region II mode. The azimuthal order of both modes is the same and is indicated in the expanded expressions below by the integer n. These spacial constants do not depend on the axial dependences of the fields and are made dimensionless by dividing off appropriate factors.

The spacial constants found in Equations (4-136) through (4-139) of the Method I solution are given by

$$\langle E, e^{TM}\rangle_{pi} = R_n(k_{\rho 1}a) - \frac{k_{\rho 1}^2}{k_{\rho 2}^2} \frac{J_n(k_{\rho 1}a)\,S_n(k_{\rho 2}a)}{F_n(k_{\rho 2}a)} + n^2 J_n(\lambda_{np}\frac{a}{b})$$

$$\times \frac{k_o}{\gamma_i}\left[\frac{\mu_1}{\mu_o} - \frac{\mu_2 k_{\rho 1}^2}{\mu_o k_{\rho 2}^2}\right] J_n(k_{\rho 1}a)\sqrt{\frac{G_n(k_{\rho 2}a)}{F_n(k_{\rho 2}a)}}\,\frac{U_n}{V_n}\,,$$

(C-2)

$$\langle H, h^{TM}\rangle_{pi} = R_n(k_{\rho 1}a) - \frac{\epsilon_2 k_{\rho 1}^2}{\hat\epsilon_1 k_{\rho 2}^2} \frac{J_n(k_{\rho 1}a)\,S_n(k_{\rho 2}a)}{F_n(k_{\rho 2}a)} + n^2 J_n(\lambda_{np}\frac{a}{b})$$

$$\times \frac{\gamma_i \epsilon_o}{k_o \epsilon_1}\left[1 - \frac{k_{\rho 1}^2}{k_{\rho 2}^2}\right] J_n(k_{\rho 1}a)\sqrt{\frac{G_n(k_{\rho 2}a)}{F_n(k_{\rho 2}a)}}\,\frac{U_n}{V_n}\,,$$

(C-3)

with V_n and U_n given by Equations (3-93) and (3-95), the functions F_n and G_n given by Equations (3-76) and (3-78), and the functions $R_n(k_{\rho 1}a)$ and $S_n(k_{\rho 2}a)$ given by

$$R_n(k_{\rho 1}a) = \frac{\lambda_{np}k_{\rho 1}b}{\left(\lambda_{np}^2 - k_{\rho 1}^2 b^2\right)}\left[\lambda_{np}\frac{a}{b}J_n(\lambda_{np}\frac{a}{b})J_n'(k_{\rho 1}a)\right.$$

(C-4)

$$\left. - k_{\rho 1}a J_n(k_{\rho 1}a)J_n'(\lambda_{np}\frac{a}{b})\right],$$

$$S_n(k_{\rho 2}a) = \frac{\lambda_{np}k_{\rho 2}b}{\left(\lambda_{np}^2 - k_{\rho 2}^2 b^2\right)}\left[\lambda_{np}\frac{a}{b}J_n(\lambda_{np}\frac{a}{b})F_n'(k_{\rho 2}a)\right.$$

(C-5)

$$\left. - k_{\rho 2}a F_n(k_{\rho 2}a)J_n'(\lambda_{np}\frac{a}{b})\right].$$

The spacial constants found in Equations (4-157) through (4-160) of the Method I solution are given by

$$\left\langle E, e^{TE} \right\rangle_{pi} = Q_n(k_{\rho 1} a) - \frac{\mu_2 k_{\rho 1}^2}{\mu_1 k_{\rho 2}^2} \frac{J_n(k_{\rho 1} a) \, T_n(k_{\rho 2} a)}{G_n(k_{\rho 2} a)} + n^2 J_n(\lambda'_{np} \tfrac{a}{b})$$

$$\text{(C-6)}$$

$$\times \frac{k_0 \gamma_i}{k_1^2} \frac{\hat{\epsilon}_1}{\epsilon_0} \left[1 - \frac{k_{\rho 1}^2}{k_{\rho 2}^2} \right] J_n(k_{\rho 1} a) \sqrt{\frac{F_n(k_{\rho 2} a)}{G_n(k_{\rho 2} a)}} \frac{U_n}{W_n} \, ,$$

$$\left\langle H, h^{TE} \right\rangle_{pi} = Q_n(k_{\rho 1} a) - \frac{k_{\rho 1}^2}{k_{\rho 2}^2} \frac{J_n(k_{\rho 1} a) \, T_n(k_{\rho 2} a)}{G_n(k_{\rho 2} a)} + n^2 J_n(\lambda'_{np} \tfrac{a}{b})$$

$$\text{(C-7)}$$

$$\times \frac{k_0}{\gamma_i} \left[\frac{\hat{\epsilon}_1}{\epsilon_0} - \frac{\epsilon_2 k_{\rho 1}^2}{\epsilon_0 k_{\rho 2}^2} \right] J_n(k_{\rho 1} a) \sqrt{\frac{F_n(k_{\rho 2} a)}{G_n(k_{\rho 2} a)}} \frac{U_n}{W_n} \, ,$$

with W_n and U_n given by Equations (3-94) and (3-95), F_n and G_n given by Equations (3-76) and (3-78), and the functions $Q_n(k_{\rho 1} a)$ and $T_n(k_{\rho 2} a)$ given by

$$Q_n(k_{\rho 1} a) = \frac{\lambda'_{np} k_{\rho 1} b}{\left(\lambda'^2_{np} - k_{\rho 1}^2 b^2 \right)} \left[\lambda'_{np} \frac{a}{b} J_n(\lambda'_{np} \tfrac{a}{b}) J'_n(k_{\rho 1} a) \right.$$

$$\text{(C-8)}$$

$$\left. - k_{\rho 1} a \, J_n(k_{\rho 1} a) J'_n(\lambda'_{np} \tfrac{a}{b}) \right] ,$$

$$T_n(k_{\rho 2} a) = \frac{\lambda'_{np} k_{\rho 2} b}{\left(\lambda'^2_{np} - k_{\rho 2}^2 b^2 \right)} \left[\lambda'_{np} \frac{a}{b} J_n(\lambda'_{np} \tfrac{a}{b}) G'_n(k_{\rho 2} a) \right.$$

$$\text{(C-9)}$$

$$\left. - k_{\rho 2} a \, G_n(k_{\rho 2} a) J'_n(\lambda'_{np} \tfrac{a}{b}) \right] .$$

For method II the constants above are augmented by

$$\langle E, H \times \hat{z}\rangle_{jj}^{TM} = (k_{\rho 1}a)^2 \left\{ \frac{1}{2}\left[1 + n^2\frac{\epsilon_0\mu_1 G U_n^2}{\hat{\epsilon}_1\mu_0 F V_n^2}\right]\langle J,J'\rangle + n^2\frac{J^2}{k_{\rho 1}^2 a^2}\right.$$

$$\times \frac{k_0}{\gamma}\sqrt{\frac{G}{F}}\frac{U_n}{V_n}\left[\frac{\mu_1}{\mu_0}\left(1+\frac{\gamma^2}{k_1^2}\right) - \frac{\epsilon_2\mu_2 k_{\rho 1}^4}{\hat{\epsilon}_1\mu_0 k_{\rho 2}^4}\left(1+\frac{\gamma^2}{k_2^2}\right)\right]$$ (C-10)

$$+\frac{1}{2}\frac{\epsilon_2 J^2 k_{\rho 1}^2}{\hat{\epsilon}_1 F^2 k_{\rho 2}^2}\left[\frac{b^2}{a^2}F_n'^2(k_{\rho 2}b) - \langle F,F'\rangle\right] + \frac{1}{2}n^2\frac{\epsilon_0\mu_2 k_{\rho 1}^2}{\hat{\epsilon}_1\mu_0 k_{\rho 2}^2}$$

$$\times \left. \frac{J^2 U_n^2}{FGV_n^2}\left[\frac{b^2}{a^2}G_n^2(k_{\rho 2}b)\left(1-\frac{n^2}{k_{\rho 2}^2 b^2}\right) - \langle G,G'\rangle\right]\right\},$$

and

$$\langle E, H \times \hat{z}\rangle_{jj}^{TE} = (k_{\rho 1}a)^2 \left\{ \frac{1}{2}\left[1 + n^2\frac{\hat{\epsilon}_1\mu_0 F U_n^2}{\epsilon_0\mu_1 G W_n^2}\right]\langle J,J'\rangle + n^2\frac{J^2}{k_{\rho 1}^2 a^2}\right.$$

$$\times \frac{k_0}{\gamma}\sqrt{\frac{F}{G}}\frac{U_n}{W_n}\left[\frac{\hat{\epsilon}_1}{\epsilon_0}\left(1+\frac{\gamma^2}{k_1^2}\right) - \frac{\epsilon_2\mu_2 k_{\rho 1}^4}{\mu_1\epsilon_0 k_{\rho 2}^4}\left(1+\frac{\gamma^2}{k_2^2}\right)\right]$$ (C-11)

$$+\frac{1}{2}n^2\frac{\epsilon_2\mu_0 k_{\rho 1}^2}{\epsilon_0\mu_1 k_{\rho 2}^2}\frac{J^2 U_n^2}{FGW_n^2}\left[\frac{b^2}{a^2}F_n'^2(k_{\rho 2}b) - \langle F,F'\rangle\right]$$

$$+\frac{1}{2}\frac{\mu_2 k_{\rho 1}^2 J^2}{\mu_1 k_{\rho 2}^2 G^2}\left[\frac{b^2}{a^2}G_n^2(k_{\rho 2}b)\left(1-\frac{n^2}{k_{\rho 2}^2 b^2}\right) - \langle G,G'\rangle\right]\left.\right\},$$

where

$$\langle J,J'\rangle = \left[J'^2 + J^2\left(1-\frac{n^2}{k_{\rho 1}^2 a^2}\right) + \frac{2}{k_{\rho 1}a}JJ'\right],$$ (C-12)

$$\langle F, F' \rangle = \left[F'^2 + F^2 \left[1 - \frac{n^2}{k_{\rho 2}^2 a^2} \right] + \frac{2}{k_{\rho 2} a} FF' \right], \qquad \text{(C-13)}$$

and

$$\langle G, G' \rangle = \left[G'^2 + G^2 \left[1 - \frac{n^2}{k_{\rho 2}^2 a^2} \right] + \frac{2}{k_{\rho 2} a} GG' \right]. \qquad \text{(C-14)}$$

The variables J, J', F, F', G, and G' are defined in Chapter 3 in Equations (3-84). U_n, V_n, and W_n are defined in Equations (3-92) through (3-95). The left hand side expressions of Equations (C-10) and (C-11), as noted in Equation (4-187) of Chapter 4, are related such that

$$\langle E, H \times \hat{z} \rangle_{jj}^{\text{TE}} = \frac{\mu_1}{\hat{\epsilon}_1} A_{B_j}^2 \langle E, H \times \hat{z} \rangle_{jj}^{\text{TM}}, \qquad \text{(C-15)}$$

where A_{B_j} is given by Equation (4-83) of Chapter 4.

Appendix D
TIME-AVERAGE VALUE OF A DECAYING, ROTATING FIELD

D.1 Introduction

In order to understand the behavior of the natural mode electromagnetic fields inside a cavity loaded with a lossy dielectric, it is useful to define a time-average value of the field. Since the fields of the natural modes decay exponentially in time in the presence of losses, their time-average over all time is zero. One means of overcoming this difficulty is to neglect the time decay in the definition of the average to obtain a relative average, i.e., an average relative to the decay factor. Another solution is to define the time-average for a specific finite time period and include reference to the time period in the result.

For the decaying fields of the natural modes of a cavity containing boundaries between lossy media, a relative time-average value cannot be defined by simply neglecting the time decay factor. Since, as will be shown, the fields rotate with time, such an evaluation does not fairly represent the relative magnitudes of each of the field components. Instead, a time-average value is defined for a specific finite time period. The definition takes into consideration the differing field component phases which account for the rotation. With a proper choice of time period, a time-independent, relative time-average may be derived from the finite time period average.

D.2 Time-Average Field Values for a Given Time Period

For a non-decaying periodic function it is common to define a root mean squared (RMS) value for the magnitude of the function. This definition is given by

$$F_{RMS} = \sqrt{\frac{1}{T} \int_{t_o}^{t_o + T} [f(t)]^2 \, dt} \,, \qquad (D-1)$$

where T is the period of the function and t_o is the initial time for the period over

which the average is taken. For non-decaying periodic functions with T a half-integer multiple of the period, the RMS value is independent of t_0 and is equal to the time-average of the function over all time.

The time-average value of a decaying function may be defined similarly to the RMS value for the periodic function. In particular, the time-decaying expression for one vector component of the electric field of a natural lossy cavity mode is given by

$$E(t) = \text{Re}(e^{j\hat{\omega}t}\hat{E}), \qquad (D\text{-}2)$$

where $\hat{\omega}$ and $\hat{E}$ are the complex natural radian frequency and the complex electric field component respectively. In terms of purely real and purely imaginary numbers they may be expressed in the form

$$\hat{\omega} = \omega' + j\omega'',$$
$$\hat{E} = E e^{j\delta}. \qquad (D\text{-}3)$$

The real time value of the electric field component may then be written

$$E(t) = e^{-\omega''t} E \cos(\omega't + \delta). \qquad (D\text{-}4)$$

To render a time-average value of the magnitude this expression is substituted into Equation (D-1). Choosing $T = 2m\pi/\omega'$, the resulting time-average electric field component over m cycles is

$$E_{av} = \sqrt{\frac{\omega' E^2}{2m\pi} \int_{t_0}^{t_0 + \frac{2m\pi}{\omega'}} e^{-2\omega''t} \cos^2(\omega't + \delta)\, dt}. \qquad (D\text{-}5)$$

Performing the integration the time-average value is given by

$$E_{av} = E \sqrt{\frac{\omega'}{2m\pi\omega''}} X(m, t_0, \omega', \omega'', \delta), \qquad (D\text{-}6)$$

where

In

D.3

is t
inte

whe
the
seve
the

wher
wher
the c
or dif
exist

$$X^2(m,t_0,\omega',\omega'',\delta) = \frac{1}{4} e^{-2\omega''t_0} \left(1 - e^{-4m\omega''\pi/\omega'}\right)$$

$$\times \left\{ 1 - \frac{\omega''\omega'}{\omega''^2 + \omega'^2} \left[\sin 2(\omega't_0 + \delta) - \frac{\omega''}{\omega'} \cos 2(\omega't_0 + \delta) \right] \right\}. \tag{D-7}$$

In the limit as α approaches zero, X^2 approaches $m\pi\omega''/\omega'$, thus

$$\lim_{\alpha \to 0} E_{av} = \frac{E}{\sqrt{2}} = E_{RMS}. \tag{D-8}$$

D.3 Field Rotation of the Natural Modes

The unresolved question in defining the time-average value by Equation (D-6) is the specification of t_0. It might seem that t_0 would best be specified such that the integration begins and ends at a field zero or a field peak, i.e.,

$$t_0 = -\frac{\delta}{\omega'}, \quad \text{or} \quad t_0 = \frac{\frac{n\pi}{2} - \delta}{\omega'},$$

where n is an integer. However, it must be remembered that only one component of the vector field has been considered so far. The total electric field is composed of several vector components which peak at different times. In cylindrical coordinates the total field is composed of axial, radial, and azimuthal components such that

$$\vec{E} = \hat{E}_\rho \vec{\rho} + \hat{E}_\phi \vec{\phi} + \hat{E}_z \vec{z}$$

$$= E_\rho e^{j\delta_\rho} \vec{\rho} + E_\phi e^{j\delta_\phi} \vec{\phi} + E_z e^{j\delta_z} \vec{z}, \tag{D-10}$$

where the phases δ_ρ, δ_ϕ, and δ_z are in general different. For the lossless case, or when losses are present but no boundaries exist between regions of lossy media, as in the case of a cavity homogeneously loaded with lossy materials, the phases are equal or differ by $\pm\pi$. In contrast, when the cavity contains regions where boundaries exist between media, of which at least one is lossy, the phases of the field

components differ by arbitrary amounts dependent on the cavity/load configuration and the frequency. Furthermore, the phases are functions of spacial coordinates.

A consequence of arbitrary phase differences between field components is a change in field direction with time. Since the field components change in time according to Equation (D-4), an arbitrary phase difference between two components indicates that in general they will not be zero at the same instant of time. Neglecting the time decay factor, the tip of a vector representing two field components at a point within the cavity may be understood to trace out an elliptical boundary in time as the field rotates about the center of the ellipse. If the phase difference is exactly $\pm n\pi$ (n equals zero or an integer), the eccentricity of the ellipse is 1 with its minor axis equal to zero and there is no field rotation, rather the field oscillates sinusoidally in a constant direction.

Figure D-1 is a drawing of an ellipse with major and minor axes labeled a and b. The axes of the ellipse are rotated away from the coordinate axes by an angle φ. If the ellipse is described parametrically with θ the parametric variable, the point on
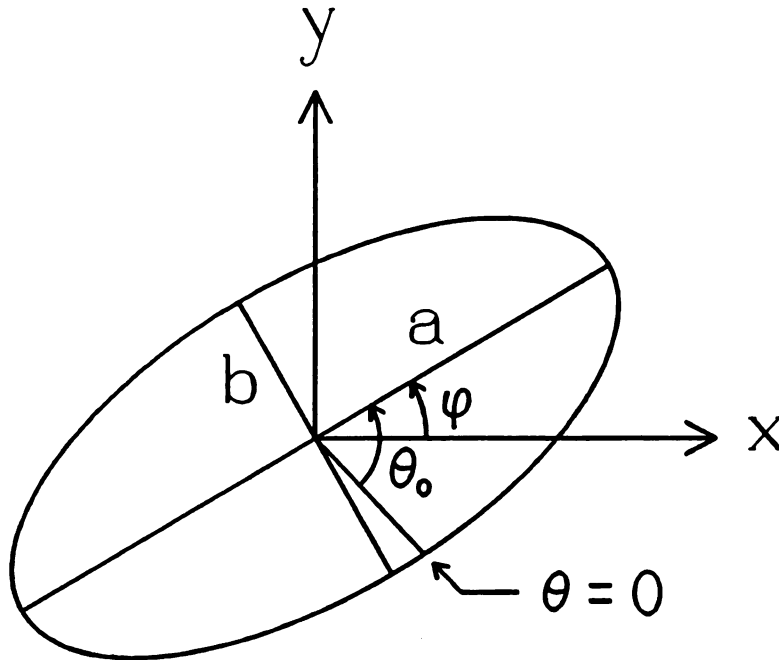
Figure D-1 Ellipse rotated by φ away from coordinate axes.

the ellipse for $\theta = 0$ is located at the angle θ_0 away from φ as shown. The point on the ellipse moves counterclockwise with θ for $ab > 0$ or clockwise against θ for $ab < 0$. The parametric equations describing the ellipse for θ starting at polar coordinate angle $\varphi - \theta_0$ are given by

$$x = a \cos(\theta - \theta_0) \cos\varphi - b \sin(\theta - \theta_0) \sin\varphi$$

$$y = a \cos(\theta - \theta_0) \sin\varphi + b \sin(\theta - \theta_0) \cos\varphi .$$

(D-11)

The rotation ellipse followed by the tip of the vector representing two field components may be put into the form of Equations (D-11). Suppressing the time decay factor, the field components are given by

$$E_x(t) = E_x \cos(\omega t + \delta_x),$$

$$E_y(t) = E_y \cos(\omega t + \delta_y).$$

(D-12)

With ωt as the parametric variable, it may be shown that the features of the ellipse are written in terms of the field magnitudes and phases as

$$a = \frac{1}{2} \left[\sqrt{E_x^2 + E_y^2 + 2 E_x E_y \sin(\delta_x - \delta_y)} \right.$$

$$\left. + \sqrt{E_x^2 + E_y^2 - 2 E_x E_y \sin(\delta_x - \delta_y)} \right] ,$$

(D-13)

$$b = \frac{1}{2} \left[\sqrt{E_x^2 + E_y^2 + 2 E_x E_y \sin(\delta_x - \delta_y)} \right.$$

$$\left. - \sqrt{E_x^2 + E_y^2 - 2 E_x E_y \sin(\delta_x - \delta_y)} \right] ,$$

(D-14)

$$\varphi = \frac{1}{2} \left[\arctan\left(\frac{E_x \sin\delta_x + E_y \cos\delta_y}{E_x \cos\delta_x - E_y \sin\delta_y} \right) \right.$$

$$\left. + \arctan\left(\frac{-E_x \sin\delta_x + E_y \cos\delta y}{E_x \cos\delta_x + E_y \sin\delta y} \right) \right] ,$$

(D-15)

$$\theta_o = \frac{1}{2} \left[\arctan \left(\frac{-E_x \sin\delta_x + E_y \cos\delta_y}{E_x \cos\delta_x + E_y \sin\delta_y} \right) \right.$$

$$\left. - \arctan \left(\frac{E_x \sin\delta_x + E_y \cos\delta y}{E_x \cos\delta_x - E_y \sin\delta y} \right) \right] . \qquad \text{(D-16)}$$

It is useful to note that a as defined in Equation (D-13) is always greater than zero so that the direction of rotation may be determined solely from the sign of b. For the lossless case b is zero. The direction of rotation may also be determined from the phase values alone. Choosing the principal values of the phases to lie between $-\pi$ and $+\pi$ the direction of rotation is found as indicated in Table D-1 below.

From Equations (D-13) and (D-14) it may also be shown that

$$E_x^2 + E_y^2 = a^2 + b^2 . \qquad \text{(D-17)}$$

This quantity is the square of the distance between the points were the major and minor axis intersect the rotation ellipse.

Since the fields decay with time, the tip of the field vector does not remain on the rotation ellipse boundary but draws inward toward the origin as the field rotates. In order to adequately represent the field, the actual path of the vector during one cycle is inscribed in the rotation ellipse as shown in Figure D-2. By inscribing the time-decaying field path the direction of rotation is also indicated.

Phase Angle Difference	Rotation Direction
$-2\pi < \delta_x - \delta_y < -\pi$	counterclockwise
$-\pi < \delta_x - \delta_y < 0$	clockwise
$0 < \delta_x - \delta_y < \pi$	counterclockwise
$\pi < \delta_x - \delta_y < 2\pi$	clockwise

Table D-1 Rotation direction in relation to phase differences.

$$E_y$$

$$t = \frac{2\pi}{\omega'}$$

$$E_x$$

$$t = 0$$
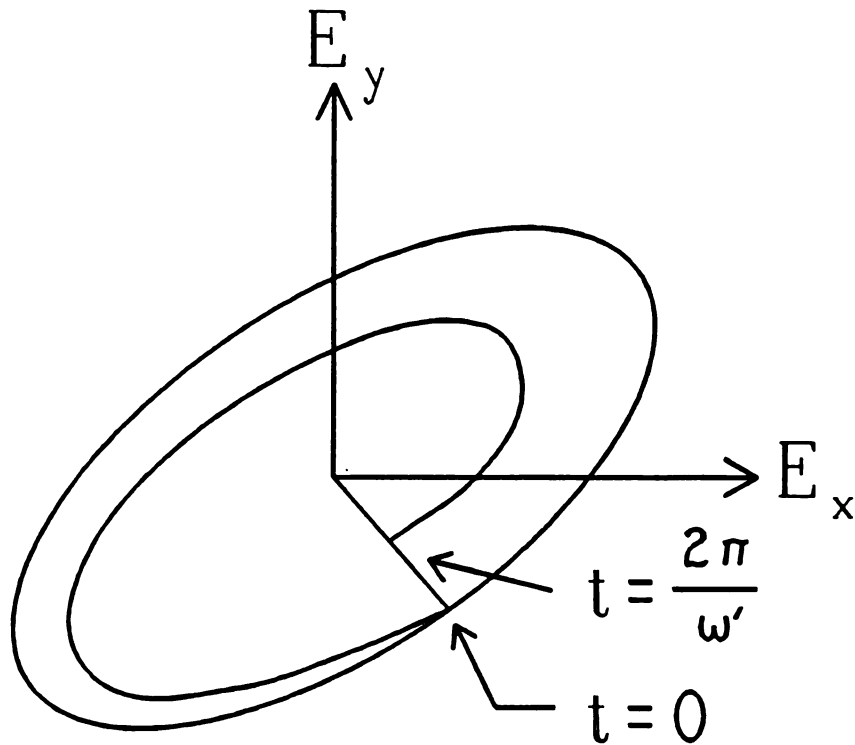
Figure D-2 Rotation ellipse with inscribed field trajectory.

Field rotation ellipses, such as the one shown in Figure D-2, may be drawn for any given point inside the cavity. By drawing a rotation ellipse at each point on a grid representing a plane of points in the cavity, a representation may be made for the rotating vector fields of the natural modes. Such a representation is analogous to the representation of a time constant vector field produced by drawing the appropriate vector at a number of equally spaced points.

This rotation of the natural mode fields gives cause for speculation on its possible effects on materials heating processes. The first question is, does this field rotation take place under sinusoidal steady-state conditions? If it does, then there is probably nothing new to be gained from examining the effect of field rotation on heating, since it has been a factor all along. However, if this rotation occurs only when the fields decay with time in natural mode fashion, an investigation of materials heating using a sharp pulse signal might exhibit interesting heating patterns. In order to deliver an appreciable amount of energy while maintaining a narrow pulse width,

the frequency of the pulses would have to be on the order of ω'. This prompts the designation of *extremely rapid pulse* (ERP) for the process.

It is possible that the ERP process would provide more uniform heating. On the other hand, since field rotation occurs only when there are boundaries between materials in a cavity, perhaps ERP heating would preferentially heat the boundary regions. If that is the case, the ERP process could be used for bonding and joining of materials, similar to the way sinusoidal steady-state heating is used already.[1]

D.4 Relative Time-Average Field Values

It should now be clear that the choice of t_0 in determining the time-average values of the field components is very important. Even if a field at a point is primarily radial at $t = 0$, selecting t_0 such that the field is axial at $t = t_0$ may produce the impression that the time-average value of the field is primarily axial. The larger ω'' the more such distortion is likely to occur because, due to the decay in time, the contribution from the field at t_0 is relatively greater than the contribution a quarter of a cycle later.

It is proposed here that the best means of obtaining an idea of the relative contributions of each component of the field to the time-average value is to set t_0 to zero and integrate over a large number of cycles, i.e., referring to Equations (D-5) through (D-7), set $m = \infty$. The value for m in the denominator of Equation (D-6) may be neglected since it is common to all components. This procedure yields a value which is a true relative time average over all time.

Upon examining Equation (D-7) it may be seen that the relative time-average field values from the above procedure may be obtained irrespective of m by using any t_0 of the form

$$t_0 = 0, \quad \text{or} \quad t_0 = \frac{n\pi}{\omega'}, \tag{D-18}$$

where n is an integer. This indicates that the first (or nth) half cycle after $t_0 = 0$ is a

---

[1]Clark, Gac, and Sutton, 487-521.

sufficient representative of the relative time-average value of the field components over all time. In simplest form, the relative time-average value of one field component may be written

$$E_{av}(rel.) = \frac{E}{\sqrt{2}} \sqrt{1 - \frac{\omega''\omega'}{\omega''^2 + \omega'^2}\left(\sin2\delta - \frac{\omega''}{\omega'}\cos2\delta\right)} \quad . \qquad \text{(D-19)}$$

Equation (D-19) provides a time-independent means of comparing time-average values of the various field components at a single point, or for comparing values of a single component at different points within the cavity and load. It reduces to the RMS value of E for $\omega'' = 0$.

Appendix E
COMPLEX ROOT-FINDING ALGORITHMS
USED IN THIS DISSERTATION

Root-finding lies at the heart of numerical solutions of boundary value problems. For real functions with real arguments there are a number of methods which can be used to find the function's zeros. Among these methods are bisection, the false position method (linear approximation), Müller's method (approximation using a quadratic), and Newton's method. Depending on the character of the function, any of these might be used with good results. In any event, when a root is bracketed, the bisection method will always find it or another zero or singularity within the bracketed region. Unfortunately, when the function is complex and its argument is complex the problem of finding its roots is far more difficult.

Searching for the complex roots of a complex function can be understood as the solution of two simultaneous functions of two variables. The real and imaginary parts of the complex function are the two simultaneous functions, while the real and imaginary parts of the complex variable are the two variables. If the complex function is f and the complex argument is z, the roots are the solutions to the simultaneous equations

$$\mathrm{Re}\big[f\big(\mathrm{Re}(z),\mathrm{Im}(z)\big)\big] = 0,$$

$$\mathrm{Im}\big[f\big(\mathrm{Re}(z),\mathrm{Im}(z)\big)\big] = 0.$$

(E-1)

Formulating the problem this way helps to clarify the difficulty involved in searching for complex roots of a complex function. The authors of *Numerical Recipes* put the matter succinctly when they say, "We make an extreme, but wholly defensible, statement: There are *no* good, general methods for solving systems of

378

more than one nonlinear equation. Furthermore, it is not hard to see why (very likely) there *never will be* any good, general methods" (emphasis theirs).[1]

This prediction proved to be true for the complex functions arising in the problem considered in this dissertation. It was necessary to use two different complex root-finding techniques in the process of finding the complex natural frequencies of the cavity-open or cavity-image type cavities. The first root-finding technique was used to find the wavenumbers in the coaxially-loaded waveguide section of the cavity. The same root-finder was also used to solve for the wavenumbers in the coaxially-loaded .waveguide and for the natural frequency of the cavity-short type cavity. The technique is based on Traub's recension of Müller's method and works extremely well for smoothly varying functions.[2] The FORTRAN implementation used in this research is called *ROOT* and was developed by N. P. de Koo and Anton G. Tijhuis of the Laboratory of Electromagnetic Research in the Department of Electrical Engineering at Delft University of Technology in the Netherlands.[3] It is an especially safe and efficient algorithm and should be useful to anyone who finds occasion to search for complex roots of a smoothly varying complex function. The code is reproduced here by permission:

```
      SUBROUTINE ROOT(FUNC,A,B,EPS,M,NULP,KEY,ITR)
C
C /**************************************************************/
C /*                                                          */
C /* Subroutine ROOT determines a zero of the function FUNC    */
C /* starting from the initial estimates A < > B.              */
C /* Method employed: Muller's method.                         */
C /*                                                          */
C /* Directions for use: see file USER.DOK .                   */
C /*                                                          */
C /* Reference: Traub, J.F., "Iterative methods for the solution of */
```

[1]William H. Press, Brian P. Flannery, Saul A. Teukolsky, and William T. Vetterling, *Numerical Recipes: The Art of Scientific Computing* (Cambridge: Cambridge University Press, 1986), 269.

[2]J. F. Traub, *Iterative Methods for the Solution of Equations* (Englewood Cliffs, NJ: Prentice-Hall, 1964), ch. 10.

[3]N. P. de Koo and Anton G. Tijhuis, *ROOT* (Laboratory of Electromagnetic Research, Department of Electrical Engineering, Delft University of Technology, P.O. Box 5031, 2600 GA Delft, The Netherlands). From the same address may also be obtained some excellent subroutines by A. G. Tijhuis and R. M. van der Weiden for the evaluation of complex Bessel functions. Alternatively, according to Dr. Tijhuis, these zero-finding and complex Bessel function evaluation subroutines may be obtained from Rick Whittaker at McDonnell Douglas Research Laboratories in Saint Louis.

```fortran
C /* equations", Prentice - Hall, Englewood Cliffs, New Jersey (1964), */
C /* Chapter 10.                                                       */
C /*                                                                   */
C /* Author        : N.P. de Koo                                       */
C /* English version : A.G. Tijhuis (1984)                             */
C /*                                                                   */
C /* (C) : 1975                                                        */
C /*        Laboratory of Electromagnetic Research                     */
C /*        Department of Electrical Engineering                       */
C /*        Delft University of Technology                             */
C /*        P.O. Box 5031, 2600 GA Delft, The Netherlands.             */
C /*                                                                   */
C /* Fortran language translation:                                     */
C /*                                                                   */
C /*        11/85                                                      */
C /*        Chander Sabharwal                                          */
C /*        McDonnell Douglas Research Laboratories                    */
C /*        P.O. Box 516                                               */
C /*        St. Louis, MO 63166                                        */
C /*        USA                                                        */
C /*                                                                   */
C /*        (Modified by Ben Manring 9/89 to return also the number of */
C /*        iterations carried out.)                                   */
C /*                                                                   */
C /*******************************************************************/
C
      INTEGER    M,N,ITR
C
      COMPLEX*16 A,B,NULP,Z3,Z2,F3,F2,Z23,F23,Z1,F1,DZ23,Z12,F12,DZ12,
     1           Z13,F13,DZ123,OHM,OHM2,W2,W,N1,N2,CORR,Z,FUNC
C
      DOUBLE PRECISION EPS,ABS1,ABS2
C
      LOGICAL    KEY
C
      EXTERNAL   FUNC
C
         Z3=A
         Z2=B
         F3=FUNC(A)
         F2=FUNC(B)
         IF(KEY) THEN
            WRITE(6,61) A,F3,B,F2
  61        FORMAT(/1X,'Initial value of A = ',2D15.7,' F3 = ',2D15.7,
     1             /1X,'Initial value of B = ',2D15.7,' F2 = ',2D15.7)
         ENDIF
         Z23=Z2-Z3
         F23=F2-F3
         DZ23=F23/Z23
         Z1=Z2-F2/DZ23
         N=-1
         F1=FUNC(Z1)
         Z=Z1
  10     CONTINUE
         N=N+1
         IF(KEY) THEN
            WRITE(6,62) N,Z,F1
  62        FORMAT(1X,'N = ',I4,'Z = ',2D15.7,'F1 = ',2D15.7)
         ENDIF
         Z12=Z1-Z2
         F12=F1-F2
         DZ12=F12/Z12
         Z13=Z1-Z3
         F13=DZ12-DZ23
         DZ123=F13/Z13
         OHM=Z12*DZ123+DZ12
         OHM2=OHM*OHM
         W2=OHM2-4E0*F1*DZ123
         W=CDSQRT(W2)
         N1=W+OHM
         N2=OHM-W
         ABS1=CDABS(N1)
         ABS2=CDABS(N2)
         IF(ABS1 .GT. ABS2) THEN
            CORR=F1/N1*2D0
```

```
      ELSE
        CORR=F1/N2*2D0
      ENDIF
      Z3=Z2
      Z2=Z1
      Z=Z1-CORR
      F3=F2
      F2=F1
      F1=FUNC(Z)
      Z1=Z
      DZ23=DZ12
      IF(M .EQ. N) THEN
        WRITE(6,63)
63      FORMAT(1X,'Too many iteration steps.')
        GOTO 20
      ENDIF
      ABS1=CDABS(Z1)
      IF(CDABS(CORR) .GT. EPS*ABS1)  GOTO 10
C
      IF(KEY) WRITE(6,64) EPS
. 64    FORMAT(/1X,'The specified accuracy,EPS = ',E15.7
   1              ,' has been reached.')
C
20    CONTINUE
      IF(KEY) THEN
        WRITE(6,65) N+1,Z1,F1
65      FORMAT(1X,'Number of iteration steps : ',I10
   1           /1X,'Z1 = ',2D25.14
   2           /1X,'F1 = ',2D25.14)
      ENDIF
      ITR=N+1
      NULP=Z1
      RETURN
      END
```

While this root-finder worked very well in solving the boundary condition equations for coaxially-loaded waveguide sections, it was not able to locate roots of the matrix determinants produced by equating tangential E and H fields across the boundaries between homogeneous and coaxially-loaded waveguide regions. The reason for this is that both the real and the imaginary parts of the determinant are step functions. The roots of step functions are difficult to find by any means except bisection, which is not directly applicable to the complex case. An analog to bisection does exist for analytic complex functions with no branch cuts in the vicinity of the root. For an analytic function, contour integration in the complex plane may be used to determine the number of roots enclosed in the contour. Roots may be found by taking successively smaller contours around the root until it is located to sufficient precision. This method is not restricted to single roots. Such an approach was briefly attempted to solve the cavity-image type problem, but without success. It is possible that there are branch cuts in the region near the roots.

Instead, a rather cumbersome, but effective method of finding complex roots was developed for this application. It is based on finding the roots of the real and

imaginary parts of the determinant independently. The roots of either part form a curve on the complex argument plane. The point at which a curve of zeros of the real part of the determinant crosses a curve of zeros of the imaginary part is a zero of the complex determinant, both the real and imaginary parts being zero. This is illustrated in Figure E-1. The Figure shows two curves. The nearly vertical curve is a plot of the roots of the imaginary part of the determinant; the other curve is for the real part of the determinant. The Figure shows a complex natural frequency for the cavity/load system where the two curves cross at $f = 2.416815 + j\, 1.327$ GHz.[†]

It is not necessary to plot the zeros in order to find the complex root, as shown in Figure E-1. It is easier to include the bookkeeping details in a computer program and locate the crossing points by linear interpolation in the vicinity of the root. These capabilities are included in the complex root-finder *COMBIS*. *COMBIS* finds complex roots as described above by using bisection individually on the real and imaginary parts of the determinant. The FORTRAN code for *COMBIS* is given below and the algorithm is briefly outlined here.

Figure E-2 shows portions of the curves formed by the zeros of the real and imaginary parts of a hypothetical function on the complex argument plane. In this example, the first step is to find a root of the imaginary part of the complex function. This is done by choosing a value for the imaginary part of the root, y_o, as shown in Figure E-2. With y_o fixed, the root of the imaginary part of the function is x_1. In general, x_1 may be found using any kind of real root-finder, but bisection is probably necessary if it is necessary to resort to a method like *COMBIS* to find the complex roots of the total function.

x_1 is then used as the fixed real part of the root and y_1 is sought as the root of the real part of the function. When y_1 is located it is used as the fixed imaginary part of the root while x_2 is sought as the root of the imaginary part of the function. Similarly, y_2 is found by fixing x_2 as the real part of the root and solving for the root of the real part of the function. Referring to Figure E-2, when points 1, 2, 3, and 4 are found, a new starting point is calculated from the crossing point, point 5 in the

---

[†]The data plotted derives from the Method I type solution with a 5 x 5 matrix.

TM012 mode, 7" cavity, 1/2" nylon rod

5x5 Determinant

Ls = 14.65 cm

b = 3.5 in

a = .25 in

l = 2.5 cm

ϵ = 3.03 − j0.039

▫—▫ Zeros of Imag (Det)
⊙—⊙ Zeros of Real (Det)

Imag (f) GHz

2.1E−05
1.9E−05
1.7E−05
1.5E−05
1.3E−05
1.1E−05
9.0E−06

2.41670   2.41676   2.41682   2.41688   2.41694   2.41700

Real (f) GHz
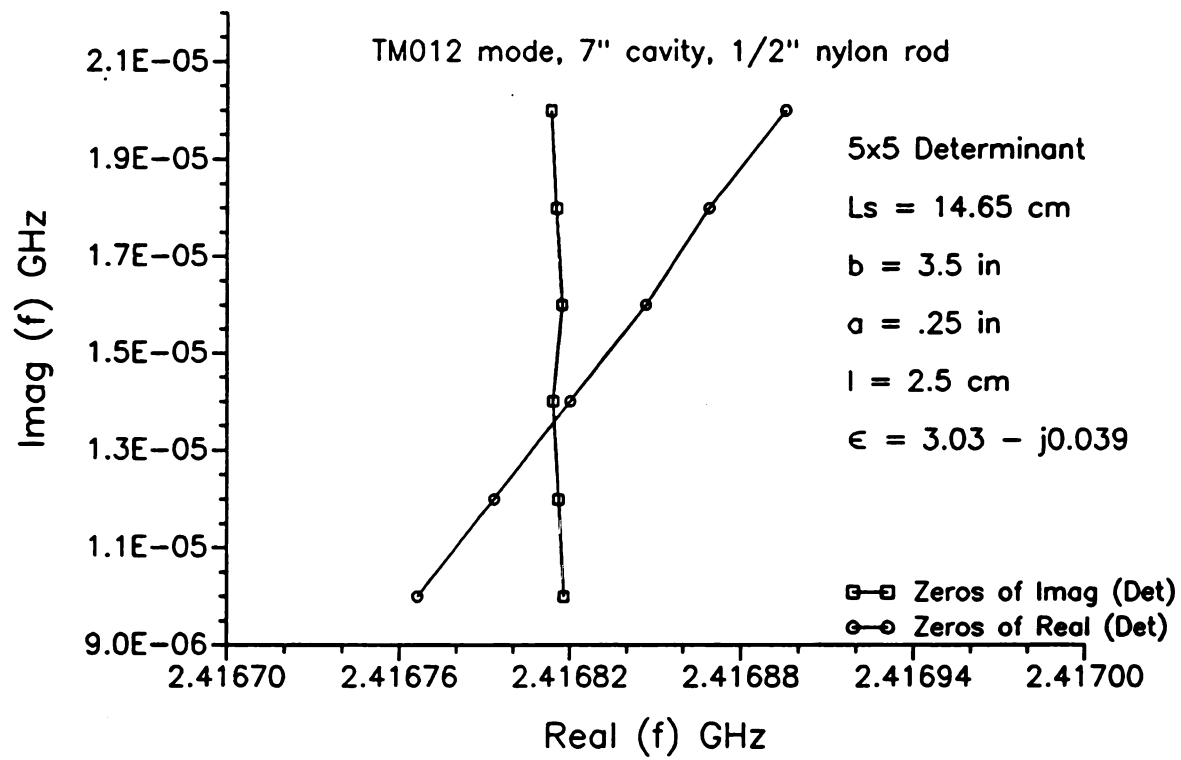
Figure E-1 Complex roots located by crossing of real and imaginary root curves.
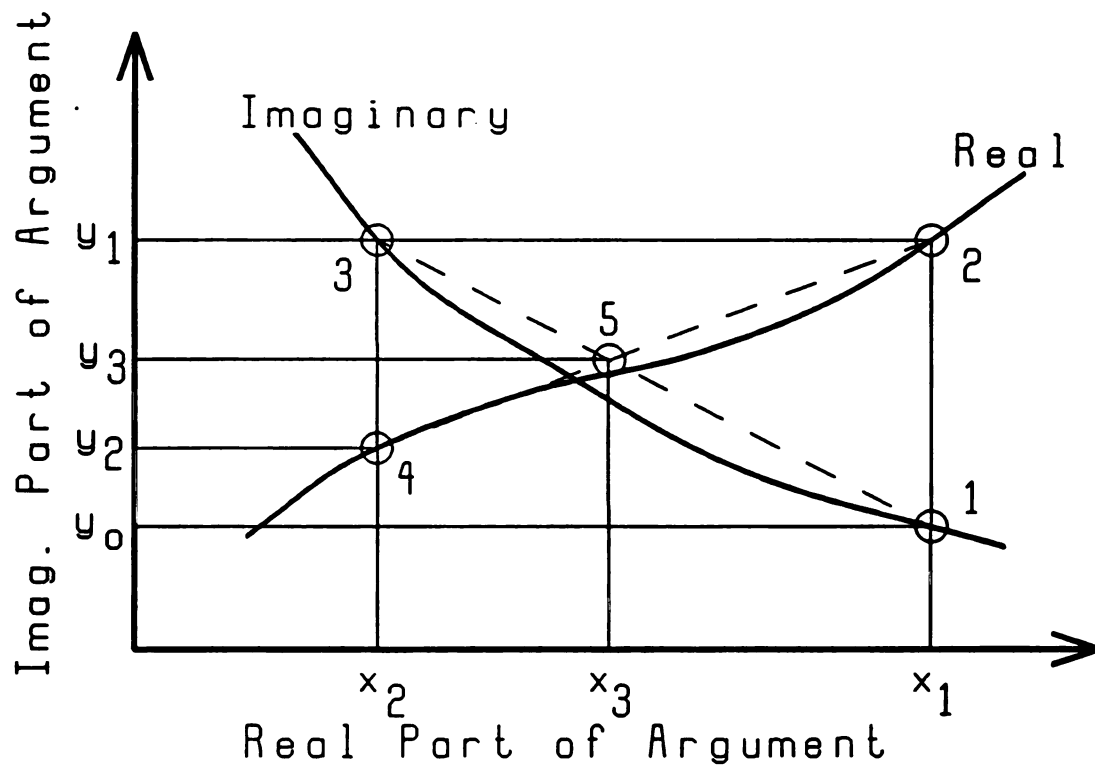
Figure E-2 Points used by *COMBIS* in finding complex roots.

Figure. Thus y_3 becomes the new initial imaginary part of the root, i.e., y_3 becomes the new y_0, and another iteration is carried out. *COMBIS* determines when enough iterations have been carried out by comparing points 1, 2, 3, and 4. If they are close enough together, i.e., they differ by an amount less than the specified accuracy, and point 5 is located inside the rectangle composed of the lines connecting them, *COMBIS* returns point 5 as the root.

It may be observed that there is a difficulty if one of the curves of zeros forms a horizontal or a vertical line on the plane. Two courses of action are available. First, one may test for this condition beforehand. If it exists, then all that is necessary is that the value represented by the vertical or horizontal line be set appropriately as the value of one part of the root. The other part of the root is then found by one application of bisection to the component of the function whose zeros did not fall into the vertical or horizontal line.

Second, the actual argument plane may be transformed by rotation into a plane which *COMBIS* uses to represent the argument. This is the method employed in the version of *COMBIS* below. Rotation is also useful even when the zero curves are not horizontal or vertical. Sometimes it is simply easier to find the complex zeros for a certain function by a rotation of the axes. $90°$ was a common rotation used in solving for the roots of the determinants in this dissertation. In addition to rotation, the axes may also be scaled or inverted. Scaling is used in the version of *COMBIS* below. Inversion may easily be added if desired:

```
      SUBROUTINE COMBIS(GUESS1,GUESS2,ACC,THETA,NITR,NULP,ITR)
C
C/*********************************************************************/
C/*                                                                 */
C/*    (C) : 1992, E. B. Manring                                    */
C/*                                                                 */
C/*    Subroutine COMBIS is designed to find the complex zeros of the */
C/*    complex function, FUNC=RLFUNC + j IMFUNC. It does so using REAL */
C/*    root finding techniques, bisection here, although any real zero */
C/*    finding technique could be substituted. However, the reason   */
C/*    one would use COMBIS instead of a Muller's method, a secant   */
C/*    method, or some other complex zero-finding technique is because */
C/*    the real and imaginary parts of the function are step functions */
C/*    whose roots cannot be found easily by other means. So, bisec- */
C/*    tion is probably needed if COMBIS is needed.                  */
C/*                                                                 */
C/*    METHOD of attack: COMBIS finds zeros of the real and imag-    */
C/*    inary parts of the function separately. These zeros will form */
C/*    two curves on the complex argument plane, one curve will rep- */
```

```
C/*    resent the zeros of real part, the other curve the zeros of    */
C/*    the imaginary part. Where the two curves cross, both real and  */
C/*    imaginary parts are zero simultaneously. COMBIS attempts to    */
C/*    find that crossing point by linear approximation in the        */
C/*    vicinity of the root.                                          */
C/*                                                                   */
C/*    IMPORTANT NOTE: COMBIS assumes that the initial guess is       */
C/*                    close enough to the result that the pattern    */
C/*                    made in the complex argument plane by the      */
C/*                    curve for the zeros of the imaginary part      */
C/*                    of the function and the curve for the zeros    */
C/*                    of the complex part of the function looks      */
C/*                    like an X or a + in the "vicinity" of the      */
C/*                    guess. COMBIS may work anyway under certain    */
C/*                    circumstances; however, even if this rather    */
C/*                    vague criterion is satisfied, COMBIS may       */
C/*                    wander off the zero. There are no guarantees   */
C/*                    made by the author.                            */
C/*                                                                   */
C/*                                                                   */
C/*    VARIABLES:                                                     */
C/*                                                                   */
C/*    GUESS1    Complex*16.  The initial guess for the root.         */
C/*                                                                   */
C/*    GUESS2    Complex*16.  A second guess, close to GUESS1.        */
C/*                                                                   */
C/*    ACC       Real*8.  The absolute accuracy desired in the root.  */
C/*                                                                   */
C/*    THETA     Real*8.  The offset angle of the X-Y coordinates used */
C/*              by COMBIS from the REAL(Z)-IMAG(Z) coordinates of the */
C/*              complex argument plane: radians.                     */
C/*                                                                   */
C/*    SCALE     Real*8.  This variable is the ratio of the real part */
C/*              of the initial guess to the imaginary part of the    */
C/*              initial guess. ·It is used to scale the imaginary    */
C/*              argument axis to the same order as the real argument */
C/*              axis.  This makes the absolute accuracy specified by */
C/*              ACC applicable to both real and imaginary parts of   */
C/*              the argument.  It is also helpful to have both axes  */
C/*              of nearly the same order in order that the rotation  */
C/*              be effective.                                        */
C/*                                                                   */
C/*    NITR      Integer.  Number of allowed iterations.              */
C/*                                                                   */
C/*    NULP      Complex*16.  The Root found by COMBIS.               */
C/*                                                                   */
C/*    ITR       Integer.  Number of iterations COMBIS took to find   */
C/*              the root.                                            */
C/*                                                                   */
C/*                                                                   */
C/*    The PRM variable is a parameter which is made common to RLFUNC */
C/*    or IMFUNC as a fixed second variable (X or Y while the other is */
C/*    being sought).                                                 */
C/*                                                                   */
C/*    NOTE:  FUNCTION NAME                                           */
C/*                                                                   */
C/*    The name of the function is not in the argument list.  Rather, */
C/*    it is named in the external function subroutines RLFUNC and    */
C/*    IMFUNC.  These subroutines should be modified to specify the   */
C/*    function whose roots are being sought.                         */
C/*                                                                   */
C/*                                                                   */
C/*    NOTE:  SUBROUTINE "PAUSED"                                     */
C/*                                                                   */
C/*    The subroutine PAUSED is used to allow the screen to pause     */
C/*    for TIM seconds so that intermediate results may be viewed     */
C/*    The intrinsic functions called by PAUSED may not be available  */
C/*    on all systems.                                                */
C/*                                                                   */
C/*    CREDITS:                                                       */
C/*                                                                   */
C/*    Subroutines ZBRAC and RTBIS are modified forms of bracketing   */
C/*    and bisection subroutines found in Numerical Recipes: The Art  */
C/*    of Scientific Computing (Cambridge: Cambridge University Press, */
C/*    1986), pp. 245-247, by W. H. Press, B. P. Flannery, S. A.      */
```

387

```
C/*    Teukolsky, and W. T. Vetterling.                              */
C/*                                                                  */
C/*****************************************************************/
C
      INTEGER    NITR,ITR,GSIGN,FITR
C
      INTEGER*2  TIM
C
      COMPLEX*16 GUESS1,GUESS2,NULP,DC
C
      REAL*8     ACC,IMFUNC,RLFUNC,Y1,X1,Y2,X2,Y3,A,B,PRM,THETA,
     *           THETAC,S,C,SCALE,DX,DY
C
      LOGICAL    CROSS
C
      EXTERNAL   IMFUNC,RLFUNC
C
      COMMON/ CPARAM / PRM,THETAC,SCALE
      COMMON/ PAUSTM / TIM
C
.     GSIGN=1
      ITR=1
      THETAC=THETA
      SCALE=DABS(DREAL(GUESS1)/DIMAG(GUESS1))
C
      THETAC=THETA
      S=DSIN(THETA)
      C=DCOS(THETA)
C
  100 A=DREAL(GUESS1)*C + SCALE*DIMAG(GUESS1)*S
      B=DREAL(GUESS2)*C + SCALE*DIMAG(GUESS2)*S
      Y1=SCALE*DIMAG(GUESS1)*C - DREAL(GUESS1)*S
C
      PRINT *, ' '
      PRINT *, 'NOW CALLING IMAGINARY PART OF THE FUNCTION'
      PRINT *, ' ---------------------------------------- '
      PRINT *, ' '
      PRM=Y1
      DX=A-B
      CALL BISEC(IMFUNC,A,B,ACC,FITR,X1)
C
      PRINT *, ' '
      PRINT *, 'NOW CALLING REAL PART OF THE FUNCTION'
      PRINT *, ' --------------------------------- '
      PRINT *, ' '
      A=Y1
      B=SCALE*DIMAG(GUESS2)*C - DREAL(GUESS2)*S
      PRM=X1
      DY=A-B
      CALL BISEC(RLFUNC,A,B,ACC,FITR,Y2)
C
      PRINT *, ' '
      PRINT *, 'NOW CALLING IMAGINARY PART OF THE FUNCTION'
      PRINT *, ' ---------------------------------------- '
      PRINT *, ' '
      A=X1+DX/3.1
      B=X1-DX/3.
      PRM=Y2
      CALL BISEC(IMFUNC,A,B,ACC,FITR,X2)
C
      PRINT *, ' '
      PRINT *, 'NOW CALLING REAL PART OF THE FUNCTION'
      PRINT *, ' --------------------------------- '
      PRINT *, ' '
      A=Y2+DY/3.1
      B=Y2-DY/3.
      PRM=X2
      CALL BISEC(RLFUNC,A,B,ACC,FITR,Y3)
C
   55 CROSS=(Y2-Y3)*(Y2-Y1).GE.0.
C
      PRINT *, ' '
      PRINT *, 'POINT 1:',X1*C-Y1*S,(X1*S+Y1*C)/SCALE
      PRINT *, 'POINT 2:',X1*C-Y2*S,(X1*S+Y2*C)/SCALE
      PRINT *, 'POINT 3:',X2*C-Y2*S,(X2*S+Y2*C)/SCALE
```

```fortran
      PRINT *, 'POINT 4:',X2*C-Y3*S,(X2*S+Y3*C)/SCALE
      PRINT *, ' '
      IF ((X1.EQ.X2.AND.DABS(Y2-Y3).LT.10*ACC) .OR.
     *    (Y2.EQ.Y3.AND.DABS(X1-X2).LT.10*ACC)      ) THEN
         NULP=DCMPLX(X2*C-Y3*S,(X2*S+Y3*C)/SCALE)
         RETURN
      ELSE IF (X1.EQ.X2 .OR. Y2.EQ.Y3) THEN
         A=X2
         B=Y3
      ELSE
         A=(X2*(Y1-Y2)+X1*(Y3-Y2))/((Y1-Y2)+(Y3-Y2))
         B=((Y3-Y2)*A+Y2*X2-Y3*X1)/(X2-X1)
      ENDIF
      PRINT *, 'CROSSING POINT:',A*C-B*S,(A*S+B*C)/SCALE
      PRINT *, ' '
C
      IF (CROSS) THEN
           PRINT*, 'Crossing point inside rectangle!'
           CALL PAUSED (TIM)
      ELSE
           PRINT*, 'CAUTION.  CROSSING POINT OUTSIDE RECTANGLE.'
           CALL PAUSED (TIM)
      GSIGN=-GSIGN
      ENDIF
C
C
C/*   Now that we have found four points around the zero we draw an
C/*   X and use the center as the new starting point.
C
C
      IF (DABS(X2-X1).LT.10.*ACC .AND.
     *    DABS(Y2-Y3).LT.10.*ACC .AND.
     *    DABS(Y2-Y1).LT.10.*ACC .AND.
     *    CROSS                         ) THEN
           NULP=DCMPLX(A*C-B*S,(A*S+B*C)/SCALE)
           RETURN
      ENDIF
C
      DC=GSIGN*(GUESS1-GUESS2)/23.
      GUESS2=DCMPLX(A*C-B*S,(A*S+B*C)/SCALE)-2.1*DC
      GUESS1=DCMPLX(A*C-B*S,(A*S+B*C)/SCALE+3.1*DIMAG(DC))
      ITR=ITR+1
      PRINT *, ' '
      PRINT *, 'ITERATIONS OF COMBIS:'
      PRINT *, ' '
      PRINT *, ITR,' ',ITR
      PRINT *, ITR,' ',ITR,' ',ITR
      PRINT *, ITR,' ',ITR,' ',ITR,' ',ITR
      PRINT *, ITR,' ',ITR,' ',ITR,' ',ITR,' ',ITR
      PRINT *, ITR,' ',ITR,' ',ITR,' ',ITR,' ',ITR,' ',ITR
      PRINT *, ITR,' ',ITR,' ',ITR,' ',ITR,' ',ITR,' ',ITR
      PRINT *, ITR,' ',ITR,' ',ITR,' ',ITR,' ',ITR,' ',ITR
      PRINT *, ITR,' ',ITR,' ',ITR,' ',ITR,' ',ITR
      PRINT *, ITR,' ',ITR,' ',ITR,' ',ITR
      PRINT *, ITR,' ',ITR,' ',ITR
      PRINT *, ITR,' ',ITR
      IF (ITR.LT.NITR) GOTO 100
      PRINT *, 'Too many iterations in COMBIS.'
      NULP=GUESS1
C
      RETURN
      END
C
C&&&&&&&&&&&&&&&&&&&&&&&&&&&&&&&&&&&&&&&&&
C
      SUBROUTINE BISEC(FUNC,A,B,ACC,ITR,ZERO)
C
C/*****************************************************************/
C/*                                                             */
C/*   BISEC is a combination of ZBRAC and RTBIS, respectively brack- */
C/*   eting and bisection routines for real functions of real   */
C/*   variables.                                                */
C/*                                                             */
C/*****************************************************************/
C
```

```
      INTEGER    ITR
C
      REAL*8     FUNC,A,B,ACC,ZERO,RTBIS,FA,FB
C
      LOGICAL    SUCCES
C
      EXTERNAL FUNC
C
      CALL ZBRAC(FUNC,A,B,FA,FB,SUCCES)
      IF (SUCCES) THEN
        ZERO=RTBIS(FUNC,A,B,FA,FB,ACC,ITR)
      ELSE
        PAUSE 'Could not bracket the root. Hit <Control><Break> to end.'
      ENDIF
C
      RETURN
      END
C
C&&&&&&&&&&&&&&&&&&&&&&&&&&&&&&&&&&&&
C
      SUBROUTINE ZBRAC(FUNC,X1,X2,F1,F2,SUCCES)
C
      INTEGER J,NTRY
C
      REAL*8  FACTOR,X1,X2,FUNC,F1,F2
C
      LOGICAL SUCCES
C
      EXTERNAL FUNC
C
      PARAMETER (FACTOR=.50,NTRY=40)
C
      IF(X1.EQ.X2) PAUSE 'You have to guess an initial range.'
      F1=FUNC(X1)
      F2=FUNC(X2)
      SUCCES=.TRUE.
      DO 100, J=1,NTRY
        IF (F1*F2.LT.0.) RETURN
        IF(DABS(F1).LT.DABS(F2)) THEN
          X1=X1+FACTOR*(X1-X2)
          F1=FUNC(X1)
        ELSE
          X2=X2+FACTOR*(X2-X1)
          F2=FUNC(X2)
        ENDIF
  100 CONTINUE
      SUCCES=.FALSE.
      RETURN
      END
C
C&&&&&&&&&&&&&&&&&&&&&&&&&&&&&&&&&&&&
C
      DOUBLE PRECISION FUNCTION RTBIS(FUNC,X1,X2,F1,F2,ACC,ITR)
C
      REAL*8     FUNC,X1,X2,ACC,F,FMID,DX,XMID,F1,F2
C
      INTEGER    J,JMAX,ITR
C
      EXTERNAL FUNC
C
      PARAMETER (JMAX=50)
C
      FMID=F2
      F=F1
      IF(F*FMID.GE.0.) PAUSE 'Root must be bracketed for bisection.'
      IF(F.LT.0.) THEN
        RTBIS=X1
        DX=X2-X1
      ELSE
        RTBIS=X2
        DX=X1-X2
      ENDIF
      DO 100, J=1,JMAX
        DX=DX*.5
        XMID=RTBIS+DX
```

```
      FMID=FUNC(XMID)
      ITR=J
      IF(FMID.LE.0.) RTBIS=XMID
      IF(DABS(DX).LT.ACC .OR. FMID.EQ.0.) RETURN
  100 CONTINUE
      PAUSE 'Too many bisections'
      END
C
C&&&&&&&&&&&&&&&&&&&&&&&&&&&&&&&&&&&
C
      REAL*8 FUNCTION RLFUNC(Y)
C
      REAL*8      X,Y,THETA,C,S,RARG,IARG,SCALE
C
      COMPLEX*16  ARG,FUNC
C
      COMMON/ CPARAM / X,THETA,SCALE
C
      EXTERNAL FUNC
C
      C=DCOS(THETA)
      S=DSIN(THETA)
C
      RARG=X*C-Y*S
      IARG=(X*S+Y*C)/SCALE
      PRINT *, ' '
      PRINT *, 'Argument:',RARG,IARG
      ARG=DCMPLX(RARG,IARG)
C
      RLFUNC=DREAL(FUNC(ARG))
C
      PRINT*, 'REAL part of the function:',RLFUNC
C
      RETURN
      END
C
C&&&&&&&&&&&&&&&&&&&&&&&&&&&&&&&&&&&&&
C
      REAL*8 FUNCTION IMFUNC(X)
C
      REAL*8      IARG,RARG,X,Y,THETA,C,S,SCALE
C
      COMPLEX*16  ARG,FUNC
C
      COMMON/ CPARAM / Y,THETA,SCALE
C
      EXTERNAL FUNC
C
      C=DCOS(THETA)
      S=DSIN(THETA)
C
      RARG=X*C-Y*S
      IARG=(X*S+Y*C)/SCALE
      PRINT *, ' '
      PRINT *, 'Argument:',RARG,IARG
      ARG=DCMPLX(RARG,IARG)
C
      IMFUNC=DIMAG(FUNC(ARG))
C
      PRINT*, 'IMAGINARY part of the function:',IMFUNC
C
      RETURN
      END
C
C&&&&&&&&&&&&&&&&&&&&&&&&&&&&&&&&&&&&&
C
      SUBROUTINE PAUSED(TIM)
C
      INTEGER*2 TIM,IHR,IMIN,ISEC,IHND,PSEC,PMIN,PHR
C
      CALL GETTIM(IHR,IMIN,ISEC,IHND)
      PMIN=IMIN
      PSEC=ISEC
  100 IF ( ( (PMIN.EQ.IMIN).AND.(PSEC.GT.(ISEC+TIM)) ) .OR.
     *     ( (PMIN.NE.IMIN).AND.((PSEC+59).GT.(ISEC+TIM)) ) ) RETURN
```

```
        CALL GETTIM(PHR,PMIN,PSEC,IHND)
        GOTO 100
 C
        END
```

No finesse is claimed for *COMBIS*. It is cumbersome and slow compared to most other complex root-finders. In some cases it may require more than a hundred function calls to accurately locate a root. Also, it should be noted that while bisection is a nearly fool proof method of finding the roots of the individual components of the function, *COMBIS* is not as reliable as it constituent parts. It may have difficulty locating a root for a given axis scale and rotation, particularly if a good guess is not available. It may also return a result which is not a root. An example where something like this might happen is illustrated in Figure E-3.

Nevertheless, there are some situations which require the brute force method embodied in *COMBIS*. In that case it is the only means by which a result may be obtained. Therefore, it is a valuable root finding technique and may be used with great profit when nothing else will work.
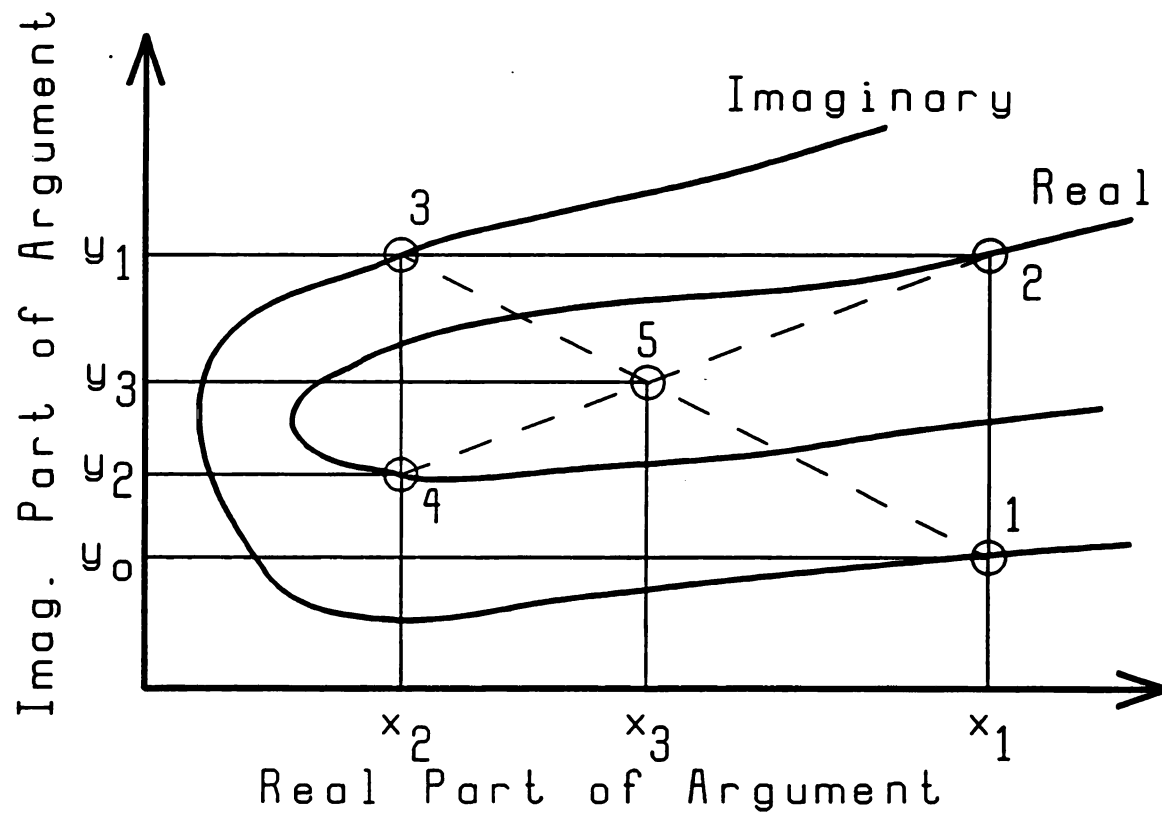
Figure E-3 Non-existent root located by *COMBIS*.

Appendix F

CHARACTERISTIC EQUATION FOR THE
SLAB-LOADED CAVITY

A special case of the cavity-image or cavity-open type configuration exists
when the load radius, a, is equal to the cavity radius, b. This special case is known
as the slab-loaded cavity configuration, shown below in Figure F-1. It may be
thought of as the radial counterpart of the cavity-short type configuration. In general,
the load or slab is of thickness ℓ with its center at height h above the cavity floor.

The cavity fields and natural frequencies are found by writing the fields for
each region in terms of the homogeneous waveguide expressions and matching
appropriate field components at the dielectric boundaries. Since the regions are
homogeneous, the fields in each region are either TE or TM. Furthermore, it is not
necessary to write the fields as summations over all modes because the homogeneous
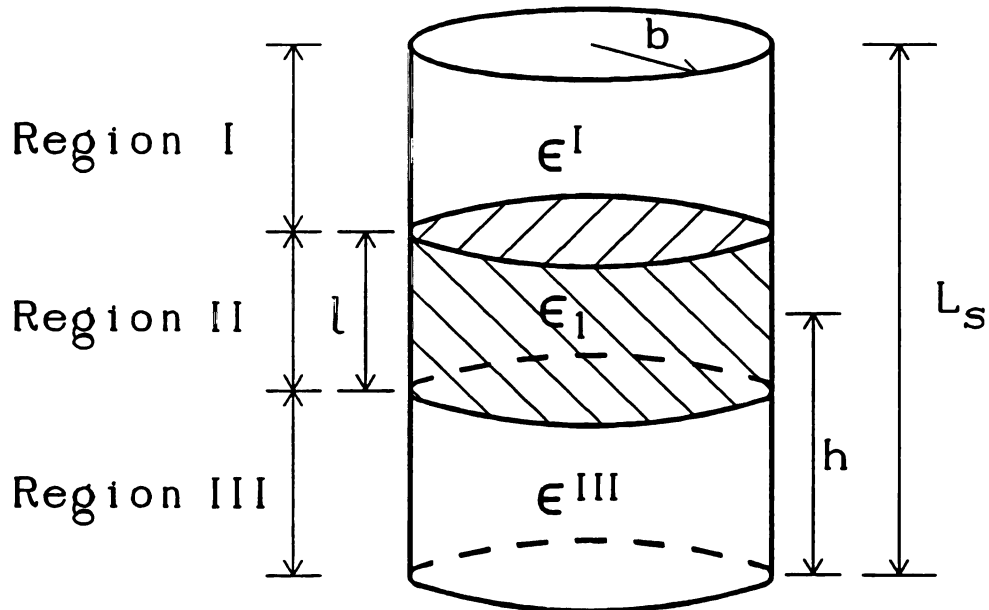

Figure F-1 General slab-loaded cavity configuration.

waveguide modes are orthogonal to one another. They match by one-to-one correspondence across the boundaries. For example, a TM_{01} mode in Region I couples to a TM_{01} mode in Region II and to no other. This fact greatly simplifies the solutions, not only by removing infinite sums from the boundary condition equations, but also because the transverse coordinate functional dependence is the same on each side of the equation and may be divided off.

For example, the axial electric field for TM modes in Region I may be written as

$$E_z^I = A \frac{\lambda_{np}^2}{j \omega \epsilon^I b^2} J_n(\frac{\lambda_{np} \rho}{b}) \cos(n\phi) \cos[k_z^I (z - L_s)] , \qquad (F-1)$$

while the axial electric field for the corresponding mode in Region II is given by

$$E_z^{II} = \frac{\lambda_{np}^2}{j \omega \epsilon_1 b^2} J_n(\frac{\lambda_{np} \rho}{b}) \cos(n\phi) [C \cos(k_z^{II} z) + D \sin(k_z^{II} z)] . \qquad (F-2)$$

Equating ϵE_z at the dielectric boundary yields

$$A \cos[k_z^I (h^+ - L_s)] = C \cos(k_z^{II} h^+) + D \sin(k_z^{II} h^+) , \qquad (F-3)$$

where $h^+ = h + \frac{1}{2} \ell$. In Equation (F-3) the transverse functional dependence has been canceled and only the axial dependence is left. However, information from the transverse dependence remains in the value of k_z, since

$$k_z = \sqrt{\omega^2 \mu \epsilon - k_c^2} , \qquad (F-4)$$

where k_c is the transverse wavenumber. In the cylindrical case $k_c = \frac{\lambda_{np}}{b}$. The transverse coordinate functional dependence also cancels for the other boundary condition equations.

An interesting corollary of the cancellation of the transverse functional dependence is that the characteristic equations for the circular cylindrical slab-loaded

cavity apply to slab-loaded cavities of general cylindrical cross section. The only difference between them is the value of k_c which depends on the geometry of the cross section. In a rectangular cavity, for example, k_c is given by

$$k^2_{c(rec)} = (\frac{n\pi}{L_x})^2 + (\frac{p\pi}{L_y})^2,$$ where L_x and L_y are the cross sectional dimensions of the cavity and n and p are integers. As long as it is possible to find an expression or a number for k_c, the characteristic equations derived below may be used for slab-loaded cavities of general cross section.

The characteristic equation for the configuration of Figure F-1, or a similarly configured cavity of general cylindrical cross section, may be written as in the form of a matrix equation as

$$\begin{bmatrix} X^+ & Y^+ \\ X^- & Y^- \end{bmatrix} \begin{bmatrix} C \\ D \end{bmatrix} = 0,$$ (F-5)

where for TM modes

$$X^+ = \frac{k_z^{II}}{\epsilon_1} \sin(k_z^{II} h^+) \cos[k_z^{I}(h^+ - L_s)] - \frac{k_z^{I}}{\epsilon^{I}} \cos(k_z^{II} h^+) \sin[k_z^{I}(h^+ - L_s)],$$

$$Y^+ = -\frac{k_z^{II}}{\epsilon_1} \cos(k_z^{II} h^+) \cos[k_z^{I}(h^+ - L_s)] - \frac{k_z^{I}}{\epsilon^{I}} \sin(k_z^{II} h^+) \sin[k_z^{I}(h^+ - L_s)],$$

(F-6)

$$X^- = \frac{k_z^{II}}{\epsilon_1} \sin(k_z^{II} h^-) \cos(k_z^{III} h^-) - \frac{k_z^{III}}{\epsilon^{I}} \cos(k_z^{II} h^-) \sin[k_z^{III}(h^-)],$$

$$Y^- = -\frac{k_z^{II}}{\epsilon_1} \cos(k_z^{II} h^-) \cos(k_z^{III} h^-) - \frac{k_z^{III}}{\epsilon^{III}} \sin(k_z^{II} h^-) \sin(k_z^{III} h^-).$$

The values $h^\pm$ are given by $h^\pm = h \pm \frac{1}{2}\ell$. The coefficients C and D are the axial dependence coefficients in Region II as used above in Equation (F-2). The characteristic equation is found by setting the determinant of the matrix in Equation (F-5) equal to zero. For TM modes the characteristic equation is

$$\frac{k_z^{\mathrm{II}\,2}}{\epsilon_1^2}\,\tan(k_z^{\mathrm{II}}\,\ell) \;+\; \frac{k_z^{\mathrm{I}}k_z^{\mathrm{III}}}{\epsilon^{\mathrm{I}}\epsilon^{\mathrm{III}}}\,\tan(k_z^{\mathrm{II}}\,\ell)\,\tan(k_z^{\mathrm{III}}h^-)\,\tan[k_z^{\mathrm{I}}(h^+ - L_s)]$$

(F-7)

$$-\,\frac{k_z^{\mathrm{II}}k_z^{\mathrm{I}}}{\epsilon_1\epsilon^{\mathrm{I}}}\,\tan[k_z^{\mathrm{I}}(h^+ - L_s)] \;+\; \frac{k_z^{\mathrm{II}}k_z^{\mathrm{III}}}{\epsilon_1\epsilon^{\mathrm{III}}}\,\tan(k_z^{\mathrm{III}}h^-) \;=\; 0\,.$$

Solving this equation, the frequency obtained may be returned to the matrix expression of Equation (F-5) to find C in terms of D, or vice versa. Knowing the coefficients, the fields may be determined.

When the slab lies on the bottom of the cavity, Equation (F-7) becomes much simpler. This configuration is shown below in Figure F-2. The characteristic equation for the configuration of Figure F-2 is derived from Equation (F-7) by setting h^- equal to zero. In this case the second and fourth terms disappear and the TM characteristic equation is

$$\frac{k_z^{\mathrm{II}}}{\epsilon_1}\,\tan(k_z^{\mathrm{II}}\,\ell) \;=\; \frac{k_z^{\mathrm{I}}}{\epsilon^{\mathrm{I}}}\,\tan[k_z^{\mathrm{I}}(\ell - L_s)]\,.$$
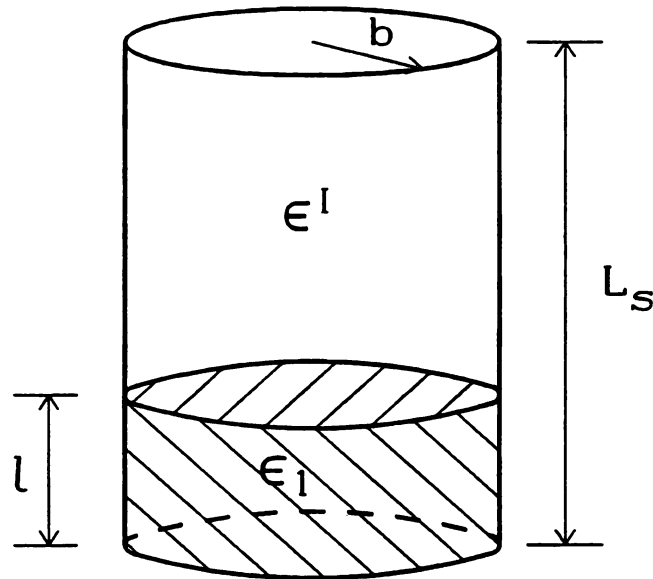
(F-8)

Figure F-2 Slab-loaded cavity with slab at one end.

The TE mode equations may be written in a similar manner to the TM mode equations. Using the same matrix equation, Equation (F-5), the matrix elements for the TE modes are given by

$$X^+ = k_z^I \sin(k_z^{II} h^+) \cos[k_z^I (h^+ - L_s)] - k_z^{II} \cos(k_z^{II} h^+) \sin[k_z^I (h^+ - L_s)],$$

$$Y^+ = k_z^I \cos(k_z^{II} h^+) \cos[k_z^I (h^+ - L_s)] + k_z^{II} \sin(k_z^{II} h^+) \sin[k_z^I (h^+ - L_s)],$$

$$X^- = k_z^{III} \sin(k_z^{II} h^-) \cos(k_z^{III} h^-) - k_z^{II} \cos(k_z^{II} h^-) \sin(k_z^{III} h^-),$$

$$Y^- = k_z^{III} \cos(k_z^{II} h^-) \cos(k_z^{III} h^-) + k_z^{II} \sin(k_z^{II} h^-) \sin(k_z^{III} h^-).$$

(F-9)

The general TE characteristic equation is

$$k_z^I k_z^{III} \tan(k_z^{II} \ell) + k_z^{II2} \tan(k_z^{II} \ell) \tan(k_z^{III} h^-) \tan[k_z^I (h^+ - L_s)]$$

$$- k_z^{II} k_z^{III} \tan[k_z^I (h^+ - L_s)] + k_z^{II} k_z^I \tan(k_z^{III} h^-) = 0.$$

(F-10)

For the configuration of Figure F-2 with $h^- = 0$, Equation (F-10) is simplified to

$$k_z^{II} \cot(k_z^{II} \ell) = k_z^I \cot[k_z^I (\ell - L_s)].$$

(F-11)

Solutions for the cavity-open type configuration when the load radius is near that of the cavity may be compared with solutions from Equations (F-7) and (F-10) which are much easier to solve, require less numerical manipulation, and are therefore more likely to return an accurate result. Similarly, cavity-image type solutions may be compared with solutions from Equations (F-8) and (F-11). These comparisons are especially useful in providing a verification that the more complicated cavity-open and cavity-image type solutions are converging to the expected answers.

LIST OF WORKS CITED

LIST OF WORKS CITED

Abramowitz, Milton, and Irene Stegun. *Handbook of Mathematical Functions.* New York: Dover Publications, n.d.

Adler, R. B. "Waves on Inhomogeneous Cylindrical Structures." *Proceedings of the I.R.E.* (40) (March 1952): 339-48.

Agdur, B., and B. Enander. "Resonances of a Microwave Cavity Partially Filled with a Plasma." *J. App. Phy.* 33 (2) (Feb. 1962): 575-81.

Asmussen, J., H. H. Lin, B. Manring, and R. Fritz. "Single-Mode or Controlled Multimode Microwave Cavity Applicators for Precision Materials Processing." *Rev. Sci. Instrum.* 58 (8) (August 1987): 1477-86.

Asmussen, Jes Jr., Raghuveer Mallavarpu, John R. Hamann, and Hee Chung Park. "The Design of a Microwave Plasma Cavity." *Proc. IEEE* 62 (1) (Jan. 1974): 109-117.

Beam, R. E., and H. M. Wachowski. "Shielded Dielectric Rod Waveguides." *Trans. Amer. Inst. Elec. Eng.* 70 (1951): 874-80.

Beam, R. E., M. M. Astrahan, W. C. Jakes, H. M. Wachowski, and W. L. Firestone. "Dielectric Tube Waveguides." Report ATI 94929, Ch. V, Northwestern University, Evanston, IL (1949).

Bhartia, P., and M. A. K. Hamid. "Field distribution in a Centrally Loaded Circular Cylindrical Cavity." *IEEE Trans. Nuc. Sci.* NS-16 (2) (April 1969): 27-34.

Bolle, D. M. "Eigenvalues for a Centrally Loaded Circular Cylindrical Cavity." *IRE Trans. Microwave Thry. Tech.* MTT-10 (3) (March 1962): 133-38.

Bruck, G. G., and E. R. Wicher. "Slow Transverse Waves in Cylindrical Guides." *J. App. Phys.* 18 (1947): 766-70.

398

Bruno, William M., and William B. Bridges. "Flexible Dielectric Waveguides with Powder Cores." *IEEE Trans. Microwave Thry. Tech.* 36 (5) (May 1988): 882-90.

Bucholz, Von Herbert. "Der Hohlleiter von kreisformigen Querschnitt mit Geschichtetem Dielektrischen Einsatz." *Annalen der Physik* (Leipzig) 43 (1943): 313-68. Quoted in R. E. Beam and H. M. Wachowski. "Shielded Dielectric Rod Waveguides." *Trans. Amer. Inst. Elec. Eng.* 70 (1951): 874-80.

Buchsbaum, S. J., L. Mower, and S. C. Brown. "Interaction Between Cold Plasmas and Guided Electromagnetic Waves." *Phys. Fluids* 3 (5) (Sept.-Oct. 1960): 806-819.

Chen, Chunming, and Kawthar A. Zaki. "Resonant Frequencies of Dielectric Resonators Containing Guided Complex Modes." *IEEE Trans. Microwave Thry. Tech.* 36 (10) (Oct. 1988): 1455-57.

Chou, Ri-Chee, and Shung-Wu Lee. "Modal Attenuation in Multilayered Coated Waveguides." *IEEE Trans. Microwave Thry. Tech.* 36 (7) (July 1988): 1167-76.

Clark, D. E., F. D. Gac, W. H. Sutton, eds. *Microwaves: Theory and Application in Materials Processing: Ceramic Transactions 21, Symposium Held During the 93rd Meeting of the American Ceramic Society at Cincinnati, Ohio 29 April-3 May, 1991.* Westerville, Ohio: The American Ceramic Society, 1991.

Clarricoats, P. J. B. "Circular-Waveguide Backward-Wave Structures." *Proc. Inst. Elec. Eng.* 110 (2) (Feb. 1963): 261-70.

_____. "Propagation Along Unbounded and Bounded Dielectric Rods—pts. 1 and 2." *Proc. Inst. Elec. Eng.,* 108 (3), pt. C (March 1961): 170-86.

Clarricoats, P. J. B., and B. C. Taylor. "Evanescent and Propagating Modes of Dielectric-Loaded Circular Waveguide." *Proc. Inst. Elec. Eng.* 111 (12) (Dec. 1964): 1951-56.

Clarricoats, P. J. B., and K. R. Slinn. "Experimental Observation of Travelling Backward Waves in Dielectric-Loaded Circular Waveguide." *Proc. Inst. Elec. Eng.* 111 (6) (June 1964): 1090-92.

Collin, R. E. *Foundations for Microwave Engineering*. New York: McGraw-Hill, 1966.

de Koo, N. P., and Anton G. Tijhuis. *ROOT*. Laboratory of Electromagnetic Research, Department of Electrical Engineering, Delft University of Technology, P.O. Box 5031, 2600 GA Delft, The Netherlands.

Frankel, S. "TM_{01} Mode in Circular Wave Guides with Two Coaxial Dielectrics." *J. App. Phys.* 18 (1947): 650-55.

Frasch, Lydell L. "An Experimental and Theoretical Study of a Microwave Cavity ·Applicator Loaded with Lossy Materials." Ph.D. diss., Michigan State University, 1987.

Fredericks, Robert Michael. "An Experimental and Theoretical Study of Resonantly Sustained Plasma in Microwave Cavities." Ph.D. diss., Michigan State University, 1971.

Gradshteyn, I. S., and I. M. Ryzhik. *Table of Integrals, Series, and Products*. San Diego: Academic Press, 1980.

Hahn, W. C. "A New Method for the Calculation of Cavity Resonators." *J. App. Phy.* 12 (January 1941): 62-68.

Hansen, W. W. "On the Resonant Frequency of Closed Concentric Lines." *J. App. Phy.* 10 (Jan. 1939): 38-45.

Harrington, Roger F. *Time-Harmonic Electromagnetic Fields*. New York: McGraw-Hill, 1961.

Jackson, J. D. *Classical Electrodynamics*. New York: John Wiley & Sons, 1975.

Kajfez, Darko. "Indefinite Integrals Useful in the Analysis of Cylindrical Dielectric Resonators." *IEEE Trans. Microwave Thry. Tech.*, MTT-35 (9) (Sep. 1987): 873-74.

King, L. V. *Phil. Mag.* 21 (1936). Quoted in W. C. Hahn. "A New Method for the Calculation of Cavity Resonators." *J. App. Phy.* 12 (January 1941): 62-68.

Kobayashi, Yoshio, and Shuzo Tanaka. "Resonant Mods of a Dielectric Rod
Resonator Short-Circuited at Both Ends by Parallel Conducting Plates." *IEEE
Trans. Microwave Thry. Tech.* MTT-28 (10) (Oct. 1980): 1077-85.

Kobayashi, Yoshio, Nobushige Fukuoka, and Sink-ichiro Yoshida. "Resonant Modes
for a Shielded Dielectric Rod Resonator." *Elect. Comm. Jap.* 64-B (11).
Trans. Scripta Publishing Co., 1983: 44-51. Translated from *Denshi Tsushin
Gakkai Ronbunshi* 64-B (5) (1981): 433-40.

Lin, Haw-Hwa. "Theoretical Formulation and Experimental Investigation of a
Cylindrical Cavity Loaded with Lossy Dielectric Materials." Ph.D. diss.,
·Michigan State University, 1989.

Mallavarpu, R. J. Asmussen, and M. C. Hawley. "Behavior of a Microwave Cavity
Discharge Over a Wide Range of Pressures and Flow Rates." *IEEE Trans.
Plasma Sci.* PS-6 (4) (Dec. 1978): 341-54.

Mallavarpu, Raghuveer. "An Investigation of the Electromagnetic Behavior of a
Microwave Plasma Source Over a Wide Range of Pressures and Flow Rates."
Ph.D. diss., Michigan State University, 1976.

Manring, Edward B. "An Experimental Investigation of the Microwave Heating of
Solid Non-Reactive Materials in a Circular Cylindrical Resonant Cavity."
M.S. thesis, Michigan State University, 1988.

Mathematica, Ver. 2.0. Wolfram Research, Inc., Champaign, Ill., 1991.

Maystre, D., P. Vincent, and J. C. Mage. "Theoretical and Experimental Study of
the Resonant Frequency of a Cylindrical Dielectric Resonator." *IEEE Trans.
Microwave Thry. Tech.* MTT-31 (10) (Oct. 1983): 844-48.

Montgomery, C. G. *Technique of Microwave Measurements.* New York: McGraw-
Hill, 1947.

Nilsson, James W. *Electric Circuits.* Reading, Mass.: Addison-Wesley, 1983.

Offermanns, Stephan. "Electrodeless High-Pressure Microwave Discharges." *J. App.
Phy.* 67 (1) (January 1990): 115-23.

Offermanns, Stephan. "Resonance Characteristics of a Cavity-Operated Electrodeless High-Pressure Microwave Discharge System." *IEEE Trans. Microwave Thry. Tech.* 38 (7) (July 1990): 904-11.

Omar, Abbas S., and Klaus F. Schünemann. "Complex and Backward Wave Modes in Inhomogeneously and Anisotropically Filled Waveguides." *IEEE Trans. Microwave Thry. Tech.* MTT-35 (3) (March 1987): 268-75.

Passow, M. L., M. L. Brake, P. Lopez, W. B. McColl, and T. E. Repetti. "Microwave Resonant-Cavity-Produced Air Discharges." *IEEE Trans. Plasma Sci.* PS-19 (2) (April 1991): 219-28.

Pincherle, L. "Electromagnetic Waves in Metal Tubes Filled Longitudinally with Two Dielectrics." *Phys. Rev.* 2:66 (5, 6) (September 1 and 15, 1944): 118-30.

Press, William H., Brian P. Flannery, Saul A. Teukolsky, and William T. Vetterling. *Numerical Recipes: The Art of Scientific Computing.* Cambridge: Cambridge University Press, 1986.

Reitz, John R., Frederick J. Milford, and Robert W. Christy. *Foundations of Electromagnetic Theory,* 3d ed. Reading, Mass.: Addison-Wesley, 1979.

Rogers, James R. "Properties of Steady State, High Pressure, Argon Microwave Discharges." Ph.D. diss., Michigan State University, 1982.

Shohet, J. L., and C. Moskowitz. "Eigenvalues of a Microwave-Cavity-Lossy-Plasma System." *J. App. Phy.* 36 (5) (May 1965): 1756-59.

Snitzer, E. "Cylindrical Dielectric Waveguide Modes." *J. Opt. Soc. Am.* 51 (5) (May 1961): 491-98.

Snyder, Wm. B., et al., eds. *Microwave Processing of Materials II: Materials Research Society Symposia Proceedings 189, Symposium Held at San Francisco, California 17-20 April 1990.* Pittsburgh: Materials Research Society, 1991.

Sphicopoulos, T., L. G. Bernier, and F. Gardiol. "Theoretical Basis for the Design of the Radially Stratified Dielectric-Loaded Cavities Used in Miniaturised Atomic Frequency Standards." *Proc. Inst. Elec. Eng.* 131 (2), pt. H (April 1984): 94-98.

Sutton, W. H., M. H. Brooks, and I. J. Chabinsky, eds. *Microwave Processing of Materials: Materials Research Society Symposia Proceedings 124, Symposium Held at Reno, Nevada 5-8 April 1988.* (Pittsburgh: Materials Research Society, 1988).

Teasdale, R. D., and T. J. Higgins. "Electromagnetic Waves in Circular Waveguides Containing Two Coaxial Media." *Proc. Nat. Elec. Conf.* 5 (1949): 427-41.

Traub, J. F. *Iterative Methods for the Solution of Equations.* Englewood Cliffs, NJ: Prentice-Hall, 1964.

Trivelpiece, A. W. "Slow Wave Propagation in Plasma Waveguides." Ph.D. diss., California Institute of Technology, 1958.

Trivelpiece, A. W., and R. W. Gould. "Space Charge Waves in Cylindrical Plasma Columns." *J. App. Phy.* 30 (11) (Nov. 1959): 1784-93.

Vigneron, S., and P. Guillon. "Mode-Matching Method for Determination of the Resonant Frequencies of a Dielectric Resonator Placed in a Metallic Box." *Proc. Inst. Elec. Eng.* 134, pt. H (2) (April 1987): 151-55.

Zaki, Kawthar A., and Ali E. Atia. "Modes in Dielectric-Loaded Waveguides and Resonators." *IEEE Trans. Microwave Thry. Tech.* MTT-31 (12) (Dec. 1983): 1039-45.

Zaki, Kawthar A., and Chunming Chen. "Intensity and Distribution of Hybrid-Mode Fields in Dielectric-Loaded Waveguides." *IEEE Trans. Microwave Thry. Tech.* MTT-33(12) (Dec. 1985): 1442-47.

_____. "Loss Mechanisms in Dielectric-Loaded Resonators." *IEEE Trans. Microwave Thry. Tech.* MTT-33 (12) (December 1985): 1448-52.

_____. "New Results in Dielectric-Loaded Resonators." *IEEE Trans. Microwave Thry. Tech.* MTT-34 (7) (July 1986): 815-24.